

Optical Biosensors for Improved Neurochemical Sensing Using Single-Walled Carbon Nanotubes

Présentée le 25 septembre 2020

à la Faculté des sciences de base
Laboratoire de nanobiotechnologie
Programme doctoral en chimie et génie chimique

pour l'obtention du grade de Docteur ès Sciences

par

Alice Judith GILLEN

Acceptée sur proposition du jury

Prof. V. Hatzimanikatis, président du jury
Prof. A. A. Boghossian, directrice de thèse
Dr A. Beyene, rapporteur
Dr C. Backes, rapporteuse
Prof. P. Ramdya, rapporteur

*It's no use going back to yesterday,
because I was a different person then.*

Lewis Carroll,
Alice's Adventures in Wonderland

For Daniel and my family
- I love you

Acknowledgements

I used to think that I was a person that could do most things in life without other people, however, throughout this thesis experience I have learnt that I could not have been more wrong. This is a document culminating an incredible experience in my life and one that I am sure would not have been possible without the help of so many people. I will do my best to express my gratitude to you all, but honestly I do not think words can do it justice.

Firstly, I would like to thank my advisor, Prof. **Ardemis A. Boghossian**. Thank you for giving me the opportunity to join LNB and allowing me the chance to pursue independent research from the get-go. Ardemis has supported me throughout my PhD and given me ample opportunities to embed myself into the wider nanotube community. Thank you for your support and encouragement to do great things.

I would also like to extend my sincere thanks to my committee members, Dr. **Claudia Backes**, Prof. **Pavan Ramdya**, and Dr. **Abraham Beyene** for their insightful discussion during the exam and their kind words after. I must also thank my jury president, Prof. **Vassily Hatzimanikatis**, not only for his support during the exam but also for his support over the last four years. You always made time to have a chat with me over a cup of tea and as a mentor have offered me invaluable advice - thank you for this unending hospitality.

To my colleagues at LNB, both past and present, thank you. You have all provided me with continuous entertainment, good memories, and lots of laughs throughout the last four years. Most of all though thank you for putting up with me! To **Nils Schuergers**, thank you for helping me to find my feet and trust my intuition at the beginning - and for the many beers that were shared. **Melania Reggente**, thank you for your support and encouragement, but also for encouraging me to do fun things as well as science. To **Mary Wood**, thank you for taking the time to help me with all the edits for my thesis and for bringing such a bright energy to the office. **Vitalijs Zubkovs**, thank you first for teaching me about fluorescence spectroscopy and microscopy, and second for always being up for a drink. **Benjamin Lambert**, **Shang-Jung Wu** and **Mo Mouhib**, thank you for all the laughs, many coffee breaks, and the endless entertainment your bets brought me. Shang-Jung you have a rigor in science I can not help but admire. Mo you have such an infectious optimism and contagious positivity, I hope that you always stay like this. Benjamin, together since day 1 at LNB; thank you for being one of

Acknowledgements

the kindest people I have ever met - I know you are someone who I can count on for whatever I may need and please know that you can count on me too (bubblegum). I also want to thank all the semester projects and masters students I had the opportunity to work with: **Carlo Gigli, Edward Honein, Josephine Pratiwi, Xingbo Shang, Claire Bourmaud, Marie Demonceaux, and Marine Degors**. Thank you for trusting me and providing me with an opportunity to discover how much there is to learn from teaching. To the rest of LNB, **Amirmostafa Amirjani, Liu Xuewen, Charlotte Roullier, and Niloufar Sharif** thank you for the fond memories. I must also extend my thanks to **Daniel Morales**, my brain guy. Thank you for introducing me to the world of *Drosophila* and helping me learn and understand the many intricacies of biology.

To my work wives, **Rebekah Wells** and **Alessandra Antonucci**. You have both been there for me whenever I needed you, no matter the time or scale of the demand. Ale, you have been my best friend in LNB since the beginning and I know we will have a friendship that will last for years to come. Your unending optimism and ability to look on the bright side of everything and everyone will never fail to amaze me. Rebekah, I cannot express my gratitude to you, especially over the last 12 months. You managed to ensure I didn't go completely crazy (or starve) and encouraged me to enjoy my last year here in Switzerland. You are an incredibly generous person and I am eternally indebted to you.

I would also like to thank my other friends here in Switzerland for making my time so much more enjoyable: **Oskari Pakari, Valentyn Bykov, Vincent Lamirand, Stefania Bertella, Lorenz Manker, Radmila Faizova, Alex Holloway, Arnaud Gelb, Austin Zadoks, Meike Ramon, Harshal Sonar, Marc Checkley, and Lee Sze Chuin**. Of course I also have to say *go raibh míle* to my friends back home in Ireland for continuing to put up with me after all these years, especially **Adam Hagan, Colm O'Donoghue**, and the Moyville crew (special mention to **Gary** and **Claire**).

Thanks must also be given to Cadbury chocolate and Lyons tea for helping me get through the writing of this thesis.

Finally to my family (#tni), I am who I am today because of your unending love and support. I am incredibly lucky to have grown up in such a supportive environment with parents who both accepted me and pushed me to the best I could be. **Mom** and **Dad** I love you so much. Thank you for always being there for me both to celebrate and also when I had a problem or needed to be calmed down. **Ruth**, my best friend from the beginning, thank you for being you (despite how annoying this can sometimes be) and being a person I know will always be there for me. I know you always support me in whatever I do and I hope that I make you proud because I am so proud of you. A list of thank yous would not be near completion without mentioning my **Deedee** who has cheered me on and never once doubted my ability to achieve my dreams throughout my entire life. Finally, to my husband **Daniel**, I have never been more happy in my entire life than with you and Rollo. You have always supported me, both in my

Acknowledgements

achievements and when I was having problems, and I can always count on your being there for me whether you are 100 m or 9323 km away. You are my best friend and I am so excited to finally get back in the same country so that we can continue to have all of life's adventures together and get back to our spontaneous coffee breaks. I love you more than I can ever manage to express, in words or otherwise.

Lausanne, September 7, 2020

A. J. G.

Abstract

Irregularities in neuromodulation can create a variety of diseases. As a result, accurate measurement of neurotransmitter concentrations is imperative to improve clinical diagnostics. Biosensing technologies help by permitting real-time monitoring of these molecules. However, despite intense global focus on optimizing biosensing technologies, their ultimate potential remains limited by inadequate sensitivity and selectivity. The extra requirement for high spatiotemporal resolution in neurochemical sensing imposes barriers that are not yet surmountable with existing biosensor technologies. This has hindered our studies of the complex nature of neurotransmitters and neuromodulators and prevented us from improving our understanding of their role in regulating biological functions.

To address these challenges, we present new optical biosensors for serotonin and dopamine using single-walled carbon nanotubes (SWCNTs). The unique physiochemical and optoelectronic properties of SWCNTs can be readily tuned, creating a versatile material for imaging and sensing applications. Their intrinsic near-infrared fluorescence overlaps with the optical transparency window for biological tissue, which coupled with their indefinite photostability, increases their suitability for *in vitro* and *in vivo* applications.

In this thesis, we systematically explore the use of surfactants, DNA, and xeno nucleic acids (XNAs) to improve the brightness and selectivity of SWCNT sensors. We highlight the trade-offs typically encountered for these approaches and propose new semi-rational methods to overcome these limitations.

We begin by examining the impact of exposed surface area on the optical response of SWCNTs. We subsequently use this understanding to achieve previously unreported molecular selectivity through controlled, adsorption-based tuning of the nanotube surface of sub-critical colloidal suspensions of sodium cholate (SC)-SWCNTs. Owing to the increased biocompatibility of DNA, we expand our study to DNA-SWCNTs and demonstrate the impact of the dispersion method on both sensor brightness and responsivity using chemically modified DNA. This thesis culminates in several major findings for improving DNA-SWCNTs in ionically complex environments using XNAs. We introduce locked nucleic acid (LNA) to control the unwanted cation-induced fluorescence changes typically encountered by DNA-SWCNTs and show that this improvement does not come at the expense of their sensing capabilities. Our results suggest that the LNA-SWCNTs may uniquely enable simultaneous monitoring of dopamine

Abstract

and calcium, providing an improved sensor for studying the process of neuromodulation.

In the final chapter of this thesis we demonstrate that the LNA-SWCNTs retain their sensing capabilities following extended periods of time in the presence of salts, proteins, antibiotics, and even whole cells. Furthermore, we expand upon the possibilities achievable using XNA-SWCNTs and present a new peptide nucleic acid (PNA) sensor for the rapid detection of an additional biomarker, microRNA. The synthetic biology approaches presented in this work serve as a complementary means for enhancing nanotube optoelectronic behaviour, unlocking previously unexplored possibilities for developing nano-bioengineered sensors with augmented capabilities.

Keywords: single-walled carbon nanotubes (SWCNT), near-infrared fluorescence, xeno nucleic acids (XNAs), locked nucleic acid (LNA), peptide nucleic acid (PNA), optical biosensors, neurotransmitters, dopamine

Résumé

De nombreuses affections, telles que la maladie de Parkinson ou la maladie d'Alzheimer, peuvent résulter d'irrégularités dans la neuromodulation. Par conséquent, il est impératif de pouvoir mesurer précisément la concentration des neurotransmetteurs concernés afin d'améliorer les diagnostics et le traitement des patients. Les biosenseurs peuvent aider à cela en permettant le suivi, en temps réel, des concentrations de biomarqueurs liés à certaines maladies. Cependant, malgré les efforts intenses déployés afin de développer et optimiser ces types de senseurs, ils restent limités par leur sensibilité, spécificité et extensibilité. En outre, les limites en termes de résolution spatiotemporelle lors de mesures neurochimiques restent, pour l'instant, insurmontables par les biosenseurs actuels. Ces difficultés ont entravé l'étude de ces molécules aux caractéristiques complexes et a, par conséquent, empêché la compréhension du rôle de ces molécules dans la régulation des fonctions biologiques.

Afin de faire face à ces complexités, nous décrivons dans cette thèse la création de nouveaux biosenseurs pour la détection de sérotonine et de dopamine se basant sur l'émission, dans le proche infrarouge, des nanotubes de carbone monoparoi (SWCNTs). Les propriétés physico-chimiques et opto-électroniques uniques des SWCNTs peuvent être aisément modifiées afin d'obtenir des transducteurs pour l'imagerie ou la détection. La fluorescence intrinsèque des SWCNTs dans le proche infrarouge chevauche la fenêtre optique d'absorption minimale des tissus biologiques, permettant ainsi une propagation plus grande de la lumière. Cela, associé à une photostabilité quasi-illimitée, octroie aux SWCNTs la possibilité de créer des senseurs *in vitro* et *in vivo*. Comme il est montré dans cette thèse, la fonctionnalisation de la surface du nanotube peut permettre de contrôler la stabilisation de la dispersion, l'intensité de sa fluorescence, sa biocompatibilité et la spécificité du senseur créé. Nous présentons de nouvelles approches utilisées pour la création de senseurs avec l'utilisation de tensioactifs, ADN et acides xénonucléiques (XNAs). Nous mettons l'accent sur les avantages et désavantages de chacune de ces fonctionnalisations et proposons de nouvelles façons d'approcher ces problèmes.

Dans cette étude, nous introduisons le tout premier senseur SWCNT-tensioactif avec spécificité, créé à partir de SWCNTs dispersés dans du cholate de sodium (SC). En contrôlant l'adsorption des molécules de SC sur la surface du nanotube, nous montrons qu'il est possible d'obtenir des spécificités moléculaires supérieures à celles précédemment démontrées par les

capteurs ADN-SWCNT. De plus, cette sp  cificit   est obtenue sans compromettre l'intensit   de la fluorescence des capteurs.

Toutefois, les capteurs ADN-SWCNTs ont l'avantage d'avoir une biocompatibilit   plus   lev  e. Nous avons alors explor   les strat  gies permettant d'am  liorer les performances de ces capteurs sans pour autant sacrifier leurs avantages. Nous pr  sentons des r  sultats d  montrant l'importance de la m  thode de pr  paration de ces capteurs et montrant   galement comment des modifications chimiques sur l'ADN peuvent am  liorer la fluorescence du capteur. Ces travaux aboutissent par la d  couverte de plusieurs facteurs pouvant am  liorer les performances des capteurs ADN-SWCNT dans des milieux ioniques complexes    l'aide des XNAs. Nous utilisons l'acide nucl  ique bloqu   (LNA) afin de contr  ler les changements de fluorescence observ  s pour les complexes ADN-SWCNT en pr  sence de cations et montrons que cela n'a pas d'effet sur les capacit  s de d  tection du capteur. En effet, bien que les LNA-SWCNTs soient plus r  sistants face    de possibles changements dans les concentrations ioniques du milieu, ils gardent malgr   tout leur r  ponse caract  ristique en pr  sence de dopamine. Nos r  sultats montrent que les LNA-SWCNTs sont capables de d  tecter, en m  me temps, les concentrations de dopamine et de calcium, mesures d'une importance capitale afin d'  tudier la neuromodulation. Par ailleurs, dans le dernier chapitre de la th  se, nous montrons que ces capteurs sont capables de maintenir leur capacit   de d  tection pendant de longues p  riodes et dans des milieux complexes contenant des sels, prot  ines, antibiotiques et cellules.

Enfin, nous d  veloppons notre discussion sur les possibilit  s des acides nucl  iques modifi  s et pr  sentons un nouveau capteur cr      partir d'acide nucl  ique peptidique (ANP) pour la d  tection rapide de micro-ARN. Cette approche, inspir  e par la biologie de synth  se, montre une fois de plus qu'il est possible d'am  liorer les propri  t  s de ces capteurs au-del   des limites pr  c  demment   tablies.

Mots-cl  s : single-walled carbon nanotubes (SWCNT), near-infrared fluorescence, xeno nucleic acids (XNAs), locked nucleic acid (LNA), peptide nucleic acid (PNA), optical biosensors, neurotransmitters, dopamine

Contents

Acknowledgements	v
Abstract	ix
Résumé	xi
Abbreviations	xix
List of Figures	xxii
List of Tables	xxxiv
Introduction	1
Background and Context	1
Properties of Single-Walled Carbon Nanotubes (SWCNTs)	2
Neurochemical Sensing	7
SWCNT Optical Biosensors for Neurochemical Sensing	9
Objectives of the Thesis	12
1 Non-covalent Methods of Engineering Optical Sensors Based on Single-Walled Carbon Nanotubes	15
1.1 Abstract	15
1.2 Introduction	16
1.3 Surfactant-Coated SWCNTs	18

xiii

Contents

1.4	Biopolymer-Suspended SWCNTs	22
1.5	Polymer Engineering of SWCNT Sensor Specificity	26
1.6	Conclusions	27
2	The Impact of Surface Area on the Response of SWCNT Optical Sensors	29
2.1	Abstract	29
2.2	Introduction	30
2.3	Results and Discussion	31
2.4	Conclusions	38
2.5	Materials and Methods	38
2.5.1	Preparation of SWCNT solutions	38
2.5.2	Fluorescence spectroscopy measurements	39
2.5.3	Spectral fitting	39
2.5.4	Rinsing procedure for sensor regeneration	40
3	Modifying DNA-SWCNT Sensors for Improved Dopamine Detection	43
3.1	Abstract	43
3.2	Introduction	44
3.3	Results and Discussion	45
3.4	Conclusions	53
3.5	Materials and Methods	54
3.5.1	Materials	54
3.5.2	Preparation of the DNA-SWCNT suspensions	55
	(1) Direct sonication	55
	(2) MeOH-assisted surfactant exchange	55
	Amicon rinsing for DNA-SWCNT purification	56
3.5.3	Absorption spectroscopy	56

3.5.4	Fluorescence spectroscopy measurements	57
	Photoluminescence measurements	57
	Dopamine detection assay	57
	Surfactant replacement assay	58
	pH and DTT assay	58
	Confocal Raman microscopy	58
	Gel electrophoresis	58
4	XNA-Nanosensors for Enhanced Stability Against Ion-Induced Fluorescence Perturbations	61
4.1	Abstract	61
4.2	Introduction	62
4.3	Results and Discussion	63
4.4	Conclusions	70
4.5	Materials and Methods	71
4.5.1	DNA-suspension of SWCNTs	71
4.5.2	Gel sensor construction	72
4.5.3	Fluorescence spectroscopy measurements	73
5	XNA-Nanosensors for Improved Neurochemical Sensing	75
5.1	Abstract	75
5.2	Introduction	75
5.3	Results and Discussion	77
5.4	Conclusions	89
5.5	Materials and Methods	90
5.5.1	Materials	90
5.5.2	Preparation of SWCNT solutions	90

Contents

5.5.3	Fluorescence spectroscopy measurements	90
5.5.4	Surfactant replacement	91
5.5.5	AFM imaging and sample preparation	91
5.5.6	ζ -potential measurements	91
5.5.7	Circular dichroism measurements	92
6	Outlook on Potential Applications of XNA-SWCNTs for Improved Optical Biosensing	93
6.1	Abstract	93
6.2	Using XNA-SWCNTs for <i>In Vitro</i> Sensing Applications	94
6.2.1	Results and Discussion	95
6.3	XNA-SWCNTs for miRNA Detection	101
6.3.1	Results and Discussion	103
6.4	Conclusions	110
6.5	Materials and Methods	111
6.5.1	Using XNA-SWCNTs for <i>In Vitro</i> Sensing Applications	111
	<i>Drosophila</i> growth and neuron extraction	111
	NIR widefield imaging	112
	Fluorescence spectroscopy measurements	113
6.5.2	XNA-SWCNTs for miRNA Detection	114
	Preparation of DNA-SWCNT solutions	114
	Preparation of PNA and miRNA solutions	115
	Absorbance spectroscopy	116
	Fluorescence spectroscopy measurements	116
	General Conclusion	117
A	The Impact of Surface Area on the Response of SWCNT Optical Sensors	121

B	Modifying DNA-SWCNT Sensors for Improved Dopamine Detection	131
	DNA-dimer formation of thiol-modified DNA	131
	Azide-modified (GT) ₁₅	133
C	Xeno Nucleic Acid Nanosensors for Enhanced Stability Against Ion-Induced Perturbations	167
D	XNA-Nanosensors for Improved Neurochemical Sensing	181
E	Outlook on Potential Applications of XNA-SWCNTs for Improved Optical Biosensing	205
	E.1 Using XNA-SWCNTs for <i>In Vitro</i> Sensing Applications	205
	E.2 XNA-SWCNTs for miRNA Detection	223
	Bibliography	246
	Curriculum Vitae	271

Abbreviations

A	Adenine
Ace	Acetylcholine
AFM	Atomic Force Microscopy
ATP	Aqueous Two-Phase
bp	base pair
C	Cytosine
CD	Circular Dichroism
CMC	Critical Micelle Concentration
CoPhMoRe	Corona Phase Molecular Recognition
CoMoCAT	Cobalt Molybdenum CATalyzed process
Cys	Cysteine
DA	Dopamine neurons
DA-CsChrimson	Transgenic dopamine neurons induced to express CsChrimson and Venus
DA-GFP	Transgenic dopamine neurons induced to express GFP
DI	DeIonised Water
DNA	DeoxyriboNucleic Acid
Dop	Dopamine
DOS	Density Of States
dsDNA	double-stranded DeoxyriboNucleic Acid
DPPE	DiPalmitoyl-pPhosphatidylEthanolamine
DTT	DiThioThreitol
DX	DeXtran
EDTA	EthyleneDiamineTetraAcetic acid
ELISA	Enzyme-Linked ImmunoSorbent Assays
eV	electron Volt
ex.	excitation
FBS	Fetal Bovine Serum
FFN	False Fluorescent Neurotransmitters
FMN	Flavin MonoNucleotides
FRET	Förster Resonance Energy Transfer
Fruc	Fructose
FSCV	Fast-Scan Cyclic Voltametry

Abbreviations

FWHM	Full-Width at Half-Maximum
G	Guanine
GABA	γ -aminobutyric acid
Gal	Galactose
GFP	Green Fluorescent Protein
Gluc	Glucose
Gluta	Glutamate
Gly	Glycine
GOx	Glucose Oxidase
HEPES	(4-(2-hydroxyethyl)-1-piperazineethanesulfonic acid)
HiPco	High-Pressure carbon monoxide process
His	Histidine
InGaAs	Indium Gallium Arsenide
LDS	Lithium Dodecyl Sulfate
LNA	Locked Nucleic Acid
LP	Long-Pass
Mal	Maltose
Man	Mannose
Met	Methionine
MeOH	Methanol
miREIA	miRNA Enzyme ImmunoAssay
miRNA	micro-RiboNucleic Acid
mRNA	messenger RiboNucleic Acid
MWCO	Molecular Weight Cut-Off
MCMC	Markov Chain Monte Carlo
NIR or near-IR	Near-InfraRed
NO	Nitric Oxide
PAGE	Polyacrylamide gel electrophoresis
PAM	PolyAcrylaMide
PBS	sodium Phosphate-Buffered Saline
PCI	Phenol-Chloroform Isoamyl
PCR	Polymerase Chain Reaction
PEG	Poly(Ethylene Glycol)
Pen/Strep	Penicillin Streptomycin
Phen	Phenylalanine
PL	PhotoLuminescence
PNA	Peptide Nucleic Acid
PVP	Poly(VinylPyrrolidone)
QY	Quantum Yield
RNA	RiboNucleic Acid
RT	Room Temperature
RT-PCR	Reverse-Transcription Polymerase Chain Reaction

SC	Sodium Cholate
SDOC	Sodium DeOxyCholate
SDS	Sodium Dodecyl Sulfate
SDBS	Sodium DodecylBenzene Sulfate
Sero	Serotonin
SNP	Single Nucleotide Polymorphisms
STEM	Scanning Transmission Electron Microscope
ssDNA	single-stranded DeoxyriboNucleic Acid
SSM	Supplemented Schneider's Medium
Suc	Sucrose
SWCNT	Single-Walled Carbon Nanotube
T	Thymine
TBE buffer	Tris/Borate/EDTA buffer
TIRF	Total Internal Reflection Fluorescence
Try	Tryptophan
Tyr	Tyrosine
UV	UltraViolet
Vis	Visible
XNA	Xeno Nucleic Acid
Xyl	Xylose
ZP	ζ-Potential / Zeta-Potential

List of Figures

1	Illustration of chiral vector and nanotube chiralities projected onto a graphene lattice.	3
2	Optical properties of SWCNTs.	4
3	Optical response of SWCNTs.	6
4	Neurons and neural communication.	8
5	Role of Ca^{2+} in neurotransmitter release.	11
1.1	Noncovalent functionalisation of SWCNTs.	16
1.2	Illustration of the trade-offs between specificity and quantum yield for different wrappings.	17
1.3	Chemical structures of example dispersants used to suspend SWCNTs.	18
1.4	Conformations of non-selective wrappings on the surface of SWCNTs.	20
1.5	Non-specific interactions of polymer wrappings on the surface of SWCNTs.	24
2.1	Schematic of analyte interactions with surfactant-coated nanotubes at high and low surface coverage.	30
2.2	Fluorescence response of $(\text{GT})_{15}$ -SWCNTs to dopamine and serotonin at different NaCl concentrations.	32
2.3	Change in the fluorescence response of SC-SWCNTs to dopamine and serotonin at different SC concentrations.	34
2.4	Fluorescence wavelength and intensity responses of SC-suspended and DNA-wrapped SWCNTs to various bioanalytes.	36
3.1	Structure of the DNA modifications.	46

List of Figures

3.2	Differences in the suspension quality and chirality distribution of modified and unmodified (GT) ₁₅ sequences prepared via direct sonication and MeOH-assisted surfactant exchange.	47
3.3	Fluorescence characterisation of SWCNTs suspended with modified and unmodified (GT) ₁₅ using direct sonication and MeOH-assisted surfactant exchange.	49
3.4	Dopamine response of modified and unmodified (GT) ₁₅ -SWCNTs prepared using direct sonication or MeOH-assisted surfactant exchange.	52
3.5	Schematic of MeOH-assisted surfactant exchange protocol for SWCNT suspension preparation.	56
4.1	Effect of monovalent and divalent cations on DNA-SWCNTs.	64
4.2	Concentration-dependent shift in the wavelength position of the (7,5) peak for DNA-SWCNTs upon the addition of various M ²⁺ ions.	66
4.3	Salt induced conformational changes of DNA on the surface of SWCNTs.	68
4.4	Comparison of the fluorescence response of LNA- and DNA-SWCNTs.	69
4.5	Comparison of the proposed conformational changes of DNA and LNA on a SWCNT in the presence of M ²⁺	71
4.6	Schematic of the gel preparation process in a 96-well plate set-up.	72
5.1	Schematic of LNA(GT) ₁₅ sequences.	77
5.2	Suspension quality and chirality specificity of LNA sequences.	78
5.3	AFM characterization of DNA and LNA sequences.	81
5.4	Wrapping behavior of DNA and LNA sequences.	82
5.5	Response of DNA- and LNA- sensors to CaCl ₂	84
5.6	Concentration-dependent intensity response of DNA- and LNA-SWCNTs to dopamine in the absence of CaCl ₂	86
5.7	Deconvoluting the response of LNA sensors to dopamine and CaCl ₂	87
6.1	Comparison of DNA- and LNA-SWCNT sensors for dopamine sensing in complex media.	96

6.2	Effect of media composition on the fluorescence response of SWCNT films to dopamine addition.	97
6.3	Comparison of the NIR spectral response of LNA _{every5} -SWCNTs to dopamine in complex solutions.	99
6.4	Nanotube films for <i>in vitro</i> cell imaging.	100
6.5	Structures of DNA, LNA, and PNA.	102
6.6	Detection of miRNA using PNA-DNA-SWCNT hybrids.	104
6.7	Schematic of the PNA-DNA-SWCNT configurations differing in length of the hybrid portion and directionality of the hybridization.	107
6.8	Dependency of the wavelength shifting response of PNA-DNA-SWCNTs on the length of the hybrid portion.	108
6.9	Fluorescence wavelength shift response of PNA-DNA _{15bp} -SWCNTs to complementary and non-complementary miRNA.	109
A.1	Chemical structures for the library of analytes (neurotransmitters, amino acids, sugars) tested using SC-SWCNT sensors.	121
A.2	Normalized absorbance spectra for the (6,5) chirality E ₁₁ peak for SC-SWCNT solutions diluted to varying concentrations of SC.	123
A.3	Concentration-normalized fluorescence spectra of the (6,5) chirality peak for SC-SWCNT solutions diluted to varying concentrations of SC.	123
A.4	Fluorescence intensity change of the (6,5) chirality following the addition of serotonin for SC-SWCNT solutions diluted to varying concentrations of SC. . .	124
A.5	Concentration calibration curves for the intensity change the (6,5) chirality peak of 0.5 mM and 1.5 mM SC-SWCNT solutions following the addition of serotonin.	125
A.6	Concentration calibration curves for the wavelength shift of the (6,5) chirality peak of 0.5 mM and 1.5 mM SC-SWCNT solutions following the addition of serotonin.	125
A.7	Concentration calibration curves for the intensity change the (6,5) chirality peak of 0.5 mM and 1.5 mM SC-SWCNT solutions following the addition of dopamine.	126
A.8	Concentration calibration curves for the wavelength shift of the (6,5) chirality peak of 0.5 mM and 1.5 mM SC-SWCNT solutions following the addition of dopamine.	126

List of Figures

A.9	Normalized fluorescence emission spectra 1.5 mM, 5 mM, and 10 mM-SWCNTs before and after the addition of dopamine and serotonin.	127
A.10	Reversibility of the wavelength shift for 1.5 mM SC-SWCNT sensors following serotonin addition.	128
A.11	Spectral reversibility of 1.5 mM SC-SWCNT sensors following serotonin addition.	128
B.1	Denaturing 15% polyacrylamide gels of DNA extracted from sonicated and MeOH assisted surfactant exchanged DNA-SWCNT samples.	131
B.2	Chemical structure of amino-dT base used for internal modification of DNA sequences with an amino functional group.	132
B.3	Maps of electron distribution for guanine (G) modelled as electrostatic potential on electronic density.	132
B.4	Comparison of normalized absorbance spectra for the (6,5) chirality E ₁₁ peak of unmodified and modified (GT) ₁₅ -SWCNTs prepared via direct sonication and MeOH assisted surfactant exchange.	132
B.5	Absorbance spectra for Azide5'- and Azide3'-(GT) ₁₅ -SWCNTs prepared using MeOH assisted surfactant exchange.	133
B.6	Comparison of the suspension quality and chirality distribution of modified and unmodified (AT) ₁₅ - and (N) ₃₀ -SWCNTs prepared using MeOH assisted surfactant exchange.	134
B.7	Fluorescence spectra for Am5'3'Int-(GT) ₁₅ - and Azide5'-(GT) ₁₅ -SWCNTs samples prepared by direct sonication and MeOH assisted surfactant exchange. . .	135
B.8	Comparison of the fluorescence emission under 575 nm excitation for modified and unmodified (GT) ₁₅ -SWCNTs prepared by direct sonication and MeOH assisted surfactant exchange.	136
B.9	Absolute peak intensities of the (7,5) chirality (excitation: 660 nm) for SWCNTs suspended with modified- and unmodified-(GT) ₁₅ by direct sonication and MeOH assisted surfactant exchange.	137
B.10	PLE maps for modified and unmodified (GT) ₁₅ -SWCNT solutions prepared via direct sonication.	138
B.11	PLE maps for modified and unmodified (GT) ₁₅ -SWCNT solutions prepared using MeOH assisted surfactant exchange.	139

B.12 Raman characterisation of modified and unmodified DNA-SWCNTs prepared by direct sonication and MeOH assisted surfactant exchange.	140
B.13 Quantification of DNA adsorbed on the surface of the nanotube.	141
B.14 Fluorescence characterisation of modified- and unmodified (AT) ₁₅ - and (N) ₃₀ -SWCNTs prepared using MeOH assisted surfactant exchange.	142
B.15 PLE maps for modified and unmodified (AT) ₁₅ - and (N) ₃₀ -SWCNTs prepared using MeOH assisted surfactant exchange.	143
B.16 Fluorescence response of modified- and unmodified-(GT) ₁₅ -SWCNTs prepared via direct sonication towards SDOC.	144
B.17 Fluorescence response of modified- and unmodified-(GT) ₁₅ -SWCNTs prepared using MeOH assisted surfactant exchange towards SDOC.	145
B.18 Absorbance spectra of modified and unmodified (GT) ₁₅ -, (AT) ₁₅ -, and (N) ₃₀ -SWCNTs prepared using MeOH assisted surfactant exchange following the addition of SDOC.	146
B.19 Fluorescence response of modified- and unmodified-(AT) ₁₅ - and (N) ₃₀ -SWCNTs prepared using MeOH assisted surfactant exchange towards SDOC.	147
B.20 Response of modified and unmodified (GT) ₁₅ -SWCNTs prepared via direct sonication following the addition of dopamine.	148
B.21 Response of modified and unmodified (GT) ₁₅ -SWCNTs prepared using MeOH assisted surfactant exchange following the addition of dopamine.	149
B.22 Response of modified and unmodified (AT) ₁₅ -SWCNTs prepared using MeOH assisted surfactant exchange following the addition of dopamine.	151
B.23 Response of modified and unmodified (N) ₃₀ -SWCNTs prepared using MeOH assisted surfactant exchange following the addition of dopamine.	152
B.24 Response of modified and unmodified DNA-SWCNTs towards DTT.	153
B.25 Spectral response of modified and unmodified (GT) ₁₅ -SWCNTs prepared via direct sonication towards DTT.	154
B.26 Spectral response of modified and unmodified (GT) ₁₅ -SWCNTs prepared using MeOH assisted surfactant exchange towards DTT.	155
B.27 Spectral response of modified and unmodified (AT) ₁₅ -SWCNTs prepared via MeOH assisted surfactant exchange towards DTT.	156

List of Figures

B.28 Spectral response of modified and unmodified (N) ₃₀ -SWCNTs prepared via MeOH assisted surfactant exchange towards DTT.	157
B.29 Response of modified and unmodified DNA-SWCNTs towards NaOH 0.02M (pH adjustment to pH 7).	158
B.30 Spectral response of modified and unmodified (GT) ₁₅ -SWCNTs prepared by direct sonication towards NaOH 0.02M (pH adjustment to pH 7).	159
B.31 Spectral response of modified and unmodified (GT) ₁₅ -SWCNTs prepared using MeOH assisted surfactant exchange towards NaOH 0.02M (pH adjustment to pH 7).	160
B.32 Spectral response of modified and unmodified (GT) ₁₅ -SWCNTs prepared using MeOH assisted surfactant exchange towards NaOH 0.1M (pH adjustment to pH 9).	161
B.33 Spectral response of modified and unmodified (AT) ₁₅ -SWCNTs prepared using MeOH assisted surfactant exchange following pH adjustments to pH 7 and pH 9).	162
B.34 Spectral response of modified and unmodified (N) ₃₀ -SWCNTs prepared using MeOH assisted surfactant exchange following pH adjustments to pH 7 and pH 9).	163
B.35 Response of modified and unmodified DNA-SWCNTs prepared using MeOH assisted surfactant exchange towards NaOH 0.1M (pH adjustment to pH 9).	164
B.36 Effect of excess unbound DNA on the absorbance spectra and suspension quality of DNA-SWCNTs.	164
B.37 Effect of starting DNA concentration on the dispersion quality for MeOH-assisted surfactant exchanged SWCNT suspensions.	165
C.1 Effect of MgCl ₂ and CaCl ₂ on DNA-SWCNT fluorescence.	168
C.2 Shift in the wavelength position of the (7,6) chirality peak for DNA-SWCNTs on addition of MgCl ₂ and CaCl ₂	169
C.3 Wavelength shifting response of the (7,6) chirality peak for DNA ₁₅₅ -SWCNTs on addition of various divalent metal cations.	170
C.4 Wavelength shifting response of the (7,5) and (7,6) chirality peaks for DNA ₁₅₅ -SWCNTs on addition of NaCl and KCl.	171
C.5 Wavelength shifting response of the (7,5) chirality peak for DNA ₁₅₅ -SWCNTs with increasing concentration of various divalent metal cations.	172
C.6 Change in wavelength shifting response of the (7,6) chirality peak for DNA ₁₅₅ -SWCNTs with increasing concentration of various divalent metal cations.	173

C.7	Circular dichroism results of DNA ₁₅₅ , (GT) ₁₅ , and (GT) ₂₃ before and after the addition of CaCl ₂ or MgCl ₂	174
C.8	Kinetic responses of the intensity and wavelength position of the (7,6) peak of DNA ₁₅₅ -SWCNTs on addition of various divalent cations.	175
C.9	Reversibility of the fluorescence response of the (7,6) chirality peak for DNA-SWCNTs.	176
C.10	Wavelength shift of the (7,5) and (7,6) peaks for PVA (10%)-suspended SWCNTs following the addition of M ²⁺ ions.	177
C.11	Spectral response of LNA-SWCNTs on addition of CaCl ₂ and MgCl ₂	178
C.12	Comparison of the response of DNA- and LNA-SWCNTs on addition of CaCl ₂ and MgCl ₂	179
C.13	Effect of gel percentage on the response kinetics of DNA-SWCNTs encapsulated in agarose gel following the addition of MgCl ₂	180
D.1	Image of freshly prepared DNA- and LNA-SWCNT suspensions.	182
D.2	Concentration normalised absorbance spectra of DNA- and LNA-SWCNTs. . .	182
D.3	Absorbance spectra of DNA- and LNA-SWCNTs before and after SDOC replacement.	183
D.4	Absorbance spectra of DNA- and LNA-SWCNTs at various time points following SDOC addition.	184
D.5	Wavelength shift of absorbance peak positions following SDOC addition. . . .	185
D.6	Wavelength shift of the (7,5) and (7,6) fluorescence peak positions following SDOC addition.	186
D.7	Additional AFM images collected for (GT) ₁₅ ⁻ , LNA _{every3} ⁻ , LNA _{every5} ⁻ , LNA _{every6G} ⁻ , LNA _{every6T} ⁻ , LNA _{33mid} ⁻ , and LNA _{20mid} -SWCNTs.	187
D.8	Comparison of nanotube cross-section and longitudinal AFM height profiles for LNA _{33mid} -SWCNTs.	188
D.9	Comparison of nanotube cross-section and longitudinal AFM height profiles for LNA _{20mid} -SWCNTs.	188
D.10	Correction for the height measurements for LNA _{every6G} -SWCNTs.	189

List of Figures

D.11 Circular dichroism measurements of DNA- and LNA-SWCNTs on addition of CaCl_2	189
D.12 Solvatochromic shift as a function of the SWCNT diameter to the power of negative 4 (d^{-4}).	190
D.13 Fluorescence spectral response of DNA- and LNA-SWCNTs following the addition of CaCl_2	192
D.14 Intensity changes and wavelength shifts of DNA- and LNA-SWCNTs following the addition of CaCl_2	193
D.15 Fluorescence spectral response of LNA-SWCNTs following the addition of dopamine.	194
D.16 Concentration-dependent wavelength shifting response of DNA- and LNA-SWCNTs towards dopamine in the absence of CaCl_2	194
D.17 Concentration-dependent intensity response of DNA- and LNA-SWCNTs towards dopamine in the absence of CaCl_2	195
D.18 Fluorescence spectral response of LNA-SWCNTs following the addition of CaCl_2 and dopamine.	196
D.19 Fluorescence response of the (7,5) peak for $(\text{GT})_{15}$ - and LNA-SWCNTs following the addition of dopamine in the presence of various concentrations of CaCl_2 . .	197
D.20 Fluorescence response of the (7,6) peak for $(\text{GT})_{15}$ - and LNA-SWCNTs following the addition of dopamine in the presence of various concentrations of CaCl_2 . .	198
D.21 Comparison of the fluorescence response of $(\text{GT})_{15}$ - and LNA-SWCNTs for the (7,5) and (7,6) peaks following the addition of CaCl_2 and dopamine at different time points.	199
D.22 Change in the absorbance spectrum due to ageing effects of the DNA- and LNA-SWCNT suspensions.	200
D.23 PLE maps of the DNA- and LNA-SWCNT suspensions following 180 days of incubation at 4°C	200
D.24 Wavelength shift of the (7,5) and (7,6) fluorescence peak positions for DNA- and LNA-SWCNTs following SDOC addition of samples prepared using the surfactant exchange protocol.	201
D.25 Data correlation matrix for the $(\text{GT})_{15}$ - and LNA-SWCNT sensors.	201

D.26 Comparison of the fluorescence response of the (7,5) peak for (GT) ₁₅ - and LNA-SWCNTs prepared via sonication and surfactant exchange following the addition of CaCl ₂ and dopamine.	202
D.27 Comparison of the fluorescence response of the (7,6) peak for (GT) ₁₅ - and LNA-SWCNTs prepared via sonication and surfactant exchange following the addition of CaCl ₂ and dopamine.	203
E.1 Single molecule response behavior of (GT) ₁₅ -SWCNT sensor films towards dopamine in DI water.	205
E.2 Single molecule response behavior of LNA _{every5} -SWCNT sensor films towards dopamine in DI water.	206
E.3 Single molecule response behavior of (GT) ₁₅ -SWCNT sensor films towards dopamine in supplemented Schneider's medium (10% FBS, 1% Pen/Strep). . .	207
E.4 Single molecule response behavior of LNA _{every5} -SWCNT sensor films towards dopamine in supplemented Schneider's medium (10% FBS, 1% Pen/Strep). . .	208
E.5 Single molecule response of LNA _{every5} -SWCNT sensor films towards dopamine addition following a 24 h incubation in DPBS.	209
E.6 Single molecule response of LNA _{every5} -SWCNT sensor films towards dopamine following a 24 h incubation in Rinaldini solution.	210
E.7 Single molecule response of LNA _{every5} -SWCNT sensor films towards dopamine following a 24 h incubation in supplemented Schneider's medium.	211
E.8 Single molecule response of LNA _{every5} -SWCNT sensor films towards dopamine following a 24 h incubation in 10 % FBS.	212
E.9 Improving the single molecule response of SWCNT films by increasing the density of the films - supplemented Schneider's medium.	213
E.10 Improving the single molecule response of SWCNT films by increasing the density of the films - 10% FBS.	214
E.11 Comparison of LNA _{every5} -SWCNT sensor films following 48 h of incubation in supplemented Schneider's medium both with and without cells.	215
E.12 Widefield visible images of <i>Drosophila</i> neurons.	216
E.13 Fluorescence intensity increase of LNA _{every5} films in DI water following the addition of different media samples.	217

List of Figures

E.14 Single molecule response of LNA _{every5} -SWCNT sensor films in DI water to the addition of supplemented Schneider's medium.	218
E.15 Single molecule response of LNA _{every5} -SWCNT sensor films in DI water to the addition of supplemented Schneider's medium spiked with 100 μ M dopamine.	219
E.16 Single molecule response of LNA _{every5} -SWCNT sensor films in DI water to the addition medium extracted from a neuronal cell culture containing dopamine neurons induced to express CsChrimson.	220
E.17 Single molecule response of LNA _{every5} -SWCNT sensor films in DI water to the addition medium extracted from a neuronal cell culture containing dopamine neurons induced to express GFP.	221
E.18 Fluorescence response of LNA _{every5} -SWCNTs towards the addition of medium extracted from <i>Drosophila</i> neuronal cell cultures.	222
E.19 Schematic of the protocol used to extract <i>Drosophila</i> neurons from adult or larvae brains.	222
E.20 Normalized absorbance spectra for all DNA-SWCNT suspensions.	223
E.21 PLE maps for PNA-DNA _{8bp-rev} -SWCNTs before and after the addition of complementary miRNA.	224
E.22 Comparison of the fluorescence spectra for DNA _{8bp-rev} -SWCNTs, PNA-DNA _{8bp-rev} -SWCNTs, and PNA-DNA _{8bp-rev} -SWCNTs following the addition of complementary miRNA for hybrids created using PNA ₁₅₅ , PNA ₁₈₄ , or PNA ₁₉₅	226
E.23 Comparison of the fluorescence spectra of DNA _{8bp-rev} -SWCNTs, PNA-DNA _{8bp-rev} -SWCNTs, and PNA-DNA _{8bp-rev} -SWCNTs with complementary miRNA for hybrids created using PNA ₁₅₅ , PNA ₁₈₄ , PNA ₁₉₅ , or PNA ₂₀₂ acquired after an incubation period of 16 h.	227
E.24 Fluorescence wavelength shift following the addition of PNA, miRNA, or PNA + miRNA to DNA _{8bp-rev} -SWCNTs.	228
E.25 Comparison of the chirality dependent wavelength shifts and intensity changes for DNA _{8bp-rev} -SWCNTs following addition of miRNA, PNA, and PNA with miRNA.	229
E.26 Comparison of the chirality dependent wavelength shifts and intensity changes for DNA _{8bp} -SWCNTs following addition of miRNA, PNA, and PNA with miRNA.	230
E.27 Comparison of the chirality dependent wavelength shifts and intensity changes for DNA _{10bp} -SWCNTs following addition of miRNA, PNA, and PNA with miRNA.	231

E.28 Comparison of the chirality dependent wavelength shifts and intensity changes for DNA _{15bp} -SWCNTs following addition of miRNA, PNA, and PNA with miRNA.	232
E.29 Comparison of the chirality dependent wavelength shifts and intensity changes for DNA _{20bp} -SWCNTs following addition of miRNA, PNA, and PNA with miRNA.	233
E.30 Dependency of the wavelength shifting response of PNA ₁₅₅ , PNA ₁₈₄ -, and PNA ₁₉₅ -DNA-SWCNTs on the length of the hybrid portion.	234
E.31 Comparison of the chirality dependent wavelength shifts and intensity changes for DNA _{15bp} -SWCNTs following addition of miRNA, PNA, and PNA with miRNA for solutions with higher relative concentrations of miRNA versus PNA.	235
E.32 PLE maps for PNA-DNA _{15bp} -SWCNTs before and after the addition of complementary and non-complementary miRNA.	236
E.33 Comparison of the normalized absorbance spectra for PNA ₁₅₅ and PNA _{10b} -DNA _{15bp} -SWCNTs following the addition of complementary or non-complementary miRNA.	237
E.34 Comparison of the normalized absorbance spectra for DNA _{15bp} -SWCNTs, PNA ₁₅₅ -DNA _{15bp} -SWCNTs, and PNA ₁₅₅ -DNA _{15bp} -SWCNTs following the addition of either complementary or non-complementary miRNA.	237
E.35 PLE maps for PNA-DNA _{10bp} -SWCNTs before and after the addition of complementary and non-complementary miRNA.	238
E.36 PLE maps for PNA-DNA _{20bp} -SWCNTs before and after the addition of complementary and non-complementary miRNA.	239
E.37 Comparison of the changes in fluorescence spectra for PNA _{10b} -DNA-SWCNTs prepared using different hybrid section lengths (10, 15, or 20 bases) following the addition of non-complementary miRNA.	240
E.38 Comparison of the changes in fluorescence spectra for PNA ₁₅₅ -DNA-SWCNTs prepared using different hybrid section lengths (10, 15, or 20 bases) following the addition of complementary and non-complementary miRNA.	241
E.39 Comparison of the changes in fluorescence spectra for PNA ₁₈₄ -DNA-SWCNTs prepared using different hybrid section lengths (10, 15, or 20 bases) following the addition of complementary and non-complementary miRNA.	242
E.40 Comparison of the changes in fluorescence spectra for PNA ₁₉₅ -DNA-SWCNTs prepared using different hybrid section lengths (10, 15, or 20 bases) following the addition of complementary and non-complementary miRNA.	243

List of Figures

- E.41 Comparison of the changes in fluorescence spectra for PNA₁₉₅-DNA-SWCNTs prepared using different hybrid section lengths (10, 15, or 20 bases) following the addition of complementary and non-complementary miRNA. 244
- E.42 Fluorescence wavelength shift response of PNA-DNA_{10bp}-SWCNTs and PNA-DNA_{20bp}-SWCNTs to complementary and non-complementary miRNA. 245

List of Tables

3.1	List of functional groups and modification positions tested for improving the fluorescence intensity of (GT) ₁₅ -SWCNTs.	46
3.2	Comparison of the concentration yields of SWCNTs suspended using direct sonication and MeOH-assisted surfactant exchange.	50
3.3	Fluorescence intensity change of the (6,5) and (7,5) chiralities for modified (GT) ₁₅ -SWCNTs compared to the respective (GT) ₁₅ -SWCNT complex.	50
4.1	Summary of metal ion complexes and the corresponding range of concentrations studied in the presence of DNA-SWCNTs.	65
6.1	Wavelength shift following the addition of PNA sequences to DNA _{8bp-rev} -SWCNTs.	105
6.2	List of miRNA sequences.	115
6.3	List of PNA sequences used to create PNA-DNA-SWCNTs.	115
A.1	List of Chemicals and Suppliers.	122
A.2	Wavelength shifts (in nm) for all nanotube samples following 15 min of incubation with analyte solution.	129
A.3	Percentage (%) intensity change ($\frac{I_f - I_0}{I_0}$) for all nanotube samples following 15 min of incubation with analyte solution.	130
B.1	Additional DNA sequences, functional groups, and modification positions tested for improved fluorescence intensity of nanotube suspensions prepared using the MeOH assisted surfactant exchange protocol.	132
B.2	Fluorescence intensity increase for modified and unmodified (GT) ₁₅ -SWCNTs following the addition of dopamine.	150

List of Tables

B.3	Penetration depth enhancement for modified (GT) ₁₅ -SWCNTs.	166
C.1	List of oligonucleotides used to examine the effect of divalent cations on nanotube fluorescence.	167
C.2	Wavelength shift response as a function of agarose gel percentage.	180
D.1	List of DNA and LNA sequences.	181
D.2	Fit parameters for the solvatochromism shift model.	190
D.3	Chirality dependent energy shifts, E_{11}^2 (ΔE), for all DNA and LNA sequences. . .	191
E.1	List of DNA sequences used to prepare the DNA-SWCNT suspensions.	225

Introduction

*Why, sometimes I've believed as many as
six impossible things before breakfast.*

Lewis Carroll
Alice's Adventures in Wonderland

Background and Context

Patient outcomes are strongly impacted not only by the treatments available but also by the stage at which a disease is diagnosed. As a result, new biosensing technologies that enable earlier intervention are imperative for improved patient care. A need for early intervention is especially important for many neurological disorders, such as Parkinson's disease or Alzheimer's disease, as the burden of disease is exacerbated by the long timescales of the disease and the loss of healthy life an individual may experience. This means that earlier diagnosis can have an even greater impact on the patient's quality of life by enabling earlier intervention to slow the progression of the disease before symptoms present themselves.

Despite an intense, global focus on developing and optimizing biosensing technologies, their ultimate potential remains limited. Biosensors continue to be restricted by their sensitivity, selectivity, and scalability, which constrains their ability to aid in the early detection and intervention of life-altering complications. This is further complicated for neurochemical sensing as applications for neurotransmitter detection also require high temporal and spatial resolution that is difficult to achieve *in vivo* using existing technologies [1–4]. Although genetically encoded sensors have enabled increased spatiotemporal resolution [5–7], due to their nature they have thus far been limited to use in animal models. Therefore, it remains difficult to achieve accurate real-time measurements of neuromodulator concentration in humans, reducing the success of treatments for patients suffering from these diseases. To overcome the limitations of existing biosensing technologies, we require a new generation of biosensors that offer rapid response times, increased sensor stability, decreased costs, and improved selectivity towards an increased variety of biomarkers.

Optical biosensors based on single-walled carbon nanotubes (SWCNTs) have been presented

as an attractive solution for this problem. Their unique physical and chemical properties, in particular the fluorescence properties of semi-conducting SWCNTs [8, 9], make them an ideal candidate for designing the next generation of optical sensors. SWCNTs have already been successfully incorporated into devices to detect a variety of analytes, particularly in the field of biomedical diagnostics [10–12] and neurochemical sensing [13–17]. However, the extent of the selectivity of their response remains unclear. A better understanding of the side interactions of nanotubes with non-target molecules in solution is essential for enabling the transition of this technology to real-world applications and use in point-of-care diagnostics.

The work presented in this dissertation aims to provide greater insight into the fundamental mechanisms of detection for SWCNT optical sensors, presenting new methods to overcome the current limitations faced by the community. Specifically, we present new procedures to engineer nanotube-based sensors for neurotransmitter detection with increased selectivity using easily scalable methods. We show how synthetic biology can be implemented to reduce response interference for oligonucleotide-SWCNT sensors. Furthermore, we demonstrate that these sensors can be used for the label-free optical detection of neurotransmitters in complex biological media. The hope is that these tools can be used to design sensors that are viable in crude, untreated samples, which could significantly advance biomedical diagnostic technologies by enabling faster and more efficient sensors, without needing to compromise sample integrity.

Properties of Single-Walled Carbon Nanotubes (SWCNTs)

Understanding the basic physical and chemical properties of SWCNTs, and the impact these have on their optoelectronic properties, is crucial for optimizing biosensor design. SWCNTs are commonly conceptualised as individual sheets of graphene that have been cylindrically rolled, and axiomatically have a diameter on the order of a few nm. Each nanotube species can be assigned a chiral index that is classified by a pair of integers (n, m) [18], which define its electronic structure [19] and diameter. These integers define individual nanotube species by the chiral vector, \mathbf{C}_h , which is expressed by unit vectors of the graphene lattice [20] (**Figure 1**):

$$\mathbf{C}_h = n\hat{\mathbf{a}}_1 + m\hat{\mathbf{a}}_2 \quad (1)$$

The nanotube diameter relates to \mathbf{C}_h and more specifically the (n, m) indices according to

$$d = \frac{\sqrt{3}}{\pi} a_{cc} \sqrt{n^2 + nm + m^2} \quad (2)$$

where a_{cc} is the length of a carbon-carbon (C-C) bond, ~ 0.14 nm. By changing the chiral angle (Eq. 3), α , or the direction of rolling, it is possible to obtain all possible nanotube chiralities. This angle denotes the angle at which the hexagons of the graphene lattice are tilted along the nanotube axis and is measured as the angle between the \mathbf{C}_h and $\hat{\mathbf{a}}_1$ vectors (**Figure 1**).

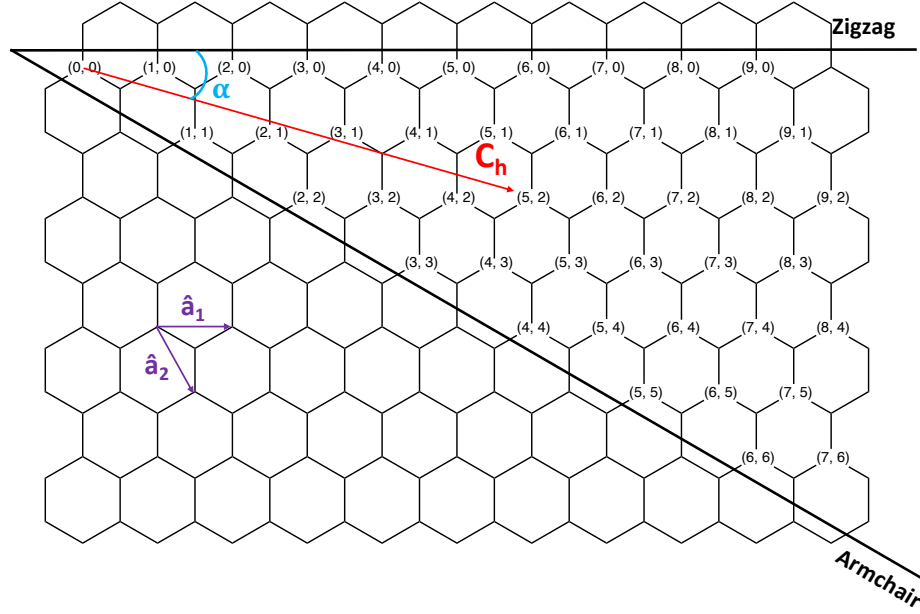


Figure 1 – Illustration of chiral vector and nanotube chiralities projected onto a graphene lattice. C_h is the chiral vector that signals the direction of rolling and α indicates the chiral angle, measured between the C_h and \hat{a}_1 vectors.

$$\alpha = \tan^{-1} \left(\frac{\sqrt{3}m}{2n+m} \right) \quad (3)$$

The arrangement of the C-C bonds around the circumference of the nanotube can be in one of three configurations depending on (n, m) and α : **armchair** ($n = m$, $\alpha = 30^\circ$), **zigzag** ($n = 0$ or $m = 0$, $\alpha = 0^\circ$) or **chiral** (any other n and m , $0^\circ < \alpha < 30^\circ$). SWCNT fluorescence emissions demonstrate a unique chirality dependency and the individual nanotubes may be classified as metallic (when $n - m = 3k$ where k is a non-zero integer), semi-metallic, or semiconducting. For the purpose of this study, we have focused our interest on semiconducting SWCNTs given their unique electronic and optical properties.

The electronic properties of SWCNTs are governed by the existence of Van Hove singularities¹ intrinsic to their density of state (DOS) distribution (**Figure 2 (A)**). These singularities are a result of the unidirectionality of the 1-dimensional (1D) electronic states, with each singularity corresponding to a quantum sub-band [20]. Due to the existence of these Van Hove singularities, the absorption spectra of SWCNTs exhibit sharp peaks associated with allowed transitions that can occur between singularities of the same index (e.g. $v_1 \rightarrow c_1$). Absorption spectra of two mixtures of nanotubes produced by two different synthesis methods are shown in **Figure 2 (B)**. Differences between the two spectra arise from the variation in chirality distributions obtained, which can be affected by factors such as the catalyst or method of preparation.

¹The DOS of 1D materials is not a continuous function of energy but instead contains sharp, discontinuous peaks. These non-smooth points, or singularities, in the DOS are called Van Hove singularities.

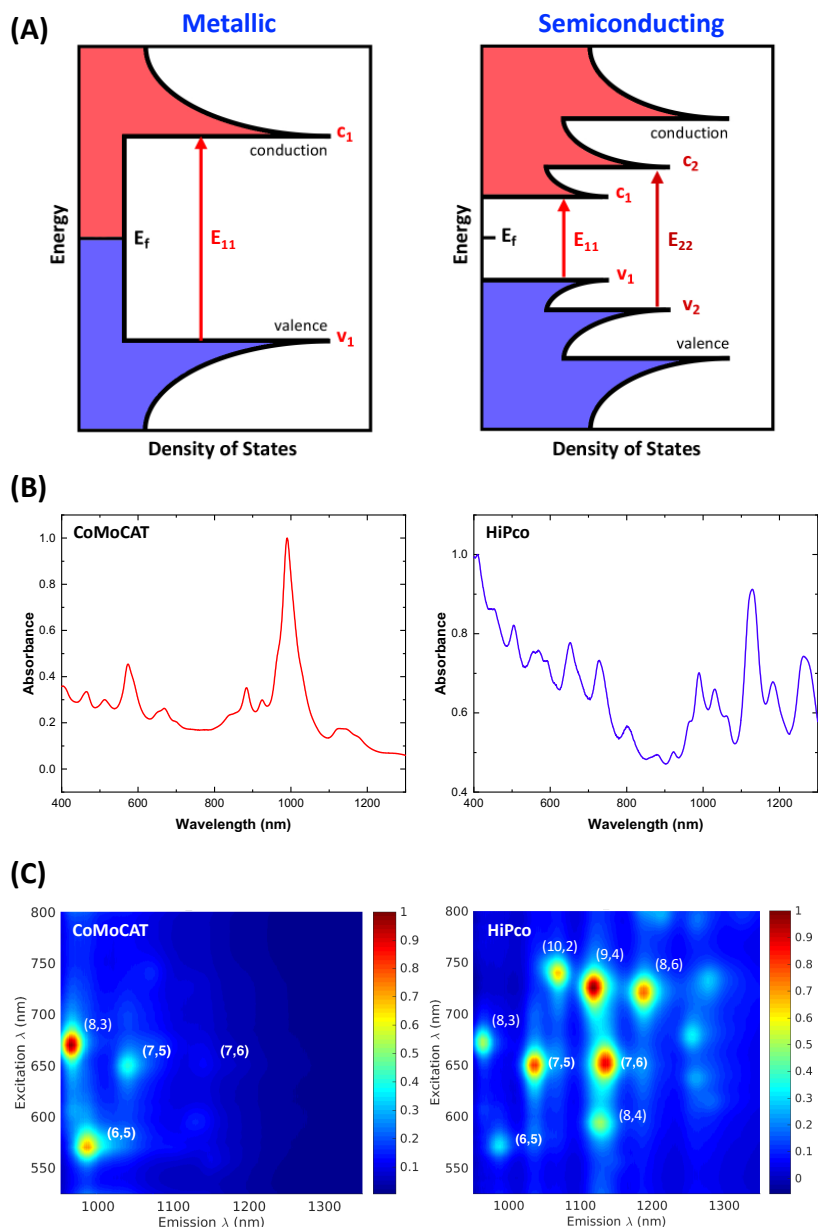


Figure 2 – Optical properties of SWCNTs. (A) DOS of metallic and semiconducting SWCNTs. Illustrative density of states diagrams for metallic (**left**) and semiconducting (**right**) SWCNTs. Van Hove singularities in the DOS are a result of the unidirectionality of the 1D electronic states. Semiconducting nanotubes have a band-gap at the Fermi level (E_f) while metallic SWCNTs do not. Electronic transitions are permitted between bands of the same index and may be denoted as E_{ii} . (B) Normalised absorbance spectra for sodium cholate suspended SWCNTs. The UV-Vis-NIR absorption spectrum of SWCNTs exhibit distinct peaks due to the sharp inter-band transitions associated with the Van Hove singularities. The relative abundance of SWCNT chiralities is dependent on the method of nanotube preparation, which results in different ratios of the peaks in the absorption spectra. Nanotubes were synthesized using either the CoMoCAT (**left**) or HiPco (**right**). (C) Normalised photoluminescence excitation plots for sodium cholate suspended CoMoCAT (**left**) and HiPco (**right**) SWCNTs show the emission peaks of distinct nanotube chiralities. Relaxation of excited electrons from the conduction band to valence band results in fluorescence emission of semiconducting SWCNTs.

However, in both instances convoluted spectra are obtained due to the heterogeneity of the (n, m) species present in the samples. In addition to convolution effects, absorption peak broadening can result from nanotube aggregates present in the suspension. These aggregates are due to the strong van der Waals attractions that exist between nanotubes that can hinder the separation and individualisation of nanotube powders into solution and also lead to re-aggregation post suspension.

Due to the existence of the band gap in the DOS of semiconducting SWCNTs (**Figure 2 (A)**), relaxation of photo-excited electrons results in fluorescence emission [9]. SWCNT fluorescence emission is excitonic rather than electronic in nature, with typical exciton lifetimes ranging from 1 to 100 picoseconds [13]. The band gap emission of individual SWCNTs is a function of the chiral index (n, m) and nanotube diameter [8, 21–24]. Consequently, different nanotube chiralities exhibit distinct fluorescence emission peaks with energy ranges in the near-infrared (NIR) region from 900 – 1400 nm (**Figure 2 (C)**) [8, 25, 26]. Although the emission from the E_{11} transition only exhibits a small Stokes shift² from its absorption maximum [8], larger Stokes shifts can be obtained by exciting the nanotubes at the E_{22} transition and recording the emission from the E_{11} . By using many different excitation wavelengths, we can generate 3D excitation-emission profiles that can be used to study nanotube photoluminescence (**Figure 2 (C)**). The exact wavelength of emission is not only dependent on the nanotube chirality and diameter [8, 27, 28], but also on the local dielectric environment [29, 30] and any structural or chemical defects on the nanotube surface [31–34]. Due to the sensitivity of nanotube fluorescence to any changes in the surrounding environment, modulations of the emission can be used to detect a variety of different molecules [10, 35–37].

The NIR fluorescence of SWCNTs overlaps with the optical transparency window of biological tissue where absorption by water, proteins, haemoglobin, melanin, and DNA is low [38, 39]. Furthermore, SWCNT fluorescence has also been shown to be indefinitely photostable and resistant to photobleaching even under continuous illumination [40], making SWCNTs attractive for long-term biomedical imaging and continuous biosensing applications *in vivo* and *in vitro*. One of the primary challenges when using SWCNTs for any optical sensing applications is their tendency to aggregate in aqueous solutions, which diminishes their fluorescent capabilities [41] and hinders their interaction potential with surrounding molecules. Despite this, the strong van der Waals forces and hydrophobic nature of nanotubes can be overcome to obtain colloidal dispersions in aqueous solutions using a variety of functionalisation techniques [30]. As non-covalent methods of functionalisation preserve the nanotube's intrinsic fluorescence, this method is more commonly used when creating optical biosensing devices, as will be discussed further in **Chapter 1**.

A variety of different molecules, including surfactants, synthetic polymers, biopolymers (such as DNA), or proteins can be used to functionalize and disperse SWCNTs. In addition to improving the solubility of the SWCNTs, these wrappings also impart secondary characteristics

²The Stokes shift is the difference in energy between the positions of the band maxima of the absorbance and emission spectrum for the same electronic transition.

Introduction

such as enhanced bio-compatibility and improved molecular sensitivity. Furthermore, as the exciton relaxation process is very sensitive to the surrounding chemical environment, the presence of additional molecules on the SWCNT surface means that different wrappings result in distinct changes to properties such as the emission energy or quantum yield. These differences can also be due to perturbations in pH, charge, dielectric constant, polarity, and water accessibility between the different wrappings, as well as the chemical nature of the wrappings themselves.

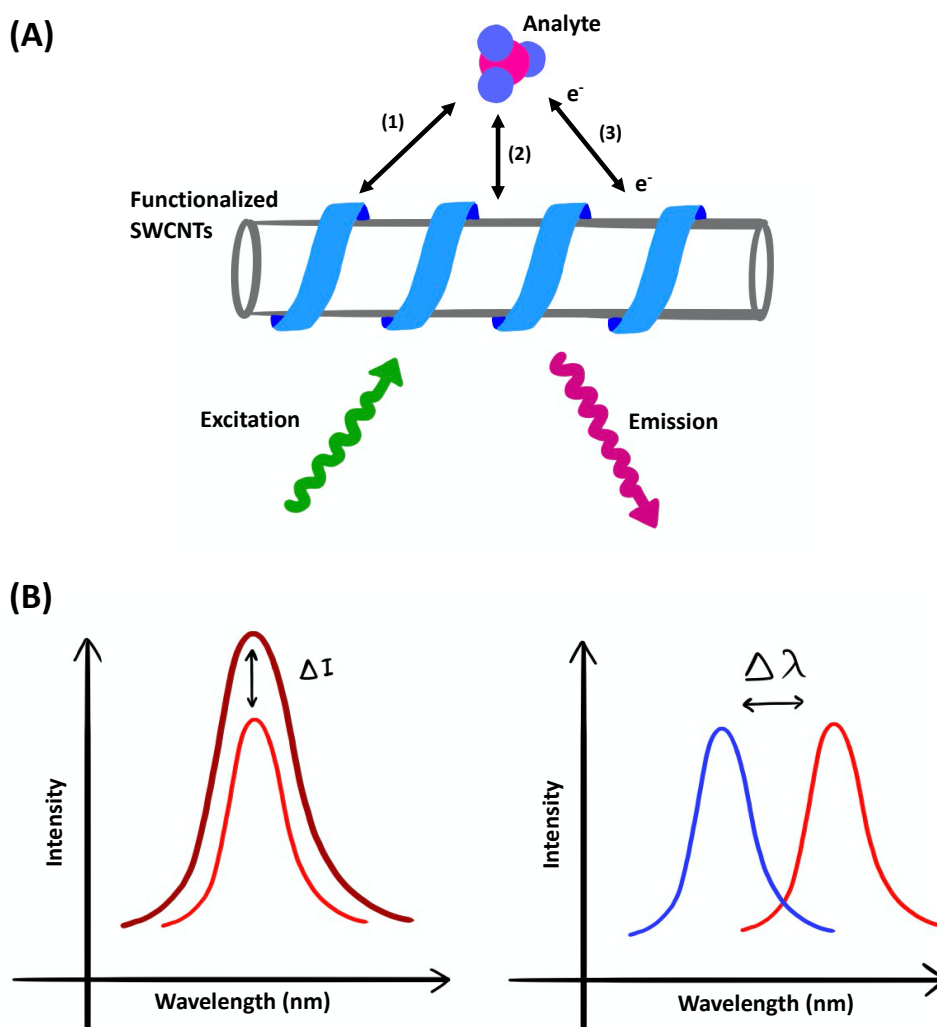


Figure 3 – Optical response of SWCNTs. **(A)** Common mechanisms of interaction between small molecules and suspended SWCNTs. Analyte molecules can interact with functionalized nanotubes by **(1)** causing conformational changes of the wrapping on the surface of the nanotube; **(2)** directly adsorbing onto the exposed surface of the nanotube; or **(3)** electron transfer between the analyte and nanotube or nanotube wrapping. **(B)** Interactions between the analyte and functionalized nanotube can result in changes to the SWCNT fluorescence emission spectrum. These changes can be either intensity changes (**left**) and wavelength shifting (**right**) or a combination of the two.

Moreover, these wrappings modulate the mechanisms via which target analytes can interact with the nanotube (**Figure 3 (A)**) [30, 36]. Depending on the combination of analyte and wrapping, these interactions can result in an optical response of the SWCNT, indicated by changes in the fluorescence emission spectrum (**Figure 3 (B)**). Changes in the fluorescence spectra can be either intensity changes (increases or decreases) or wavelength shifts (blue-shifting or red-shifting), or any combination of the two. Furthermore, the exact change to the fluorescence spectrum is not only a function of the nanotube wrapping and target analyte, but also strongly dependent on the nanotube chirality. The endless combinations obtainable from interfacing different wrapping molecules with specific nanotube chiralities can be used to create a myriad of optical biosensors for various applications. Throughout this work, we examine how surfactants, DNA, and synthetic xeno nucleic acids (XNAs) can be used to tune the response of SWCNT-based optical biosensors with a focus towards differentiating different neurotransmitter molecules.

Neurochemical Sensing

A deeper understanding of how cells transfer and process information is crucial for expanding our knowledge of the biological processes involved in both health and disease. In the brain, communication is mediated by a series of electrical and chemical signaling between neurons, the latter of which is known as chemical neurotransmission. Neurons communicate with each other at specialised junction structures called the synapse (**Figure 4**), which constitute the fundamental processing unit of the brain [15]. At the synapses, signals are transmitted from the presynaptic neuron to the postsynaptic neuron through the synaptic cleft, which is a gap of $\sim 20 - 40$ nm [42]. These signals are triggered by an electric pulse, known as an action potential, that originates in the postsynaptic cell following sufficient depolarisation of the cell membrane. This action potential propagates along the neuron's axon to the presynaptic terminal where the depolarisation of the membrane results in the opening of voltage-gated Ca^{2+} channels. The subsequent influx of Ca^{2+} into the cell causes a Ca^{2+} transient that activates the protein synaptotagmin and triggers fusion-pore opening and the release of neurotransmitters or neuromodulators into the synaptic cleft [43–46]. Neurotransmitters and neuromodulators released during this process diffuse across the cleft to bind with chemoreceptors on the postsynaptic neuron, causing them to activate [42, 47]. Chemical neurotransmission can be either fast- or slow-acting depending on whether ligand-gated ion channels or G-protein-coupled receptors (GPCRs) are activated.

Neurotransmitter binding to ligand-gated ion channels can cause either excitatory or inhibitory effects. Known as fast synaptic transmission, this occurs on millisecond timescales and results in an influx of ions in the adjacent postsynaptic neurons [47], which in turn increases (excitatory) or decreases (inhibitory) the likelihood of a postsynaptic neuron firing an action potential. Following recognition and activation, neurotransmitter molecules are released by the postsynaptic neuron back into the synaptic cleft. These neurotransmitter molecules can then either diffuse away from the cleft into the surrounding medium, get recycled by transport proteins into the presynaptic neuron, or be enzymatically destroyed [48].

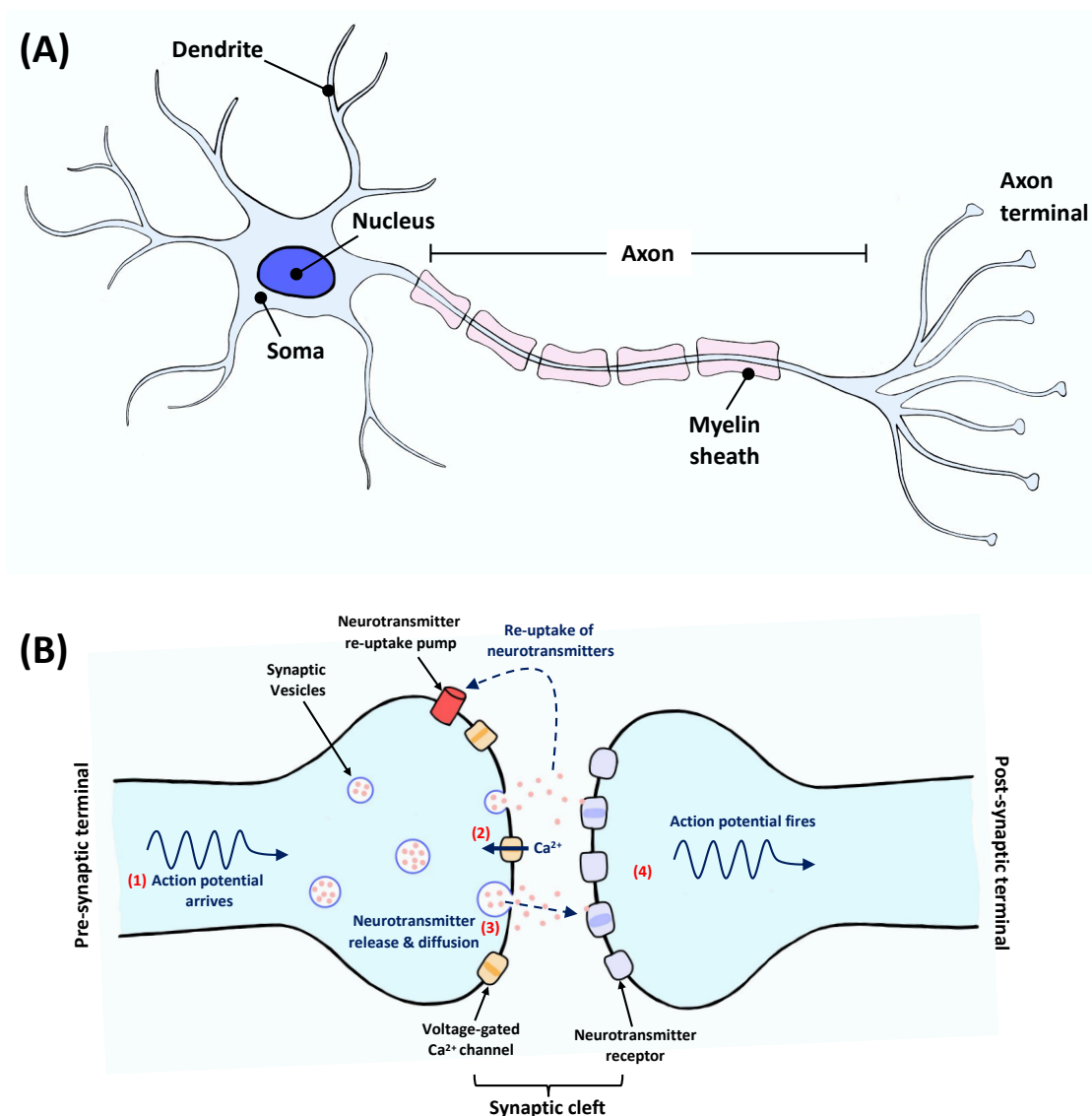


Figure 4 – Neurons and neural communication. **(A)** Diagram illustrating the key structural components of a neuron. Cellular communication occurs following stimulation of a neuron that depolarizes the cell and results in the generation of an action potential. This action potential travels along the axon of the neuron to the axon terminal where signals can be transmitted to neighboring cells through the synapse. **(B)** Illustration of the neural synapse. The synapse is the space where cells transmit signals from the pre-synaptic cell (transmitting cell) to the postsynaptic cell (receiving cell). **(1)** Cellular communication is triggered when an action potential reaches the axon terminal, resulting in depolarization of the membrane. **(2)** This depolarization results in voltage-gated Ca^{2+} channels opening, which in turn leads to an inward flow of Ca^{2+} cations. **(3)** The influx of Ca^{2+} triggers the synaptic vesicles to fuse to the plasma membrane, leading to exocytosis and a release of the neurotransmitter molecules. **(4)** The released neurotransmitters diffuse into the synaptic cleft and can bind to the neurotransmitter receptors on the postsynaptic terminal of the postsynaptic cell. Binding of the neurotransmitters to the receptors results in either a negative (inhibitory effect) or positive (excitatory effect) change in the membrane potential. If the neurotransmitter results in an excitatory effect, the postsynaptic neuron becomes more likely to fire an action potential, whereas if the neurotransmitter has an inhibitory effect the postsynaptic neuron is less likely to fire an action potential. Pink dots represent neurotransmitter molecules.

Contrary to neurotransmitters, which interact with ligand-gated ion channels, neuromodulators interact with postsynaptic neurons via GPCRs [47, 49]. This interaction induces secondary messenger responses that alter the intrinsic biochemical properties of the receiving neuron and consequently modulate its electrophysiological responsiveness [50]. This process mediates the biophysical properties of ion channels, receptors, transporters and other effector substrates, over longer time periods (100s of milliseconds to seconds) and results in slower neurotransmission. Neuromodulators can also escape the synaptic cleft and diffuse more broadly, where they can then influence a population of surrounding neurons in a state-dependent manner enabling a much greater range of action [47].

Problems in the regulation of neural systems, specifically the dysfunction of communication pathways, contribute to the pathology of many neurological disorders and diseases [2]. For example, irregularities in the dopaminergic pathways have been linked to Parkinson's disease, schizophrenia, and depression [1, 5, 51–54]. However, in many instances the cause of this dysfunction remains elusive, leading to difficulties in finding appropriate treatments for these diseases. This underlines the importance of continuing to develop a deeper knowledge of neural communication to obtain a more holistic comprehension of neurochemical function in the brain [55, 56]. However, as synaptic transmission is both rapid and highly localised [57], sensors with high spatiotemporal precision are required to accurately study the dynamic behavior of neural systems [2, 5].

Unfortunately, many of the traditional techniques for monitoring neurotransmitter transients are not well suited for use in *in vitro* and *in vivo* conditions due to limitations with their spatial and temporal precision. For example, fast-scan cyclic voltametry (FSCV) has been widely used to measure changes in dopamine concentrations over long periods of time at specific locations. However, FSCV is invasive and implanted electrodes are typically much larger than the site of the signalling process [17], meaning this technique lacks the spatial resolution required to visualize dopamine release from single neurons [2, 3]. Contrary to this, the use of false fluorescent neurotransmitters (FFN) can enable high spatial resolution but, due to a reliance on intracranial infusions, lacks the ability to be used for longitudinal measurements [4, 58]. Recent efforts to overcome these limitations have led to the discovery of several genetically encoded biosensors, such as dLight1 [5] and GRAB_{DA} [6]. Despite the success of these protein-based probes for addressing the limits of spatiotemporal resolution, they present their own shortcomings, most notably that they require genetic manipulation and so are limited to genetically tractable model organisms. This further motivates the need for developing alternative sensors that address the critical attributes for spatiotemporal resolution, while also providing a platform that can be seamlessly adapted to facilitate a myriad of applications across many biological species.

SWCNT Optical Biosensors for Neurochemical Sensing

When designing probes for continuous monitoring applications *in vivo* and *in vitro*, attributes such as fluorescence quantum yield and emission photostability become increasingly im-

portant. Additionally, a key limitation for deep imaging in biological structures is photon absorption and scattering of visible light by biological material, leading to attenuated fluorescence [38, 59]. This creates a need for fluorophores with peak emissions outside of the visible spectral range to enable increased tissue penetration [39, 60]. The indefinite photostability and inherent NIR fluorescence of SWCNTs addresses these concerns, providing an attractive alternative to traditional optical sensing technologies. This has led to an increasing use of nanotubes over the past decade to create non-genetically encoded biosensors. As mentioned previously, by carefully selecting the method of surface functionalisation and wrappings used, these sensors can be imparted with chemical selectivity for range of applications including neurochemical sensing [14, 61, 62] and miRNA³ detection [10]. Moreover, their capability for single molecule detection and small size means that these sensors have the spatiotemporal resolution necessary for monitoring single cell activity [62].

Although surfactant nanotubes exhibit higher fluorescence quantum yields compared to other wrapping molecules, their lack of inherent selectivity has prevented their application as biosensor complexes. Instead, the first generation of nanotube optical sensors relied on biological macromolecules, such as antibodies and aptamers, to impart selectivity to the sensors [70]. Specific folding within these macromolecules creates unique three-dimensional structures that act as binding pockets or interfaces to recognize target molecules [71, 72]. However, these macromolecules are expensive, fragile, and relatively unstable for extended use with SWCNTs, which limited their widespread applicability. The introduction of CoPhMoRe (Corona Phase Molecular Recognition) by the Strano research group provided a new method for obtaining selective SWCNT sensors [73] for a wider range of molecules. The initial work focused on using synthetic heteropolymers or non-selective biopolymers (such as single-stranded DNA (ssDNA)) to create nanotube-templated recognition sites that act as synthetic antibodies for specific molecules [73, 74]. An advantage of this technique is that polymers, which previously had little to no connection or affinity for the target analytes, create highly selective recognition sites by adopting unique configurations as they pin to the nanotube surface. These conjugates provide a platform that can be tuned to create sensors for a much wider range of target analytes than previously possible by providing effective chemical interfaces for molecular recognition. The versatility of this technique has led to the proliferation of nanotube sensors for a plethora of applications [75, 76] including a number of sensors for neurotransmitter detection [14, 15, 17, 36, 61, 62, 77, 78].

The first ‘turn-on’ CoPhMoRe sensors for dopamine detection were achieved using ssDNA-wrapped SWCNTs (DNA-SWCNTs), specifically using the (GT)₁₅ sequence [14]. These sensors exhibited excellent spatial and temporal resolution, which is necessary for monitoring highly stochastic neuromodulatory events and visualizing fast chemical transients [15, 62, 79]. Subsequent work aimed at improving both the turn-on response and selectivity of these sensors

³microRNA (miRNA) are small non-coding RNA molecules, typically between 15 to 25 nucleotides in length. miRNAs play important roles in regulating gene expression and are involved in a variety of biological processes [63]. These small molecules have been reported as potential noninvasive biomarkers for many diseases, including several types of cancer [64–69].

by altering either the base sequence or the length of the wrapping DNA [15, 77]. Although these improvements led to sensors with turn-on responses of up to 3500% [15], problems with selectivity remained, and these sensors suffered from lower initial fluorescence intensities. Recent studies have demonstrated that the fluorescence of DNA-SWCNTs can be severely impacted by fluctuations in the local concentrations of different cationic species [35, 80]. The presence of these cations can lead to intensity changes and/or wavelength shifts [35, 80], which calls into question the sensing accuracy of DNA-SWCNTs in complex environments and hence their suitability for *in vivo* applications.

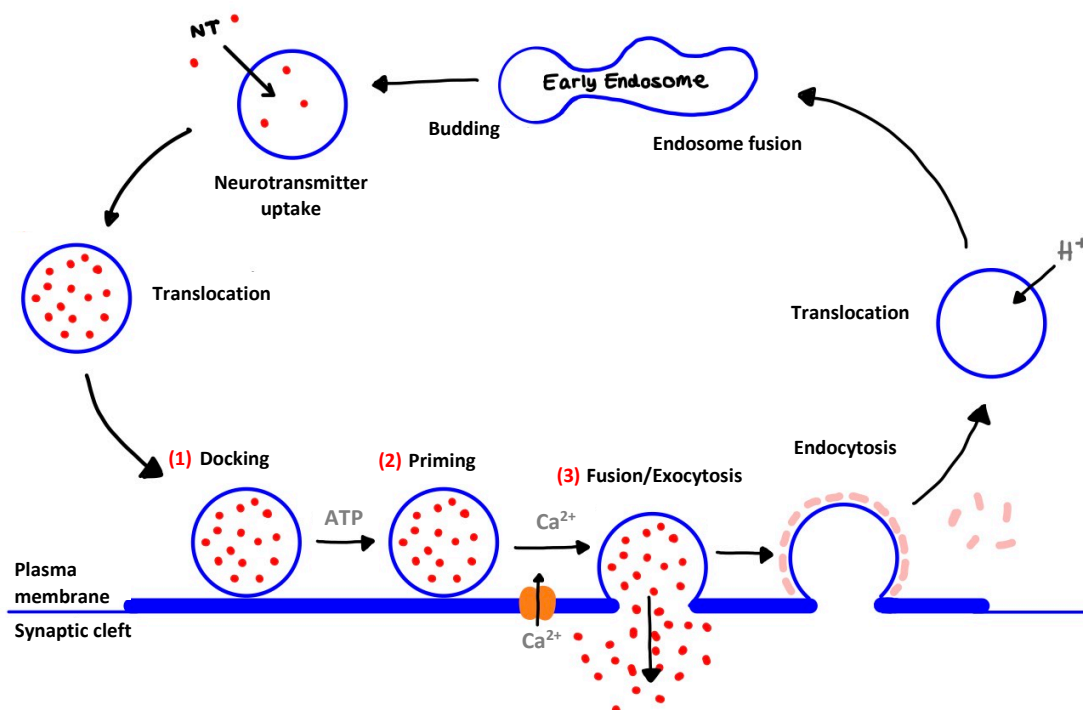


Figure 5 – Role of Ca^{2+} in neurotransmitter release. Illustration (adapted from [45, 57]) of the steps of the synaptic vesicle cycle in the presynaptic terminal. Key steps involved in neurotransmitter release are highlighted: (1) Vesicles filled with neurotransmitter molecules dock at an active zone in the cell membrane to establish initial contact; (2) Once docked, vesicles are primed via a maturation process making them competent for fast Ca^{2+} -triggered membrane fusion. Following priming, vesicles arrest, awaiting a Ca^{2+} signal; (3) Primed vesicles are stimulated for rapid fusion/exocytosis by a spike in Ca^{2+} during an action potential. The Ca^{2+} ions activate synaptotagmins by binding via two C2-domains, which triggers fusion-pore opening and the release of neurotransmitters into the synaptic cleft [43]. Following the release of neurotransmitter molecules, empty vesicles are rapidly internalised and recycled. Red dots represent neurotransmitter molecules and pink ellipses represent clathrin⁴.

This is especially problematic for neurosensing applications, such as dopamine detection, given the role of Ca^{2+} in neurotransmitter release and signalling at the synapse (**Figure 5**). Prior to fusion, synaptic vesicles filled with neurotransmitters are docked close to Ca^{2+} channels in the membrane (**Figure 5**). Depolarisation of the membrane creates pulses of Ca^{2+} , up

⁴Clathrin is a ~ 180 KDa protein that plays a major role in the formation of coated transport vesicles. Clathrin-coated vesicles are found in all eukaryotic cells, but they are particularly enriched in the brain [43, 81, 82].

to ~ 0.2 mM, which initiate vesicle exocytosis and neurotransmitter release [45, 57]. This proximity and dependency of dopamine release on Ca^{2+} fluxes means that any convolution in signal responses to calcium and dopamine can be detrimental to efforts in untangling the complex signalling dynamics of neurotransmitter signalling and release. The convergence of these two events imposes further requirements for SWCNT sensors to be able to differentiate between Ca^{2+} and neurotransmitter fluxes with very little spatial separation, ideally giving optical responses to neurotransmitters invariant to changes in Ca^{2+} concentration. An ability to rationally design sensors that could address this problem with improved quantum yields would enable improved imaging of the dynamic behavior of neuromodulation and could provide a robust pathway for translating SWCNT sensors into *in vivo* sensing applications at increased penetration depths.

Objectives of the Thesis

Ideal probes for bioimaging applications must satisfy several requirements, including high sensitivity, molecular selectivity, spatiotemporal resolution, photostability and resistance to signal interference from surrounding molecules. This thesis aims to address these concerns while engineering nanotube optical biosensors for improved neurochemical sensing. To achieve this goal, several approaches were taken to address problems with the selectivity and stability of SWCNT sensors. Herein we present new methods for designing both surfactant- and DNA-SWCNTs, culminating with the design of a novel XNA-wrapped SWCNT (XNA-SWCNT) sensor that can separate the optical response of dopamine and Ca^{2+} to enable multimodal sensing. This thesis consists of six chapters, several of which have already been published or submitted to peer-reviewed journals. An outline for each chapter is provided below.

Chapter 1: *Non-covalent Methods of Engineering Optical Sensors Based on Single-Walled Carbon Nanotubes*

The first chapter of this thesis, provides an overview of several different strategies that can be employed to non-covalently functionalize the surface of SWCNTs. We review various wrappings, beginning with surfactant molecules and expanding the discussion to biomolecules such as DNA. We compare the advantages and disadvantages associated with each wrapping, highlighting the trade-offs that typically exist between selectivity and brightness between different wrappings. Finally, we discuss how novel synthetic modifications and empirical approaches can be used to overcome some of the current limitations of both surfactant- and biomolecule-suspended SWCNTs. Specifically we introduce polymer engineering and the use of synthetic biopolymers as a means of selectively engineering SWCNT-based sensors with improved capabilities.

Chapter 2: *The Impact of Surface Area on the Response of SWCNT Optical Sensors*

Chapter 2 investigates the role of exposed surface area on the optical response behavior of both DNA- and surfactant-suspended SWCNTs. The surface area was modulated using NaCl

for DNA-SWCNTs and by changing the bulk surfactant concentration for sodium cholate-SWCNTs. Based on these findings, we present a new method for controlling the selectivity of surfactant-suspended optical SWCNT sensors through colloidal templating of the exposed surface area. Surfactant-sensor responses were measured against a library of bioanalytes, including neurotransmitters, amino acids, and sugars, and their performances were compared to DNA-SWCNT optical sensors. We detected an intensity response towards dopamine and serotonin for all sodium cholate-suspended SWCNT concentrations. Furthermore, a selective 14.1 nm and 10.3 nm wavelength red-shifting response to serotonin was observed for SWCNTs suspended in 1.5 and 0.5 mM sodium cholate, respectively. Importantly, the modulation in surface area did not significantly affect the quantum yield of the sodium cholate nanotubes. Thus, through controlled, adsorption-based tuning of the nanotube surface, we demonstrated the applicability of sub-critical colloidal suspensions to achieve selectivities exceeding those previously reported for DNA-SWCNT sensors, without needing to compromise on the superior brightness of surfactant-SWCNT sensors, further highlighting the role of surface area in nanotube response behavior.

Chapter 3: *Modifying DNA-SWCNT Sensors for Improved Dopamine Detection*

Chapter 3 outlines a new approach for increasing the fluorescence intensity of DNA-SWCNTs by using chemically modified DNA sequences. We examined the impact of the type, position, and number of modifications on the fluorescence properties of the DNA-SWCNTs, with a specific focus on (GT)₁₅-SWCNTs. In addition, we investigate the impact that the method of preparation has on the resulting DNA-SWCNT complex, both in terms of the intensity of fluorescence emissions and the reactivity and sensitivity of the complexes to target analytes. We show that while nanotube suspensions prepared using MeOH-assisted surfactant exchange display higher intensities, they also suffer from considerably reduced turn-on responses to dopamine. Conversely, sonicated preparations of SWCNTs using modified DNA exhibited improved fluorescence intensity values compared to unmodified (GT)₁₅-SWCNTs while simultaneously retaining a strong dopamine response. The increased fluorescence intensities before and after dopamine addition significantly increases the theoretical penetration depths for these sensors for *in vivo* applications. This approach presents an attractive alternative to current methods of improving the fluorescence intensity of SWCNT-based sensors as it circumvents the need for any exogenous additives. Furthermore, as it does not rely on making changes to the base sequence, this method can be applied to nearly any DNA sequence to increase the brightness of a variety of DNA-SWCNT sensors.

Chapter 4: *XNA-Nanosensors for Enhanced Stability Against Ion-Induced Fluorescence Perturbations*

Chapter 4 introduces XNAs as a method of improving the performance of DNA-SWCNT sensors. In this study, we performed a systematic investigation on the effects of multivalent salts on the fluorescence emission of ssDNA-wrapped nanotubes. These salts are commonly found in biofluids and are of central importance in cellular signalling within the body. We observed

fluorescence wavelength shifting for DNA-SWCNT-based optical sensors in the presence of divalent cations. This shifting was independent of the cation and counterion species, and also found to be independent of the DNA length and base composition. Through concomitant monitoring of both fluorescence intensity and wavelength shifting, we furthermore identified the transient formation of intermediate DNA-SWCNT optical states within our system. By then introducing XNAs, specifically LNA, we could limit ion-induced fluorescence drift in the presence of cations for concentrations more than two orders of magnitude higher than for pure DNA-SWCNTs. In addition, transient fluorescence measurements revealed distinct optical transitions for the ssDNA- and LNA-based wrappings during ion-induced conformation changes, with LNA-based sensors showing increased permanence in conformational and signal stability. This demonstration introduces synthetic biology as a complementary means for enhancing nanotube optoelectronic behavior with an aim of creating sensors that are more suitable for use in unprocessed biological samples.

Chapter 5: *XNA-Nanosensors for Improved Neurochemical Sensing*

In **Chapter 5** we expand on our findings in **Chapter 4** and seek to further develop XNA-SWCNTs for neurochemical sensing applications. We present new rational approaches using LNA to engineer SWCNT sensors with improved stability towards cation-induced fluorescence changes that can also be used for the label-free imaging of dopamine. By investigating the effect of both position and percentage of introduced locked bases on the resulting LNA-SWCNT sensors, we could identify locking patterns that enable improved sensors for use in the presence of Ca^{2+} . Not only do the LNA-SWCNTs demonstrate improved stability compared to $(\text{GT})_{15}$ -SWCNTs towards undesirable fluorescence modulation in the presence of Ca^{2+} , but they also demonstrated improved label-free imaging of dopamine. These approaches are introduced as a complementary means for enhancing nanotube optoelectronic behavior, unlocking previously unexplored possibilities for developing nano-bioengineered sensors with augmented capabilities.

Chapter 6: *Outlook on Potential Applications of XNA-SWCNTs for Improved Optical Biosensing*

The final chapter of the thesis presents an outlook on ongoing and future developments using XNAs to design SWCNT based optical sensors with improved capabilities. We present findings on using the LNA-SWCNT sensors designed in **Chapter 5** in more complex media solutions. We examine how both incubation time and medium composition can impact the fluorescence intensity of LNA sensor films, and furthermore confirm that our sensors retain their ability to detect dopamine in whole cell cultures. In addition, we present preliminary findings on a new class of XNA-SWCNT sensors, a family of peptide nucleic acid (PNA)-DNA-SWCNT sensors designed for miRNA detection. We present a novel stepwise methodology for constructing PNA-DNA-SWCNTs and demonstrate how this modular design can be used to create multiple miRNA sensors for different target sequences.

1 Non-covalent Methods of Engineering Optical Sensors Based on Single-Walled Carbon Nanotubes

It takes all the running you can do, to keep in the same place. If you want to get somewhere else, you must run at least twice as fast as that!

Lewis Carroll,
Alice's Adventures in Wonderland

*Portions of this chapter are reproduced with permission from [30]: Gillen, A.J.; Boghossian, A.A. **Non-covalent Methods of Engineering Optical Sensors Based on Single-Walled Carbon Nanotubes**, *Frontiers in Chemistry* (2019).*

1.1 Abstract

Optical sensors based on single-walled carbon nanotubes (SWCNTs) demonstrate trade-offs that overall limit their use in *in vivo* and *in vitro* environments. Sensor characteristics are primarily governed by the non-covalent wrapping used to suspend the hydrophobic SWCNTs in aqueous solutions, and we herein review the advantages and disadvantages of several of these different wrappings. Whereas sensors based on surfactant wrappings can show enhanced quantum efficiency, high stability, scalability, and diminished selectivity, sensors based on synthetic and bio-polymer wrappings conversely tend to show lower quantum efficiency, stability, and scalability, while demonstrating improved selectivity. Major efforts to date have focused on optimizing sensors based on DNA wrappings, which have intermediate properties that can be improved through synthetic modifications. Though empirical approaches have been used to engineer sensors based on DNA wrappings, we highlight alternative techniques based on iterative screening that offer a more guided approach to tuning DNA-based sensor properties. These more rational techniques can yield DNA sequences that combine the advantages of the diverse nanotube wrappings to create high-performance optical sensors.

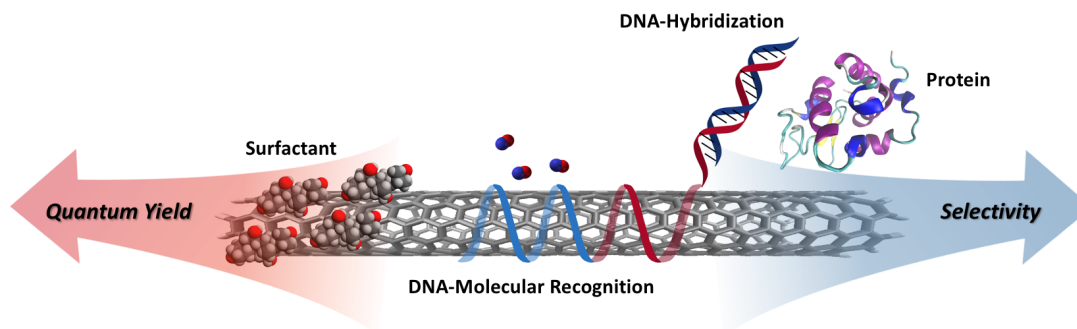


Figure 1.1 – Schematic illustrating the trade-offs between quantum yield and selectivity for various non-covalent surface functionalizations.

1.2 Introduction

Optical sensors use light as a means of contactless detection for real-time sensing. Distinct optical signals from a single device enables multimodal detection of several analytes simultaneously, a feature that is especially advantageous for remote *in vivo* biosensing applications. Fluorescence-based optical sensors require two elements for operation: a molecular recognition element that selectively interacts with the analyte of interest and an optical transducer, such as a fluorophore, that converts this interaction into a measurable optical signal.

As described in several reviews [13, 40, 83, 84], single-walled carbon nanotubes (SWCNTs) are among the most promising fluorescence-based transducers for biosensing applications. They are one-dimensional nanostructures with optoelectronic properties that are tuned by tube diameter as a result of quantum confinement. Conceptualised as cylindrically rolled-up sheets of graphene, SWCNTs can be either metallic or semiconducting, depending on the direction, or chiral angle, the sheet is rolled to yield a nanotube with a distinct diameter. In 2002, O’Connell *et al.* demonstrated that semiconducting forms of SWCNTs dispersed in aqueous solutions emit photoluminescence at near-infrared (NIR) wavelengths [9]. This emission lies within the optical transparency window for biological material [40] which, when coupled with the nanotube’s indefinite photostability and capabilities for single-molecule detection, makes SWCNTs attractive for *in vivo* continuous monitoring applications.

The use of SWCNTs as fluorescent transducers requires surface functionalization to impart optical stability and molecular recognition. Non-functionalized SWCNTs are inherently hydrophobic and exhibit a strong tendency to aggregate into bundles in aqueous solutions. Since most SWCNT preparations contain metallic nanotubes, these bundles contribute to the fluorescence quenching of semiconducting SWCNTs through the non-radiative exciton decay channels within the bundle [9, 85]. Therefore, the bundles need to be exfoliated to generate individually suspended nanotubes in a liquid phase for most practical applications [86]. Specifically, this suspension allows the semi-conducting nanotubes to fluoresce in the NIR. In addition to enabling solubilization and fluorescence, surface functionalization can

also modify the nanotube surface to promote selective interactions with particular analytes of interest (**Figure 1.2**). The underlying mechanism for this selectivity depends on the wrapping and remains an ongoing area of research for many wrappings [16, 35–37, 62, 77, 78, 87–90].

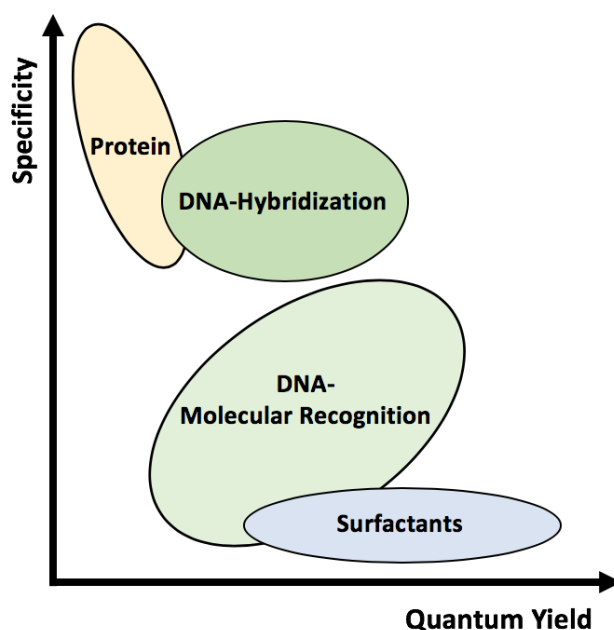


Figure 1.2 – Schematic representation of the various wrappings used to suspend SWCNTs. Different wrappings can alter the quantum yield and specificity of the complexes.

Since covalent functionalization of the nanotube surface is known to strongly affect, or even diminish, the nanotube fluorescence, non-covalent modifications are typically used for creating optical sensors. The most common approach for non-covalently separating SWCNT bundles is liquid-phase exfoliation and stabilization [86]. This approach typically involves using forced dispersion (with ultrasound, for example) in the presence of wrappings such as surfactants, synthetic polymers, oligonucleotides, and proteins that can stabilize the suspended SWCNTs (**Figure 1.3**). In addition to improving the solubility of the SWCNTs, these wrappings can also impart secondary characteristics such as enhanced bio-compatibility and improved molecular sensitivity, overcoming problems associated with the chemical inertness of raw SWCNTs [91].

In this chapter, we present an overview of several key methods used for the non-covalent functionalization of SWCNTs. Beginning with surfactant-coated SWCNTs, we progress towards the use of biomolecules to suspend nanotubes, highlighting key benefits and disadvantages associated with each wrapping. Finally, we conclude with a consideration of new approaches aimed at overcoming some of the limitations of both surfactant- and biomolecule-suspended SWCNTs. These examples highlight emerging methods to selectively engineer improved SWCNT-based optical sensors in complex environments.

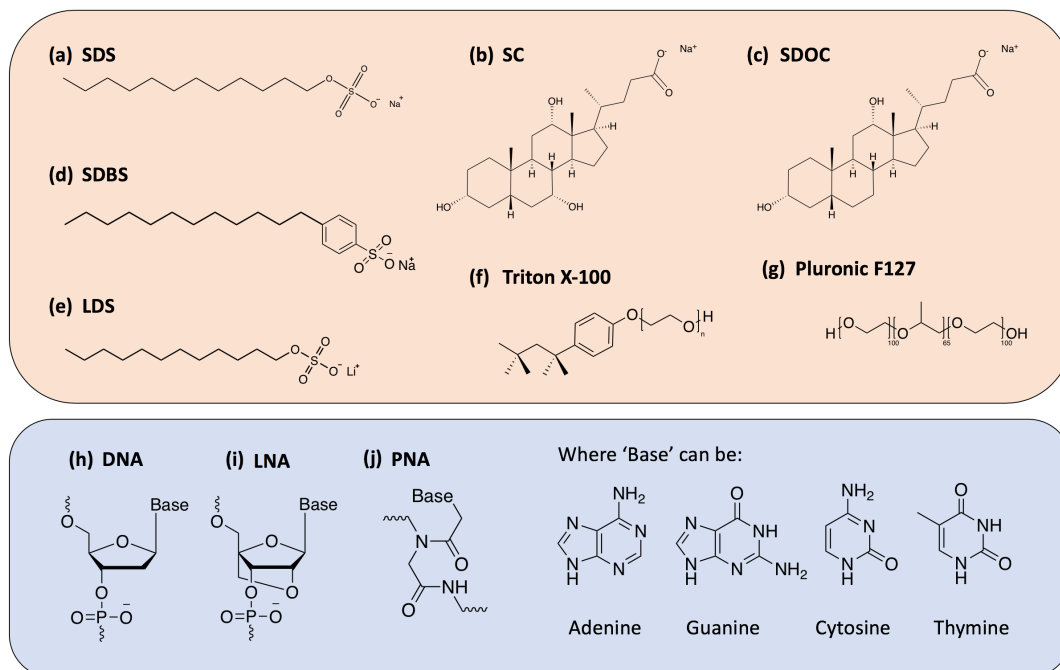


Figure 1.3 – Chemical structures of the various dispersants discussed in this chapter. Surfactant molecules (**top box**) (a) Sodium Dodecylsulfate (SDS); (b) Sodium Cholate (SC); (c) Sodium Deoxycholate (SDOC); (d) Sodium Dodecylbenzenesulfonate (SDBS); (e) Lithium Dodecylsulfate (LDS); (f) Triton X-100; (g) Pluronic F127; and oligonucleotide-derived molecules (**bottom box**) (h) Deoxyribonucleic Acid (DNA); (i) Locked Nucleic Acid (LNA); (j) Peptide Nucleic Acid (PNA).

1.3 Surfactant-Coated SWCNTs

Surfactant-coated SWCNTs represent a standard comparative benchmark for nanotube suspensions, particularly with respect to achieving scalable wrapping procedures and the high quantum yields necessary for optical sensing. Historically, the first reported suspensions of individual SWCNTs were achieved using an aqueous surfactant, sodium dodecylsulfate (SDS) [8, 9, 92]. The resulting isolation of the nanotubes from surrounding bundles greatly improved the optical resolution of the absorbance spectra. Additionally, the authors were able to characterize the direct band gap of individual semiconducting SWCNTs with fluorescence spectroscopy [8, 9], which was first hypothesized in the early 1990s [93–95] and previously detected using Raman and STEM [28, 96].

To prevent re-bundling and obtain a thermodynamically stable suspension, the strong cohesion energy of the isolated tubes ($\sim 120 \text{ kT nm}^{-1}$) must be compensated by either tube-solvent, or in the case of surfactant-suspended SWCNTs, tube-surfactant interactions [97]. However, SWCNT suspensions often exist in a kinetically meta-stable state. Kinetic stabilization does not fully overcome the cohesion energy of the tubes and instead involves creating a repulsive force between the tubes that reduces the likelihood of forming tube-tube contacts, hence slowing aggregation [97]. The ability of the surfactant to prevent re-aggregation of the SWCNTs

is attributed to its contribution to this repulsive force, further driven by the enthalpic and entropic contributions from the favored hydrophobic surface interactions on the nanotube surface, similar to the interactions in the kinetic stabilization of colloids [97–101]. Previous studies hypothesized that the individual nanotubes are encased in the hydrophobic interiors of the micelle. The hydrophilic part of the surfactant molecules is believed to face outwards, creating a cylindrical micelle and a repulsive force between the nanotubes that renders a thermodynamically meta-stable suspension (**Figure 1.4**) [97, 102].

The use of surfactants to suspend SWCNTs has since expanded to include other anionic, cationic, and non-ionic surfactants [103–109] such as sodium cholate (SC), sodium deoxycholate (SDOC), sodium dodecylbenzenesulfonate (SDBS), lithium dodecyl sulfate (LDS), Triton X-100, and pluronic F127. Depending on the surfactant used, high-quality dispersions can be achieved with large populations of individualized nanotubes [86] and SWCNT concentrations > 1 mg/mL. However, different surfactants have been found to vary greatly in the degree of dispersion and stability of the resulting suspensions. This variation is, in part, attributed to the hydrophobic interactions between the surfactant and nanotube, which result in the formation of different structures with varying degrees of surface coverage [110]. In addition to cylindrical micelle SWCNT encapsulation, as was proposed for the SDS-suspended SWCNTs, two additional structures have been suggested detailing how surfactant molecules adsorb onto the SWCNT surface [97, 111]: (i) Langmuir-type (random molecular adsorption) layer and (ii) adsorbed spherical and hemispherical micelles [112–114] (**Figure 1.4 (A)**). The latter, spherical and hemispherical micelle formation, is adopted only by strong amphiphiles that prefer higher curvature aggregates. This formation of hemimicellar aggregates on the surface of the SWCNTs typically involves adsorption of the surfactant onto the nanotube followed by the self-assembly of the molecules, which is enabled by diffusion along the nanotube surface [113]. In contrast, the former, random adsorption of the surfactant on the SWCNT surface, is adopted by weakly amphiphilic molecules (such as flavin mononucleotides (FMN)) and bile acid surfactants (including SC and SDOC) where adsorption is competitive, i.e. follows a Langmuir isotherm [97, 105, 115–117].

According to both experiment and simulation, the degree of exposed SWCNT surface coverage following adsorption of surfactant molecules under all three regimes is largely dependent on surfactant concentration [110]. Indeed, Wang *et al.* [118], have shown that for Triton-X, the optimal surfactant dispersion concentration is different from the critical micelle concentration (CMC) and results from competition between maximizing surfactant adsorption on the nanotube surface and micelle-mediated depletion interaction between adjacent SWCNT bundles. Moreover, previous reports have shown vast differences in the maximum relative solubility of SWCNT complexes using the same surfactant, with an apparent dependence on the processing method and conditions. For example, suspensions made with SDBS can have maximum SWCNT concentrations of 20 mg/mL [114] or no more than ~ 0.01 mg/mL [119], depending on the dispersion approach.

Another factor believed to impact the stability of surfactant-dispersed SWCNTs is the ζ -

potential (ZP). When surfactant molecules adsorb onto the surface of SWCNTs, the surfactant counterion (commonly Na^+ or Li^+) is dissociated from the hydrophilic head group of the surfactant. These counterions are spatially separated from the tail group of the molecular ions, arranging in a diffuse cloud that acts as a multi-pole. As a result, surfactant-suspended nanotubes appear, from a distance, to carry an effective charge associated with this double layer, which is denoted as the ZP [86]. This potential is equivalent to the electrostatic potential measured at the edge of the layer at the bound surfactant tail groups, and it acts as a repulsive interaction potential between neighboring SWCNTs. In a study by Coleman *et al.* [120], the dispersion quality of six surfactant molecules was tested. Each of the dispersion-quality metrics were found to scale well with the measured ZP of the dispersion, with SDS suspending better than both SDBS and SC, corresponding to ZP values of -70.0 mV, -68.8 mV, and -48.8 mV respectively. These findings indicate that the dispersion quality of surfactant-SWCNTs may be controlled by the magnitude of the electrostatic repulsive forces between the coated SWCNTs [120, 121], a property that can be tuned in order to improve the long-term stability of these solutions.

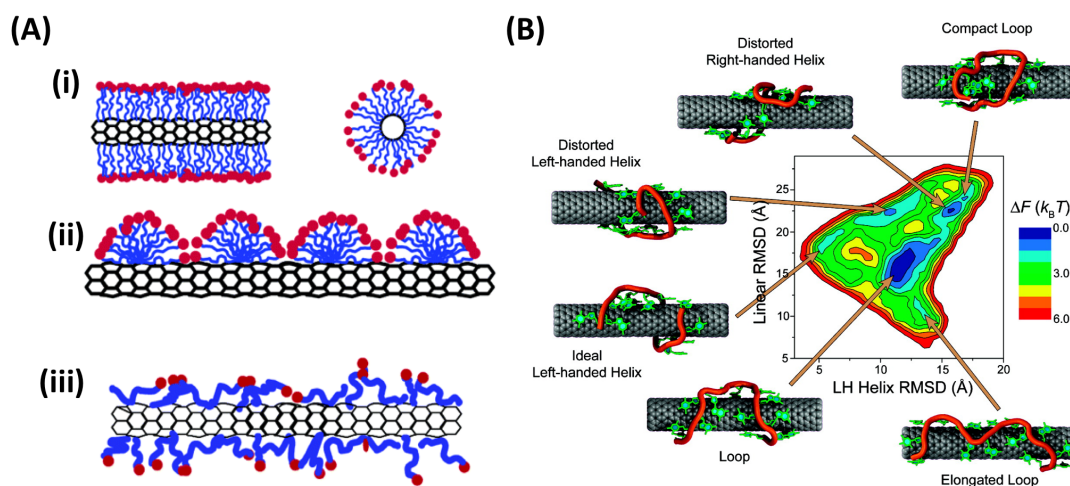


Figure 1.4 – Conformations of non-selective wrappings on SWCNT surface. **(A)** A schematic representation of the various mechanisms by which surfactant molecules interact and disperse SWCNTs. **(i)** Cylindrical micelle encapsulation; **(ii)** Hemimicellar adsorption; and **(iii)** Random adsorption. Reprinted with permission from [122] Copyright © 2004, American Chemical Society. **(B)** Free energy landscape of $(\text{GT})_7$ -SWCNT hybrid at room temperature. Representative conformations for each local minimum are displayed. The sugar-phosphate backbone is depicted in orange, and bases are shown in green. Reprinted with permission from [123] Copyright © 2009, American Chemical Society.

Given the dependence of maximum dispersion concentration and stability on surfactant type, we focus the remainder of our discussion on the four most commonly used surfactants for SWCNT suspension, SC, SDOC, SDS, and SDBS. These surfactants have been shown to achieve stable dispersions with relatively high yields [104], all with reported suspension efficiencies above 40%. Despite the similar structures of SC and SDOC, which only differ by a hydroxy group, SDOC shows a marked increase in suspension yield (+17%). In addition to dispersion

efficiency, the resolution of the optical absorption spectrum can be used to determine differences in the quality of SWCNT suspensions. Distinct absorption peaks are observed for both SC and SDOC, while SDS and SDBS show much broader peaks. In instances where SWCNTs are not effectively exfoliated, the van der Waals interactions between aggregated nanotubes result in broad, weak absorption peaks [90]. This observation therefore suggests that SC and SDOC can generally yield more monodisperse SWCNTs under the studied preparation conditions. On the other hand, the broader peaks observed for SDS and SDBS indicate that these surfactants do not effectively de-bundle the nanotubes, resulting in a poorer dispersion quality despite the apparently high suspension yields.

In addition to their high dispersion efficiencies, these surfactants also benefit from a number of other advantages. Compared to most biopolymers, these wrappings yield SWCNT suspensions that are relatively cheap and stable, and the preparation procedures are scalable enough to produce large volumes of monodisperse SWCNTs, which is an important consideration for the industrialization of nanotube sensors. Furthermore, surfactant-suspended SWCNTs typically exhibit much larger suspension [86] and quantum yield values [104] compared to both protein- and DNA-suspended SWCNTs. The increased fluorescence intensity is attributed, in part, to the increased surface coverage of the surfactant on the SWCNT surface. The increased coverage results in higher levels of oxygen and water shielding, which has been shown to decrease nanotube fluorescence [124], thereby leading to brighter SWCNT complexes. This increase in brightness is particularly important for biosensing applications, where penetration depth and sensor sensitivity have been linked to quantum yield [15, 59, 125, 126].

Toxicity is an additional metric when considering surfactant-suspended SWCNTs for *in vitro* and *in vivo* biosensing applications. Surfactants allow SWCNTs to disperse in water, the universal biological solvent, permitting researchers to flexibly carry out a variety of environmental, biocompatibility, and safety analyses [86]. However, certain surfactants, such as SDS and SDBS, are known to be cytotoxic to cells even at concentrations as low as 0.05 mg/mL [127], and similar effects have been observed for nanotubes suspended with these surfactants [127, 128]. In studies performed by Dong *et al.* [127, 128], neither the proliferation nor viability of the cells was affected by pristine SWCNTs in the absence of surfactant. Furthermore, conjugates of SWCNTs suspended with various concentrations of SC also showed no negative impact on cell viability and growth, and proliferation was comparable to that of untreated cells. The observed cytotoxicity of the nanotube-surfactant conjugates was therefore believed to be driven by the inherent cytotoxicity of the surfactant in the suspension [127, 128]. These studies illustrate the importance surfactant selection in overcoming challenges in toxicity. Although issues such as toxicity can be mitigated through appropriate selection of surfactant type and concentration, surfactant-suspended SWCNTs are limited for biosensing applications due to their lack of inherent selectivity. As a result, current efforts focus on the use of alternative wrappings to suspend SWCNTs, including biopolymers such as single-stranded DNA (ssDNA) and proteins.

1.4 Biopolymer-Suspended SWCNTs

DNA is one of the most extensively studied wrappings used to suspend SWCNTs for optical sensing applications based on Raman, fluorescence emission, and absorption spectroscopies [74, 89, 129–133]. The non-covalent functionalization of nanotubes using ssDNA is based on π -stacking of the aromatic nucleotide bases with the sp^2 -hybridized side-wall of carbon nanotubes [130]. In turn, this arrangement exposes the negatively charged sugar-phosphate backbone of the DNA, which is hydrophilic and easily solvated, towards the water, enabling suspension of the ssDNA-SWCNT (DNA-SWCNT) complexes in aqueous solutions [130]. These favorable side-wall-DNA and DNA-water interactions yields suspensions that are facile and stable at room temperature for several months [130]. Work carried out by Zheng *et al.* [130] showed that almost any ssDNA sequence could be used to successfully suspend SWCNTs in the presence of a denaturant and mild sonication. Although atomic force microscopy (AFM) measurements and simulations show DNA to helically self-assemble around the SWCNT [130, 134], the final binding structure has been shown to be sequence-dependent, and short ssDNA strands may also assume other configurations on the nanotube surface [123, 130, 135] (**Figure 1.4 (B)**). The sparser surface coverage of the DNA compared to surfactants (such as SC) exposes a larger carbon surface to water, resulting in a decrease in the intensity and emission energy of the SWCNT fluorescence. For example, the (7,5) chirality undergoes a bathochromic shift of 17.6 meV (15.6 nm) when wrapped in ssDNA instead of SC due to the greater water accessibility of the DNA wrapping and the resulting increase in the local dielectric constant at the nanotube surface [87, 136]. Such changes in the local dielectric have been shown to yield an expected fluorescence shift in SWCNT emission peaks [29].

In addition to the facile suspension procedure and stable assembly, ssDNA benefits from additional features ideal for scale-up sensor design. DNA-SWCNT suspensions can be further concentrated to achieve dispersion yields as high as 4 mg/mL [130]. Additionally, the nearly limitless variability in sequence length and composition, as well as the well-established chemistries available for DNA functionalization, make ssDNA an incredibly malleable polymer for tuning the characteristics of the suspended SWCNTs. For example, Zheng *et al.* modified DNA-SWCNTs at one end with biotin that was used for immobilization onto streptavidin-coated beads [130]. This study demonstrates one of many biochemical approaches for controlling DNA-SWCNT behavior by specifically engineering DNA-SWCNT complexes. Furthermore, both sequence length and base composition has been shown to impact the interaction potential of ssDNA with the surface of SWCNTs [130, 137], which has also recently been shown to vary with SWCNT chirality [138, 139].

The ability of DNA to form chirality-specific interactions has been exploited for a variety of applications, most notably, chirality separation. Chirality separation is key for multi-modal sensing applications where each chirality selectively responds to a distinct analyte in a solution mixture. Following separation, the individual chiralities can each be functionalized with a wrapping that selectively responds to particular analyte of interest, and the analyte is detected by monitoring the corresponding wavelength. Many separation mechanisms have been

devised [41, 130, 134, 140–151] with varying degrees of success; however, a facile approach for scalable, complete and total fractionation into all the single chiralities remains elusive. Aqueous two-phase (ATP) separation [152–156] has emerged at the forefront of methods currently employed in chirality separation. Briefly, an ATP system consists of two separate, but permeable, water phases of slightly different structures that is created by polymer phase separation [155]. Studies have shown that the partitioning of DNA-SWCNT complexes has a strong dependence on both the DNA sequence and SWCNT structure (i.e. chirality) [153]. Moreover, this partitioning can be modulated by changing the polymer compositions of the two phases in order to rescale the hydration energies. For example, the addition of dextran (DX) to a poly-(ethylene glycol)/polyacrylamide (PEG/PAM) system pulls down DNA-SWCNTs from the top to the bottom phase (due to increased hydrophilicity) while the addition of poly(vinylpyrrolidone) (PVP) has the opposite effect. The effectiveness of this method was demonstrated in work carried out by Ao *et al.* [152–155], where over 300 DNA sequences were screened using ATP separation techniques, resulting in the isolation of 23 different chiralities.

Aside from their chirality specificity and selectivity, different DNA lengths and sequences have also shown preferences towards molecular recognition with certain analytes (**Figure 1.5**). Small nucleotide and microRNA (miRNA) sequences are promising biomarkers for a variety of pathologies, including cancer [10]. However, current methods of detection are complex and time-consuming, leading to difficulties in their implementation for point-of-care diagnostics. An advantage of DNA-SWCNT optical sensors is the ability to engineer selectivity towards target oligonucleotides by taking advantage of DNA's natural preference for specific complementary base pairing. Many studies have demonstrated the use of DNA-SWCNTs to quantitatively detect a range of both miRNA and DNA sequences [10, 87, 129, 157]. Work carried out by Jeng *et al.* and Harvey *et al.* have shown that these fluorescence-based sensors are even capable of detecting single nucleotide polymorphisms (SNPs) [157] and can be multiplexed to detect several sequences simultaneously [10]. In the study by Jeng *et al.*, the addition of complementary DNA is believed to increase the surface coverage of the SWCNT upon hybridization, resulting in a decrease in the effective dielectric constant of the surrounding SWCNT environment and a shifting of the SWCNT fluorescence peak. Similarly, Harvey *et al.* propose an underlying mechanism based on changes in dielectric constant and electrostatic charge, which can modulate SWCNT emission wavelengths upon hybridization. The fluorescence shifting observed in both studies in response to complementary hybridization is particularly advantageous for detecting diseases such as heart and kidney disease, as well as various cancers, which can be associated with different combinations of specific miRNA sequences [69, 158–162].

In addition to detecting hybridization, DNA-SWCNTs can also be engineered to detect a variety of other molecules, including neurotransmitters, sugars, and peptides [62, 76, 164, 165], though the underlying mechanism of these sensors remains an ongoing area of research [166, 167]. While certain DNA-SWCNT sensors are based on oligonucleotides that act as molecular sieves, like the (AT)₁₅-SWCNTs designed to detect NO [74], an alternative approach is based on displacement or conformational changes of the DNA-wrapping [15, 35, 80, 131, 165, 168].

Chapter 1. Non-covalent Methods of Engineering Optical Sensors Based on Single-Walled Carbon Nanotubes

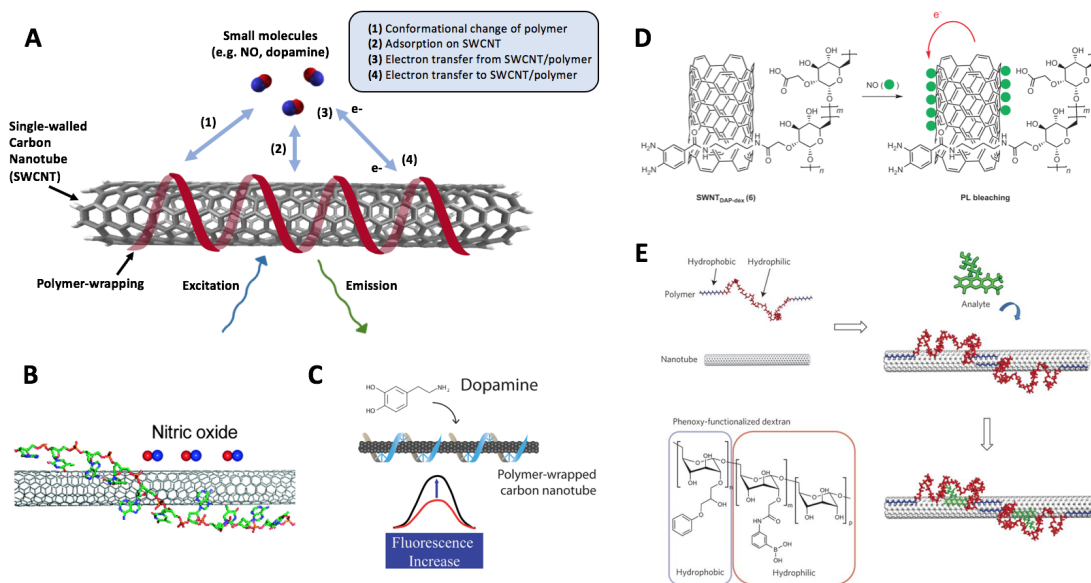


Figure 1.5 – Non-specific interactions of polymer wrappings on SWCNT surface. **(A)** Common mechanisms of interaction between small molecules and polymer-wrapped SWCNTs. **(B)** The optical response of (AT)₁₅-wrapped SWCNT ((AT)₁₅-SWCNT) upon exposure to NO. A side schematic view of one of the several binding structures of (AT)₁₅-SWCNT simulated from a HyperChem simulation package. Bases of the DNA stack on the sidewall of the SWCNT, and the sugar-phosphate backbone extends away from the surface. Adapted with permission from [74] Copyright © 2011, American Chemical Society. **(C)** Schematic of the fluorescent turn-on sensor for dopamine. Adapted with permission from [14] Copyright © 2006, American Chemical Society. **(D)** Schematic illustration for NO detection using SWCNT-polymer hybrids, highlighting the mechanism for NIR fluorescence bleaching by NO with SWCNT-DAP-dextran complexes. PL = photoluminescence. Reprinted with permission from [163] Copyright © 2009, Nature Publishing Group. **(E)** A synthetic polymer with an alternating hydrophobic and hydrophilic sequence adopting a specific conformation when adsorbed to the nanotube. The polymer is pinned in place to create a favored recognition site for the molecules of interest, leading to either a wavelength or intensity change in SWCNT fluorescence. Adapted with permission from [73] Copyright © 2013, Nature Publishing Group.

Early studies in this area screened libraries of molecules of interest against SWCNTs suspended using several different DNA sequences by monitoring the changes in the fluorescence emission of these sensors upon addition of the analyte. Through this approach, researchers were able to identify particular sequences with an enhanced affinity to certain chemicals, such as (AT)₁₅ towards nitric oxide (NO) [74] (**Figure 1.5 (B)**) and (GT)₁₅ towards catecholamines [62, 74, 77] (**Figure 1.5 (C)**). Further studies have also demonstrated that DNA length can also be used to tune the fluorescence properties of DNA-SWCNT hybrids, offering a new approach to controlling the behavior of these sensors [15, 138].

Recent studies carried out by Landry *et al.* and Lee *et al.* have shown that DNA aptamers on SWCNT scaffolds can be used to also detect certain biologically relevant proteins [165, 169]. This label-free fluorescence detection offers many advantages over conventional immunological analytical methods, such as enzyme-linked immunosorbent assays (ELISA) or mass spectroscopy, which lack temporal resolution for real-time quantification of protein levels.

Furthermore, this method obviates cumbersome purification and labelling steps typically required by more classical approaches. Both RAP1 and HIV-1 [165] and platelet-derived growth factor [169] were successfully detected using DNA aptamer-SWCNT complexes. Moreover, the RAP1 and HIV-1 sensors were also reported as to selectively respond to their target proteins in molecularly complex environments such as crude, unpurified cell lysates [165].

Although DNA-SWCNTs have shown improved selectivity towards small molecules compared to surfactant-SWCNTs [73], they still lag behind their protein- and peptide-based counterparts, which offer exceptional molecular recognition. Proteins are capable of not only differentiating between molecularly similar targets, but also different chiralities of the same molecule. For example, whereas proteins such as glucose oxidase (GOx) selectively interact with D-glucose [37], sensors based on the (GT)₁₅ DNA wrapping interact with a family of catecholamines [14, 62, 77]. Although glucose sensors based on DNA-SWCNTs have also been developed, these sensors ultimately require the addition of GOx for specificity due to the structural similarities of competing sugar molecules. Furthermore, the underlying sensing mechanisms for protein-based sensors are often more clearly identified. Their sensing mechanisms are quite diverse, varying from protein charge-transfer [37, 170] to exciton quenching due to protein conformational changes [171], both of which have been shown to alter the SWCNT fluorescence intensity.

Protein-based wrappings, however, suffer from their own disadvantages; a lack of precise control during the protein immobilization process, for example, can result in unfavorable orientations that limit access to the active site [172]. Similarly, structural rearrangements may occur that inhibit, or in some cases destroy, the bioactivity of these molecules [90, 91]. In addition, protein-based wrappings exhibit limited dispersion efficiency, which has been shown to depend on the protein and is generally less efficient than DNA- and surfactant-based suspensions. Several methods of functionalization have been proposed [90, 91, 173–175] and used to create sensors based on Luciferase-suspended SWCNTs [70], AnnexinV-suspended SWCNTs [176], and anti-uPA-suspended SWCNTs [12], for example. However, these sensors require an intermediate linker or wrapping for stability, as opposed to the non-specific adsorption possible with GOx. In fact, other protein-based glucose sensors, such as those based on glucose-binding protein [125, 171], typically require more complex conjugative chemistries compared to GOx, highlighting the importance of understanding the underlying protein mechanism when determining the most appropriate method for functionalization. Although these intermediate wrappings can improve solubilization and help maintain protein structure and function on the SWCNT surface, more complex functionalization procedures with multiple conjugation steps could limit the scalability of the sensors.

Irrespective of the improved selectivity offered by DNA and especially protein-suspended SWCNTs, these sensors suffer from relatively low quantum yields compared to surfactant-suspended nanotubes [104]. The low intensities restrict the depth at which these biosensors can be implanted for use *in vivo* and *in vitro*. Moreover, studies have shown that both protein- and DNA-SWCNTs are sensitive to local variations in pH [90, 177] and ionic strength [35,

80, 131, 178]. The latter raises a specific problem for a number of fluorescence biosensing applications, as these ions are often involved in biological signaling pathways (such as Ca^{2+} in dopamine regulation). Therefore, fluctuations in the local concentrations throughout the day would compromise the sensing capabilities of the DNA-SWCNT complexes.

1.5 Polymer Engineering of SWCNT Sensor Specificity

The trade-offs between surfactant-suspended SWCNTs and biopolymer-suspended SWCNTs have encouraged researchers to seek an alternative means of detection based on synthetic or bioengineered polymers. *Xeno* nucleic acids (XNAs), for example, can be used to improve the sensing capabilities of DNA-SWCNTs in ionically complex systems [35]. XNAs are synthetic alternatives to naturally occurring DNA and RNA. Due to their modularity, nucleic acids can be readily adjusted using a variety of chemical modifications [179–182] and XNAs can contain modifications to either the nucleobase, phosphate, or sugar in an otherwise native oligonucleotide sequence [181, 183, 184]. Although XNAs were initially developed to emulate the DNA replication processes found in nature, these synthetic oligomers were quickly realized for their advantages in *in vivo* stability and specificity [179, 184–186]. Larger base modifications can result in altered physico-chemical properties, such as a tendency to adopt non-standard helical conformations, but certain chemical modifications to the N7 (in purines) or C5 (in pyrimidines), sites that extend into the major DNA groove, can be reasonably tolerated without significant steric impact [180]. Backbone modifications can also alter the physico-chemical properties of oligonucleotides. One example is peptide nucleic acid (PNA), where the sugar phosphate backbone is substituted with aminoethylglycine. This substitution results in a charge-neutral polymer that is capable of strong canonical base pairing. The type and extent of the modification depends on the intended application. For example, locked nucleic acid (LNA) can greatly improve the stability of SWCNT sensors in the presence of high ionic concentrations [35]. Previous studies showed that salt cations can alter the DNA conformation on the nanotube surface, changing the emission wavelengths [35, 80, 131]. Since the added methyl bridge in the backbone of LNA increases the rigidity of the polymer, LNA exhibits increased conformation stability in the presence of fluctuating salt concentrations. By modifying 25% of the sequence with a ‘locked’ base, bioengineered sensors based on LNA have been shown to withstand over two orders of magnitude higher salt concentrations without any perturbations in fluorescence. These complexes offer a strong promise for use in ionically complex media, such as blood or urine, without compromising the biocompatibility or nearly inexhaustible sequence space offered by oligonucleotide wrappings. The added chemical modifications also carry untapped potential for further narrowing selectivity through bio-conjugative chemistries that are specific to functional groups in the desired target.

Similarly, recent work by Chio *et al.* has employed the use of peptoids, N-substituted glycine polymers, to serve as protein molecular recognition elements for SWCNT-based sensors [34]. These peptoids draw inspiration from biological peptides, however display greater resistance to degradation by proteases, analogous to how certain XNAs have higher resistance

to naturally occurring exo- and endo-nucleases [183]. The tunability of these sequence-defined synthetic polymers enables greater chemical diversity by providing a larger monomer space of primary amines [187]. Although the stability of the peptoid wrapping on the nanotube surface was shown to vary depending on composition, length, charge and polarity, Chio *et al.* demonstrated that these sensors could be used to engineer a selective sensor for the fluorescence detection of lectin protein wheat germ agglutinin [34].

In addition to peptoids and oligonucleotide derivatives, purely synthetic heteropolymers have also been used to augment sensor properties. One such platform uses Corona Phase Molecular Recognition (CoPhMoRe) and relies on SWCNT-adsorbed heteropolymers to template preferential recognition sites for target analytes. The final structures adopted by the polymer on the surface control the selectivity of the sensor towards a target. Though the mechanism for modulating SWCNT fluorescence in response to binding is likely analyte- and polymer-specific, its precise characterisation remains an area of active research [166, 167]. Typically, the heteropolymers employed contain both hydrophobic and hydrophilic segments. The former interacts with the SWCNT surface, while the latter extends into solution to suspend the complex in aqueous solutions. CoPhMoRe-based sensors have been developed to detect neurotransmitters [13, 73, 168], vitamins [73], and steroids [73], as well as small molecules such as NO and H₂O₂ [163, 188, 189] (**Figure 1.5**).

Furthering the development of these sensors, Bisker *et al.* [16] extended the capabilities of CoPhMoRe sensors to detect larger macromolecules, such as proteins. A variant of a CoPhMoRe screening approach was used to identify polymeric wrappings that could be used to create synthetic, non-biological antibody analogs capable of recognizing biological macromolecules. This approach yielded a selective sensor for fibrinogen based on dipalmitoylphosphatidylethanolamine (DPPE)-PEG (5kDa)-suspended SWCNT. This sensor was capable of detecting fibrinogen in a competitive binding assay in the presence of albumin, which can passivate the sensor by binding to non-specific binding sites [16]. This observation suggests that CoPhMoRe is more likely due to a combination of factors related to both the specific corona phase formed by the polymer-SWCNT complex and the unique elongated conformation of the fibrinogen protein, rather than sensing mechanisms based on aggregation, molecular weight, or protein hydrophobicity.

1.6 Conclusions

Since the first reported aqueous suspension of individual SWCNTs with surfactant [8, 9, 92], researchers have learned to suspend SWCNTs using a variety of natural and synthetic wrappings. Polymer wrappings in particular have served the dual purpose of both solubilizing SWCNTs and regulating the selectivity of SWCNTs towards specific analytes in biological media. As a result, polymers such as DNA have become standard wrappings for optical SWCNT-based biosensing, and recent efforts have focused on modifying these polymers to improve the quantum yield, stability, scalability, and selectivity of these sensors. However, with

the exception of protein-based wrappings and complementary DNA-strand hybridization, the nature of the selectivity of polymer wrappings towards specific analytes remains unclear. As a result, most DNA and synthetic polymer-based SWCNT sensors are empirically engineered through random library screening and selection. These techniques evaluate the responsivity of several different polymer-wrapped SWCNTs against a variety of analytes, and the polymer-analyte combinations that yield relatively strong fluorescence responses are used to identify suitable polymer wrappings for SWCNT-based sensing [73, 74]. Though this approach has been quite successful in identifying wrappings that can trigger a fluorescence response towards particular analytes, the sensors often show compromised selectivity. Moreover, the polymer wrappings also yield sensors with lower stability and brightness compared to surfactant wrappings.

At present, the optimization of empirically engineered sensors largely entails screening larger libraries to increase the chances of identifying a more desirable hit [73, 74]. This overlooks opportunities for designing and implementing predictive approaches based on systematic trend analysis. Furthermore, there is a lack of iterative or incremental development for further improvement, stagnating the optimization of the final device. In order to overcome these limitations, we require novel rational and even semi-rational approaches for engineering nanotube wrappings with improved brightness, selectivity, and stability. Such techniques could be used to strengthen the understanding of the mechanisms and the empirical specificity of the interactions between different SWCNT sensors and their target molecules. Such a fundamental understanding is needed to not only improve existing sensors, but also to ultimately design molecular probes in a rational and predictive manner. In this thesis we present new methods that aim to address these limitations using surfactant, DNA, and XNA wrappings while creating improved sensors for neurochemical sensing applications.

2 The Impact of Surface Area on the Response of SWCNT Optical Sensors

'Why,' said the Dodo, 'the best way to explain it is to do it.'

Lewis Carroll,
Alice's Adventures in Wonderland

*Portions of this chapter are reproduced with permission from [61]: Gillen, A.J.; Siefman, D.J.; Wu, S.-J.; Bourmaud, C.; Lambert, B.; Boghossian, A.A. **Templating colloidal sieves for tuning nanotube surface interactions and optical sensor responses**, *Journal of Colloid and Interface Science* (2019).*

2.1 Abstract

Surfactants offer a tunable approach for modulating the exposed surface area of a nanoparticle. They further present a scalable and cost-effective means for suspending single-walled carbon nanotubes (SWCNTs), which have demonstrated practical use as fluorescence sensors. Though surfactant suspensions show good quantum yields for mixed SWCNT disperions in aqueous solutions, they lack the selectivity that is vital for optical sensing. We present a new method for controlling the selectivity of optical SWCNT sensors through colloidal templating of the exposed surface area. Colloidal nanotube sensors were obtained using various concentrations of sodium cholate, and their performances were compared to DNA-SWCNT optical sensors in order to elucidate the role of exposed surface area on nanotube optical response behavior. Sensor responses were measured against a library of bioanalytes, including neurotransmitters, amino acids, and sugars. We report an intensity response towards dopamine and serotonin for all sodium cholate-suspended SWCNT concentrations. We further identify a selective, 14.1 nm and 10.3 nm wavelength red-shifting response to serotonin for SWCNTs suspended in 1.5 and 0.5 mM sodium cholate, respectively. Through controlled, adsorption-based tuning of the nanotube surface, this study demonstrates the applicability of sub-critical colloidal suspensions to achieve selectivities exceeding those previously reported for DNA-SWCNT sensors.

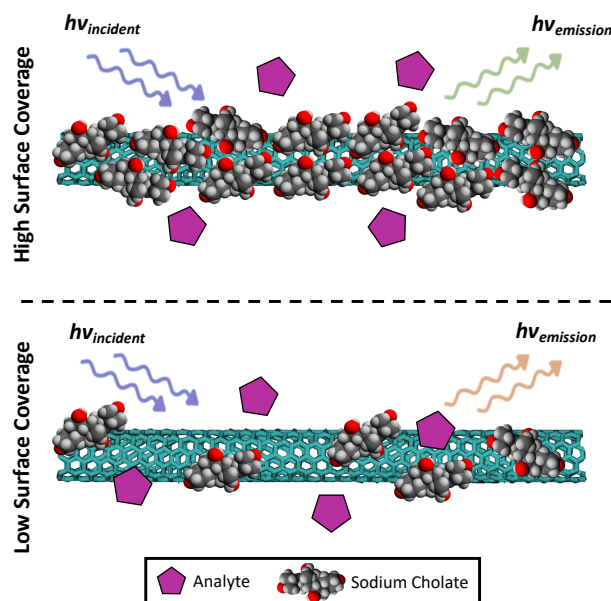


Figure 2.1 – Schematic of analyte interactions with surfactant-coated nanotubes at high and low surface coverage

2.2 Introduction

Biosensors are a bottleneck for disease diagnosis and healthcare monitoring. Their performance is defined by a combination of several key attributes, such as sensitivity and selectivity. For example, biosensors that are used for point-of-care diagnostics must be sensitive enough to detect a target molecule at biologically relevant concentrations, while sufficiently selective to only respond to the target molecule in complex biological media. However, the optimization of these individual attributes often results in trade-offs, limiting the sensor's overall performance.

For optical sensors based on the near-infrared (NIR) fluorescence of single-walled carbon nanotubes (SWCNTs), certain attributes can be altered via surface functionalization of the SWCNT. The light emitted from SWCNT sensors benefits from increased tissue penetration and indefinite photostability [10, 14, 74, 190–193], which makes these sensors attractive for biosensing applications [8, 9, 104, 107]. As covalent functionalization can diminish SWCNT fluorescence, attributes such as brightness, sensitivity, and selectivity are preferentially tuned through the use of non-covalent wrappings on the SWCNT surface [30]. To date, a lack of orthogonal approaches to independently optimize multiple attributes has yielded sensors with compromised performances.

One of the most extensively studied non-covalent surface wrappings for SWCNTs is deoxyribonucleic acid (DNA) [89, 130–132, 134, 164, 194–196]. Since the pioneering work of Zheng *et al.*, the versatility of this wrapping in suspending SWCNTs has been successfully demonstrated

with many different single-stranded DNA (ssDNA) sequences [78, 130, 132, 134, 139]. Furthermore, the molecular recognition capabilities of ssDNA-SWCNT (DNA-SWCNT) complexes have been shown to vary with DNA length and sequence [15, 62, 74]. However, the underlying mechanisms driving the recognition capabilities DNA-SWCNTs remain unclear [15, 74], leading to difficulties in rationally designing DNA-SWCNT sensors for specific analytes. In addition, these complexes suffer from low quantum yields compared to most conventional fluorophores, which reduces the penetration depth for these sensors *in vivo* [78, 104].

Surfactants, such as sodium cholate (SC), sodium dodecyl sulfate (SDS), or sodium dodecylbenzenesulfonate (SDBS), are also commonly used to non-covalently disperse SWCNTs [107, 110, 119, 151, 197, 198]. These SWCNT conjugates benefit from a number of advantages over DNA-SWCNTs, including a higher fluorescence quantum yield [104, 107]. Moreover, this method of suspension is more scalable and cost-effective compared to suspension methods that use proteins or other biopolymers such as DNA or RNA. However, whereas the selectivity of DNA-based sensors can be tuned with a DNA sequence, surfactant-suspended SWCNTs are inherently non-selective and also currently lack techniques to tune their molecular recognition [73].

In this study, we explore the effects of exposed nanotube surface area on the response characteristics of both DNA- and surfactant-suspended SWCNTs. In particular, we have chosen to study SC-suspended SWCNTs as a model surfactant system, as previous studies on surface coverage and critical micelle concentration (CMC) demonstrated that this system can offer a molecular understanding of SWCNT surface interactions [105, 199–201]. Furthermore, SC benefits from greater biocompatibility compared to more strongly denaturing surfactants, as well as an ability to tune exposed surface area with sub-CMC dispersions [201, 202]. Herein, we exploit this tunability to introduce an approach based on designing colloidal templates to tune the analyte specificity of surfactant-suspended nanotubes. This increase in selectivity is achieved without sacrificing the increased fluorescence quantum yield of these conjugates. We apply these colloidal sensors and study their response to a library of analytes including neurotransmitters, amino acids, and sugars, and we show that we can selectively detect serotonin. These findings demonstrate a semi-rational approach for altering analyte specificity through the modulation of exposed surface area.

2.3 Results and Discussion

The presence of certain salts, such as NaCl, alters the conformation of the DNA wrapping on the SWCNT surface. As reported in previous studies [35, 80], Na^+ cations screen intramolecular repulsion forces along the negatively charged phosphate backbone, allowing the DNA to adapt a tighter conformation around the nanotube. The tighter wrapping is believed to increase oxygen exclusion and hence, increase the fluorescence intensity of the sensor.

To examine the effects of DNA conformation on sensor response, fluorescence emission spectra of the (6,5) peak were obtained following the addition of specific analytes for (GT)₁₅-

SWCNTs in the absence and presence of NaCl (**Figure 2.2**). The added analytes, serotonin and dopamine (1 mM final concentration), are neurotransmitters that have been previously shown to alter the fluorescence of DNA-SWCNTs in the presence of salt [14, 36]. In agreement with these findings, we observe a fluorescence increase, as well as a shifting, of the (6,5) peak on dopamine and serotonin addition in the presence of 100 mM NaCl (**Figure 2.2 (A)**). In the 100 mM NaCl solutions, the serotonin and dopamine can also interact with the cations present via cation- π interactions [203, 204]. The greater binding energy of the indole group with Na^+ may contribute to the larger shifts observed for serotonin compared to dopamine [204].

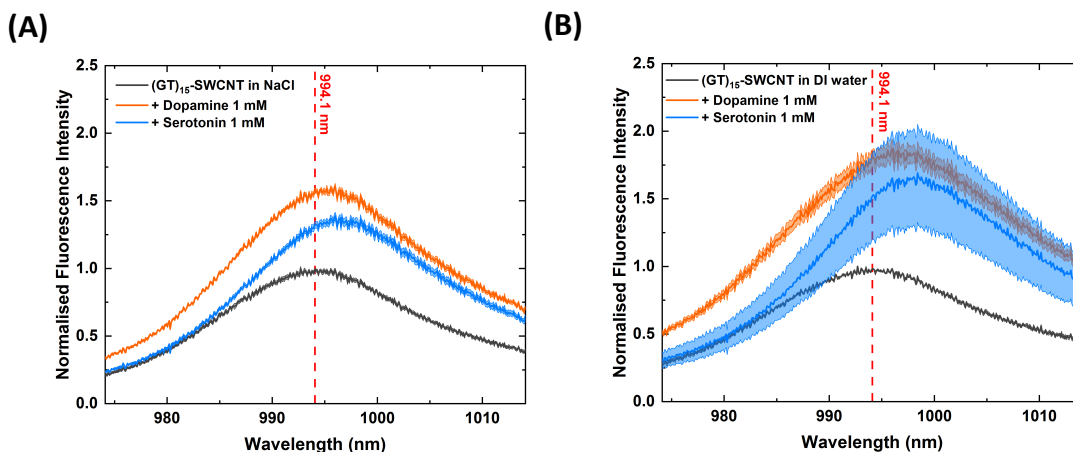


Figure 2.2 – Fluorescence response of $(\text{GT})_{15}$ -SWCNTs to dopamine and serotonin at different NaCl concentrations. Fluorescence response (A) in the presence of 100 mM NaCl and (B) in the absence of NaCl following the addition of 1 mM dopamine (orange) and 1 mM serotonin (blue) (excitation: 575 nm). All shaded regions represent 1σ standard deviation ($n = 3$ technical replicates). All peaks were normalized to the (6,5) maximum fluorescence emission intensity prior to addition of the neurotransmitters.

In the absence of NaCl, we observe a larger fluorescence intensity response and greater variability for both analytes (**Figure 2.2 (B)**). Since DNA is believed to adapt a looser conformation at lower salt concentrations [80], increases in exposed surface area may facilitate charge transfer or aromatic stacking on the nanotube that is responsible for the observed red-shift in both the fluorescence and absorbance (**Appendix Figure A.2**). Previous reports have shown that, similar to NaCl, dopamine alone can interact with the phosphate groups in the DNA backbone to yield tighter wrapping conformations [62]. However, this capability was attributed to the presence of the two hydroxyl groups, and hence only believed possible for catecholamines. As we also observe intensity and wavelength responses on addition of serotonin, which contains only one hydroxyl group, we hypothesize that additional mechanisms beyond phosphate group interactions may contribute to the red-shifting of these sensors. Furthermore, the serotonin response in particular showed a significant increase in variability at lower NaCl concentrations. This increase in variability is attributed, in part, to an increase in nanotube sensitivity as a result of larger exposed surface area, though the precise mechanism is the subject of future investigations.

Several factors are believed to contribute to the distinct responses in the absence and presence of NaCl. Although the addition of cationic species can be used, in theory, to tune the exposed surface area of DNA-SWCNTs, this tunability is convoluted due to electronic screening along the DNA backbone and secondary interactions between the target molecules and cations [35, 80, 131]. As such, in addition to differences in exposed surface area, cationic concentration may itself play a role in modulating sensor response. Alongside conformational restrictions that favor DNA base-stacking, these factors are expected to limit the tunability of surface coverage with DNA for sensing applications.

Surfactants, including SC, show concentration-dependent surface coverage of solubilized particles and can offer greater tunability in modulating the exposed surface area of suspended nanoparticles [105, 198, 205–207]. For SWCNTs in particular, recent work by Bergler *et al.* has shown that even low concentrations of SC can yield suspensions with increased fluorescence intensity compared to DNA wrappings [104, 105]. In these suspensions, the cholate ions have been shown to wrap around the nanotube with the hydrophobic group directed inwards [198]. Bergler *et al.* proposed a SC micellization reaction on SWCNT surfaces that is analogous to the closed association model for free micelle formation [105]:



where n represents the aggregation number and β is the fraction of sodium counterion binding [105, 208]. Importantly, this model enables a thermodynamic analysis of the SC-SWCNT micelle formation equilibrium within the same framework as that used for the association of ionic surfactants in bulk water. As such, the SC can self-assemble at the surface of the nanotube at concentrations lower than the CMC in the bulk due to the higher local concentration and ion stabilization at the nanotube core [101, 105, 209, 210]. At low concentrations, SC undergoes Langmuir-type adsorption that is dominated by immobilization of isolated monomers with low nanotube surface coverage. However, at higher concentrations, co-operatively formed SC-SWCNT micelles enable increased surface coverage, with a Hill coefficient of 65 ± 6 monomers, much greater than that for the formation of free SC micelles (4 monomers) [105]. Based on this understanding of SWCNT solubilization, the exposed nanotube surface area can therefore be increased by decreasing the surfactant concentration in the solution to concentrations below the bulk CMC.

In agreement with Bergler *et al.* [105], we observe abrupt changes in the absorption and fluorescence emission spectra when diluting the SC concentration of SC-SWCNTs to concentrations below the predicted secondary CMC (7 – 12 mM) (**Figure 2.3, top**) [105, 211]. Compared to the stock 46 mM SC-SWCNT solution, we observe an 8.3 nm red-shift of the (6,5) fluorescence peak for 0.5 mM SC-SWCNT, as well as a 7.5 nm red-shift of the (6,5) absorption peak (**Appendix Figure A.2**). These findings suggest that the shift is due to the significant change in surface coverage that is expected at concentrations well below the secondary CMC,

which is expected

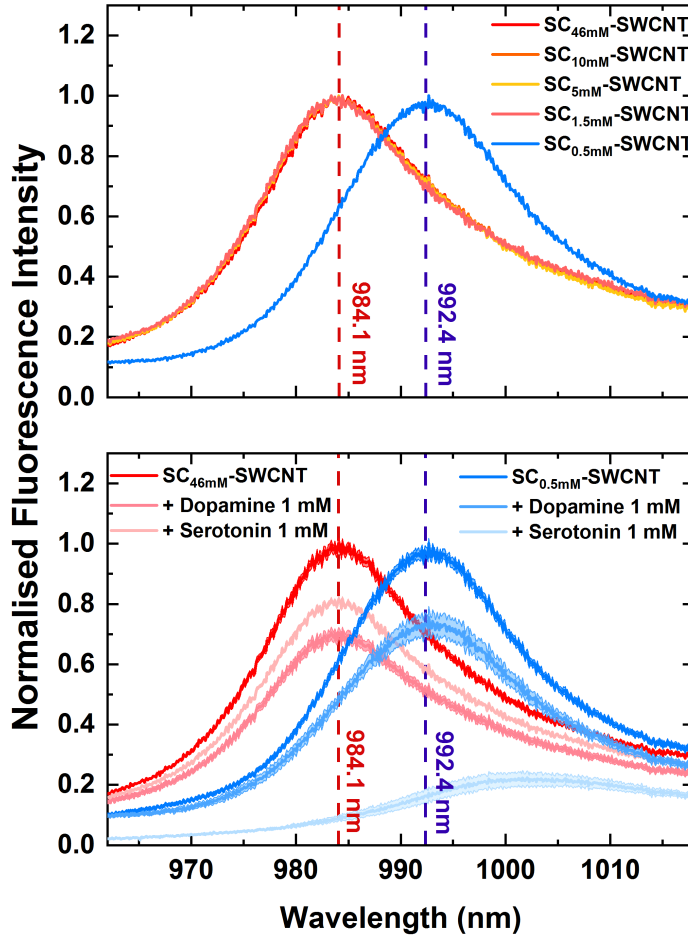


Figure 2.3 – Change in the fluorescence response of SC-SWCNTs to dopamine and serotonin at different SC concentrations. **(Top)** Representative fluorescence spectra of the (6,5) chirality peak for SC-SWCNTs in varying concentrations of SC (excitation: 575 nm). All peaks were normalized to the maximum fluorescence emission intensity at the (6,5) emission peak. **(Bottom)** Fluorescence response of 46 mM (red curves) and 0.5 mM (blue curves) SC-SWCNTs to 1 mM dopamine (darker curves) and 1 mM serotonin (lighter curves) (excitation: 575 nm). The shaded regions represent 1σ standard deviation ($n = 3$ technical replicates). All peaks were normalized to the maximum fluorescence emission intensity at the (6,5) emission peak prior to the addition of analyte.

to increase water accessibility to the SWCNT surface and consequently alter the local dielectric constant [35, 105, 190]. In addition, only small differences in fluorescence intensity (2 – 14%) were observed among samples across all SC concentrations (**Appendix Figure A.3**) when normalized by the SWCNT concentration.

The addition of neurotransmitters to the SC-SWCNTs was shown to alter the fluorescence emission of the SWCNT (**Figure 2.3**, **Appendix Figure A.9**). Contrary to the (GT)₁₅-suspended SWC-

NTs, which exhibited fluorescence intensity increases on addition of serotonin or dopamine, the SC-SWCNTs showed a decrease in fluorescence intensity for all SC concentrations. Within the high coverage regime (46 mM SC concentration), the fluorescence emission intensity decreased by almost 19% following the addition of serotonin. Larger decreases of up to 76% were observed as the surface area was increased for lower SC concentrations (**Figure 2.3**, **Appendix Figure A.4**, **A.9**).

In addition to fluorescence intensity, we also observed changes in the peak wavelength emission of the (6,5) peak on addition of dopamine and serotonin (**Figure 2.3**). Whereas no shifting was observed for the 46 mM SC-SWCNTs, the 0.5 mM and 1.5 mM concentrations showed red-shifting of over 10 nm on addition of serotonin (**Figure 2.3**, **Appendix Figure A.9**). This concentration-dependent shifting at SC concentrations considerably lower than the secondary CMC suggests that exposed surface area could play a critical role in determining sensor sensitivity, particularly in inducing shifting responses.

The selectivity of both DNA- and surfactant-suspended nanotubes was further characterized by monitoring changes in fluorescence intensity and peak position against a library of bioanalytes including various neurotransmitters (**Figure 2.4 (A)**), amino acids (**Figure 2.4 (B)**), and sugars (**Figure 2.4 (C)**). For the DNA-SWCNTs, we observe a generally more selective intensity response following the addition of NaCl. In the absence of NaCl, the DNA is believed to adopt a looser conformation that increases the accessibility of the nanotube surface. Furthermore, the lack of ionic screening can make the SWCNT more susceptible to changes in ionic strength [80]. In agreement with previous observations by Salem *et al.* [80], we can achieve large intensity increases for both the (GT)₁₅- and (AT)₁₅-SWCNTs by increasing the ionic strength of the solution following the addition of PBS (**Figure 2.4 (C)**). While the responsivity of the DNA-SWCNTs was greatly reduced following the addition of NaCl, significant intensity changes were still recorded following the addition of several analytes (**Figure 2.4 (A)**, **2.4 (B)**, **2.4 (C)**), in agreement with previous observations in the literature [37, 62, 212–215]. Smaller increases (< 15%) were also observed for a number of other small molecules, whose adsorption onto the nanotube surface has been shown to contribute to water and oxygen shielding (**Appendix Table A.2** and **A.3**) [213].

Like the DNA-SWCNTs, SC-SWCNTs similarly showed intensity changes in response to dopamine and serotonin; however, the SC-SWCNTs generally showed considerably less reactivity to the library of analytes screened, with little response to both amino acids or sugars. Furthermore, whereas the shifting response of the (6,5) peak of (AT)₁₅-SWCNTs was blue-shifted (>1.5 nm) in the absence of NaCl, the shifting response of the (6,5) peak of the SC-SWCNTs was red-shifted. The contrasting shifting behaviors allude to fundamental differences in the sensing mechanisms of these sensors, specifically in how they alter the solvent accessibility at the nanotube surface.

Moreover, in the case of SC-SWCNTs, we were able to tune analyte selectivity with surfactant concentration, particularly at low concentrations (1.5 mM and 0.5 mM) [105, 211]. No wave-

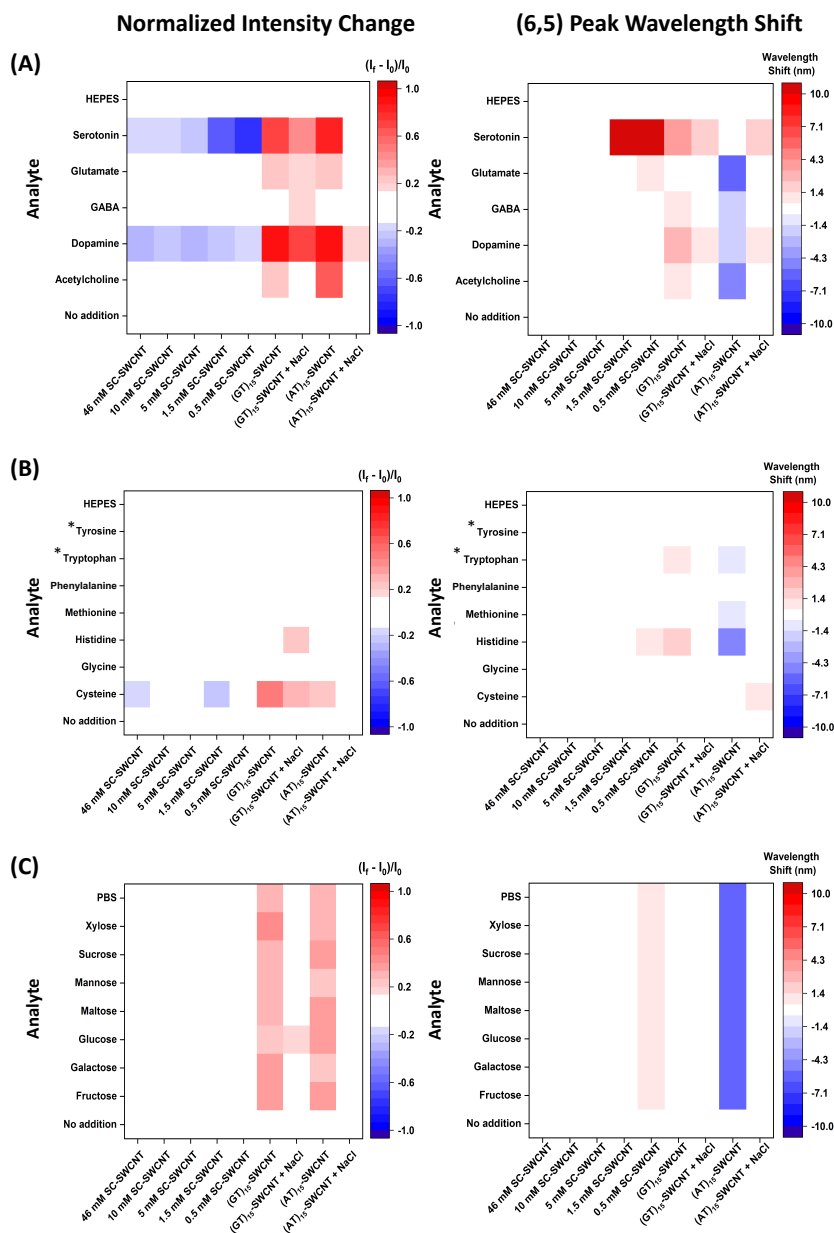


Figure 2.4 – Fluorescence wavelength and intensity responses of SC-suspended and DNA-wrapped SWCNTs to various bioanalytes. Normalized fluorescence changes $(I_f - I_0)/I_0$ (**left**) and wavelength shifts (**right**) were recorded for the (6,5) emission peak following the addition of **(A)** neurotransmitters, **(B)** amino acids, and **(C)** sugars. **Red** indicates an intensity increase or redshift in the wavelength position of the (6,5) peak, and **blue** represents an intensity decrease or blueshift in the wavelength position. Fluorescence measurements are also included for the suspending buffer solution of each library in the first row of each heatmap. Except for tyrosine and tryptophan (noted with an asterisk), all samples were incubated for 15 min in the presence of 1 mM analyte prior to measurement. The final concentrations of the tyrosine and tryptophan solutions used were 0.03 mM and 0.56 mM, respectively, due to their lower solubility. The responses reported in the figure show at least a $0.15 \times$ change in intensity. A table quantifying the magnitude of all responses is included in the Appendix (**Appendix Table A.2** and **A.3**). The full name and supplier of all analyte chemicals used are included in the Appendix (**Appendix Table A**).

length peak shifts were recorded for the 46 mM, 10 mM, nor the 5 mM SC concentrations of SC-SWCNTs in the presence of any of the selected analytes. In agreement with colloid theory [101, 105, 198, 205–207, 209, 210], this observation suggests that sufficient surfactant coverage can limit analyte accessibility to the SWCNT surface, thereby preventing any wavelength response of the fluorescence emission. We further observe a general increase in reactivity for SC-SWCNTs at lower surfactant concentrations, particularly in the presence of sugars and neurotransmitters. In particular, the 1.5 mM and 0.5 mM SC-SWCNT suspensions underwent a 14.1 nm and 10.3 nm wavelength red-shift, respectively, in the presence of serotonin (**Figure 2.4A**). This shifting response was shown to be reversible (**Appendix Figure A.10**) and exhibited a limit of detection of 10 μ M (**Appendix Figure A.4, A.5, A.6**). The lower shift observed for the 0.5 mM SC-SWCNT sensor is attributed to the more red-shifted initial wavelength position of the peak.

The concentration-dependent selectivity observed in this study demonstrates surfactant-suspended SWCNTs as a model system for probing the effects of exposed surface area on fluorescence response. Since pure dopamine and serotonin solutions (100 mM concentration) are unable to suspend SWCNTs (data not shown), such analytes are believed to largely interact with exposed surface area of the surfactant-suspended nanotube, rather than competitively displace the solubilizing surfactant on the nanotube surface. This mechanism is supported by the retained SWCNT solubility following analyte addition. Differences between similarly sized analytes suggest that although the exposed surface area can play a significant role in controlling the accessibility of the nanotube surface, factors such as an analyte's interaction with the nanotube surface also play a role in modulating SWCNT fluorescence [36, 73]. For example, despite tryptophan and serotonin being relatively structurally similar analytes, they demonstrated significantly different response behaviors. Whereas serotonin resulted in considerable quenching for 1.5 mM and 0.5 mM SC-SWCNTs (-61% and -76.2%), tryptophan showed only slight intensity changes (-2.8% and +1.9%, respectively). We do not attribute this disparity to differences in the final concentration of analyte (1 mM versus 0.53 mM), as substantial quenching (-22.5% and -32.7% for 1.5 mM and 0.5 mM SC, respectively) is still observed following the addition of 0.1 mM serotonin (**Appendix Figure A.5**). Furthermore, in spite of differences in their topological polar surface areas (79.1 Å and 62 Å for tryptophan and serotonin respectively) [216, 217], we mainly attribute the variations in response to differences in analyte reactivity and adsorption on the exposed SWCNT surface. For example, previous studies have reported slower electron transfer kinetics for tryptophan compared to redox active molecules such as serotonin and dopamine [218–222]. Similar analyte-specific interactions can also account for the stronger response observed for the serotonin molecule compared to the dopamine molecule at low SC concentrations (**Appendix Figure A.5, A.6, A.7, and A.8**) [217, 223].

2.4 Conclusions

The findings presented herein illustrate that colloidal templating can be used to alter the analyte specificity and selectivity of nanotube optical sensors. Whereas previous approaches have modified the corona phase of a polymer to impart analyte specificities [13, 14, 16, 62, 224, 225], colloidal sensors enable more rational modulation of the exposed surface area with surfactant concentration. Surfactants benefit from tunability in modulating surface coverage, enabling a semi-rational approach to engineering selectivity. By modulating the exposed surface area of surfactant-suspended SWCNTs, we engineered a SWCNT sensor for the selective detection of serotonin. To the best of our knowledge, this sensor represents the first example of specific target recognition by surfactant-suspended SWCNTs. In addition, surfactant-based SWCNT sensors benefit from higher quantum yields, lower costs, greater stability, and scalable preparative procedures compared to DNA-SWCNTs. Though the use of surfactants could limit the applicability of these sensors for *in vivo* measurements, *in vitro* analysis of biological samples can still be achieved with appropriate surfactants at designated concentrations. Furthermore, surfactants offer a range of physiochemical properties, such as differences in toxicity, solubility, CMCs, charge, and polarity, that can accommodate a variety of biosensing conditions. While the underlying mechanisms responsible for modulating SWCNT fluorescence remain elusive and analyte-specific, surfactant-based wrappings offer an approach to de-couple the effects of surface accessibility from analyte reactivity. In conjunction with SWCNT sensors based on DNA and synthetic polymer wrapping, these surfactant-suspended SWCNTs can provide an additional avenue for further studying analyte-wrapping interactions and their effects on modulating SWCNT fluorescence.

2.5 Materials and Methods

2.5.1 Preparation of SWCNT solutions

A (6,5)-enriched mixture of purified CoMoCAT SWCNTs was suspended in 2% (w/v) SC (Sigma-Aldrich) according to the procedure by Zubkovs *et al.* [37]. Briefly, 25 mg of CoMoCAT SWCNTs (CHASM SG65i, Lot No. SG65i-L59) were added to 25 mL of SC 2% (w/v) solution (equivalent to 46 mM SC). The mixture was homogenized for 20 min at 5,000 rpm (Polytron PT 1300 D, Kinematica) prior to probe-tip sonication (1/4 in. tip, Q700 Sonicator, Qsonica) for 1 h (10% amplitude) in an ice bath. The resulting solution was centrifuged at $164,000 \times g$ (30,000 rpm) for 4 h at 20°C (Optima XPN-80 Ultracentrifuge, Beckman) to remove nanotube aggregates. Absorbance spectra were taken for the supernatant using a UV-vis-NIR scanning spectrometer (Shimadzu 3600 Plus). The SWCNT concentration of each sample was calculated by absorbance using an extinction coefficient $\epsilon_{739} = 0.025 \text{ L mg}^{-1} \text{ cm}^{-1}$ [196, 226]. Solutions of SC-SWCNTs, with SC concentrations of 0.5 mM, 1 mM, 5 mM, and 10 mM, were obtained via dilution of the 2% (46 mM) SC-SWCNT stock solution immediately prior to use. The same stock SC solution was used for all dilutions to ensure a similar distribution of nanotube lengths for all samples.

SWCNTs were suspended with (GT)₁₅- and (AT)₁₅-DNA sequences (Microsynth) using a modified surfactant exchange protocol [78, 189, 190, 227]. In the surfactant exchange method, methanol (final solvent percentage 60% (v/v)) is added to surfactant-suspended SWCNTs in the presence of DNA to increase the critical micelle concentration (CMC) of the surfactant [227], allowing the DNA to replace the surfactant on the SWCNT surface. The exchange was performed on the 2% SC-suspended CoMoCAT SWCNTs, prepared as described above, mixed with a final concentration of 15 μ M DNA (as measured by Nanodrop 2000 Spectrophotometer). 800 μ L of the DNA/SC-SWCNT solution was added to 1.2 mL of methanol, and the resulting mixture was incubated at room temperature for 2 h.

Following incubation, the surfactant and unbound DNA were removed using centrifugal ultra-filtration devices (Amicon Ultra 0.5 mL 100 kDa Filters, Merck) by rinsing the solution ten times with DI water. The rinsed solution was then collected and centrifuged for 4 h at $16,750 \times g$ and 4°C to remove any aggregates formed during the surfactant exchange protocol. Final concentrations for the supernatants were calculated from absorbance measurements at 739 nm, as described above.[196, 226] For measurements taken in the presence of salt, NaCl was added to yield a final concentration of 100 mM in the presence of the purified DNA-SWCNT samples.

2.5.2 Fluorescence spectroscopy measurements

Fluorescence emission spectra were acquired using a custom-built optical setup on an inverted Nikon Eclipse Ti-E microscope (Nikon AG Instruments), as described previously [37]. Briefly, 49.5 μ L of SWCNT solution (5 mg/L concentration) was placed in a 384-well plate and excited at 575 ± 5 nm (resonance excitation for the (6,5) SWCNT chirality). Following the acquisition of the initial spectrum, 0.5 μ L of target analyte solution (prepared as described in the Appendix) was added and the mixture was incubated for 15 min prior to recording a final spectrum. A fine grating (600 lines mm^{-1}) was used to collect the nanotube emission at wavelengths between 961 and 1018 nm. Fluorescence emission data were fit to a skewed-Lorentzian using a custom Python program based on non-linear least-squares. The fit was used to determine the maximum intensity and corresponding wavelength position of the (6,5) chirality emission. More detailed information on the spectral fitting is outlined below.

2.5.3 Spectral fitting

A non-linear-least-squares fit was applied to the experimental data to calculate the intensity and wavelength of the SWCNT emission peaks. The fitting procedure minimizes an objective function that represents the deviation between the experimental data and the mathematical representation of the peak. The objective function was defined as the chi-squared statistic (χ^2), and the model contains fitting variables that minimize the χ^2 . In other words, the residual between the experimental data and the model is minimized by varying the parameters of the model. The least-squares fit is done with the Levenburg-Marquardt algorithm [228, 229], or

damped least squares as implemented in the software `lmfit` in Python [230].

This fit does not give a probability distribution on the fitted model, i.e. the experimental uncertainty is disregarded in the fitting. To estimate the associated uncertainty, we employ probabilistic data analysis. This analysis marginalizes nuisance parameters, thereby propagating the effects of the experimental uncertainty to the final result. The probabilistic data analysis was performed with the affine-invariant ensemble sampler for Markov chain Monte Carlo (MCMC) [231]. The prior is taken as the center and amplitude of the photoppeak from the experimental data. We assume a uniform prior for these parameters such that all possible values are equally likely considered to be the prior. MCMC samples are drawn from the prior distributions and representative data sets from the likelihood function to give the posterior, or the estimated uncertainty on the fitted parameters.

Nanotube emission peaks are traditionally fitted using either Voigt [10, 232–235] or Lorentzian [9, 27, 236] probability density functions. However, since the acquired data sets typically exhibit varying degrees of skewness [237], the use of these probability density functions results in inaccurate fits. In order to account for the skewness, a skewed Lorentzian was used as the fitting model [238]. The Lorentzian is given in **Eq. 2.2** where ν is the energy (converted from wavelength), ν_0 is the peak center, A is the area under the peak, and γ is the full width at half maximum. The skewed Lorentzian has γ as a function of ν , i.e. the width is allowed to vary sigmoidally as seen in **Eq. 2.3**. The nuisance parameter a is a measure of symmetry that accounts for skewness. When a is zero, the formulation gives the standard Lorentzian with a symmetric profile. Meanwhile, a positive a skews the peak towards lower wave numbers and a negative a towards higher wave numbers.

$$L(\nu) = \frac{2A/\pi\gamma}{1 + 4[(\nu - \nu_0)/\gamma]^2} \quad (2.2)$$

$$\gamma(\nu) = \frac{2\gamma_0}{1 + \exp[a(\nu - \nu_0)]} \quad (2.3)$$

2.5.4 Rinsing procedure for sensor regeneration

Fluorescence emission spectra were acquired using the custom-built optical setup on an inverted Nikon Eclipse Ti-E microscope (Nikon AG Instruments), as previously outlines. As before, 49.5 μL of 1.5 mM SC-SWCNT solution (5 mg/L concentration) was placed in a 384-well plate and excited at 575 ± 5 nm (resonance excitation for the (6,5) SWCNT chirality). Following the acquisition of the initial spectrum, 0.5 μL of serotonin solution (100 mM) was added and the mixture was incubated for 30 min prior to recording a final spectrum.

The sensors were rinsed using centrifugal ultra-filtration devices (Amicon Ultra 0.5 mL 100

kDa Filters, Merck). Prior to use, the devices were rinsed twice using 500 μL of 46 mM SC solution and centrifuging at $14,000 \times g$ for 2 min at 20°C . Following the acquisition of the initial response, a total volume of 500 μL serotonin-SWCNT solution (495 μL SC-SWCNT 5 mg/L and 5 μL serotonin 100 mM) was added to the rinsed devices, and centrifuged at $14,000 \times g$ for 90 s at 20°C . SC solution (46 mM, 400 μL) was added to the devices to resuspend the sensors, and the resuspended solution was then rinsed at $14,000 \times g$ for 90 s at 20°C . This was repeated twice to ensure all the serotonin was removed from the solution. Following rinsing the sensors were resuspended in 500 μL 1.5 mM SC and collected. The sensor solution was vortexed briefly and 49.5 μL of the rinsed solution (not concentration adjusted) was placed in a 384-well plate and excited at 575 ± 5 nm. As before, following the acquisition of the initial spectrum, 0.5 μL of serotonin solution (100 mM) was added and the mixture was incubated for 30 min prior to recording a final spectrum. A fine grating (600 lines mm^{-1}) was used to collect the nanotube emission at wavelengths between 961 and 1018 nm.

3 Modifying DNA-SWCNT Sensors for Improved Dopamine Detection

*It sounded an excellent plan, no doubt,
and very neatly and simply arranged;
the only difficulty was, that she had not
the smallest idea how to set about it.*

Lewis Carroll, *Alice's Adventures in
Wonderland*

3.1 Abstract

The sensitivity of fluorescent SWCNT-based sensors strongly depends on sensor brightness, with the brightest sensors demonstrating enhanced sensitivity and greater penetration depths *in vivo*. As shown in the previous chapters, SWCNT brightness can be increased through non-covalent functionalization using various surfactants, such as sodium cholate. Although we have shown in **Chapter 2** that it is possible to improve the selectivity of surfactant-SWCNTs by controlling the amount of exposed surface area, ultimately these sensors remain limited for *in vivo* and *in vitro* applications by their lower biocompatibility and the impracticality of maintaining constant bulk surfactant concentrations. In this chapter, we explore methods of increasing the brightness of DNA-SWCNTs by using chemically modified DNA sequences with the aim of creating brighter sensors that are also more suitable for use *in vivo* and *in vitro*.

We show that both the fluorescence intensity and sensor reactivity is strongly impacted not only by the chemical modification of the DNA but also by the method of preparation. Sensors prepared using MeOH-assisted surfactant exchange exhibited higher overall fluorescence, however the responsivity of these sensors is significantly reduced compared to SWCNTs prepared by direct sonication. We further demonstrate that modified DNA can enhance the fluorescence intensity of sonicated (GT)₁₅-SWCNTs while retaining their responsivity to dopamine, making these sensors an attractive alternative for dopamine sensing *in vivo* by enabling significantly higher penetration depths. As the increases in fluorescence intensity

were achieved without needing to alter the base sequence of the DNA wrapping or to add any exogenous compounds, these modifications can - in theory - be applied to nearly any DNA sequence to increase the brightness and penetration depths of a variety of DNA-SWCNT sensors without affecting biocompatibility or reducing the near-limitless sequence space available.

3.2 Introduction

The ultimate goal when designing biomedical sensors is to create a technology that can be used for continuous and long-term monitoring applications *in vivo*. In the brain, realizing such technologies could revolutionize health care by improving our understanding and treatment of many different neurological, psychiatric, and cognitive disorders. However, in order to understand both signalling between single neurons and through extended neural networks, it is essential to monitor neural activity over much larger volumes, ideally at high speeds while achieving synaptic resolution [239]. Unfortunately despite significant progress, no single technology or approach has yet been able to accomplish all the analytical requirements for widespread *in vivo* use in humans [62, 240, 241]. In addition, for *in vivo* brain imaging, sensors need to be able to transmit through not only tissue and skin, but also trans-cranially. This causes additional attenuation in the fluorescence of optical sensors, creating a need for the removal of overlying brain tissue and for craniotomies to enable sensing in subcortical structures [242].

An effective strategy for addressing this limitation is to use fluorophores, such as SWCNTs, with longer emission wavelengths, where light absorption and scattering by biological tissue is minimised [8, 9, 38, 190]. The molecular recognition capabilities of DNA-SWCNTs make them an attractive material for neurotransmitter detection and *in vivo* neural biosensing applications [14, 17, 36, 62, 77, 243–245]. However, low photoluminescence quantum yield (QY) values have limited the optical performance of DNA-SWCNTs and constrained their widespread applicability [30, 246, 247]. As shown in **Chapter 1** and **Chapter 2**, DNA-SWCNTs typically exhibit much lower fluorescence compared to surfactant-suspended nanotubes [30, 61, 104, 108, 248]. As the sensitivity of all nanosensor optical devices is strongly linked to the brightness of the emitting fluorophore [60], this creates problems for *in vivo* sensing applications. Furthermore, this limits the practical application of the sensors by reducing the penetration depth of the fluorescence emission [78, 249]. While there are advantages to using alternative wrappings, like surfactants, to increase the quantum yields of nanotube sensors [61], ultimately any wrapping replacing DNA sacrifices the increased biocompatibility and vast combinatorial library available for this biopolymer.

Previous attempts to increase DNA-SWCNTs have relied on modifications to the DNA base sequence [78] or the addition of exogenous compounds. However, many of the exogenous compounds reduce the biocompatibility of the sensors, as the additives (such as reducing agents or nanoparticles) can increase cytotoxicity and diminish sensitivity and/or selectivity of

the sensors. Moreover, as the fluorescence properties and molecular recognition capabilities of DNA-SWCNTs have been shown to vary depending on DNA sequence and length [17, 73, 78] there remains a need to identify alternative methods for increasing the fluorescence intensity of DNA-SWCNTs without substituting the wrapping sequence.

Recent work by Yang *et al.* has demonstrated that the method (direct sonication of MeOH-assisted surfactant exchange) used to prepare DNA-SWCNT suspensions can also significantly impact the resulting DNA-SWCNT complex [250]. Disparities in the fluorescence spectra for DNA-SWCNTs produced by the two methods indicated that the replacement process did not always result in the same DNA wrapping configuration compared to using direct sonication. Differences in the secondary structures of the DNA alters the fluorescence properties of the DNA-nanotube complex, but can also impact the recognition capabilities of the DNA-SWCNTs.

In this chapter, we focus on improving the fluorescence intensity of (GT)₁₅-SWCNTs through the preparation process and through the incorporation of DNA modifications in engineered DNA sequences. (GT)₁₅-SWCNTs are selected for their role in neurotransmitter sensing. Furthermore, these sensors suffer from low fluorescence intensities compared to other DNA-SWCNTs [61, 248]. As a result, there is great interest in increasing the relative fluorescence intensity of (GT)₁₅-SWCNTs, without compromising their sensitivity to dopamine, in order to increase the penetration depths of these sensors for *in vivo* applications. We examine how the fluorescence of DNA-SWCNTs is affected by the addition of different functional groups in the DNA wrapping sequence. Although the presence of the modifications did not hinder the sensor's ability to detect dopamine, we demonstrate that the preparation method significantly impacted the responsivity of the sensors and reduced the maximal fluorescence changes obtained on addition of analyte. Moreover, for sonicated samples, we show that using modified-DNA results in a significant increase in the fluorescence intensity, both before and after dopamine addition, that can increase the theoretical penetration depth for the sensors *in vivo*. These findings demonstrate a new approach for tuning the fluorescence behavior of DNA-SWCNTs for a given sequence and length, without compromising the sensing capabilities of the sensors or requiring the addition of any exogenous compounds.

3.3 Results and Discussion

Modified DNA sequences were chemically synthesized (Microsynth) to contain one of three functional groups: amino-, azide-, or thiol- (**Figure 3.1**). Due to the formation of DNA dimers, thiol-modified DNA was excluded from subsequent characterization (see **Appendix B** for more information). To investigate the impact of the location and number of modifications on the fluorescence behavior of the DNA-SWCNTs several amino-group modification combinations were designed for (GT)₁₅-SWCNTs. Details on the modifications and positions examined during this study are included in **Table 3.1**.

Chapter 3. Modifying DNA-SWCNT Sensors for Improved Dopamine Detection

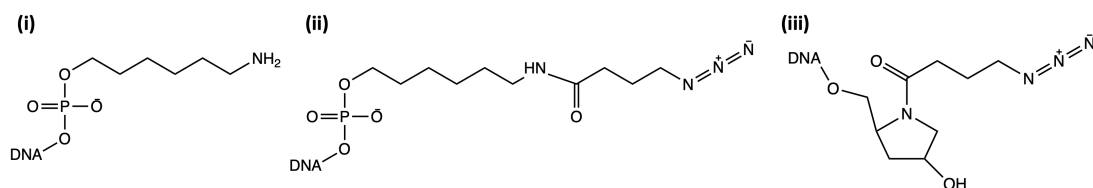


Figure 3.1 – Chemical structures of the functional groups and linker molecules used for terminal DNA modification: **(i)** amino, **(ii)** azide 5' and **(iii)** azide 3'. All chemical structures were drawn in ChemDraw. Internal modifications for the amino functionalisation were introduced using an amino-dT base (**Appendix Figure B.2**).

Table 3.1 – A list of functional groups and modification positions tested for improving the fluorescence intensity of (GT)₁₅-SWCNTs in this study. Internal modifications for the -NH₂ functional group were introduced using an amino-dT base (Microsynth) (**Appendix Figure B.2**).

	Modification	[Linker]	[Position]	Sequence Name
(GT) ₁₅	Unmodified		N/A	(GT) ₁₅
	Amino, -NH ₂	[C ₆]	[5']	(GT) ₁₅ Amino5'
			[3']	(GT) ₁₅ Amino3'
			[5' + 3']	(GT) ₁₅ Amino5'3'
			[5' + Interior]	(GT) ₁₅ Amino5'Int
			[5' + 3' + Interior]	(GT) ₁₅ Amino5'3'Int
	Azide, -N ₃	[NHS Ester]	[5']	(GT) ₁₅ Azide5'
			[3']	(GT) ₁₅ Azide3'

The absorbance spectra of all (GT)₁₅-SWCNTs were used to compare the wrapping behavior and suspension quality of the solutions that were prepared using direct sonication and MeOH-assisted surfactant exchange (**Figure 3.2**). All modified and unmodified DNA sequences were able to suspend the CoMoCAT SWCNTs, as evidenced by the distinct bands in the absorbance spectra and the low non-resonant background (**Figure 3.2 (A)**) [108]. As expected, the predominant peak in all spectra was observed at around 994 nm, which was associated with the first sub-band E₁₁ exciton transition for the (6,5) chirality nanotube. However, we observed differences in the relative absorbance values of the (6,5) peak depending on both the DNA modification and the method of preparation. Furthermore, the differences in full width half max (FWHM) values and peak-to-background ratios obtained for the different sequences indicated significant heterogeneity in the quality of suspension. Lower FWHM and higher peak-to-background values alongside higher yields indicate improved nanotube dispersion.

With the exception of the (GT)₁₅ Amino5'3'Int sequence, all modified (GT)₁₅-SWCNT suspensions prepared via direct sonication had lower FWHM values for the (6,5) chirality (**Figure 3.2 (B) (i)**) and higher peak-to-background ratios (**Figure 3.2 (B) (ii)**). These observations indicate an improved dispersion quality for these solutions compared to suspensions using the unmodified sequence (**Figure 3.2 (B)**). These observations suggest that the addition of the

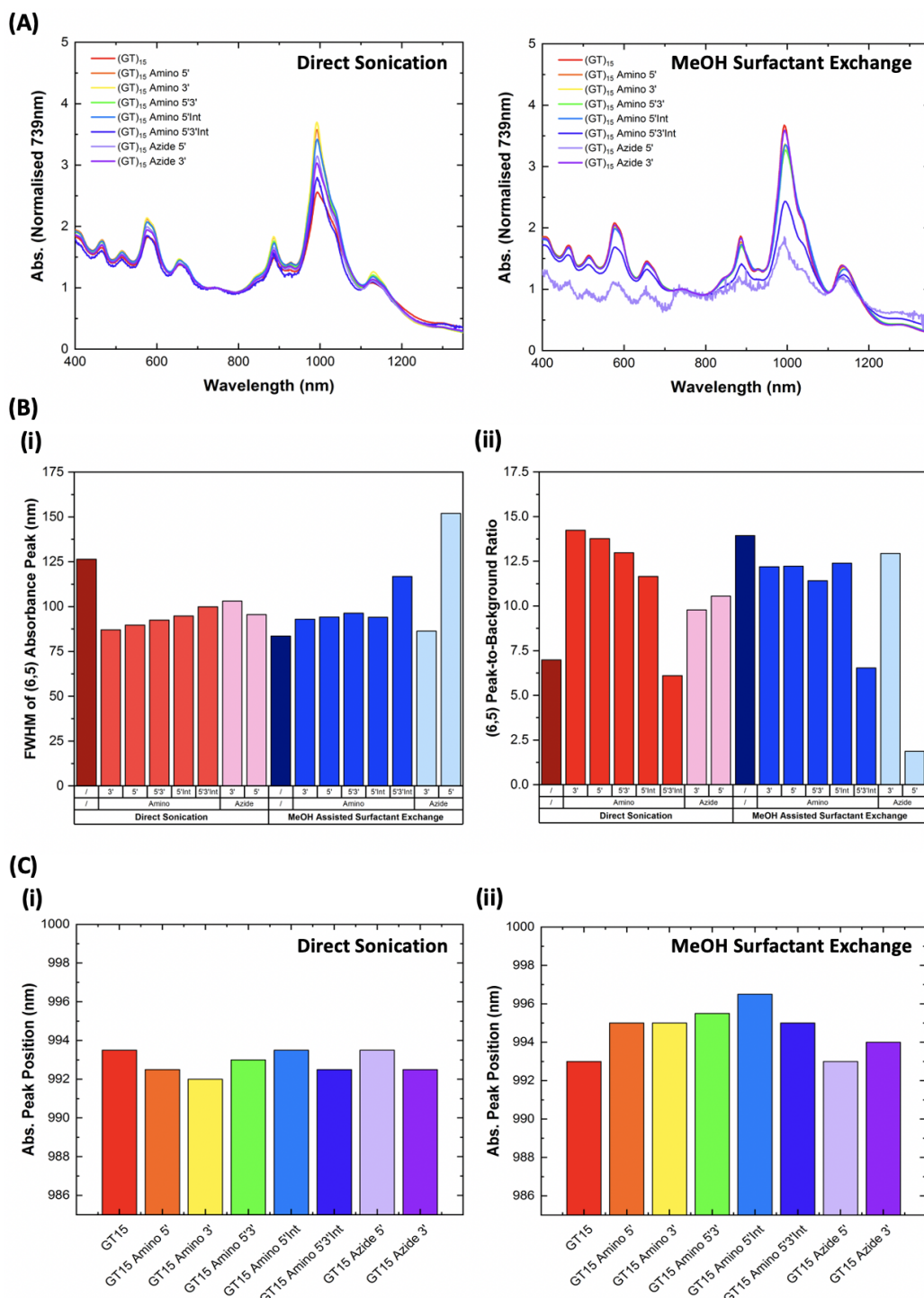


Figure 3.2 – Differences in the suspension quality and chirality distribution of modified and unmodified (GT)₁₅ sequences for SWCNT solutions prepared via direct sonication and MeOH-assisted surfactant exchange. **(A)** Absorbance spectra for all modified and unmodified DNA-SWCNT samples examined in this study. All spectra are normalized to concentration using an extinction coefficient of 0.0253 mg/L at Abs_{739nm}. **(B)** Comparison of the absorbance peak positions of the (6,5) chirality for modified and unmodified (GT)₁₅-SWCNTs prepared via **(i)** direct sonication and **(ii)** MeOH-assisted surfactant-exchange. **(C)** Characterisation of the quality of suspension based on the **(i)** FWHM and **(ii)** peak-to-background ratio for the (6,5) absorbance peaks of each suspension.

functional groups assisted with the exfoliation of the nanotube bundles during the sonication process, resulting in the higher yields and more individually dispersed solutions. (GT)₁₅ Amino5'3'Int-SWCNTs resulted in well dispersed nanotubes, indicated by the low FWHM. However, we obtained significantly lower total nanotube concentrations and observed a reduced peak-to-background ratio due to a lower relative concentration of suspended (6,5) nanotubes (**Table 3.2**). The reduced yield was, in part, attributed to the presence of the internal modification that was attached via an amino-dT base in the middle of the sequence (chemical structure detailed in **Appendix Figure B.2**). The addition of this internal modification could disrupt the π - π stacking of the DNA-sequence, which in turn destabilizes the wrapping or imposes additional steric restrictions. Interestingly, despite the same number of modifications, (GT)₁₅ Amino5'Int-SWCNTs exhibited a lower peak-to-background ratio, higher FWHM, and significantly lower maximum concentration-yield compared to (GT)₁₅ Amino5'3'-SWCNTs, again indicating that the presence of the internal modification reduced the suspension capabilities of the DNA sequence.

With the exception of (GT)₁₅ Azide5', the concentration of nanotube solutions was significantly higher for those prepared using the surfactant exchange protocol compared to direct sonication. In addition, contrary to the sonicated samples, the unmodified (GT)₁₅ yielded the highest quality and most concentrated SWCNT dispersions with the MeOH-assisted surfactant exchange method. In agreement with previous observations for sonicated samples, (GT)₁₅ Amino5'3'Int-SWCNTs resulted in a poorer suspension quality, although the yield and relative absorbance of the (6,5) peak was considerably higher for the surfactant exchanged samples. Due to the lower suspension quality and yields of samples prepared using (GT)₁₅ Azide5' and (GT)₁₅ Amino5'3'Int modifications, these samples were excluded from subsequent fluorescence characterization (see **Appendix B** for more detailed information, **Appendix Figure B.5, B.6, B.7**).

The electronic properties of SWCNTs are very sensitive to changes in their local environment, which can shift the position of peak absorbance and fluorescence [29, 250]. For suspensions prepared using direct sonication, the peak absorbance for the E₁₁ transition of the (6,5) peak remained at around 992.8 ± 0.6 nm independent of the modification type, position, or quantity. However, for surfactant exchanged samples, we observed a red-shift in the peak absorbance from 993.0 nm (unmodified) to 995.4 ± 0.7 nm for the amino modified sequences. Furthermore, the absorbance peak position was increasingly red-shifted as additional amino functional groups were added (from 0 to 1 to 2), with the largest red-shifting recorded for (GT)₁₅ Amino5'Int-SWCNTs. Red-shifted absorbance is commonly attributed to decreasing surface coverage [61, 250]. This suggests that the addition of the amino modifications to the (GT)₁₅ sequence resulted in reduced surface coverage for suspensions prepared via surfactant exchange. These findings highlight the impact of functional groups and linker molecules on both the physical and optical properties of the DNA-SWCNT, and furthermore support the hypothesis that sequences can wrap differently on the nanotube when different preparation methods are used to obtain SWCNT dispersions [250].

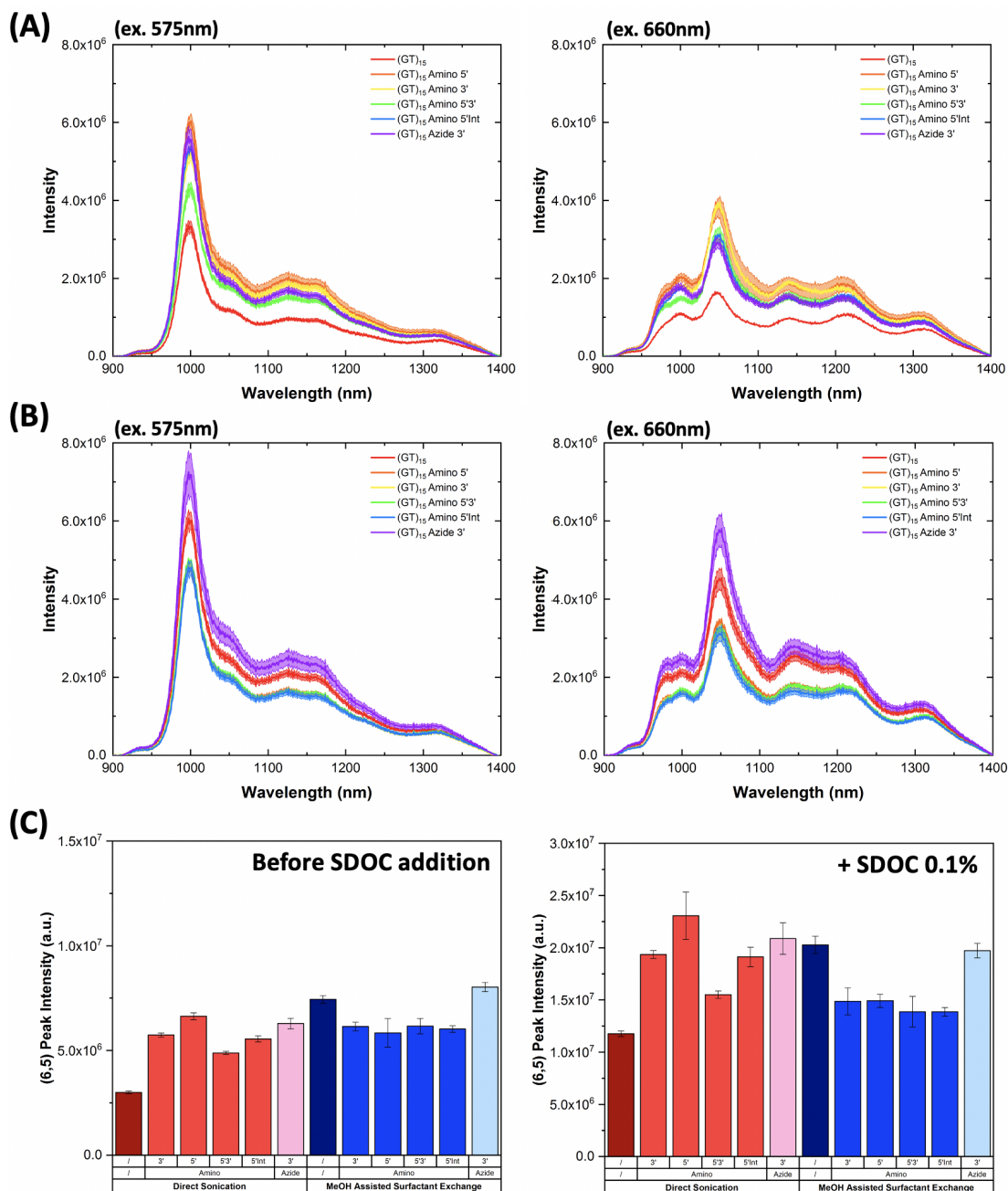


Figure 3.3 – Fluorescence characterisation of SWCNTs suspended with modified and unmodified DNA using direct sonication and MeOH-assisted surfactant exchange. **(A - B)** Fluorescence spectra of (GT)₁₅ samples suspended via **(A)** direct sonication and **(B)** using MeOH-assisted surfactant exchange. Graphs include spectra for SWCNTs suspended with unmodified (GT)₁₅ (red line) and modified (GT)₁₅. For all spectra, the central line represents the average spectrum with the shaded regions representing 1 σ standard deviation (n = 3 technical replicates) (excitation: 575 nm (left) and 660 nm (right)). All fluorescence spectra were normalized to concentration measured at 739 nm in the 384-well plate immediately prior to measurement to account for any minor variations. **(C)** Comparison of the absolute peak intensity of the (6,5) chirality (excitation: 575 nm) for modified and unmodified (GT)₁₅-SWCNTs before and after addition of SDOC (final SDOC concentration: 0.1%). Error bars represent 1 σ standard deviation (n = 3 technical replicates).

Chapter 3. Modifying DNA-SWCNT Sensors for Improved Dopamine Detection

Table 3.2 – A comparison of the concentration yields of SWCNTs suspended using direct sonication and MeOH-assisted surfactant exchange for both modified and unmodified (GT)₁₅.

Sequence	Direct Sonication (mg/L)	MeOH-assisted Surfactant Exchange (mg/L)
(GT) ₁₅	40.74	209.01
(GT) ₁₅ Amino 5'	72.50	195.01
(GT) ₁₅ Amino 3'	77.10	173.19
(GT) ₁₅ Amino 5'3'	125.50	168.91
(GT) ₁₅ Amino 5'Int	45.60	169.08
(GT) ₁₅ Amino 5'3'Int	10.22	41.99
(GT) ₁₅ Azide 5'	56.96	2.67
(GT) ₁₅ Azide 3'	62.84	158.36

To examine whether the chemical modifications affected the fluorescence behavior of the DNA-SWCNTs, we determined the *relative* quantum efficiency of the different suspensions by comparing fluorescence emission spectra collected under the exact same imaging conditions [78]. Significant increases were obtained in the peak fluorescence intensities for all modified (GT)₁₅-SWCNTs compared to unmodified (GT)₁₅-SWCNTs for suspensions prepared via direct sonication (**Figure 3.3 (A)**, **Appendix Figure B.8 (A)**, **B.9**). In addition to increases in the integrated fluorescence emissions, we also observed a chirality dependence of the fluorescence enhancement for certain modifications; for example the (GT)₁₅ Amino5'3' sequence produced a much larger intensity increase for the (7,5) than the (6,5) chirality. This chirality dependence was also observable in the PLE maps collected for the different suspensions (**Appendix Figure B.10**). A quantitative comparison of changes in the integrated intensity, as well as for the (6,5) and (7,5) chiralities, relative to the unmodified (GT)₁₅-SWCNT complex is shown in **Table 3.3**.

Table 3.3 – Fluorescence intensity change of the (6,5) and (7,5) chiralities for modified (GT)₁₅-SWCNTs compared to the respective (GT)₁₅-SWCNT complex. The integrated fluorescence intensity under the 575 nm excitation is labelled as ALL.

DNA Sequence	Direct Sonication			MeOH-assisted Surfactant Exchange		
	(6,5)	(7,5)	ALL	(6,5)	(7,5)	ALL
(GT) ₁₅ Amino3'	55.4 ± 5.8%	136.6 ± 2.0%	70.7%	-17.8 ± 4.1%	-30.2 ± 2.4%	-18.5%
(GT) ₁₅ Amino5'	79.6 ± 5.3%	132.1 ± 7.2%	87.2%	-19.6 ± 4.4%	-23.6 ± 2.2%	-18.4%
(GT) ₁₅ Amino5'3'	28.7 ± 5.5%	90.6 ± 6.2%	44.1%	-17.0 ± 3.8%	-27.4 ± 2.0%	-16.7%
(GT) ₁₅ Amino5'Int	58.7 ± 4.4%	89.1 ± 1.4%	62.0%	-20.6 ± 5.3%	-30.6 ± 3.4%	-20.5%
(GT) ₁₅ Azide3'	67.9 ± 6.4%	77.3 ± 4.5%	63.6%	19.5 ± 8.5%	27.9 ± 6.9%	18.4%

On the contrary, for samples prepared using MeOH-assisted surfactant exchange, only one sequence ((GT)₁₅ Azide3') exhibited higher fluorescence compared to unmodified (GT)₁₅ with an increase of 19.5 ± 8.5% for the (6,5) chirality. Furthermore, as shown in the PLE maps (**Appendix Figure B.10, B.11**), all surfactant exchanged samples contained much greater

amounts of large diameter chiralities compared to their sonicated counterparts. Similar chirality distributions were also observed for (AT)₁₅ and (N)₃₀-SWCNTs that were prepared by surfactant exchange. Interestingly, unmodified (GT)₁₅-SWCNTs that were prepared using the MeOH-assisted surfactant exchange method had significantly higher fluorescence intensities ($55.4 \pm 5.6\%$) compared to (GT)₁₅-SWCNTs prepared by direct sonication. Subsequent Raman analysis showed similarity in all Raman modes, specifically the D, G, and G' bands for samples prepared by direct sonication and MeOH-assisted surfactant exchange. This implies a common degree of disorder for both preparation methods, suggesting that the changes in fluorescence intensity were not a result of differences in defect density (see **Appendix Figure B.12** for more information).

To determine whether the increased fluorescence intensities were due to increasing surface coverage, we compared the fluorescence intensity of solutions before and after the addition of excess sodium deoxycholate solution (SDOC), which shows preferential binding affinity to SWCNTs [138]. Changes in wrapping homogeneity and exposed surface area of the nanotube are known to effect the QY of SWCNT suspensions [30, 61, 78]. However, at the same concentration, DNA-SWCNTs with fluorescence intensities that only differ due to QY should exhibit overlapping emission spectra following equilibration with SDOC [78]. As shown in **Figure 3.3 (C)**, differences in the fluorescence intensity values of modified and unmodified (GT)₁₅-SWCNTs (normalised to concentration at Abs_{739nm}) remained following the SDOC replacement for both sonicated and surfactant exchanged samples. Similarly, fluorescence spectra for (AT)₁₅- and (N)₃₀-SWCNTs also differed post-SDOC replacement, indicating that this was not a sequence specific effect (**Appendix Figure B.17, B.19**). The continued variance of peak intensity values post-replacement implies that the differences in fluorescence intensity are not exclusively a QY effect, but rather largely a result of chirality preferences during the suspension process for the different DNA sequences. Additionally, absorbance spectra collected post-SDOC replacement also showed differences in the relative peak intensities for samples which had been prepared by MeOH-assisted surfactant exchange, further supporting the hypothesis that the modified wrappings showed different affinities towards specific chiralities (**Figure B.18**). As a result, we attributed the increase in fluorescence observed for the (6,5) peak under resonance excitation (575 nm) to differences in the relative abundance of this chirality in the different suspensions. Nevertheless, the increase we obtained for modified (GT)₁₅-SWCNTs prepared via sonication would enable much greater penetration depths compared to their non-modified counterpart using either the 575 nm or 660 nm excitation (**Appendix Table B.3**).

As recent studies have shown that DNA sequences can have different equilibrium structures depending on their preparation methods [250], we sought to investigate the differences in the maximal turn-on response for non-modified (GT)₁₅-SWCNTs prepared via sonication and surfactant exchange (**Figure 3.4**). Consistent with previous observations [14, 15, 61, 62], the addition of dopamine increased the fluorescence intensity of all samples. However, while the initial fluorescence intensity of the (6,5) peak was higher for (GT)₁₅-SWCNTs prepared via MeOH-assisted surfactant exchange, we observed a reduction of more than 50% in the

Chapter 3. Modifying DNA-SWCNT Sensors for Improved Dopamine Detection

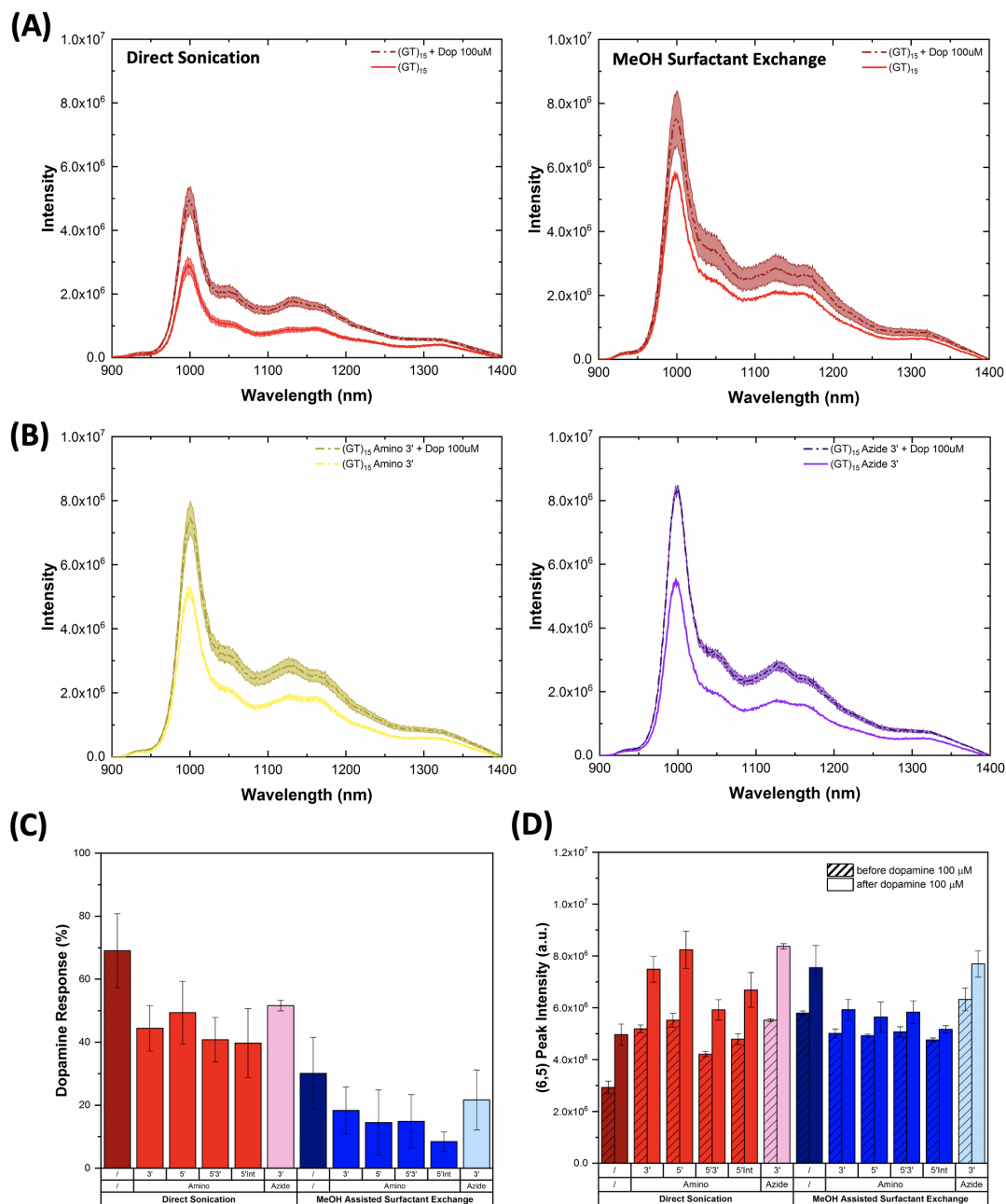


Figure 3.4 – Dopamine response of modified and unmodified (GT)₁₅-SWCNTs. **(A)** Fluorescence spectra of (GT)₁₅-SWCNTs prepared via direct sonication and MeOH-assisted surfactant exchange before (solid line) and after (dashed line) addition of dopamine (final concentration: 100 μ M, excitation: 575 nm). **(B)** Representative fluorescence spectra of modified (GT)₁₅-SWCNTs prepared by direct sonication before (solid line) and after (dashed line) addition of dopamine (final concentration: 100 μ M, excitation: 575 nm). For all spectra, the central line represents the average spectrum with the shaded regions representing 1 σ standard deviation (n = 3 technical replicates). **(C)** Fluorescence intensity increase following the addition of dopamine. Error bars represent 1 σ standard deviation (n = 3 technical replicates). **(D)** (6,5) peak intensity values before (dashed colour) and after (solid colour) dopamine addition (final concentration 100 μ M, excitation: 575 nm). Error bars represent 1 σ standard deviation (n = 3 technical replicates).

turn-on response of the sensor following the addition of dopamine (reduced from 69% to 30%). Moreover, maximal changes in fluorescence (defined as $(I_f - I_0)/I_0$, where I_f is the final intensity and I_0 is the initial intensity) were reduced for all modified (GT)₁₅-SWCNTs prepared using the surfactant exchange method (**Figure 3.4 (C)**, **Appendix Figure B.21**). The decrease in responsivity for these SWCNT suspensions was attributed to the different wrapping configurations of the DNA on the surface of the nanotube [250]. Supporting this hypothesis, all nanotube suspensions prepared using MeOH-assisted surfactant exchange also exhibited lower reactivity towards changes in pH and towards the addition of reducing agents such as dithiothreitol (DTT) (**Appendix Figure B.24, B.26-B.28, B.29, B.31-B.35**). These observations suggest that, independent of any chemical modifications, each preparation method resulted in a fundamentally different DNA configuration on the surface of the nanotube, in agreement with recent observations by Yang *et al.* [250].

While we did observe a slight decrease in the turn-on response, the fluorescence enhancement of the modified (GT)₁₅-SWCNTs relative to the unmodified sequence (for sonicated samples) was retained following the addition of dopamine (**Figure 3.4 (C)**, **Appendix Figure B.20**). Furthermore, all sonicated samples exhibited maximum intensity changes of at least $2.4 \times$ that of their surfactant-exchanged counterpart. As shown in **Table B.2**, the absolute intensity increase following dopamine addition ($I_f - I_0$) to the sonicated samples was comparable to the magnitude obtained using unmodified (GT)₁₅-SWCNTs and even increased for certain modifications. Moreover, given that both the baseline fluorescence and fluorescence post dopamine addition was higher for modified (GT)₁₅-SWCNTs, these sensors could enable *in vivo* sensing at significantly higher penetration depths than unmodified (GT)₁₅-SWCNTs (**Appendix Table B.3**) [78, 249], without comprising on responsivity.

3.4 Conclusions

In this chapter we examined the effect of DNA modifications on the fluorescence properties of the resulting SWCNT complexes. We demonstrated that modified DNA can alter the fluorescence behavior of resulting SWCNT complexes, both in terms of fluorescence intensity and responsivity. Furthermore, we showed more generally that the properties of a DNA-SWCNT complex are strongly dependent on which preparation method is used, even for SWCNTs suspended using unmodified DNA. This dependence is largely attributed to differences in the secondary structures adopted by the DNA on the surface of the nanotube, in agreement with recent findings by Yang *et al.* [250].

While the presence of DNA modifications resulted in higher fluorescence intensities for SWCNT complexes produced by direct sonication, lower intensities were observed for modified DNA samples prepared using the MeOH-assisted surfactant exchange process. Moreover, we observed that the fluorescence intensity of unmodified (GT)₁₅-SWCNTs was also significantly lower for sonicated samples compared to those prepared via surfactant exchange. Further examination into these differences using Raman spectroscopy found no appreciable

difference in the density of defects between the samples. Additional studies using surfactant replacement suggested that the observed fluorescence changes were due to chirality enhancement, rather than exclusively QY effects. This also explains the variance in chirality distributions observed between the PLE maps of sonicated and surfactant replacement samples as the preparation method is known to influence the equilibrium structures of DNA-SWCNT hybrids in a way that is dependent on the DNA-sequence and chirality [250]. However, this enhancement still enabled significant improvements in the theoretical penetration depths for all modified (GT)₁₅-SWCNTs prepared via direct sonication compared to their unmodified counterpart for both the (6,5) and (7,5) chirality peaks.

Interestingly, despite the higher baseline fluorescence of SWCNTs prepared using the MeOH-assisted surfactant exchange method, these samples suffered from a significantly reduced turn-on response to dopamine. A similar lack in responsivity was also observed towards reducing agents and pH changes. This lack of responsivity was furthermore shown to be largely independent of base composition. On the contrary, modified (GT)₁₅-SWCNTs prepared by sonication retained the sensitivity to dopamine in spite of their higher baseline fluorescence. This retention is particularly important for many applications *in vivo* where a high fluorescence intensity is crucial for improved sensing at higher penetration depths.

In summary, although MeOH-assisted surfactant exchange is a versatile and scalable approach to preparing SWCNTs, this method of preparation can alter the wrapping of the DNA on the surface of the nanotube compared to sonication. Such changes in the wrapping configurations can decrease the reactivity of the sensors to target analytes meaning that MeOH-assisted surfactant exchange may not always be the best approach for producing SWCNT suspensions for sensing applications. This observation highlights the importance of carefully selecting which preparation method is used to prepare SWCNT suspensions for sensing applications to avoid any unwanted loss of sensitivity or responsivity. Furthermore, for (GT)₁₅-SWCNTs prepared by direct sonication we observed that the incorporation of chemical modifications on DNA sequences could be used to increase the intensity of the fluorescence emission. Moreover, the enhancement described herein was achieved without changing the base composition or adding any exogenous compounds, which is important for retaining the intrinsic properties of the DNA-SWCNT complex. We believe that this knowledge can be used as a generic methodology to artificially engineer DNA-SWCNTs for various sensing applications by creating sensors with enhanced fluorescence that enable significantly increased imaging depths *in vivo*.

3.5 Materials and Methods

3.5.1 Materials

All DNA oligomers were purchased from Microsynth. Chemicals were purchased from Sigma-Aldrich, unless otherwise specified. Purified CoMoCAT SWCNTs were purchased from CHASM Technologies, Inc. (SG65i, batch LOT No. SG65i-L59).

3.5.2 Preparation of the DNA-SWCNT suspensions

Suspensions of purified CoMoCAT (Sigma Aldrich SWeNT SG65i, batch MKBN5945V) SWCNTs were prepared using two different methods (1) direct sonication and (2) MeOH-assisted surfactant exchange. All DNA-SWCNT solutions were stored at 4°C between measurements in order to mitigate aggregation of the SWCNTs [225]. Three ssDNA sequences were used in this study, (GT)₁₅, (AT)₁₅, and N₃₀ both unmodified and with various modifications (see **Table 3.1** and **Appendix Table B.1** for more information on the modifications used). N₃₀ is a random mixture of 30-mer DNA sequences where the exact sequences are not known (1.15×10^{18} unique DNA sequences).

(1) Direct sonication

1 mg of CoMoCAT SWCNTs was added to a 1 mL solution of ssDNA (100 μ M in DI water, Microsynth) and sonicated (140mm, Q700, Qsonica) for 90 min (power = 40 W) in an ice-bath. This was followed by a 4 h centrifugation step (Eppendorf Centrifuge 5424R) at $21,130 \times g$ and 4°C to remove SWCNT aggregates. The supernatant of the suspensions (~ 80% of the solution) was extracted and subsequently washed as detailed below to remove any impurities and unbound DNA from the solution (**Figure B.36**).

(2) MeOH-assisted surfactant exchange

Sodium cholate (SC)-suspended SWCNTs were used for the modified surfactant exchange protocol as previously described in Chapter 2 [61]. The SC-SWCNTs used for the procedure were prepared according to the procedure by Zubkovs *et al.* [37]. Briefly, 25 mg of CoMoCAT SWCNTs were added to 25 mL of 2% (w/v) SC solution. The mixture was homogenized for 20 min at 5,000 rpm (Polytron PT 1300 D, Kinematica) and subsequently sonicated using probe-tip sonication (1/4 in. tip, Q700 Sonicator, Qsonica) for 1 h (10% amplitude) in an ice bath. The resulting solution was centrifuged at $164,000 \times g$ (30,000 rpm) for 4 h at 20°C (Optima XPN-80 Ultracentrifuge, Beckman) to remove any remaining nanotube aggregates.

To perform the MeOH-assisted surfactant exchange, 400 μ L of SC-SWCNTs were mixed with 400 μ L of ssDNA solution (75 μ M in DI water). The same SC-SWCNT stock was used for all suspensions to ensure a similar starting distribution of nanotube chiralities and lengths for all samples. DNA concentrations were measured and adjusted based on absorbance measurements (Nanodrop 2000, Thermo Scientific). 1.2 mL of methanol (VWR Chemicals) was added to the DNA and SC-SWCNT mixture to obtain a final solvent percentage of 60% (v/v) and a final DNA concentration of 15 μ M (**Figure B.37**). The solution was vortexed briefly to mix and subsequently incubated for 2 h at room temperature. Following the incubation, all MeOH, displaced surfactant, and unbound DNA was removed by rinsing the solutions according to the procedure detailed below.

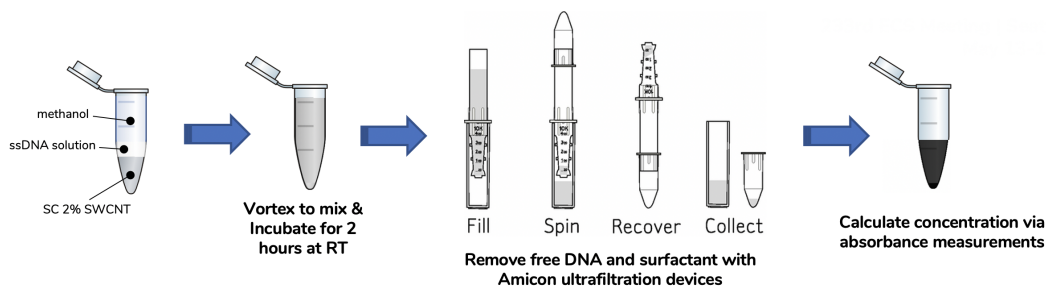


Figure 3.5 – Schematic of MeOH-assisted surfactant exchange protocol for SWCNT suspension preparation.

Amicon rinsing for DNA-SWCNT purification

In order to remove impurities (such as remaining catalyst particles, surfactant, MeOH) and unbound DNA from the DNA-SWCNT suspensions, all solutions were purified using Amicon centrifugal ultra-filtration devices (Amicon Ultra-2, Sigma Aldrich, 100 kDa membrane, Merck). Prior to use, the filtration devices were rinsed two times with DI water in accordance with the manufacturer's recommendations. The solution of DNA-SWCNTs was subsequently added to the filtration device and rinsed eight times with 1 mL aliquots of DI water (devices were centrifuged at $3,000 \times g$ 4°C for 2 min for each rinsing step). The rinsed suspension was collected from the filtration device and centrifuged for a minimum of 1 h at $21,130 \times g$ and 4°C to remove any additional SWCNT aggregates that may have formed during the rinsing process. The supernatant solution was extracted and subsequently characterised using a UV-Vis-NIR scanning spectrometer (Shimadzu 3600 Plus) with a quartz cuvette (Suprasil quartz, path length 3 mm, Hellma).

3.5.3 Absorption spectroscopy

Absorbance spectra were acquired for all samples using a UV-Vis-NIR scanning spectrometer (UV-3600 Plus, Shimadzu) with a quartz cuvette (Suprasil quartz, path length 3 mm, Hellma). The concentrations for all samples were calculated using an extinction coefficient $\epsilon_{739\text{nm}} = 0.0253 \text{ L mg}^{-1} \text{ cm}^{-1}$ [226]. All nanotube suspensions were diluted to 33 mg/L, corresponding to $\text{Abs}_{739\text{nm}} = 0.253$, unless otherwise specified.

SDOC replacement samples were prepared by mixing 90 μL of SWCNT solution (33 mg/L) with 10 μL of SDOC 1% (w/v). Spectra for the samples were collected prior to addition and following a period of 10 min incubation post-addition.

3.5.4 Fluorescence spectroscopy measurements

Fluorescence emission spectra were acquired using a custom-built optical set-up with an inverted Nikon Eclipse Ti-E microscope (Nikon AG Instruments), as described previously [37]. Briefly, samples were excited using a pulsed super-continuum laser coupled with a tuneable band-pass filter unit (SuperK Extreme EXR-15 and Super K VARIA, NKT Photonics). The fluorescence signal was collected using an IsoPlane SCT-320 spectrometer (Princeton Instruments) coupled to an InGaAs NIR camera (NIRvana 640 ST, Princeton Instruments). Measurements were recorded with LightField (Princeton Instruments) in combination with a custom-built LabView (National Instruments) software for automation purposes. An exposure time of 5 s and laser excitation with band width of 10 nm and relative power of 100% was used for all measurements, unless stated otherwise. Fluorescence emission spectra were collected at wavelengths between 900 nm and 1400 nm using a dispersive grating of 75 lines mm^{-1} . All experiments were performed in 384-well plates (Clear Flat-Bottom Immuno Nonsterile 384-Well Plates, MaxiSorp, Life Technologies) which were sealed (Empore Sealing Tape Pad, 3M) prior to each fluorescence measurement to prevent evaporation.

Photoluminescence measurements

50 μL aliquots of DNA-SWCNT solutions ($\sim 33 \text{ mg/L}$) were added to a 384-well plate and photoluminescence excitation (PLE) maps were acquired between 500 nm and 800 nm using a 5 nm step and 5 s exposure time. Additional samples were used to acquire on a resonance fluorescence emission spectra for the (6,5) chirality (at $575 \pm 5 \text{ nm}$) and (7,5) chirality (at $660 \pm 5 \text{ nm}$). Absorbance values at 575, 632, 660, 739, and 808 nm were collected immediately prior to measurement using a Varioskan LUX microplate reader to ensure that the concentrations of the nanotubes were comparable. All spectra were normalised to the concentration determined at $\text{Abs}_{739\text{nm}}$. Results were analysed using a custom Matlab code (Matlab R2017b, Mathworks) for the PLE maps and custom Python codes for the on-resonance spectra.

Dopamine detection assay

10 mM solutions of dopamine (dopamine hydrochloride) were freshly prepared in DI water immediately prior to measurement. Fluorescence spectra were initially acquired for all DNA-SWCNT solutions (49.5 μL , $\sim 33 \text{ mg/L}$) in a 384-well plate using a laser excitation of $575 \pm 5 \text{ nm}$. Following the initial measurement, 0.5 μL of dopamine solution (10 mM) was added to the SWCNT suspension. Solutions were mixed by pipetting up and down several times. The suspensions were incubated for 10 min at room temperature in the dark prior to recording the second fluorescence spectrum.

Chapter 3. Modifying DNA-SWCNT Sensors for Improved Dopamine Detection

Surfactant replacement assay

Surfactant replacement of the DNA-SWCNT solutions was performed using 1% (w/v) SDOC. 5 μL of SDOC was mixed with 45 μL aliquots of the DNA-SWCNT solutions ($\sim 33 \text{ mg/L}$) and incubated at room temperature for 10 min. Fluorescence spectra were acquired before and after SDOC addition using an excitation of $575 \pm 5 \text{ nm}$.

pH and DTT assay

Baseline fluorescence spectra were acquired for all DNA-SWCNT solutions (49.5 μL , $\sim 33 \text{ mg/L}$) in a 384-well plate using an excitation of $575 \pm 5 \text{ nm}$. Following this, 0.5 μL of either NaOH 0.02 M, NaOH 0.1 M, or DTT was added to the SWCNT suspension. Solutions were mixed by pipetting up and down several times. Prior to recording the second spectrum, suspensions were incubated for 10 min at room temperature.

Confocal Raman microscopy

Samples were prepared for Raman microscopy by drop casting 10 μL of DNA-SWCNT solution (10 mg/L) onto cleaned glass slides (Coverslip $24 \times 55 \times 0.15 \text{ mm}$, Fisher Scientific). Raman spectra were recorded at an excitation wavelength of 532 nm at 100% relative power with 5 s exposure time. The spectrometer was calibrated before measurements using an internal standard. Spectra were collected between $100 - 2750 \text{ cm}^{-1}$ using a water-immersion $100 \times$ L objective on a confocal spectroscope (inVia Raman Microscope, Renishaw) with a grating of $1,800 \text{ lines mm}^{-1}$.

Gel electrophoresis

Unbound DNA was removed from DNA-SWCNT samples prepared by direct sonication and MeOH-assisted surfactant exchange by rinsing with Amicon centrifugal ultra-filtration devices (Amicon Ultra-2, Sigma Aldrich, 100 kDa membrane, Merck), as detailed above. Samples were diluted to a concentration of 1 mg/L (extinction coefficient $\epsilon_{739\text{nm}} = 0.0253 \text{ L mg}^{-1} \text{ cm}^{-1}$ [226]) and DNA was extracted using phenol-chloroform isoamyl (PCI). Equal volumes of DNA-SWCNT suspension and PCI solution (Sigma-Aldrich 25:24:1) were combined and vortexed for 30 s. The solution was centrifuged at $16,000 \times g$ for 5 min (at room temperature). The aqueous top phase was collected and DNA was subsequently precipitated by ethanol precipitation in the presence of sodium acetate and glycogen (Carl Roth, final concentration of 1 g/L) [251]. The DNA pellet was washed with 70% ethanol to remove salts and finally resuspended in 10 μL of DI water.

Extracted DNA was mixed with equal volumes of $2 \times$ formamide loading buffer. The samples were denatured by incubating the mixture at 95°C for 5 min and immediately quenching it on ice before loading the solution onto the gel. The samples were run on a denaturing 15%

3.5. Materials and Methods

urea-polyacrylamide gel in 1 × Tris/Borate/EDTA (TBE) buffer at 200 V for 1 h. Three dilutions (1 ×, 0.5 ×, and 0.2 ×) were run for each DNA sequence. SYBR Gold dye (0.2 ×, Thermo Fisher) as used to stain the DNA. Fluorescence was recorded following 30 min of staining on a blue-light gel image (E-Gel, Thermo Fisher). In order to compare the size of the DNA fragments, a ssDNA ladder (10 – 100 nucleotides) was run in the last lane of the gel.

4 XNA-Nanosensors for Enhanced Stability Against Ion-Induced Fluorescence Perturbations

*But if I'm not the same, the next question
is, Who in the world am I?
Ah, that's the great puzzle!*

Lewis Carroll, *Alice's Adventures in
Wonderland*

*Portions of this chapter are reproduced with permission from [35]: Gillen, A.J.; Kupis-Rozmyslowicz, J.; Gigli, C.; Schuergers, N.; Boghossian, A.A. **Xeno Nucleic Acid Nanosensors for Enhanced Stability Against Ion-Induced Perturbations**, *Journal of Physical Chemistry Letters* (2018).*

4.1 Abstract

The omnipresence of salts in biofluids creates a pervasive challenge in designing sensors suitable for *in vivo* applications. Fluctuations in ion concentrations have been shown to affect the sensitivity and selectivity of optical sensors based on single-walled carbon nanotubes wrapped with single-stranded DNA (DNA-SWCNTs). We herein observe fluorescence wavelength shifting for DNA-SWCNT-based optical sensors in the presence of divalent cations at concentrations above 3.5 mM. In contrast, no shifting was observed for concentrations up to 350 mM for sensors bioengineered with increased rigidity using xeno nucleic acids (XNAs). Transient fluorescence measurements reveal distinct optical transitions for DNA- and XNA-based wrappings during ion-induced conformation changes, with XNA-based sensors showing increased permanence in conformational and signal stability. This demonstration introduces synthetic biology as a complementary means for enhancing nanotube optoelectronic behavior, unlocking previously unexplored possibilities for developing nano-bioengineered sensors with augmented capabilities.

4.2 Introduction

The near-infrared (NIR) emission of single-walled carbon nanotubes (SWCNTs) lies within the optical transparency window of biological materials [9], where water, blood, and tissue absorption are minimal. The increased tissue penetration of SWCNT NIR fluorescence, combined with their indefinite photo-stability [40], makes optical SWCNT-based sensors attractive for continuous monitoring applications in biological samples and even for use *in vivo*. Optical SWCNT sensors have already been successfully used for miRNA detection in urine and serum [10], real-time deep-tissue brain imaging [252, 253], and glucose detection in both whole blood and *in vivo* [215]. Single-stranded DNA (ssDNA)-wrapped SWCNTs (DNA-SWCNTs) are among the most widely used SWCNT-based conjugates for optical biosensing [10, 90, 133]. The non-covalent functionalisation of SWCNTs with DNA is based on π -stacking of the aromatic nucleotide bases with the hydrophobic side-wall of carbon nanotubes [130]. This functionalisation preserves the optoelectronic properties and enhances biocompatibility in addition to greatly improving nanotube solubility in aqueous solutions. In contrast to other wrapping polymers, DNA allows for nearly limitless sequence variation, with DNA-suspended SWCNTs showing sequence-dependent fluorescence intensity and wavelength responses [14, 36, 124]. These favorable attributes have motivated numerous studies on the behavior of various oligonucleotide wrapping sequences, both in how they suspend and interact with different SWCNT chiralities and how they can be used to detect various analytes of interest [10, 40, 130, 134, 147, 215].

The majority of studies on oligonucleotide-suspended SWCNTs, including applications in biosensing and bio-imaging, have focused on bio-analyte detection in deionized (DI) water or in buffered solutions containing standardised salt concentrations. Several studies have previously explored the effects of metal ions and counterions on both surfactant-suspended [254–256] and bio-functionalised [80, 131, 257–259] nanotubes [260–262]. In both types of SWCNT suspensions, the presence of certain ions was shown to induce aggregation of the nanotubes in solution. Brege *et al.* demonstrated fluorescence quenching of sodium dodecylbenzenesulfonate (SDBS)-suspended nanotubes in the presence of low amounts (< 0.5 mM) of certain metal ions, particularly group II and XII cations such as Mg^{2+} , Ca^{2+} , and Zn^{2+} . Recently, Salem *et al.* reported that DNA undergoes a conformation change on the surface of the SWCNT, identifiable via a fluorescence intensity increase that is triggered by varying the concentration of NaCl present in the system [80]. In addition, the varying monovalent salt concentration was shown to affect the fluorescence response of the DNA-SWCNT complex to both pH changes and the molecular recognition of riboflavin. Since the majority of optical SWCNT sensors rely on increases or decreases in fluorescence intensity across different chiralities for analyte detection [14, 36, 37, 80, 215, 263], these findings suggest that inherent variation in bio-fluid salt concentrations may alter the fluorescence intensity and sensing capabilities of these oligonucleotide-based sensors [264].

In this study, we performed a systematic investigation on the effects of multivalent salts on the fluorescence emission of DNA-wrapped nanotubes by exploring varying ion concentra-

tions covering the physiological ranges found in common biofluids. Through concomitant monitoring of both fluorescence intensity and wavelength shifting, we identified the transient formation of intermediate DNA-SWCNT optical states within our system. This study further introduces the use of *xeno nucleic acid* (XNA) based wrappings, synthetic oligonucleotides with tailored mechanochemical properties, designed to limit ion-induced fluorescence drift in unprocessed biological samples, offering a new basis for improving sensor performance.

4.3 Results and Discussion

Semiconducting HiPco SWCNTs were individually dispersed using known sequences of DNA, including (GT)₁₅, (GT)₂₃, and DNA₁₅₅ (detailed sequence information is provided in **Appendix Table C.1**). Since the (7,6) and (7,5) chiralities were the most dominant species within the samples, we focused on monitoring the responses of these chiralities in the presence of the metal cations. SWCNT solutions were encapsulated into a gel matrix to eliminate aggregation in the presence of metal cations [131, 257, 261] (assembly information provided in **Methods and Preparation, Figure 4.6**). As shown in **Figure 4.1 (A)**, the addition of divalent cations (0.5 M CaCl₂) induces a shift in the wavelength position of certain SWCNT chiralities. Contrary to this, no shift in peak position was observed upon addition of < 0.5 M of NaCl, in agreement with the recent study by Salem *et al.* [80], which showed a dependence of fluorescence intensity on the ionic strength of monovalent salts due to changes in oxygen accessibility. We therefore focus the remainder of this study on the behavior of DNA-SWCNT in the presence of divalent cations, where red-shifts (> 4 nm) in the fluorescence peak wavelength position were observed.

Fluorescence emission spectra were collected for DNA₁₅₅-SWCNT (**Figure 4.1 (B)**), DNA(GT)₁₅-SWCNT (**Appendix Figure C.1 (B), C.1 (D)**), and DNA(GT)₂₃-SWCNT (**Appendix Figure C.1 (C), C.1 (E)**) over a range of CaCl₂ and MgCl₂ concentrations to investigate the dependence of the divalent cation-induced wavelength shift on DNA sequence and length. Concentration-dependent shifting is seen across multiple SWCNT chiralities (**Figure 4.1 (B)**), with pronounced changes observed for the (7,5) chirality. In addition, the introduction of Ca²⁺ and Mg²⁺ cations is shown to trigger a comparable response, irrespective of the DNA sequence, demonstrating an overall increase in the degree of shifting with increasing cation concentration. These results suggest that the response is independent of both sequence length and nucleotide composition for the sequences studied.

Additional measurements were carried out in the presence of a wider selection of salts for the DNA₁₅₅ sequence, given the particular interest of this sequence in possible applications for

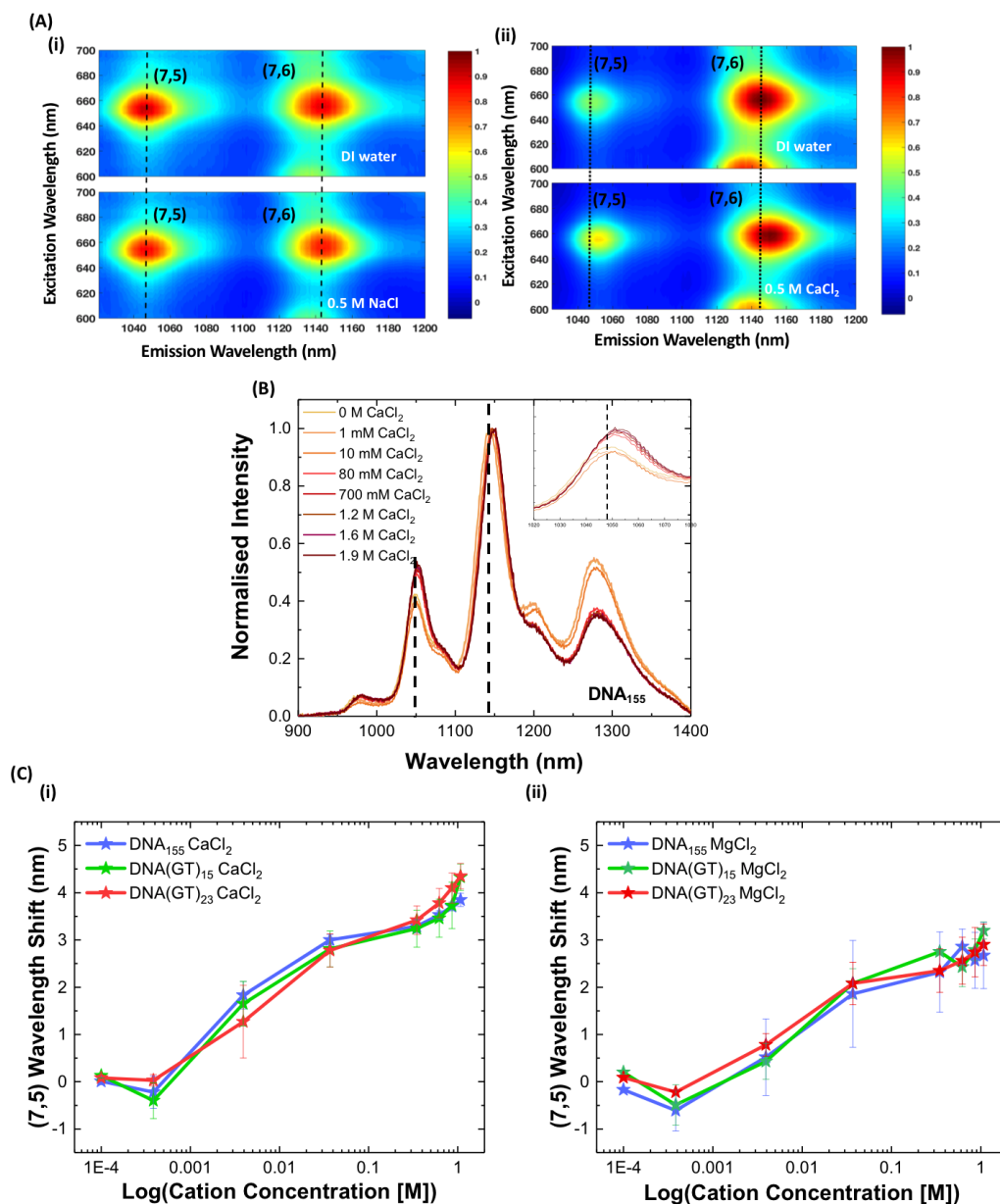


Figure 4.1 – (A) Monovalent vs. divalent salt effects on DNA-SWCNT fluorescence. Representative photoluminescence map illustrating DNA-SWCNT fluorescence response of (7,5) and (7,6) chirality peaks for DNA₁₅₅ upon addition of (i) 0.5 M NaCl and (ii) 0.5 M CaCl₂. All peaks were normalised to the maximum fluorescence emission intensity, corresponding in both instances to the (7,6) chirality emission. The vertical dashed lines at 1049.5 nm and 1142.9 nm are shown to highlight the corresponding (7,5) and (7,6) peaks, respectively. (B) Response of SWCNTs in the presence of varying CaCl₂ concentrations. Representative normalised fluorescence emission spectra show the wavelength response of DNA₁₅₅-suspended SWCNTs (excitation: 660 nm. Inset: response of the (7,5) chirality peak). (C) Comparison of the wavelength shift of the (7,5) chirality peak for DNA₁₅₅-SWCNT, (GT)₁₅-SWCNT, and (GT)₂₃-SWCNT following the addition of various concentrations of (i) CaCl₂ or (ii) MgCl₂. All error bars represent 1 σ standard deviation (n = 3 technical replicates, excitation: 660 nm, emission: 1045 nm).

miRNA detection [10]. Salts commonly found in biological fluids, such as Ca^{2+} and Mg^{2+} , which can range between 5 – 12 mM, or Fe^{2+} , which can range between 9 – 30 mM in blood [265–268], vary widely not only across different patients, but also over time within the same patient. As such, we examined a wide range of concentrations (**Table 4.1**) within the solubility limits of each salt. Spectra were collected over a period of 30 minutes for the predominant (7,5) and (7,6) peaks at 660 nm excitation. A concentration-dependent red-shift in the fluorescence peak position of the (7,5) (**Figure 4.2**) and (7,6) (**Appendix Figure C.3**) chiralities was observed, with maximum recorded shifts exceeding 4 nm. Similar behavior was observed for both chiralities in the presence of a range of divalent ions, irrespective of the counteranion species (individual ion measurements are presented in **Appendix Figure C.5** and **C.6**). Comparable shifting occurred in mixed solutions of CaCl_2 and MgCl_2 , where the total ion concentration equalled that of the pure solutions, suggesting that total ionic strength, rather than cation identity, is responsible for the observed fluorescence shifting.

Table 4.1 – Summary of metal ion complexes and the corresponding range of concentrations studied in the presence of DNA-SWCNTs. Varying salt concentrations were added to gel-encapsulated SWCNTs to eliminate effects of dilution or potential aggregation. An asterisk indicates solutions where a narrower concentration range was analysed due to limited solubility of the salt in DI water at room temperature.

Metal Cation	Counterion	Concentration Range
Na^+	Cl^-	0.4 mM - 1.1 M
K^+	Cl^-	0.4 mM - 0.9 M*
Mg^{2+}	Cl^-	0.4 mM - 1.1 M
	Br^-	0.4 mM - 0.6 M*
	SO_4^{2-}	0.4 mM - 0.6 M*
Ca^{2+}	Cl^-	0.4 mM - 1.1 M
	Br^-	0.4 mM - 1.1 M
Mn^{2+}	Cl^-	0.4 mM - 1.1 M
Fe^{2+}	Cl^-	0.4 mM - 1.1 M

Variations in the fluorescence emission of DNA-SWCNTs have been previously linked to DNA conformational changes on the surface [10, 131, 257], suggesting that changes in DNA conformation may also account for the wavelength shifting observed in this study (**Figure 4.3 (A)**). Phenomena such as solvatochromism (solvent Stark effect) have been shown to induce wavelength shifting in the fluorescence spectra of DNA-SWCNTs. This effect is caused by a change in the dipole moment upon photoexcitation, which results in the rearrangement of the surrounding solvent molecules. In turn, this rearrangement induces a difference in the solvation energy of the molecule between the ground and excited states for different micro-environments and solvents, stabilising the latter [29, 233]. Solvatochromic shifts, ΔE , can be understood in terms of dipolar interactions between the polarised SWCNT and the solvent, and they are found to vary with the polarity or, more specifically, the local dielectric constant of the solvent. Since the SWCNT is more strongly polarised in the excited state, the excited state enjoys greater stabilisation with increased access to polar solvents such as water, resulting in a diminished energy gap and red-shifting of the fluorescence emission [233, 264].

Chapter 4. XNA-Nanosensors for Enhanced Stability Against Ion-Induced Fluorescence Perturbations

Choi *et al.* proposed a proportional relationship between the dielectric constant of the solvent, ϵ , and the E_{ii} transitions [29],

$$(E_{ii})^2 \Delta E_{ii} \propto \frac{\epsilon - 1}{2\epsilon + 1} \quad (4.1)$$

where E_{ii} is measured in vacuum. Since the local dielectric constant is a function of the adsorbed wrapping and intercalating solvent molecules [29, 40], this relationship suggests that the observed fluorescence red-shifting on addition of the metal cations is due to an increase in the dielectric constant of the local SWCNT environment. This change is believed to be a result of alterations to wrapping conformation that affect solvent accessibility, which, in turn, modulates the transition energy.

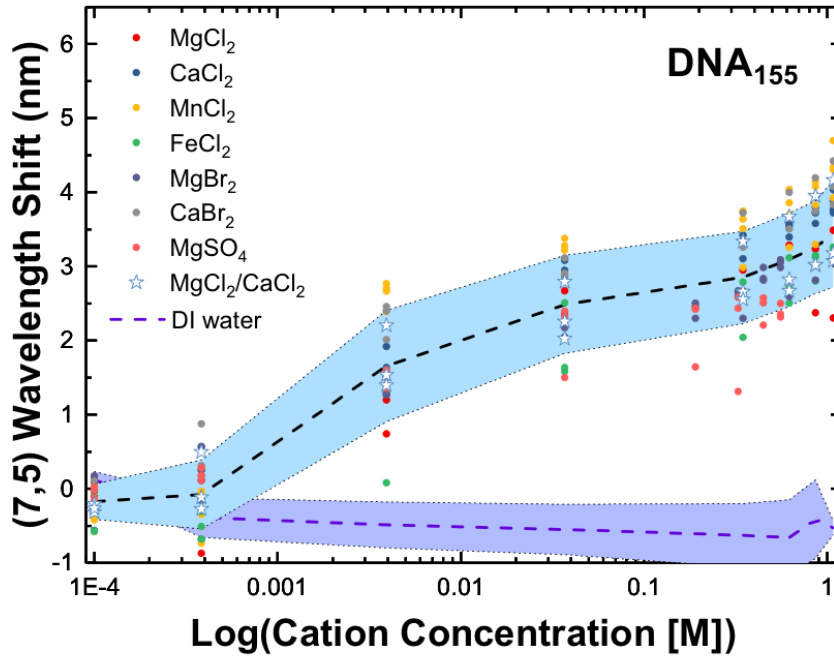


Figure 4.2 – Concentration-dependent shift in the wavelength position of the (7,5) peak upon the addition of various M^{2+} ions (excitation: 660 nm). The dashed line represents the average wavelength shift for the maximum emission peak upon addition of M^{2+} ions or water only, with the shaded regions representing 1σ standard deviation ($n = 3$ technical replicates). These measurements were performed using SWCNTs wrapped with DNA₁₅₅. A 1:1 molar ratio of MgCl₂ and CaCl₂ was used for the MgCl₂/CaCl₂ mixture.

To study the DNA conformation changes, we continuously monitored DNA-SWCNT fluorescence upon addition of various metal cations using the gel-based system (**Figure 4.6**). Compared to solution, the gel matrix is expected to decrease the diffusion of the analyte and consequently slow the rate of the kinetics of the DNA conformational changes. As shown in **Figure 4.3 (B)** (and **Appendix Figure C.13**), the DNA-SWCNTs undergo a comparable, though

more attenuated and gradual, fluorescence response when encapsulated within an agarose gel matrix compared to the response in aqueous solution. The slower kinetics in the gel system allowed us to capture a transient spike in fluorescence intensity (**Figure 4.3 (C)**), suggesting the formation of a metastable intermediate state between the two equilibrium DNA conformations on the SWCNT surface. The increased fluorescence intensity of this intermediate state, schematically shown in the center panel of **Figure 4.3 (A)**, overlaps with the maximum rate of fluorescence shifting. Similar intermediate states have been reported for free dsDNA, which is believed to adopt a stretched transient state during a salt-induced conformational change [269].

Several factors have been reported to contribute to fluorescence intensity increases, including oxygen exclusion, charge-transfer, and electronic interactions [124, 138, 270]. Increased oxygen exclusion can occur with increased DNA surface coverage, which has been shown to concomitantly alter the accessibility of water molecules. As discussed by Choi *et al.* and Salem *et al.*, dielectric and charge screening effects of salts have been shown to reversibly modulate fluorescence intensity, with fluorescence increasing with salt concentrations [29, 80, 138, 271, 272]. These studies suggest that cation accumulation in the surrounding microenvironment of the SWCNT (center panel of **Figure 4.3 (A)**) can give rise to increased SWCNT coverage in the intermediate state by screening the negatively charged phosphate groups of the DNA. The resulting intensity peak in this model would thus be attributed to either increased water and oxygen shielding due to the tighter wrapping conformation or altered electronic interactions between the DNA and SWCNT [124, 138]. The simultaneous red-shifting of the SWCNT fluorescence, which has been linked to decreased water shielding [10, 264], suggests that the latter mechanism based on altered electronic interactions may dominate. This tightly-bound transient conformation is hypothesised to relax with time to adjust for cation-cation repulsion at higher local ionic concentrations. Furthermore, the observed fluorescence recovery and transitional dip in fluorescence intensity upon salt removal through EDTA chelation (**Figure 4.3 (C)**) shows that this process is reversible.

The solution-phase conformational changes of DNA in the presence of divalent salts were directly studied using circular dichroism (CD) measurements. Salt-induced conformation changes have been firmly established for free dsDNA solutions [269], including the B-to-Z transformation that is observed in the presence of high salt concentrations [273–276]. Increased cation concentrations increase the screening of the negative phosphate group along the DNA backbone [277], enabling a tighter wrapping conformation around the SWCNT [257]. Conformational changes for DNA₁₅₅-SWCNT, DNA(GT)₁₅-SWCNT, and DNA(GT)₂₃-SWCNT in the presence of divalent salts were confirmed via changes in the ellipticity upon addition of either 0.5 M Ca²⁺ or 0.5 M Mg²⁺ (**Figure C.7**). Immediate changes in the CD spectra were observed for all DNA strands, with only marginal differences in the spectra detected with respect to time, indicating that the new steady-state equilibrium was reached in a matter of seconds. This behavior is in agreement with that reported for dsDNA [269] and the kinetics obtained from the fluorescence measurements collected in solution (**Figure 4.3 (B)**).

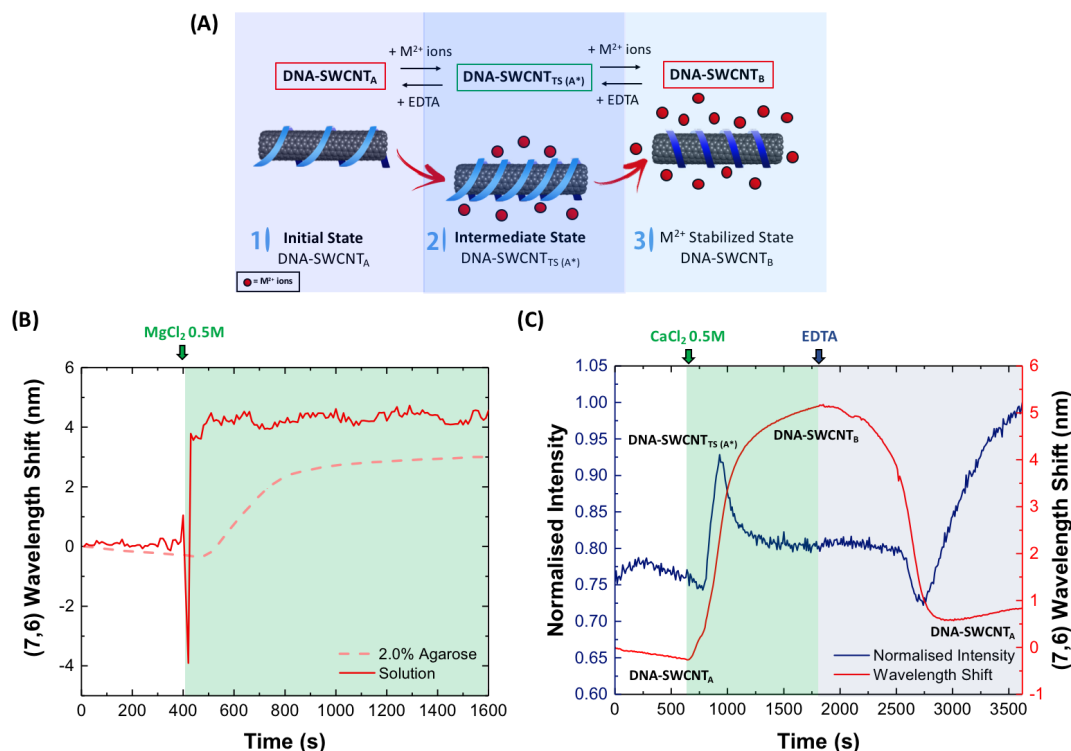


Figure 4.3 – Reaction kinetics and proposed mechanism. **(A)** Schematic of the proposed reversible conformational change of DNA on a SWCNT in the presence of M^{2+} . The light blue ribbon represents the suspending DNA wrapped around the SWCNT in one conformation and the dark blue ribbon represents DNA in another conformation. Metal cations are represented by red dots. **(B)** Fluorescence response of the (7,6) peak of DNA₁₅₅-SWCNTs upon addition of 0.5 M MgCl₂ in solution (solid line) and the agarose gel matrix (dotted line) (excitation: 660 nm). **(C)** Kinetic measurements of the fluorescence response in terms of both wavelength (red) and intensity (blue) of the (7,6) chirality peak for (GT)₁₅ DNA-wrapped SWCNTs upon addition of 0.5 M CaCl₂ (excitation: 660 nm). The fluorescence intensity is normalised by the maximum recorded intensity. The arrows show the addition times of CaCl₂ and EDTA.

The proposed mechanism would suggest that oligonucleotides with increased conformational rigidity, such as certain synthetic organic polymers or XNAs, should be more resistant to salt-induced fluorescence shifting. An advantage of choosing XNAs over other synthetic polymers is that increased steric restriction is achieved without compromising the biocompatibility or sequence variability offered by oligonucleotide wrappings. To explore the effect of rigidity on shifting, SWCNTs were suspended with locked nucleic acid (LNA), which is a synthetic nucleic acid analogue of ribonucleic acid (RNA) containing a methyl bridge within the sugar groups along the polymer backbone. The presence of these bridges restricts the movement of the nucleotides and locks the strand into the 3'-endo (North) conformation that is often found in A-form DNA duplexes [278–282]. LNA₁₅₅, which shares sequence identity with DNA₁₅₅ except for having all thiamine bases locked (25% of the sequence), showed a diminished fluorescence response to divalent metal cations compared to DNA₁₅₅ (**Figure 4.4**). In contrast to DNA, the CD measurements of LNA (**Figure 4.4 (A)**) show no change in ellipticity

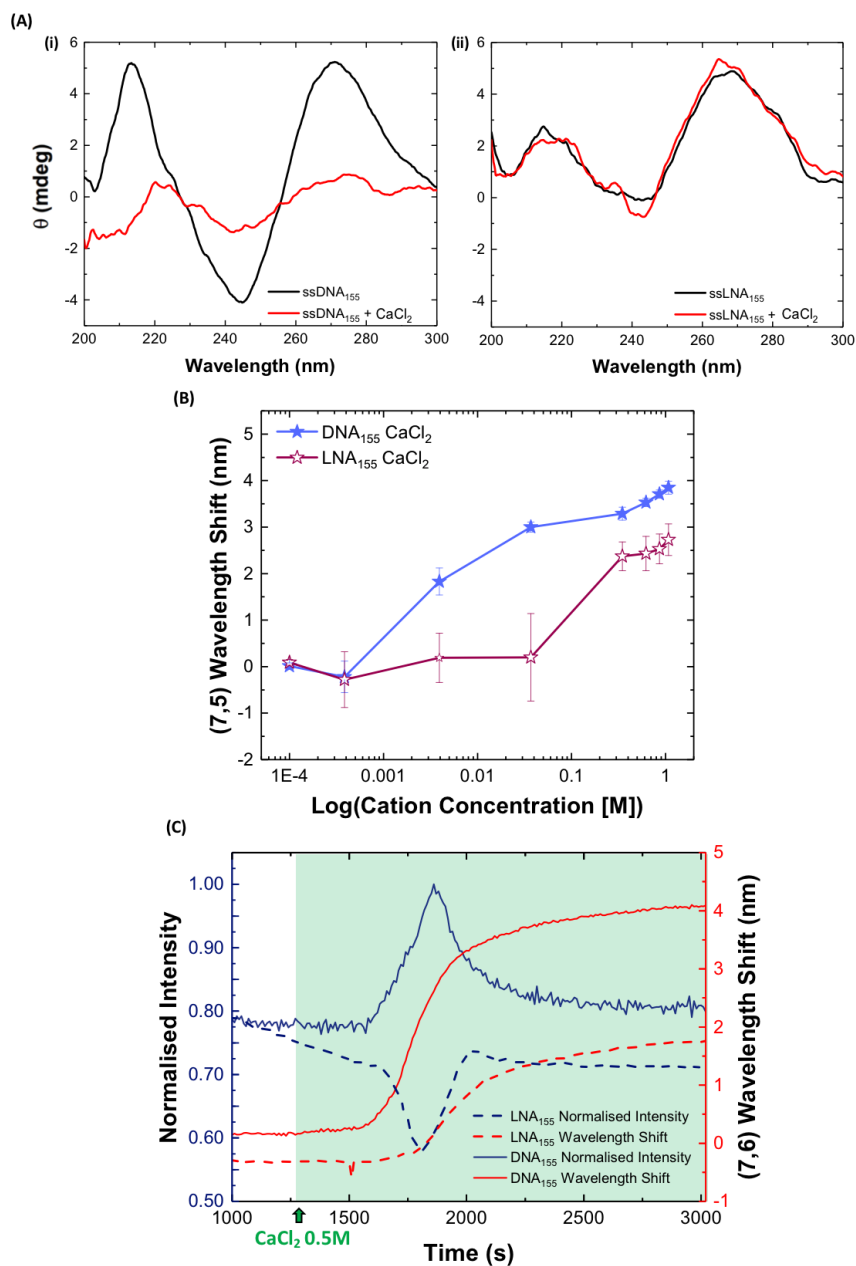


Figure 4.4 – Response of LNA-SWCNT complexes in the presence of Ca^{2+} ions. **(A)** Circular dichroism measurements of DNA₁₅₅ and LNA₁₅₅ before and after addition of CaCl_2 . **(B)** Wavelength shifting of the (7,5) chirality peak for the DNA₁₅₅- and LNA₁₅₅-wrapped SWCNTs upon addition of Ca^{2+} ions. All error bars represent the standard deviation ($n = 3$ technical replicates, excitation: 660 nm, emission: 1045 nm). **(C)** Time-lapse fluorescence emission response of the (7,6) chirality peak for DNA₁₅₅-SWCNTs and LNA₁₅₅-SWCNTs in the presence of CaCl_2 .

at equivalent concentrations of CaCl_2 (0.5 M). Compared to DNA₁₅₅, over two orders of magnitude higher concentrations of M^{2+} ions are needed to induce a fluorescence response (**Figure 4.4 (B)**). Moreover, even at high concentrations, the magnitude of the peak shifts is reduced by approximately 30% for the (7,5) (**Figure 4.4 (B)**) and 15% for the (7,6) peaks (**Appendix**

Figure C.12), indicative of greater LNA conformational-stability in the presence of high salt concentrations.

A comparison of the time-lapse measurements (**Figure 4.4 (C)**) shows a local minimum in the intensity response for the LNA sequence with increasing salt concentrations, instead of the characteristic intensity spike seen for the DNA intermediate. This drop in intensity is hypothesised to be caused by a weakening of the interaction between the LNA and the surface of the SWCNT in its intermediate state, a mechanism that is consistent with the electronic interactions that are proposed to dominate the DNA-SWCNT intensity change. Whereas DNA can freely re-orientate along the surface of the nanotube to maximise the π -stacking interaction, the presence of the methyl bridges restricts the movement of the LNA, forcing the LNA to withdraw from the surface of the nanotube during the intermediate state of the conformational change.

4.4 Conclusions

The results presented in this study show a reversible, concentration-dependent wavelength shift of DNA-SWCNT fluorescence in the presence of divalent cations. This fluorescence shifting occurs in the presence of divalent cations and is distinct from the fluorescence response towards monovalent ions where only intensity changes have been reported [80]. Although the nature of this multivalent-specificity remains an ongoing area of research, comparisons of concentration thresholds and the time-lapse fluorescence response offer several key insights into the underlying mechanism of salt-induced conformational and optoelectronic responses. Monovalent cations induce no measurable shifting, even when exceeding twice the concentration that prompts fluorescence shifting by divalent ions, suggesting that the increased ionic strength of divalent salts is not solely responsible for the recorded shifting. Instead, we suggest that the differences in the response behavior upon addition of monovalent and divalent ions is due to an inability of monovalent ions to interact with more than one phosphate group in the DNA backbone, resulting in a reduced screening effect at equivalent ion concentrations [273].

A transient fluorescence intensity spike, which occurs when the rate of fluorescence shifting is maximum, suggests the formation of a metastable intermediate state as the DNA undergoes a conformational change. Based on previous reports in the literature [29, 80, 124, 138, 271, 272] and our own observations, this suggests that cation accumulation in the surrounding microenvironment affects the interaction of the DNA with the SWCNT surface. This change affects the arrangement of the DNA, resulting in an intensity peak, which we attribute to heightened π -stacking interactions between the DNA bases and SWCNT. In agreement with this hypothesis, a decrease in the fluorescence intensity of LNA-SWCNTs was observed during the intermediate state of the conformational changes due to weaker base stacking interactions as a result of the increased conformational restrictions.

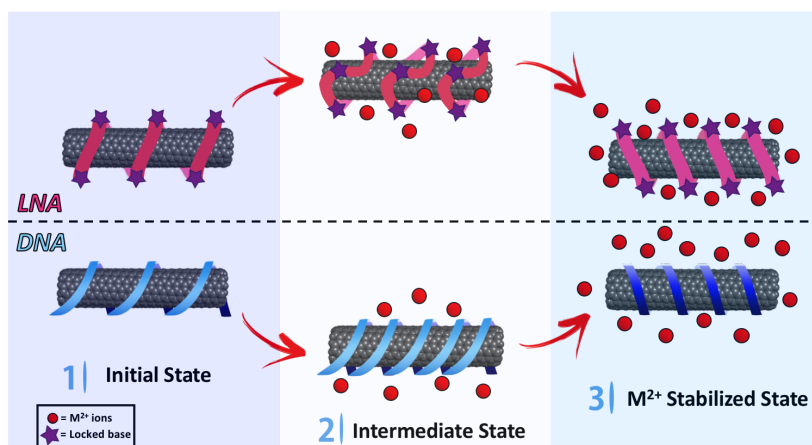


Figure 4.5 – Comparison of the proposed conformational changes of DNA and LNA on a SWCNT in the presence of M^{2+} . The pink and blue ribbons represent the suspending LNA and DNA, respectively, wrapped around the SWCNT, and the purple stars the locked bases. Metal cations are represented by red dots.

The salt-induced conformational changes, which were corroborated using CD measurements, are in agreement with observations in literature for free dsDNA [257, 273–275, 277]. LNA-SWCNTs, which are rigid biopolymers with locked conformations, show no measurable conformational changes and a diminished fluorescence shift in the presence of equivalent salt concentrations. Instead, salt concentrations above the physiological range [267, 268] are required to induce a fluorescence response with LNA-based complexes. These nano-bioengineered hybrids therefore contribute a previously unexplored approach to addressing the pervasive challenge of ion-induced fluorescence drift in optical biosensing. Given the variability of salts in electrolyte-rich biofluids such as urine and blood, the additional stability these hybrids confer is essential for accurate trend analysis used for continuous *in vivo* monitoring. This stability is especially crucial for monitoring patients suffering from hyperparathyroidism, electrolyte imbalances, or recovering from recent surgery, which show elevated calcium and magnesium concentrations. The permanence of LNA to salt-induced fluorescence perturbations can thus be used as a general basis for designing sensors with improved diagnostic capabilities.

4.5 Materials and Methods

4.5.1 DNA-suspension of SWCNTs

Purified HiPco SWCNTs (1 mg, NanoIntegris Lot. No. HP26-019 and HP29-064) were suspended in 1 mL of oligonucleotide solution (100 μ M dissolved in DI water, Microsynth (DNA) and Exiqon (LNA)). The mixture was sonicated using a Cup Horn sonicator (140 mm, Qsonica) for 90 min (power = 40 W) in an ice-bath, followed by a centrifugation step (Eppendorf Centrifuge 5424R) for 4 h at $16,750 \times g$ and 4°C to remove SWCNT aggregates. The subsequent

Chapter 4. XNA-Nanosensors for Enhanced Stability Against Ion-Induced Fluorescence Perturbations

supernatant was dialysed for 12 h in 2 L of DI water using a 14,000 Da MWCO cellulose membrane (Sigma Aldrich). The DNA sequences used for suspension included a sequence referred to as DNA₁₅₅, as well as (GT)₁₅ and (GT)₂₃. The XNA used in this investigation was LNA₁₅₅, which is equivalent in sequence to DNA₁₅₅ with all the T bases in the sequence locked via a methyl bridge, and it was purchased from Exiqon (Denmark). Detailed sequence information is provided in **Appendix Table C.1**. Absorbance spectra were acquired using a UV-Vis-NIR scanning spectrometer (Shimadzu 3600 Plus). The concentrations for HiPco samples were calculated using an extinction coefficient $\text{Abs}_{632\text{nm}} = 0.036 \text{ L mg}^{-1} \text{ cm}^{-1}$ and all samples were diluted to a final SWCNT concentration of 50 mg/L.

4.5.2 Gel sensor construction

35 μL of DNA-SWCNTs in DI water (50 mg/L) were concentrated using a 10 μL silica bead suspension and 500 μL PE buffer (QIAEX II Preparation Kit, QIAGEN). The DNA wrapped around the SWCNT is electrostatically adsorbed to the silica beads, and hence the complex can be extracted from solution using this technique, while the ethanol-containing PE buffer efficiently removes salt contaminants. This mixture was incubated at room temperature for 10 – 30 min. The samples were centrifuged for 90 s at $21,130 \times g$ (Eppendorf Centrifuge 5424R). The supernatant was discarded and the remaining pellet of DNA-SWCNTs and silica beads was allowed to dry briefly before being re-suspended in 10 μL of PE buffer. 40 μL of 2% agarose gel (Ultrapure Agarose, Invitrogen) was added to a well of a 96-well plate and gels were allowed to solidify for 1 – 3 minutes). The silica-bound DNA-SWCNT hybrids were added to the top of the gel. Once the beads are added to the gel, the DNA-SWCNT complex diffuses from the surface of the bead to give locally high concentrations of sensor complexes. The DNA-SWCNT complexes are assumed to have detached from the beads on contact with the agarose gel due to the disrupted electrostatic interaction. As a result, the silica beads are not limiting the movement of DNA on the SWCNT surface nor affecting the behavior of the sensor, which is corroborated by the similar response observed in the absence of beads (**Figure 4.3 (B)**). An additional layer of 2% agarose (40 μL) was added on top to create the concentrated SWCNT ‘sandwich gel’.

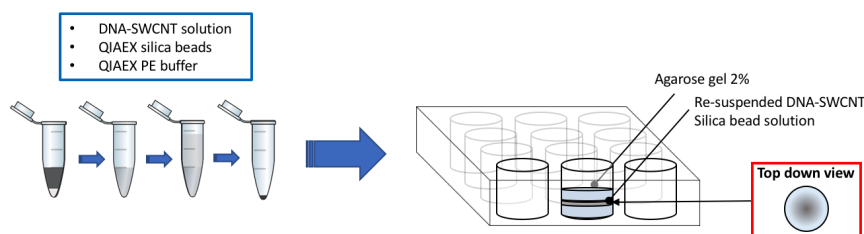


Figure 4.6 – Schematic of the gel preparation process in a 96-well plate set-up.

4.5.3 Fluorescence spectroscopy measurements

Fluorescence emission spectra were acquired from gel-based sensor systems in a 96-well plate setup using a custom-built optical setup with an inverted Nikon Eclipse Ti-E microscope (Nikon AG Instruments) as described previously [37]. Briefly, sandwich gel sensors were prepared using 2% agarose gel (Ultrapure Agarose, Invitrogen) in a 96-well plate (as described above) and excited at 660 ± 5 nm (HiPco SWCNT). Emission spectra were collected at wavelengths between 900 nm and 1400 nm and spectral data were fitted using custom Lorentzian fitting functions in MATLAB. For measurements shown in **(Figure 4.2)**, spectra were collected over a period of 30 min for the predominant (7,5) and (7,6) peaks at 660 nm excitation.

5 XNA-Nanosensors for Improved Neurochemical Sensing

Curiouser and curiouser!

Lewis Carroll, *Alice's Adventures in Wonderland*

5.1 Abstract

To date, the engineering of single-stranded DNA-SWCNT (DNA-SWCNT) optical biosensors have largely focused on creating sensors for new applications with little focus on optimising existing sensors for *in vitro* and *in vivo* conditions. As previously described in **Chapter 4**, recent studies have shown that nanotube fluorescence can be severely impacted by changes in local cation concentrations. This is particularly problematic for neurotransmitter sensing applications as spatial and temporal fluctuations in the concentration of cations, such as Na^+ , K^+ , or Ca^{2+} , play a central role in neuromodulation. This can lead to inaccuracies in the determination of neurotransmitter concentrations using DNA-SWCNT sensors, which limits their use for detecting and treating neurological diseases.

In this chapter, we present new approaches using locked nucleic acid (LNA) to engineer SWCNT sensors with improved stability towards cation-induced fluorescence changes. By incorporating LNA bases into the $(\text{GT})_{15}$ -DNA sequence, we create sensors that are not only more resistant towards undesirable fluorescence modulation in the presence of Ca^{2+} but that also retain their capabilities for the label-free detection of dopamine. The synthetic biology approach presented in this work therefore serves as a complementary means for enhancing nanotube optoelectronic behavior, unlocking previously unexplored possibilities for developing nano-bioengineered sensors with augmented capabilities.

5.2 Introduction

Neurotransmitters play a central role in a variety of biological functions that rely on chemical communication [55, 283]. Imbalances or signalling problems of key neurotransmitters, such

as dopamine, serotonin, and γ -aminobutyric acid (GABA) [283–286], are often linked to the pathology of many neurological diseases, including Alzheimer's and Parkinson's disease. The prevalence of these diseases is unfortunately expected to increase as the global population ages [287], contributing to not only greater mortality, but also a severely compromised quality of life. State-of-the-art treatments could be improved by real-time measurements of neurotransmitter concentrations, however the current lack of selective, responsive, and minimally invasive technologies limits personalized treatment options and patient comfort.

Several of these limitations have been overcome with the development of optical biosensors based on single-walled carbon nanotubes (SWCNTs). SWCNTs can be conceptualised as cylindrically rolled sheets of graphene whose optoelectronic properties vary with diameter and chirality. The semiconducting chiralities show distinct intrinsic fluorescence emissions that enable multimodal sensing in mixed chirality samples. Furthermore, these emissions span the second near-infrared optical window, which overlaps with the optical transparency window for biological tissue. This optical overlap, along with the SWCNT's resistance to photobleaching, makes SWCNTs suitable for deep-tissue, long-term, and continuous *in vitro* and *in vivo* imaging [30]. SWCNTs have also shown high spatial and temporal resolution, which is particularly important for the real-time, spatiotemporal monitoring of neurotransmitters [15, 62]. The selectivity preferences of these SWCNT-based optical sensors toward neurotransmitters, such as dopamine [14, 17, 62, 78] and serotonin [61, 288] can be modulated by non-covalently functionalizing the SWCNT surface with specific sequences of single-stranded DNA (ssDNA). Following either direct sonication or dialysis exchange, the ssDNA has been shown to self-assemble onto the SWCNT surface through π - π stacking of the bases. In addition to solubilizing the nanotubes, the ssDNA can alter the nanotube fluorescence response towards specific analytes in a sequence- and length-dependent manner, thus enabling preferential selectivity towards analytes of interest. Such optical SWCNT sensors have been used for *in vivo* brain imaging and *in vitro* spatiotemporal dopamine mapping of neurons [17, 59, 62, 252, 289].

As discussed in **Chapter 4**, nanotube fluorescence can be severely impacted by changes in local cation concentrations [35, 80]. This sensitivity to fluctuating cation concentrations is particularly detrimental to neurotransmitter sensing applications, where cells communicate via changes in concentrations of neurotransmitters and neuromodulators that are often triggered by fluxes of cations such as Ca^{2+} [55, 290–293]. In fact, the competitive responsivity of many existing ssDNA-SWCNT dopamine sensors to such cations limits the application of these sensors in efforts to untangle the complex signalling dynamics of the brain [17, 35, 80]. Consequently, the real-time, selective detection of physiological concentrations of dopamine in the absence of ionic or salt interference remains an ongoing challenge.

In this chapter, we build upon our previous observations in **Chapter 4** and present a SWCNT-based sensor capable of detecting dopamine with suppressed cation responsivity. We bioengineer a DNA(GT)₁₅¹, which has previously been shown to respond to both dopamine [14] and

¹DNA(GT)₁₅ represents a DNA sequence that is 30 bases long consisting of 15 repeating GT units.

various cations [35], by incorporating locked nucleic acid (LNA) bases at various positions throughout the sequence. We characterized the different LNA wrappings, examining their suspension quality, morphologies, and optoelectronic effects. We identified certain LNA sequences that showed increased conformational resilience to fluctuating cation concentrations [35]. In addition, all the LNA sensors sustained their selective dopamine responsivity, allowing us to demonstrate dopamine detection in the presence of cationic species. Furthermore, via concomitant monitoring of multiple chiralities, we showed that certain LNA sequences enable, for the first time, the selective detection of both Ca^{2+} and dopamine simultaneously.

5.3 Results and Discussion

We compared the solubilisation and fluorescence properties of the original $(\text{GT})_{15}$ to those of seven distinct single-stranded LNA-based derivatives (**Figure 5.1**). As summarized in **Figure 5.1**, the designed LNA sequences differed in terms of the percentage of locking, the type of base locked (either T or G), and the location and distribution of locking (detailed sequence information is provided in **Appendix Table D.1**). All tested LNA sequences were able to suspend the SWCNTs to varying extents, as evidenced by the dark solutions obtained post dialysis (**Appendix Figure D.1**) as well as from the bright fluorescence peaks and distinct bands in the absorption spectrum for each of the solutions (**Figure 5.2 (A) and (B)**, **Appendix Figure D.2**).

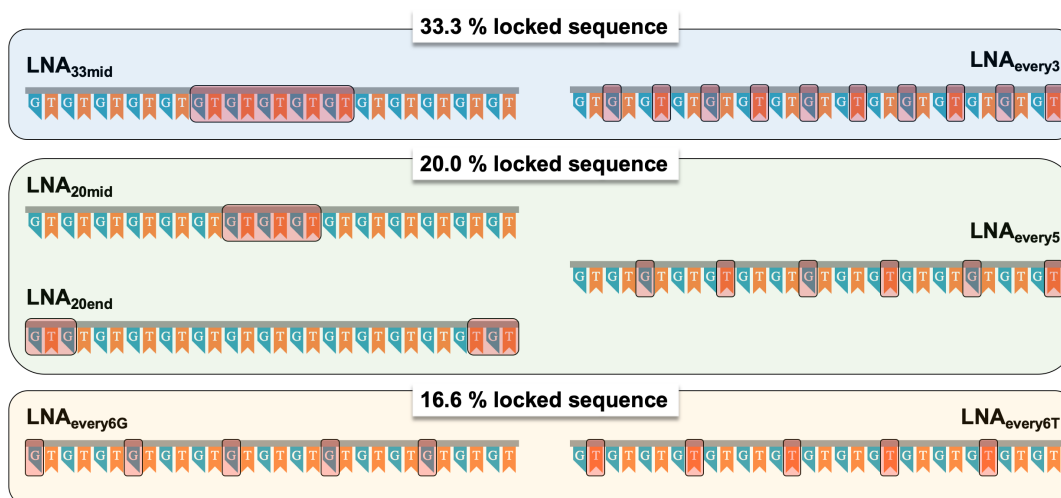


Figure 5.1 – Schematic of all single-stranded LNA $(\text{GT})_{15}$ sequences tested in this study. Locked bases are indicated by a shaded red box.

As shown in the photoluminescence excitation/emission (PLE) maps (**Figure 5.2 (A)**), the LNA-SWCNTs showed preferential, chirality-specific fluorescence emissions, depending on the locking positions of the sequence. The $(\text{GT})_{15}$ SWCNTs showed the highest fluorescence emissions for the (7,5) nanotube chirality with 660 nm excitation, as expected for HiPco SWCNT samples. In contrast, LNA sequences that contained blocks of consecutively locked bases ($\text{LNA}_{20\text{mid}}$, $\text{LNA}_{20\text{end}}$, and $\text{LNA}_{33\text{mid}}$) showed higher fluorescence emissions from the

larger diameter chiralities that appear at longer excitation and emissions wavelengths. On the other hand, the fluorescence was more pronounced for small diameter nanotubes, such as the (6,5) chirality, for sequences with an increased locking periodicity (LNA_{every6T}, LNA_{every5}, and LNA_{every3}).

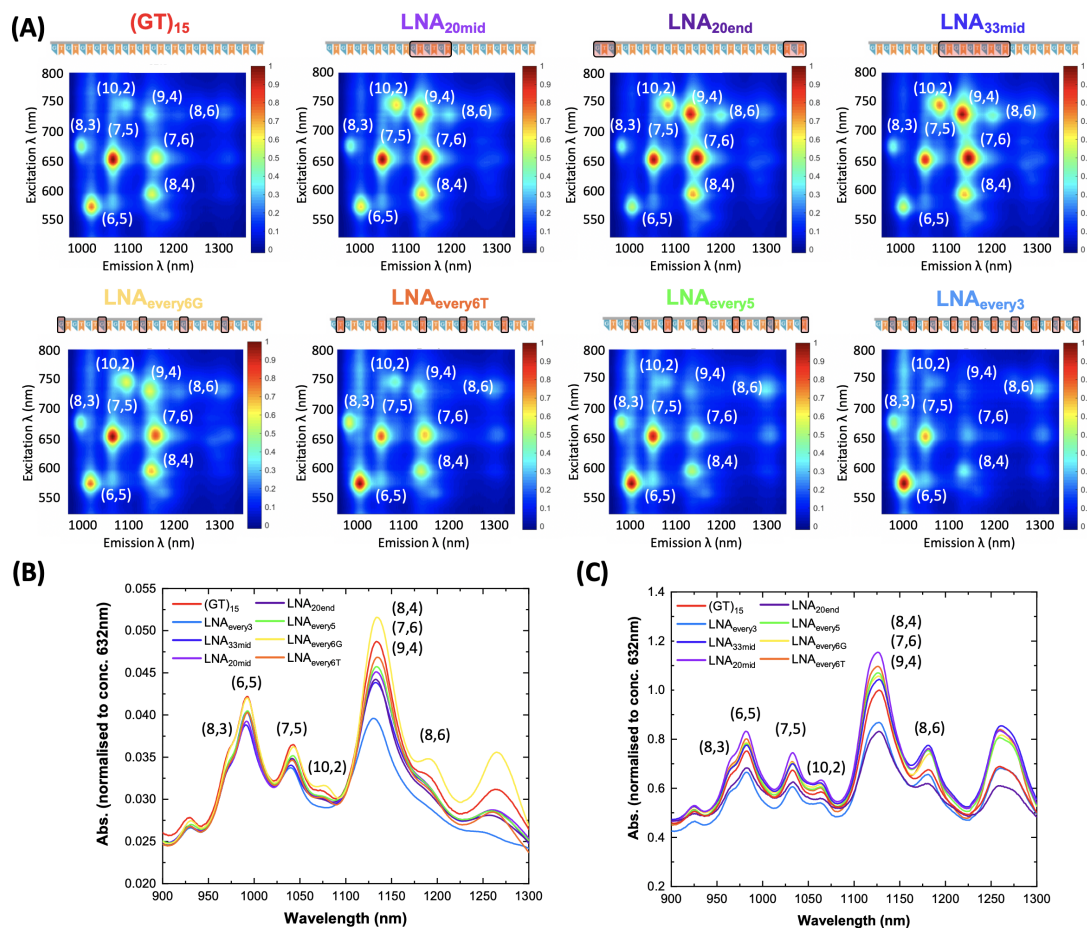


Figure 5.2 – Suspension quality and chirality specificity of LNA sequences. **(A)** PLE maps of the original (GT)₁₅- and all LNA-SWCNT solutions. **(B)** Absorbance spectra for all DNA- and LNA-SWCNT samples examined in this study. All spectra are normalized to concentration as determined using an extinction coefficient of 0.036 mg/L at Abs_{632nm}. **(C)** Absorbance spectra of all sequences following SDOC replacement of original solutions collected following 16 h of incubation. Spectra were normalized to nanotube concentration as determined using an extinction coefficient of 0.036 mg/L at Abs_{632nm} and subsequently normalized to the (GT)₁₅ spectrum (red) for comparison.

To determine whether the chirality-specific differences in fluorescence emissions were due to selective increases in quantum yield or chirality enrichment, we compared the chirality distribution of the nanotubes using absorption spectroscopy (**Figure 5.2 (B)**). Although all LNA-SWCNT suspensions were synthesized from the same initial distribution of SWCNT chiralities, differences in the absorption peak ratios for the different LNA sequences suggests that the LNA preferentially enriches certain chiralities. Chirality enrichment was further

confirmed by displacing all LNA and DNA wrappings with the same wrapping, sodium deoxycholate (SDOC) [138]. Following equilibration with the preferentially adsorbed SDOC (**Appendix Figure D.3, D.4, D.5**), we observed that none of the SDOC-suspended SWCNTs had overlapping absorbance spectra (**Figure 5.2 (C)**). These observations confirm that the LNA is not simply altering the quantum yield in a chiral-dependent manner but rather that the different LNA sequences exhibit preferences for suspending certain nanotube chiralities.

The wrapping morphology of the different oligonucleotide sequences was subsequently characterized using atomic force microscopy (AFM) (**Figure 5.3, Appendix Figure D.7 – D.10**). Because of the increased vertical (compared to lateral) resolution of AFM measurements, we examined the differences between the wrappings by comparing coated (peaks, **Figure 5.3 (center)**) and uncoated (valleys, **Figure 5.3 (right)**) regions along the nanotube. This enabled us to examine the wrapping homogeneity along the nanotube for the different sequences by comparing the variance in the height distribution of the peaks (**Figure 5.3 (left)**). We could also qualitatively assess the periodicity of the wrappings by counting the number of peaks observed per unit length along the nanotube.

The (GT)₁₅ exhibited an overall regularized wrapping along the nanotube length (**Figure 5.3 (A)**). This consistency is in agreement with previous reports that have suggested helical wrapping of DNA onto the SWCNT surface [139, 245]. Similarly, all LNA sequences with periodic lockings (LNA_{every5}, LNA_{every6T}, LNA_{every6G}, and LNA_{every3}) displayed regular wrapping heights along the surface of the nanotube (**Figure 5.3 (B – E)**). In addition, we note that the SWCNTs suspended using the periodic LNA sequences were smaller in height (LNA_{every3} - 1.17 ± 0.12 nm, LNA_{every5} - 1.09 ± 0.09 nm, LNA_{every6T} - 1.02 ± 0.25 nm, LNA_{every6G} - 0.82 ± 0.22 nm)² compared to (GT)₁₅-SWCNTs (1.48 ± 0.16 nm). Conversely, SWCNTs suspended using LNA sequences with blocks of locked bases (**Figure 5.3 (F – G)**) appeared to preferentially suspend larger diameter SWCNTs (LNA_{33mid} - 2.16 ± 0.03 nm, LNA_{20mid} - 1.47 ± 0.20 nm). We attribute these differences to the relative increase of certain chiralities (such as the (6,5) for periodic lockings and the (10,2) or (9,4) for blocks of locked bases) in the LNA suspensions, in agreement with our observations from the PLE maps and absorbance spectra (**Figure 5.2**).

Examining the regularity of the wrapping for the different sequences, we observed a distinct difference between periodically locked sequences and the sequences with a block of continuous locking. Whereas the former showed frequent peaks regularly dispersed along the length of the nanotube, similar to (GT)₁₅, LNA_{33mid} and LNA_{20mid} exhibited a more sporadic coverage. Rather than periodic peaks, LNA_{33mid} showed longer coated sections along the nanotubes. In addition, there were larger spacings between wrapped regions (**Appendix Figure D.8**). Similar trends were observed for the LNA_{20mid} (**Appendix Figure D.9**).

²Due to the presence of an additional layer of material on the substrate of the LNA_{every6G}-SWCNTs, the heights estimated by the cross-section analysis shown in **Figure 5.3** were slightly underestimated. Additional measurements, taken across the nanotubes into exposed parts of the substrate show the true height of the nanotubes, which is used for comparison to the other wrappings **Appendix Figure D.10**.

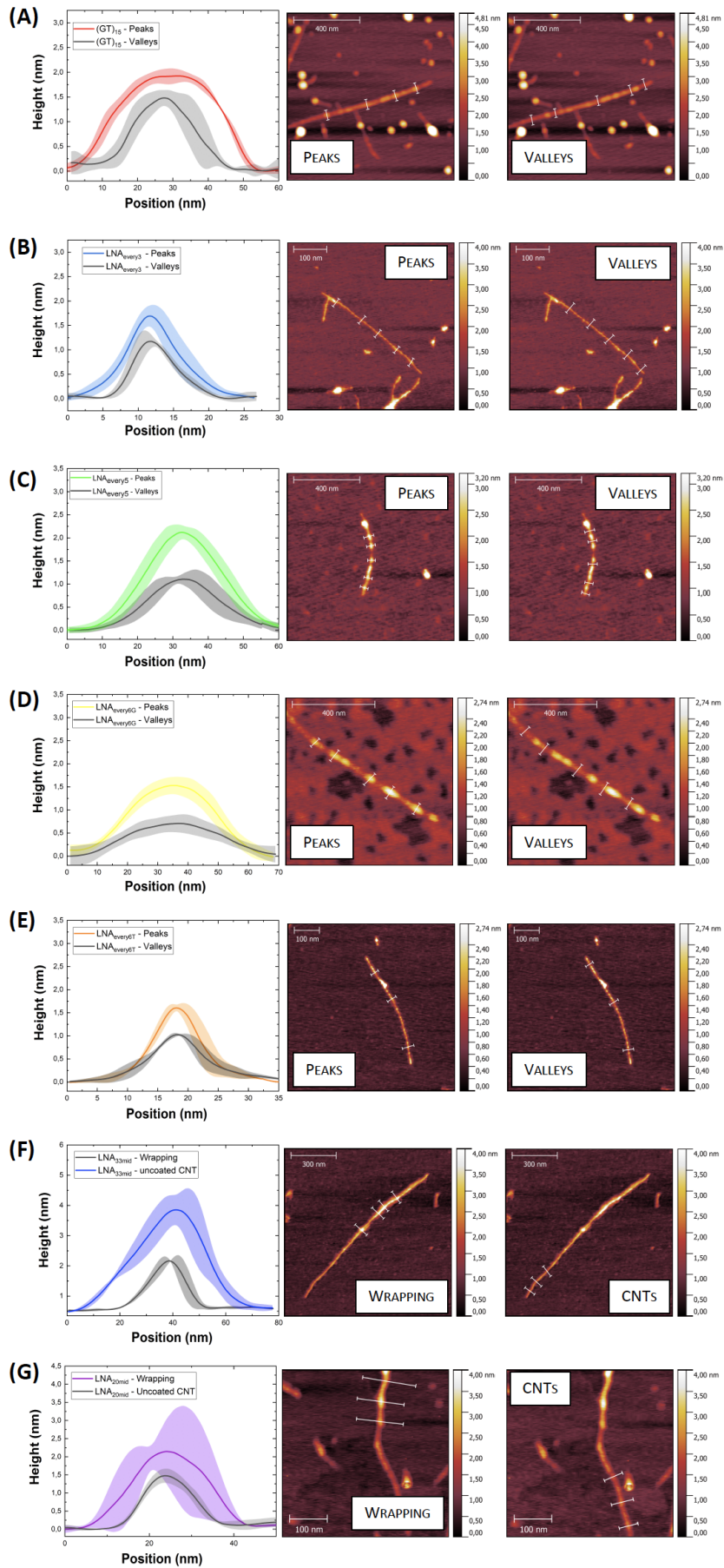


Figure 5.3 – AFM characterization was performed to examine differences in the wrapping behavior of (A) (GT)₁₅, (B) LNA_{every3}, (C) LNA_{every5}, (D) LNA_{every6G}, (E) LNA_{every6T}, (F) LNA_{33mid}, and (G) LNA_{20mid}. Average height profiles were extracted from coated (peaks) and uncoated (valleys) cross sections along the nanotube. A minimum of three positions were selected along the nanotube to extract the height profiles (indicated by the white lines in AFM height images). Solid lines in the height profiles represent the average height and shaded regions represent 1 σ standard deviation (n = 3 – 5 profiles).

Subsequent analysis of the coated regions of LNA_{33mid} qualitatively demonstrated the consistency of the wrapping over these sections (**Appendix Figure D.8, D.9**). In addition, we observed that the wrapping heights of LNA with blocks of locked bases were much greater than both the periodically locked sequences and (GT)₁₅. We attribute the distinct wrapping pattern of LNA_{33mid} and LNA_{20mid} to the bundled locking of bases in the middle of the sequence. The presence of locked bases limits the ability of this sequence to reconfigure on the nanotube surface, which may, in turn, limit the ability of these sequences to tightly wrap around the nanotube resulting in the higher wrapping heights observed.

While the free rotation of natural DNA enables a majority of bases in a wrapping sequence to π -stack onto the nanotube [139, 245], steric restrictions of LNA sequences at locked positions into the 3'-endo north conformation (**Appendix Figure D.11**) may result in only a fraction of these bases being able to stack onto the SWCNT surface. Other bases may either self-stack onto each other or protrude from the nanotube surface disrupting any helical wrapping [245, 294] and lead to differences in the wrapping heights. The variability in wrapping behavior can also affect the amount of DNA/LNA that can stack onto the nanotube surface per unit area.

To further investigate differences in the wrapping behavior, we characterized all SWCNT solutions using ζ -potential (ZP) (**Figure 5.4 (A)**), which measures a nanoparticle's surface charge. Due to a lack of salt in the DNA- and LNA-SWCNT solutions, we assume that only a single layer of DNA or LNA can adsorb onto the nanotube surface as the electrostatic repulsion between the phosphate groups along the backbone should prevent multilayer adsorption. Hence, we can use ZP values as a proxy for the relative amount of negatively charged oligonucleotides adsorbed onto the surface [245, 295]. The ZP measurements showed only slight variations for the majority of LNA-SWCNTs compared to (GT)₁₅-SWCNTs. Two exceptions were LNA_{33mid}, which showed a notably lower ZP, and LNA_{every3}, which showed the most negative ZP of all complexes. Both of these sequences had the same percentage of locking, however as was shown in the AFM images (**Figure 5.3, Appendix Figure D.7, D.8**) due to differences in the locking periodicity, these sequences adopted very different wrapping structures on the nanotube surface. While LNA_{33mid} had certain areas with a dense coverage, a majority of the nanotube surface remained uncoated (indicated by the lower height profile extracted from the AFM images). We hypothesize that these areas of uncoated SWCNT reduce the overall charge density of the complex, resulting in a lower than expected ZP value. Conversely, LNA_{every3} had a very dense wrapping, with almost the entirety of the nanotube surface covered by frequent and tightly packed peaks, which could result in a higher charge density and hence the more negative ZP value observed.

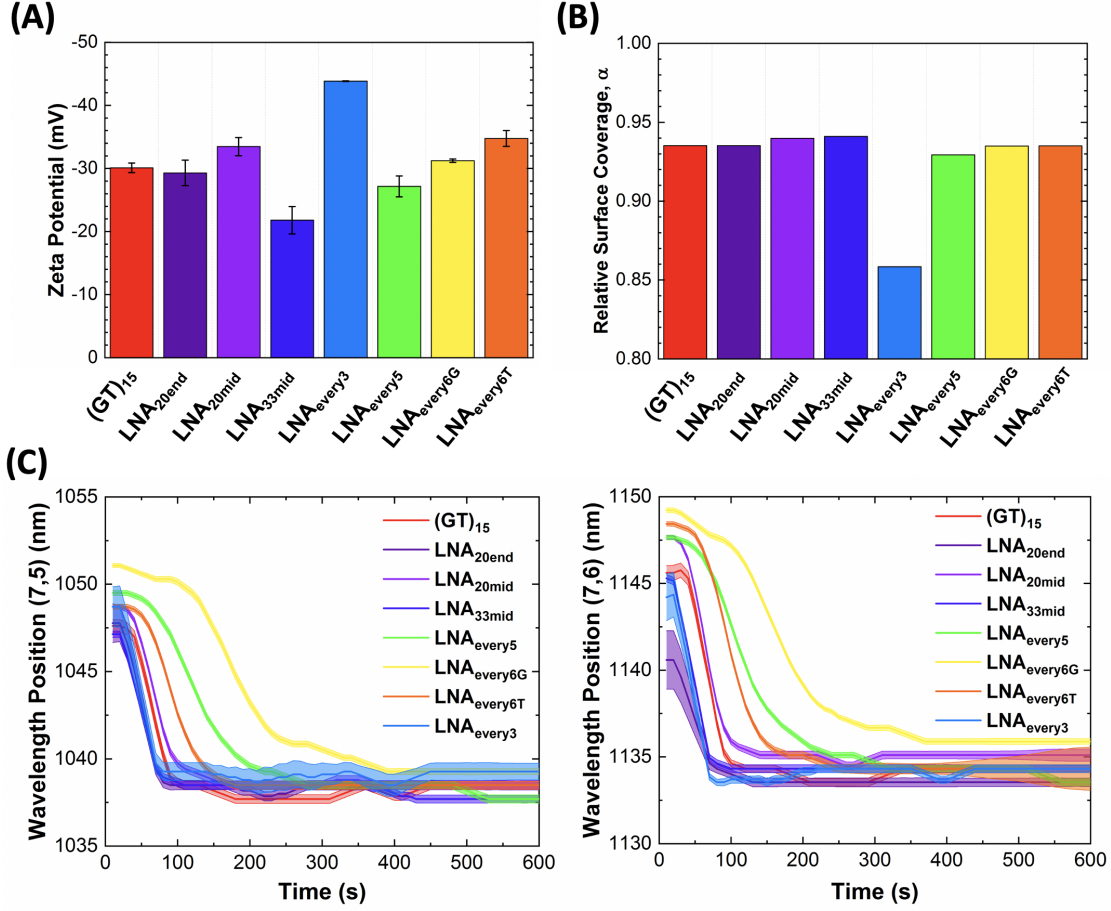


Figure 5.4 – Wrapping behavior of DNA and LNA sequences. **(A)** ζ -potential of SWCNTs functionalized with (GT)₁₅ and LNA analogues in DI water. Measurements were performed in triplicates with error bars representing 1σ standard deviation, as calculated from individual data shown in **Appendix Table D.2**. **(B)** The relative surface coverage of the different DNA and LNA polymer wrappings calculated relative to N-Methyl-2-pyrrolidone (NMP) [29]. **(C)** Modulation of the fluorescence emission wavelength position of the (7,6) and (7,5) chirality peaks of all sequences parameters as a function of time following SDOC addition. Shaded regions represent the standard deviation (3σ) of the peak fit used at each time point.

In order to further probe differences in surface coverage between the wrappings, the relative surface coverage, α , was estimated based on the effective dielectric constant, ϵ_{eff} [16, 29] (**Figure 5.4 (B)**)

$$\alpha = \frac{\epsilon_{\text{eff}} - \epsilon_{\text{water}}}{\epsilon_{\text{p}} - \epsilon_{\text{water}}} \quad (5.1)$$

where ϵ_{water} and ϵ_{p} are the contributions to the dielectric constant from the surrounding water and wrapping polymer, respectively. For both LNA and DNA sequences, $\epsilon_{\text{p}}=4$ was used [131]. ϵ_{eff} is obtained from the slope of the linear fit of the solvatochromic shift, $(E_{11})^2 \Delta E_{11}$, versus the diameter of the nanotube to the power of negative 4, d^{-4} , for the various chiralities present in each suspension (**Appendix Figure D.12**). The experimental solvatochromic shifts were de-

terminated by extracting the peak positions for the different chiralities in the PLE plots obtained (**Figure 5.2**). All data used to calculate the values of ϵ_{eff} and α are included in **Appendix Table D.2** and energy shift values are included in **Appendix Table D.3**. All LNA sequences had similar calculated surface coverage values to nanotubes suspended using (GT)₁₅ with the exception of LNA_{every3} (**Figure 5.4 (B)**). As this approach considers all nanotube chiralities to approximate an average surface coverage independent of chirality, it is not capable of capturing chirality specific effects. This is particularly problematic for the LNA_{every3}, which exhibits a strong preference towards the (6,5) chirality. We note that while the energy shift values were the same for LNA_{every3} and all other sequences when examining the (6,5) chirality, large deviations were observed for the larger diameter nanotubes, such as the (10,2), suspended using the LNA_{every3} (**Appendix Table D.3**). Furthermore, as a result of the selectivity of LNA_{every3} towards the (6,5) chirality, the fluorescence intensity of the other chirality peaks was significantly lower. This in turn leads to a poorer fit of the data (indicated by the lower Adj. R² value **Appendix Table D.2**), which can result in a significant underestimation of α . More generally, we believe that this method of approximating surface coverage can lead to discrepancies if strong chirality preference is displayed by the different wrappings. However, it does provide information on the relative accessibility of the nanotube surface to water by comparing the experimentally determined solvatochromic shifts for a given chirality (**Appendix Table D.3**).

The effective binding affinities of the different wrappings were characterized by examining surfactant displacements kinetics, as done previously [138]. In this method, surfactants (such as SDOC) added to the solution competitively bind to the nanotube surface and displace the DNA wrapping. This displacement results in blue-shifting of the fluorescence peak positions at a rate that depends on the DNA binding affinity [138]. The relative binding affinities of the various oligonucleotide wrappings can therefore be inferred by continuously monitoring the positions of the (7,6) and (7,5) fluorescence emission peaks following SDOC addition (final concentration 0.1%). As shown in **Figure 5.4 (C)** and **Appendix Figure D.6**, the LNA_{every6T}, LNA_{every6G}, and LNA_{every5} showed slower displacement kinetics compared to (GT)₁₅ for both the (7,5) and (7,6) peaks, implying stronger binding affinity for these engineered wrappings to both of these chiralities.

We further examined the fluorescence stability of the different wrappings in the presence of CaCl₂ (**Figure 5.5 (A)**, **Appendix Figure D.13, D.14**). As shown in **Chapter 4**, the fluorescence of (GT)₁₅-SWCNT sensors undergoes changes in the presence of varying cation concentrations [35]. In agreement with these observations, we observe both quenching ($-22.6 \pm 2.7\%$ and $-12.4 \pm 2.7\%$) and wavelength red-shifting (1.6 ± 0.0 nm and 2.3 ± 0.2 nm) for the (7,5) and (7,6) (GT)₁₅-SWCNT chirality peaks following the addition of CaCl₂ (**Figure 5.5 (A)**). Similarly, certain LNA-SWCNTs, including LNA_{20end}, LNA_{33mid}, and LNA_{every3}, exhibited large fluorescence changes upon addition of CaCl₂ (**Appendix Figure D.13, D.14**). We attribute this to an instability of these wrappings on the (7,5) and (7,6) chiralities, in line with our observations from the SDOC replacement experiments (**Figure 5.4 (C)**).

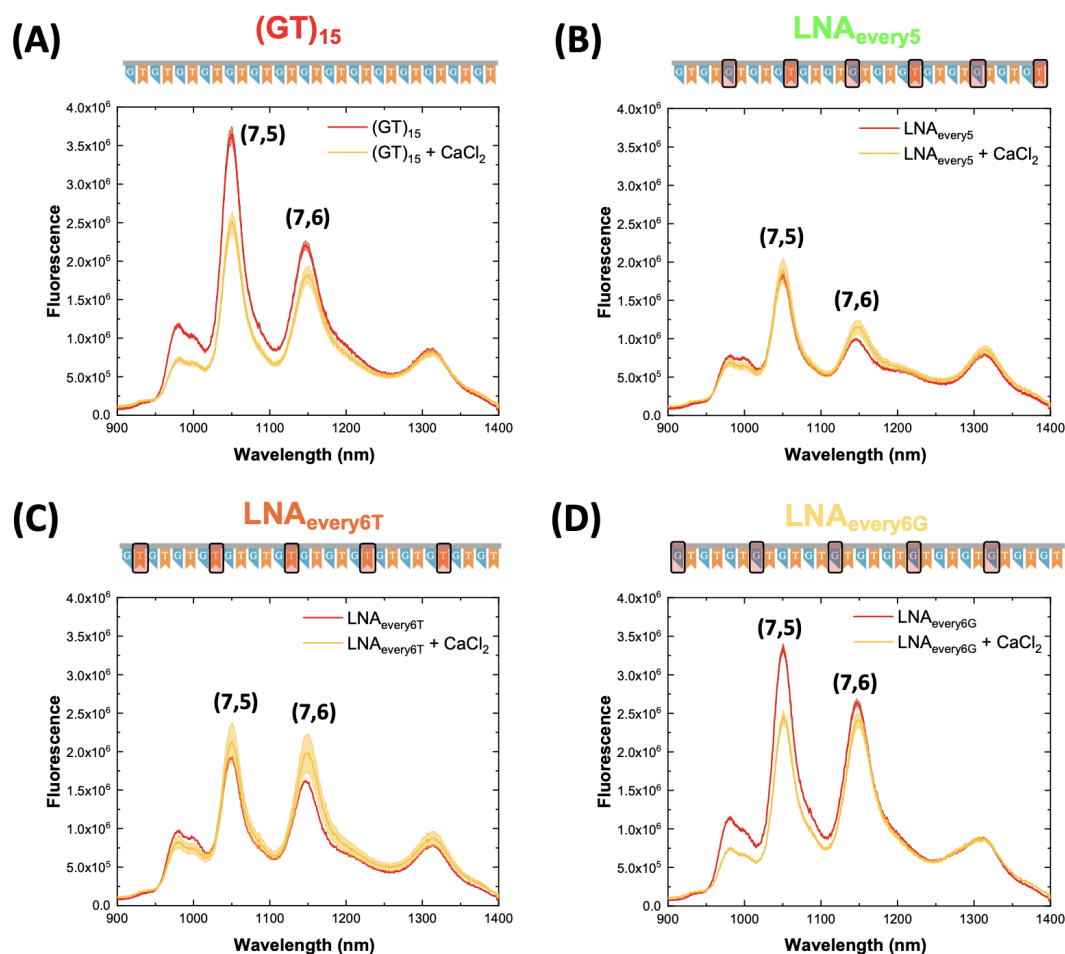


Figure 5.5 – Response of DNA- and LNA- sensors to CaCl_2 . Representative spectra of the response of (i) $(\text{GT})_{15}$, (B) $\text{LNA}_{\text{every}5}$, (C) $\text{LNA}_{\text{every}6\text{T}}$, and (D) $\text{LNA}_{\text{every}6\text{G}}$ sensors following the addition of 0.5 M CaCl_2 (final concentration: 5 mM, excitation: 660 nm). Graphs include the spectra before (red) and after addition of CaCl_2 (yellow). The solid line represents the average wavelength shift with the shaded regions representing 1σ standard deviation ($n = 3$ technical replicates). All samples were incubated for 30 min. Spectra for all other LNA sequences are included in **Appendix Figure D.13**.

Conversely, LNA-SWCNT complexes with more spaced locking demonstrated superior stability in the presence of the divalent cations. For example, the $\text{LNA}_{\text{every}5}$ -SWCNT (**Figure 5.5 (B)**) showed only minor changes in the fluorescence intensity of both the (7,5) or (7,6) peaks ($-6.5 \pm 1.0\%$ and $+4.6 \pm 1.0\%$, respectively) and the shifting of the (7,5) was reduced by approximately 44% (**Appendix Figure D.14**). Interestingly, despite the same periodicity of locking for both the $\text{LNA}_{\text{every}6\text{T}}$ (**Figure 5.5 (C)**) and $\text{LNA}_{\text{every}6\text{G}}$ (**Figure 5.5 (D)**) sequences, we observed pronounced differences in the behavior of these sensors. Whereas the $\text{LNA}_{\text{every}6\text{T}}$ -SWCNT exhibited only a minor increase in the fluorescence intensity of the (7,5) chirality ($+0.3 \pm 3.2\%$), the $\text{LNA}_{\text{every}6\text{G}}$ -SWCNT had pronounced quenching ($-24.5 \pm 3.4\%$). This suggests that the base itself, and not only the periodicity of locking, can greatly impact the stability of the LNA-SWCNT sensors. Moreover, the differences in the response of the (7,5) and (7,6) peaks

implies that the fluorescence changes are dependent on the interaction of a particular LNA sequence with a specific chirality and not simply a direct function of the percentage locking. This observed chirality specificity further supports our previous observations of different fluorescence behaviors for certain LNA sequences in the PLE plots (**Figure 5.2 (A)**). Chirality specific responses are also observed for the LNA_{20mid}-SWCNT (**Appendix Figure D.13**), where the changes in intensity and wavelength position of the (7,5) chirality ($+19.3 \pm 16.3\%$ and 0.9 ± 0.2 nm) were much lower than for the (7,6) peak ($+55.6 \pm 20.4\%$ and 3.2 ± 0.2 nm).

Current dopamine sensors based on (GT)_x-SWCNTs are ‘turn-on’ sensors, exhibiting strong relative fluorescence intensity changes on recognition of the neurotransmitter [15, 62]. As a result, any competing changes in the fluorescence intensity could result in inaccurate concentration measurements. Given the variability of Ca²⁺ concentrations in different biofluids and the fluctuations of Ca²⁺ involved in neurotransmission, large intensity responses of SWCNT-based sensors to this cation could be detrimental to their applicability *in vitro* and *in vivo*. At high Ca²⁺ concentrations, we show that the (GT)₁₅-SWCNTs exhibit the largest intensity decrease for both the (7,5) and (7,6) chiralities. Furthermore, as we have shown in **Chapter 5**, absolute cation concentration is more important than the nature of the individual cations [35]. Therefore, in ionically complex solutions the (GT)₁₅-SWCNT would lead to a significant underestimation of dopamine concentration. Conversely, the LNA_{33mid}-, LNA_{20mid}-, and LNA_{every3}-SWCNTs showed large intensity increases after the addition of CaCl₂, which would lead to overestimation of the dopamine concentration. To overcome the problems associated with significant underestimation or overestimation, an ideal sensor would exhibit minimal intensity changes, if any, in the presence of the Ca²⁺.

Additional measurements were carried out across a wider range of CaCl₂ concentrations (0.05 mM – 50 mM) to further probe the stability of these sequences. Spectra were collected following an incubation period of 30 min and peak wavelength shifts and intensity changes were calculated for the predominant (7,5) and (7,6) chiralities (**Appendix Figure D.14**). Concentration-dependent wavelength red-shifting was observed for the (7,5) and (7,6) chiralities for all sequences, with maximum recorded shifts exceeding 6 nm for the LNA_{33mid}. At the highest Ca²⁺ concentration tested, five of the LNA sequences (LNA_{20end}, LNA_{20mid}, LNA_{every6G}, LNA_{every5}, and LNA_{every6T}) showed lower shifting than (GT)₁₅-SWCNTs for the (7,5) chirality peak. Moreover, compared to (GT)₁₅, over one-order-of-magnitude higher concentration of Ca²⁺ was required to induce any wavelength response for the (7,5) peak for four of these sequences (LNA_{20end}, LNA_{20mid}, LNA_{every6G}, and LNA_{every6T}). Although the magnitude of shifting for the (7,6) peak compared to (7,5) peak was greater for all sensors at higher Ca²⁺ concentrations, several LNA-SWCNTs again exhibited superior stability towards cation-induced wavelength changes, indicative of greater LNA conformational stability [35]. For example, the magnitude of shifting for the LNA_{every6T}-SWCNTs (1.8 ± 0.5 nm) was 38% lower than for the (GT)₁₅-SWCNTs (3.0 ± 0.3 nm). It is also worth noting that at the highest Ca²⁺ concentration, the red-shift of the LNA_{20mid} and LNA_{20end} sensors was 4.4 ± 0.7 nm and 2.3 ± 0.2 nm, respectively, compared to the 2.9 ± 0.3 nm shift of the (GT)₁₅, despite their shifting response being significantly lower than the (GT)₁₅-SWCNT for the (7,5) peak. This

large disparity in the (7,5) and (7,6) shifting response again highlights the chirality specific behavior of the different LNA sequences.

These observations further emphasize the importance of considering locking position, in addition to total locking percentage, when designing LNA-SWCNT sensors. Furthermore, these results prove that for LNA, increasing the percentage of locked bases does not always equate to a more stable LNA sensor as is clearly shown by comparing the LNA_{every6T} (16.6% locked) sensor to LNA_{33mid} and LNA_{every3} (33.3% locked). These findings enabled us to identify several LNA-SWCNTs that exhibit superior signal stability in varying Ca²⁺ concentrations compared to (GT)₁₅-SWCNTs. Amongst the sequences studied, LNA_{every6T}- and LNA_{every5}-SWCNTs were found to provide the greatest stability against undesirable intensity changes across the range of calcium concentrations for both the (7,5) and (7,6) peaks. At high Ca²⁺ concentrations, the LNA_{every6G}- and LNA_{20end}-SWCNTs also demonstrated improved stability compared to the (GT)₁₅-SWCNT complex (**Appendix Figure D.14**).

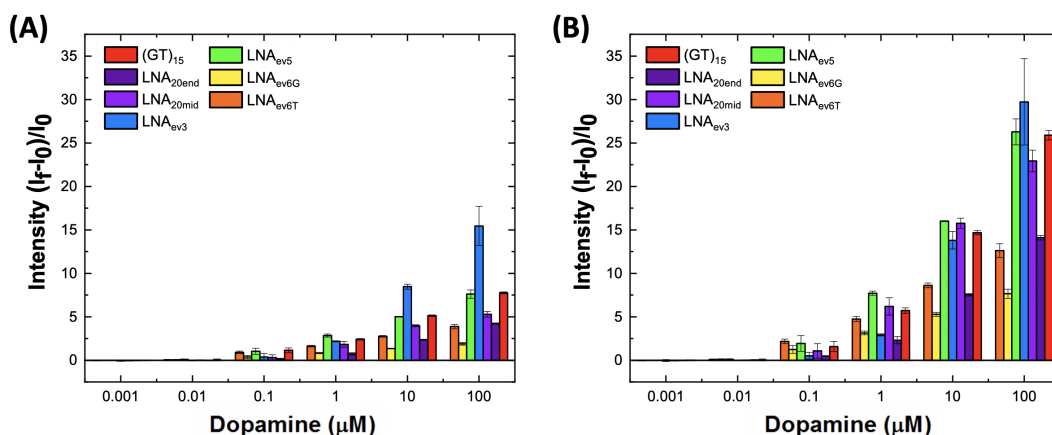


Figure 5.6 – Concentration-dependent intensity response of DNA- and LNA-SWCNTs to dopamine in the absence of CaCl₂ (excitation: 660 nm). Relative intensity change of the (A) (7,5) peak and (B) (7,6) peak following the addition of Dopamine. All samples were incubated for 30 min. Error bars represent 1 σ standard deviation (n = 3 technical replicates). Both graphs are plotted on the same axis scales for comparison.

The increased resistance of certain LNA sequences towards ion-induced fluorescence changes has been attributed to the increased conformational rigidity of these sequences [35]. Owing to this, it was uncertain whether these sensors would retain the ability to interact with other bioanalytes, especially those such as dopamine which are thought to modulate DNA-SWCNT fluorescence by also inducing DNA conformational changes [35, 62]. In order to determine the validity of this concern, we examined the response of our DNA- and LNA-SWCNT sensors to a range of dopamine concentrations in the absence of CaCl₂ (**Figure 5.6**, **Appendix Figure D.15**, **D.16**). Concentration-dependent intensity changes were seen across multiple SWCNT chiralities (**Figure 5.6**), with pronounced increases observed for both the (7,5) and (7,6) chiralities. Although some LNA-SWCNTs have reduced turn-on responses

compared to (GT)₁₅-SWCNTs, all LNA sensors retained their ability to interact with dopamine (**Appendix Figure D.15**) despite the changes in their sensitivity to Ca²⁺. As shown in **Figure 5.6** (and **Appendix Figure D.17**), the limit of detection for the LNA sensors matched the (GT)₁₅-SWCNTs at 10 nM dopamine. We also note that the turn-on response of LNA_{every3}-SWCNTs was significantly greater than for (GT)₁₅-SWCNTs for the (7,5) peak (15.5× versus 7.7×). Similarly, the LNA_{every5}-SWCNTs had comparable responses to the (GT)₁₅-SWCNTs for the (7,5) peak and marginally higher turn-on responses for the (7,6) peak, especially at intermediate dopamine concentrations (7.7× versus 5.7× in 1 μM dopamine and 16.0× versus 14.7× in 10 μM dopamine).

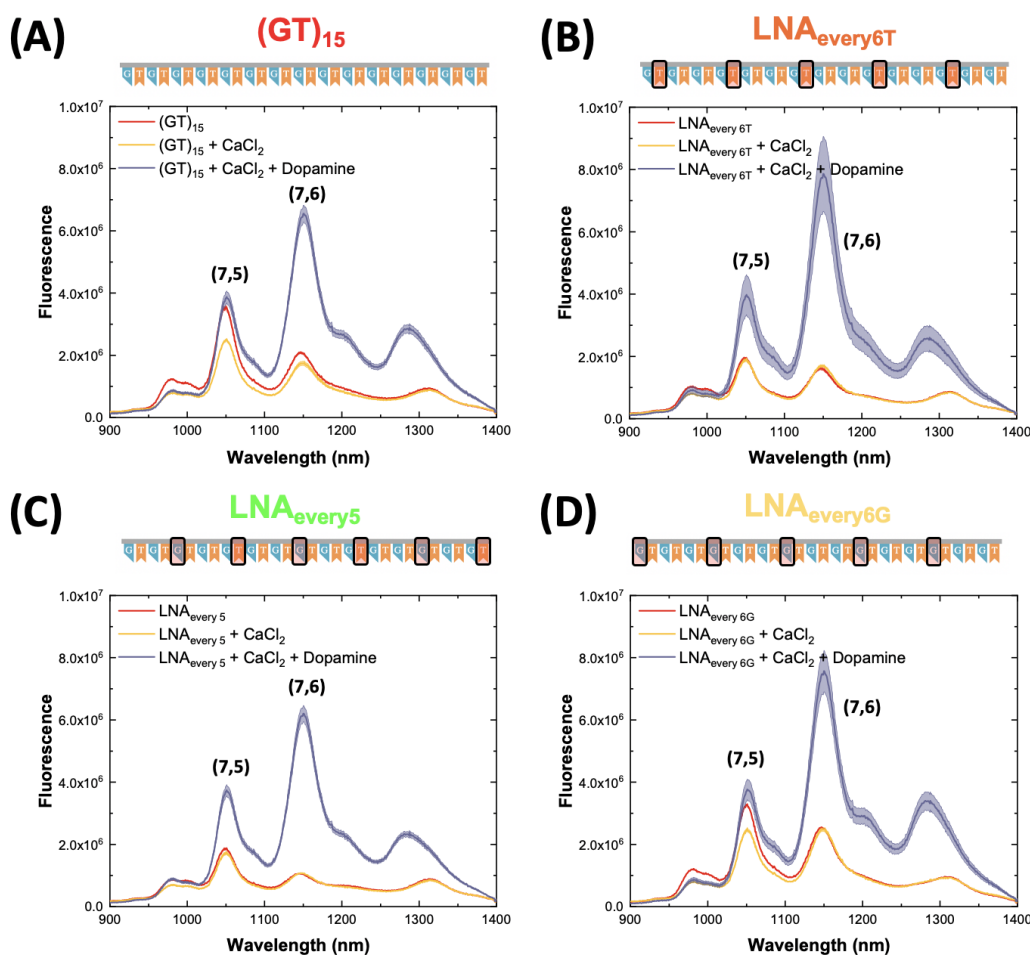


Figure 5.7 – Deconvoluting the response of LNA sensors to dopamine and CaCl₂. **(A-D)** Spectral response of (GT)₁₅ and representative LNA sensors following the addition of 0.5 M CaCl₂ (final concentration: 5 mM) and 10 mM dopamine (final concentration: 100 μM, excitation: 660 nm). Graphs include the spectra before addition (**red**), following the addition of CaCl₂ (**yellow**) and following subsequent addition of dopamine (**purple**). All samples were incubated for 30 min post-addition. The solid line represents the average wavelength shift with the shaded regions representing 1σ standard deviation (n = 3 technical replicates).

The resilience of LNA-sensors to salt-induced fluorescence perturbations [35], coupled with their retained ability to interact with dopamine, can thus provide a general basis for designing sensors with improved diagnostic capabilities. To this end, we tested the ability of the DNA- and LNA-SWCNTs to detect dopamine (100 μ M) in the presence of CaCl_2 (5 mM) (**Figure 5.7, Appendix Figure D.18**). Sensors were first incubated with CaCl_2 and spectra were recorded after 30 min. Freshly prepared dopamine solution was subsequently added to the sensor solution and spectra were again acquired following an additional incubation period. In line with our previous observations, following the addition of CaCl_2 the fluorescence intensity of the (GT)₁₅-SWCNTs decreased for both the (7,5) and (7,6) chiralities. As expected, the addition of dopamine increased the fluorescence of the sensor, however, due to the lower starting fluorescence in the presence of Ca^{2+} , the (7,5) peak only marginally increased versus the initial spectrum (**Figure 5.7 (A)**).

The undesirable fluorescence modulation was further exacerbated at higher Ca^{2+} concentrations for the (GT)₁₅-SWCNTs, to the point where in the presence of 50 mM CaCl_2 the (7,5) peak in the final spectrum (post dopamine addition) even appeared to quench compared to the original intensity (**Appendix Figure D.19**). Contrary to this, the LNA_{every6T}- (**Figure 5.7 (B)**), LNA_{every5}- (**Figure 5.7 (C)**), and LNA_{20mid}-SWCNTs (**Appendix Figure D.18**) showed only minor changes in the fluorescence intensity of both the (7,5) and (7,6) peaks in the presence of 5 mM Ca^{2+} . Furthermore, the presence of the cations did not interfere with the ability of these sensors to interact with dopamine, with significant turn-on responses observed for each of these LNA-SWCNTs.

Although the fluorescence of the LNA_{every6G}-SWCNT (7,5) peak quenched following the addition of Ca^{2+} , the (7,6) peak intensity was unchanged within error. In line with the observations for (GT)₁₅-SWCNTs, the addition of dopamine recovered the fluorescence of the (7,5) peak, although final intensity increases were marginal versus the original spectrum. Despite not reacting to the Ca^{2+} cations, the (7,6) peak fluorescence intensity was significantly enhanced by the addition of dopamine. In fact, the final intensity of the LNA_{every6G}-SWCNTs was higher (normalized to sensor concentration) than the (GT)₁₅-SWCNTs, implying that these sensors would additionally benefit from increased penetration depth in biological samples [78, 249]. Furthermore, the distinct responses of the (7,5) and (7,6) peaks to CaCl_2 and dopamine enabled simultaneous multi-modal sensing of these two analytes. By exciting the sensors at 660 nm and monitoring the fluorescence intensity of the two peaks over time, information on the concentration of both calcium (via the (7,5) peak) and dopamine (via the (7,6) peak) could be inferred. This is, to the best of our knowledge, the first optical sensor that can simultaneously detect calcium and dopamine, opening the door to a plethora of new and improved biosensing opportunities.

5.4 Conclusions

SWCNTs provide a platform that can overcome many of the restrictions currently facing biosensing technologies as they enable real-time continuous monitoring [17, 37] and provide a means of increasing spatiotemporal resolution [17, 62]. Research into DNA-SWCNTs has thus far largely focused on expanding biochemical detection capabilities, and many sensors are now capable of long-term imaging for a wide variety of analytes [10, 15, 16, 73, 225]. Despite this every growing library of DNA-SWCNT sensors, little work has been done to optimise existing sensors for *in vitro* and *in vivo* conditions.

In this work, we took the (GT)₁₅-SWCNT sensors, known for their ability to detect dopamine [14, 15, 36] and introduced locked bases along the sequence in order to examine the effect of ‘locking’ on their sensing behavior. Initial characterization of the sensors showed that both locking periodicity and percentage affects the relative affinity of the sequences towards certain chiralities. Further experiments sought to examine the differences between the optical response of the sensors to increasing concentrations of Ca²⁺ cations [35]. Optical fluctuations caused by the presence of calcium may lead to inaccuracies in concentration readouts and, owing the central role of Ca²⁺ cations in the neurotransmission [293], could limit the use of these sensors for *in vitro* and *in vivo* applications. By incorporating certain LNA bases we improved the stability of (GT)₁₅-SWCNTs towards undesirable fluorescence modulation in the presence of Ca²⁺. This stability appeared to depend strongly on the nature of the base that is locked, with no systematic dependence observed to the percentage of locking. Furthermore, we observed a strong chirality specificity where depending on the periodicity of locking and nature of bases (G or T) locked, only certain nanotube chiralities exhibited improved resilience towards salt induced fluorescence changes.

In addition to studying the optical behavior of these sensors in the presence of Ca²⁺, we also probed their response to dopamine. The presence of locked bases did not destroy the ability of the sensors to interact with dopamine nor did it reduce the limit of detection. In fact, for LNA_{every3}-SWCNTs and LNA_{every5}-SWCNTs, an improved turn-on response rate versus (GT)₁₅-SWCNTs was obtained for the (7,5) and (7,6) chiralities, respectively. Moreover, not only did the LNA sensors show superior sensing capabilities to dopamine in the presence of Ca²⁺ cations, but the nanobioengineered hybrid LNA_{every6G}-SWCNT also provided an unprecedented sensing capability to monitor both Ca²⁺ and dopamine simultaneously. This is, to the best of our knowledge, the first optical sensor that is capable of detecting these two analytes concurrently, a differentiation that could be used to push forward our understanding of the intricate mechanisms of neuronal signalling.

Based on these findings, we believe that this methodology can be used to generate a new class of SWCNT sensors, which could be more promising for *in vitro* and *in vivo* applications. The use of LNA provides a solution for the limitations currently faced by DNA-SWCNTs in ionically complex solutions while enabling more rational design of SWCNT based sensors for a wider range of biological applications and conditions. Furthermore, it does not reduce the

biocompatibility or sequence space offered by DNA-SWCNTs. Specifically, the ability of our sensors to identify and measure dopamine with higher selectivity provides a powerful tool for use in the clinical diagnostics of diseases such as Parkinson's Disease.

5.5 Materials and Methods

5.5.1 Materials

All chemicals and materials were purchased from Sigma-Aldrich, unless specified otherwise. Purified HiPco-SWCNTs were purchased from NanoIntegris (Lot. No. HP29-064). All DNA and LNA sequences were purchased from Microsynth.

5.5.2 Preparation of SWCNT solutions

Purified HiPco-SWCNTs (~0.5 mg) were suspended in 500 μL of either DNA or LNA solution (100 μM dissolved in DI water). The mixture was sonicated in an ice bath for 90 min (power = 40 W) using a Cup Horn sonicator (140 mm, Qsonica). Following sonication, the samples were centrifuged (Eppendorf Centrifuge 5424R) for 4 h at $21,130 \times g$ and 4°C to remove SWCNT aggregates. The supernatant was collected and dialysed for 23 h in 2 L of DI water (14,000 Da MWCO cellulose membrane). Post-dialysis, all samples were centrifuged again for 4 h ($21,130 \times g$ and 4°C) to remove any additional aggregates that may have formed.

Absorbance spectra of all samples were acquired using a UV-Vis-NIR scanning spectrometer (Shimadzu 3600 Plus) with a quartz cuvette (Suprasil quartz, path length 3 mm, Hellma). The concentrations for all samples were calculated using an extinction coefficient $\text{Abs}_{632\text{nm}} = 0.036 \text{ L mg}^{-1} \text{ cm}^{-1}$ and diluted to 10 mg/L for all measurements, unless otherwise stated. All DNA- and LNA-SWCNT solutions were stored at 4°C in order mitigate aggregation of the SWCNTs [225].

5.5.3 Fluorescence spectroscopy measurements

Fluorescence emission spectra were collected using a custom built NIR optical setup on an inverted Nikon Eclipse Ti-E microscope (Nikon AG Instruments), as described previously [37, 78]. Measurements were recorded with LightField (Princeton Instruments) in combination with a custom-built LabView (National Instruments) software for automation purposes. An exposure time of 10 s and laser excitation with band width of 10 nm and relative power of 100% was used for all measurements, unless stated otherwise.

Sample preparation was carried out in 384-well plates (MaxiSorp, Nunc). For all sensor response experiments, 49 μL of DNA- or LNA-SWCNT solution (10 mg/L) was added to a well and excited at $660 \pm 5 \text{ nm}$. Following the acquisition of the initial spectrum, 0.5 μL of either CaCl_2 solution (varying concentrations, dissolved in DI water) or DI water (for control

experiments) was added, and the wells were sealed (Empore, 3M). Samples were incubated for 10 – 30 min (at room temperature) prior to recording the final spectrum. Following the acquisition of the spectra post the first addition, 0.5 μL of freshly prepared analyte solution (varying concentrations, dissolved in DI) was added. The mixture was incubated for an additional 10 – 30 min prior to acquiring the final spectra. A grating of 75 nm^{-1} was used to collect the nanotube emission between 900 – 1400 nm. Spectral fitting was performed using custom Python codes.

Photoluminescence excitation (PLE) maps were acquired between 525 nm and 800 nm with a 5 nm step. 50 μL aliquots of DNA- and LNA-SWCNT solutions (10 mg/L) were added to a 384-well plate, which was then sealed (Empore, 3M) to avoid evaporation during the measurement. The results were analysed using a custom Matlab code (Matlab R2017b, Mathworks).

5.5.4 Surfactant replacement

Surfactant replacement of the DNA- and LNA-SWCNT solutions was performed using 1% (w/v) sodium deoxycholate (SDOC). All fluorescence experiments involving the real-time addition of SDOC were performed in a 384-well plate (MaxiSorp, Nunc). Following an initial time period of ~ 60 s to collect sufficient DNA/LNA-SWCNT control data, 2.5 μL of 1% SDOC was added to 22.5 μL of SWCNT solution (10 mg/L) to give a final SDOC concentration of 0.1%. Spectra were then collected continuously for 1 h with a constant exposure time of 10 s.

Samples for absorbance experiments were prepared by mixing 63 μL of SWCNT solution (10 mg/L) with 7 μL of SDOC 1%. Spectra for the samples were collected prior to addition and at various time points post-addition. All measurements were carried out using a UV-Vis-NIR scanning spectrometer (Shimadzu 3600 Plus) with a quartz cuvette (Suprasil quartz, path length 3 mm, Hellma).

5.5.5 AFM imaging and sample preparation

DNA- and LNA-SWCNT solutions (20 μL) were drop-casted onto freshly cleaved mica substrates and dried at room temperature. Morphological characterization of the samples was performed using a commercial AFM setup (Cypher, Asylum Research) equipped with a commercial Si cantilever (AC240TS-R3, Asylum Research). Topography, phase, and amplitude images were acquired in standard tapping mode. Images were analysed with standard tools (e.g. plane subtraction and profile extraction) featured in the AFM data analysis software (Gwyddion 2.52).

5.5.6 ζ -potential measurements

ζ -potential measurements were carried out with a Zetasizer Nano ZS analyzer (Malvern), using folded capillary cells. All DNA- and LNA-SWCNT solutions were diluted in DI water to yield a

final concentration of 2 mg/L.

5.5.7 Circular dichroism measurements

Samples were analysed in a circular dichroism spectrometer across a wavelength range 200 – 300 nm in 0.2 nm intervals, using a quartz cuvette (Suprasil quartz, path length 1 mm, Hellma). DNA and LNA samples were diluted to a final concentration of 7.5 μ M in either DI water or 0.25 M CaCl_2 and a volume of 300 μ L was used for all experiments.

6 Outlook on Potential Applications of XNA-SWCNTs for Improved Optical Biosensing

'Would you tell me, please, which way I ought to walk from here?'
'That depends a good deal on where you want to get to.'

Lewis Carroll, *Alice's Adventures in Wonderland*

6.1 Abstract

The enhanced stability of the fluorescence signal from LNA-SWCNTs in ionically complex solutions demonstrated in previous chapters of this thesis suggests that these sensors could provide an alternative to DNA-SWCNTs for improved *in vitro* and *in vivo* sensing. In this chapter, we present findings on the use of LNA-SWCNTs in more complex solutions. Building upon our observations in **Chapter 4** and **Chapter 5**, we expand our study to examine the impact of proteins, antibiotics, and whole neuronal cell cultures on the fluorescence properties and sensing abilities of LNA-SWCNTs. We examine how both incubation time and medium composition can impact the fluorescence intensity of sensor films and furthermore confirm that our LNA-SWCNT sensors retain the ability to detect dopamine in whole cell cultures.

In addition, we present preliminary findings on a new class of XNA-SWCNT sensors, a family of PNA-DNA-SWCNT sensors designed for miRNA detection. We present a novel stepwise methodology for preparing PNA-DNA-SWCNTs, which provides a proof-of-concept for the modular design and assembly of multiple miRNA sensors. We examine the impact of the length of the PNA-DNA hybrid section on the sensing capabilities of the final complex and verify that our sensors exhibit selectivity for complementary miRNA. We further demonstrate that these sensors can be used for the rapid optical detection of several miRNA sequences using either absorbance (< 15 min) or fluorescence spectroscopy (< 1 h).

6.2 Using XNA-SWCNTs for *In Vitro* Sensing Applications

Despite the remarkable developments in SWCNT-based optical biosensors in recent years, their application into *in vivo* and *in vitro* sensing applications is still relatively limited [10, 17, 240, 296, 297]. This is in part due to the difficulties associated with translating non-covalently functionalized SWCNTs from buffered conditions to complex biological media without losing the sensing capabilities of the sensors. By its nature, non-covalent functionalization of SWCNTs is a dynamic process [298]. As such, the corona phase on the surface of the nanotube is in constant flux with molecules exchanging between the bulk and surface regions. This process can lead to complications when nanotube sensors are taken from carefully controlled buffer solutions and placed into biological fluids. When a nanotube, or any nanoparticle, is introduced into complex biological fluids or media, different proteins and small molecules (including various salt and cationic species) can associate to the SWCNT surface creating a new, more complex corona [296, 298]. The binding of these proteins and small molecules can disrupt the conformation of the original wrapping on the nanotube surface, which in turn effects the biological and optical behavior of the SWCNTs [15, 296, 298]. In turn, this can reduce the optical response of the nanotube to target analytes creating the illusion of a loss of previously validated results from under buffered conditions, and ultimately hindering the efficacy and functionality of the SWCNT *in vivo* or *in vitro* [10, 15, 299]. Understanding the key components of this process, such as interaction strength and exchange kinetics of different molecules, is critically important for the future success of SWCNT sensors in biological environments.

Recent work by Pinals *et al.* demonstrated that protein adsorption onto the nanotube surface can attenuate the optical response of (GT)₆-SWCNT sensors to dopamine [298]. The dopamine turn-on response was diminished by 52.2% or 78.2% for sensors that were incubated with human serum albumin or fibrinogen solutions, respectively [298]. This decrease was attributed to protein adsorption on the nanotube surface, which resulted in both an increase of the baseline fluorescence and decrease of the final fluorescence intensity post-dopamine addition. Furthermore, this study found that higher affinity wrappings, which in this instance were longer DNA sequences, had reduced protein adsorption. Gravely *et al.* similarly observed that SWCNTs suspended with longer DNA sequences had greater physical and optical stability following internalization into murine macrophages [300]. These findings suggest that higher affinity wrappings could address many of the limitations currently facing DNA-SWCNT sensors. Moreover, this indicates that increased wrapping affinity can be used as a guideline for rationally engineering SWCNTs with improved functionality and performance in more complex *in vitro* and *in vivo* conditions.

Our previous studies have shown that LNA-SWCNTs can be used to mitigate unwanted fluorescence fluctuations in the presence of different divalent cation species. Furthermore, we have observed that our LNA sensors exhibit a higher wrapping affinity compared to their DNA counterparts. In this chapter we build upon our previous observations and examine whether the LNA sensors presented in **Chapter 5** can also retain their superior sensing capabilities

in more complex media, specifically supplemented Schneider's medium, which we selected due to its use for *Drosophila melanogaster* (*Drosophila*) neuron culturing [301]. LNA_{every5}-SWCNTs were selected as they simultaneously demonstrated a greater resistance fluorescence changes in the presence of Ca²⁺ cations while also retaining similar turn-on responses following dopamine addition compared to the (GT)₁₅-SWCNTs. Our results show that while (GT)₁₅-SWCNTs have significantly reduced turn-on responses in both deionized (DI) water and supplemented Schneider's medium when immobilized in films, LNA_{every5}-SWCNTs retain a significant turn-on response of 90.1% and 63.7%, respectively. Furthermore, we showed that the LNA_{every5} sensors retain their ability to sense dopamine in the presence of cultured neurons and also following cellular incubation periods of up to 24 hours.

6.2.1 Results and Discussion

Experiments were performed on surface immobilized SWCNTs to demonstrate the dopamine response of individual SWCNTs using a custom-built NIR confocal microscope [302]. Given the additional complexity of biofluids, we sought to compare the sensing capability of the LNA-SWCNTs and DNA-SWCNTs in DI water (**Figure 6.1 (A)**) versus in a complex medium, supplemented Schneider's medium (10% FBS, 1% Pen/Strep) (**Figure 6.1 (B)**). Supplemented Schneider's medium was chosen due to its widespread use in culturing *Drosophila* neurons [301]. We freshly prepared nanotube films using either (GT)₁₅-SWCNTs or LNA_{every5}-SWCNTs. Nanotube films were subsequently covered with 200 μ L of DI water or supplemented Schneider's medium and left to incubate for 5 min prior to acquiring any images. Both (GT)₁₅- and LNA_{every5}-SWCNTs had lower starting fluorescence in DI water than in supplemented Schneider's medium, in agreement with previous observations for other protein-rich solutions [298]. Moreover, in all preparations LNA_{every5}-SWCNTs produced denser films leading to higher fluorescence compared to (GT)₁₅ (**Figure 6.1 (A-B)**, **Appendix Figure E.1 – E.4**) under the 780 nm excitation. This was in part attributed to differences in the surface binding affinity of the LNA- and DNA-SWCNTs [139], but also to differences in the relative fluorescence of these sensors using a 780 nm excitation (**Figure 5.2 (A)**).

The addition of dopamine resulted in an intensity increase of all sensor films in both DI water and supplemented Schneider's medium. The relative intensity increase (**Figure 6.1 (C)**) normalized to the initial intensity was determined using the mean intensity values from the wide-field images collected (**Appendix Figure E.1 – E.4**). Although both sensors possessed the ability to interact with dopamine in DI water, the turn-on response of the LNA_{every5}-SWCNTs (+90.9 \pm 25.2%) was significantly higher than for (GT)₁₅-SWCNTs (+6.4 \pm 1.9%). In supplemented Schneider's medium, the ability of (GT)₁₅-SWCNTs to detect dopamine via intensity changes decreased, and no significant increase in fluorescence intensity of the film was detected (+4.5 \pm 6.0%). While the extent of the turn-on response also reduced for LNA_{every5}-SWCNTs, a substantial increase was still recorded (+63.7 \pm 8.1%) following the addition of dopamine. Furthermore, the overall intensity of the LNA_{every5}-SWCNT films both pre- and post-dopamine was greater in supplemented Schneider's medium than in DI water.

Chapter 6. Outlook on Potential Applications of XNA-SWCNTs for Improved Optical Biosensing

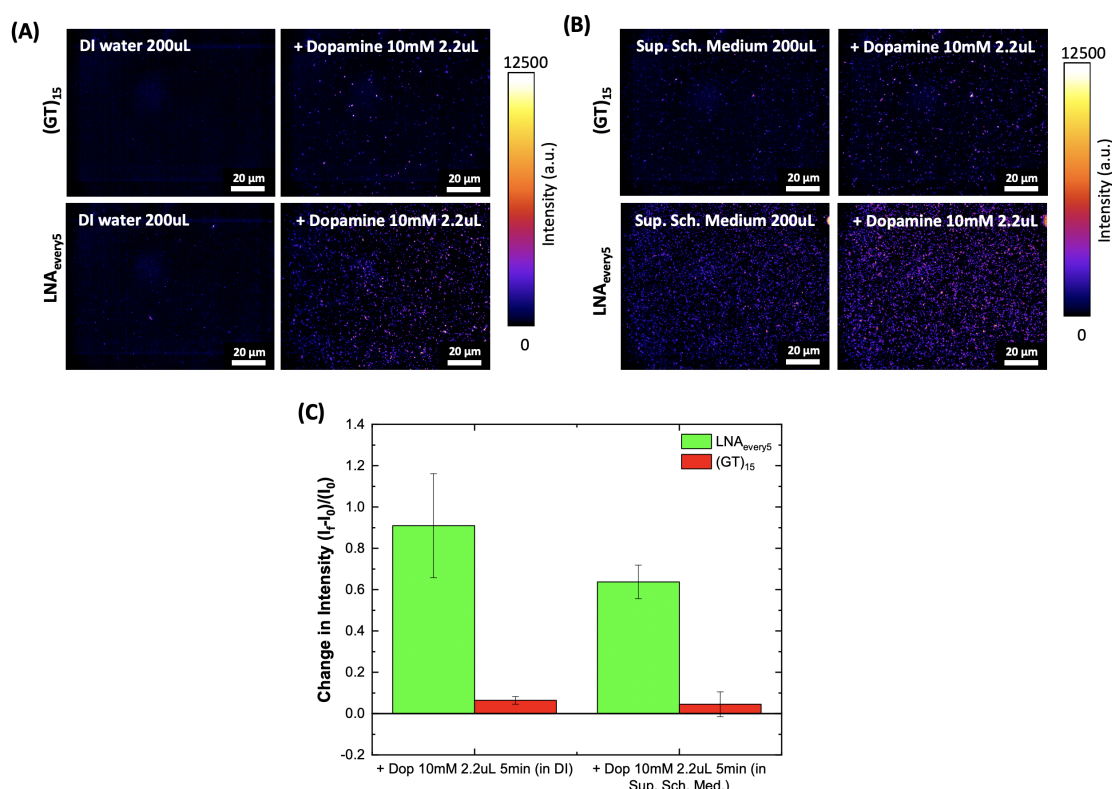


Figure 6.1 – Comparison of DNA- and LNA-SWCNT sensors for dopamine sensing in complex media. (A) NIR fluorescence images of sensors that were immobilized onto a glass surface and incubated in DI water before (**left**) and after (**right**) addition of dopamine (final concentration: 100 μ M). (B) NIR fluorescence images of sensors that were immobilized onto a glass surface and incubated in supplemented Schneider's medium (10% FBS, 1% Pen/Strep) before (**left**) and after (**right**) addition of dopamine (final concentration: 100 μ M). (C) Comparison of the intensity increase of (GT)₁₅- (**red**) and LNA_{every5}-SWCNTs (**green**) following addition of dopamine (100 μ M) in DI water and supplemented Schneider's medium. Intensity changes were calculated from the mean intensity of the wide-field images obtained before and after addition of dopamine (**Appendix Figure E.1 – E.4**, excitation: 780 nm, emission filter: 980 nm LP). All films were incubated in DI water or medium for 15 min prior to measurement. Error bars represent 1 σ standard deviation (n = 3 technical replicates). Backgrounds were subtracted using a Gaussian blur filter (sigma = 50).

In order to use our sensor films for *in vitro* measurements of dopamine release from neurons, it would be necessary grow cell cultures on top of the nanotube films. This would require incubation periods of 24 – 48 h for the *Drosophila* cell cultures in order to provide sufficient time for neurite formation in the culture [301]. Given the recent findings by Pinals *et al.*, we sought to investigate whether longer incubation periods in complex media would affect the ability of the LNA_{every5}-SWCNTs to detect dopamine.

With respect to the envisioned application to image *Drosophila* neurons *in vitro*, we tested four media compositions to examine the affect of the various components in supplemented Schneider's medium. We prepared nanotube sensor films using LNA_{every5} and covered the films with 250 μ L of the desired medium (either DPBS, DPBS with 1% Pen/Strep (also known

6.2. Using XNA-SWCNTs for *In Vitro* Sensing Applications

as Rinaldini's solution), DPBS with 10% FBS, or supplemented Schneider's medium). Covered films were left to incubate at room temperature for 24 h (**Figure 6.2 (A)**). DPBS, a pH balanced salt solution with no Ca^{2+} or Mg^{2+} ions, was used as a negative control to account for changes in the fluorescence properties of nanotube films stored at room temperature for extended periods of time. By comparing the fluorescence turn-on response following dopamine addition for films incubated in DPBS to those incubated in a more complex medium, we could examine the impact of additives such as proteins (FBS) or antibiotics (Pen/Strep).

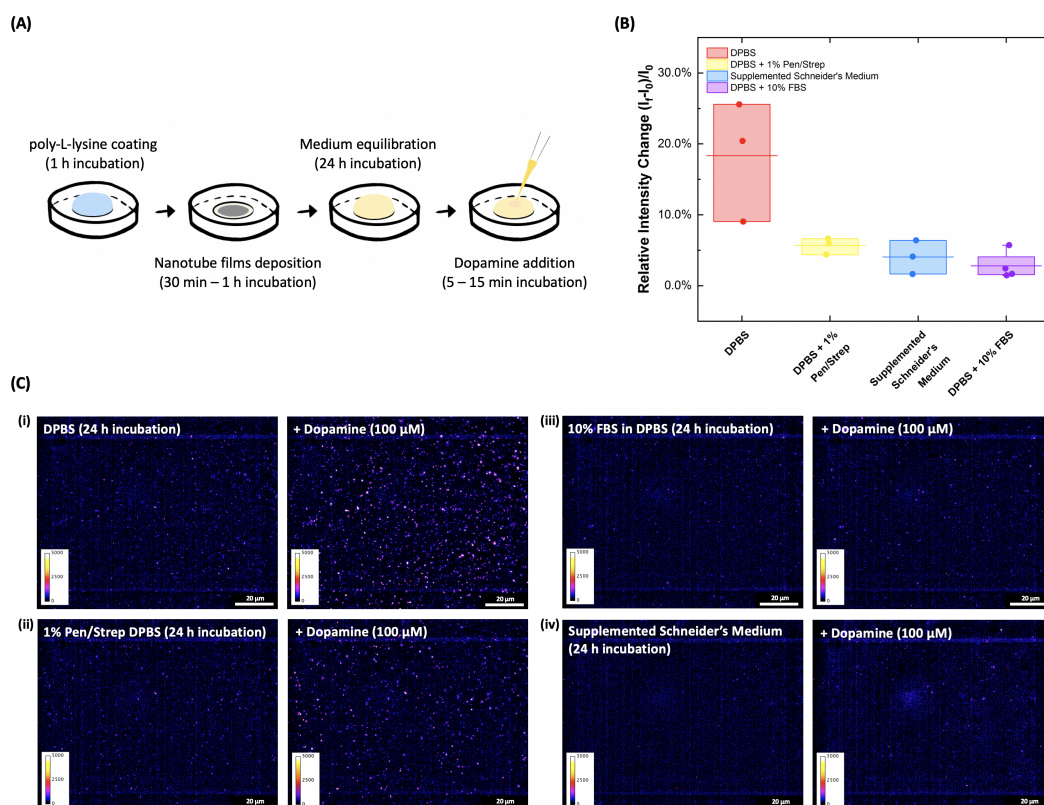


Figure 6.2 – Effect of media composition on the fluorescence response of SWCNT films to dopamine addition. **(A)** Schematic detailing the experimental procedure used to prepare nanotube films to study the effect of medium composition on nanotube fluorescence. All nanotube films were incubated in medium for 24 h prior to measurement. **(B)** Fluorescence intensity increase of the LNA_{every5} films incubated media with different composition following the addition of dopamine (final concentration: 100 μM). Intensity changes were calculated from the mean intensity of the wide-field images obtained (**Appendix Figure E.5, E.6, E.7, and E.8**). Central line represents the average turn-on response. Dots represent the turn-on response of individual replicates (n = 3 – 4 technical replicates). **(C)** Representative NIR fluorescence images of sensors that were immobilized onto a glass surface and incubated with the desired medium ((i) **DPBS**, (ii) **1% Pen/Strep in DPBS**, (iii) **10% FBS in DPBS**, and (iv) **supplemented Schneider's medium**) before (**left**) and after (**right**) addition of dopamine (final concentration: 100 μM, excitation: 780 nm, emission filter: 980 nm LP). Backgrounds were subtracted using a Gaussian blur filter (sigma = 20). Additional replicates are presented in **Appendix Figure E.5 – E.8**.

All sensor films retained an ability to interact with dopamine, however we note that the fluorescence turn-on response was significantly reduced for films incubated in a more complex medium compared to those incubated in DPBS (**Figure 6.2 (B)**). In addition, we observed a significant decrease in the mean fluorescence intensity of films (prior to dopamine addition) incubated in any medium containing FBS (**Figure 6.2 (C)**, **Appendix Figure E.5 – E.8**), although this did not significantly impact the ability of these sensors to interact with dopamine compared to sensors incubated with only antibiotics. Despite this relative decrease, by increasing the density of the nanotube sensor films, we could improve the average turn-on response of the sensors incubated in supplemented Schneider's medium following dopamine addition from $+4.0 \pm 2.4\%$ to $+7.9 \pm 0.3\%$ (**Appendix Figure E.9**). Further increases in film density enabled even greater enhancement, with the ultrahigh density films incubated in 10% FBS exhibiting a dopamine turn-on response of $+61.7 \pm 17.8\%$ (**Appendix Figure E.10**). These findings suggest that although extended incubation periods can impact the ability of the nanotube sensor films to interact with dopamine, the extent by which reactivity is reduced can be tuned by adjusting the sensor density [62].

To ensure that the immobilization of the nanotube sensors did not impact their responsivity to dopamine in complex media, we also tested the fluorescence response of the LNA_{every5}-SWCNTs in solution (**Figure 6.3 (A)**). LNA_{every5}-SWCNT solutions were mixed at a 4:1 ratio with either DI water, supplemented Schneider's medium, or supplemented Schneider's medium with dopamine (100 μM , 10 μM , or 1 μM) and imaged immediately. Although serum media are known to induce nanotube aggregate formation [303], no visible aggregation was observed in any of the samples over the time course of our experiments (< 10 min). We observed a significant fluorescence enhancement following the addition of supplemented Schneider's medium, in line with previous observations for protein-rich solutions [298]. Importantly, this increase in the baseline fluorescence did not destroy the sensors ability to detect dopamine, with significant turn-on responses observed even at low dopamine concentrations (0.2 μM). Furthermore, the sensors retained their ability to exhibit concentration dependent fluorescence intensity increases, although we note that the intensity increase appeared to saturate around 2 μM of dopamine with only a marginally larger fluorescence enhancement recorded for 20 μM of dopamine.

Based on these observations, we subsequently sought to examine whether the presence of neuron cells would impact the response behavior of the LNA_{every5}-SWCNTs to dopamine. *Drosophila* neurons were extracted from the brains of L3 larvae and re-suspended post-digestion in supplemented Schneider's medium. The neuron solution was added into an LNA_{every5}-SWCNT covered, poly-L-lysine coated well on a 96-well plate and incubated overnight. Immediately prior to measurement, an additional 50 μL of LNA_{every5}-SWCNT solution was added to the well. Kinetic measurements were collected following the addition of exogenous dopamine (final concentration: 100 μM) for both the (7,5) and (7,6) chirality (**Figure 6.3 (B)**). Significant turn-on responses were recorded for both peaks with final intensity increases of 31.5% and 36.4% for the (7,5) and (7,6) chirality peaks, respectively. This indicates that our sensors remain capable of detecting dopamine even in the presence of cells and suggests that

these sensors could be used for *in vitro* sensing applications.

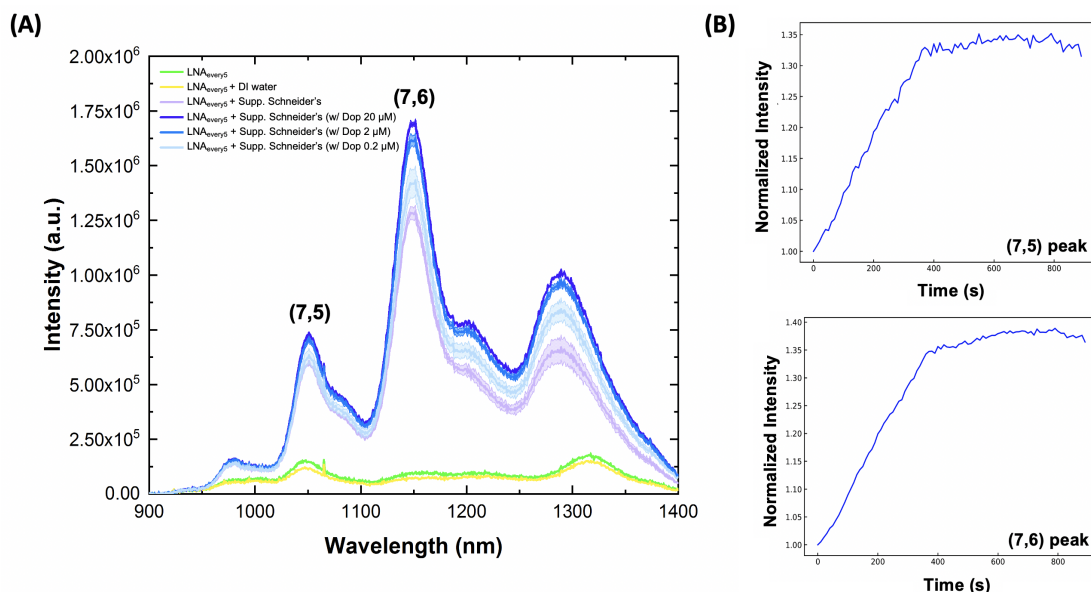


Figure 6.3 – Comparison of the NIR spectral response of LNA_{every5}-SWCNTs to dopamine in complex solutions. **(A)** Fluorescence response of LNA_{every5} following the addition of supplemented Schneider's medium both with and without dopamine (excitation: 660 nm, exposure time: 10 s). Included are the spectra before (green) and following addition of DI water (yellow), supplemented Schneider's medium (purple line), or supplemented Schneider's medium spiked with dopamine (blues, final dopamine concentrations of 20 μM, 2 μM, or 0.2 μM). The solid line represents the average wavelength shift and all shaded regions represent 1σ standard deviation (n = 3 technical replicates). **(B)** Fluorescence intensity response of the (7,5) (top) and (7,6) (bottom) chirality of LNA_{every5} sensors following the addition of exogenous dopamine (final concentration: 100 μM) in a *Drosophila* neuronal cell culture. *Drosophila* neurons were extracted from the brains of L3 larvae and re-suspended post-digestion in supplemented Schneider's medium. Neuronal cell cultures contained transgenic dopamine neurons induced to express CsChrimson (representing approximately 1% of the sample). Cells were grown for 24 h at room temperature in 96-well plates prior to measurement (excitation: 660 nm, exposure time: 10 s).

Finally, we examined the impact of LNA-SWCNTs on cell growth and the impact the cells had on the fluorescence behavior of the sensor films. Transgenic dopamine neurons (representing approximately 1% of the sample) were induced to express either GFP (DA-GFP) or CsChrimson (DA-CsChrimson), a light activated Ca²⁺ Channelrhodopsin (light activation 590 nm) [304], via the Gal4-UAS system [305]. Neurons were incubated on poly-L-lysine glass-bottomed petri dishes overnight, both in the presence and absence of SWCNTs.

Although films incubated with DA-GFP neurons showed higher baseline fluorescence following 48 h of incubation (Figure 6.4 (A)), subsequent analysis of extracted medium from these cultures indicates that it is unlikely that this increase was due to increased dopamine concentrations in the medium but rather an artefact of film heterogeneity. No significant differences were observed between the optical responses following either DA-GFP or DA-CsChrimson medium additions compared to additions of supplemented Schneider's medium,

Chapter 6. Outlook on Potential Applications of XNA-SWCNTs for Improved Optical Biosensing

indicating negligible changes in the medium composition that could effect nanotube fluorescence (Appendix Figure E.28, E.18). The overall similarity in the baseline fluorescence of sensors incubated with neuron cell cultures to those incubated in medium supports our previous observations that the presence of neurons does not negatively impact the fluorescence behavior of the LNA_{every5}-SWCNTs. This further highlights the suitability of these sensors for use in *in vitro* sensing applications.

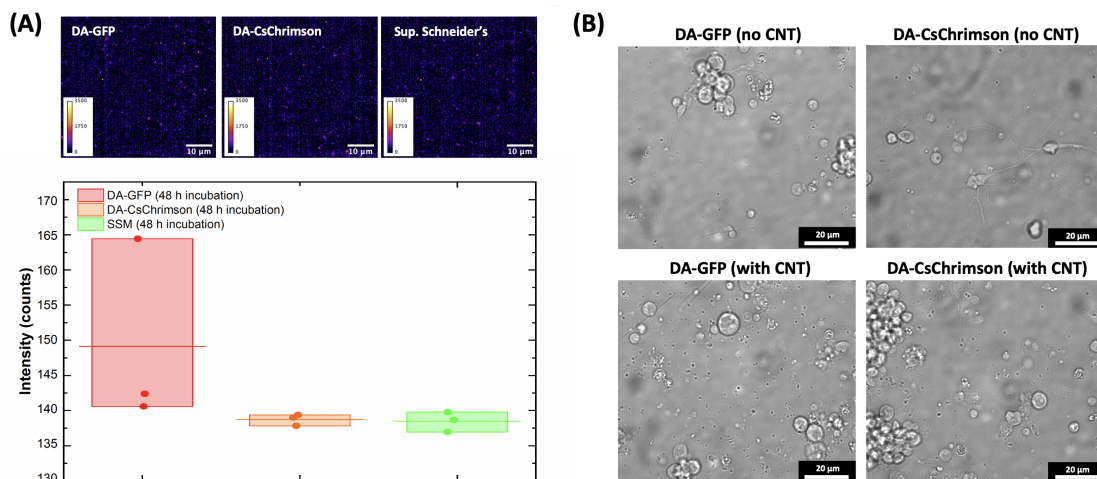


Figure 6.4 – Nanotube films for *in vitro* cell imaging. **(A) (Top)** NIR fluorescence images of LNA_{every5} sensors that were immobilized onto a glass surface and incubated with either *Drosophila* neuronal cell culture or supplemented Schneider's medium (excitation: 780 nm, emission filter: 980 nm LP). All films were incubated for a period of 48 h at room temperature. Neuronal cultures contained transgenic dopamine neurons (DA) (representing approximately 1% of the sample) induced to express either GFP (**left**) or CsChrimson (**center**). All backgrounds were subtracted using a Gaussian blur filter (sigma = 20). **(Bottom)** Fluorescence intensity of the LNA_{every5} films following 48 h incubation. Average intensity values were calculated from the mean intensity of the wide-field images obtained (Appendix Figure E.11). Central line represents the average turn-on response. Dots represent the turn-on response of individual replicates (n = 3 technical replicates). **(B)** White light visible widefield images of neurons following 48 h of growth on poly-L-lysine coated glass (**top**) or LNA_{every5}-SWCNT covered poly-L-lysine coated glass (**bottom**) for both neuronal cell cultures (additional replicates are included in Appendix Figure E.12).

For all samples, cells tended to form clusters and aggregates, however isolated cells were also observed. While cells grown on nanotube films were predominately round, those grown in the absence of nanotubes exhibited greater neurite outgrowth (Figure 6.4, Appendix Figure E.12). In addition, we observed larger amounts of debris in the samples grown on nanotube films. Previous reports in the literature suggest that this debris could consist of nanotube-protein aggregates [300, 303], although further characterisation is required to determine the exact composition.

Although we have demonstrated that our LNA-SWCNTs exhibit superior sensing capabilities in complex media compared to DNA-SWCNTs, further optimization and characterization of sensor behavior in the presence of isolated neurons is required before single-neuron mea-

measurements can be performed. This includes studying the statistical fluctuations of nanotube intensity with time as well as improving cell adhesion to the nanotube films. Promising approaches for future research on LNA-SWCNTs also include incorporating these sensors into *ex vivo* brain slices to study dopamine release and other cation-dependent processes without competing fluorescence responses.

6.3 XNA-SWCNTs for miRNA Detection

Over the past few decades, microRNAs (miRNAs) have emerged as promising biomarkers for a range of diseases [158, 159, 306]. miRNAs are short strands of non-coding RNA, typically 15 – 25 nucleotides [67], which are involved in the regulation of many cellular processes including differentiation, cell growth and cell death [68]. These molecules play an important regulatory role in gene expression by triggering degradation, affecting translation, or regulating transcription of target messenger RNAs (mRNAs) [63]. Deregulated expression of different miRNAs is associated with a range of diseases, including numerous types of cancers [64–69] and as such circulating miRNA and exosomal miRNA has immense potential to serve as noninvasive diagnostic biomarkers [67].

Despite growing interest in the detection of miRNA, clinical implementation has been limited by the trade-offs typically encountered between accuracy/sensitivity and cost/time for the detection methods currently available [67, 307]. For example, RNA-sequencing provides the most sensitive quantification and detection of miRNA, however this technique requires extensive processing and evaluation steps that increase both the time and cost of analysis. As a result, this technique is typically reserved for use in the discovery of novel miRNA rather than clinical detection. Conversely, the most common method of miRNA detection in diagnostics, reverse-transcription polymerase chain reaction (RT-PCR) [308, 309], relies on relatively standard equipment and the processing can be more or less automated leading to much faster processing times. However, an undeniable bias from unreliable background corrections/normalizations, a reliance on error-prone reverse-transcription reactions, and a lack of standardization for pre-processing steps can lead to sub-optimal specificity and problems with reproducibility when using this approach.

To address aspects of these shortcomings, Kappel *et al.* designed a new form of immunoassay, miRNA enzyme immunoassay (miREIA), for miRNA quantification [310]. In miREIA, miRNA is hybridized with complementary biotinylated DNA oligonucleotides and these duplexes are subsequently detected using a monoclonal antibody. The miREIA workflow is similar to the ELISA methodology used for antigen detection and can be run on standard immunoassay analyzers increasing its applicability and convenience in clinical settings. In addition, this approach circumvents any need for reverse-transcription or amplification/pre-amplification steps thereby increasing reproducibility. However, as this approach requires miRNA purification from blood samples it has limited use in both unprocessed samples and *in vivo* applications [310].

Chapter 6. Outlook on Potential Applications of XNA-SWCNTs for Improved Optical Biosensing

Owing to the many advantages of SWCNTs, recent works have looked to engineer SWCNT-based optical sensors for the detection of short DNA sequences or miRNA that transduce DNA hybridization into spectral changes in the emission spectrum of the SWCNT. Optical modulation of SWCNT fluorescence was first used to detect DNA hybridization by Jeng *et al.* [87]. In this study, a hypsochromic shift of 2 meV was observed following the addition of complementary DNA, with no significant wavelength shift observed on addition of a non-complementary strand [87]. The wavelength shifting observed on recognition of the complementary sequence was attributed to an increase in the surface coverage of the SWCNT following hybridization. Later work by Jeng *et al.* went on to demonstrate how these DNA-SWCNTs were also capable of detecting single nucleotide polymorphisms (SNPs) [157]. More recent work by Harvey *et al.* presented a DNA-SWCNT sensor for the optical detection of different miRNA sequences [10]. In this work, spectral changes following hybridization were attributed to the displacement of both electrostatic charge and water from the nanotube surface. Following hybridization, the newly formed duplex was hypothesized to desorb from the surface of the nanotube leaving only the nanotube-binding domain in contact, resulting in an increase of the exposed surface area. Subsequent addition of surfactant molecules led to increased water shielding and a markedly enhanced spectral response as the moieties underwent a triggered assembly on the nanotube surface. These sensors were subsequently used for the direct detection of miRNA in urine and serum and also for the first *in vivo* optical detection of target DNA and miRNA using SWCNT NIR fluorescence.

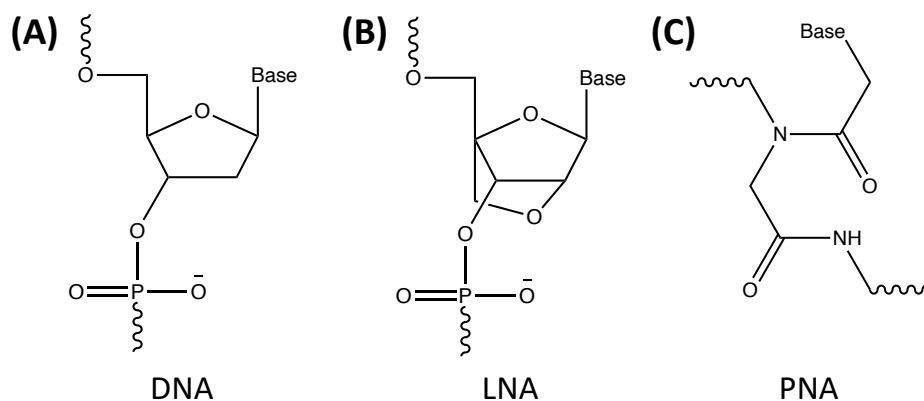


Figure 6.5 – Structures of (A) DNA, (B) LNA, and (C) PNA. LNA is an unnatural nucleic acid where the ribose ring has an additional methyl bridge between the 2' oxygen and 4' carbon. The presence of the bridge 'locks' the LNA into the 3'-endo (North) conformation, the ideal conformation for Watson-Crick binding [278]. PNA is an artificially synthesized polymer similar to DNA where the sugar-phosphate backbone has been replaced by N-(2-aminoethyl)-glycine units linked by peptide bonds [311].

The previous chapters of this thesis have highlighted several advantages of XNA-SWCNTs over conventional DNA-SWCNTs for different sensing applications. XNAs have also been extensively studied for miRNA detection, most notably LNA [184, 312–317] and peptide nucleic acid (PNA) [311, 318–322] owing to their improved efficiency compared to DNA probes (**Figure 6.5**). PNA is of particular interest due to its uncharged backbone which enables stronger

DNA hybridization due to the absence of electrostatic repulsion [323, 324]. An additional consequence of the lack of electrostatic repulsion is that PNA can hybridize with DNA virtually independently of the salt concentration [322]. PNA also demonstrates increased specificity compared to DNA or RNA, as any base pair mismatch results in greater destabilization for PNA than natural oligonucleotides [319], however the destabilisation of the mismatch is strongly impacted by its position along the sequence [325].

In this section we seek to combine the advantages of SWCNT-based sensors with those of synthetic biology oligomers, specifically PNA, and present preliminary findings on the use of PNA-DNA-SWCNT hybrids to create a platform for the label-free detection of miRNA. Our findings show that it is possible to form stable PNA-DNA-SWCNTs, which demonstrate optically distinct spectra compared to their DNA-SWCNT counterparts. In addition, our PNA-DNA-SWCNT sensors demonstrate rapid miRNA detection capabilities without a need for additional surfactant molecules during the detection process [10], making the sensors more applicable for *in vivo* sensing applications. We show that the length of the PNA-DNA hybrid section effects the performance of the sensor, indicating that the mechanism of response is not simply non-specific adsorption of the PNA/miRNA onto the DNA-SWCNT surface. Furthermore, the modular approach for designing PNA-DNA-SWCNT sensors presented in this chapter provides a proof-of-concept for a platform that can be readily adapted for a variety of different miRNA sequences. Future studies will further investigate the mechanisms of interaction for the DNA-PNA-miRNA and expand upon the library and concentration ranges of miRNA that can be detected.

6.3.1 Results and Discussion

The uncharged backbone of PNA means that this polymer cannot be used to obtain stable dispersions of isolated SWCNTs [30]. To overcome this limitation, we designed a modular assembly for PNA-DNA-SWCNTs, where DNA scaffolds were used to attach PNA to the SWCNT surface. Initial experiments used a DNA sequence containing a (GT)₁₀ anchor section and an eight base long hybrid section, whose sequence was reverse complementary to the hybrid portion for all PNA sequences (5'-GTC TCT TC-3'), hence forth referred to as DNA_{8bp-rev}. DNA_{8bp-rev} was used to prepare nanotube dispersions via MeOH-assisted surfactant exchange. In order to maximise the interaction of PNA with the DNA that was adsorbed onto the nanotube surface, free DNA was removed from the suspension using ultrafiltration devices. PNA-DNA-SWCNTs were constructed by mixing PNA solution together with the DNA-SWCNT suspension. A schematic of the assembly process for the PNA-DNA-SWCNTs is shown in **Figure 6.6 (A)**.

The optical response of DNA_{8bp-rev}-SWCNTs following the addition of PNA or PNA with miRNA was examined using fluorescence spectroscopy. All samples were incubated for a period of 1 – 2 h following addition of miRNA and PNA prior to acquiring any spectra. As shown in the photoluminescence excitation/emission (PLE) maps (**Figure 6.6 (B)**, **Appendix Figure E.21**), distinct differences were observed following the addition of PNA and following the subsequent

Chapter 6. Outlook on Potential Applications of XNA-SWCNTs for Improved Optical Biosensing

addition of complementary miRNA for all PNA-DNA-SWCNTs. Line plots were extracted from the PLE maps to more easily compare the fluorescence changes on addition of PNA or miRNA (Figure 6.6 (C), Appendix Figure E.22).

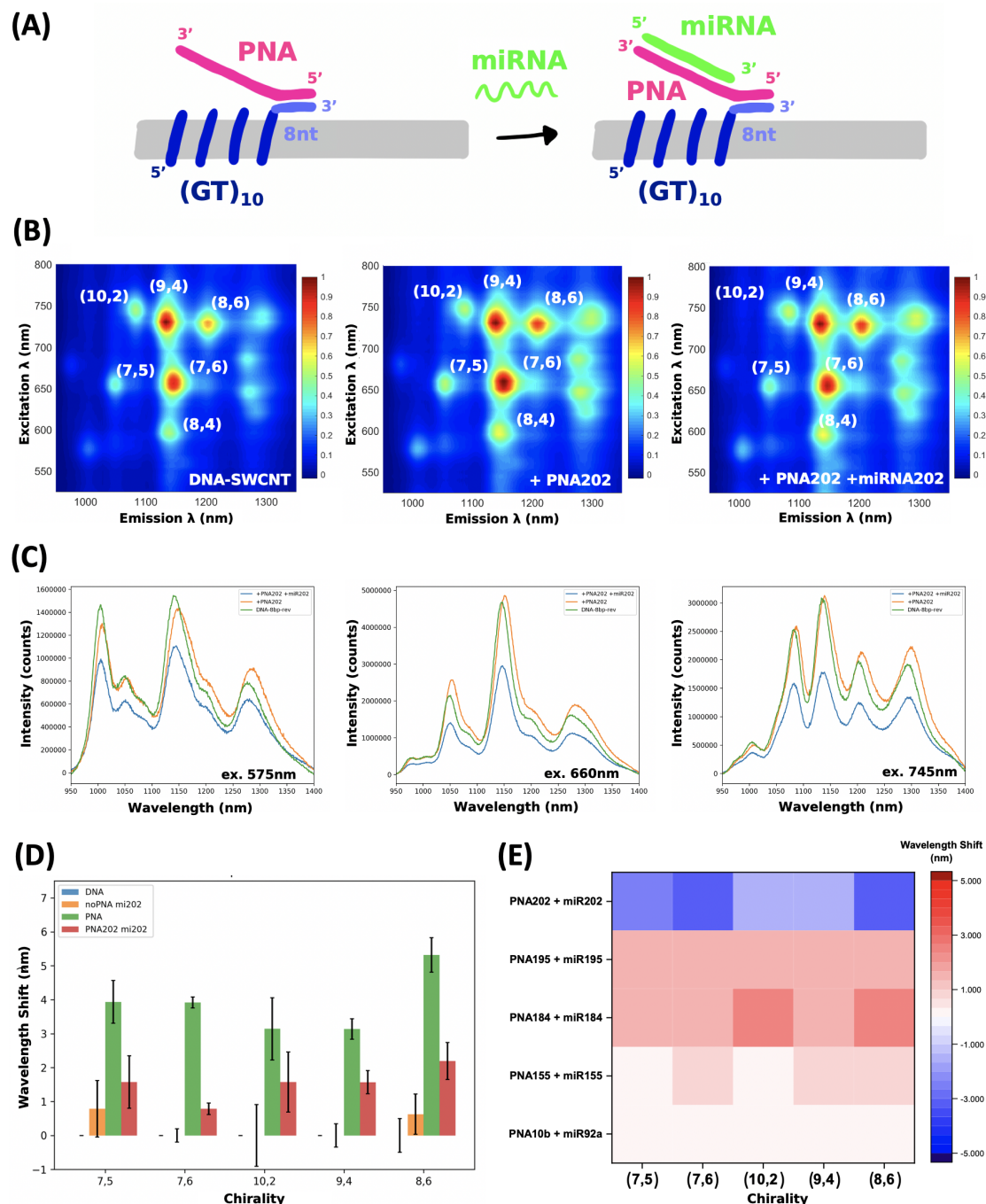


Figure 6.6 – Detection of miRNA using PNA-DNA-SWCNT hybrids. **(A)** Schematic of PNA-DNA_{8bp-rev} configuration used to create the sensor for miRNA detection. The DNA wrapping sequence consisted of a (GT)₁₀ anchor and eight bases designed to hybridize with the PNA sequence. **(B)** PLE maps of the original DNA_{8bp-rev}-SWCNT solution (**left**), the DNA_{8bp-rev}-SWCNT solution mixed with PNA₂₀₂ (PNA-DNA-SWCNT, **center**), and the PNA-DNA_{8bp-rev}-SWCNT solution mixed with complementary miRNA (miR202, **right**). The predominate chiralities are labelled in white. All fluorescence intensities were normalized to the maximum intensity in each plot (final concentration: PNA = 9.5 μ M, miRNA = 4.8 μ M). **(C)** Spectra extracted from PLE maps to compare the intensity and wavelength positions of the DNA_{8bp-rev}-SWCNTs (**green**), the PNA-DNA_{8bp-rev}-SWCNTs (**orange**), and the PNA-DNA_{8bp-rev}-SWCNTs following the addition of complementary miRNA (**blue**). The wavelength of the excitation laser used is indicated in the lower right corner (final concentration: PNA = 9.5 μ M, miRNA = 4.8 μ M). **(D)** Comparison of the chirality dependent wavelength shifts following addition of miRNA (**orange**), PNA (**green**), and PNA with complementary miRNA (**red**) (final concentration: PNA = 9 μ M, miRNA = 1 μ M). All wavelength shifts were calculated versus the wavelength positions for DNA_{8bp-rev}-SWCNTs. For DNA_{8bp-rev}-SWCNTs, error bars represent 1 σ standard error (n = 5 technical replicates). For all other samples error bars represent the error on the fit of the peak (3 σ from one technical replicate). **(E)** Fluorescence wavelength responses of PNA-DNA_{8bp-rev}-SWCNTs following the addition of complementary and non-complementary miRNA (final concentration: PNA = 9 μ M, miRNA = 1 μ M). Complementary miRNA was added to PNA₂₀₂-, PNA₁₉₅-, PNA₁₈₄-, and PNA₁₅₅-DNA_{8bp-rev}-SWCNTs. Non-complementary miRNA was added to PNA_{10b}-DNA_{8bp-rev}-SWCNTs. All wavelength shifts were calculated versus the wavelength position of each chirality for the PNA-DNA_{8bp-rev}-SWCNTs prior to miRNA addition. **Red** indicates a red-shift in the wavelength position of the chirality peak, and **blue** represents a blue-shift in the wavelength position.

In general, the addition of PNA (final concentration: PNA = 9 μ M) resulted in a red-shift in the wavelength position corresponding to the peak fluorescence of the predominate chiralities. Despite this, the extent of the red-shift was sequence dependent; PNA₂₀₂ resulted in the largest shift (5.3 ± 0.5 nm) and PNA₁₉₅ the smallest shift (0.6 ± 0.5 nm) both for the (8,6) chirality (all other wavelength shifts are listed in **Table 6.1**).

Table 6.1 – Wavelength shift following the addition of PNA sequences to DNA_{8bp-rev}-SWCNTs

PNA sequence	Wavelength shift (nm)				
	(7,5)	(7,6)	(10,2)	(9,4)	(8,6)
PNA _{10b}	1.6 ± 0.8	0.8 ± 0.2	1.6 ± 0.9	1.6 ± 0.4	1.4 ± 0.5
PNA ₁₅₅	2.4 ± 0.8	1.6 ± 0.2	1.6 ± 0.9	1.6 ± 0.4	2.2 ± 0.5
PNA ₁₈₄	2.4 ± 0.8	2.4 ± 0.2	1.6 ± 0.9	1.6 ± 0.3	3.0 ± 0.5
PNA ₁₉₅	0.0 ± 0.8	0.0 ± 0.2	0.0 ± 0.8	0.0 ± 0.3	0.6 ± 0.6
PNA ₂₀₂	3.9 ± 0.6	3.9 ± 0.2	3.1 ± 0.9	3.1 ± 0.3	5.3 ± 0.5

The addition of PNA₂₀₂ resulted in the largest red-shift of any of the PNA sequences for all chiralities. Increased water accessibility or increased anionic charge is known to result in red-shifting of nanotube emission wavelengths, while decreases in local anionic charge density or water density at the nanotube surface can cause blue-shifting [10, 35]. As PNA is uncharged, we attribute this red-shifting to an increase in the accessible surface area (decrease of surface coverage), which results in increased water accessibility to the nanotube surface. We hypothesize that this increase in surface area is a result of the dissociation of the partial duplex formed from the nanotube surface [10]. The larger increase relative to the other PNA

sequences may result from the shorter sequence length of PNA₂₀₂.

For PNA₂₀₂-DNA_{8bp-rev}-SWCNTs, subsequent addition of complementary miRNA (miR202, final concentration: 1 μ M) resulted in blue-shifting of the fluorescence back towards the original positions of the DNA_{8bp-rev}-SWCNTs. Importantly, the addition of miR202 in the absence of PNA₂₀₂ did not result in any significant shifting of the wavelength position for any of the chirality peaks measured (**Figure 6.6 (D)**) indicating that the response observed was due to the interaction of the PNA and complementary miRNA sequence. While it is possible that PNA preferentially binds with miRNA before fully hybridizing with the DNA-SWCNT or that post-hybridization the PNA complex detaches from the DNA_{8bp-rev}-SWCNT, the strong stability of PNA-DNA complexes means this is unlikely even accounting for the increased stability of the PNA-RNA complex [319]. Instead, we attribute the blue-shift of PNA₂₀₂ following miR202 addition to increased surface coverage following hybridization, which we believe is due to the PNA-miRNA duplex adsorbing onto the nanotube surface [89]. Although decreases in the local anionic charge density can also result in blue-shifting, due to the neutral charge of the PNA, we do not believe that there would be a significant change even if the hybridized sequence was partially desorbed from the nanotube surface [10].

Conversely, for PNA₁₉₅, PNA₁₈₄, and PNA₁₅₅ the addition of complementary miRNA resulted in increased red-shifting (**Figure 6.6 (E)**, **Appendix Figure E.24, E.25**). This response continued to be statistically distinct from the optical response following miRNA addition in the absence of PNA for all sequences. Differences in the directionality of the shift may result from fundamentally different interaction mechanisms that result in unique structural changes depending on the PNA and miRNA combination. The enhanced red-shift may be the result of increases in the local anionic charge density either due to non-specific adsorption of the miRNA or from the phosphate backbone from the miRNA being brought into close proximity of the nanotube surface following hybridization. However, we discount the possibility that the red-shift is due to non-specific adsorption of the miRNA onto the nanotube due to a lack of significant shifting following miRNA addition in the absence of PNA (**Appendix Figure E.24**). Alternatively, the red-shift may result from increasing water accessibility due to partial desorption of the hybridized PNA-miRNA from the nanotube surface. However, in order to determine which of these effects has the largest impact, additional experiments such as molecular dynamics simulations, AFM, or FRET assays to test duplex desorption from the nanotube surface are required [10]. The addition of non-complementary miRNA (miR92a) to PNA_{10b} did not result in any significant wavelength shifts for any chirality measured, indicating that the interaction of the PNA and miRNA was sequence specific and providing further evidence that the red-shifts observed for the other PNA sequences were not a result on non-specific adsorption.

Following our initial observations using DNA_{8bp-rev}-SWCNTs, we sought to examine the impact of the length of the hybrid portion, as well as the directionality of the PNA-DNA hybridization (parallel or anti-parallel), on the sensing capabilities of the PNA-DNA constructs.

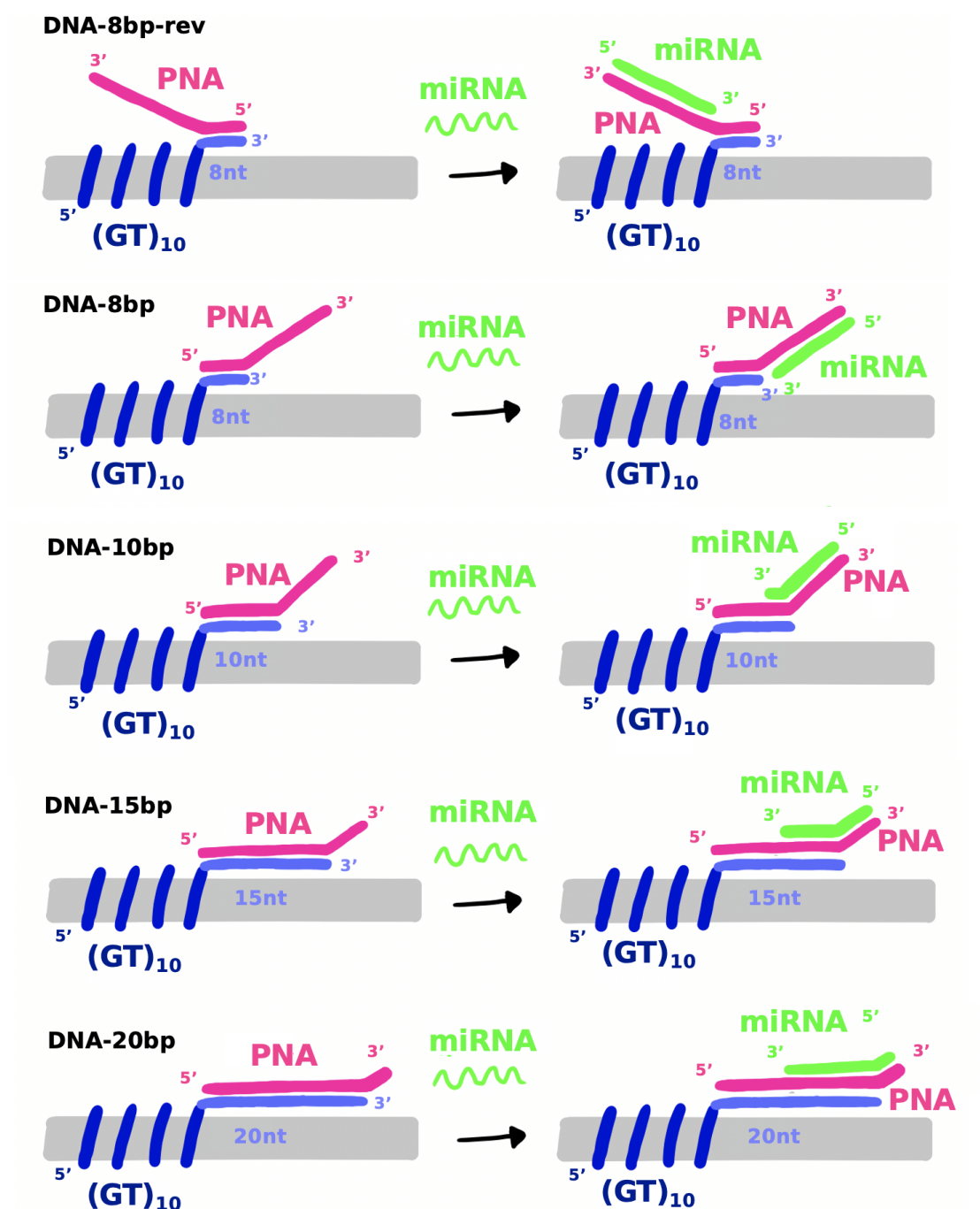


Figure 6.7 – Schematic of the PNA-DNA-SWCNT configurations differing in length of the hybrid portion (8, 10, 15, or 20 bases) and directionality of the hybridization (anti-parallel (rev) or parallel). PNA hybridizes with DNA in a sequence-dependent manner, according to the Watson-Crick hydrogen bonding scheme [322]. However, contrary to DNA, PNA can bind to complementary nucleic acids in both parallel and anti-parallel orientation, although the later is preferred and results in a more stable complex [319, 322].

Chapter 6. Outlook on Potential Applications of XNA-SWCNTs for Improved Optical Biosensing

In contrast to DNA, PNA can bind in either a parallel or anti-parallel fashion as a result of its more flexible backbone [319, 322]. However, kinetic studies have shown that, in general, PNA demonstrates a preference towards the antiparallel binding orientation with lower affinity observed for duplexes formed with parallel orientation [319]. As we want to maximise the extent by which PNA preferentially binds with the target miRNA sequence over the DNA, we predominately tested constructs that consist of a DNA-PNA hybrid section with a parallel orientation for miRNA binding on recognition in an anti-parallel fashion. This should enable significantly faster duplex formation for the PNA-miRNA duplex [319] and ideally result in a more reactive complex. A schematic illustrating the different configurations of PNA-DNA-SWCNTs tested is provided in **Figure 6.7**.

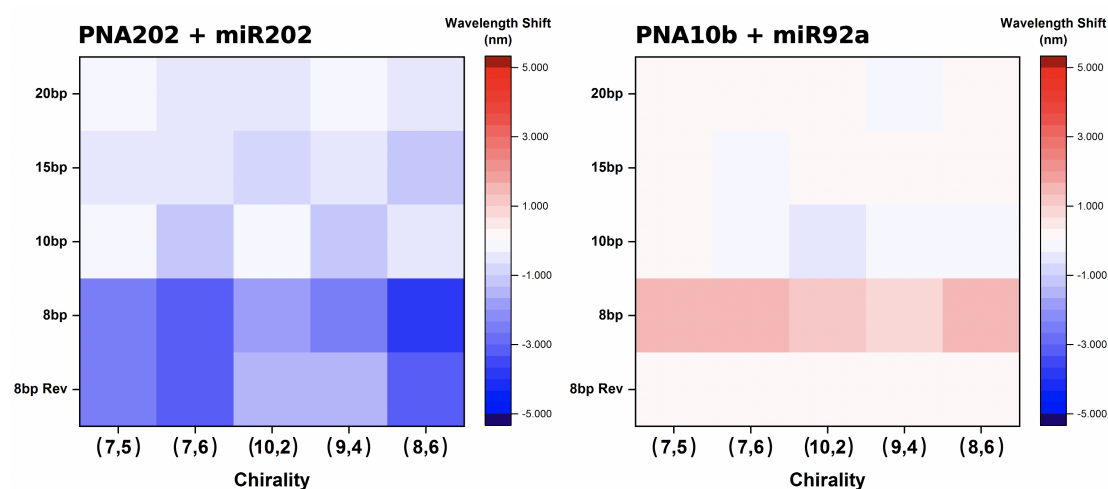


Figure 6.8 – Dependency of the wavelength shifting response of PNA-DNA-SWCNTs on the length of the DNA hybrid portion. Comparison of the wavelength shift following addition of complementary (**left**) and non-complementary (**right**) miRNA to PNA-DNA-SWCNTs (final concentration: PNA = 9 μ M, miRNA = 1 μ M). PNA-DNA-SWCNTs were formed using different lengths for the hybrid portion in the DNA sequence (8, 10, 15, or 20 bases) as well as different directionalities for the hybridization (anti-parallel (rev) or parallel). All wavelength shifts were calculated versus the wavelength position of each chirality for the PNA-DNA-SWCNTs prior to miRNA addition. **Red** indicates a red-shift in the wavelength position of the chirality peak, and **blue** represents a blue-shift in the wavelength position.

In line with expectations, the PNA₂₀₂ complexes formed using DNA_{8bp}-SWCNTs (parallel binding) had a larger blueshift in the wavelength peak positions of all chiralities following the addition of complementary miRNA compared to when using DNA_{8bp-rev}-SWCNTs (anti-parallel binding) (**Figure 6.8, Appendix Figure E.25, E.26**). Moreover, we observed a notable decrease in the wavelength shifting response for PNA₂₀₂-DNA-SWCNTs as the length of the hybrid section was increased. Interestingly, whereas PNA₁₅₅, PNA₁₈₄, and PNA₁₉₅ exhibited a red-shift in response to complementary miRNA for complexes using the DNA_{8bp-rev} sequence, complexes formed using the parallel binding sequence, DNA_{8bp}, exhibited a blue-shifting response for certain chiralities depending on the PNA sequence. Furthermore, as the length of the hybrid section was increased, we observed that all PNA-DNA-SWCNTs began to exhibit a blue-shift in the wavelength position of all chiralities following the addition of complementary

miRNA (**Appendix Figure E.25 – E.30**). On the contrary, PNA_{10b}-DNA-SWCNTs, which are used as a negative control with non-complementary miRNA, showed no significant shifting following miRNA addition for any PNA-DNA complexes with a hybrid section length of 10 or more bases (**Figure 6.8**).

We note however that a redshift in the peak positions of all chiralities was observed following the addition of non-complementary miRNA (miR92a) for the PNA_{10b}-DNA_{8bp}-SWCNTs. Although the exact reason for this observed wavelength shift remains an ongoing area of study, we rule out the possibility that it is due to non-specific adsorption of the miRNA onto the nanotube surface as no significant changes were observed following miRNA addition in the absence of PNA (**Appendix Figure E.26**).

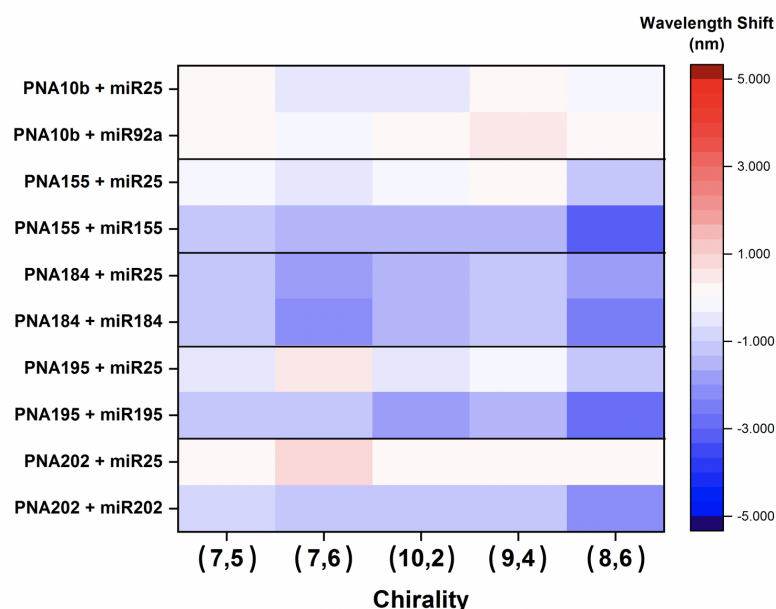


Figure 6.9 – Fluorescence wavelength shift response of PNA-DNA_{15bp}-SWCNTs to complementary and non-complementary miRNA (final concentration: PNA = 9.4 μ M, miRNA = 5.7 μ M). complementary miRNA was added to PNA₂₀₂-, PNA₁₉₅-, PNA₁₈₄-, and PNA₁₅₅-DNA_{15bp}-SWCNTs, as well as the non-complementary miR25 for comparison. Two different non-complementary miRNAs (miR25 and miR92a) were added to PNA_{10b}-DNA_{15bp}-SWCNTs. All wavelength shifts were calculated versus the wavelength position of the chiralities for the respective PNA-DNA_{15bp}-SWCNT solution prior to miRNA addition. **Red** and **blue** indicate a red-shift or blue-shift in the wavelength position, respectively.

In order to examine whether a fluorescence wavelength shift response could be engineered for the PNA-DNA-SWCNTs with longer hybrid sections, we increased the concentration of miRNA relative to the PNA. We hypothesized that in order to see significant fluorescence responses a majority of the PNA-DNA-SWCNTs would need to react with miRNA. Based on this assumption, we believed that the response to miRNA could be recovered (or enhanced) by increasing the relative concentration of the miRNA to at least 50% of the PNA concentration in solution. To test this hypothesis we examined the spectral responses for constructs made using a 15

base hybrid section following the addition of higher concentrations of either complementary or non-complementary miRNA (**Figure 6.9, Appendix Figure E.31, E.32**). As expected, no significant wavelength shift was observed for PNA_{10b}-DNA_{15bp}-SWCNTs following the addition of either non-complementary miRNA sequence. Although PNA₁₈₄ had strong blue-shifting responses following the addition of miR184 for both the (7,6) and (8,6) chiralities, this complex also strongly reacted with the non-complementary sequence indicating that this was not a sequence specific detection mechanism. Significant blue-shifts were also observed for all chiralities for PNA₂₀₂, PNA₁₉₅, and PNA₁₅₅ constructs on addition of complementary miRNA. Moreover, the addition of non-complementary miRNA induced red-shifting for all PNA₂₀₂ chiralities or a minor blue-shift for most PNA₁₉₅ and PNA₁₅₅ chiralities, indicating that the blue-shifting response to complementary miRNA was a sequence specific interaction. We also observed a red-shift of the peak position in the absorbance spectrum (**Appendix Figure E.33**) of DNA_{15bp}-SWCNTs (1136.5 nm) on addition of PNA₁₅₅ (1139.5 nm) and subsequently a blue-shift on addition of miR155 (1137.5 nm) following only 15 min of incubation (**Appendix Figure E.33**). No shift was observed on addition of non-complementary miRNA (**Appendix Figure E.33, E.34**). Additional experiments using hybrid sections with a length of 10 or 20 bases (**Appendix Figure E.35, E.36, E.42**) also demonstrated strong blue-shifting on addition of complementary miRNA and a lack of response for non-complementary miRNA.

These findings provided a proof-of-concept that PNA-DNA-SWCNTs can be used for the rapid and selective optical detection of miRNA. Future work will examine the abilities of these sensors to work in biological solutions, such as blood, serum, or urine. Additionally, further optimization of the ratio of PNA:miRNA will be required to improve the limit of detection of the sensors. Finally, to maximise the potential of these sensors, multiplexed detection for several miRNA sequences can be designed using nanotube preparations enriched with different chiralities and different PNA-DNA constructs. This would enable the creation of a versatile platform that could be customized for a plethora of different miRNA combinations, enabling rapid biomarker detection for a range of diseases.

6.4 Conclusions

The preliminary results presented in this chapter demonstrate the potential application of LNA-SWCNTs for neurosensing applications in complex media and PNA-DNA-SWCNTs for the rapid detection of miRNA.

Nanotube films made using LNA-SWCNTs exhibited superior optical sensing capabilities towards dopamine compared to their DNA-SWCNT counterparts with more than a 14-fold increase in the turn-on response observed in both DI water and supplemented Schneider's medium. Furthermore, LNA-SWCNTs films retained their dopamine sensing ability even following extended incubation periods (24 – 48 h) at room temperature in the presence of proteins, antibiotics, and whole cell cultures. Moreover, we observed that the turn-on response to dopamine following extended incubation periods could be tuned by controlling

the density of the nanotube films used. Although these findings present LNA-SWCNTs as a promising alternative to DNA-SWCNTs for *in vitro* sensing applications, further optimization is required for single-cell measurements. Specifically, cell adhesion to the nanotube films must be improved and extended studies on the fluctuations of nanotube intensity pre- and post-dopamine stimulation needs to be performed. These LNA-SWCNT sensors could also be implemented in *ex vivo* brain slices to study dopamine release or other cation-dependent processes.

The novel process introduced for the assembly of PNA-DNA-SWCNTs presents a flexible platform that can be used to design sensors for many different miRNA sequences. For all constructs studied, we observed a strong red-shift in the fluorescence of DNA-SWCNTs following the addition of PNA, up to 5.5 nm depending on the DNA and PNA sequence and the nanotube chirality. On subsequent addition of miRNA, the PNA-DNA-SWCNTs underwent either blue- or red-shifting. The extent and direction of shifting was strongly dependent on the PNA sequence used but also on the length of the PNA-DNA hybrid section and directionality of the hybridization. Highest shifts were observed for DNA_{8bp} and DNA_{8bp-rev} at low concentrations of miRNA. We also noted a strong dependency of our sensors on the concentration ratio of PNA:miRNA, with improved shifting responses observed as the relative concentration of miRNA was increased. Furthermore, several of the sensors examined showed strong sequence specificity, with little to no response detected on addition of non-complementary miRNA. Based on these observations we conclude that it may be possible to tune the sensor response for lower concentrations of miRNA by adjusting the relative amounts of PNA added. Using our PNA-DNA-SWCNTs we could detect complementary miRNA additions by monitoring wavelength shifts in both absorbance and fluorescence with detection speeds of < 15 min and < 1 h, respectively.

These findings provide a proof-of-concept that PNA-DNA-SWCNTs can be used as a promising method for the rapid optical detection of miRNA. Future work will examine the ability of these sensors to work in biological solutions (such as blood, serum, or urine), determine whether these sensors are capable of detecting single nucleotide polymorphisms, and expand on the library of miRNAs that can be detected. Ultimately this platform will be expanded for multiplexed detection of several miRNA sequences by customizing specific chiralities with different PNA-DNA constructs, providing a technology that can be used for detecting a plethora of different diseases and miRNA combinations.

6.5 Materials and Methods

6.5.1 Using XNA-SWCNTs for *In Vitro* Sensing Applications

Drosophila growth and neuron extraction

The following flies were obtained from the Bloomington *Drosophila* Stock Center: Tyrosine hydroxylase-GAL4 (Stock #8848, full genotype: w[*]; P{w[+mC]=ple-GAL4.F}3), UAS-GFP (Stock

Chapter 6. Outlook on Potential Applications of XNA-SWCNTs for Improved Optical Biosensing

#35839, full genotype: $y[1] w[*]; P\{w[+mC]=UAS-CD4-tdGFP\}8M2$), and UAS-CsChrimson (stock #55135, full genotype: $w[1118]; P\{y[+t7.7] w[+mC]=20XUAS-IVS-CsChrimson.mVenus\}attP40$). Parental flies were raised at 25°C and 50% relative humidity in 12h:12h dark:light cycles. Larval progeny of the above lines was raised in the dark, on food supplemented with all-trans retinal (~0.2 mM).

Drosophila neuronal cell culture was prepared as described by Egger *et al.* [301]. Briefly, L3 larvae were picked from food vials, washed in 70% ethanol and placed in petri dishes containing supplemented Schneider's medium (Schneider's medium (Gibco, cat. no. 21720-024) supplemented with 1% (v/v) penicillin-streptomycin (1% Pen/Strep, Life Technologies, cat. no. 15070063) and 10% (v/v) heat-inactivated fetal bovine serum (10% FBS, Sigma)). Brains were dissected out and immediately rinsed with Rinaldini solution (DPBS (Life Technologies) with 1% Pen/Strep) prior to being processed for dissociation. Tissue was digested for 1 hr at RT with collagenase I (0.5 mg/mL) (Sigma, cat. no. C9697). Digested tissue was rinsed with supplemented Schneider's medium and finally resuspended in supplemented Schneider's medium. Tissue was subsequently physically triturated by pipetting up and down at least 200 times.

NIR widefield imaging

Samples were imaged using a custom-built optical setup consisting of an inverted microscope (Eclipse Ti-E, Nikon AG Instruments) with either an oil-immersion TIRF 100 × objective (N.A. 1.49, Nikon) coupled to either an InGaAs camera (NIRvana 640 ST, Princeton Instruments) or Shamrock 303i spectrometer (Andor) or EMCCD visible camera (iXon Ultra 888, Andor). For NIR images, samples were illuminated using a TriLine LaserBank system (Cairn Research) at 780 nm and fluorescence was collected using a 980 nm long-pass (LP) filter (Semrock). For visible images, samples were illuminated using LED excitation at either 395 nm (emission filter: 417 – 477 nm) or 470 nm (emission filter: 502 – 538 nm). Images were acquired using the Nikon NIS-Elements software (Nikon Instruments).

Nanotube films were prepared on poly-L-lysine coated glass petri dishes by incubating 10 μ L of SWCNT solution (10 mg/L) and 40 μ L DI water for 30 – 60 min, followed by washing with DI water. More dense nanotube films were prepared by incubating 20 μ L of SWCNT solution (10 mg/L) and 30 μ L DI water for 60 min, followed by washing with DI water.

For single molecule images of nanotube film responses to dopamine addition, films were initially imaged in the absence of any medium or buffer. 200 μ L of either DI water or Supplemented Schneider's medium (10% FBS, 1% Pen/Strep) (200 μ L) was added to the petri dish and the samples were imaged immediately, as well as following an incubation period of 5 min. Following this, 2.2 μ L of freshly prepared dopamine solution (10 mM) was added. The samples were again imaged immediately and following 5 min of incubation. All imaging was performed using the TIRF 100 × objective, the 780 nm laser, and the 980 nm LP emission filter with an exposure time of 1 s (relative power of 100%). All collected images were analysed using ImageJ

Fiji software. Background subtractions were performed for all NIR images using a Gaussian blur filter with sigma radius = 50.

To examine the impact of different buffers on the nanotube fluorescence and responsivity, nanotube films were incubated with 250 μL of either DPBS, 10% FBS in DPBS, Rinaldini solution, or Supplemented Schneider's Medium and incubated at room temperature overnight. Samples were imaged using the TIRF 100 \times objective, 780 nm laser, and 980 nm LP emission filter with an exposure time of 1 s unless specified otherwise (relative power of 100%). A baseline measurement of the fluorescence of the films prior to any additions was acquired for 15 min. Following this, 2.5 μL of freshly prepared dopamine solution (10 mM) was added. Samples were imaged immediately and following the 15 min of incubation.

For cell culturing experiments, 150 μL – 200 μL of supplemented Schneider's medium was added to the poly-L-lysine coated petri dishes (either with or without nanotube coatings). *Drosophila* neurons were prepared for culturing as detailed above and 50 μL of re-suspended brain solution (\sim 50,000 neurons) was added to each petri dish and pipetted 2 – 3 times to mix. Cells were incubated at room temperature under ambient conditions for 24 – 48 h. Imaging of the samples was performed in both the visible and NIR.

Media response tests were performed on films wetted with 100 μL DI water. 10 μL of medium was taken from a cell culture of *Drosophila* neurons that had been plated onto poly-L-lysine coated petri dishes (with or without nanotubes) and left to incubate at room temperature under ambient conditions for 72 h. Additional supplemented Schneider's medium was added as required to the samples over the 72 h to prevent the plates from drying out. Samples were analysed both immediately following addition and after 5 min of incubation and no significant differences were observed. Fresh supplemented Schneider's medium was used as the negative control and supplemented Schneider's medium spiked with 100 μM dopamine was used as the positive control.

Fluorescence spectroscopy measurements

A custom-built optical set-up with an inverted Nikon Eclipse Ti-E microscope (Nikon AG Instruments) [37] was used to acquire all fluorescence emission spectra. A pulsed super-continuum laser coupled with a tuneable band-pass filter unit (SuperK Extreme EXR-15 and Super K VARIA, NKT Photonics) was used to excite the samples at 660 ± 5 nm. The fluorescence signal was detected using an IsoPlane SCT-320 spectrometer (Princeton Instruments) coupled to an InGaAs NIR camera (NIRvana 640 ST, Princeton Instruments). LightField software (Princeton Instruments) was used to collect fluorescence spectra at wavelengths between 900 nm and 1400 nm using a dispersive grating of 75 lines mm^{-1} .

Media response experiments were performed in 384-well plates (Clear Flat-Bottom Immuno Nonsterile 384-Well Plates, MaxiSorp, Life Technologies) which were sealed (Empore Sealing Tape Pad, 3M) prior to each measurement to prevent evaporation. 20 μL aliquots of SWCNT

Chapter 6. Outlook on Potential Applications of XNA-SWCNTs for Improved Optical Biosensing

solution (10 mg/L) were added to individual wells in the 384-well plate and a baseline fluorescence spectrum was acquired (10 s exposure time, 100% relative laser power). 5 μ L of media was removed from the cultured neuron plates and added to the nanotube solution. The solution was mixed by pipetting up and down several times. Positive control measurements were performed using supplemented Schneider's medium that had dopamine added to a final concentration: of 100 μ M, 10 μ M, or 1 μ M. Negative control measurements were performed using supplemented Schneider's medium without any dopamine present.

Samples to examine the ability of LNA_{every5}-SWCNTs to detect dopamine in the presence of cells were prepared in 96-well plates (Corning). Fluorescence spectra were collected using the custom built NIR optical setup detailed above. An exposure time of 10 s and laser excitation at 660 nm with band width of 10 nm and relative power of 100% was used for all measurements. Nanotubes were coated onto poly-L-lysine coated 96-well plates (Corning) by incubating 20 μ L of SWCNT solution (5 mg/L) and 30 μ L DI water per well for 30 min followed by washing with DI water. For cell culturing, supplemented Schneider's medium, 75 μ L, was added to a nanotube-coated well, and 75 μ L of dissociated neurons (extracted as detailed above, \sim 75,000 cells) were mixed in by pipetting up and down three times. Cells were incubated at room temperature under ambient conditions overnight. Immediately prior to measurement, an additional 50 μ L of SWCNT solution (5 mg/L) was added to the well. Following the acquisition of initial baseline fluorescence measurements, 2.22 μ L of 10 mM dopamine was added to the sample (volume 200 μ L) to achieve a final dopamine concentration of 100 μ M in solution. Spectra were collected over a period of 15 min for the predominant (7,5) and (7,6) peaks at 660 nm excitation. Spectral data was fitted using custom Python codes [61].

6.5.2 XNA-SWCNTs for miRNA Detection

All DNA and RNA oligomers were purchased from Microsynth. PNA oligomers were purchased from PANAGENE. Chemicals were purchased from Sigma-Aldrich, unless otherwise specified. Purified HiPco-SWCNTs were purchased from NanoIntegris (Lot. No. HP34-032). Nuclease free water was purchased from QIAGEN.

Preparation of DNA-SWCNT solutions

DNA-SWCNTs were prepared using a modified surfactant exchange protocol as described previously [61, 78]. This process involved the use of 2% SC-suspended SWCNTs, which were prepared according to the procedure outlined in Gillen *et al.* [61]. Briefly, 25 mg of purified HiPco-SWCNTs were added to 25 mL of SC 2% (w/v) solution. The mixture was homogenized for 20 min at 5,000 rpm (Polytron PT 1300 D, Kinematica) immediately prior to performing probe-tip sonication (1/4 in. tip, Q700 Sonicator, Qsonica) for 1 h (10% amplitude) in an ice bath. The solution was centrifuged at $164,000 \times g$ for 4 h at 20°C (Optima XPN-80 Ultracentrifuge, Beckman) to remove any nanotube aggregates. The top 80% of the supernatant was collected and the remaining solution and pellet was discarded.

400 μ L of DNA solution (33 μ M in nuclease free water (QIAGEN)) was added to 400 μ L of 2% SC-SWCNTs (40 mg/L) (detailed information about all the sequences used is included in **Appendix Table E.1**). DNA concentrations were measured and adjusted using absorbance measurements (Nanodrop 2000, Thermo Scientific). To maintain similar starting distributions of nanotube chirality and length, the same SC-SWCNT stock was used for all suspensions. Methanol (1.2 mL) was added to the mixture to reach a final solvent percentage of 60% (v/v). The solution was vortexed briefly to mix prior incubation for at least 2 h at room temperature. Post-incubation, the DNA-SWCNTs were purified to remove all unbound DNA, displaced surfactant, and MeOH using Amicon centrifugal ultra-filtration devices (Amicon Ultra-2, Sigma Aldrich, 100 kDa membrane, Merck). Amicon devices were washed 2 \times as per the manufacturers instructions prior to use with nuclease free water (4,000 \times g, 2 min, 20°C). SWCNT solutions were rinsed 6 times using 1 mL of nuclease free water for each wash (4,000 \times g, 2 min). All rinsed samples were centrifuged for 30 min at 21,130 \times g and 4°C to remove any aggregates that may have formed during the surfactant exchange protocol or washing. The top 80% of the supernatant was collected and used for subsequent experiments. All DNA-SWCNT solutions were stored at 4°C between measurements in order mitigate aggregation of the SWCNTs [225].

Preparation of PNA and miRNA solutions

PNA solutions were prepared by dissolving 50 nmoles of PNA in 500 μ L of nuclease free water. Lyophilized RNA oligomers were suspended in 500 μ L saline-sodium citrate (SSC) buffer (2 \times , stock diluted using nuclease free water). All samples were vortexed for \sim 30 s to ensure the solution was homogenous. Absorbance measurements (Nanodrop 2000, Thermo Scientific) were used to adjust the concentrations of the miRNA samples to 100 μ M. All miRNA solutions were subsequently divided into 25 μ L aliquots and stored at -20°C. Detailed information for the miRNA and PNA sequences used in this study are presented in **Table 6.2** and **Table 6.3**.

Table 6.2 – List of miRNA sequences that were used in this study.

Name	Sequence (5' to 3')	Length	GC content
miR92a	UAC CCU GUA GAA CCG AAU UUG UG	23 bases	44 %
miR155	UUA AUG CUA AUC GUG AUA GGG GUU	24 bases	38 %
miR184	UGG ACG GAG AAC UGA UAA GGG U	22 bases	50 %
miR195	UAG CAG CAC AGA AAU AUU GGC	21 bases	43 %
miR202	AGA GGU AUA GGG CAU GGG AA	20 bases	50 %

Table 6.3 – List of PNA sequences used in this study.

Name	Sequence (N-terminus to C-terminus)	Length	GC content
PNA _{10b}	GTC TCT TCC ACA AAT TCG GTT CTA CAG GGT A	31 bases	45%
PNA ₁₅₅	GTC TCT TCA ACC CCT ATC ACG ATT AGC ATT AA	32 bases	41%
PNA ₁₈₄	GTC TCT TCA CCC TTA TCA GTT CTC CGT CCA	30 bases	50%
PNA ₁₉₅	GTC TCT TCG CCA ATA TTT CTG TGC TGC TA	29 bases	45%
PNA ₂₀₂	GTC TCT TCT TCC CAT GCC CTA TAC CTC T	28 bases	50%

Absorbance spectroscopy

Absorbance spectra were acquired using a UV-Vis-NIR scanning spectrometer (UV-3600 Plus, Shimadzu) with samples contained in a quartz cuvette (Suprasil quartz, path length 3 mm, Hellma). All absorption spectra were collected using a 0.5 nm step size and medium scan speed. Baseline spectra were acquired with nuclease free water prior to measurement of the DNA-SWCNT samples. Concentrations were calculated using an extinction coefficient $Ab_{s632nm} = 0.036 \text{ L mg}^{-1} \text{ cm}^{-1}$. All DNA-SWCNT solutions were diluted to 10 mg/L, corresponding to $Ab_{s632nm} = 0.108$, unless otherwise specified.

Kinetic absorption measurements were also performed on mixtures of PNA, miRNA, and DNA-SWCNTs. A spectrum was initially collected for the DNA-SWCNT solution (67.5 μL). PNA solution (7.5 μL) was then added directly into the quartz cuvette and mixed by pipetting up and down several times. Spectra were collected immediately and then after 15, 30, 60, 90, and 120 min of incubation. miRNA solution (4.5 μL) was subsequently added and mixed by pipetting up and down. Again spectra were collected immediately and then after 15, 30, 60, 90, and 120 min of incubation.

Fluorescence spectroscopy measurements

A custom-built optical set-up with an inverted Nikon Eclipse Ti-E microscope (Nikon AG Instruments) [37] was used to acquire all fluorescence emission spectra as detailed above.

Experiments were performed in 384-well plates (Clear Flat-Bottom Immuno Nonsterile 384-Well Plates, MaxiSorp, Life Technologies) which were sealed (Empore Sealing Tape Pad, 3M) prior to each fluorescence measurement to prevent evaporation. Fluorescence spectra were required using a 575, 660, and 745 nm laser excitation source with 10 s exposure time and 100% relative power. Spectral fitting was performed on all collected fluorescence spectra using custom Python codes as detailed previously in **Chapter 2** [61]. The following ratios were used for preparing the solutions prior to fluorescence measurements (nuclease free water and SSC 2 \times solution was added in place of PNA and miRNA for the respective controls):

- 45 μL of DNA-SWCNT solution (10 mg/L) + 4.5 μL PNA (or nuclease free water) 100 μM + 0.5 μL miRNA 100 μM (or SSC 2 \times solution)
- 45 μL of DNA-SWCNT solution (10 mg/L) + 5 μL PNA (or nuclease free water) 100 μM + 3 μL miRNA 100 μM (or SSC 2 \times solution)

Photoluminescence excitation/emission (PLE) maps were acquired between 525 nm and 800 nm using a 5 nm step and 10 s exposure time. Results were analysed using a custom Matlab code (Matlab R2017b, Mathworks).

General Conclusion

She began to believe that very few things are indeed impossible.

Lewis Carroll, *Alice's Adventures in Wonderland*

Despite intense, global focus biosensing technologies continue to be restricted by their sensitivity, selectivity, and scalability, which in turn constrains their ability to aid in the early detection and intervention of various life-altering complications. This is further complicated for neurochemical sensing, as limitations in the spatiotemporal resolution achievable has hindered our ability to study the complex nature of neurotransmitter molecules and accurately elucidate their role in the pathology of diseases such as of Parkinson's or Alzheimer's disease. Therefore, it has remained difficult to achieve accurate real-time measurements of neuro-modulator concentrations, reducing the success of treatments for patients and negatively impacting patient prognosis.

To overcome the limitations of existing biosensing technologies, we require a new generation of biosensors that offer (i) scalable methods of preparation, (ii) improved sensitivity, (iii) increased sensor stability, and (iv) rapid response times. Extended work is especially needed to further understand the competing interactions that can lead to signal fluctuations when sensors are moved from buffered solutions to biological environments, which in many instances can compromise the overall sensor efficiency.

In this dissertation, focus was directed towards establishing new approaches for the non-covalent functionalisation of SWCNTs with the aim of creating optical sensors for improved neurochemical sensing. SWCNTs were selected owing to their unique optoelectronic properties, specifically their photostable NIR fluorescence emission that enables increased signal penetration in biological tissue and media. We addressed several limitations faced by existing SWCNT technologies using surfactant, DNA, and XNA wrappings, to gain fundamental insights into the sensing behavior of these complexes. This improved understanding enabled us to design sensors that demonstrated improved sensing capabilities and stability in complex media compared to current state-of-the-art SWCNT optical sensors.

Chapter 6. Outlook on Potential Applications of XNA-SWCNTs for Improved Optical Biosensing

We began by reviewing the different approaches used to non-covalently functionalize SWCNTs for sensing applications in **Chapter 1**, comparing the advantages and disadvantages associated with different methods. In particular, this work focused on examining the trade-offs that typically exist between selectivity and brightness for different wrapping molecules such as surfactants or biomolecules like ssDNA. We further introduced new synthetic biopolymers, such as LNA, as a means of overcoming certain limitations faced by DNA-SWCNTs and highlighted their capabilities to selectively engineer SWCNT-based sensors with improved capabilities.

In **Chapter 2**, we introduced a new method for controlling the selectivity of surfactant-suspended optical SWCNT sensors through colloidal templating of the exposed surface area. Changes in the bulk surfactant concentration were used to modulate the exposed surface area of SC-SWCNTs. Our surfactant-SWCNTs exhibited an intensity response to dopamine and serotonin at all concentrations, however for sub-critical colloidal suspensions of SC-SWCNTs (1.5 mM and 0.5 mM SC) we further observed a selective wavelength red-shifting response to serotonin. Not only did these sensors exhibit superior selectivity compared to DNA-SWCNTs, but moreover this approach did not compromise on the increased brightness of surfactant-SWCNTs nor their colloidal stability.

The increased biocompatibility and large sequence space that is available for DNA-SWCNT has encouraged work that aims to increase the performance of DNA-SWCNTs, specifically the intensity of their fluorescence emission. In **Chapter 3**, we outlined how chemically modified DNA could be used to alter the fluorescence behavior of DNA-SWCNTs, both in terms of fluorescence intensity and responsivity. Focusing on (GT)₁₅-SWCNTs, we examined the impact of the type, position, and number of modifications on the fluorescence properties of the resulting complex. Moreover, we examined how the method of preparing SWCNTs impacted the fluorescence behavior of the resulting complex. Notably, SWCNTs prepared via MeOH assisted surfactant exchange typically exhibit superior fluorescence intensities but typically lack the same sensor response compared to sonicated samples. This implies that depending on the preparation method, we obtain fundamentally different wrapping configurations of the DNA on the surface of the nanotube, in agreement with recent observations in the literature. Based on these findings, we concluded that careful selection of the appropriate preparation method for SWCNT solutions is necessary in order prevent any unwanted deterioration in sensor performance. In addition, we found that modified DNA-sequences could increase the fluorescence intensity of SWCNTs prepared via direct sonication. Moreover, the relative increases were retained post-dopamine addition. The enhanced optical properties of the modified DNA-SWCNTs benefit from significantly increased theoretical penetration depths, making these sensors more attractive for *in vivo* applications. Furthermore, this approach circumvents the need for any exogenous additives and does not rely on making changes to the base sequence, meaning it can be applied to nearly any DNA sequence to increase the brightness without compromising on sensor biocompatibility or selectivity.

Much of the research creating optical biosensors based on DNA-SWCNTs has focused on optimizing these sensors in buffered solutions, which can lead to problems when these sensors are transferred into more biologically relevant conditions. In **Chapter 4**, we examined the affect that changes in the concentration of multivalent cation species had on the fluorescence emission of DNA-SWCNTs. These salts are commonly found in biofluids and are of central importance in cellular signalling within the body. We observed a species-independent red-shift of the nanotube fluorescence that was also found to be independent of the DNA length and base composition. Through concomitant monitoring of both fluorescence intensity and wavelength shifting, we identified the transient formation of intermediate DNA-SWCNT optical states within our system. These findings enabled us to uncover important information on the impact of fluctuating cation concentrations on SWCNT fluorescence and further elucidate that the optical response was due to conformational reorganization of the DNA on the surface of the nanotube. By introducing XNAs, specifically LNA, into the DNA sequence we increased the conformational stability of the biopolymer on the SWCNT and demonstrated that this limited the ion-induced fluorescence drift. Our LNA-SWCNTs could withstand cation concentrations more than two orders of magnitude higher than pure DNA-SWCNTs with increased permanence in both conformational and fluorescence-signal stability. In addition, this increase in stability was achieved without compensating on the unique advantages of DNA, including biocompatibility and sequence space.

Chapter 5 builds upon our findings that LNA-SWCNTs offer improved resistance to cation-induced fluorescence changes and extends their use to neurochemical sensing applications. We show that improvements in stability can be sustained without limiting the sensors ability to detect dopamine. However, the improvements in sensors performance were shown to be highly dependent on the position and percentage of LNA bases in the sequence. We identified several locking patterns that not only demonstrated improved stability compared to (GT)₁₅-SWCNTs towards undesirable fluorescence modulation in the presence of Ca²⁺, but also demonstrated improved label-free imaging of dopamine. Furthermore, we showed that by concomitant monitoring of the (7,5) and (7,6) chirality peaks we could simultaneously detect Ca²⁺ and dopamine signal responses. Additional research in this area could look at incorporating LNA bases into other DNA sequences used to create DNA-SWCNT sensors to impart increased stability in ionically complex environments without negatively affecting the DNA-SWCNT's recognition capabilities.

Extending the use of LNA-SWCNTs, in **Chapter 6** we explored how our sensors could be used for improved sensing in complex biological media and realistic biological preparations even following extended incubation times. The LNA-SWCNTs developed exhibited superior sensing performance towards dopamine in both buffered solutions and more complex media, and showed promise for use *in vitro* or *ex vivo*. While further optimization is required to study neuromodulation at the level of individual synapses, we demonstrated that these sensors retained their ability to respond to exogenous dopamine in the presence of cells, even following extended incubation periods at room temperature. Finally, we showed that XNA-SWCNTs

Chapter 6. Outlook on Potential Applications of XNA-SWCNTs for Improved Optical Biosensing

are not limited to neurochemical sensing applications and presented preliminary findings on using a modular PNA-DNA-SWCNT platform for the detection of another clinically relevant biomarker, miRNA. Our observations indicated that this technology was capable of specific miRNA detection at unprecedented speeds using either absorbance or fluorescence spectroscopy. Furthermore, the customizability of the platform is particularly advantageous for miRNA detection where diverse combinations of miRNAs fingerprint different diseases requiring a technology that can create an equally diverse range of sensors.

In conclusion, the results presented in this thesis expanded our knowledge of non-covalent methods of nanotube functionalization and demonstrated several new experimental methodologies for preparing surfactant-, DNA-, and XNA-SWCNT complexes with improved capabilities for neurochemical sensing. The XNA-SWCNT technology introduced is promising not only for neurochemical sensing, but also as a versatile platform for miRNA detection as demonstrated by the PNA-DNA-SWCNT sensor presented. These findings unveil several avenues for future research using XNA-SWCNT complexes and show promise for achieving previously unattainable sensitivities and capabilities that we anticipate will lead to transformative technologies in the nanotube sensing community.

A The Impact of Surface Area on the Response of SWCNT Optical Sensors

Preparation of analyte solutions

The analyte suspensions were prepared with a final concentration of 100 mM, with the exception of tyrosine (3 mM) and tryptophan (56 mM) due to solubility limitations. The neurotransmitters and amino acids were suspended in HEPES buffer (1 mM, pH 7.4, Sigma), and sugars were suspended using PBS (1 ×, pH 7.4, Gibco, Life Technologies). All solutions were prepared freshly prior to use and stored at 4°C in between measurements.

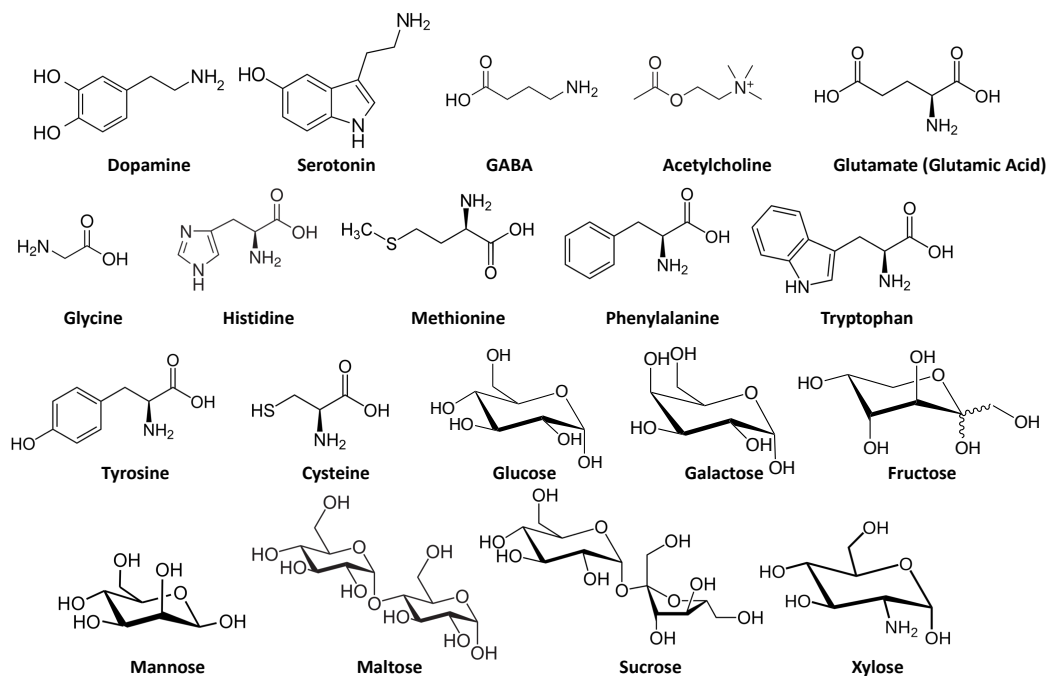


Figure A.1 – Chemical structures of target molecules tested using SC-SWCNTs. Molecules were drawn using ChemDraw Prime 17.0.

Appendix A. The Impact of Surface Area on the Response of SWCNT Optical Sensors

Table A.1 – List of Chemicals and Suppliers.

Abbreviated name	Full name	Supplier	Purity
Acetylcholine (Ace)	Acetylcholine Chloride	Merck (Sigma Aldrich)	99%
Cysteine (Cys)	L-cysteine	Merck (Sigma Aldrich)	>99%
Dopamine (Dop)	Dopamine hydrochloride	Merck (Sigma Aldrich)	<= 100%
Fructose (Fruc)	D(-)-Fructose	TCI Chemicals	>99%
GABA (Gaba)	γ -Aminobutyric acid	Merck (Sigma Aldrich)	99%
Galactose (Gal)	D(+)-Galactose	ABCR	98%
Glucose (Gluc)	b-D-Glucose (contains a-D-Glucose)	ABCR	80%
Glutamate (Gluta)	L-Glutamic acid monosodium salt monohydrate	Merck (Sigma Aldrich)	98%
Glycine (Gly)	Glycine	Carl Roth	min. 99%
Histidine (His)	L-Histidine	Carl Roth	min. 99%
Maltose (Mal)	D(+)-Maltose monohydrate	Merck (Sigma Aldrich)	>99%
Mannose (Man)	D(+)-Mannose	ABCR	99%
Methionine (Met)	L-Methionine	Carl Roth	min. 99%
Phenylalanine (Phen)	L-Phenylalanine	Carl Roth	min. 99%
Serotonin (Sero)	Serotonin hydrochloride	Carl Roth	98%
Sucrose (Suc)	D(+)-Sucrose	Acros Organics	99+%
Tryptophan (Try)	L-Tryptophan	Carl Roth	min. 99%
Tyrosine (Tyr)	L-Tyrosine	Carl Roth	min. 99%
Xylose (Xyl)	D(+)-Xylose	TCI Chemicals	>98%

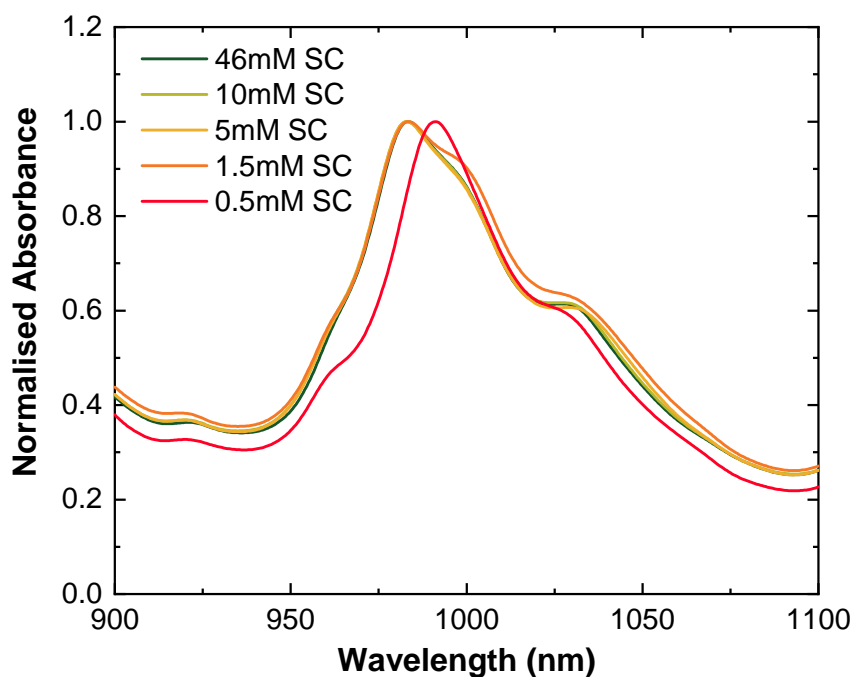


Figure A.2 – A comparison of the normalized absorbance spectra collected for the (6,5) chirality E₁₁ peak of SC-SWCNT solutions diluted to varying concentrations of SC. All spectra were normalized to the maximum absorbance recorded over the studied range.

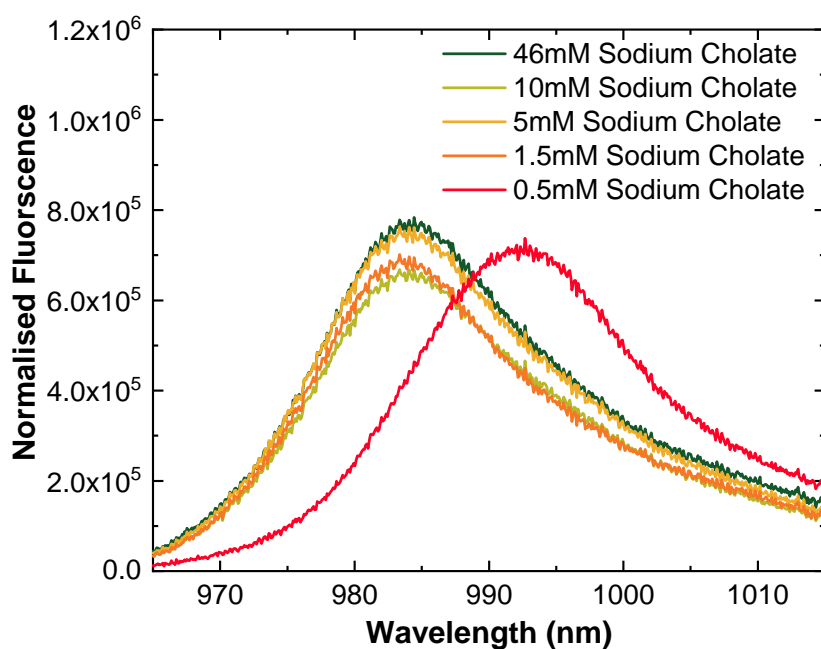


Figure A.3 – A comparison of the concentration-normalized (6,5) fluorescence peak for SC-SWCNT solutions diluted to varying concentrations of SC. All spectra were normalized by SWCNT concentration using an extinction coefficient of $\epsilon_{739\text{ nm}} = 0.0253\text{ L mg}^{-1}\text{ cm}^{-1}$ (excitation: 575 nm).

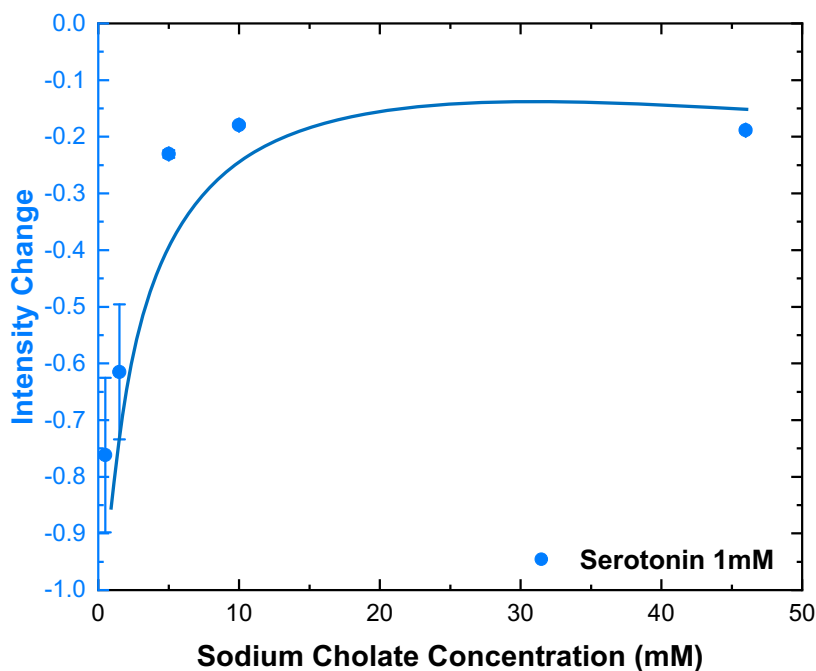


Figure A.4 – A comparison of the (6,5) fluorescence intensity change in the presence of 1 mM serotonin for SC-SWCNT solutions diluted to varying concentrations of SC. Fluorescence intensity changes were calculated by comparing the maximum intensity of the (6,5) chirality emission peak before and after the addition of serotonin. The intensity change is defined as $(I_f - I_0)/I_0$, where I_f corresponds to the maximum of the emission peak after addition and I_0 is the maximum of the peak before addition. The spectra after addition were recorded following 15 min of incubation (excitation: 575 nm).

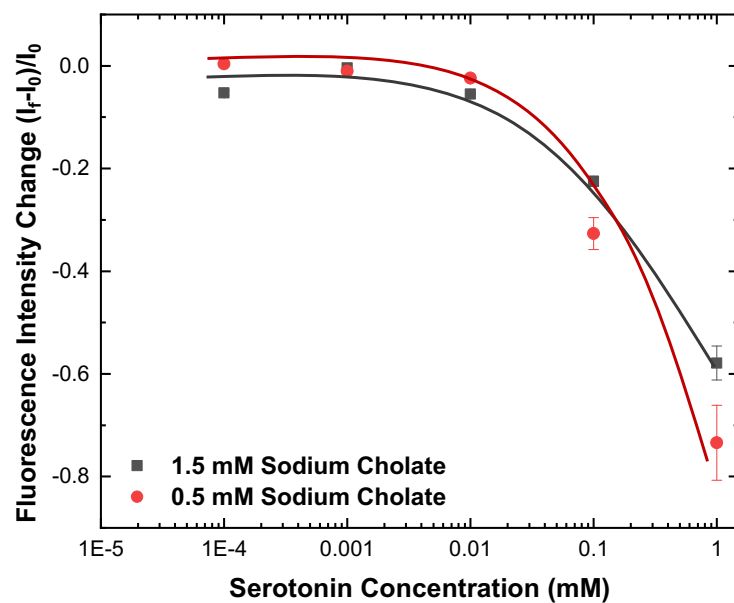


Figure A.5 – Concentration calibration curves for the intensity change of the (6,5) chirality peak for 0.5 mM and 1.5 mM SC-SWCNT solutions following the addition of serotonin. All spectra after addition were recorded following 15 min of incubation (excitation: 575 nm).

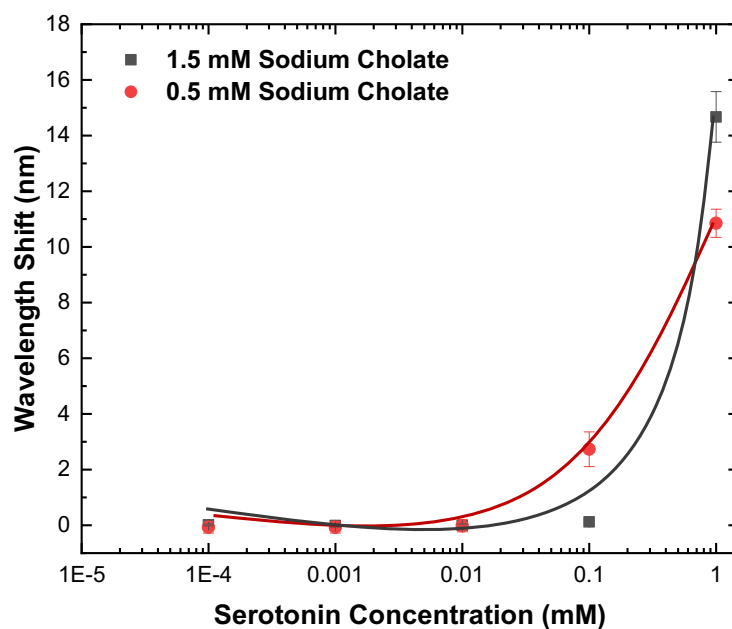


Figure A.6 – Concentration calibration curves for the wavelength shift of the (6,5) chirality peak for 0.5 mM and 1.5 mM SC-SWCNT solutions following the addition of serotonin. All spectra after addition were recorded following 15 min of incubation (excitation: 575 nm).

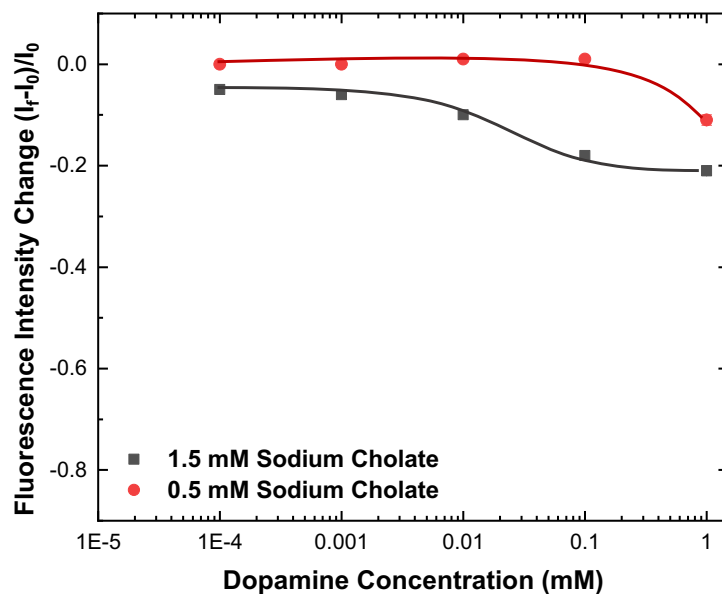


Figure A.7 – Concentration calibration curves for the intensity change of the (6,5) chirality peak for 0.5 mM and 1.5 mM SC-SWCNT solutions following the addition of dopamine. All spectra after addition were recorded following 15 min of incubation (excitation: 575 nm).

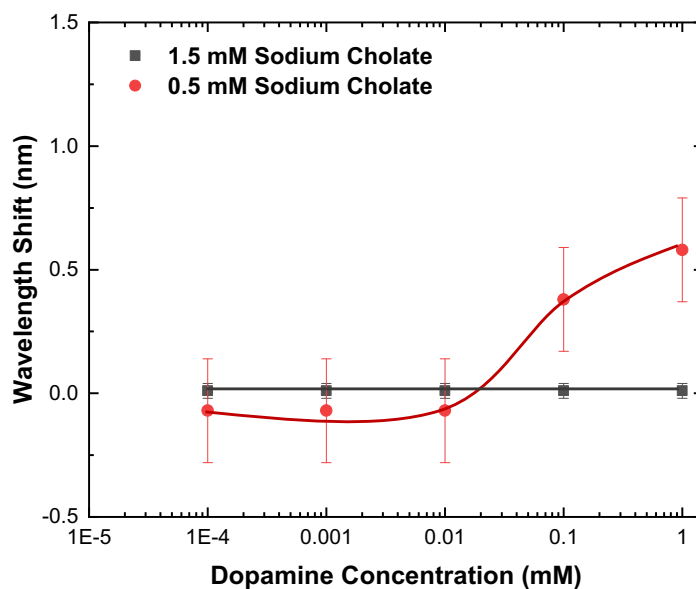


Figure A.8 – Concentration calibration curves for the wavelength shift of the (6,5) chirality peak for 0.5 mM and 1.5 mM SC-SWCNT solutions following the addition of dopamine. All spectra after addition were recorded following 15 min of incubation (excitation: 575 nm).

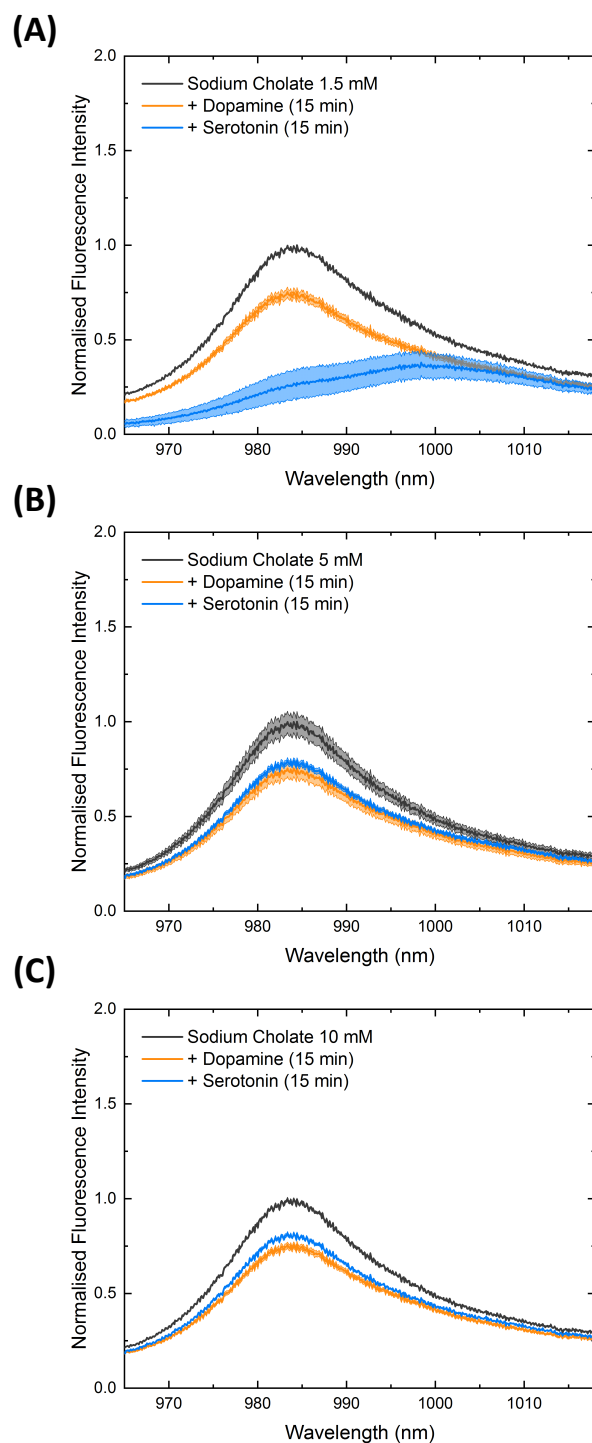


Figure A.9 – Fluorescence response of (A) 1.5 mM SC-SWCNT, (B) 5 mM SC-SWCNT, and (C) 10 mM SC-SWCNT following the addition of dopamine (orange) and serotonin (blue). Representative normalized fluorescence emission spectra show the wavelength response of the SWCNTs to the addition of 100 mM target solution (final concentration 1 mM) (excitation: 575 nm). All shaded regions represent 1 σ standard deviation ($n = 3$ technical replicates). All peaks were normalized to the maximum fluorescence emission intensity prior to addition of any target molecule, corresponding to the (6,5) chirality emission.

Appendix A. The Impact of Surface Area on the Response of SWCNT Optical Sensors

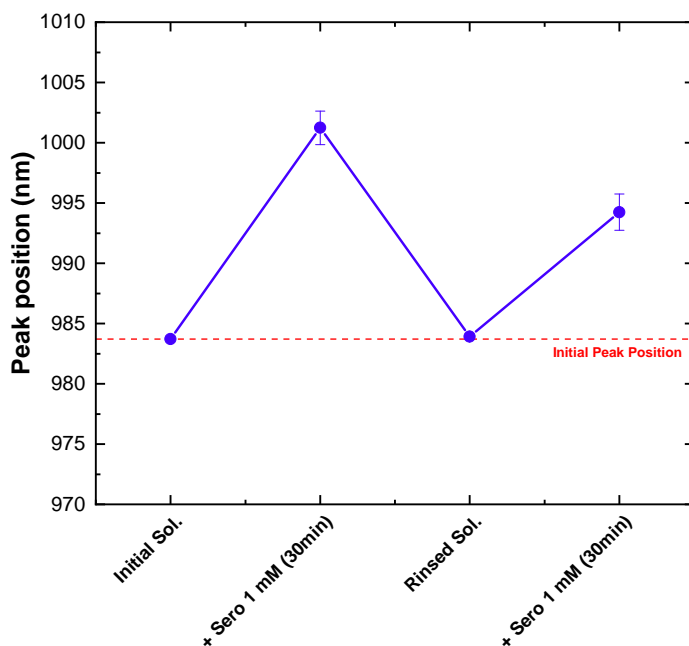


Figure A.10 – Reversibility of the fluorescence peak response of 1.5 mM SC-SWCNT on addition of serotonin (final concentration: 1 mM, excitation: 575 nm). The red dashed line represents the starting wavelength position of the sensor. Error bars represent 1σ standard deviation ($n = 3$ three technical replicates).

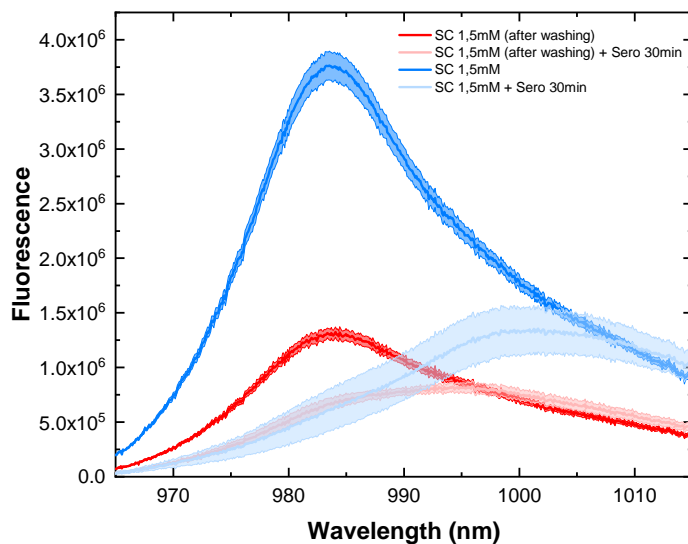


Figure A.11 – Reversibility of the fluorescence response of 1.5 mM SC-SWCNT on addition of serotonin (final concentration 1 mM) (excitation: 575 nm). **Blue** lines represent the spectra of the initial sensor before (dark) and after serotonin addition (light). **Red** lines represent the spectra of the sensor after washing before (dark) and following serotonin addition (light). The shaded regions represent 1σ standard deviation ($n = 3$ technical replicates).

Analyte	SC 46 mM	SC 10 mM	SC 5 mM	SC 1.5 mM	SC 0.5 mM	(GT) ₁₅	(GT) ₁₅ + NaCl 100 mM	(AT) ₁₅	(AT) ₁₅ + NaCl 100 mM
Ace	0.0 ± 0.03	0.0 ± 0.07	0.0 ± 0.07	-0.3 ± 1.64	0.1 ± 0.16	1.0 ± 0.08	0.1 ± 0.06	-5.2 ± 0.64	0.1 ± 0.10
Dop	-0.1 ± 0.06	0.0 ± 0.04	0.1 ± 0.04	-0.3 ± 1.64	0.3 ± 0.24	2.5 ± 0.05	1.1 ± 0.16	-2.3 ± 0.62	1.1 ± 0.17
Gaba	0.0 ± 0.03	0.0 ± 0.07	0.0 ± 0.07	-0.2 ± 1.64	0.2 ± 0.16	0.5 ± 0.08	0.1 ± 0.12	-1.5 ± 1.57	0.1 ± 0.10
Gluta	0.0 ± 0.03	0.0 ± 0.07	0.1 ± 0.04	-0.3 ± 1.64	0.7 ± 0.17	-0.2 ± 0.08	0.1 ± 0.06	-5.3 ± 0.64	0.1 ± 0.11
Sero	-0.2 ± 0.03	0.0 ± 0.07	0.1 ± 0.04	14.1 ± 4.75	10.3 ± 1.51	3.9 ± 0.10	2.3 ± 0.11	0.1 ± 0.64	2.0 ± 0.18
Cys	-0.1 ± 0.03	-0.1 ± 0.04	0.0 ± 0.04	-0.2 ± 1.64	-0.3 ± 0.20	0.4 ± 0.05	0.2 ± 0.06	0.2 ± 0.68	0.5 ± 0.39
Gly	0.0 ± 0.03	0.0 ± 0.04	0.0 ± 0.07	-0.2 ± 1.64	0.0 ± 0.17	0.1 ± 0.08	0.0 ± 0.08	-0.4 ± 1.03	0.1 ± 0.11
His	0.0 ± 0.03	0.1 ± 0.07	0.1 ± 0.07	-0.2 ± 1.64	1.1 ± 0.18	1.8 ± 0.08	0.2 ± 0.11	-4.7 ± 0.62	0.2 ± 0.10
Met	0.0 ± 0.03	0.0 ± 0.04	0.0 ± 0.07	-0.2 ± 1.64	0.0 ± 0.16	0.2 ± 0.21	0.0 ± 0.08	-0.5 ± 0.91	0.1 ± 0.11
Phe	0.0 ± 0.03	0.0 ± 0.07	0.0 ± 0.04	-0.1 ± 1.64	0.0 ± 0.16	0.3 ± 0.24	0.0 ± 0.08	0.1 ± 0.62	0.1 ± 0.11
Try	0.0 ± 0.03	0.0 ± 0.04	0.1 ± 0.04	-0.4 ± 0.15	0.0 ± 0.18	0.8 ± 0.08	0.1 ± 0.06	-0.9 ± 0.64	0.1 ± 0.10
Tyr	0.0 ± 0.03	0.0 ± 0.04	0.1 ± 0.04	-0.2 ± 1.65	0.0 ± 0.16	0.1 ± 0.05	0.1 ± 0.06	0.1 ± 0.62	0.1 ± 0.10
HEPES	0.0 ± 0.03	0.0 ± 0.06	0.0 ± 0.05	-0.1 ± 1.64	0.1 ± 0.16	0.1 ± 0.05	0.1 ± 0.06	0.0 ± 0.73	0.1 ± 0.10
Fruc	0.0 ± 0.03	0.0 ± 0.04	0.1 ± 0.04	-0.2 ± 1.64	0.7 ± 0.16	-0.2 ± 0.05	0.0 ± 0.08	-5.9 ± 0.62	0.1 ± 0.10
Gal	0.0 ± 0.03	0.0 ± 0.04	0.1 ± 0.04	-0.3 ± 1.64	0.6 ± 0.16	-0.2 ± 0.05	0.0 ± 0.08	-5.8 ± 0.65	0.1 ± 0.10
Gluc	0.0 ± 0.03	0.0 ± 0.04	0.1 ± 0.04	-0.3 ± 1.64	0.6 ± 0.17	-0.2 ± 0.05	0.1 ± 0.19	-5.9 ± 0.62	0.1 ± 0.10
Mal	0.0 ± 0.03	0.0 ± 0.04	0.1 ± 0.04	-0.3 ± 1.64	0.7 ± 0.17	-0.2 ± 0.05	0.0 ± 0.08	-5.9 ± 0.62	0.1 ± 0.10
Man	0.0 ± 0.03	0.0 ± 0.04	0.1 ± 0.04	-0.3 ± 1.64	0.6 ± 0.16	-0.2 ± 0.05	0.0 ± 0.08	-5.9 ± 0.64	0.1 ± 0.11
Suc	0.0 ± 0.03	0.0 ± 0.04	0.1 ± 0.04	-0.3 ± 1.64	0.6 ± 0.16	-0.2 ± 0.05	0.1 ± 0.06	-5.9 ± 0.62	0.1 ± 0.10
Xyl	0.0 ± 0.03	0.1 ± 0.07	0.1 ± 0.04	-0.3 ± 1.64	0.7 ± 0.17	-0.1 ± 0.08	0.1 ± 0.06	-5.8 ± 0.62	0.1 ± 0.10
PBS	0.0 ± 0.03	0.0 ± 0.04	0.1 ± 0.04	-0.3 ± 1.64	0.7 ± 0.17	-0.2 ± 0.05	0.1 ± 0.06	-5.9 ± 0.62	0.1 ± 0.11

Table A.2 – Wavelength shifts (nm) for all samples following 15 min of incubation with analyte solution. All error values reported represent 1 σ standard deviation (n = at least 3 technical replicates).

Analyte	SC 46 mM	SC 10 mM	SC 5 mM	SC 1.5 mM	SC 0.5 mM	(GT) ₁₅	(GT) ₁₅ + NaCl 100 mM	(AT) ₁₅	(AT) ₁₅ + NaCl 100 mM
Ace	-3.0 ± 0.1	-3.7 ± 0.1	0.0 ± 0.0	-3.5 ± 0.3	-2.7 ± 0.4	20.9 ± 1.6	-0.6 ± 0.0	60.3 ± 7.8	2.4 ± 0.1
Dop	-29.9 ± 1.0	-23.9 ± 0.7	-27.2 ± 1.6	-22.5 ± 1.6	-19.0 ± 3.7	88.3 ± 4.2	68.3 ± 4.7	92.2 ± 10.7	18.9 ± 0.8
Gaba	-7.3 ± 0.2	-4.6 ± 0.1	-3.1 ± 0.1	-6.6 ± 0.4	4.4 ± 0.4	-0.9 ± 0.1	18.1 ± 3.1	-1.8 ± 0.2	6.5 ± 0.2
Gluta	-7.7 ± 0.3	-3.4 ± 0.1	-2.0 ± 0.0	-2.7 ± 0.2	-0.9 ± 0.1	24.2 ± 1.7	18.3 ± 1.3	25.1 ± 2.4	8.8 ± 0.3
Sero	-18.9 ± 0.4	-17.9 ± 0.4	-23.0 ± 0.7	-61.5 ± 11.9	-76.2 ± 13.6	69.4 ± 15.1	45.0 ± 3.2	81.3 ± 9.6	12.6 ± 0.6
Cys	-14.9 ± 0.6	-10.9 ± 0.2	-12.4 ± 0.5	-22.4 ± 1.5	-9.5 ± 0.9	46.8 ± 1.6	31.0 ± 2.1	22.8 ± 1.6	-0.4 ± 0.0
Gly	-1.6 ± 0.0	-4.5 ± 0.2	-5.3 ± 0.1	-2.3 ± 0.1	3.5 ± 0.3	-8.7 ± 0.3	-12.0 ± 0.9	-5.0 ± 0.4	-5.4 ± 0.2
His	-2.9 ± 0.1	-4.5 ± 0.2	-3.2 ± 0.1	-4.6 ± 0.3	0.9 ± 0.1	-11.1 ± 1.7	24.4 ± 3.1	12.1 ± 1.6	1.3 ± 0.1
Met	-2.2 ± 0.1	-7.5 ± 0.4	-4.0 ± 0.1	-3.9 ± 0.2	3.4 ± 0.3	-3.7 ± 0.3	-8.1 ± 0.6	6.0 ± 0.5	-4.0 ± 0.2
Phe	-2.9 ± 0.1	-3.5 ± 0.1	-3.4 ± 0.1	-4.4 ± 0.3	0.5 ± 0.0	-2.9 ± 0.1	-7.4 ± 0.7	0.3 ± 0.0	-0.6 ± 0.0
Try	-2.5 ± 0.1	-2.2 ± 0.1	-2.4 ± 0.1	-2.8 ± 0.1	1.9 ± 0.2	2.9 ± 0.1	-9.9 ± 0.7	2.2 ± 0.2	-3.9 ± 0.1
Tyr	-5.2 ± 0.1	-7.1 ± 0.2	-6.4 ± 0.2	3.3 ± 0.2	3.0 ± 0.3	-2.3 ± 0.1	-12.7 ± 1.0	0.5 ± 0.0	-3.3 ± 0.1
HEPES	-0.3 ± 0.0	-2.3 ± 0.1	-1.6 ± 0.0	-1.5 ± 0.1	4.1 ± 0.4	-3.5 ± 0.2	-2.8 ± 0.2	-4.0 ± 0.3	-1.0 ± 0.0
Fruc	-1.0 ± 0.0	-3.5 ± 0.1	-3.5 ± 0.1	1.3 ± 0.1	2.6 ± 0.2	33.6 ± 1.3	-2.7 ± 0.2	38.0 ± 3.1	-3.4 ± 0.1
Gal	-2.0 ± 0.1	-1.4 ± 0.0	-2.2 ± 0.1	5.1 ± 0.3	2.1 ± 0.2	35.5 ± 1.4	-1.2 ± 0.1	23.9 ± 3.4	-3.3 ± 0.2
Gluc	-4.7 ± 0.2	-2.7 ± 0.1	-2.1 ± 0.1	2.0 ± 0.1	3.2 ± 0.3	22.9 ± 1.8	16.1 ± 4.6	34.1 ± 4.4	-5.0 ± 0.2
Mal	-0.6 ± 0.0	-1.9 ± 0.0	-1.3 ± 0.0	7.9 ± 0.5	0.1 ± 0.0	28.7 ± 2.8	-6.3 ± 0.4	39.6 ± 2.9	-5.7 ± 0.2
Man	-2.0 ± -0.1	-1.6 ± 0.0	-1.4 ± 0.0	5.5 ± 0.3	5.7 ± 0.5	30.8 ± 3.8	-3.4 ± 0.2	24.3 ± 5.2	-5.1 ± 0.2
Suc	-3.5 ± 0.1	-1.0 ± 0.0	-1.9 ± 0.0	7.6 ± 0.4	4.4 ± 0.4	29.2 ± 0.9	-4.3 ± 0.3	36.8 ± 3.4	-3.4 ± 0.1
Xyl	-3.5 ± 0.1	-4.5 ± 0.2	-0.6 ± 0.0	7.8 ± 0.5	7.9 ± 0.7	42.0 ± 6.3	-3.9 ± 0.3	28.4 ± 3.2	-0.6 ± 0.0
PBS	-2.2 ± 0.0	-2.1 ± 0.0	-2.5 ± 0.1	6.6 ± 0.6	1.9 ± 0.2	28.5 ± 2.3	-4.8 ± 0.3	28.5 ± 2.4	-3.3 ± 0.1

Table A.3 – Percentage (%) intensity change ($\frac{(I_f - I_0)}{I_0}$) for all samples following 15 min of incubation with analyte solution. All error values reported represent 1σ standard deviation (n = at least 3 technical replicates).

B Modifying DNA-SWCNT Sensors for Improved Dopamine Detection

DNA-dimer formation of thiol-modified DNA

Over time, thiol-modified DNA oxidizes, resulting in the formation of disulfide bonds between two thiol groups on the sequences. Polyacrylamide gel electrophoresis (PAGE) analysis of DNA-sequences removed from DNA-SWCNTs post-suspension showed that thiol-modified DNA formed DNA dimers during the suspension process (**Figure B.1**), resulting in an effective sequence length of 60 bases (compared to the 30 bases for the amino-, azide-, and unmodified sequences). Although reduction steps can be used to break the disulfide bonds and separate oligo dimers, reducing agents (such as dithiothreitol (DTT)) can significantly affect the fluorescence properties of DNA-SWCNTs. As a result, in order to ensure accurate comparisons between the functionalizations, thiol-modified DNA sequences were excluded from this study.

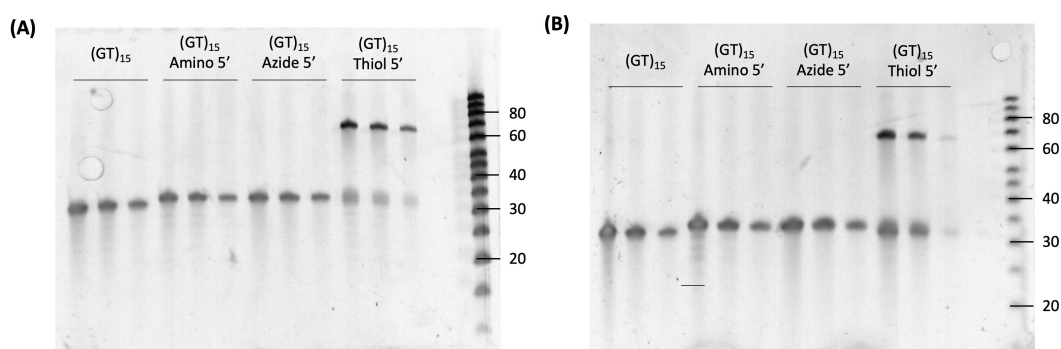


Figure B.1 – Denaturing 15% polyacrylamide gels of DNA extracted from (A) sonicated and (B) MeOH assisted surfactant exchanged DNA-SWCNT samples. The DNA samples were extracted by phenol-chloroform isoamyl (PCI) extraction and subsequently precipitated through glycogen-assisted ethanol precipitation. DNA samples were run at three concentrations for each sequence: 1 ×, 0.5 ×, and 0.2 × in the first, second, and third lanes, respectively. Both gels were stained using a SYBR Gold dye staining. A band around 30 nucleotides is observed as expected for every sequence. An additional band at ~ 60 nucleotides is also present for the thiol-modified DNA sequence, indicating the presence of dimers.

Appendix B. Modifying DNA-SWCNT Sensors for Improved Dopamine Detection

Table B.1 – Additional DNA sequences, functional groups, and modification positions tested for improved fluorescence intensity of nanotube suspensions prepared using the MeOH assisted surfactant exchange protocol.

	Functional group	[Linker]	[Modification Positions]
(AT) ₁₅	Amino (-NH ₂)	[C ₆]	[Unmodified] [5'] [3'] [5' + 3']
	Azide (-N ₃)	[NHS Ester]	[5'] [3']
(N) ₃₀	Amino (-NH ₂)	[C ₆]	[Unmodified] [5'] [5' + 3']
	Azide (-N ₃)	[NHS Ester]	[5']

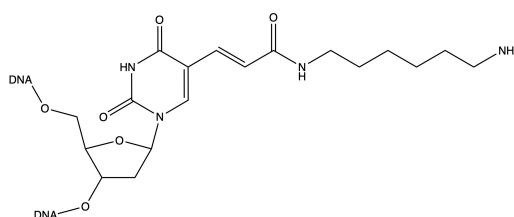


Figure B.2 – Chemical structure of amino-dT base used for internal modification of DNA sequences with an amino functional group drawn using ChemDraw Prime 17.0.

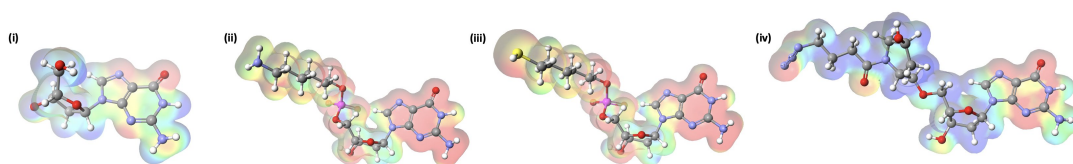


Figure B.3 – Maps of electron distribution for guanine (G) modelled as electrostatic potential on electronic density for (i) unmodified, (ii) amino-, (iii) thiol-, and (iv) azide-modified bases. All maps were generated using SCiGRESS. Areas with high relative electron density are indicated as red and low electron density regions are blue.

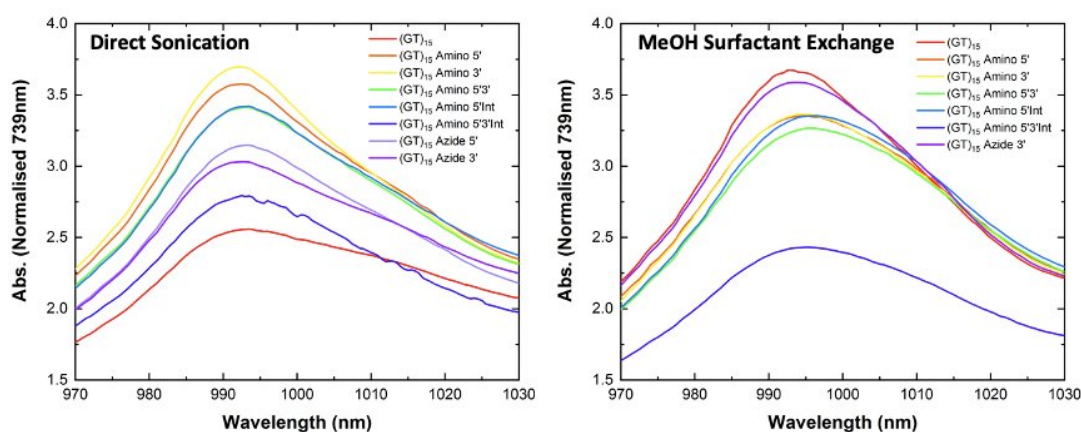


Figure B.4 – Comparison of the concentration normalized absorbance spectra for the (6,5) chirality E₁₁ peak of unmodified and modified (GT)₁₅-SWCNTs prepared via (left) direct sonication and (right) MeOH assisted surfactant exchange. All spectra were normalized to concentration using an extinction coefficient of 0.0253 mg/L at Abs_{739nm}.

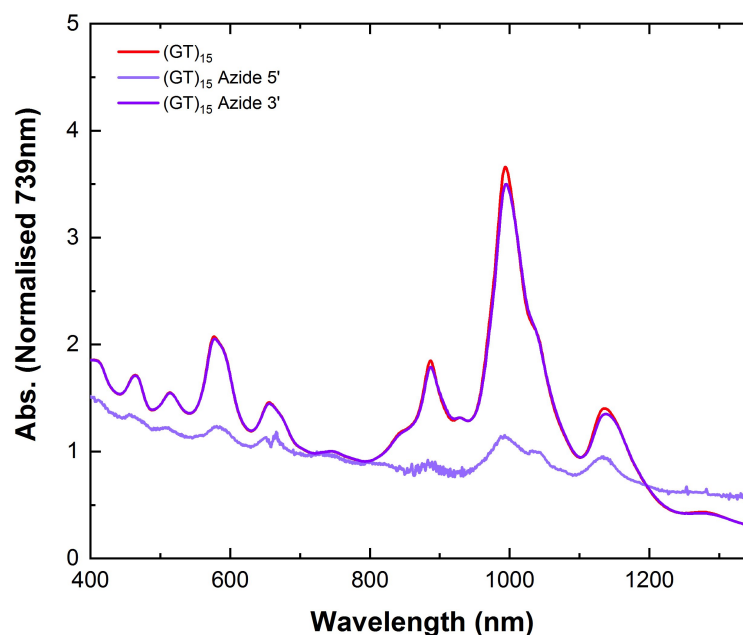


Figure B.5 – Absorbance spectra for Azide5'- and Azide3'-(GT)₁₅-SWCNTs prepared using MeOH assisted surfactant exchange. Replicate preparation of unmodified, Azide5'-, and Azide3'-(GT)₁₅-SWCNTs confirm the much lower dispersion capabilities of Azide5'-(GT)₁₅ when the MeOH assisted surfactant exchange protocol is used. All spectra were normalized to concentration using an extinction coefficient of 0.0253 mg/L at Abs_{739nm}.

Azide-modified (GT)₁₅

We observed a significant difference between (GT)₁₅ Azide5'-SWCNTs and (GT)₁₅ Azide3'-SWCNTs for suspensions prepared using MeOH-assisted surfactant exchange. While (GT)₁₅ Azide3' continued to produce well dispersed, high-yield solutions of SWCNTs with peak-to-background ratios similar to unmodified (GT)₁₅, (GT)₁₅ Azide5' was not able to effectively suspend the nanotubes. The yield of (GT)₁₅ Azide5'-SWCNTs was more than sixty times lower in concentration compared to the (GT)₁₅ Azide3'-SWCNTs and had the highest FWHM and lowest relative absorbance of all solutions. Subsequent preparations of (GT)₁₅ Azide5'-(GT)₁₅-SWCNTs using the surfactant exchange protocol resulted in equally low-yields (**Appendix Figure B.5**). Similarly, decreases in the yield and absorbance of the (6,5) peak were observed for nanotube suspensions prepared via surfactant exchange with (AT)₁₅ Azide5' but not (AT)₁₅ Azide3' (**Appendix Figure B.6**). The difference in suspension quality of Azide5' and Azide3' modifications highlights the impact of the linker molecules as well as the functional group on the dispersion capabilities of a sequence.

Appendix B. Modifying DNA-SWCNT Sensors for Improved Dopamine Detection

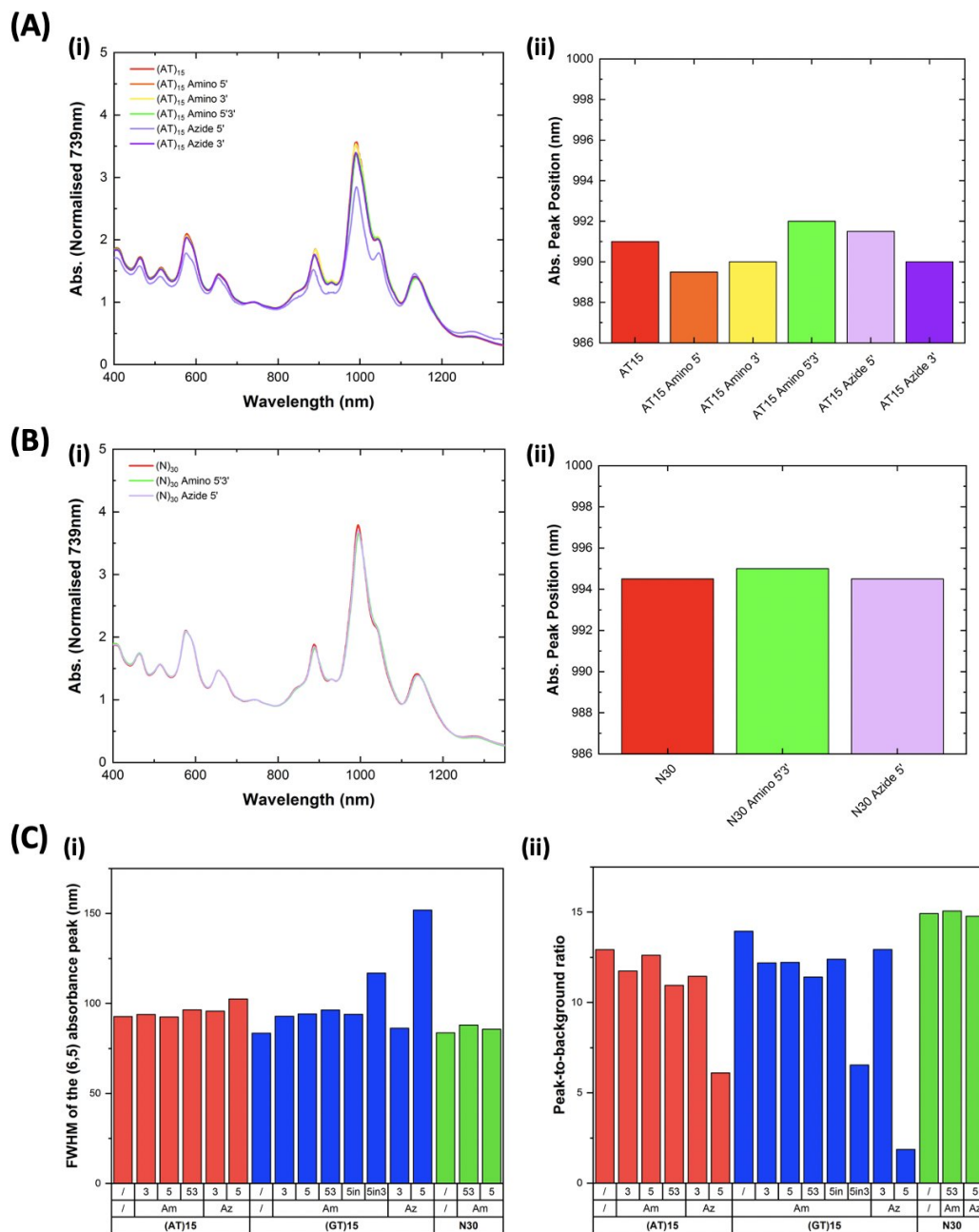


Figure B.6 – Differences in the suspension quality and chirality distribution of modified and unmodified (AT)₁₅- and (N)₃₀-SWCNTs prepared using MeOH assisted surfactant exchange. **(A)** Modified and unmodified (AT)₁₅-SWCNT samples. **(i)** Absorbance spectra and **(ii)** relative peak position of the E₁₁ transition for the (6,5) chirality for all (AT)₁₅ sequences. All spectra are normalized to concentration using extinction coefficient of 0.0253 mg/L at Abs_{739nm}. **(B)** Modified and unmodified (N)₃₀-SWCNT samples. **(i)** Absorbance spectra and **(ii)** relative peak position of the E₁₁ transition for the (6,5) chirality for all (N)₃₀ sequences examined in this study. **(C)** Characterisation of the quality of suspension for all SWCNT solutions prepared using MeOH assisted surfactant exchange. **(i)** FWHM and **(ii)** peak-to-background ratio for the (6,5) absorbance peaks of each suspension.

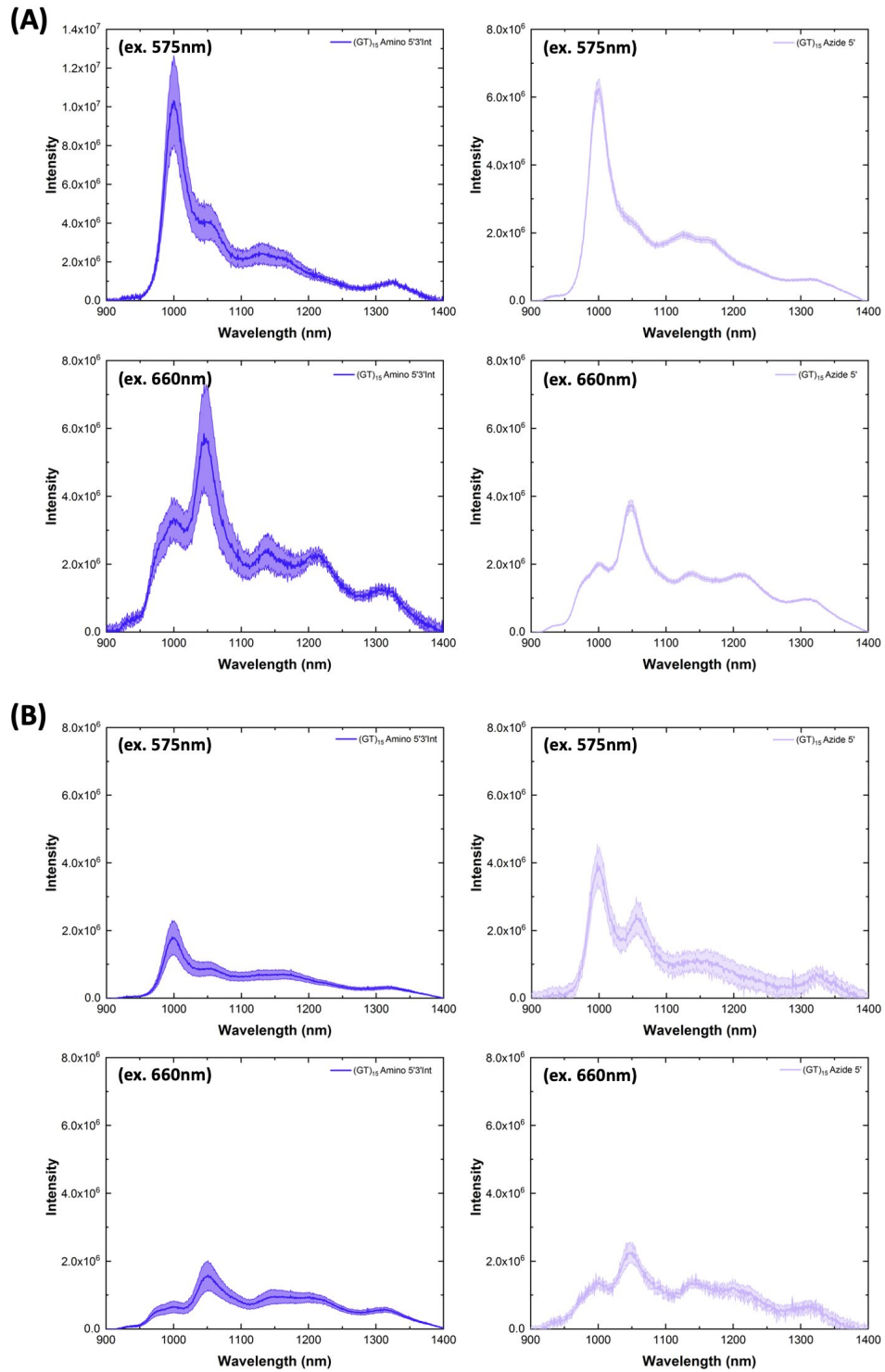


Figure B.7 – Fluorescence emission spectra for Am5'3'Int-(GT)₁₅-SWCNTs (**left**) and Azide5'-(GT)₁₅-SWCNTs (**right**) samples prepared by **(A)** direct sonication and **(B)** MeOH assisted surfactant exchange. All fluorescence spectra were normalized to nanotube concentration measured in the 384-well plate immediately prior to measurement to account for any minor variations. For all spectra, the central line represents the average spectrum with the shaded regions representing 1 σ standard deviation (n = 3 technical replicates) (excitation: 575 nm (**top**) and 660 nm (**bottom**)).

Appendix B. Modifying DNA-SWCNT Sensors for Improved Dopamine Detection

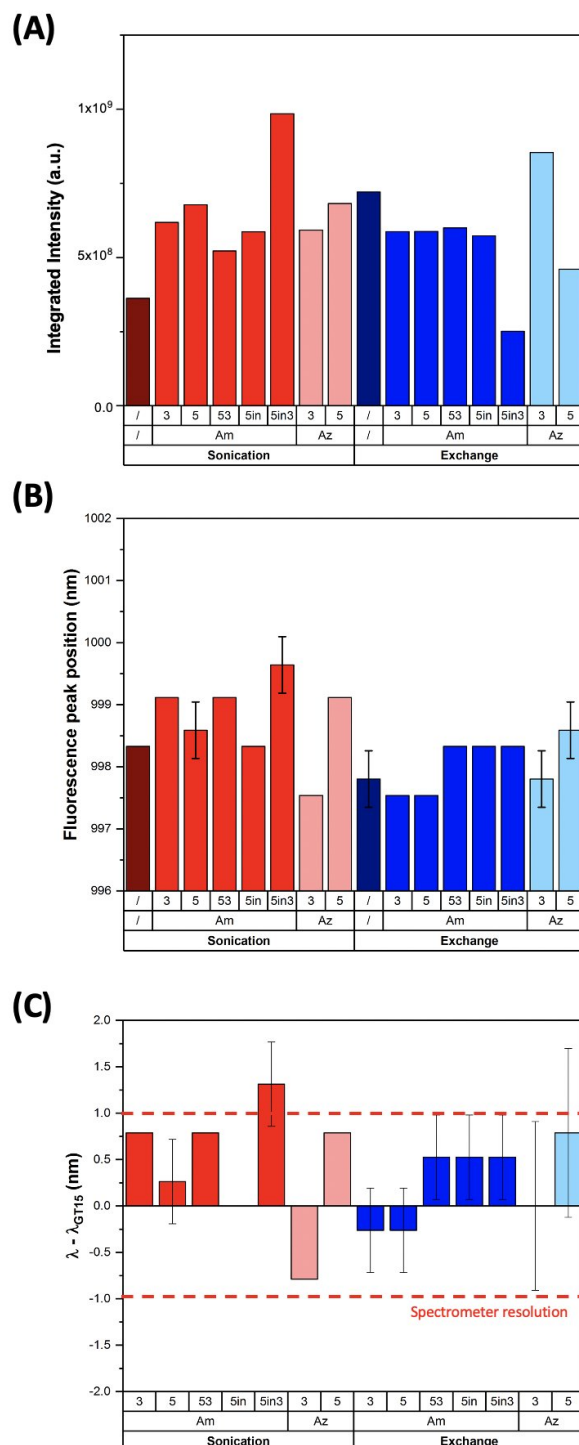


Figure B.8 – **(A)** Integrated fluorescence intensity under 575 nm excitation of modified and unmodified (GT)₁₅-SWCNTs prepared by direct sonication and MeOH assisted surfactant exchange. The integrated intensity was calculated from the additive emissions for wavelengths 900 – 1400 nm. Error bars represent 1 σ standard deviation (n = 3 technical replicates). **(B)** Fluorescence peak positions for the (6,5) chirality (excitation: 575 nm) for all modified and unmodified (GT)₁₅-SWCNTs. **(C)** Shift in the peak positions for the (6,5) peak compared to the respective (GT)₁₅-SWCNT suspension ($\lambda_{(GT)15}$). Error bars represent 1 σ standard deviation (n = 3 technical replicates). **Red** dashed lines represent the limit of resolution for the spectrometer.

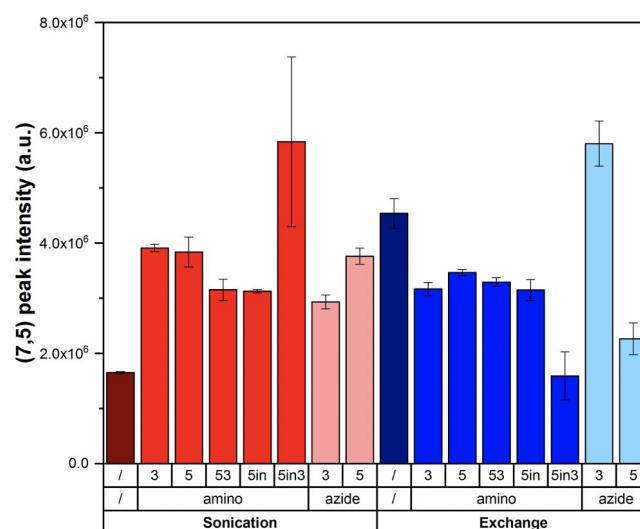


Figure B.9 – Comparison of the absolute peak intensity of the (7,5) chirality (excitation: 660 nm) for SWCNTs suspended with both modified- and unmodified-(GT)₁₅ by direct sonication and MeOH assisted surfactant exchange. Error bars represent 1 σ standard deviation (n = 3 technical replicates).

Appendix B. Modifying DNA-SWCNT Sensors for Improved Dopamine Detection

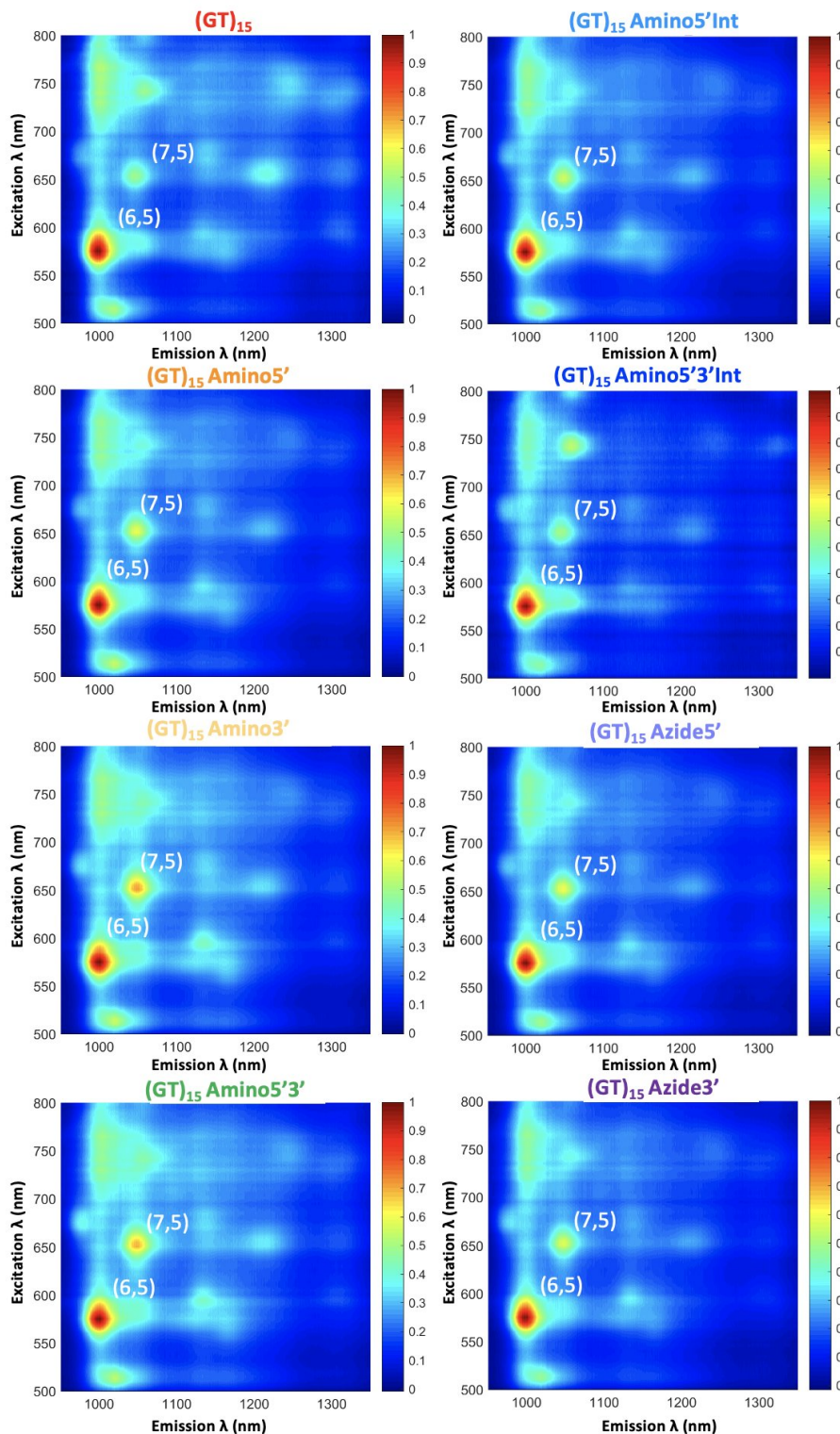


Figure B.10 – Photoluminescence excitation (PLE) maps of the modified and unmodified (GT)₁₅-SWCNT solutions prepared via direct sonication. The (6,5) and (7,5) chirality peaks are indicated in white. All fluorescence intensities were normalized to the maximum intensity in each plot.

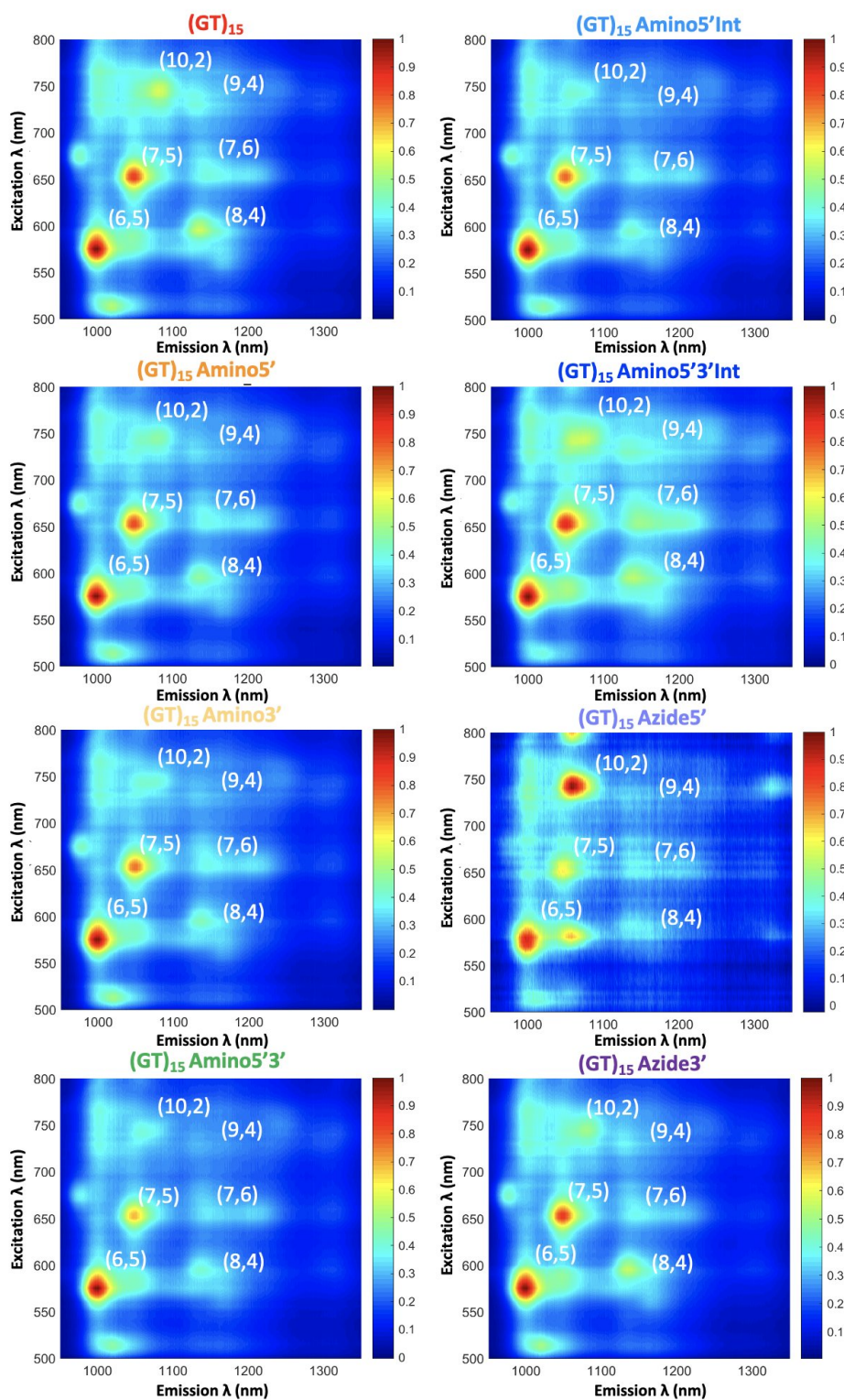


Figure B.11 – Photoluminescence excitation (PLE) maps of the modified and unmodified (GT)₁₅-SWCNT solutions prepared using MeOH assisted surfactant exchange. The (6,5) and (7,5) chirality peaks are indicated in white. All fluorescence intensities were normalized to the maximum intensity in each plot.

Appendix B. Modifying DNA-SWCNT Sensors for Improved Dopamine Detection

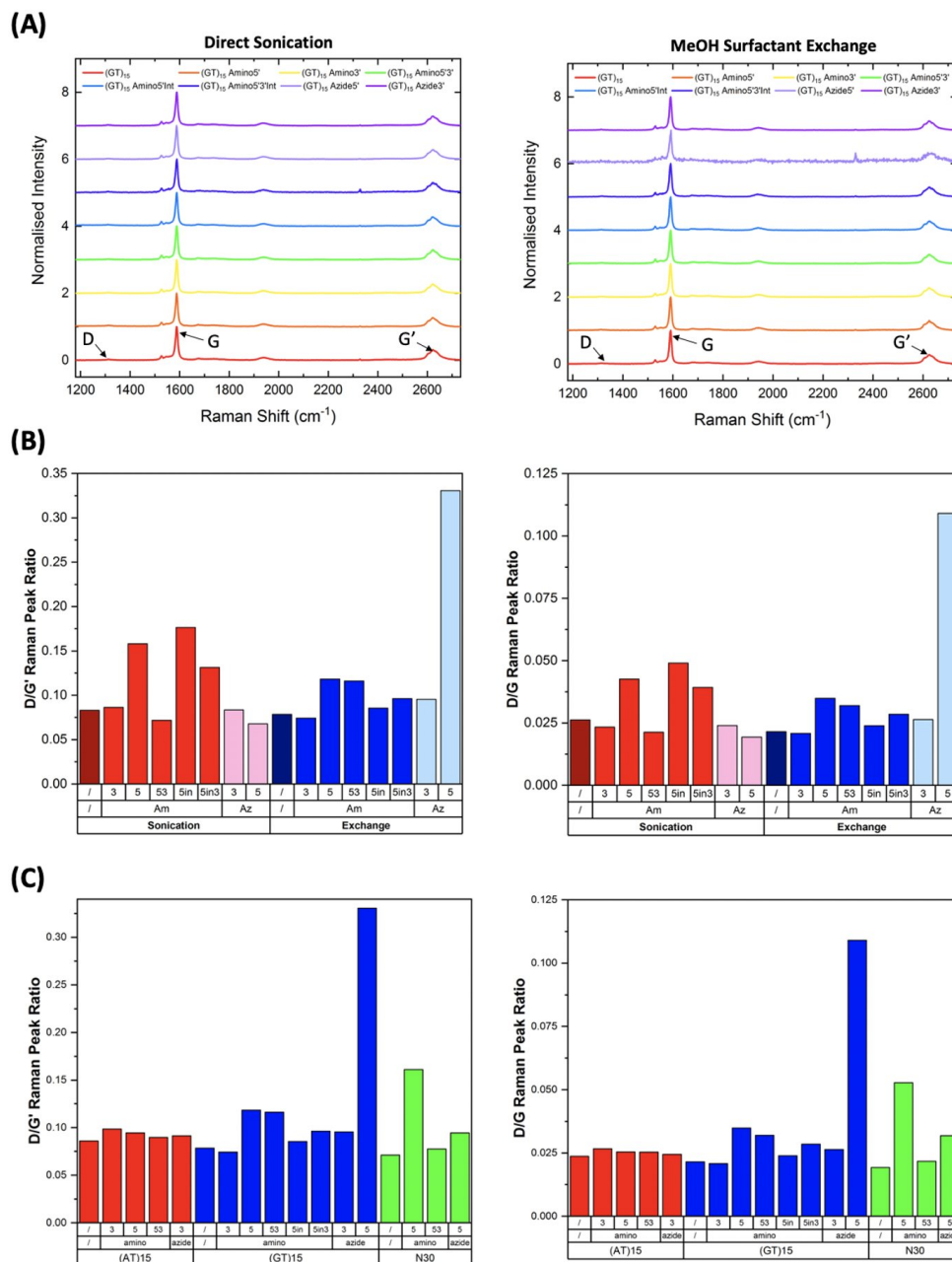


Figure B.12 – Raman characterisation of modified and unmodified DNA-SWCNTs prepared by direct sonication and MeOH assisted surfactant exchange. Nanotube surface defects provide the necessary symmetry breaking to give rise to the D-band in Raman spectra [326, 327]. As a result, comparisons of the D/G' or D/G intensity ratios provide relative measures of defect density. The similarity of all Raman modes, specifically the D, G, and G' bands, for unmodified (GT)₁₅ samples prepared by both methods implies a common degree of disorder, suggesting that changes in the fluorescence intensity were not a result of increasing defect density on the sonicated samples. **(A)** Raman spectra for modified and unmodified (GT)₁₅-SWCNTs prepared by **(left)** direct sonication and **(right)** MeOH assisted surfactant exchange. Spectra were normalized to the G-band intensity and off-set for comparison. **(B)** Comparison of the **(left)** D/G' and **(right)** D/G peak ratio for the (GT)₁₅-SWCNT suspensions. **(C)** Comparison of the **(left)** D/G' and **(right)** D/G peak ratio for all DNA-SWCNT suspensions prepared using MeOH assisted surfactant exchange.

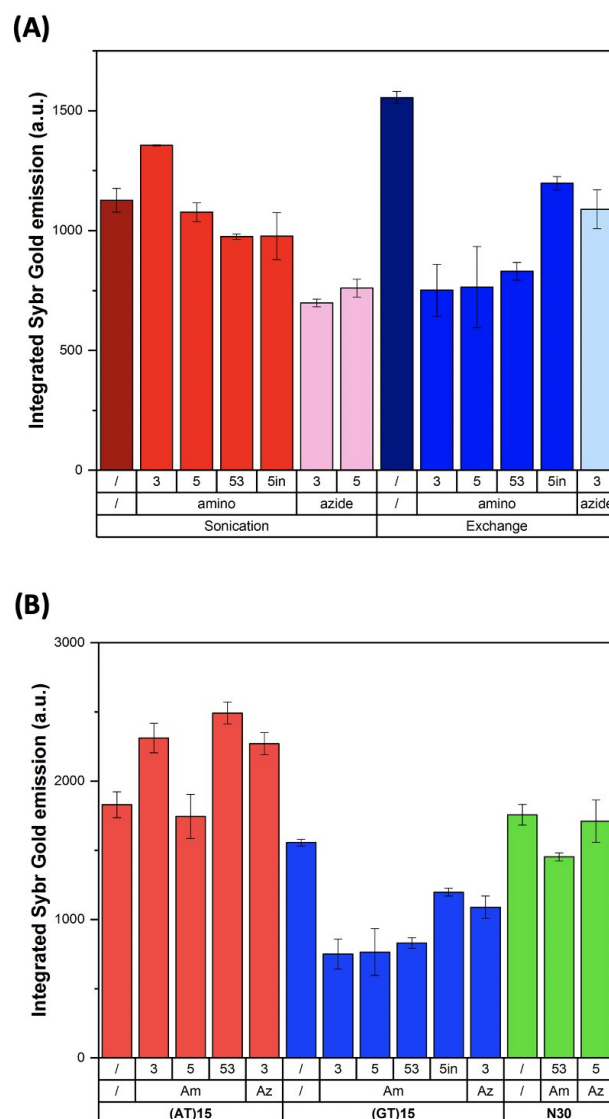


Figure B.13 – SYBR gold assay performed in order to calculate the amount of DNA adsorbed onto the surface of the nanotube for modified and unmodified **(A)** (GT)₁₅-SWCNTs prepared by direct sonication or MeOH assisted surfactant exchange and **(B)** DNA-SWCNTs prepared via MeOH assisted surfactant exchange. DNA was removed from the surface of the nanotube by phenol-chloroform isoamyl (PCI) extraction and subsequently precipitated by glycogen-assisted ethanol precipitation. Prior to DNA extraction, all DNA-SWCNT samples were rinsed using Amicon ultrafiltration devices to remove any unbound DNA that may be present in the solution. Higher integrated SYBR Gold emission values indicate higher concentrations of DNA. Error bars represent 1 σ standard deviation (n = 3 technical replicates).

Appendix B. Modifying DNA-SWCNT Sensors for Improved Dopamine Detection

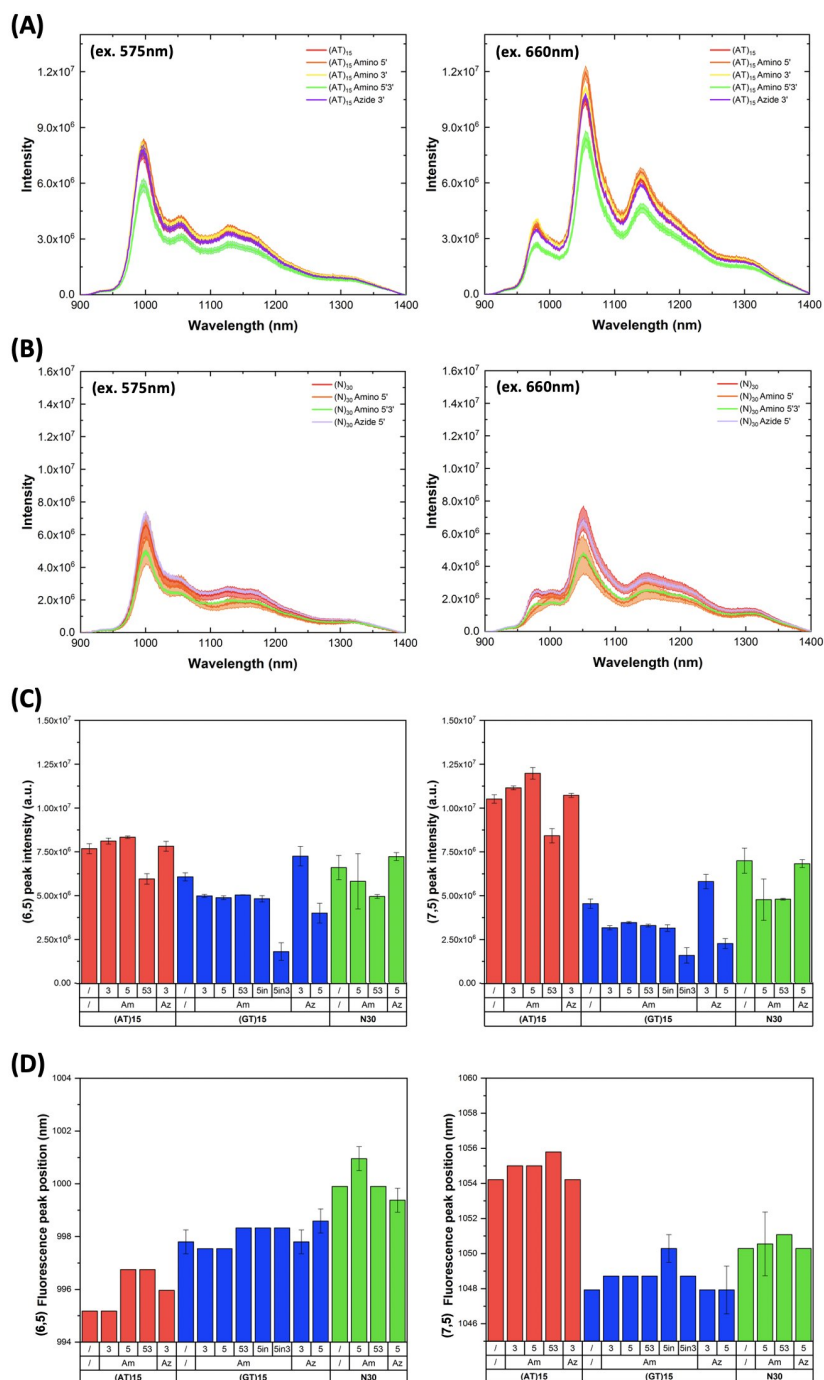


Figure B.14 – Fluorescence spectra of **(A)** (AT)₁₅- and **(B)** (N)₃₀-SWCNTs prepared using MeOH assisted surfactant exchange using both unmodified DNA (red line) and modified DNA sequences. For all spectra, the central line represents the average spectrum with the shaded regions representing 1 σ standard deviation (n = 3 technical replicates) (excitation: 575 nm (**left**) and 660 nm (**right**)). **(C)** Comparison of the absolute peak intensity of the (6,5) (excitation: 575 nm, (**left**)) and (7,5) chiralities (excitation: 660 nm, (**right**)) for modified and unmodified DNA-SWCNTs prepared using MeOH assisted surfactant exchange. Error bars represent 1 σ standard deviation (n = 3 technical replicates). **(D)** Peak position of the (6,5) (excitation: 575 nm, (**left**)) and (7,5) chiralities (excitation: 660 nm, (**right**)) for modified and unmodified DNA-SWCNTs prepared using MeOH assisted surfactant exchange. Error bars represent 1 σ standard deviation (n = 3 technical replicates).

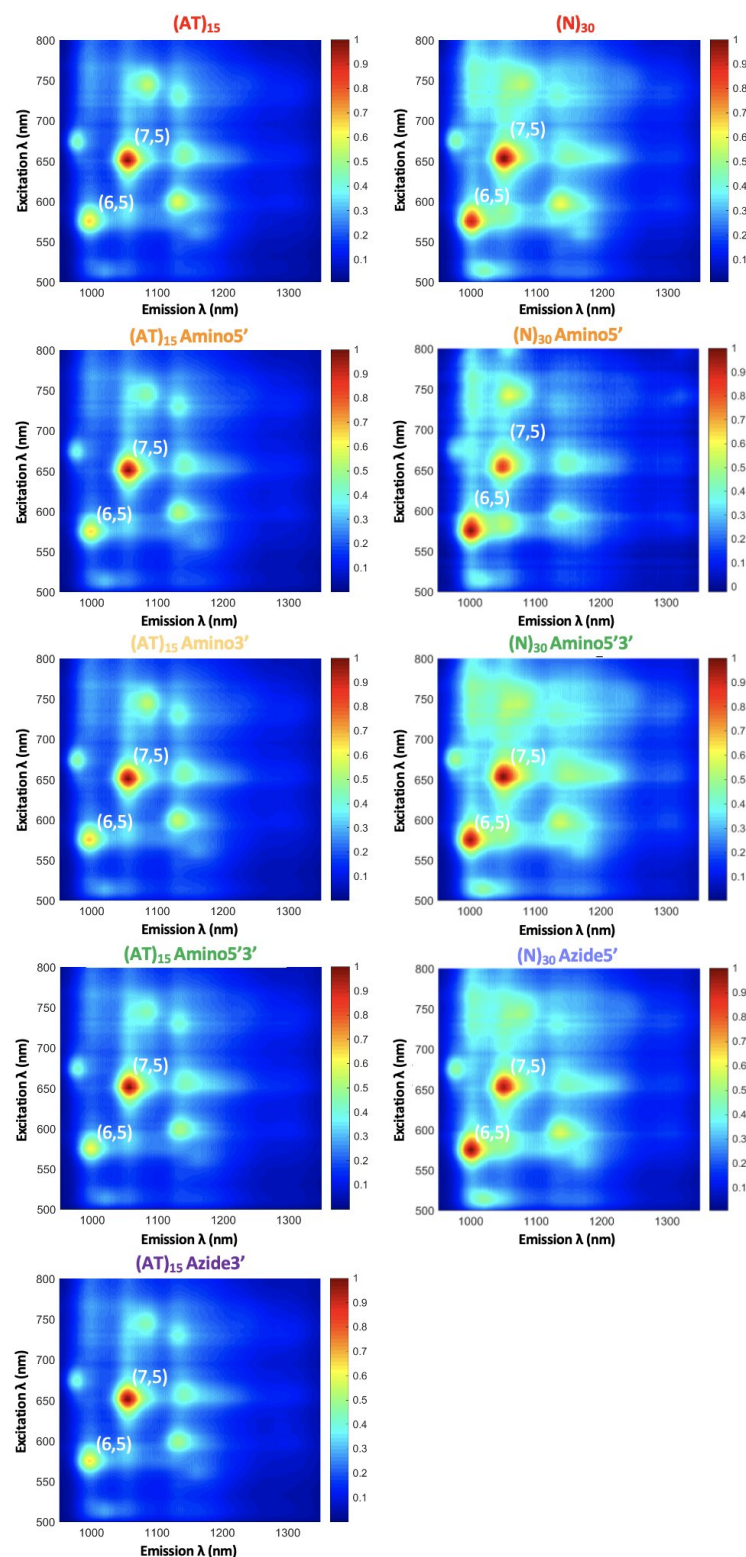


Figure B.15 – Photoluminescence excitation (PLE) maps of modified and unmodified (AT)₁₅- and (N)₃₀-SWCNTs prepared using MeOH assisted surfactant exchange. The (6,5) and (7,5) chirality peaks are indicated in white. All fluorescence intensities were normalized to the maximum intensity in each plot.

Appendix B. Modifying DNA-SWCNT Sensors for Improved Dopamine Detection

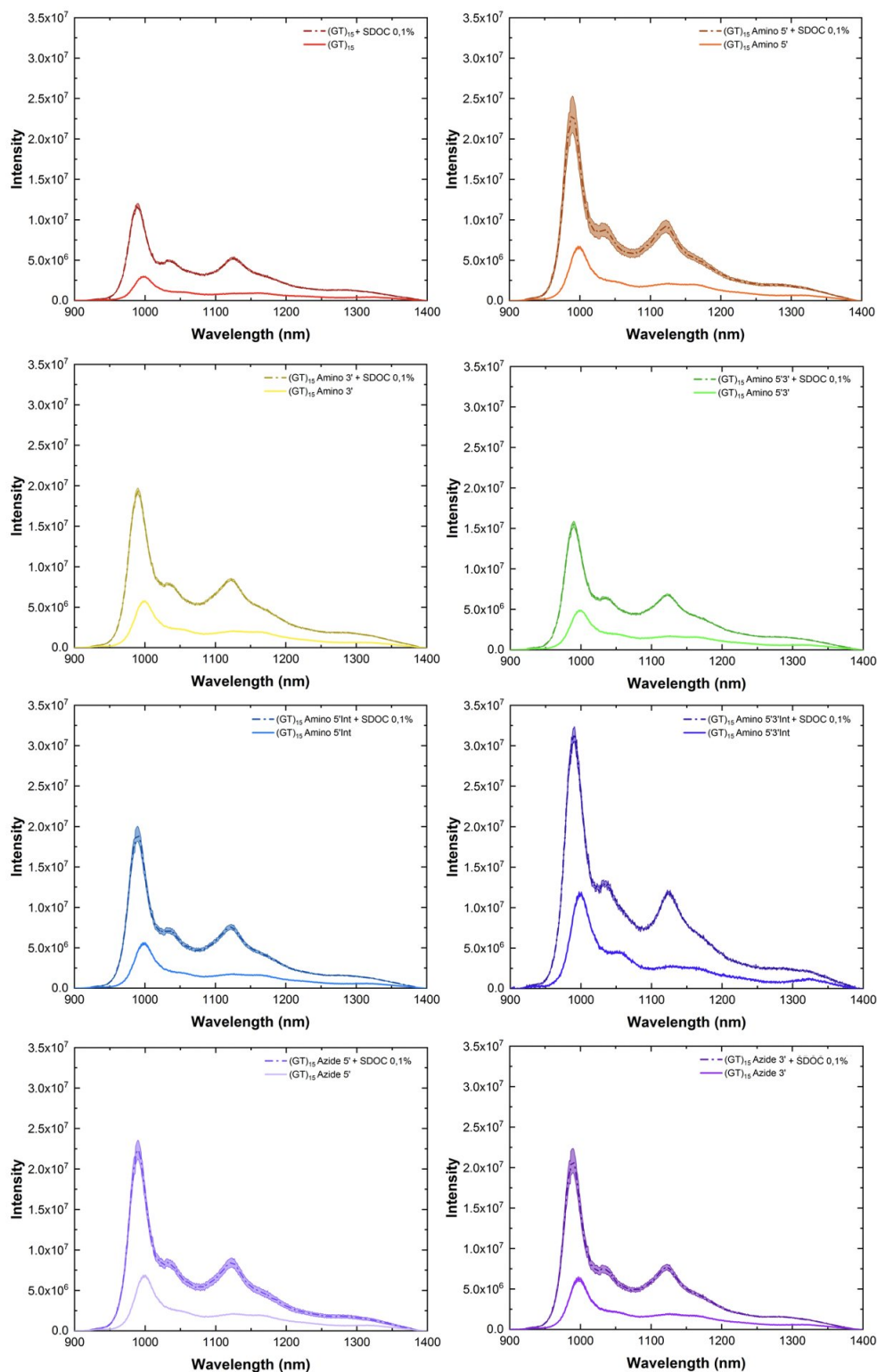


Figure B.16 – Fluorescence spectra of modified- and unmodified-(GT)₁₅-SWCNTs prepared via direct sonication before (solid light line) and after (dashed dark line) addition of SDOC (final concentration: 0.1%, excitation: 575 nm, incubation time: 10 min). For all spectra, the central line represents the average spectrum with the shaded regions representing 1 σ standard deviation (n = 3 technical replicates).

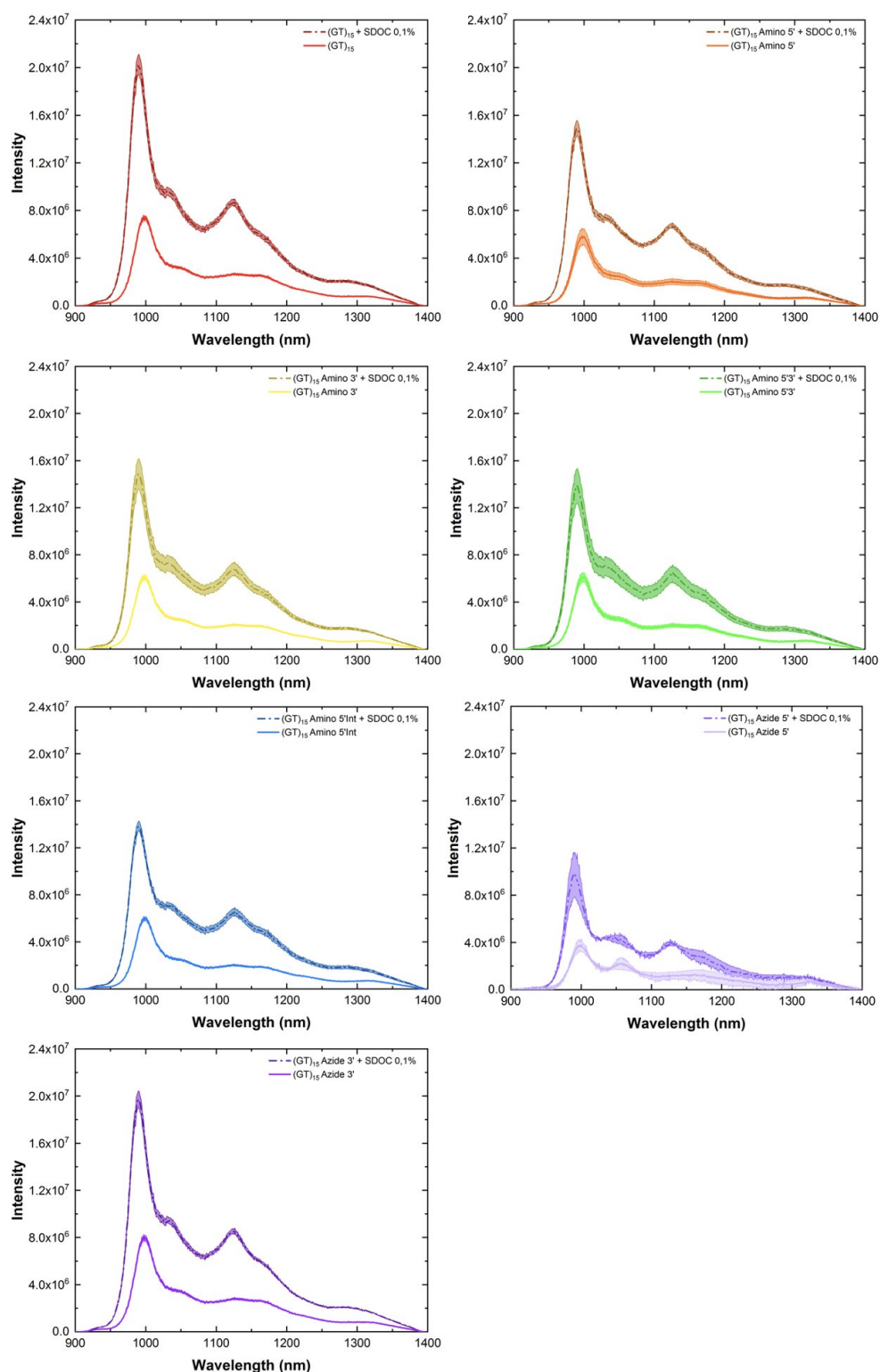


Figure B.17 – Fluorescence spectra of modified- and unmodified-(GT)₁₅-SWCNTs prepared using MeOH assisted surfactant exchange before (solid light line) and after (dashed dark line) addition of SDOC (final concentration: 0.1%, excitation: 575 nm, incubation time: 10 min). For all spectra, the central line represents the average spectrum with the shaded regions representing 1 σ standard deviation (n = 3 technical replicates).

Appendix B. Modifying DNA-SWCNT Sensors for Improved Dopamine Detection

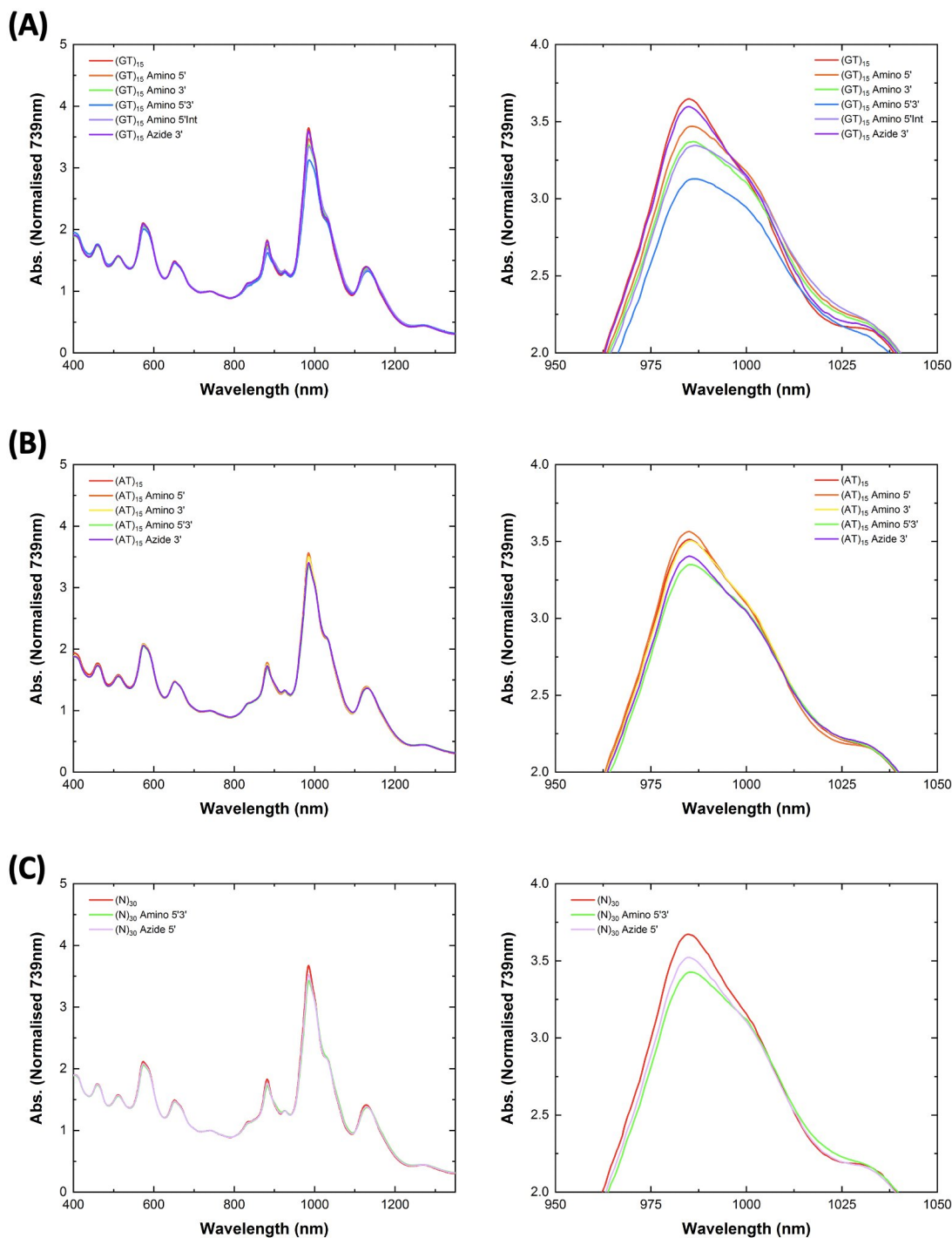


Figure B.18 – Absorbance spectra of modified and unmodified (A) (GT)₁₅-, (B) (AT)₁₅-, and (C) (N)₃₀-SWCNTs prepared using MeOH assisted surfactant exchange following the addition of SDOC (final concentration: 0.1%). Spectra on the right are a zoom-in of the absorbance for the (6,5) chirality peak highlighting that even post SDOC replacement the absorbance did not overlap indicating that there were differences in the relative abundance of this chirality in the different suspensions. All spectra were normalized to the Abs_{739nm} value to account for any differences in nanotube concentration.

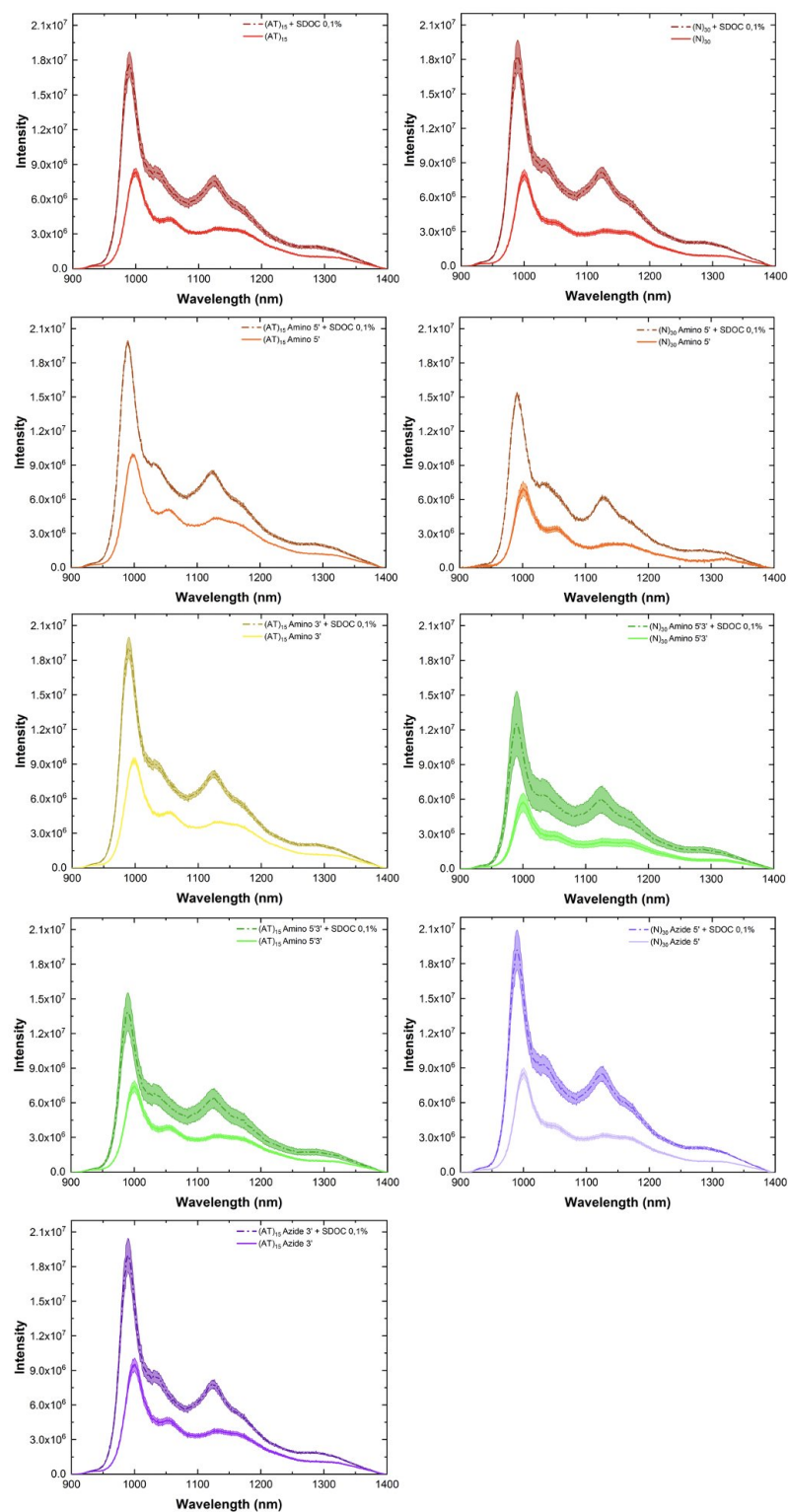


Figure B.19 – Fluorescence spectra of modified- and unmodified-(AT)₁₅-SWCNTs (**left**) and (N)₃₀-SWCNTs (**right**) prepared using MeOH assisted surfactant exchange before (solid light line) and after (dashed dark line) addition of SDOC (final concentration: 0.1%, excitation: 575 nm, incubation period: 10 min). For all spectra, the central line represents the average spectrum with the shaded regions representing 1 σ standard deviation (n = 3 technical replicates).

Appendix B. Modifying DNA-SWCNT Sensors for Improved Dopamine Detection

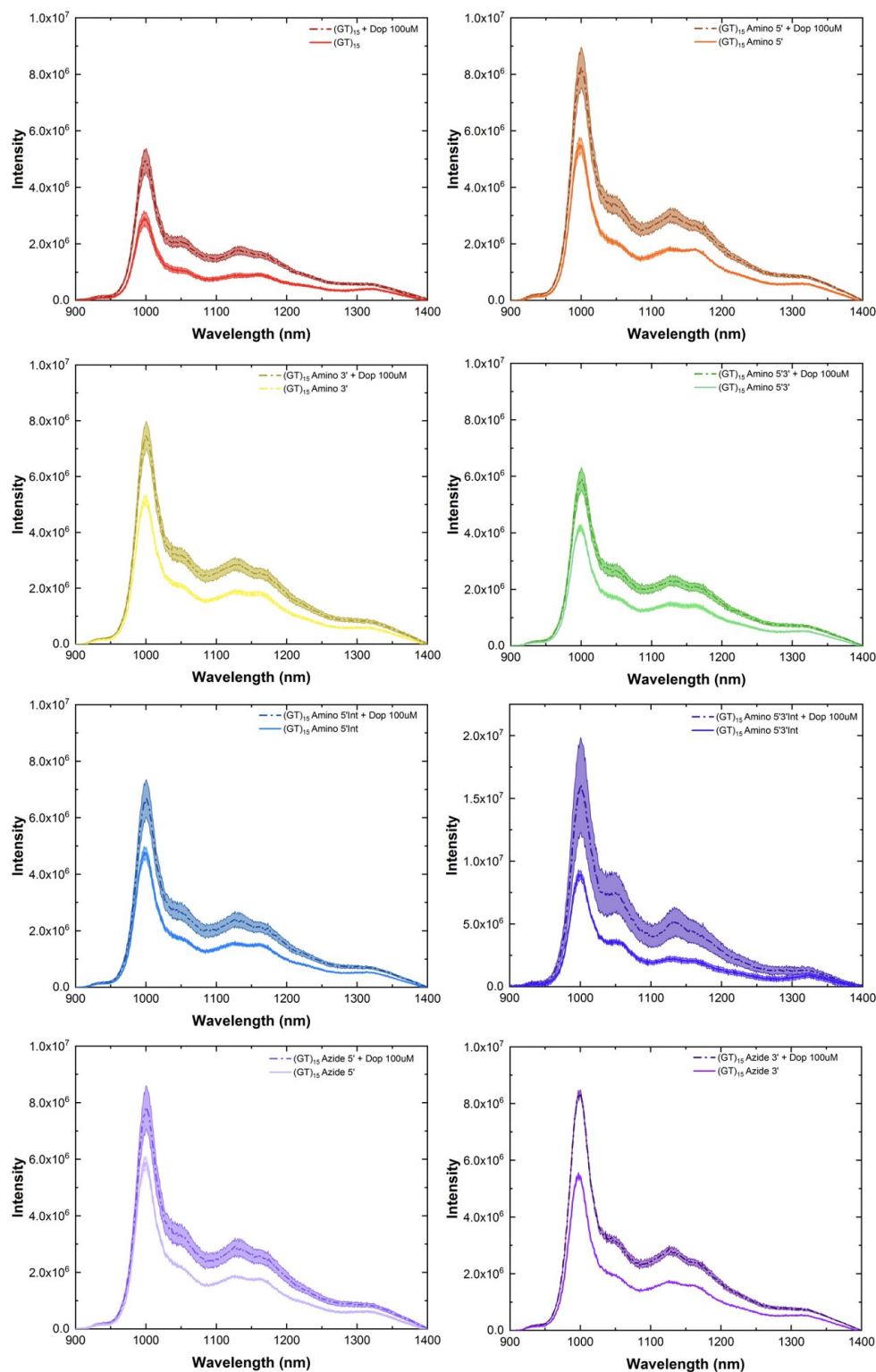


Figure B.20 – Fluorescence spectra of modified and unmodified (GT)₁₅-SWCNTs prepared via direct sonication before (solid light line) and after (dashed dark line) addition of dopamine (final concentration: 100 μ M, excitation: 575 nm, incubation period: 10 min). For all spectra, the central line represents the average spectrum with the shaded regions representing 1 σ standard deviation (n = 3 technical replicates).

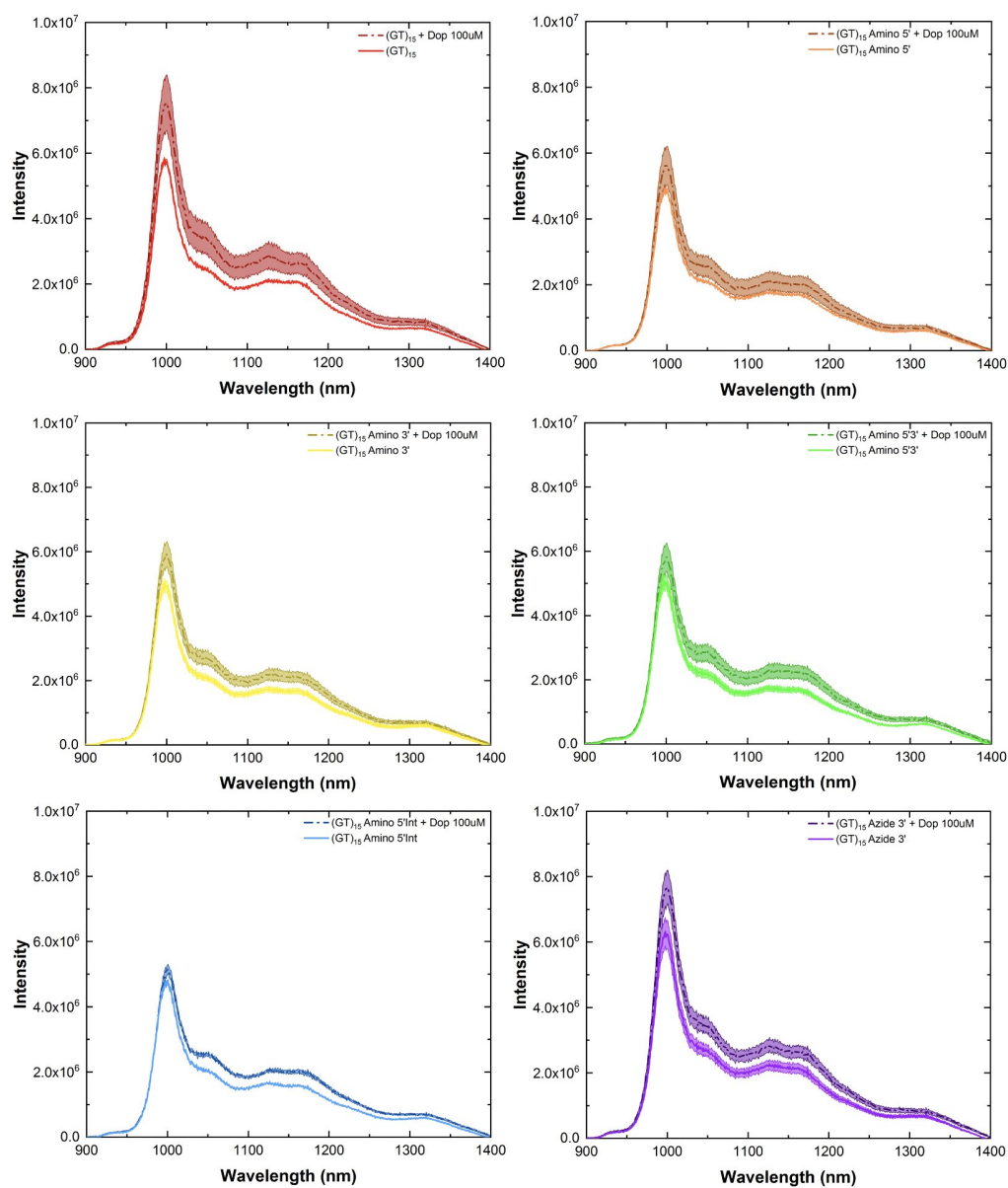


Figure B.21 – Fluorescence spectra of modified and unmodified (GT)₁₅-SWCNTs prepared using MeOH assisted surfactant exchange before (solid light line) and after (dashed dark line) addition of dopamine (final concentration: 100 μ M, excitation: 575 nm, incubation period: 10 min). For all spectra, the central line represents the average spectrum with the shaded regions representing 1 σ standard deviation (n = 3 technical replicates).

Appendix B. Modifying DNA-SWCNT Sensors for Improved Dopamine Detection

Table B.2 – Fluorescence intensity increase for modified and unmodified (GT)₁₅-SWCNTs following the addition of dopamine. Maximal fluorescence changes ($I_f - I_0 / I_0$), % change, are presented alongside the absolute magnitude of the fluorescence increase ($I_f - I_0$) for comparison.

Direct Sonication		
DNA Sequence	% Change	Absolute Increase
(GT) ₁₅ -SWCNT	69.1 ± 11.7	2.02 E+06 ± 0.48 E+06
Amino3'-(GT) ₁₅ -SWCNT	44.4 ± 7.2	2.30 E+06 ± 0.52 E+06
Amino5'-(GT) ₁₅ -SWCNT	49.4 ± 9.9	2.73 E+06 ± 0.76 E+06
Amino5'3'-(GT) ₁₅ -SWCNT	40.8 ± 7.1	1.71 E+06 ± 0.41 E+06
Amino5'Int-(GT) ₁₅ -SWCNT	39.7 ± 10.9	1.90 E+06 ± 0.70 E+06
Azide3'-(GT) ₁₅ -SWCNT	51.6 ± 1.7	2.85 E+06 ± 0.12 E+06
MeOH-assisted Surfactant Exchange		
DNA Sequence	% Change	Magnitude of Increase
(GT) ₁₅ -SWCNT	30.1 ± 11.4	1.75 E+06 ± 0.86 E+06
Amino3'-(GT) ₁₅ -SWCNT	18.3 ± 7.4	9.18 E+05 ± 4.27 E+05
Amino5'-(GT) ₁₅ -SWCNT	14.5 ± 10.3	7.14 E+05 ± 5.82 E+05
Amino5'3'-(GT) ₁₅ -SWCNT	14.9 ± 8.5	7.57 E+05 ± 4.80 E+05
Amino5'Int-(GT) ₁₅ -SWCNT	8.4 ± 3.1	4.02 E+05 ± 1.57 E+05
Azide3'-(GT) ₁₅ -SWCNT	21.7 ± 9.5	1.37 E+06 ± 0.67 E+06

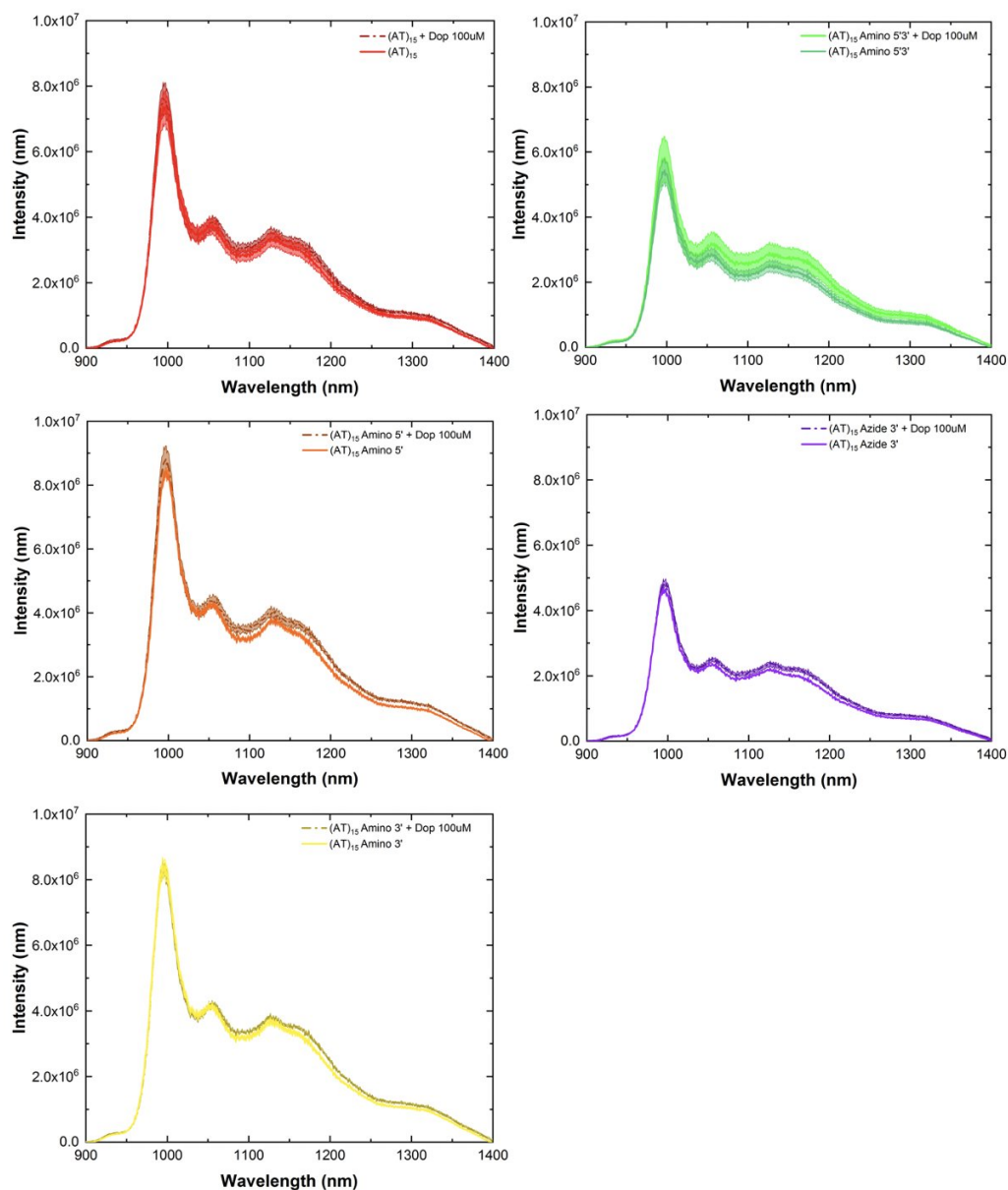


Figure B.22 – Fluorescence spectra of modified and unmodified $(AT)_{15}$ -SWCNTs prepared using MeOH assisted surfactant exchange before (solid light line) and after (dashed dark line) addition of dopamine (final concentration: 100 μ M, excitation: 575 nm, incubation period: 10 min). For all spectra, the central line represents the average spectrum with the shaded regions representing 1σ standard deviation ($n = 3$ technical replicates).

Appendix B. Modifying DNA-SWCNT Sensors for Improved Dopamine Detection

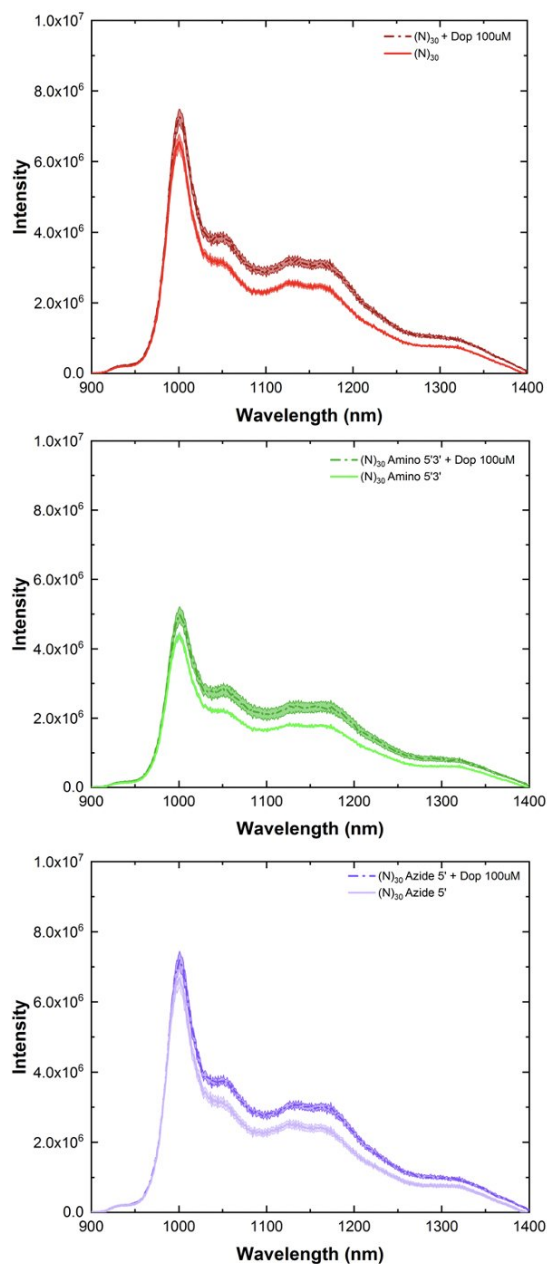


Figure B.23 – Fluorescence spectra of modified and unmodified (N)₃₀-SWCNTs prepared using MeOH assisted surfactant exchange before (solid light line) and after (dashed dark line) addition of dopamine (final concentration: 100 μM, excitation: 575 nm, incubation period: 10 min). For all spectra, the central line represents the average spectrum with the shaded regions representing 1σ standard deviation (n = 3 technical replicates).

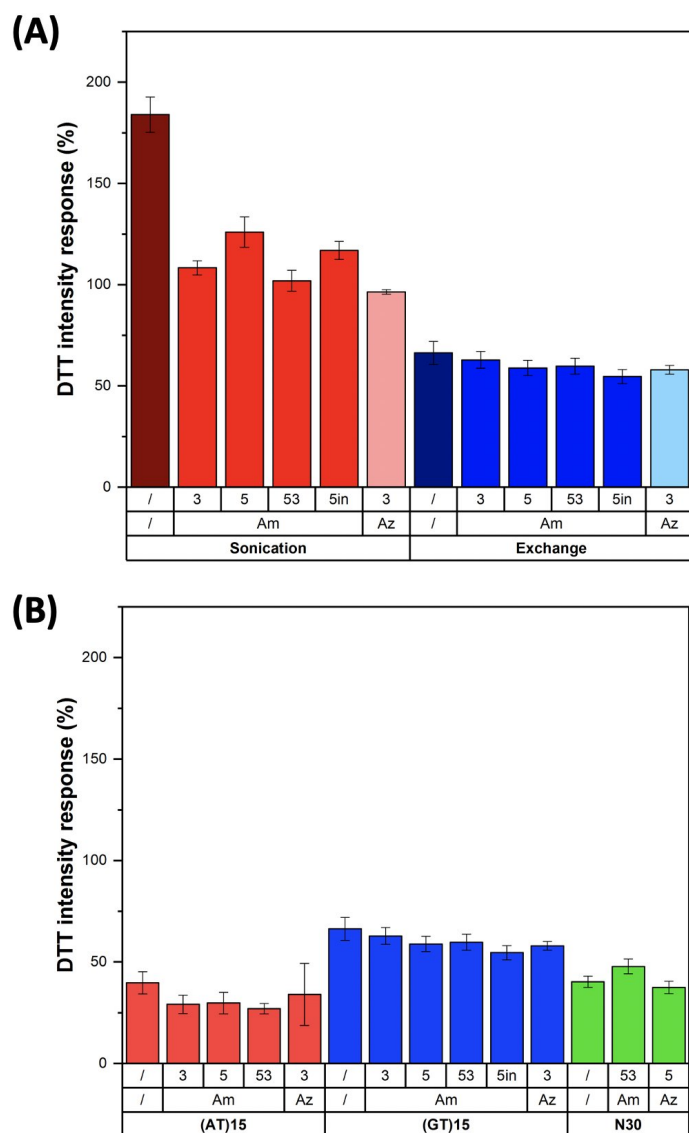


Figure B.24 – Intensity response following the addition of DTT. Comparison of the response for modified and unmodified **(A)** (GT)₁₅-SWCNTs prepared by direct sonication and MeOH assisted surfactant exchange and **(B)** DNA-SWCNTs prepared using MeOH assisted surfactant exchange towards DTT. Intensity changes were calculated as $I_f - I_0 / I_0$ for the (6,5) chirality peak (final concentration: 10 mM, excitation: 575 nm, incubation period: 10 min). Error bars represent 1σ standard deviation ($n = 3$ technical replicates).

Appendix B. Modifying DNA-SWCNT Sensors for Improved Dopamine Detection

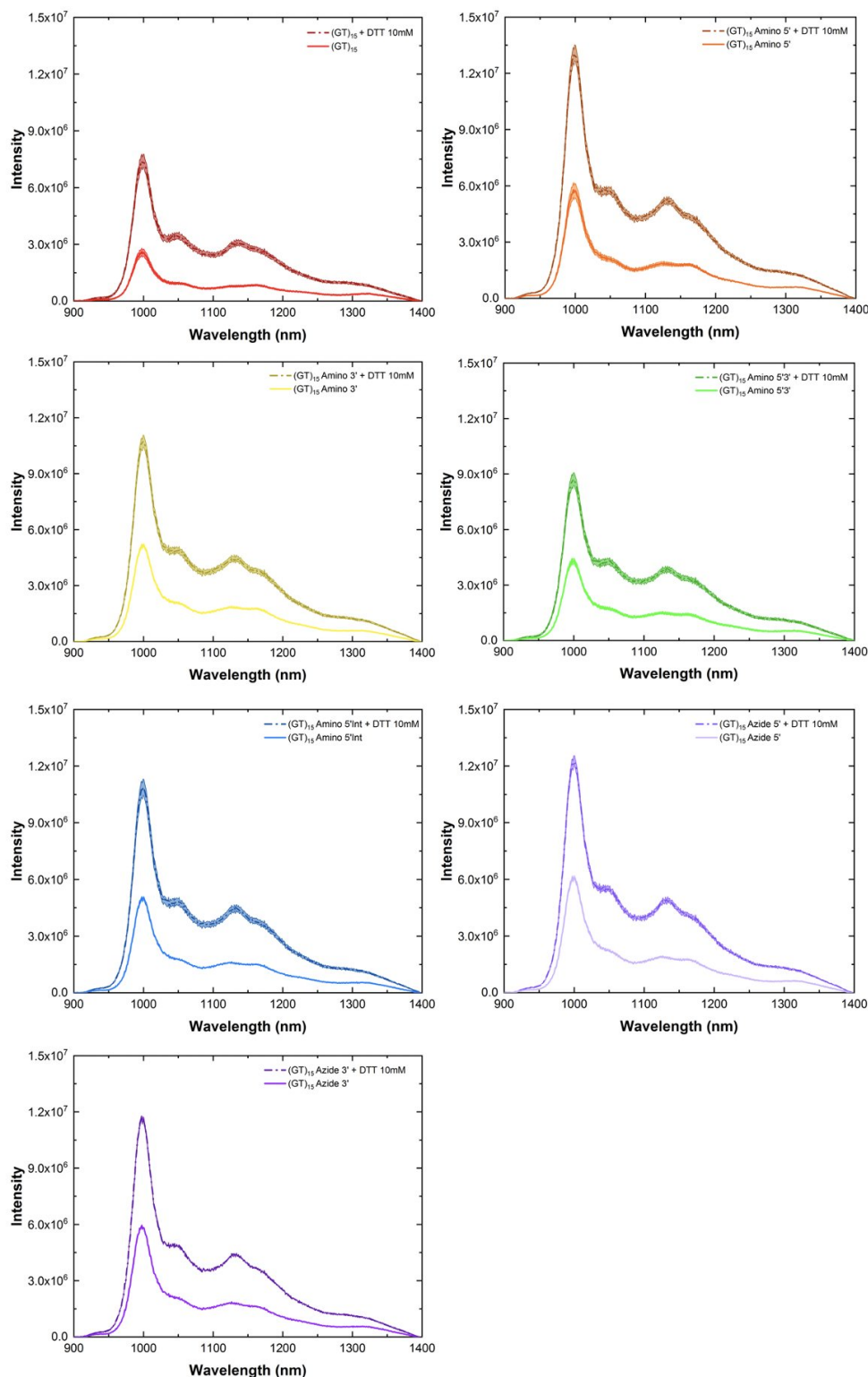


Figure B.25 – Fluorescence spectra of modified and unmodified (GT)₁₅-SWCNTs prepared by direct sonication before (solid light line) and after (dashed dark line) addition of DTT (final concentration: 10 mM, excitation: 575 nm, incubation period: 10 min). For all spectra, the central line represents the average spectrum with the shaded regions representing 1 σ standard deviation (n = 3 technical replicates).

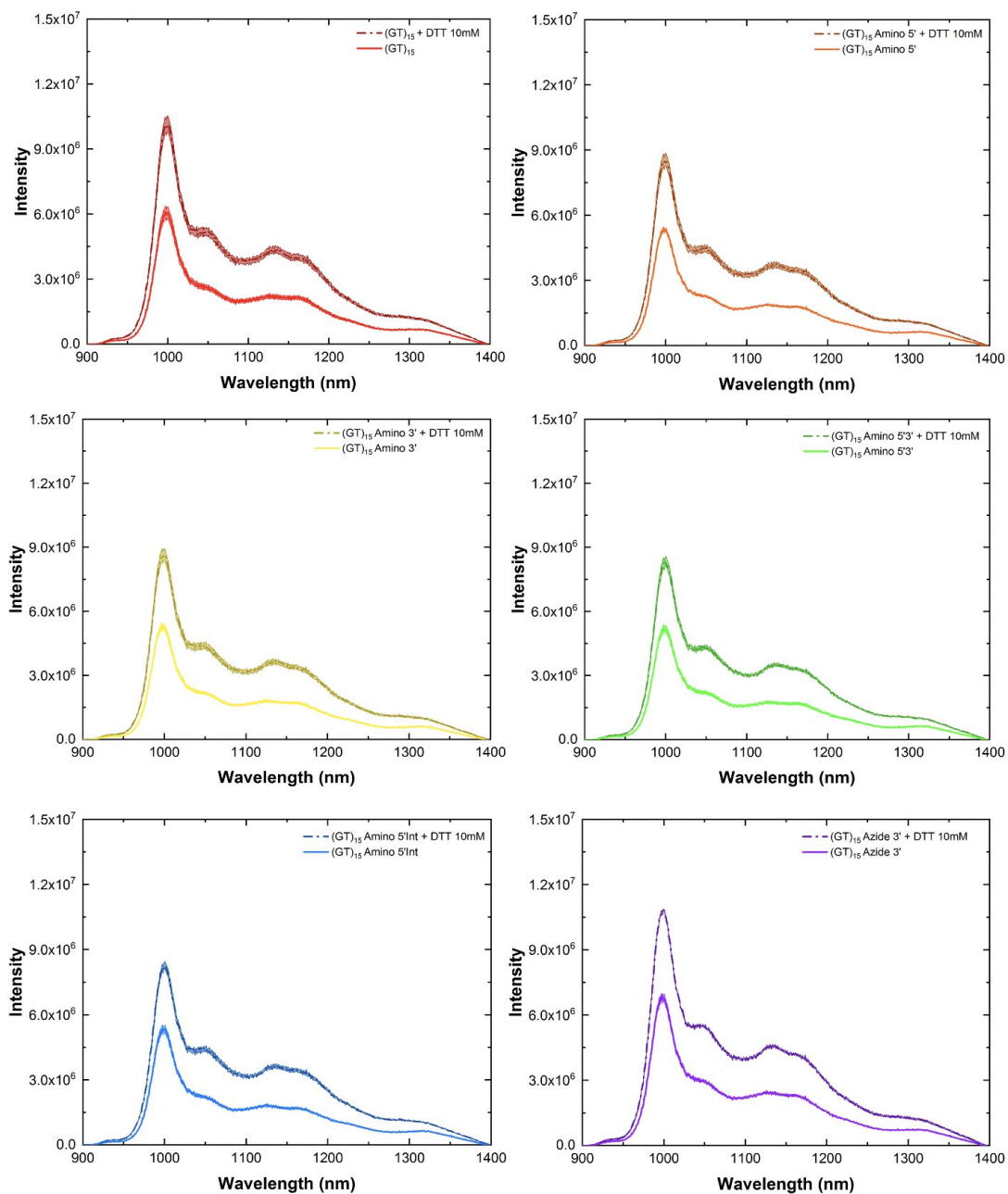


Figure B.26 – Fluorescence spectra of modified and unmodified (GT)₁₅-SWCNTs prepared using MeOH assisted surfactant exchange before (solid light line) and after (dashed dark line) addition of DTT (final concentration: 10 mM, excitation: 575 nm, incubation period: 10 min). For all spectra, the central line represents the average spectrum with the shaded regions representing 1 σ standard deviation (n = 3 technical replicates).

Appendix B. Modifying DNA-SWCNT Sensors for Improved Dopamine Detection

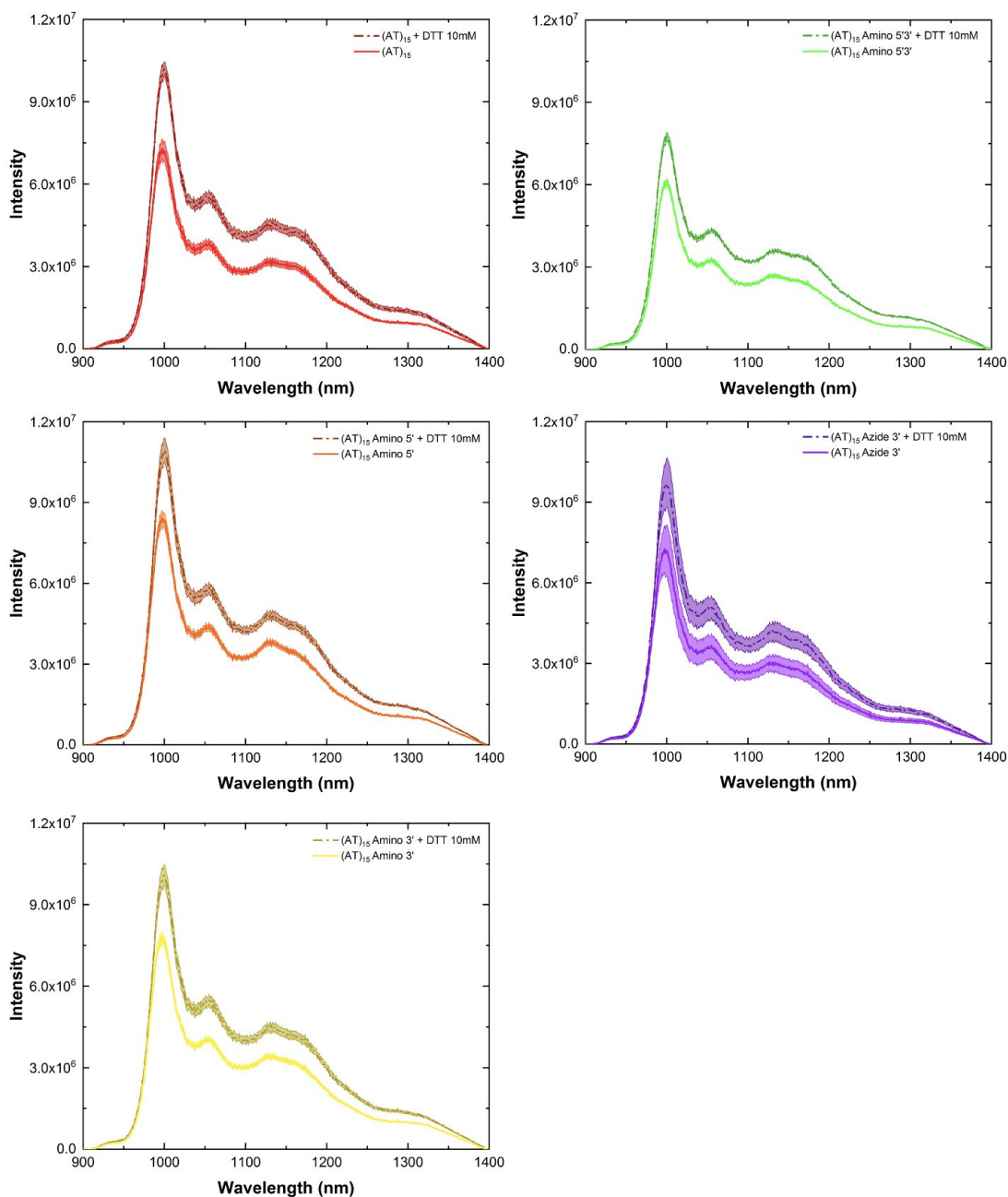


Figure B.27 – Fluorescence spectra of modified and unmodified (AT)₁₅-SWCNTs prepared using MeOH assisted surfactant exchange before (solid light line) and after (dashed dark line) addition of DTT (final concentration: 10 mM, excitation: 575 nm, incubation period: 10 min). For all spectra, the central line represents the average spectrum with the shaded regions representing 1σ standard deviation (n = 3 technical replicates).

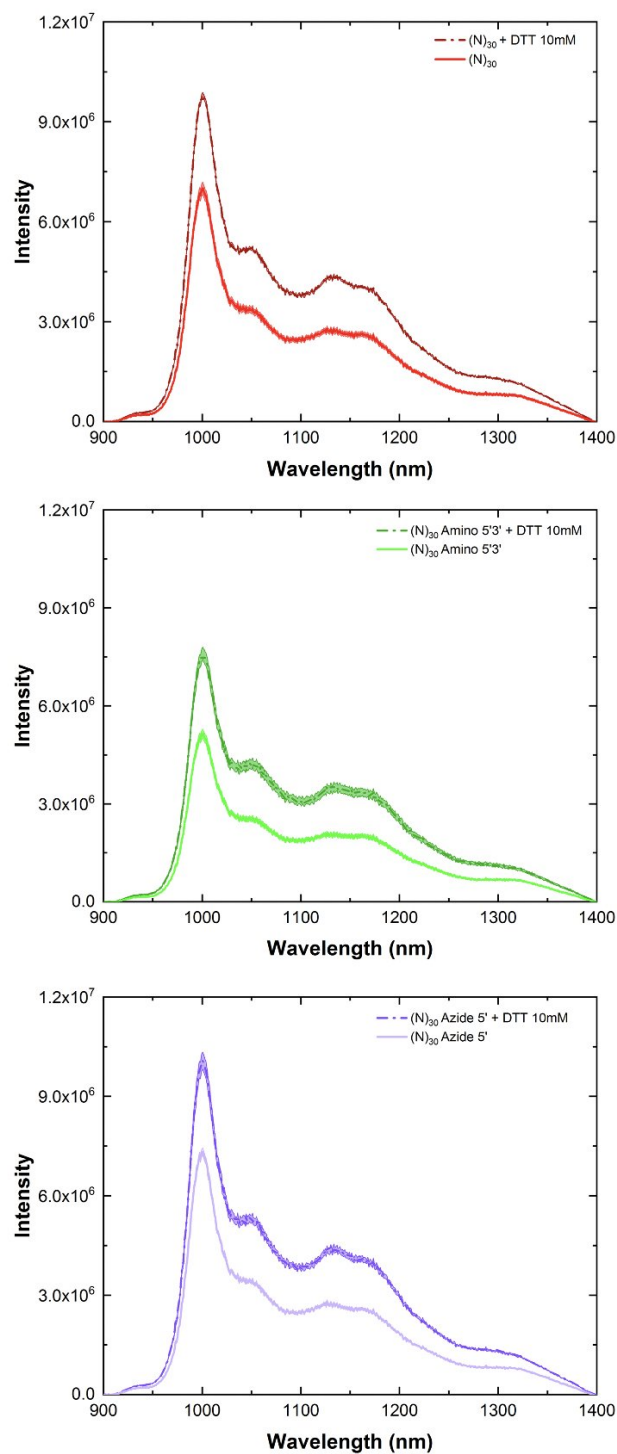


Figure B.28 – Fluorescence spectra of modified and unmodified (N)₃₀-SWCNTs prepared using MeOH assisted surfactant exchange before (solid light line) and after (dashed dark line) addition of DTT (final concentration: 10 mM, excitation: 575 nm, incubation period: 10 min). For all spectra, the central line represents the average spectrum with the shaded regions representing 1σ standard deviation ($n = 3$ technical replicates).

Appendix B. Modifying DNA-SWCNT Sensors for Improved Dopamine Detection

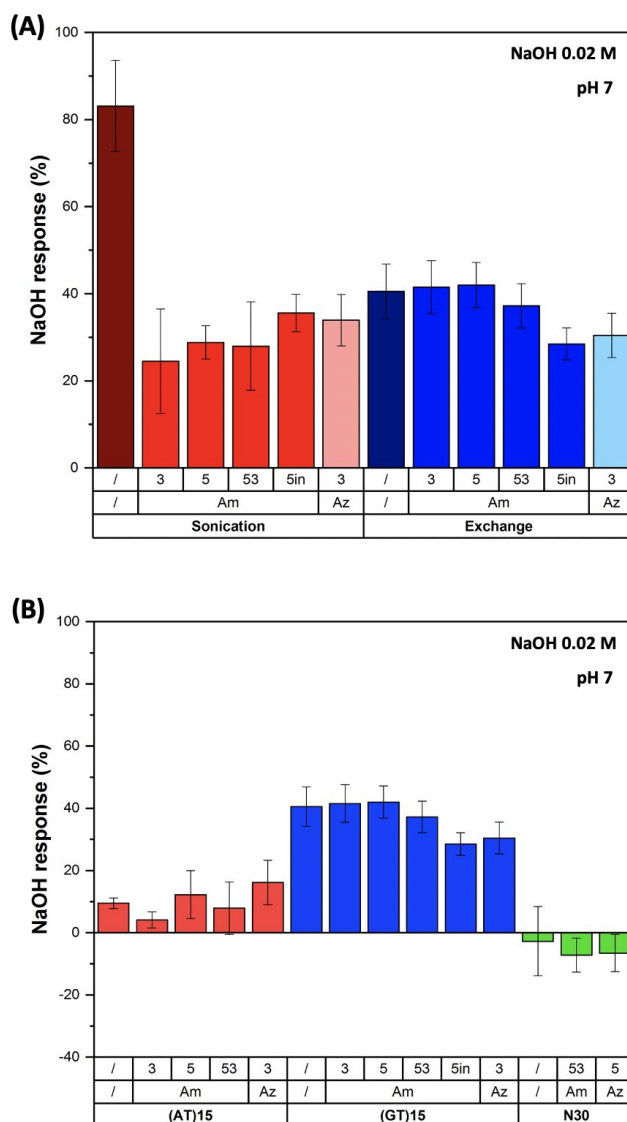


Figure B.29 – Intensity response following the addition of NaOH 0.02 M to increase the pH of the solution to pH 7. Comparison of the response for modified and unmodified **(A)** (GT)₁₅-SWCNTs prepared by direct sonication and MeOH assisted surfactant exchange and **(B)** DNA-SWCNTs prepared using MeOH assisted surfactant exchange. Intensity changes were calculated as $I_f - I_0 / I_0$ for the (6,5) chirality peak (final pH: 7, excitation: 575 nm, incubation period: 10 min). Error bars represent 1σ standard deviation (n = 3 technical replicates).

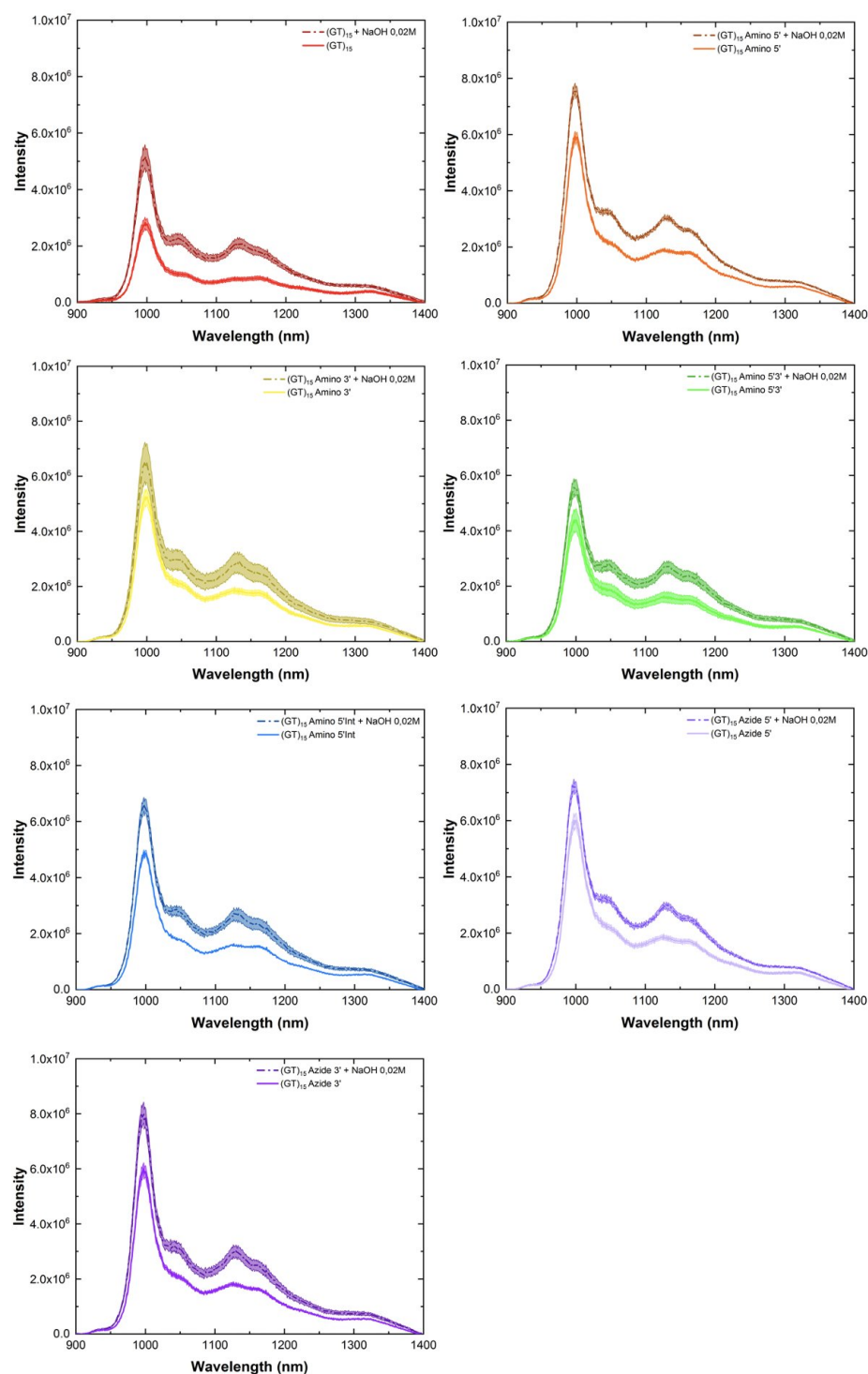


Figure B.30 – Fluorescence spectra of modified and unmodified (GT)₁₅-SWCNTs prepared by direct sonication before (solid light line) and after (dashed dark line) addition of NaOH 0.02 M (final pH: 7, excitation: 575 nm, incubation period: 10 min). For all spectra, the central line represents the average spectrum with the shaded regions representing 1 σ standard deviation (n = 3 technical replicates).

Appendix B. Modifying DNA-SWCNT Sensors for Improved Dopamine Detection

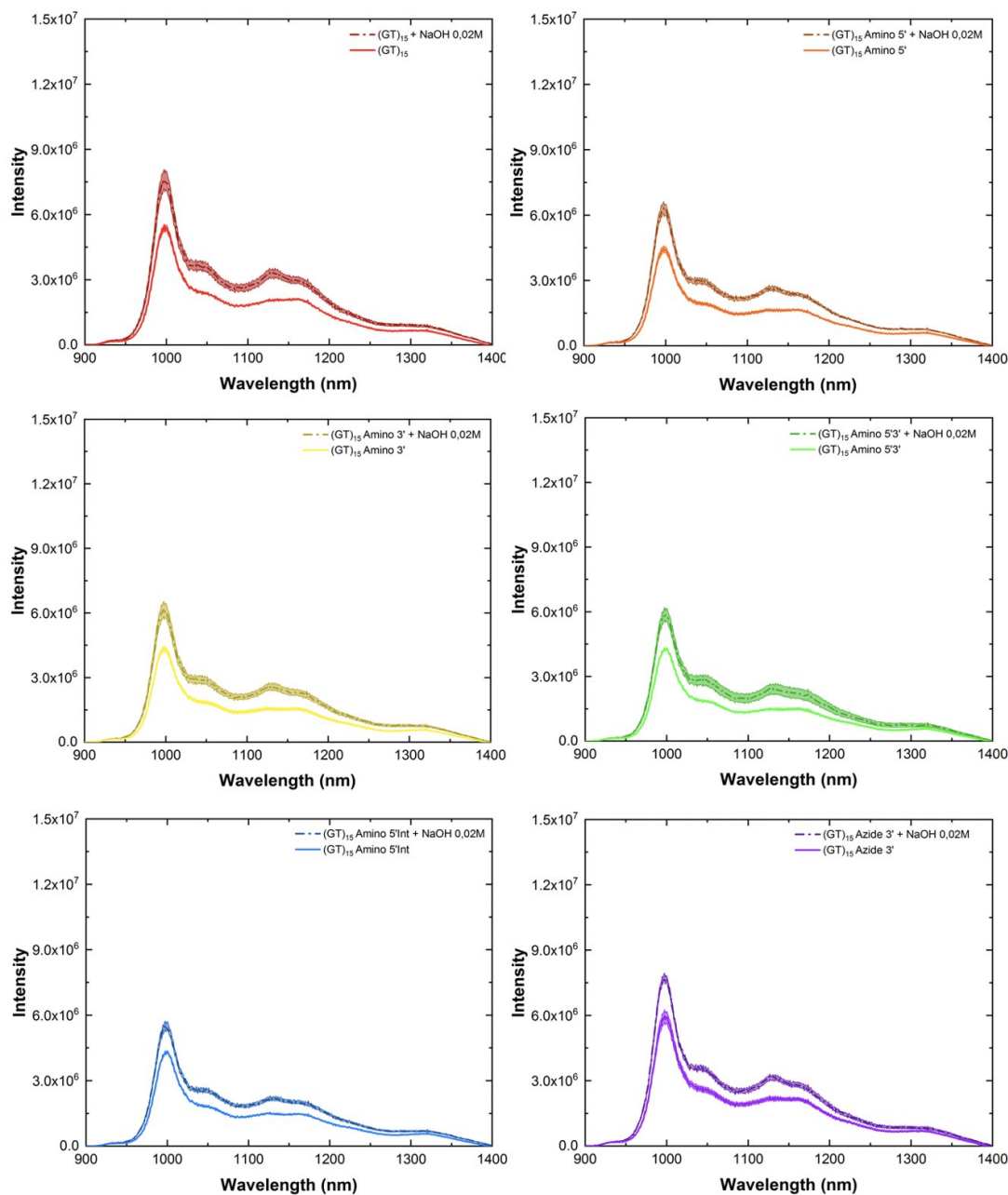


Figure B.31 – Fluorescence spectra of modified and unmodified (GT)₁₅-SWCNTs prepared using MeOH assisted surfactant exchange before (solid light line) and after (dashed dark line) addition of NaOH 0.02 M (final pH: 7, excitation: 575 nm, incubation period: 10 min). For all spectra, the central line represents the average spectrum with the shaded regions representing 1 σ standard deviation (n = 3 technical replicates).

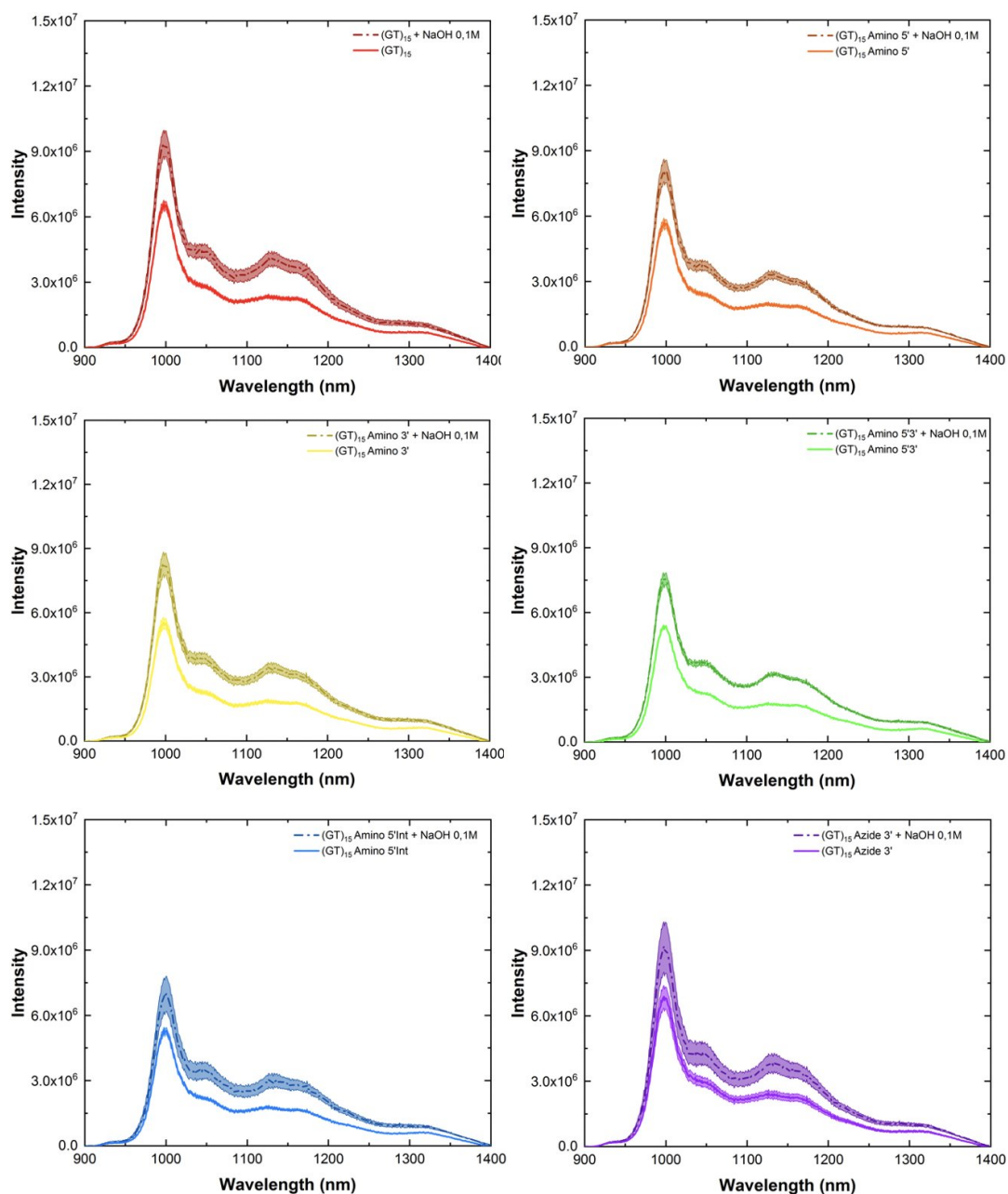


Figure B.32 – Fluorescence spectra of modified and unmodified (GT)₁₅-SWCNTs prepared using MeOH assisted surfactant exchange before (solid light line) and after (dashed dark line) addition of NaOH 0.1 M (final pH: 9, excitation: 575 nm, incubation period: 10 min). For all spectra, the central line represents the average spectrum with the shaded regions representing 1 σ standard deviation (n = 3 technical replicates).

Appendix B. Modifying DNA-SWCNT Sensors for Improved Dopamine Detection

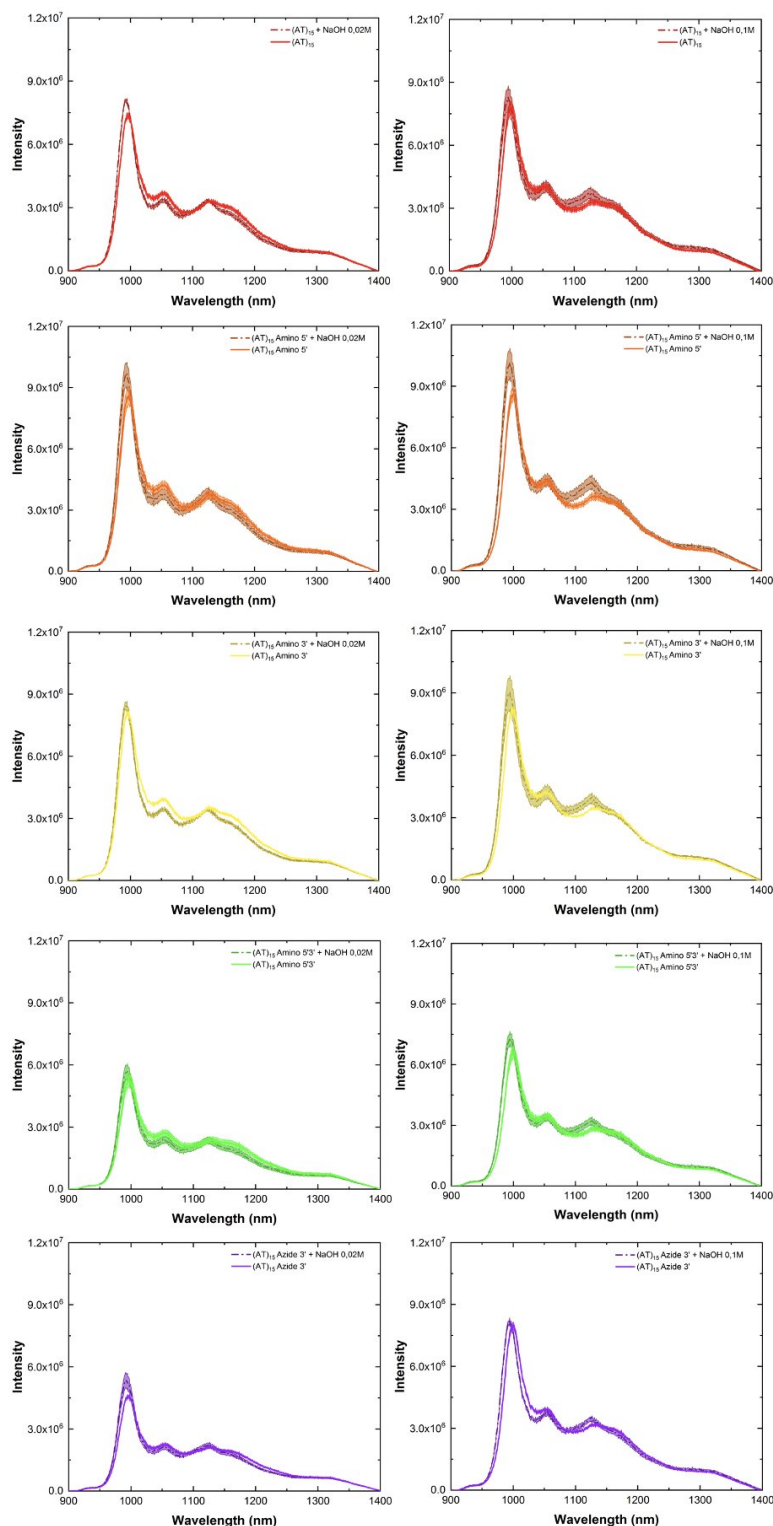


Figure B.33 – Fluorescence spectra of modified and unmodified (AT)₁₅-SWCNTs prepared using MeOH assisted surfactant exchange before (solid light line) and after (dashed dark line) addition of **(left)** NaOH 0.02 M (final pH: 7) and **(right)** NaOH 0.1 M (final pH: 9) (excitation: 575 nm, incubation period: 10 min). For all spectra, the central line represents the average spectrum with the shaded regions representing 1 σ standard deviation (n = 3 technical replicates).

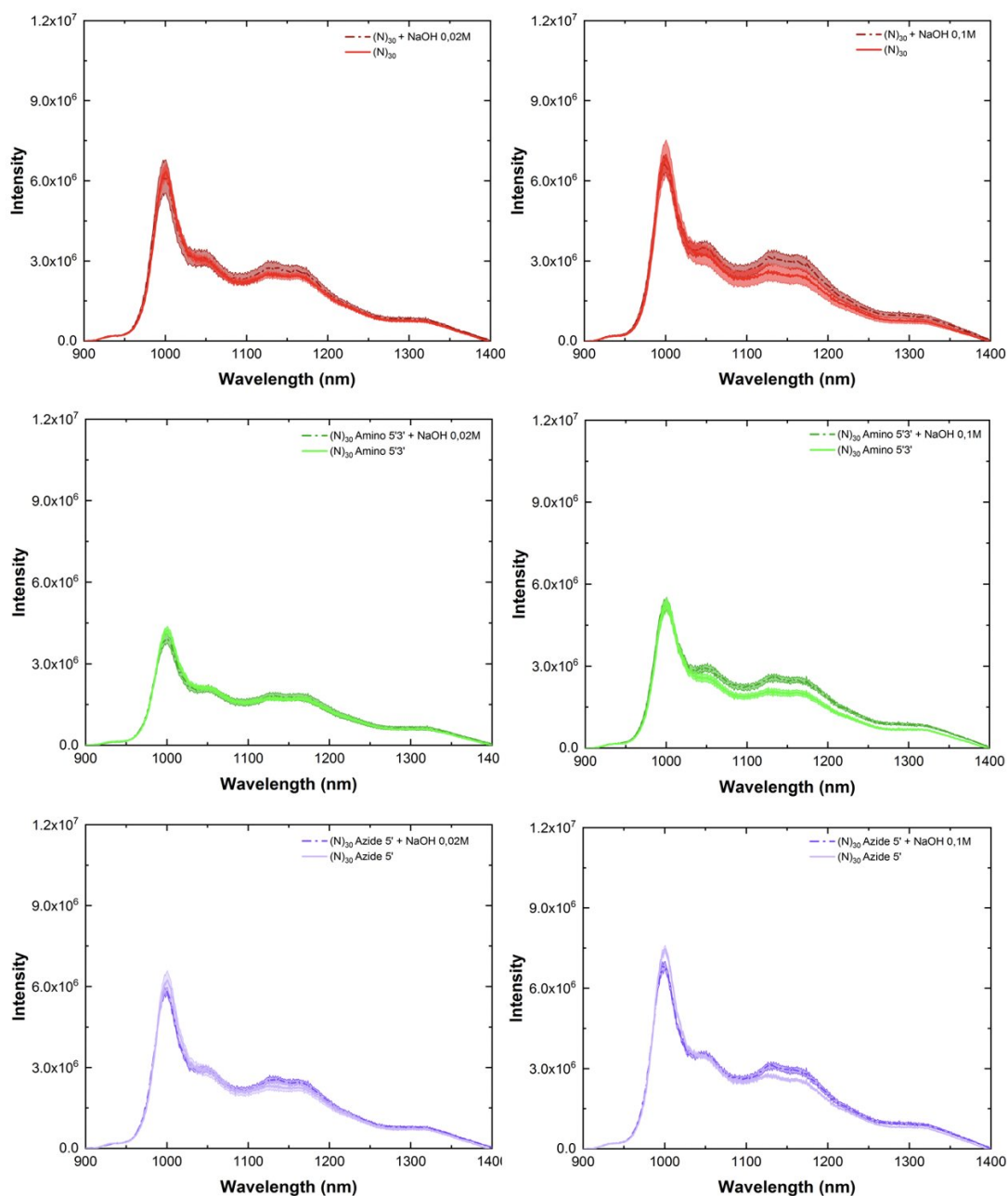


Figure B.34 – Fluorescence spectra of modified and unmodified (N)₃₀-SWCNTs prepared using MeOH assisted surfactant exchange before (solid light line) and after (dashed dark line) addition of **(left)** NaOH 0.02 M (final pH: 7) and **(right)** NaOH 0.1 M (final pH: 9) (excitation: 575 nm, incubation period: 10 min). For all spectra, the central line represents the average spectrum with the shaded regions representing 1 σ standard deviation (n = 3 technical replicates).

Appendix B. Modifying DNA-SWCNT Sensors for Improved Dopamine Detection

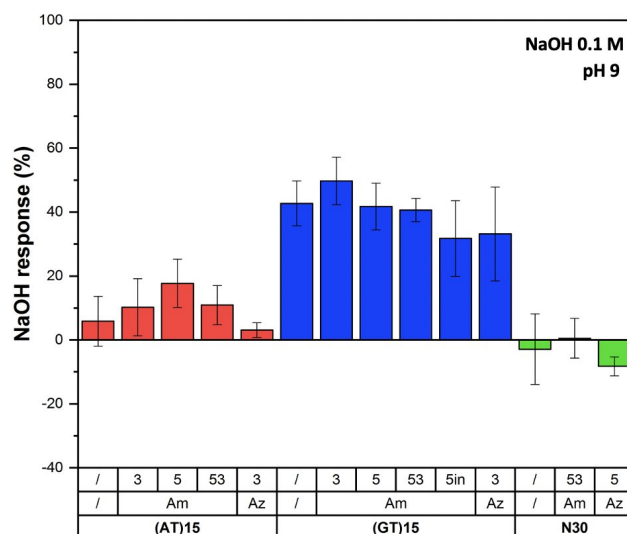


Figure B.35 – Intensity response following the addition of NaOH 0.1 M to increase the pH of the solution to pH 9. Comparison of the response for modified and unmodified DNA-SWCNTs prepared using MeOH assisted surfactant exchange. Intensity changes were calculated as $I_f - I_0 / I_0$ for the (6,5) chirality peak (final pH: 9, excitation: 575 nm, incubation period: 10 min). Error bars represent 1σ standard deviation ($n = 3$ technical replicates).

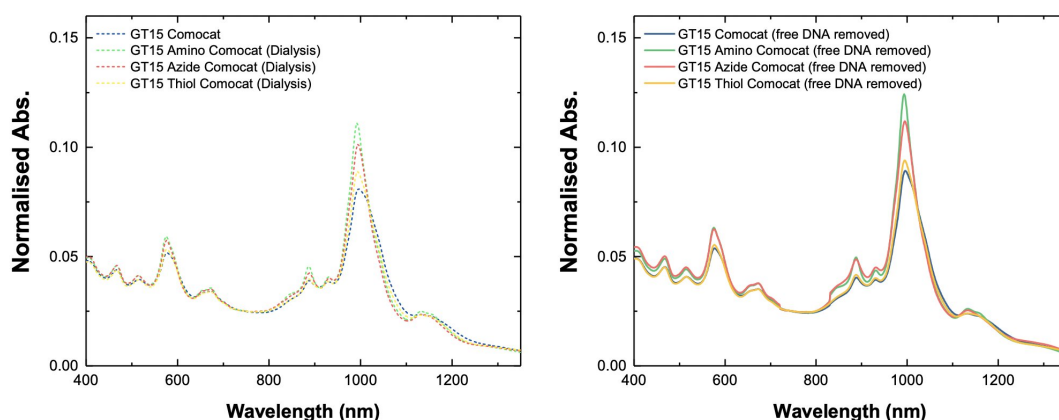


Figure B.36 – Difference between absorbance in the presence of free DNA and in the absence of free (unbound) DNA. Removing free DNA increased the relative absorbance for each sequence and decreased the FWHM of the peaks indicating improved suspension quality.

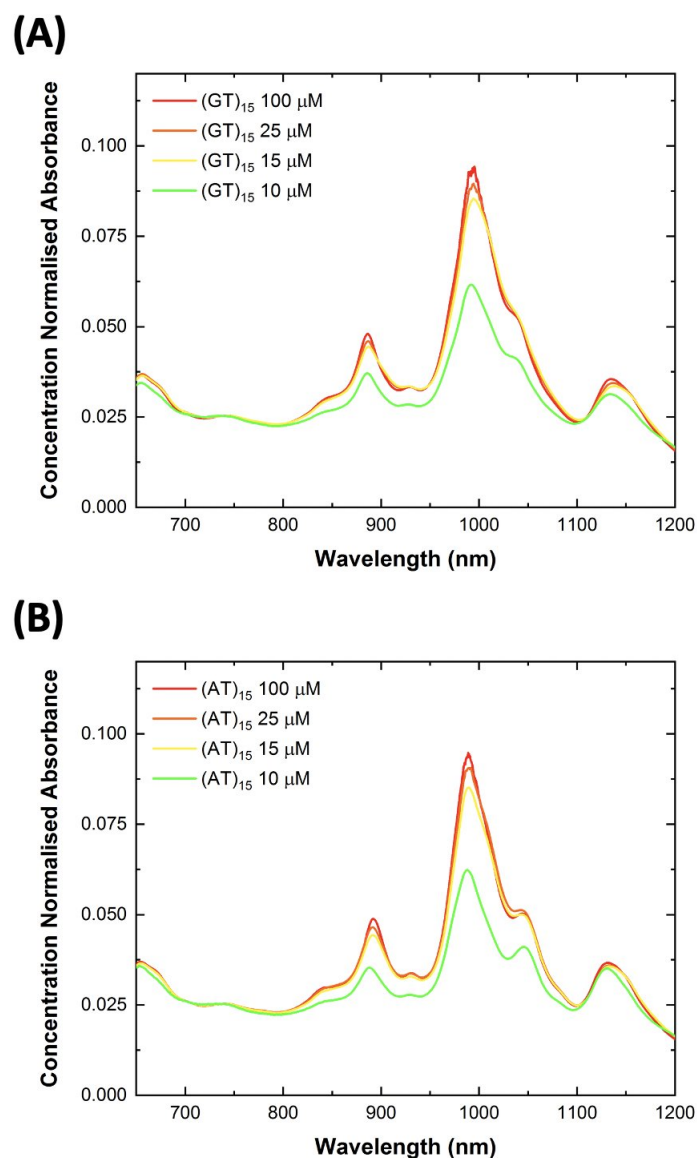


Figure B.37 – Effect of starting DNA concentration on the dispersion quality for MeOH-assisted surfactant exchanged SWCNT suspensions. The surfactant exchange protocol was carried out on the same batch of SC-SWCNTs using four different concentrations of both (GT)₁₅ and (AT)₁₅ to give final DNA concentrations of 100 μ M, 25 μ M, 15 μ M, and 10 μ M. Although a significant decrease in the dispersion yield and quality was observed for both suspensions prepared using 10 μ M final DNA concentration, no significant increases were observed as the concentration was increased above 15 μ M final concentration. For this reason 15 μ M was selected as the final concentration of DNA used in the MeOH surfactant exchange protocol for this study as it enabled good dispersion of the SWCNTs while reducing any waste of DNA by minimising the excess that remains unbound in the solution. Concentrations below 10 μ M were also tested (7.5 μ M and 5 μ M) however no stable DNA-SWCNT solutions were obtained.

Appendix B. Modifying DNA-SWCNT Sensors for Improved Dopamine Detection

Table B.3 – Estimated relative increase in penetration depths for modified (GT)₁₅-SWCNTs compared to unmodified (GT)₁₅-SWCNTs. All samples were prepared via direct sonication. Calculations were based on the findings of Lee *et al.* [249] using the equations presented by Lambert *et al.* [78] and an extinction coefficient, γ_{em} , of 10 cm⁻¹. The increase in penetration depths are shown for the (6,5) (excitation: 575 nm), (7,5) (excitation: 660 nm) and the integrated fluorescence intensity under the 575 nm excitation.

(6,5)		
DNA Sequence	α	Δ penetration depth
Am3'-(GT) ₁₅ -SWCNT	1.55	191.5 μ m
Am5'-(GT) ₁₅ -SWCNT	1.80	254.4 μ m
Am5'3'-(GT) ₁₅ -SWCNT	1.29	109.6 μ m
Am5'Int-(GT) ₁₅ -SWCNT	1.59	200.6 μ m
Am5'3'Int-(GT) ₁₅ -SWCNT	3.07	487.4 μ m
Azide3'-(GT) ₁₅ -SWCNT	1.68	225.1 μ m
Azide5'-(GT) ₁₅ -SWCNT	1.87	270.7 μ m

(7,5)		
DNA Sequence	α	Δ penetration depth
Am3'-(GT) ₁₅ -SWCNT	2.37	373.9 μ m
Am5'-(GT) ₁₅ -SWCNT	2.32	365.7 μ m
Am5'3'-(GT) ₁₅ -SWCNT	1.91	280.2 μ m
Am5'Int-(GT) ₁₅ -SWCNT	1.89	276.6 μ m
Am5'3'Int-(GT) ₁₅ -SWCNT	3.53	547.8 μ m
Azide3'-(GT) ₁₅ -SWCNT	1.77	248.8 μ m
Azide5'-(GT) ₁₅ -SWCNT	2.28	357.1 μ m

Integrated Intensity (ex. 575nm)		
DNA Sequence	α	Δ penetration depth
Am3'-(GT) ₁₅ -SWCNT	1.71	232.2 μ m
Am5'-(GT) ₁₅ -SWCNT	1.87	272.2 μ m
Am5'3'-(GT) ₁₅ -SWCNT	1.44	158.6 μ m
Am5'Int-(GT) ₁₅ -SWCNT	1.62	209.5 μ m
Am5'3'Int-(GT) ₁₅ -SWCNT	2.72	434.1 μ m
Azide3'-(GT) ₁₅ -SWCNT	1.64	213.8 μ m
Azide5'-(GT) ₁₅ -SWCNT	1.88	274.8 μ m

C Xeno Nucleic Acid Nanosensors for Enhanced Stability Against Ion- Induced Perturbations

Table C.1 – List of oligonucleotide sequences used in this study. T* indicates a ribose moiety of the tyrosine nucleotide that has been ‘locked’ through the addition of a methyl bridge connecting the 2’ oxygen and 4’ carbon

Name	Sequence (5’ to 3’)
DNA ₁₅₅	ACC CCT ATC ACG ATT AGC ATT AA ACC CCT ATC ACG ATT AGC ATT AA
DNA _{(GT)₁₅}	GTG TGT GTG TGT GTG TGT GTG TGT GTG TGT
DNA _{(GT)₂₃}	GTG TGT GTG TGT GTG TGT GTG TGT GTG TGT GTG TGT GTG TGT GTG T
LNA ₁₅₅	ACC CCT* AT*C ACG AT*T* AGC AT*T* AA ACC CCT* AT*C ACG AT*T* AGC AT*T* AA

Appendix C. Xeno Nucleic Acid Nanosensors for Enhanced Stability Against Ion-Induced Perturbations

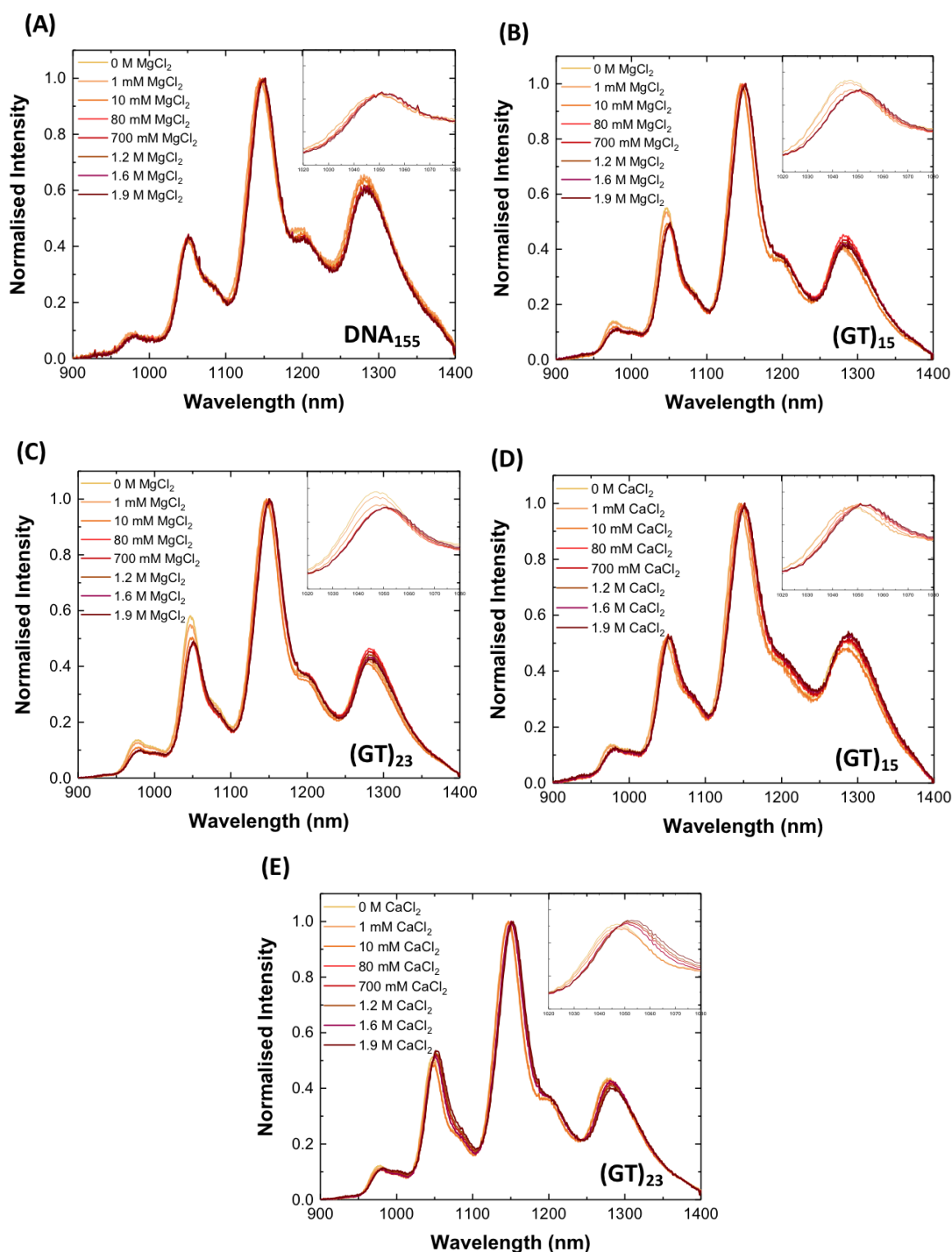


Figure C.1 – Effect of MgCl_2 (A-C) and CaCl_2 (D-E) on DNA-SWCNT fluorescence. normalized fluorescence response of (A) DNA_{155} , (B,D) $(\text{GT})_{15}$, and (C,E) $(\text{GT})_{23}$ -suspended SWCNT. (Inset: response of the (7,5) chirality peak). Fluorescence intensity is normalized to the maximum intensity value, corresponding to the maximum of the (7,6) peak.

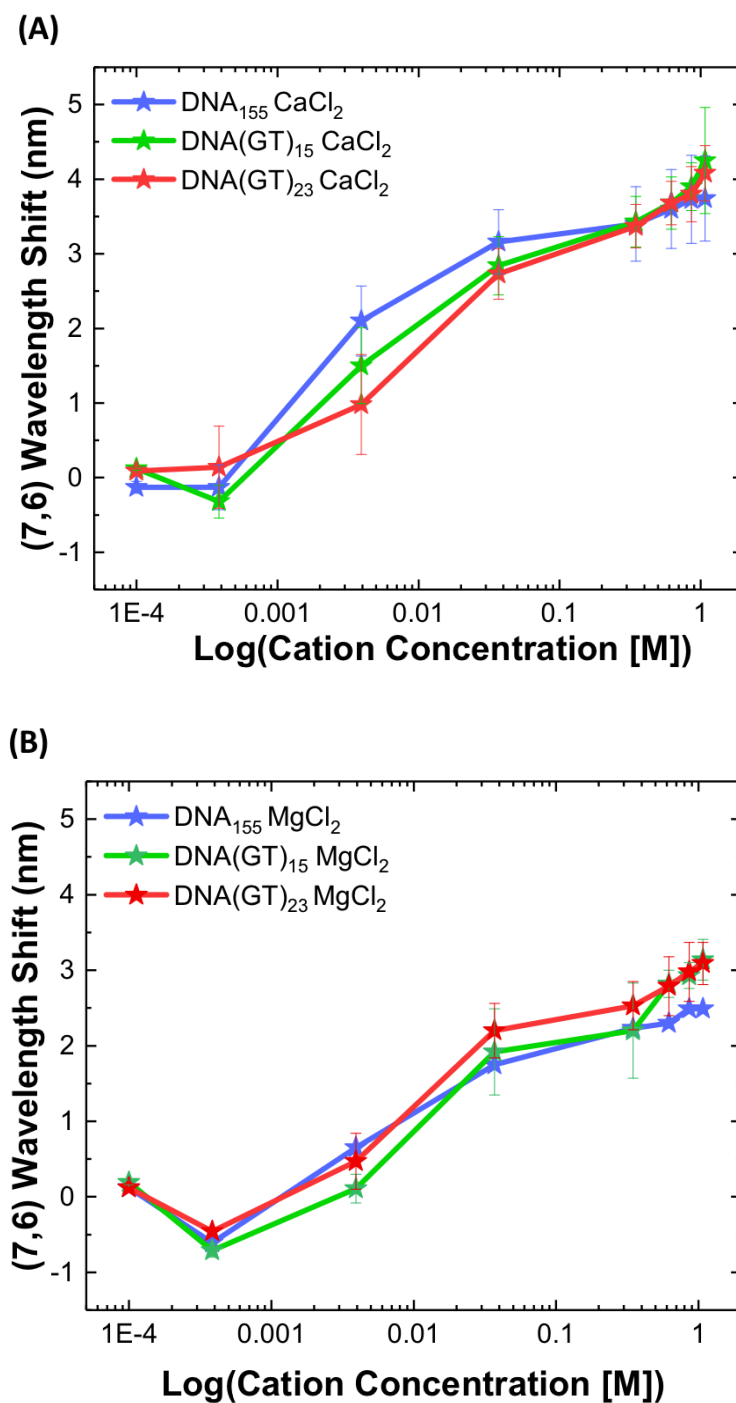


Figure C.2 – A comparison of the (7,6) peak response following the addition of (A) CaCl₂ and (B) MgCl₂ for DNA₁₅₅-SWCNT, (GT)₁₅-SWCNT, and (GT)₂₃-SWCNT. All error bars represent 1 σ standard deviation (n = 3 technical replicates).

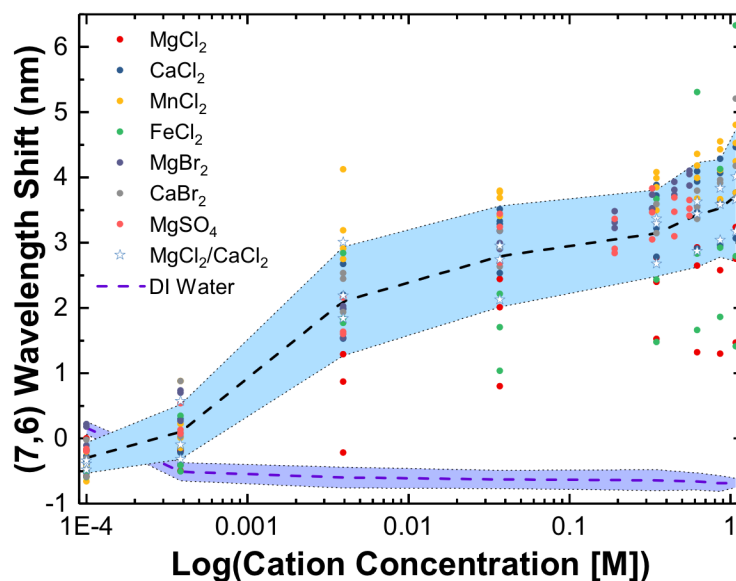


Figure C.3 – Fluorescence response of DNA₁₅₅-SWCNTs on addition of various metal cations. Change in the wavelength position of the (7,6) chirality emission peaks with respect to increasing cationic concentration. Dashed line represents the average wavelength shift for the maximum emission on addition of M²⁺ ions, with the shaded regions representing 1σ standard deviation (n = 3 technical replicates).

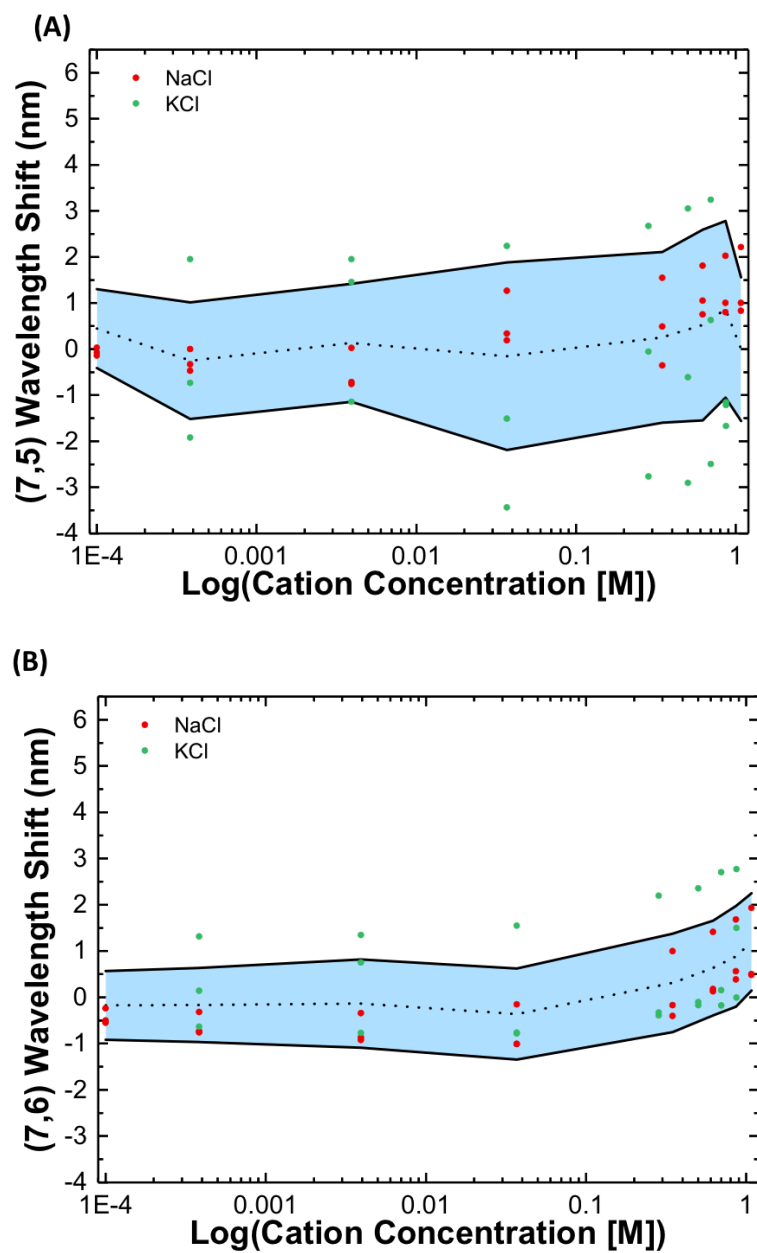


Figure C.4 – Fluorescence response of DNA₁₅₅-SWCNTs on addition of NaCl and KCl. Change in the wavelength position of the (A) (7,5) and (B) (7,6) chirality emission peaks with respect to increasing cationic concentration. Dashed line represents the average wavelength shift for the maximum emission on addition of both M⁺ ions, with the shaded regions representing 1 σ standard deviation (n = 3 technical replicates).

Appendix C. Xeno Nucleic Acid Nanosensors for Enhanced Stability Against Ion-Induced Perturbations

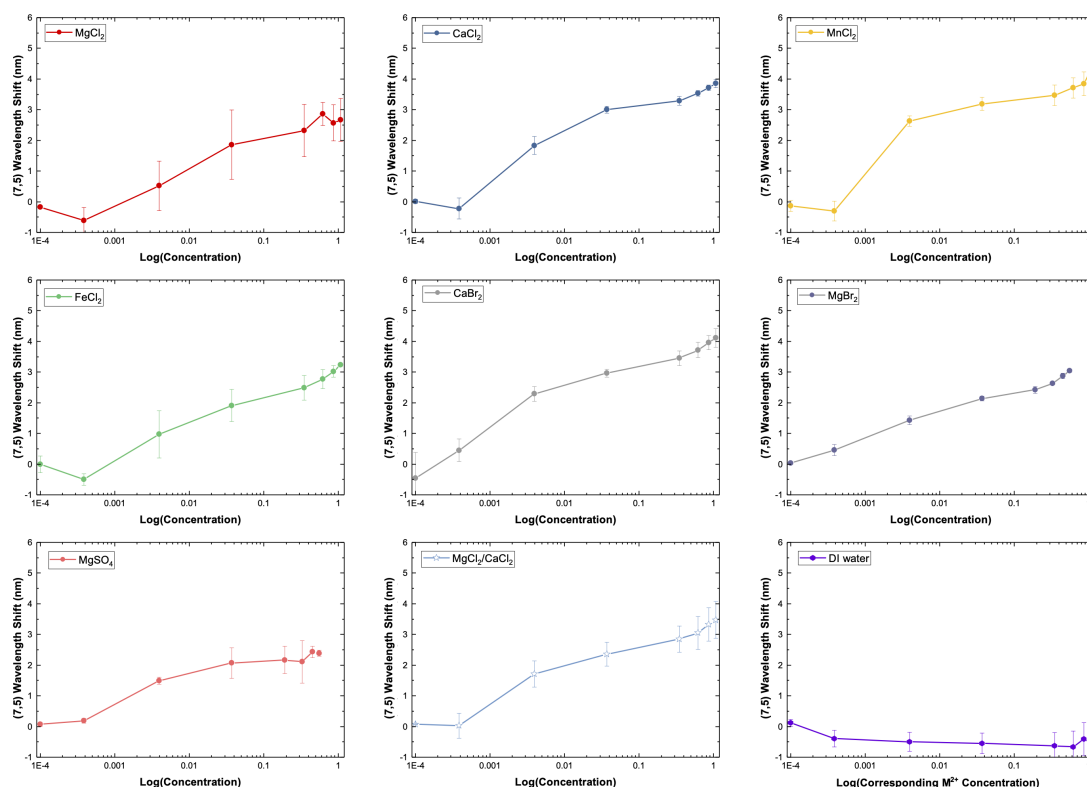


Figure C.5 – Fluorescence response of DNA₁₅₅-SWCNTs on addition of various divalent metal cation containing solutions. Change in the wavelength position of the (7,5) chirality emission peaks with respect to increasing cationic concentration. Error bars represent 1σ standard deviation over a minimum of three measurements. DI water data shown represents control measurements performed under the same conditions as a reference for each ion concentration addition.

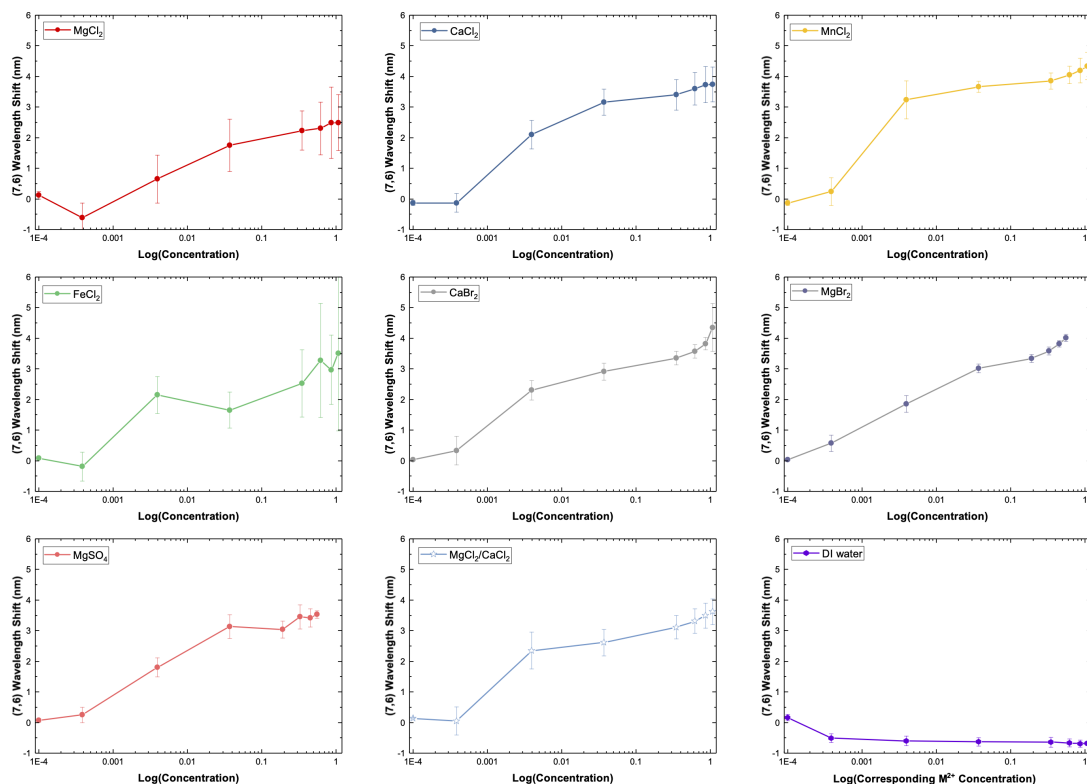


Figure C.6 – Fluorescence response of DNA₁₅₅-SWCNTs on addition of various divalent metal cation containing solutions. Change in the wavelength position of the (7,6) chirality emission peaks with respect to increasing cationic concentration. Error bars represent 1 σ standard deviation over a minimum of three measurements. DI water data shown represents control measurements performed under the same conditions as a reference for each ion concentration addition.

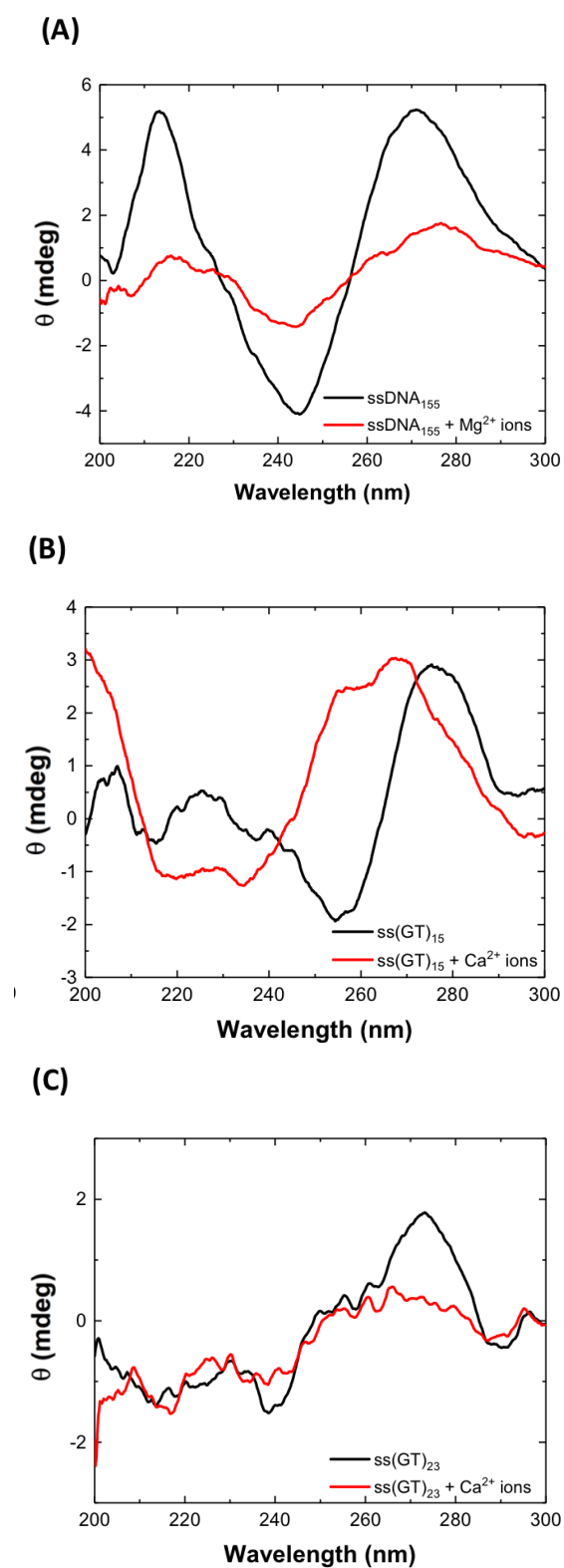


Figure C.7 – Circular dichroism measurements for (A) DNA₁₅₅, (B) (GT)₁₅ and (C) (GT)₂₃ before (**black**) and after (**red**) the addition of either 0.5 M CaCl₂ or 0.5 M MgCl₂

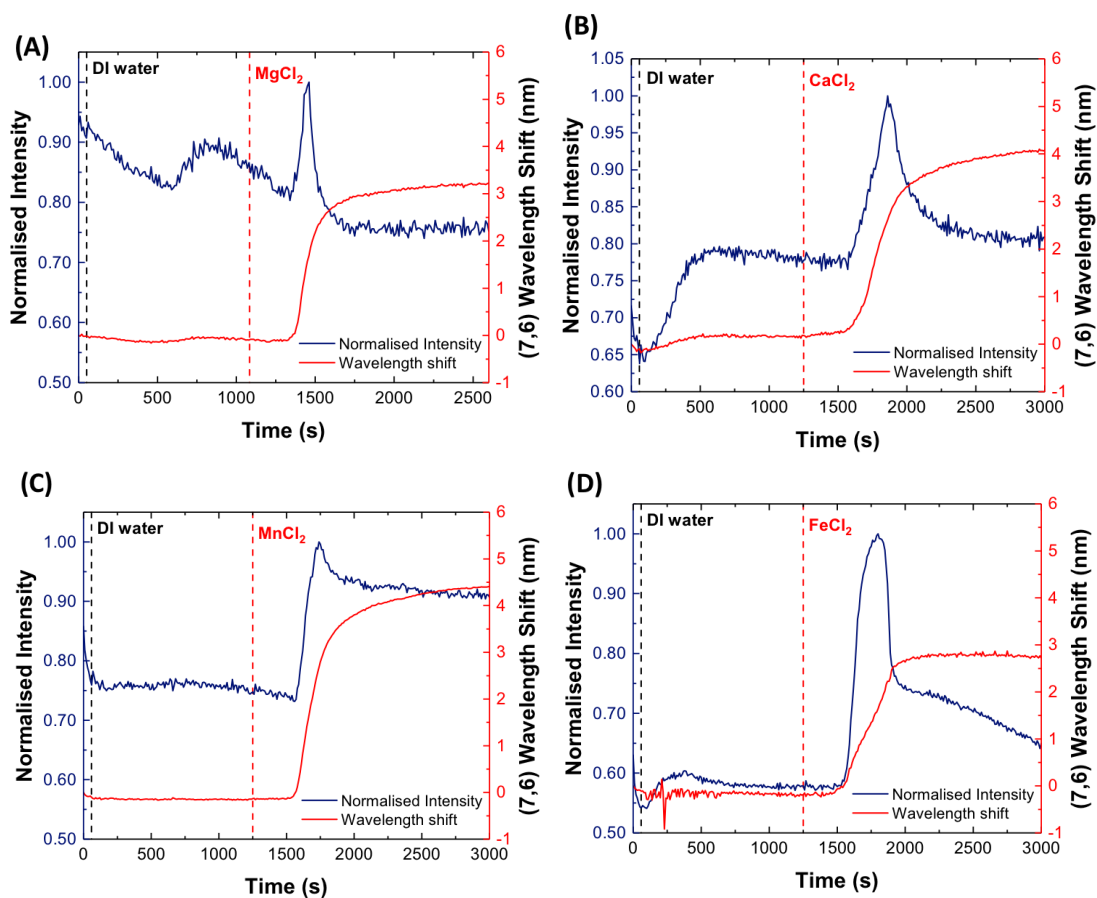


Figure C.8 – Kinetic responses of the intensity and wavelength position of the (7,6) peak of DNA₁₅₅-SWCNTs on addition of (A) MgCl₂, (B) CaCl₂, (C) MnCl₂, and (D) FeCl₂. The **red** lines indicate the change in wavelength position of the (7,6) peak with respect to time and the **navy** line indicates the change in the fluorescence intensity of the sensor. The fluorescence intensity is normalized against the initial intensity I_0 at time = 0.

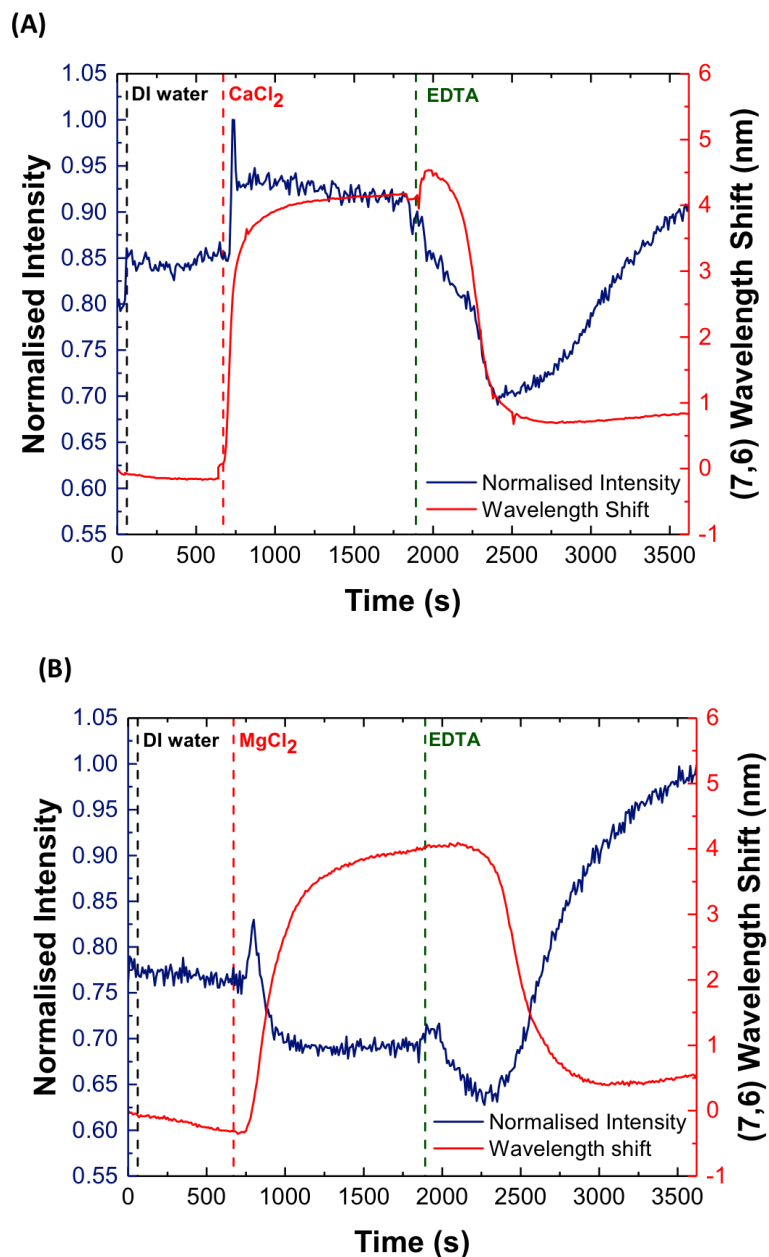


Figure C.9 – Reversibility of the fluorescence response of the (7,6) chirality peak for DNA-SWCNTs. Fluorescence response of **(A)** DNA₁₅₅- and **(B)** (GT)₁₅-wrapped SWCNTs on addition of M²⁺ ions. Reversibility of the sensor demonstrated on addition of EDTA. The **red** lines indicate the change in wavelength position of the (7,6) peak with respect to time and the **navy** line indicates the change in the fluorescence intensity of the sensor. The fluorescence intensity is normalized against the initial intensity I_0 at time = 0.

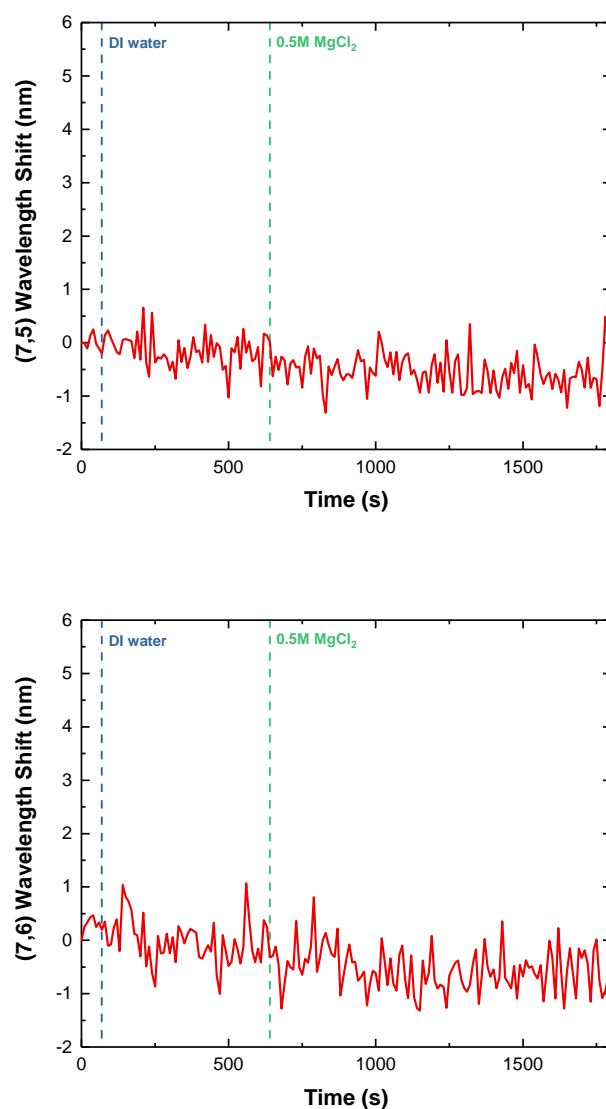


Figure C.10 – Fluorescence response of PVA (10%)-suspended SWCNTs following the addition of M^{2+} ions. No effective change in the wavelength position of the (A) (7,5) nor (B) (7,6) chirality peaks on addition of 0.5 M $MgCl_2$. Due to the fact that it was not possible to concentrate PVA-suspended SWCNTs using silica beads, as was done with DNA-SWCNTs, lower signal-to-noise ratios were obtained from the peaks, leading to increased number of apparent fluctuations in wavelength position with time.

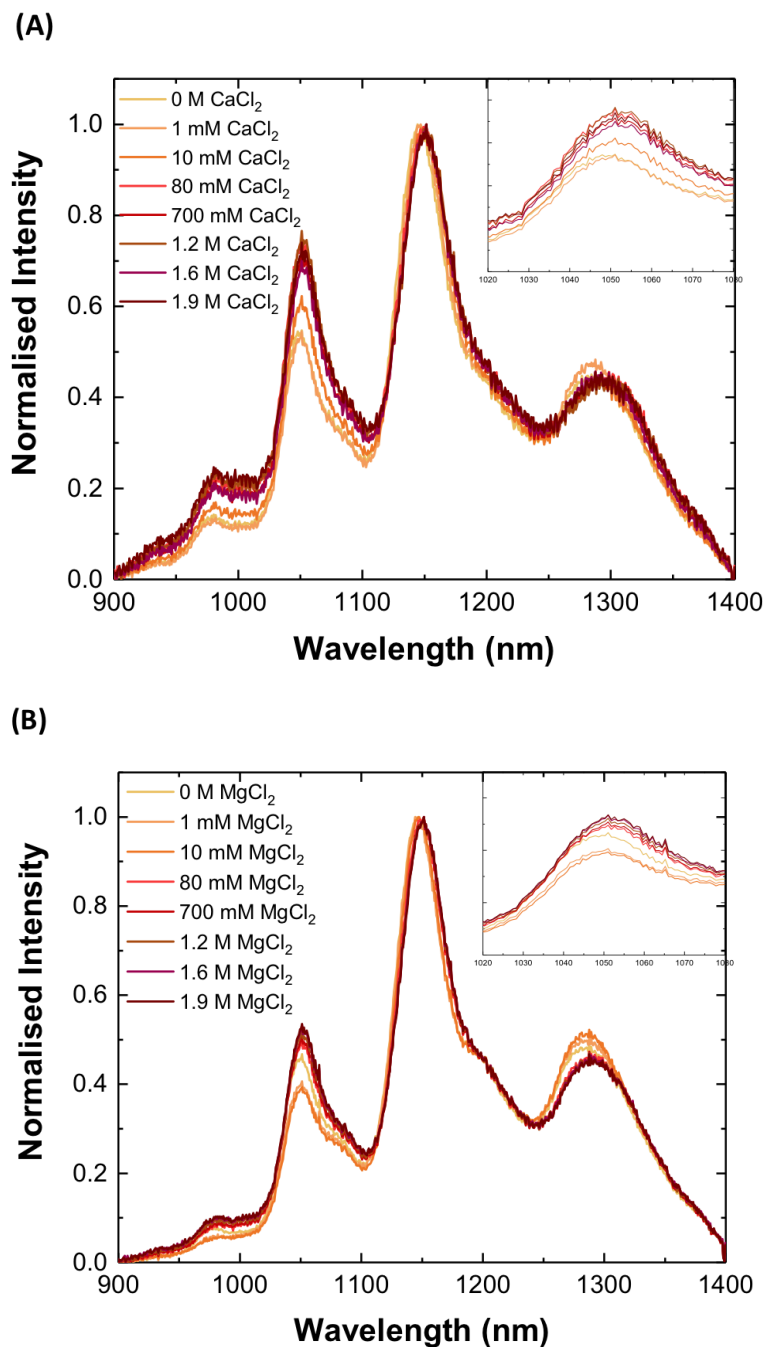
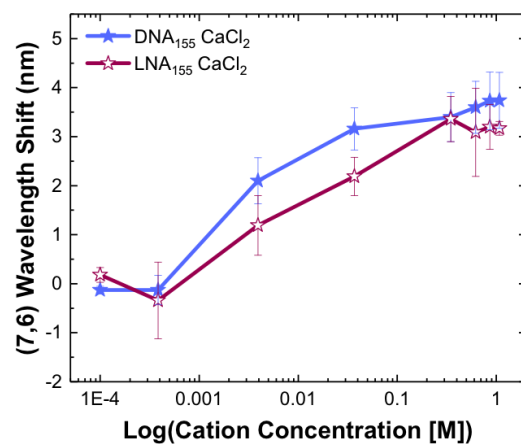
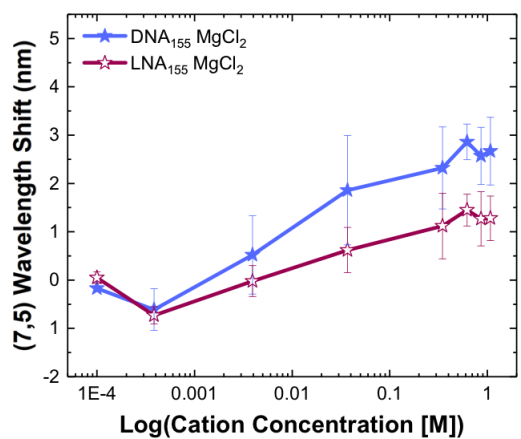


Figure C.11 – Fluorescence response of the LNA-SWCNTs on addition of (A) CaCl_2 and (B) MgCl_2 , with a focus on the (7,5) chirality peak (inset).

(A)



(B)



(C)

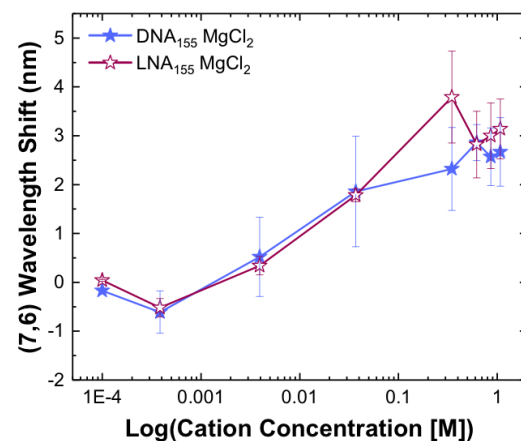


Figure C.12 – A comparison of the fluorescence wavelength response following the addition of (A) CaCl₂ to the (7,6) chirality and (B-C) MgCl₂ to (7,5) and (7,6) chirality peaks for DNA₁₅₅-SWCNTs and LNA₁₅₅-SWCNTs. All error bars represent 1 σ standard deviation (n = 3 technical replicates).

Appendix C. Xeno Nucleic Acid Nanosensors for Enhanced Stability Against Ion-Induced Perturbations

Table C.2 – Slopes of the transition curves for the wavelength shifts observed for (GT)₁₅-SWCNTs following the addition of MgCl₂ as a function of gel percentage.

Chirality Peak	Gel Type	Slope (nm/s)	Chirality Peak	Gel Type	Slope (nm/s)
(7,6)	Agarose 0.5%	1.8	(7,5)	Agarose 0.5%	2.7
	Agarose 1.0%	2.1		Agarose 1.0%	3.1
	Agarose 2.0%	2.3		Agarose 2.0%	3.4
	Agarose 3.0%	4.1		Agarose 3.0%	5.3

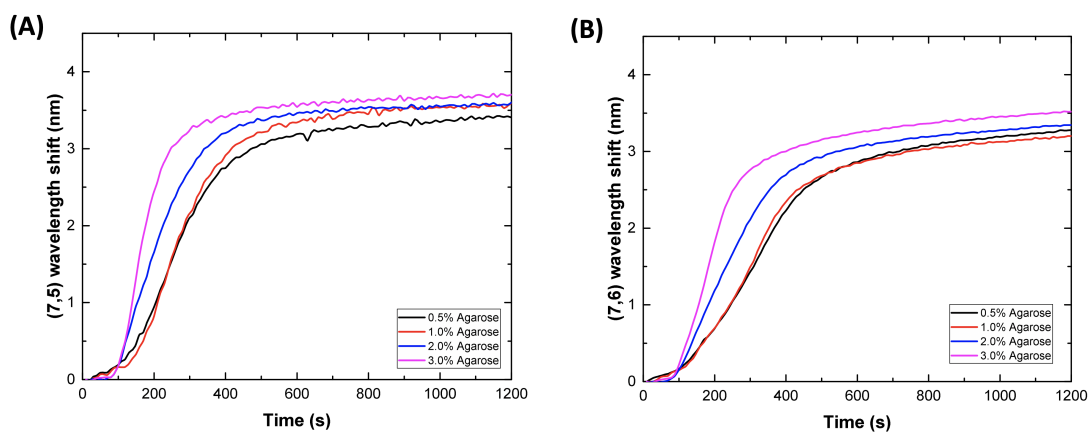


Figure C.13 – Effect of gel percentage on the response kinetics of DNA-SWCNTs encapsulated in agarose gel following the addition of MgCl₂. A comparison of the response curves show the wavelength shift of the peak position of the (A) (7,5) and (B) (7,6) chirality peaks for (GT)₁₅-SWCNTs following the addition of MgCl₂.

D XNA-Nanosensors for Improved Neurochemical Sensing

The sequences used in this study are detailed in the table below where an asterisk indicates a locked base.

Table D.1 – List of DNA and LNA sequences.

Name	Sequence
(GT) ₁₅	GTG TGT GTG TGT GTG TGT GTG TGT GTG TGT
LNA _{every6T}	GT*G TGT GT*G TGT GT*G TGT GT*G TGT GT*G TGT
LNA _{every6G}	G*TG TGT G*TG TGT G*TG TGT G*TG TGT G*TG TGT
LNA _{every5}	GTG TG*T GTG T*GT GTG* TGT GT*G TGT G*TG TGT*
LNA _{20mid}	GTG TGT GTG TGT G*T*G* T*G*T* GTG TGT GTG TGT
LNA _{20end}	G*T*G* TGT GTG TGT GTG TGT GTG TGT GTG T*G*T*
LNA _{every3}	GTG* TGT* GTG* TGT* GTG* TGT* GTG* TGT* GTG* TGT*
LNA _{33mid}	GTG TGT GTG TG*T* G*T*G* T*G*T* G*T*G TGT GTG TGT

Appendix D. XNA-Nanosensors for Improved Neurochemical Sensing

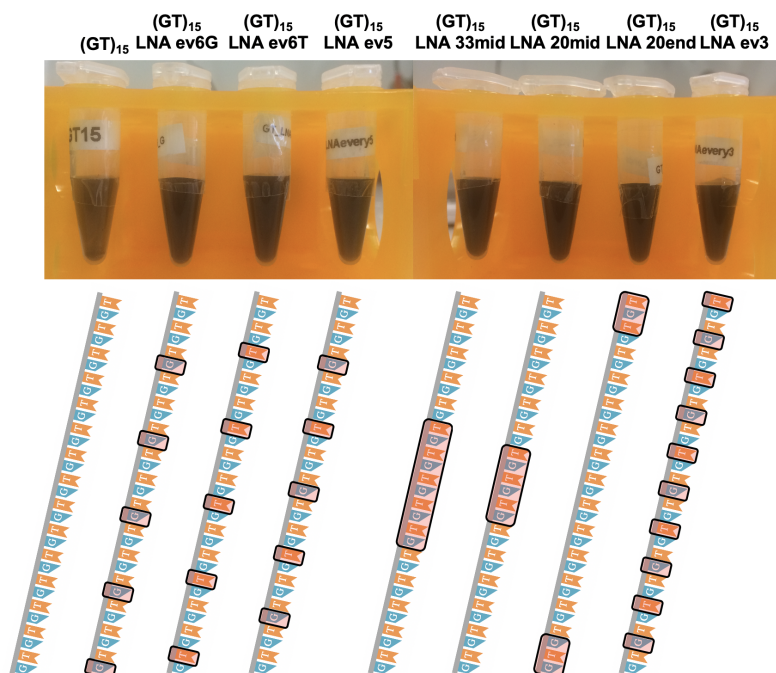


Figure D.1 – Max concentration solutions of DNA- and LNA-SWCNT suspension post sonication, dialysis, and centrifugation.

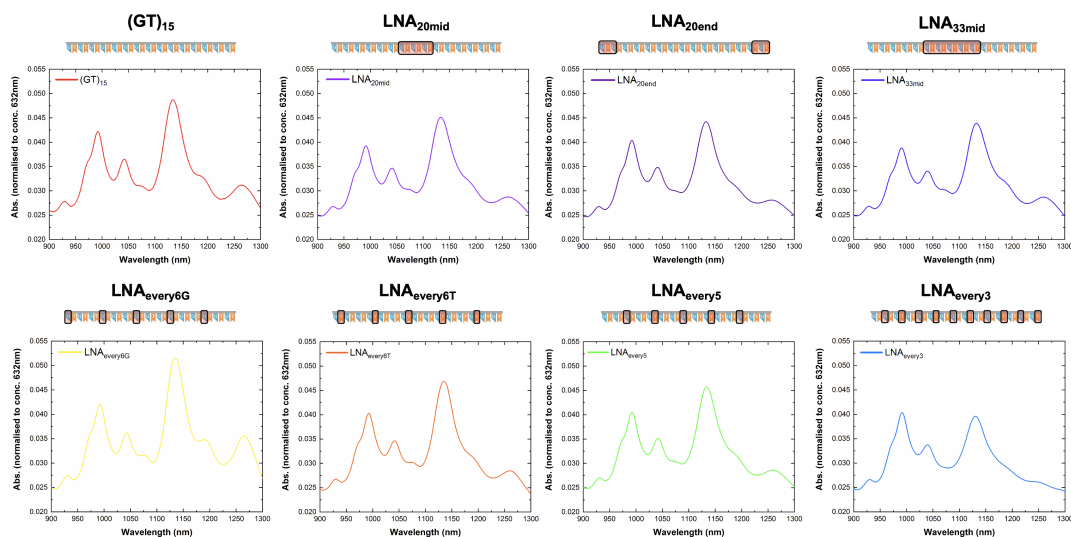


Figure D.2 – Absorbance spectra for all DNA- and LNA-SWCNT samples examined in this study. All spectra are normalized to concentration as determined using an extinction coefficient of 0.036 mg/L at Abs_{632nm}.

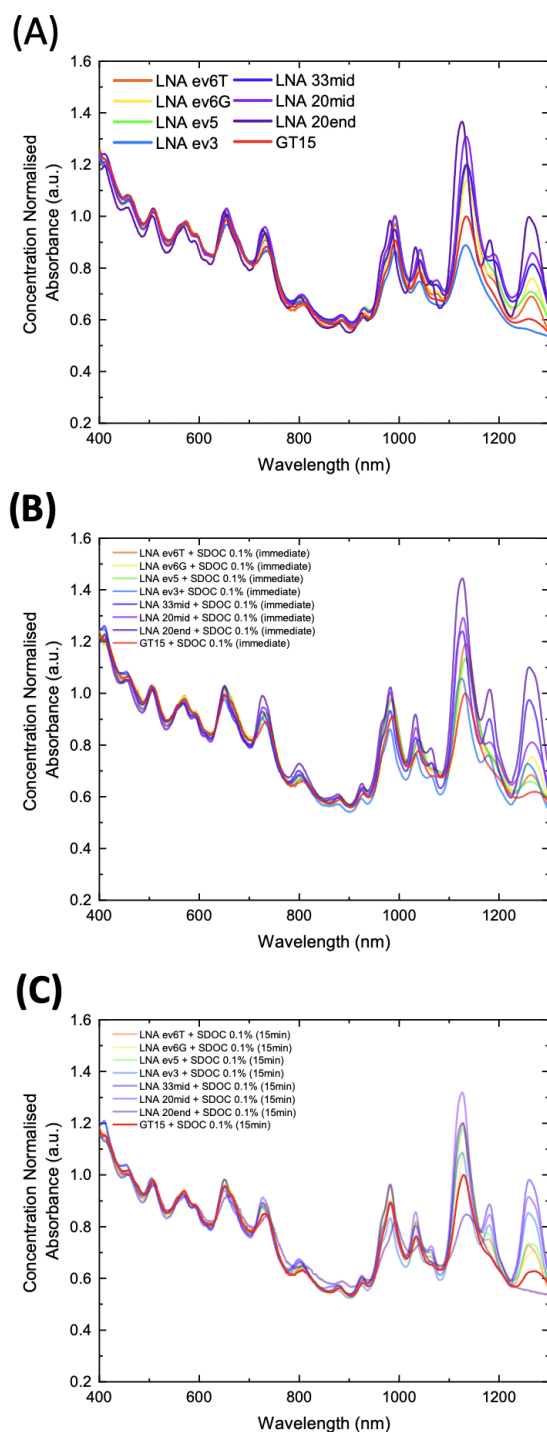


Figure D.3 – Absorbance spectra of all sequences used in this study (A) before, (B) immediately following the addition of SDOC (0.1% final concentration), and (C) following 15 min incubation post-addition. All spectra are normalized to concentration as determined using an extinction coefficient of 0.036 mg/L at Abs_{632nm} and subsequently normalized to the (GT)₁₅ spectrum for comparison.

Appendix D. XNA-Nanosensors for Improved Neurochemical Sensing

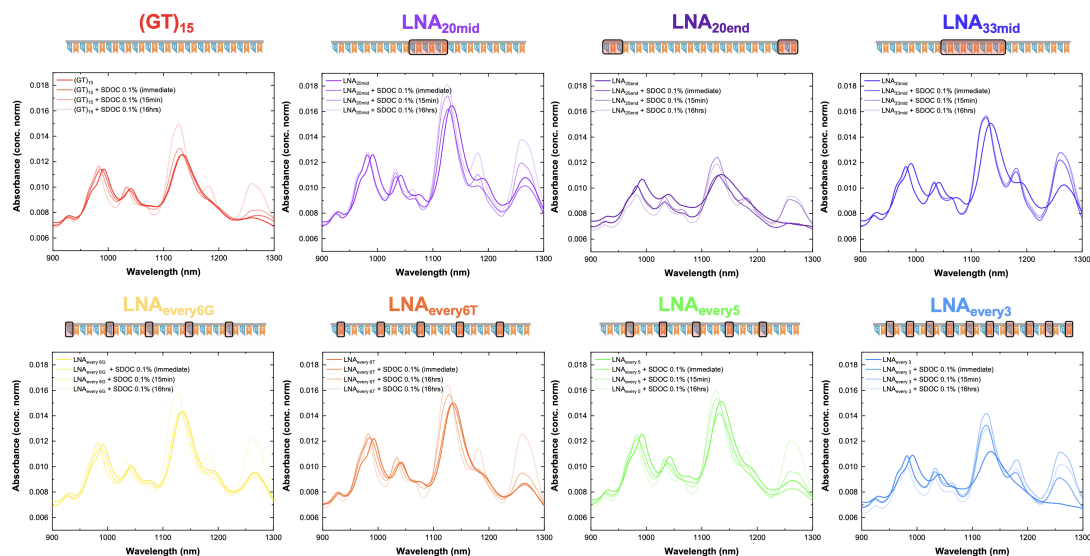


Figure D.4 – Absorbance spectra for all DNA- and LNA-SWCNT samples following addition of SDOC (0.1% final concentration) at various timepoints: immediately after addition, following 15 min of incubation, and following 16 h of incubation. All spectra are normalized to concentration as determined using an extinction coefficient of 0.036 mg/L at Abs_{632nm}.

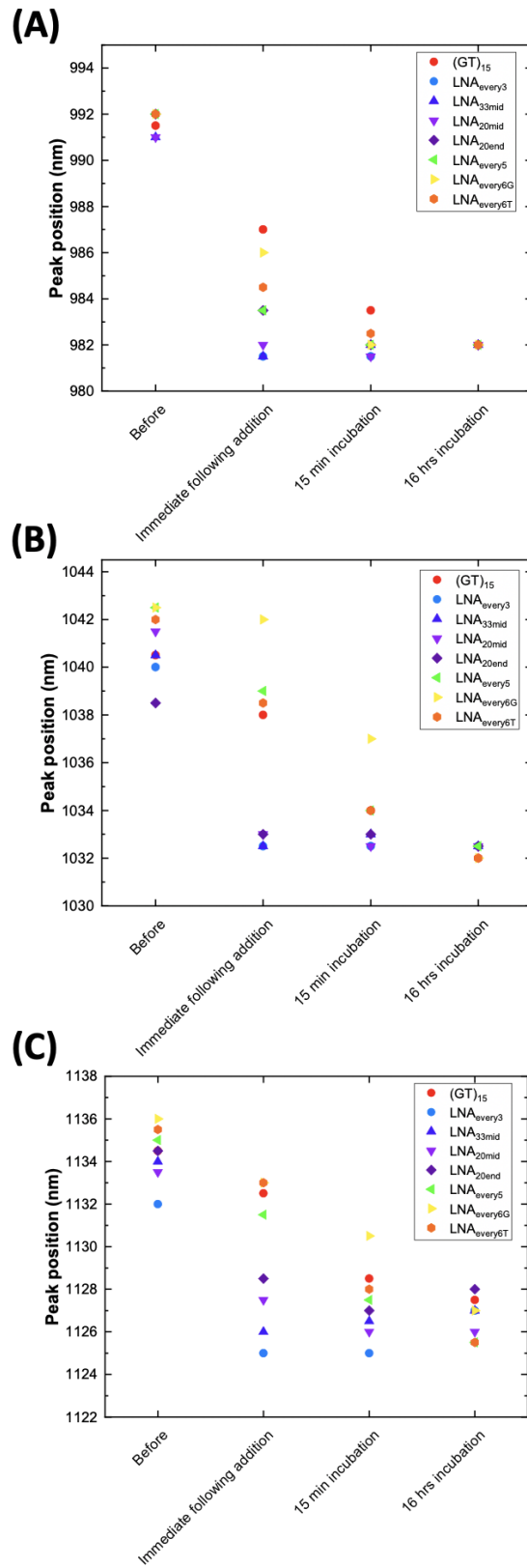


Figure D.5 – Wavelength position of the absorbance peaks at (A) ~ 990 nm, (B) ~ 1040 nm, and (C) ~ 1135 nm before SDOC addition and at three time points following SDOC addition (0.1% final SDOC concentration).

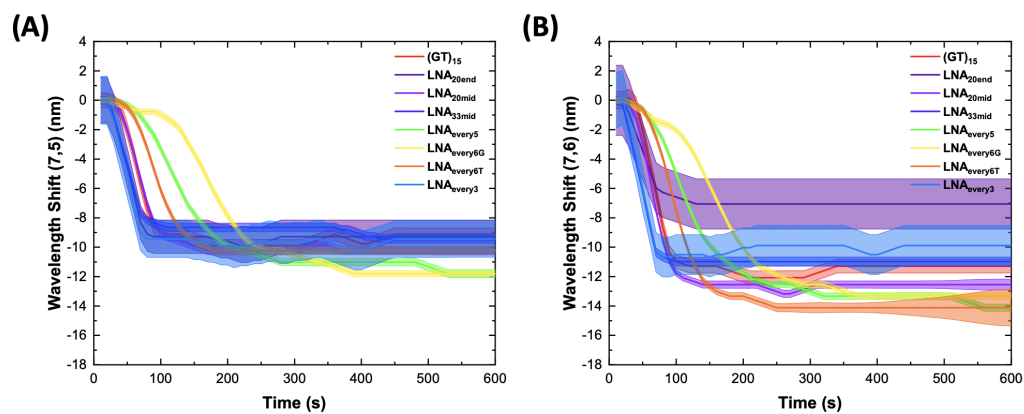


Figure D.6 – Wavelength shift of the fluorescence emission wavelength position of the (A) (7,5) and (B) (7,6) chirality peaks of all sequences parameters as a function of time following SDOC addition (0.1% final SDOC concentration).

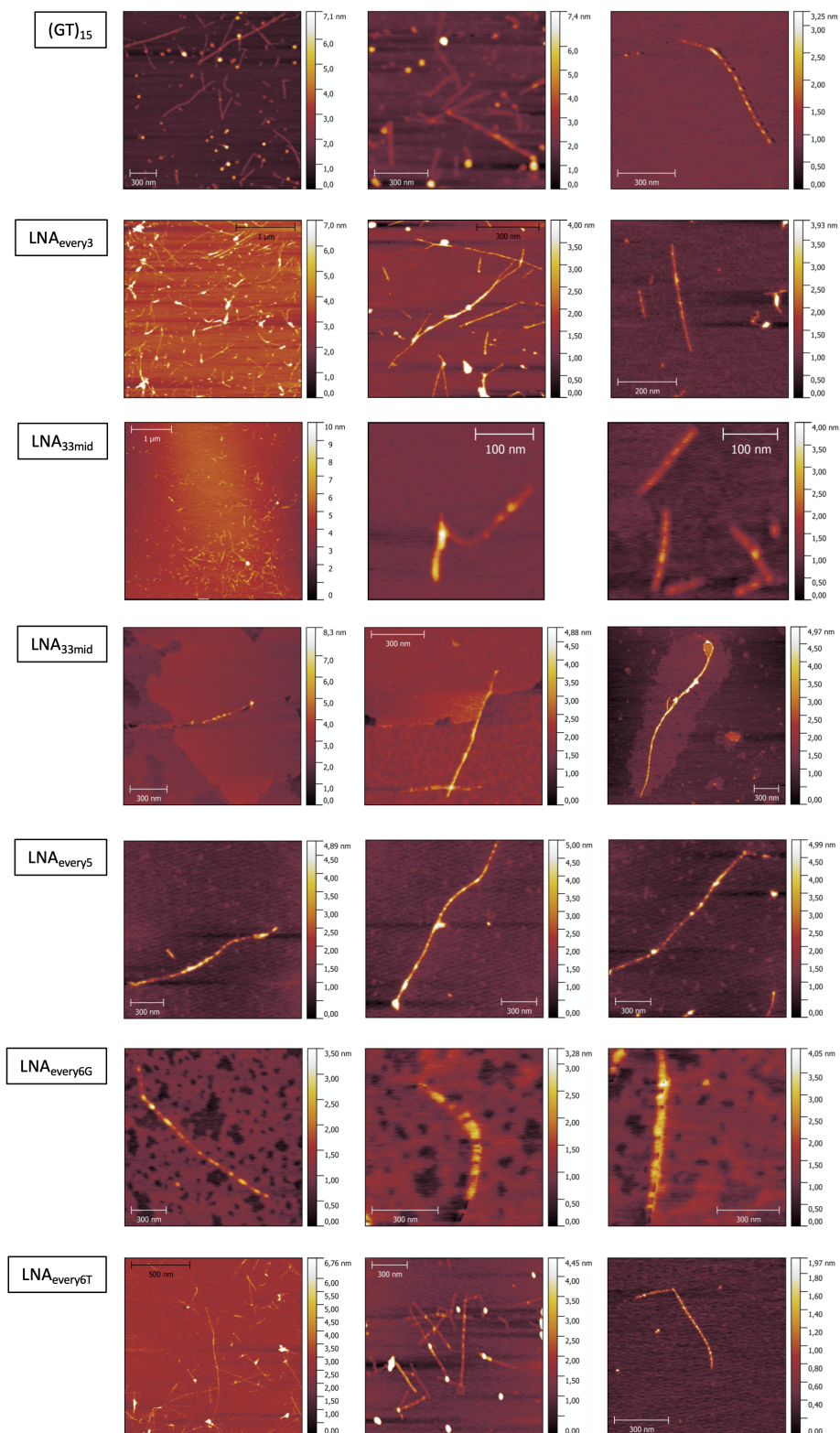


Figure D.7 – Additional AFM images collected for (GT)₁₅-, LNA_{every3}-, LNA_{every5}-, LNA_{every6G}-, LNA_{every6T}-, LNA_{33mid}-, and LNA_{20mid}-SWCNTs.

Appendix D. XNA-Nanosensors for Improved Neurochemical Sensing

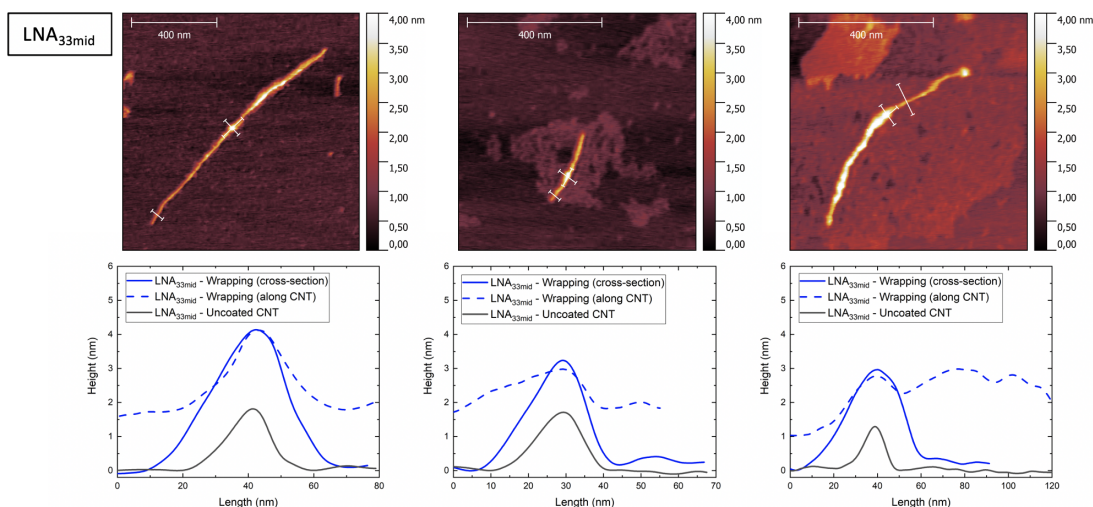


Figure D.8 – AFM height images (**top**) and extracted profiles (**bottom**) for LNA_{33mid}-SWCNTs. White lines indicate where height profiles were extracted from. The peak height extracted from cross-sectional and longitudinal profiles show good agreement. Areas of dense continuous coverage are indicated by the continuously higher peak values extracted in the profiles along the nanotube.

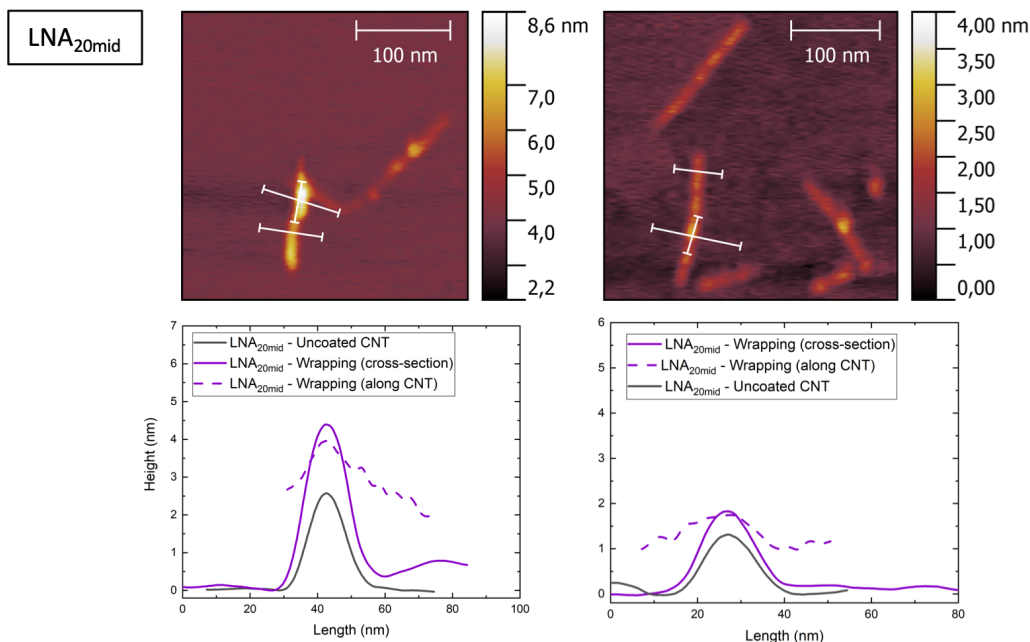


Figure D.9 – AFM height images (**top**) and extracted profiles (**bottom**) for LNA_{20mid}-SWCNTs. White lines indicate where height profiles were extracted from. The peak height extracted from cross-sectional and longitudinal profiles show good agreement. Areas of dense continuous coverage are indicated by the continuously higher peak values extracted in the profiles along the nanotube.

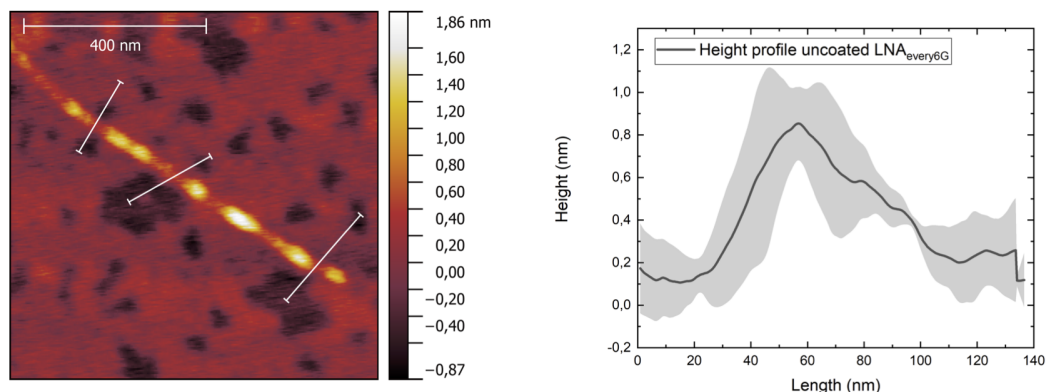


Figure D.10 – Due to the presence of an additional layer of material on the substrate of the LNA_{every6G}-SWCNTs, the heights estimated by the cross-section analysis shown in **Figure 5.3** were slightly underestimated. Additional measurements, taken from clear parts of the substrate show the true height of the nanotubes, which is used for comparison to the other wrappings. Average height profiles were extracted from three positions selected along the nanotube that overlapped with bare substrate (indicated by the white lines in AFM height images). Solid lines in the height profile represent the average height and shaded region represents 1 σ standard deviation (n = 3 profiles)

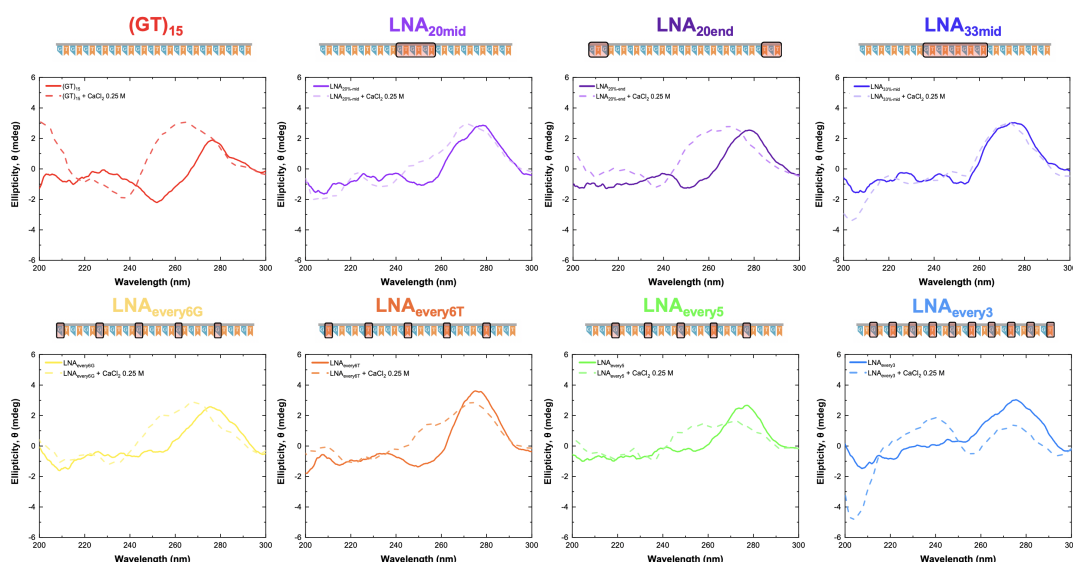


Figure D.11 – Circular dichroism measurements of DNA(GT)₁₅ and LNA(GT)₁₅ sequences on addition of CaCl₂.

Appendix D. XNA-Nanosensors for Improved Neurochemical Sensing

Table D.2 – Fit parameters for the solvatochromism shift model. The slope, Adjusted R-squared, effective dielectric constant (ϵ_{eff}), and the relative surface coverage (α).

Sequence	Slope	Adj. R ²	ϵ_{eff}	α
(GT) ₁₅	0.05886 ± 0.00622	0.93647	9.44792178	0.935221
LNA _{every6T}	0.05888 ± 0.00625	0.93601	9.459323006	0.935085
LNA _{every6G}	0.0589 ± 0.00636	0.93392	9.470750395	0.934949
LNA _{every5}	0.05969 ± 0.00627	0.93728	9.944103765	0.929321
LNA _{every3}	0.06574 ± 0.01069	0.88053	15.91040576	0.858378
LNA _{33mid}	0.05797 ± 0.00427	0.97347	8.965713056	0.940955
LNA _{20mid}	0.05815 ± 0.00547	0.94922	9.059429799	0.93984
LNA _{20end}	0.05886 ± 0.00622	0.93647	9.44792178	0.935221

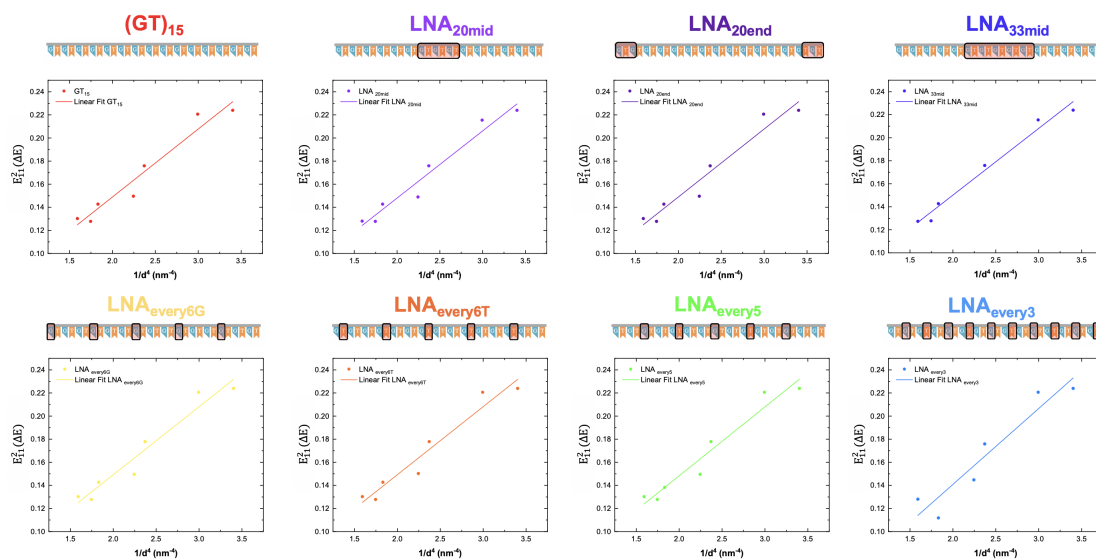


Figure D.12 – The solvatochromic shift as a function of the SWCNT diameter to the power of negative 4 (d^{-4} , dots) and corresponding linear fit (solid line).

Chirality (n,m)	$\frac{1}{d^4}$ nm ⁻⁴	$E_{11}^2(\Delta E)$							
		GT ₁₅	LNA _{every6T}	LNA _{every6G}	LNA _{every5}	LNA _{every3}	LNA _{33mid}	LNA _{20mid}	LNA _{20end}
(9,4)	1.593	0.13024	0.13024	0.13024	0.13024	0.12805	0.12731	0.12805	0.13024
(7,6)	1.747	0.12777	0.12777	0.12777	0.12777		0.12777	0.12777	0.12777
(10,2)	1.832	0.14272	0.14272	0.14272	0.1382	0.11179	0.14272	0.14272	0.14272
(8,4)	2.246	0.14961	0.15029	0.14961	0.14961	0.14475		0.14892	0.14961
(7,5)	2.371	0.17591	0.17784	0.17784	0.17784	0.17591	0.17591	0.17591	0.17591
(8,3)	2.994	0.22067	0.22067	0.22067	0.22067	0.22067	0.21548	0.21548	0.22067
(6,5)	3.402	0.22392	0.22392	0.22392	0.22392	0.22392	0.22392	0.22392	0.22392

Table D.3 – Energy shift, $E_{11}^2(\Delta E)$, as a function of nanotube chirality for all DNA and LNA sequences. Energy shifts showed a decreasing trend with increasing diameter in agreement with previous reports [29].

Appendix D. XNA-Nanosensors for Improved Neurochemical Sensing

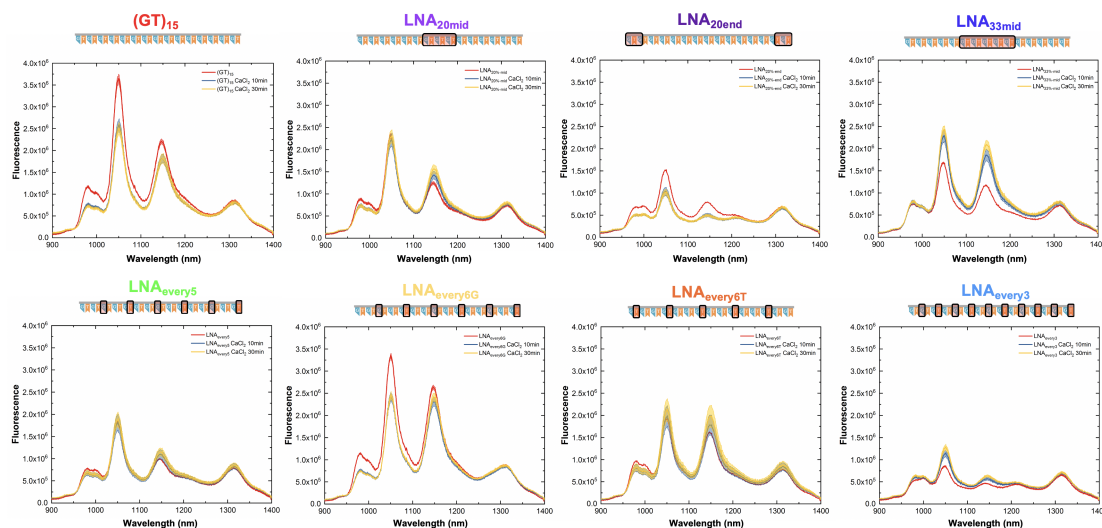


Figure D.13 – Spectral response of DNA and LNA sensors following the addition of 0.5 M CaCl₂ (final concentration: 5 mM, excitation: 660 nm). Graphs include the spectra before addition (red) and following either 10 min (blue) or 30 min (yellow) of incubation post addition. As no significant difference was observed between 10 min and 30 min incubation, 30 min incubations were used for all comparisons of wavelength shifting and intensity changes. The solid line represents the average wavelength shift with the shaded regions representing 1σ standard deviation (n = 3 technical replicates).

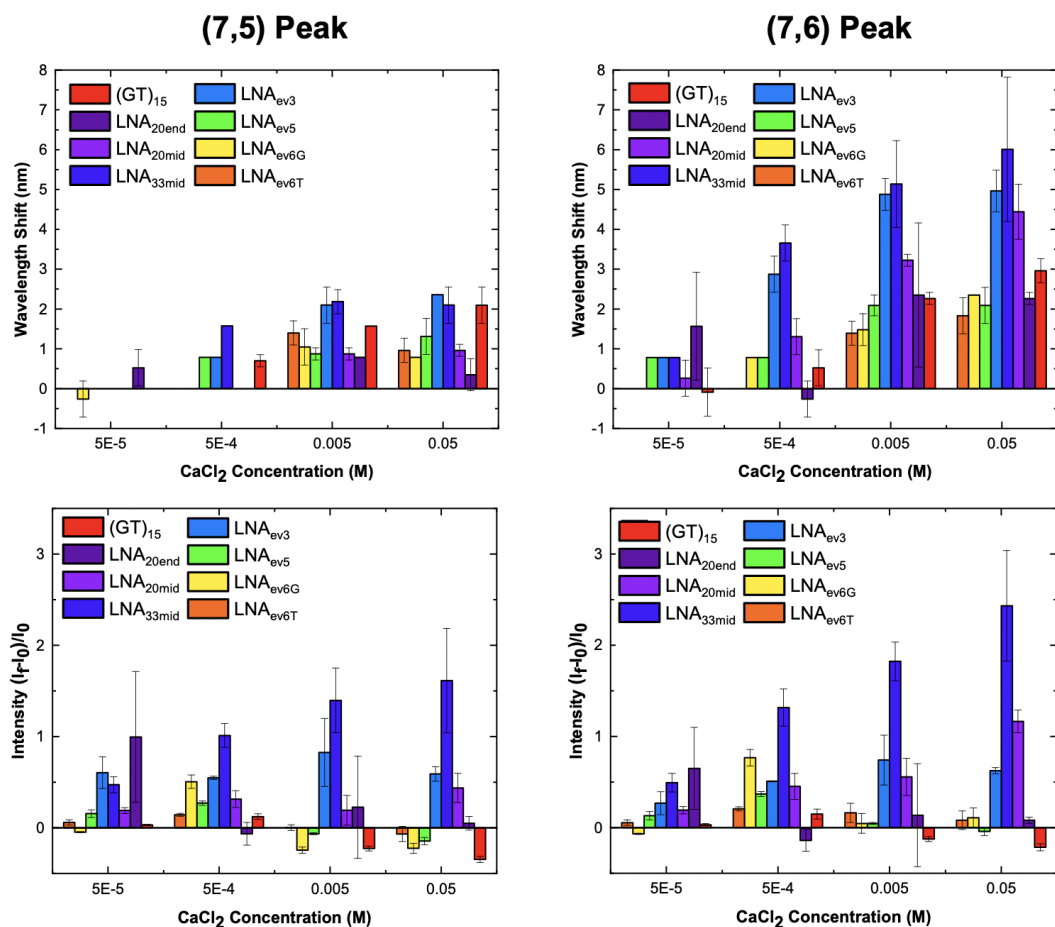


Figure D.14 – Response of DNA- and LNA- sensors to CaCl₂. Concentration-dependent (**top**) wavelength shift and (**bottom**) intensity change of the (7,5) peak (**left**) and (7,6) peak (**right**) following the addition of CaCl₂ (excitation: 660 nm). All samples were incubated for 30 min. Error bars represent 1σ standard deviation (n = 3 – 9 technical replicates).

Appendix D. XNA-Nanosensors for Improved Neurochemical Sensing

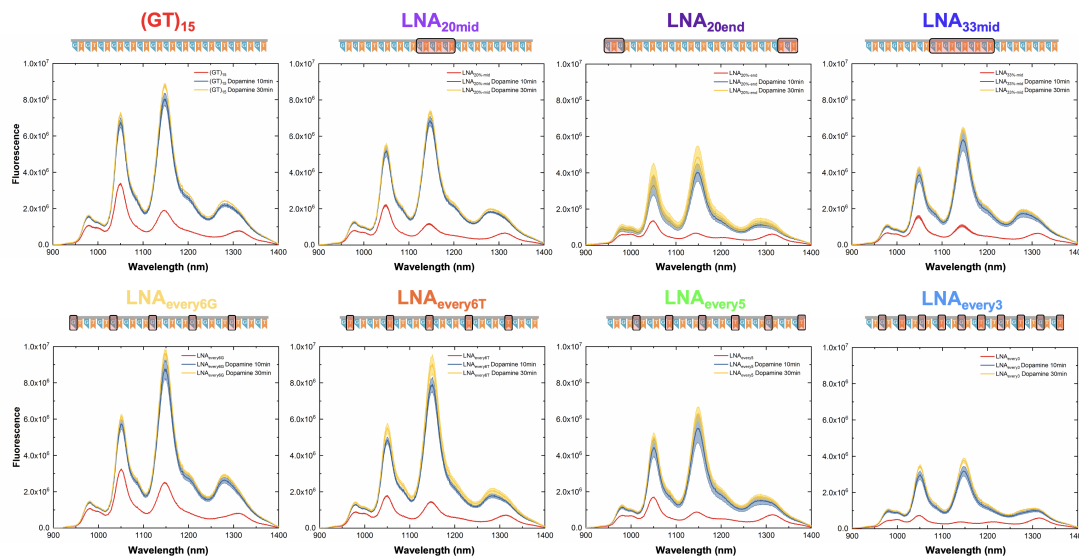


Figure D.15 – Spectral response of LNA sensors following the addition of 10 mM dopamine (final concentration: 100 μ M, excitation: 660 nm). Graphs include the spectra before addition (red) and following either 10 min (blue) or 30 min (yellow) of incubation post addition. The solid line represents the average wavelength shift with the shaded regions representing 1σ standard deviation ($n = 3$ technical replicates).

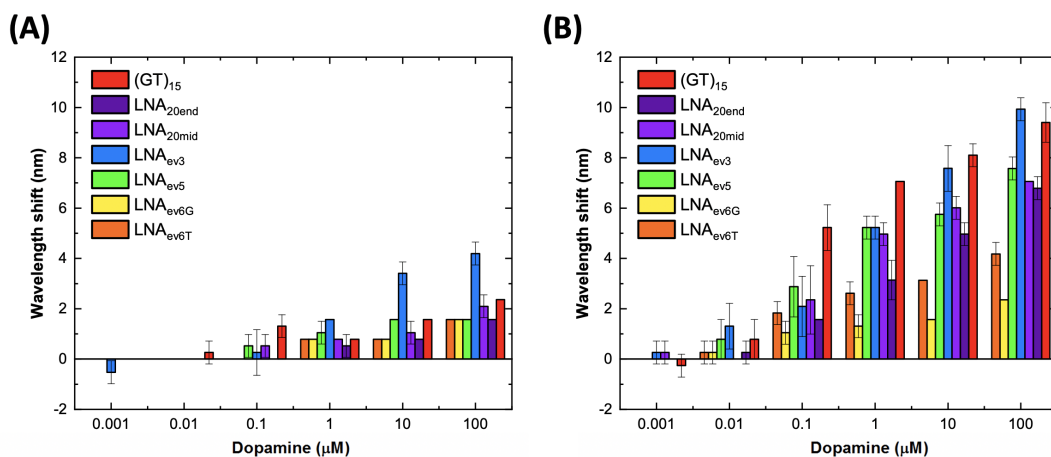


Figure D.16 – Concentration-dependent wavelength shifting response of DNA- and LNA-SWCNTs towards dopamine in the absence of CaCl_2 (excitation: 660 nm). Shift in the wavelength position of the (A) (7,5) and (B) (7,6) peak following the addition of dopamine. All samples were incubated for 30 min. Error bars represent 1σ standard deviation ($n = 3$ technical replicates).

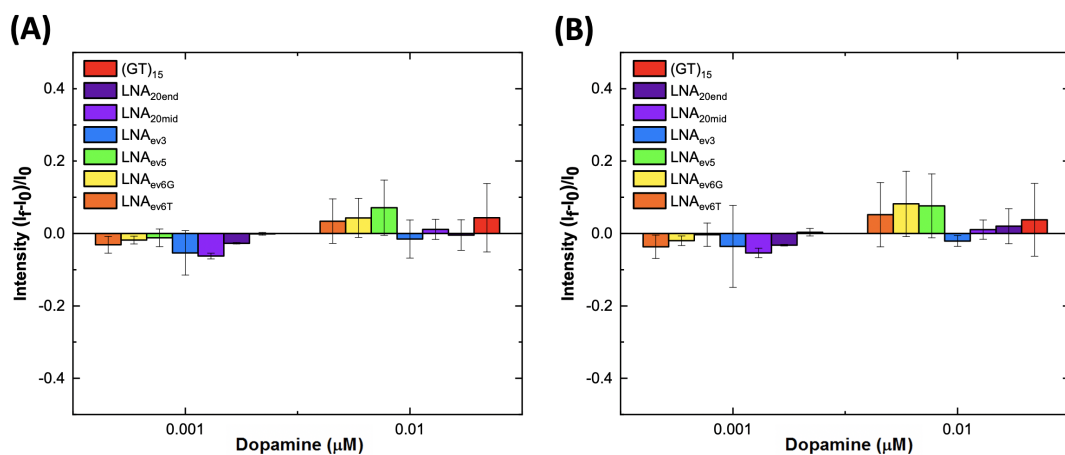


Figure D.17 – Concentration-dependent intensity response of DNA- and LNA-SWCNTs towards dopamine in the absence of CaCl_2 (excitation: 660 nm) at low concentration. Intensity change of the (A) (7,5) and (B) (7,6) peak following the addition of dopamine. All samples were incubated for 30 min. Error bars represent 1σ standard deviation ($n = 3$ technical replicates).

Appendix D. XNA-Nanosensors for Improved Neurochemical Sensing

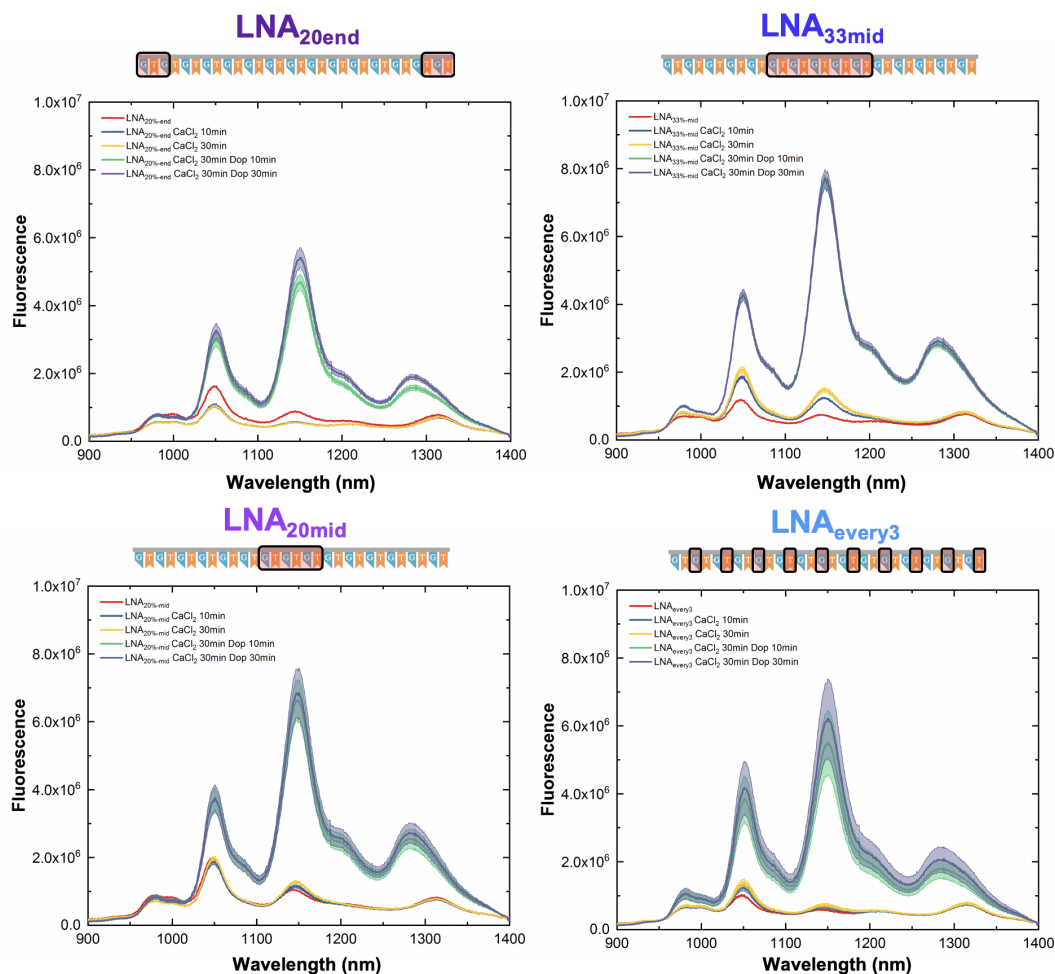


Figure D.18 – Spectral response of LNA sensors following the addition of 0.5 M CaCl₂ (final concentration: 5 μ M) and 10 mM dopamine (final concentration: 100 μ M, excitation: 660 nm). Graphs include the spectra before addition (red) and following the addition of CaCl₂ after 10 min (blue) and 30 min (yellow) of incubation and following subsequent addition of dopamine at 10 min (green) and 30 min (purple) post addition. The solid line represents the average wavelength shift with the shaded regions representing 1 σ standard deviation (n = 3 technical replicates).

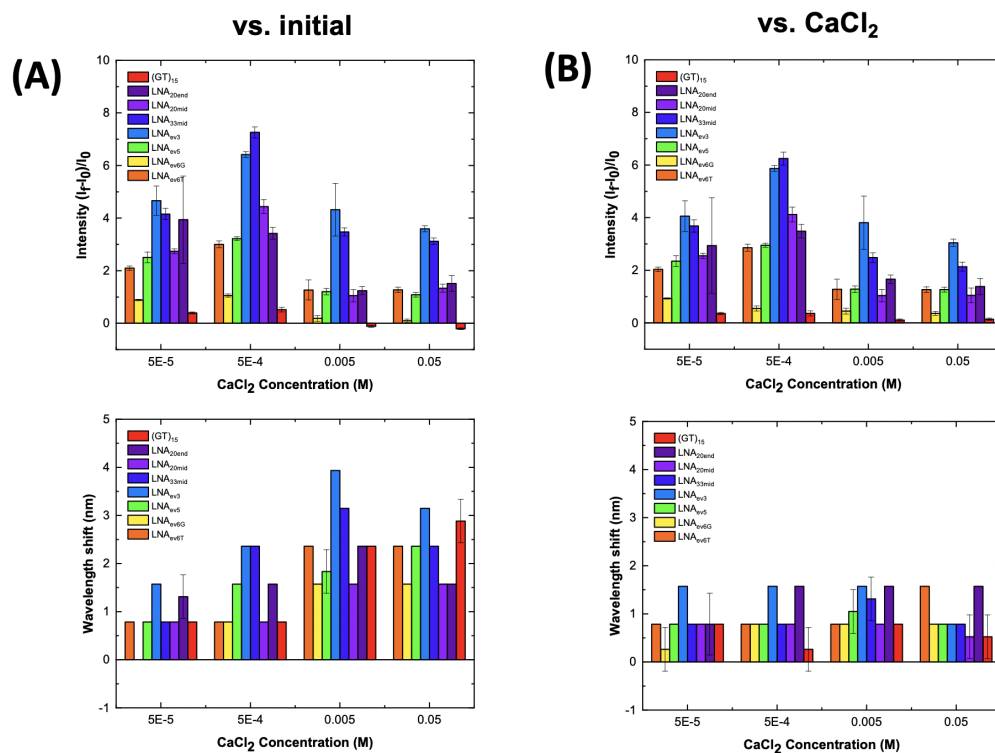


Figure D.19 – Fluorescence response of (GT)₁₅- and LNA-SWCNT sensors following the addition of 10 mM dopamine (final concentration: 100 μ M) in the presence of various concentrations of CaCl₂ (excitation: 660 nm). Intensity (**top**) and wavelength (**bottom**) response of the (7,5) peak following dopamine addition were calculated versus **(A)** the initial spectrum (before CaCl₂ addition) and **(B)** the spectrum following incubation with the CaCl₂ solutions highlighting the bias that can be introduced to the sensor response in the presence of CaCl₂. All samples were incubated for 30 min following dopamine addition. Error bars represent 1 σ standard deviation (n = 3 technical replicates).

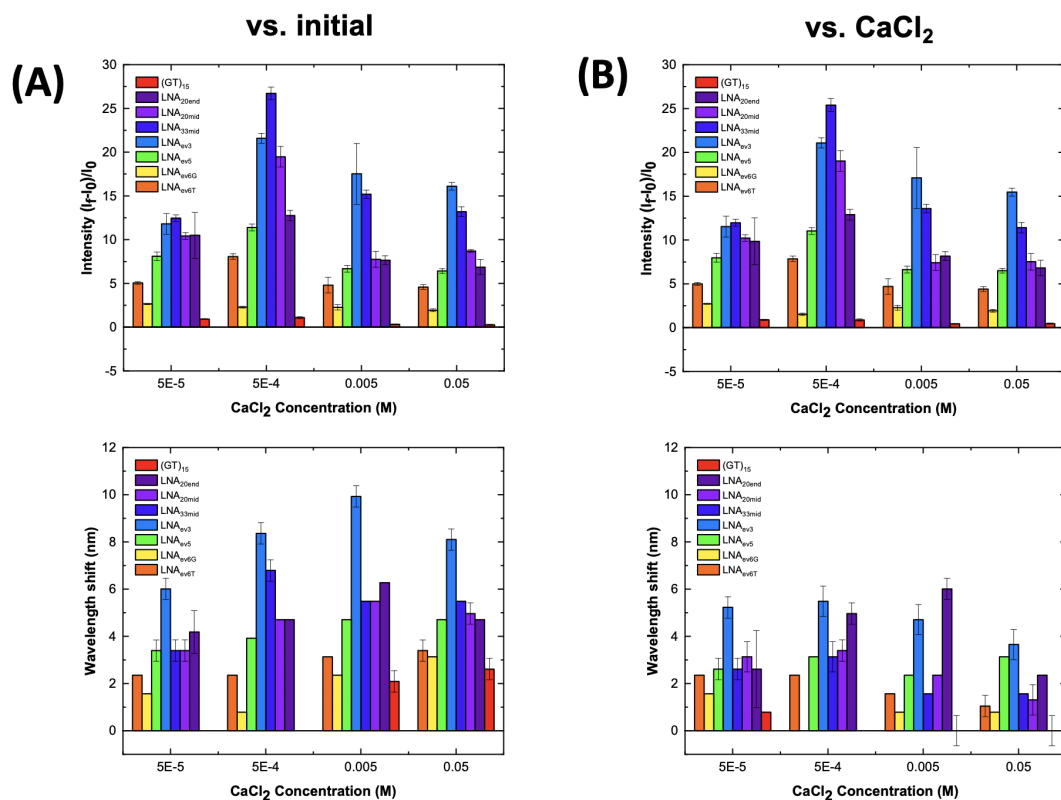


Figure D.20 – Fluorescence response of (GT)₁₅- and LNA-SWCNT sensors following the addition of 10 mM dopamine (final concentration: 100 μ M) in the presence of various concentrations of CaCl₂ (excitation: 660 nm). Intensity (**top**) and wavelength (**bottom**) response of the (7,6) peak following dopamine addition were calculated versus (A) the initial spectrum (before CaCl₂ addition) and (B) the spectrum following incubation with the CaCl₂ solutions highlighting the bias that can be introduced to the sensor response in the presence of CaCl₂. All samples were incubated for 30 min following dopamine addition. Error bars represent 1 σ standard deviation (n = 3 technical replicates).

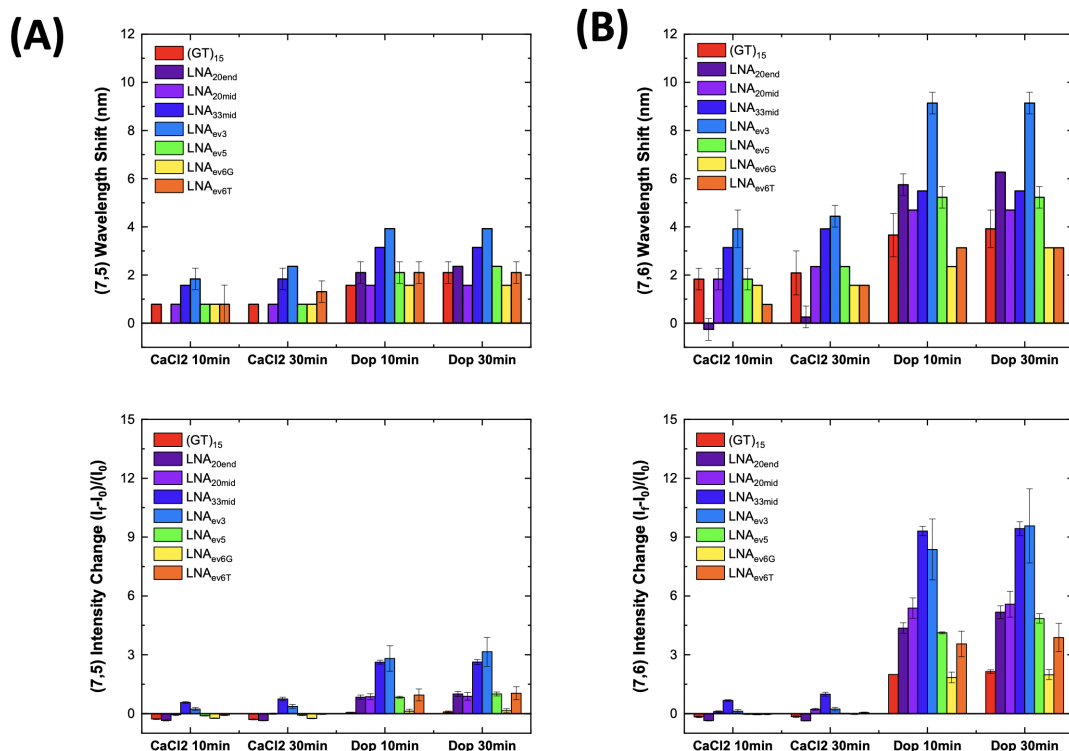


Figure D.21 – Comparison of the fluorescence response of (GT)₁₅- and LNA-SWCNTs for the (A) (7,5) and (B) (7,6) peaks following the addition of 0.5 M CaCl₂ (final concentration: 5 mM) and 10 mM dopamine (final concentration: 100 μM, excitation: 660 nm). Wavelength (top) and intensity (bottom) response of the (7,5) and (7,6) peaks following dopamine addition were calculated versus the initial spectrum (before initial CaCl₂ addition) for both time points. Error bars represent 1σ standard deviation (n = 3 technical replicates)

Appendix D. XNA-Nanosensors for Improved Neurochemical Sensing

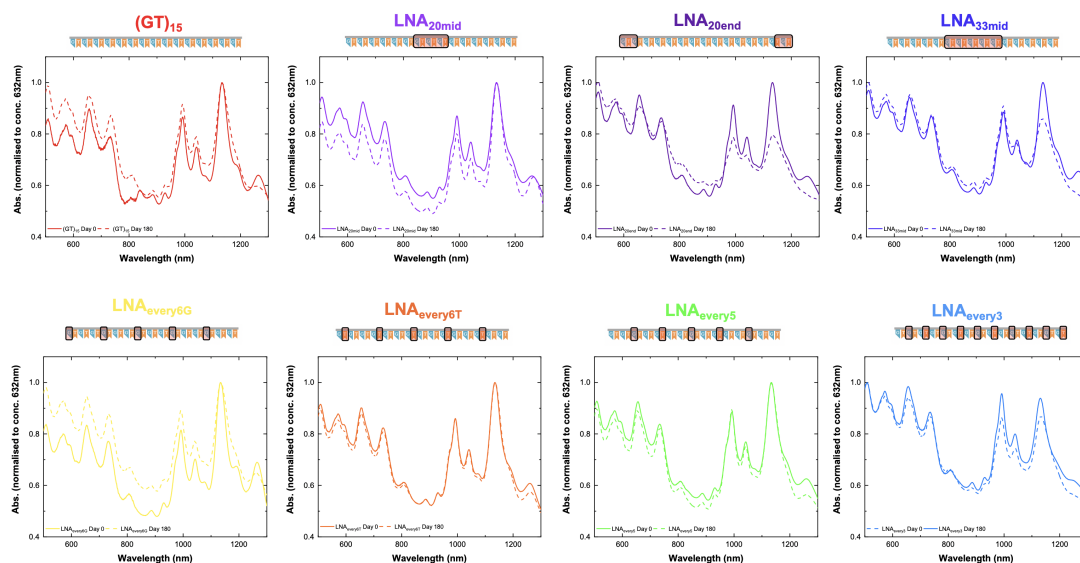


Figure D.22 – Effect of ageing on the absorbance spectra of all samples examined in this study. Absorbance spectra were collected immediately following suspension (solid line) and following 180 days incubation at 4°C (dashed line). All spectra are normalized to concentration using an extinction coefficient of 0.036 mg/L at Abs_{632nm}.

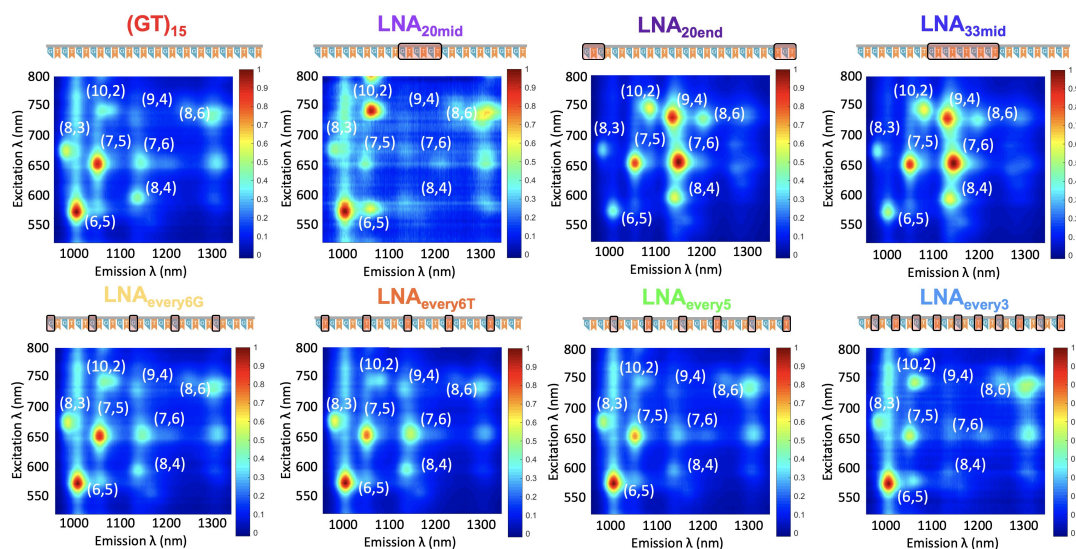


Figure D.23 – Effect of ageing on the fluorescence properties of all samples examined in this study. PLE maps of the original (GT)₁₅- and all LNA-SWCNT solutions following 180 days incubation at 4°C. All PLE maps were normalized to the maximum fluorescence intensity for comparison.

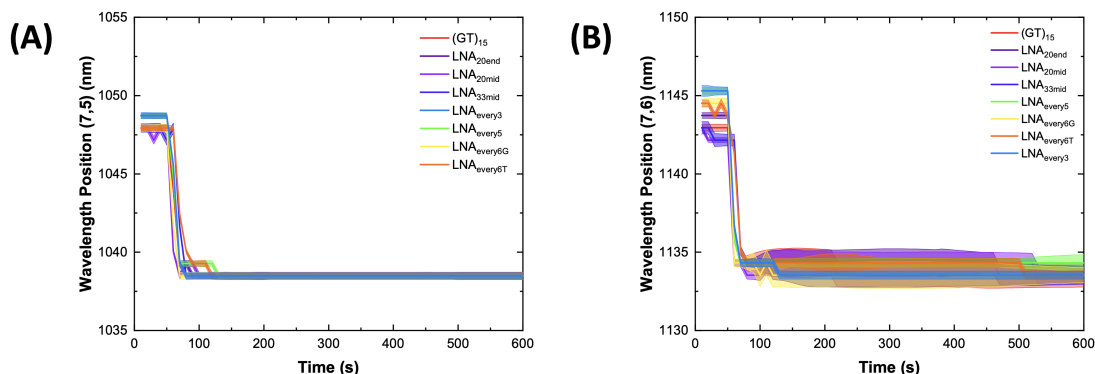


Figure D.24 – Modulation of fluorescence emission wavelength position of the (A) (7,5) and (B) (7,6) chirality peaks for all sequences as a function of time following SDOC addition. All SWCNT suspensions were prepared via the surfactant exchange method. The shaded region represents the error (3σ) of the peak fit at each time point.

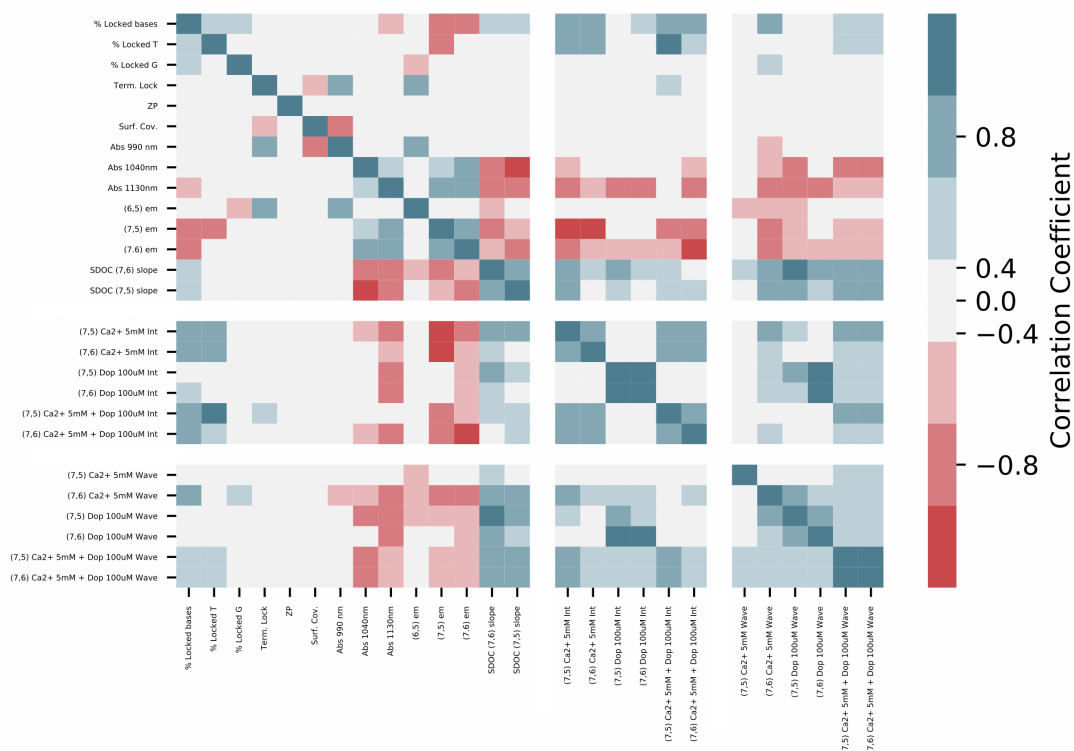


Figure D.25 – Data correlation matrix for the (GT)₁₅- and LNA-SWCNT for several different parameters measured. Blue hue indicates positive correlation and red hues indicate negative correlation.

Appendix D. XNA-Nanosensors for Improved Neurochemical Sensing

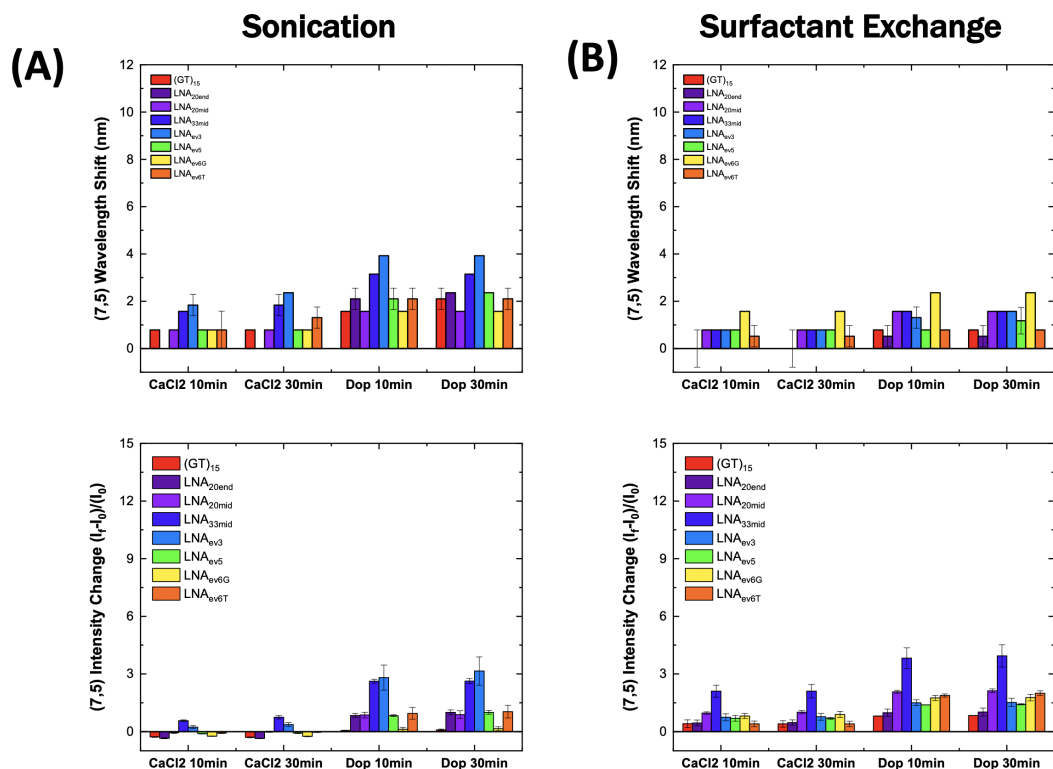


Figure D.26 – Comparison of the fluorescence response of (GT)₁₅- and LNA-SWCNTs prepared via either **(A)** sonication or **(B)** via a surfactant exchange protocol following the addition of 0.5 M CaCl₂ (final concentration: 5 mM) and 10 mM dopamine (final concentration: 100 μ M, excitation: 660 nm). Intensity (**top**) and wavelength (**bottom**) response of the (7,5) peak following dopamine addition were calculated versus the initial spectrum (before initial CaCl₂ addition) for all time points. Error bars represent 1 σ standard deviation (n = 3 technical replicates).

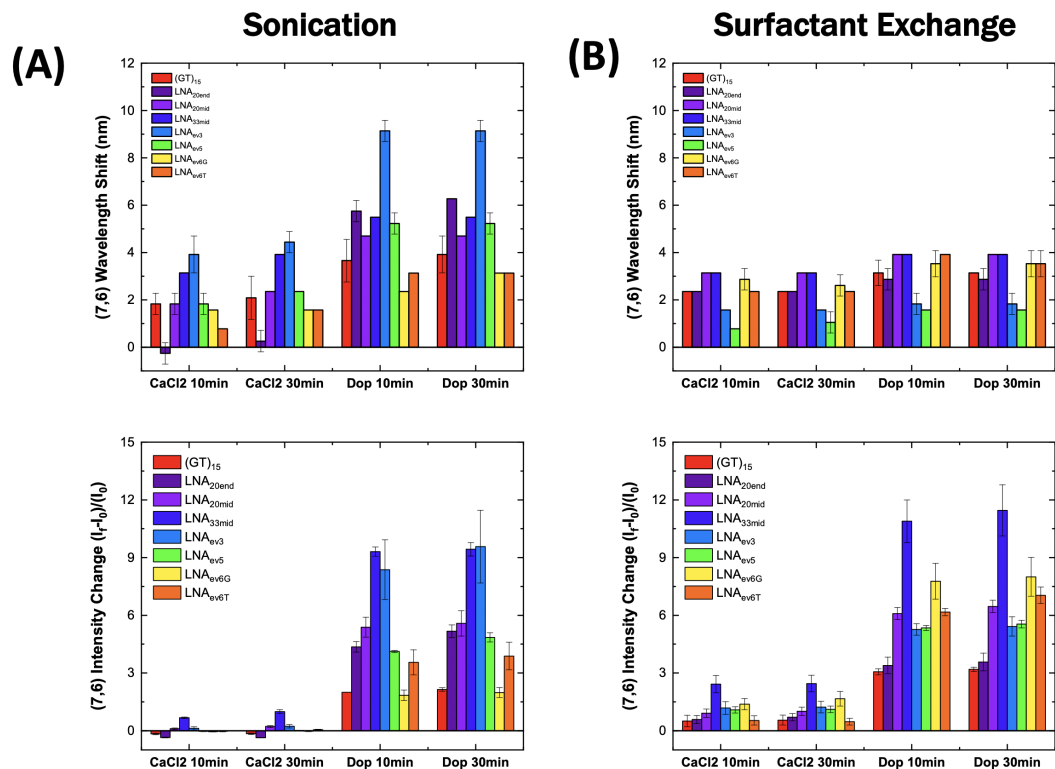


Figure D.27 – Comparison of the fluorescence response of (GT)₁₅- and LNA-SWCNTs prepared by either (A) sonication or (B) MeOH assisted surfactant exchange following the addition of 0.5 M CaCl₂ (final concentration: 5 mM) and 10 mM dopamine (final concentration: 100 μM, excitation: 660 nm). Intensity (**top**) and wavelength (**bottom**) response of the (7,6) peak following dopamine addition were calculated versus the initial spectrum (before initial CaCl₂ addition) for all time points. Error bars represent 1σ standard deviation (n = 3 technical replicates).

E Outlook on Potential Applications of XNA-SWCNTs for Improved Optical Biosensing

E.1 Using XNA-SWCNTs for *In Vitro* Sensing Applications

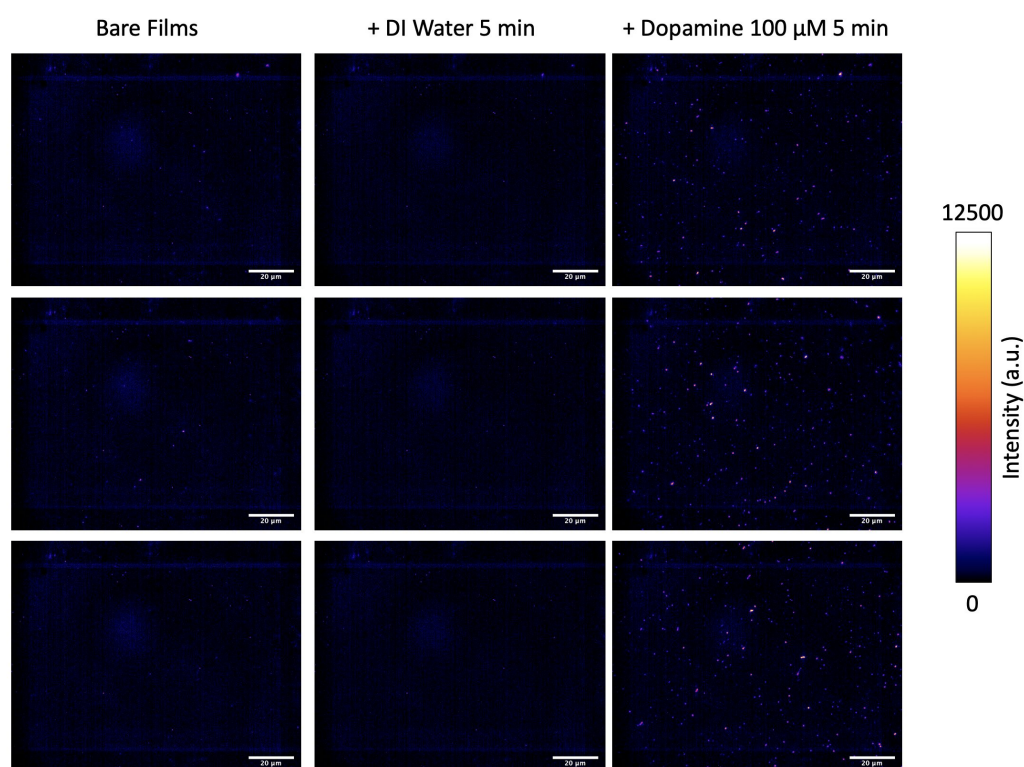


Figure E.1 – Single molecule response behavior of DNA-SWCNT sensor films towards dopamine (final concentration: 100 μ M) in DI water. Three representative images of bare (GT)₁₅ sensor films (**left**), films coated with DI water (**middle**), and following the addition of dopamine (**right**). All samples were incubated for 5 min prior to acquiring the images (excitation: 780 nm, emission filter: 980 nm LP, exposure time: 1 s). Backgrounds were subtracted using a Gaussian blur filter (sigma = 50).

Appendix E. Outlook on Potential Applications of XNA-SWCNTs for Improved Optical Biosensing

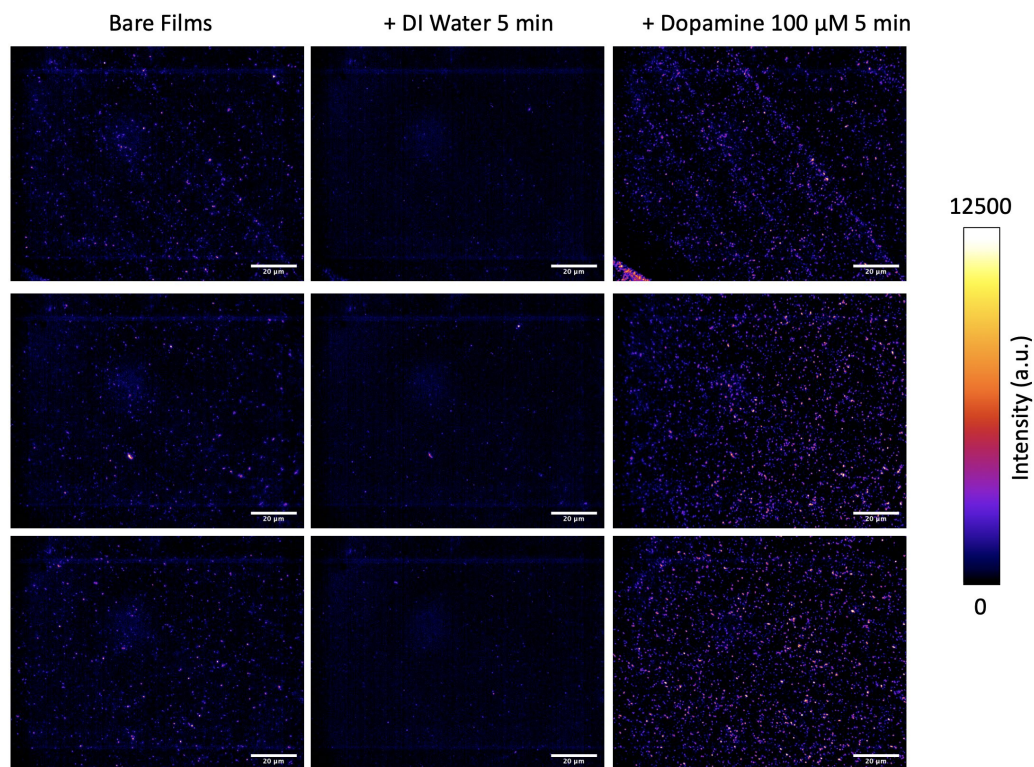


Figure E.2 – Single molecule response behavior of LNA_{every5}-SWCNT sensor films towards dopamine (final concentration: 100 μ M) in DI water. Three representative images of bare LNA_{every5} sensor films (**left**), films coated with DI water (**middle**), and following the addition of dopamine (**right**). All samples were incubated for 5 min prior to acquiring the images (excitation: 780 nm, emission filter: 980 nm LP, exposure time: 1 s). Backgrounds were subtracted using a Gaussian blur filter (sigma = 50).

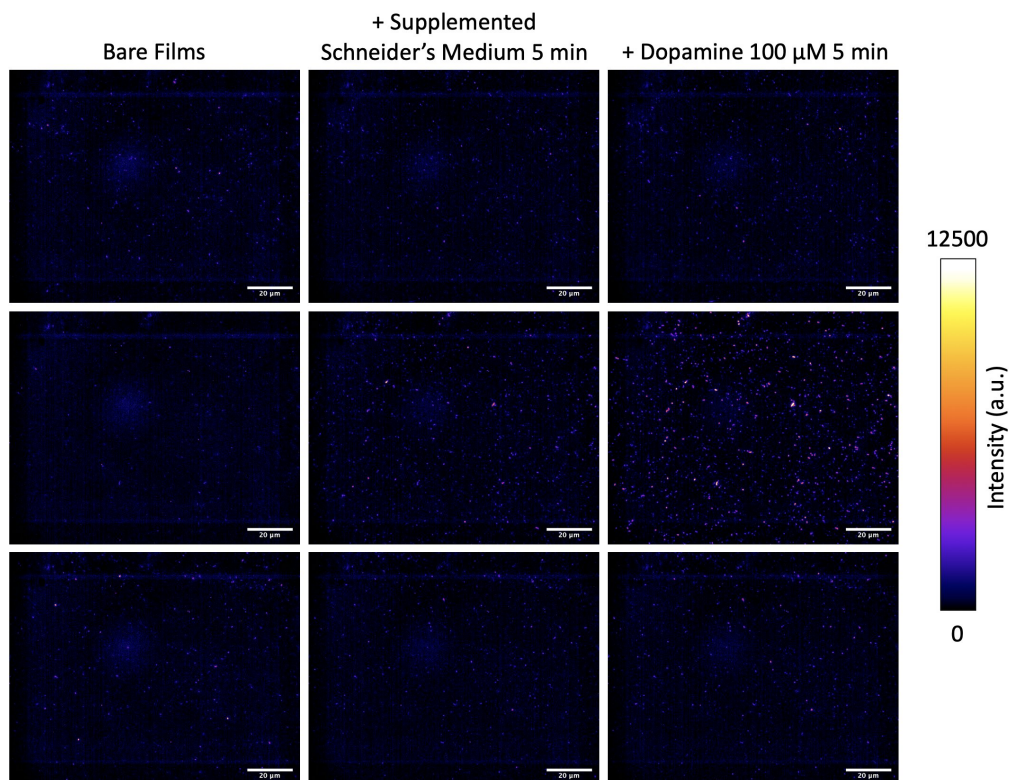


Figure E.3 – Single molecule response behavior of DNA-SWCNT sensor films towards dopamine (final concentration: 100 μ M) in supplemented Schneider's medium (10% FBS, 1% Pen/Strep). Three representative images of bare (GT)₁₅ sensor films (**left**), films coated with supplemented Schneider's medium (**middle**), and following the addition of dopamine (**right**). All samples were incubated for 5 min prior to acquiring the images (excitation: 780 nm, emission filter: 980 nm LP, exposure time: 1 s). Backgrounds were subtracted using a Gaussian blur filter (sigma = 50).

Appendix E. Outlook on Potential Applications of XNA-SWCNTs for Improved Optical Biosensing

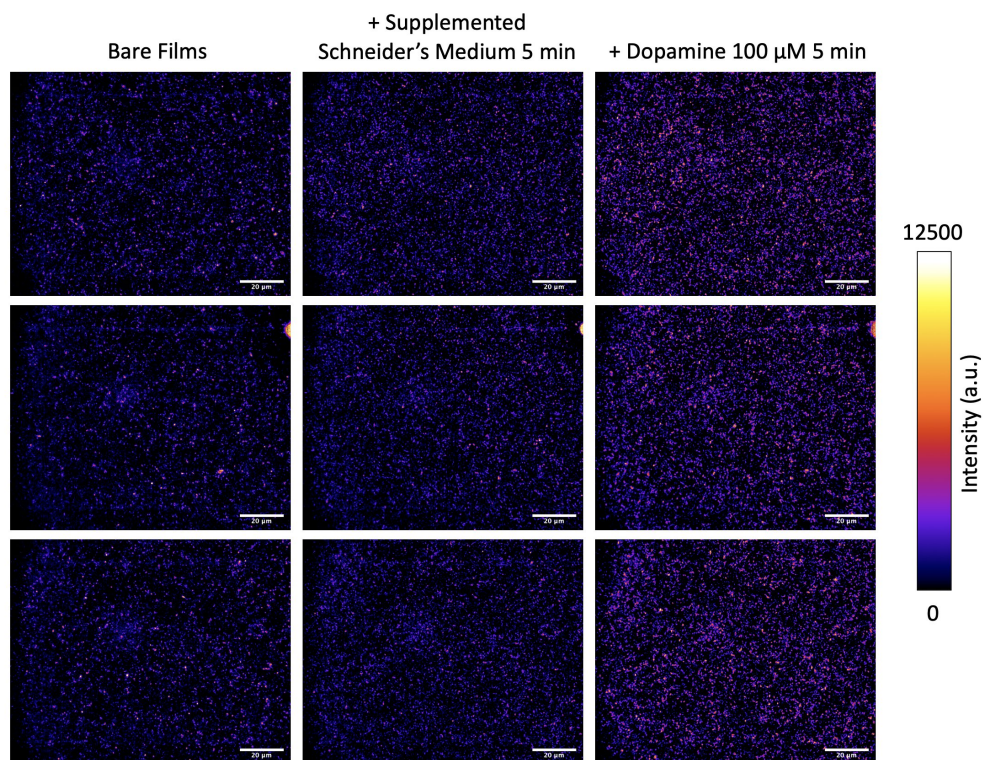


Figure E.4 – Single molecule response behavior of LNA_{every5}-SWCNT sensor films towards dopamine (final concentration: 100 μ M) in supplemented Schneider's medium (10% FBS, 1% Pen/Strep). Three representative images of bare LNA_{every5} sensor films (**left**), films coated with supplemented Schneider's medium (**middle**), and following the addition of dopamine (**right**). All samples were incubated for 5 min prior to acquiring the images (excitation: 780 nm, emission filter: 980 nm LP, exposure time: 1 s). Backgrounds were subtracted using a Gaussian blur filter (sigma = 50).

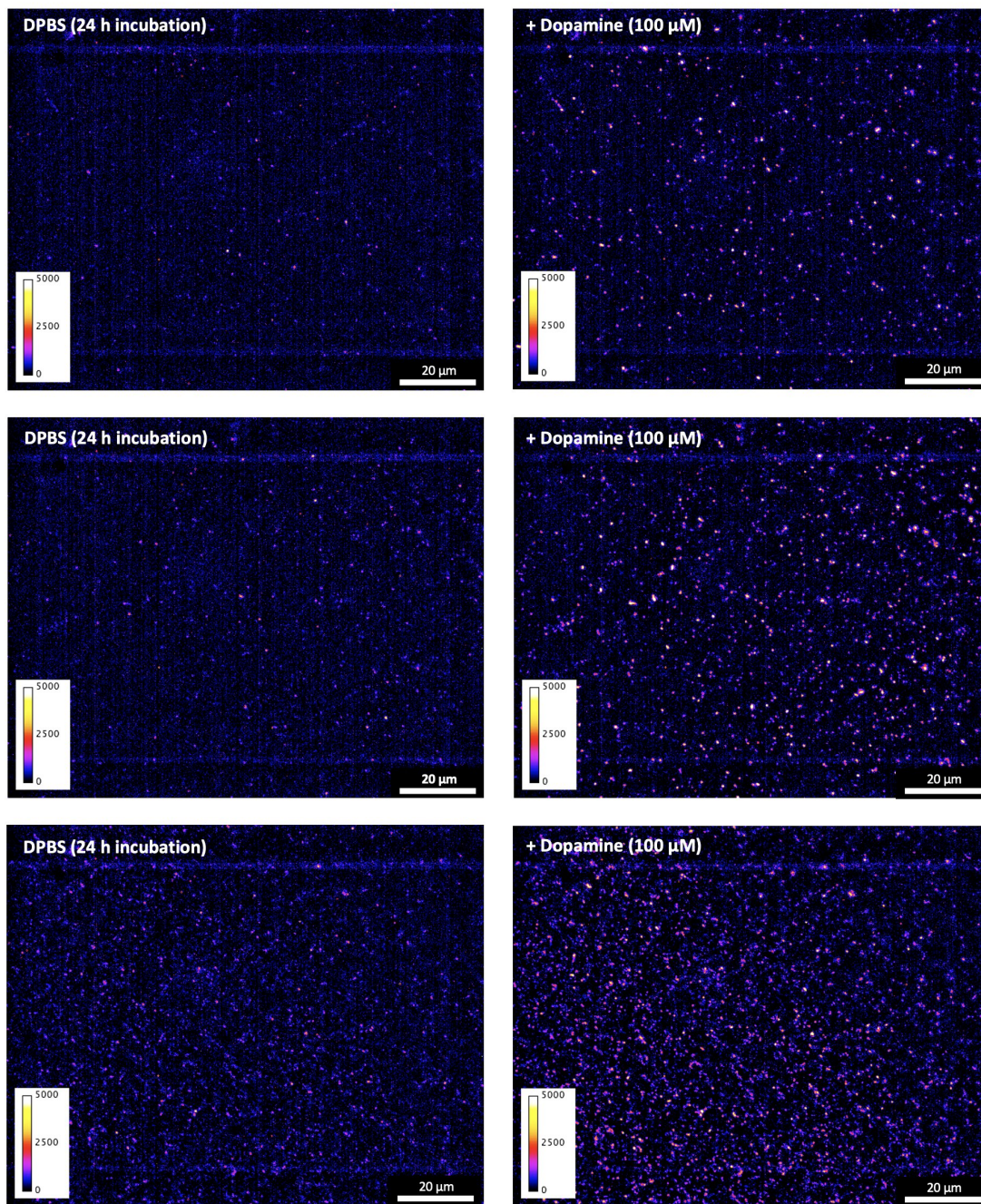


Figure E.5 – Single molecule response behavior of LNA_{every5}-SWCNT sensor films in DPBS towards dopamine (final concentration: 100 μM). All films were incubated for 24 h at room temperature prior to measurement. Three representative images of LNA_{every5} sensor films before (**left**) and after (**right**) the addition of dopamine. All samples were incubated for 15 min post-dopamine addition prior to acquiring the images (excitation: 780 nm, emission filter: 980 nm LP, exposure time: 1 s). Backgrounds were subtracted using a Gaussian blur filter (sigma = 25).

Appendix E. Outlook on Potential Applications of XNA-SWCNTs for Improved Optical Biosensing

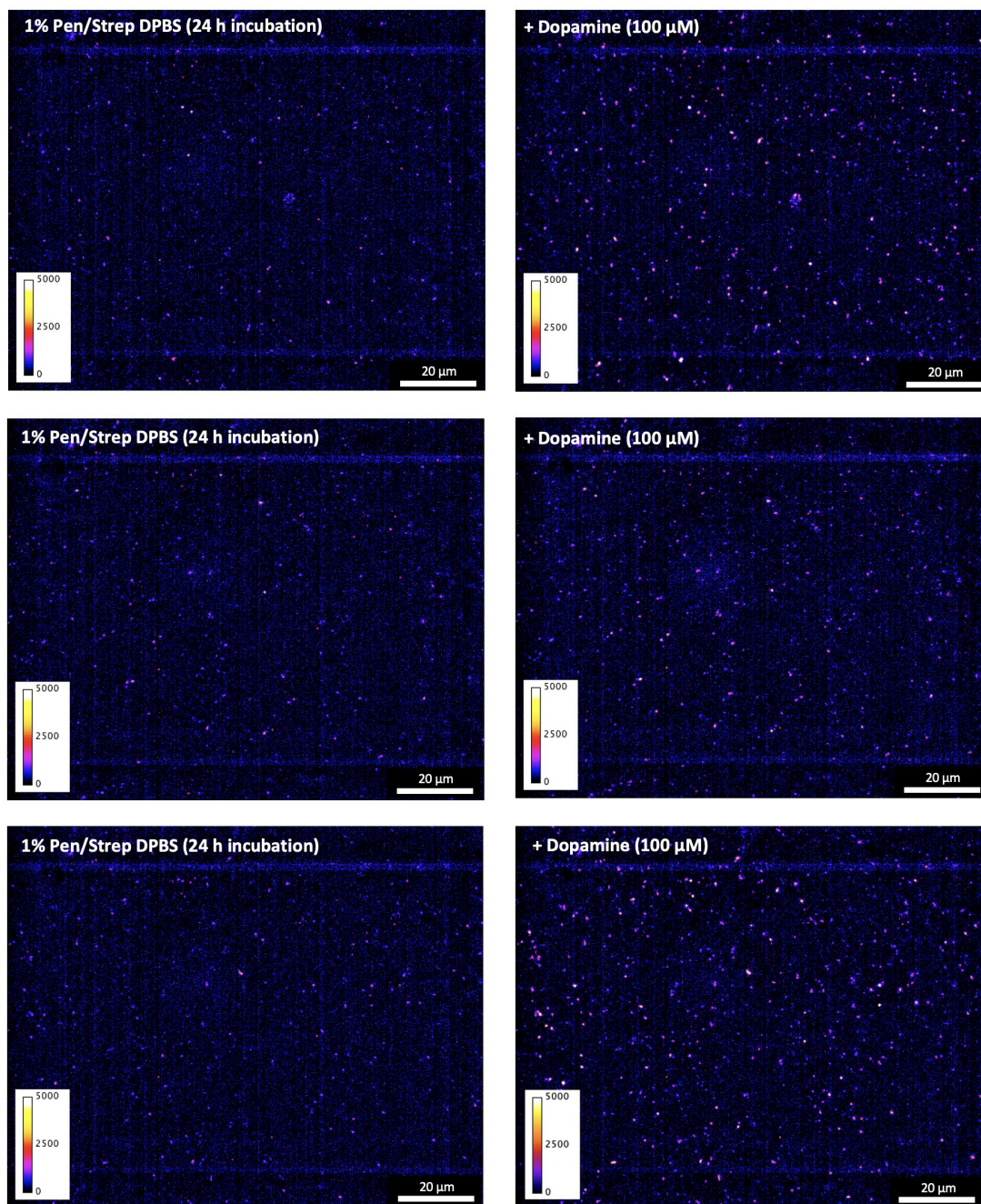


Figure E.6 – Single molecule response behavior of LNA_{every5}-SWCNT sensor films in 1% Pen/Strep in DPBS (Rinaldini solution) towards dopamine (final concentration: 100 μM). All films were incubated for 24 h at room temperature prior to measurement. Three representative images of LNA_{every5} sensor films before (**left**) and after (**right**) the addition of dopamine. All samples were incubated for 15 min post-dopamine addition prior to acquiring the images (excitation: 780 nm, emission filter: 980 nm LP, exposure time: 1 s). Backgrounds were subtracted using a Gaussian blur filter (sigma = 25).

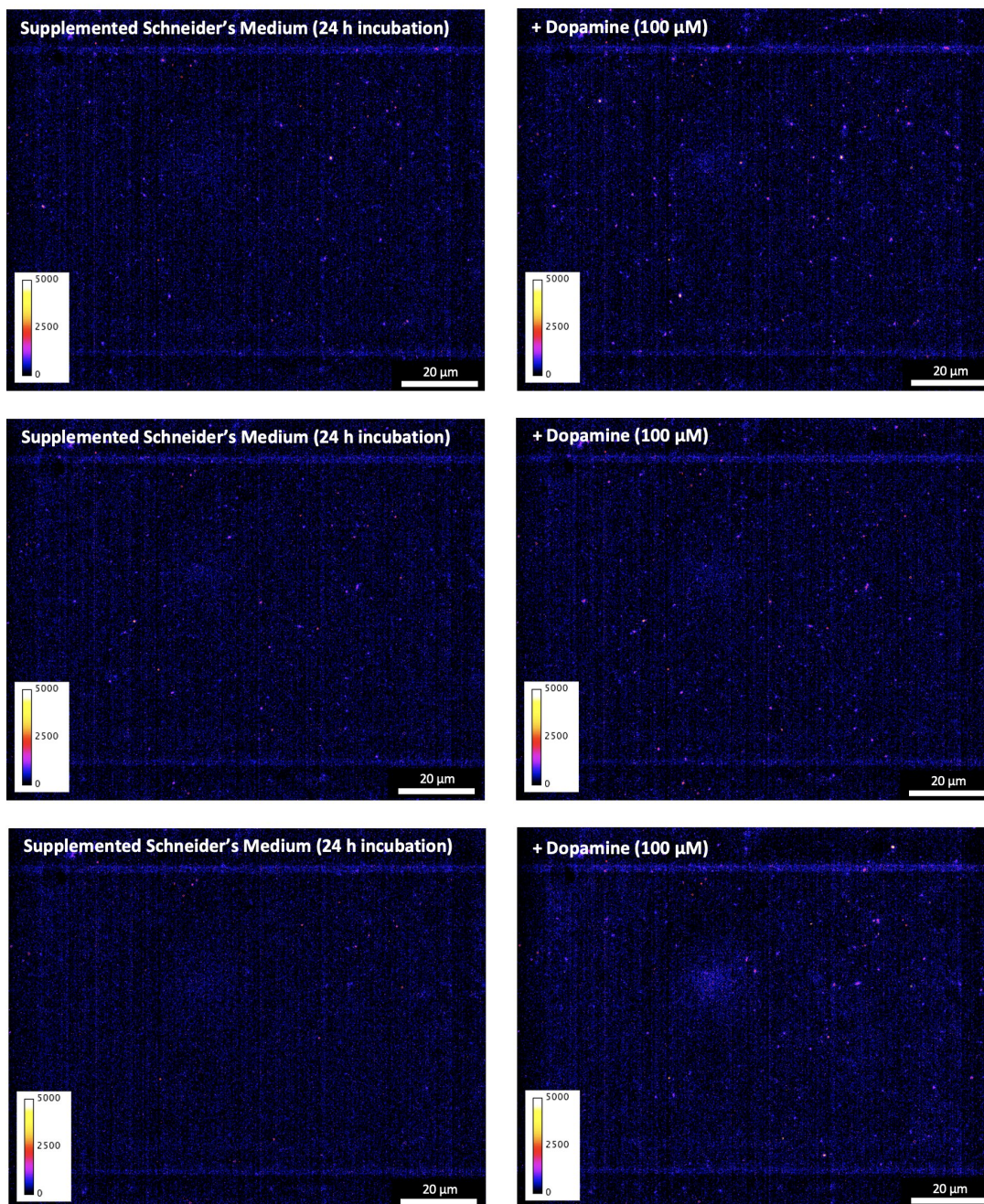


Figure E.7 – Single molecule response behavior of LNA_{every5}-SWCNT sensor films in supplemented Schneider's medium towards dopamine (final concentration: 100 μM). All films were incubated for 24 h at room temperature prior to measurement. Three representative images of LNA_{every5} sensor films before (**left**) and after (**right**) the addition of dopamine. All samples were incubated for 15 min post-dopamine addition prior to acquiring the images (excitation: 780 nm, emission filter: 980 nm LP, exposure time: 1 s). Backgrounds were subtracted using a Gaussian blur filter (sigma = 25).

Appendix E. Outlook on Potential Applications of XNA-SWCNTs for Improved Optical Biosensing

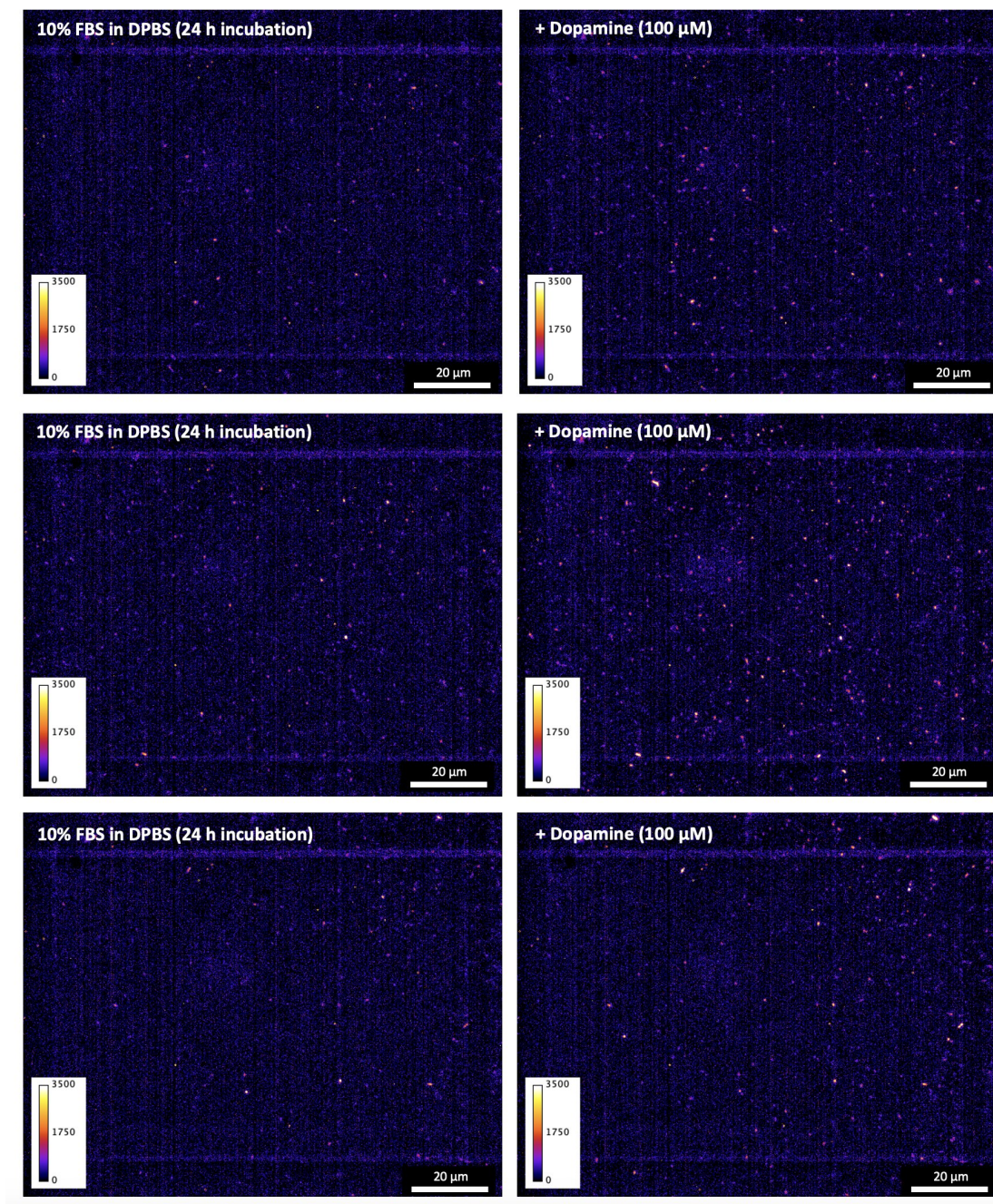


Figure E.8 – Single molecule response behavior of LNA_{every5}-SWCNT sensor films in 10% FBS (v/v) towards dopamine (final concentration: 100 μM). All films were incubated for 24 h at room temperature prior to measurement. Three representative images of LNA_{every5} sensor films before (**left**) and after (**right**) the addition of dopamine. All samples were incubated for 15 min post-dopamine addition prior to acquiring the images (excitation: 780 nm, emission filter: 980 nm LP, exposure time: 1 s). Backgrounds were subtracted using a Gaussian blur filter (sigma = 25).

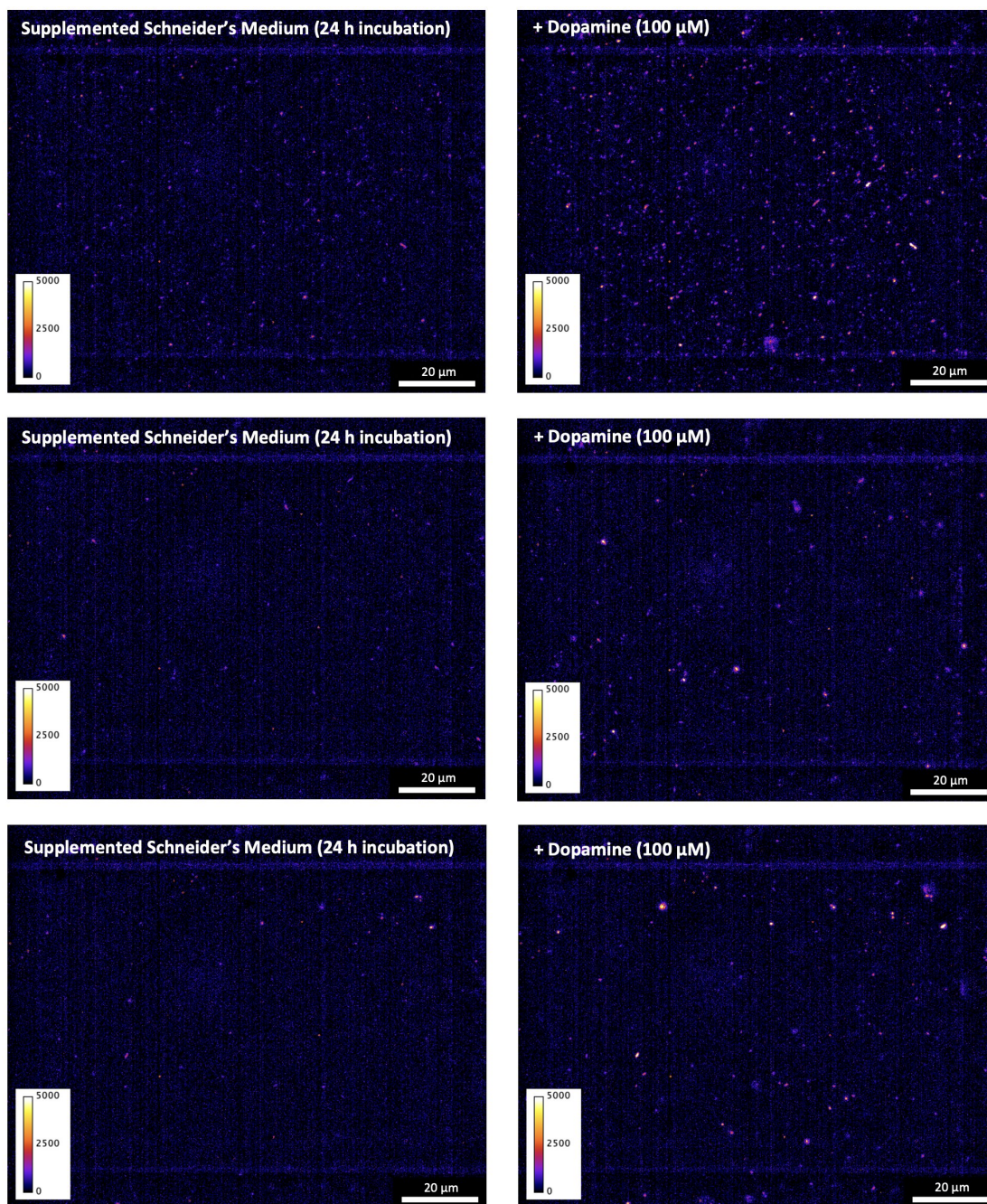


Figure E.9 – Single molecule response behavior of more dense LNA_{every5}-SWCNT sensor films in supplemented Schneider's medium towards dopamine (final concentration: 100 μM). All films were incubated for 24 h at room temperature prior to measurement. Three representative images of LNA_{every5} sensor films before (**left**) and after (**right**) the addition of dopamine. All samples were incubated for 15 min post-dopamine addition prior to acquiring the images (excitation: 780 nm, emission filter: 980 nm LP, exposure time: 1 s). Backgrounds were subtracted using a Gaussian blur filter ($\sigma = 25$).

Appendix E. Outlook on Potential Applications of XNA-SWCNTs for Improved Optical Biosensing

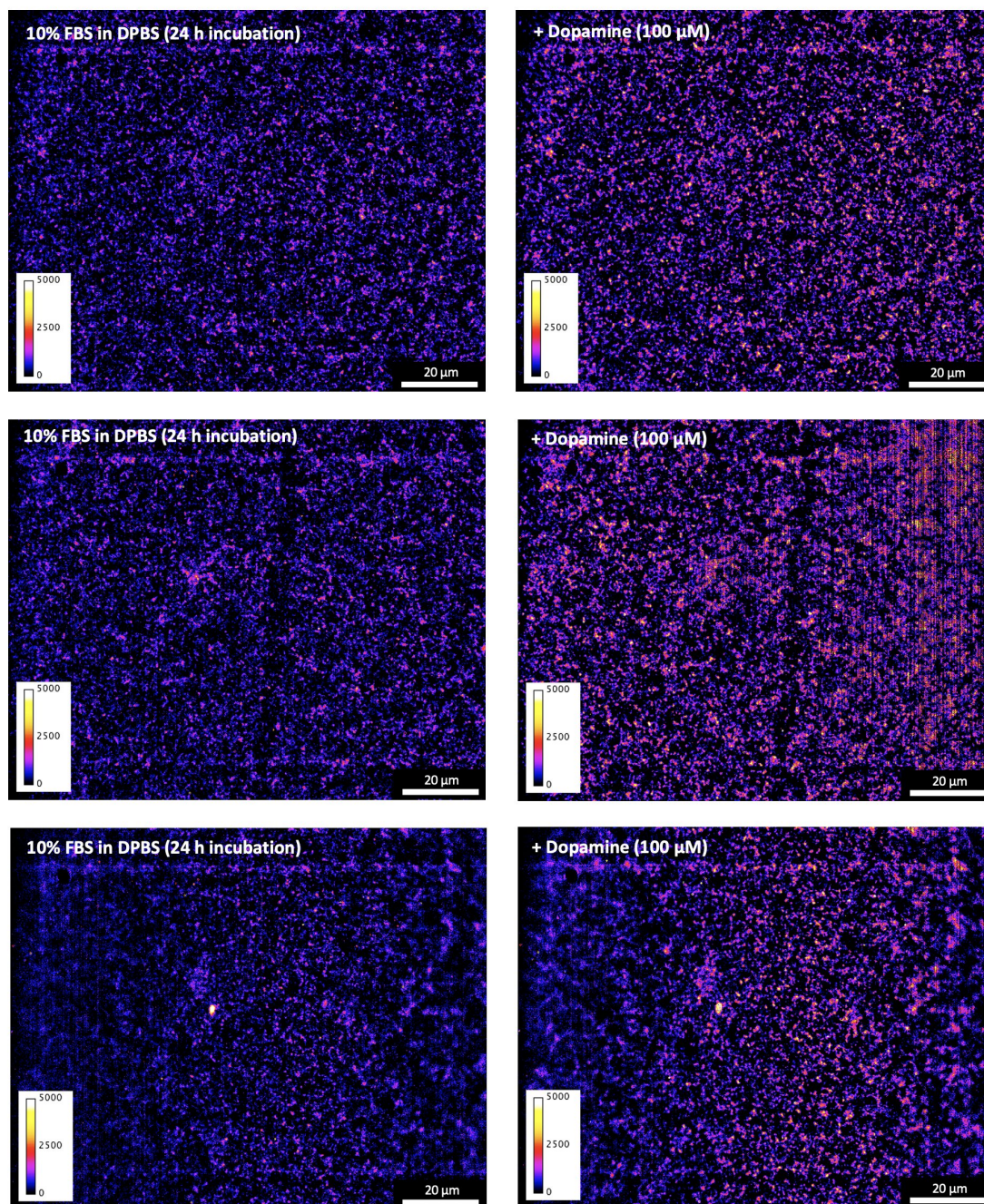


Figure E.10 – Single molecule response behavior of more ultrahigh density LNA_{every5}-SWCNT sensor films in 10% FBS (v/v) towards dopamine (final concentration: 100 μM). All films were incubated for 24 h at room temperature prior to measurement. Three representative images of LNA_{every5} sensor films before (**left**) and after (**right**) the addition of dopamine. All samples were incubated for 15 min post-dopamine addition prior to acquiring the images (excitation: 780 nm, emission filter: 980 nm LP, exposure time: 1 s). Backgrounds were subtracted using a Gaussian blur filter (sigma = 25).

E.1. Using XNA-SWCNTs for *In Vitro* Sensing Applications

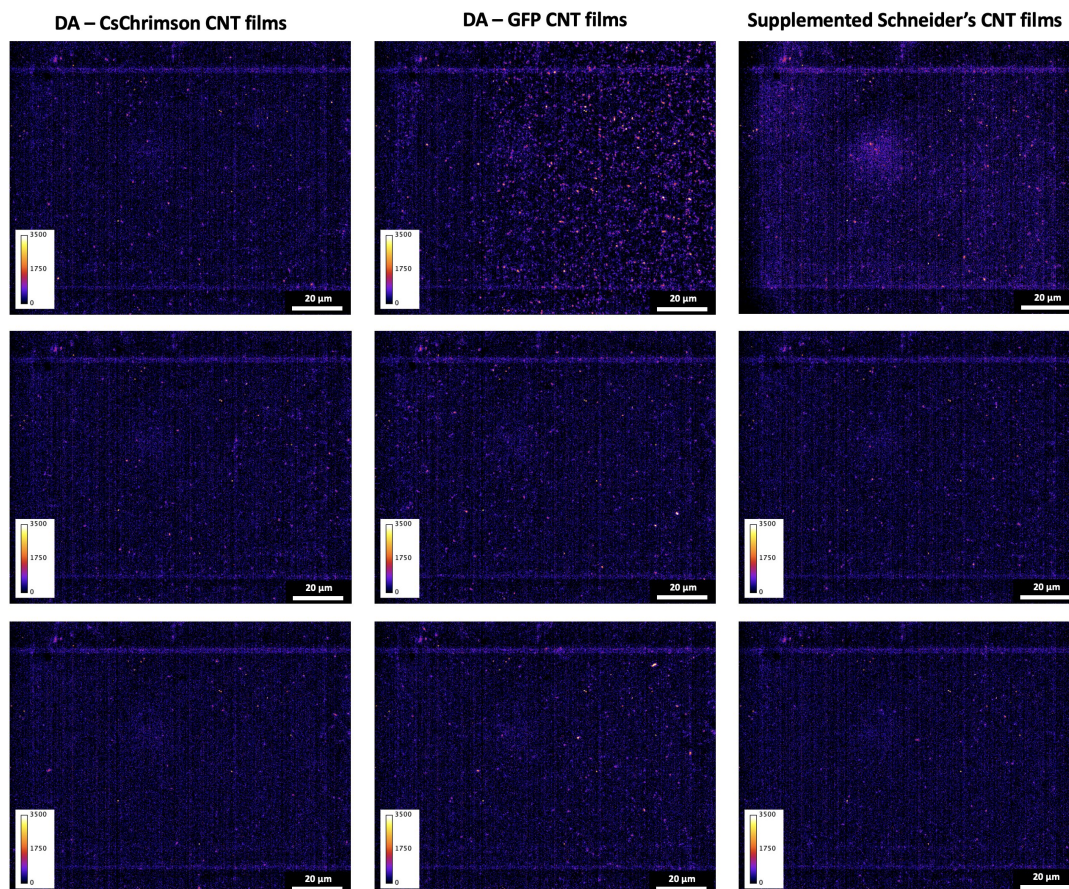


Figure E.11 – Comparison of LNA_{every5}-SWCNT sensor films following 48 h of incubation in supplemented Schneider's medium both with and without cells (excitation: 780 nm, emission filter: 980 nm LP, exposure time: 1 s). *Drosophila* neuronal cell cultures containing transgenic dopamine neurons (representing approximately 1% of the sample) induced to express either GFP (DA-GFP) or CsChrimson (DA-CsChrimson) were grown on the nanotube films for 48 h at room temperature in supplemented Schneider's medium. Films incubated in supplemented Schneider's medium at room temperature for 48 h without cells were used for comparison to examine whether there was any change in the fluorescence properties of the nanotubes due to the presence of cells. Backgrounds were subtracted using a Gaussian blur filter (sigma = 25).

Appendix E. Outlook on Potential Applications of XNA-SWCNTs for Improved Optical Biosensing

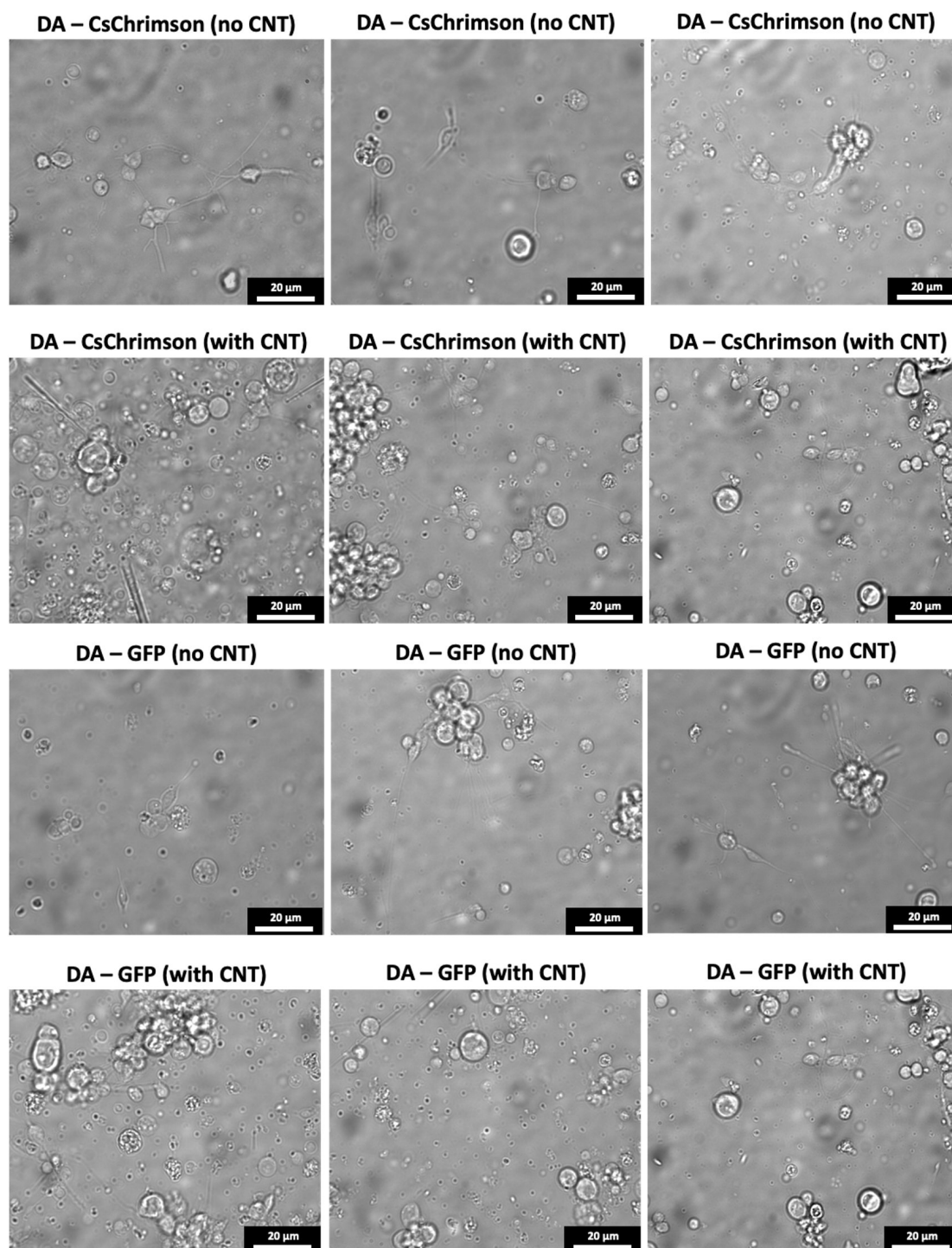


Figure E.12 – *Drosophila* neuronal cell cultures containing transgenic dopamine neurons (representing approximately 1% of the sample) were induced to express either GFP (DA-GFP) or CsChrimson (DA-CsChrimson). White light visible widefield images of the neurons were acquired following 48h of growth on poly-L-lysine coated glass petri dishes (**no CNT**) or LNA_{every5}-SWCNT covered poly-L-lysine coated glass petri dishes (**with CNT**) to examine the effect of nanotubes on cell growth.

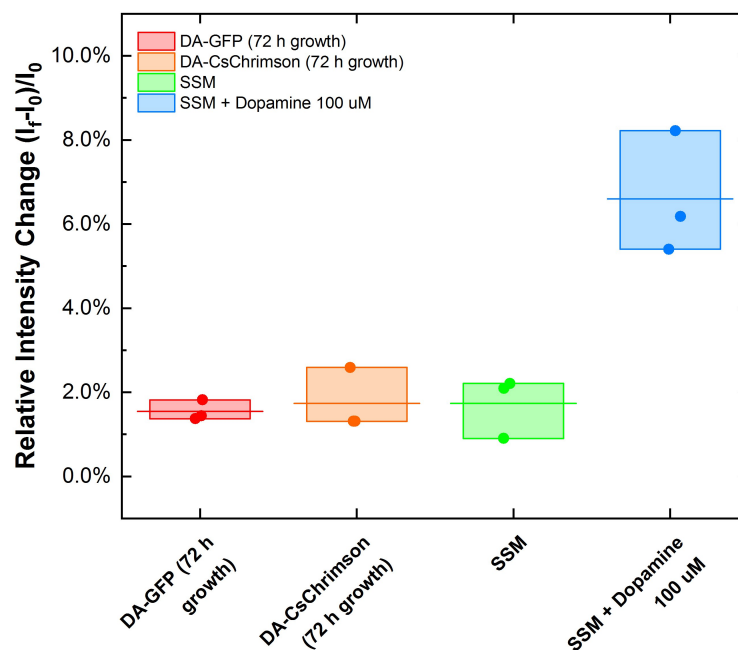


Figure E.13 – Fluorescence intensity increase of LNA_{every5} films in DI water following the addition of different media samples. Media was extracted from *Drosophila* neuronal cell cultures containing transgenic dopamine neurons (representing approximately 1% of the sample) induced to express GFP (DA-GFP) or CsChrimson (DA-CsChrimson). Cells were grown on poly-L-lysine coated glass bottom petri dishes for 72 h at room temperature in supplemented Schneider's medium. Supplemented Schneider's medium (SSM) was used as a negative control and SSM spiked with 100 μ M dopamine was used as a positive control. Intensity changes were calculated from the mean intensity of the widefield images obtained (**Appendix Figure E.14 – E.17**). The central line represents the average turn-on response. Dots represent the turn-on response of individual replicates (n = 3 technical replicates).

Appendix E. Outlook on Potential Applications of XNA-SWCNTs for Improved Optical Biosensing

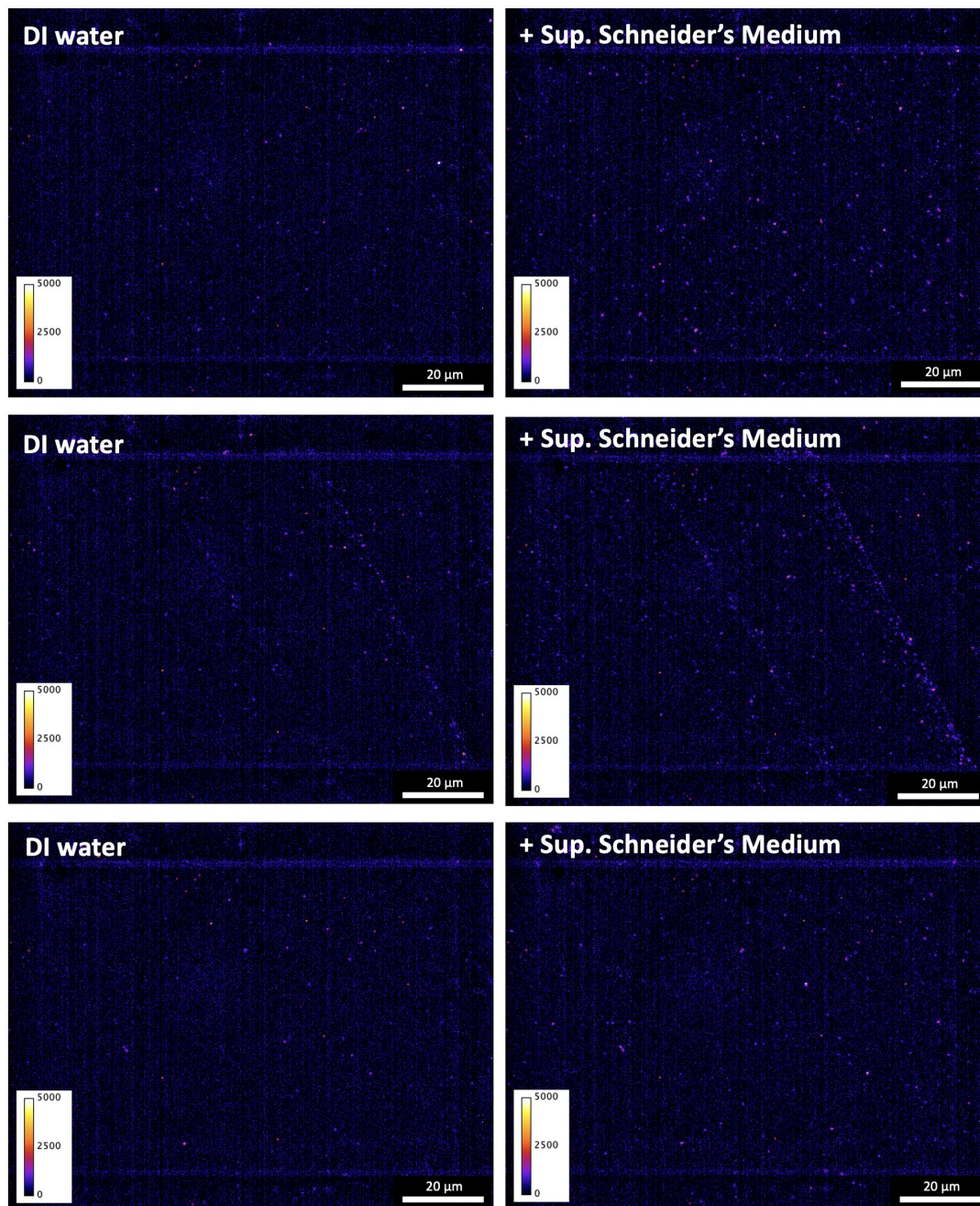


Figure E.14 – Single molecule response of LNA_{every5}-SWCNT sensor films in DI water to the addition of supplemented Schneider's medium. Films were initially wetted with 100 μ L of DI water and incubated for 15 min prior to adding 10 μ L of supplemented Schneider's medium. Three representative images of LNA_{every5} sensor films before (**left**) and after (**right**) the addition of medium were acquired. All samples were incubated for 15 min post medium addition prior to acquiring the images (excitation: 780 nm, emission filter: 980 nm LP, exposure time: 1 s). Backgrounds were subtracted using a Gaussian blur filter ($\sigma = 25$).

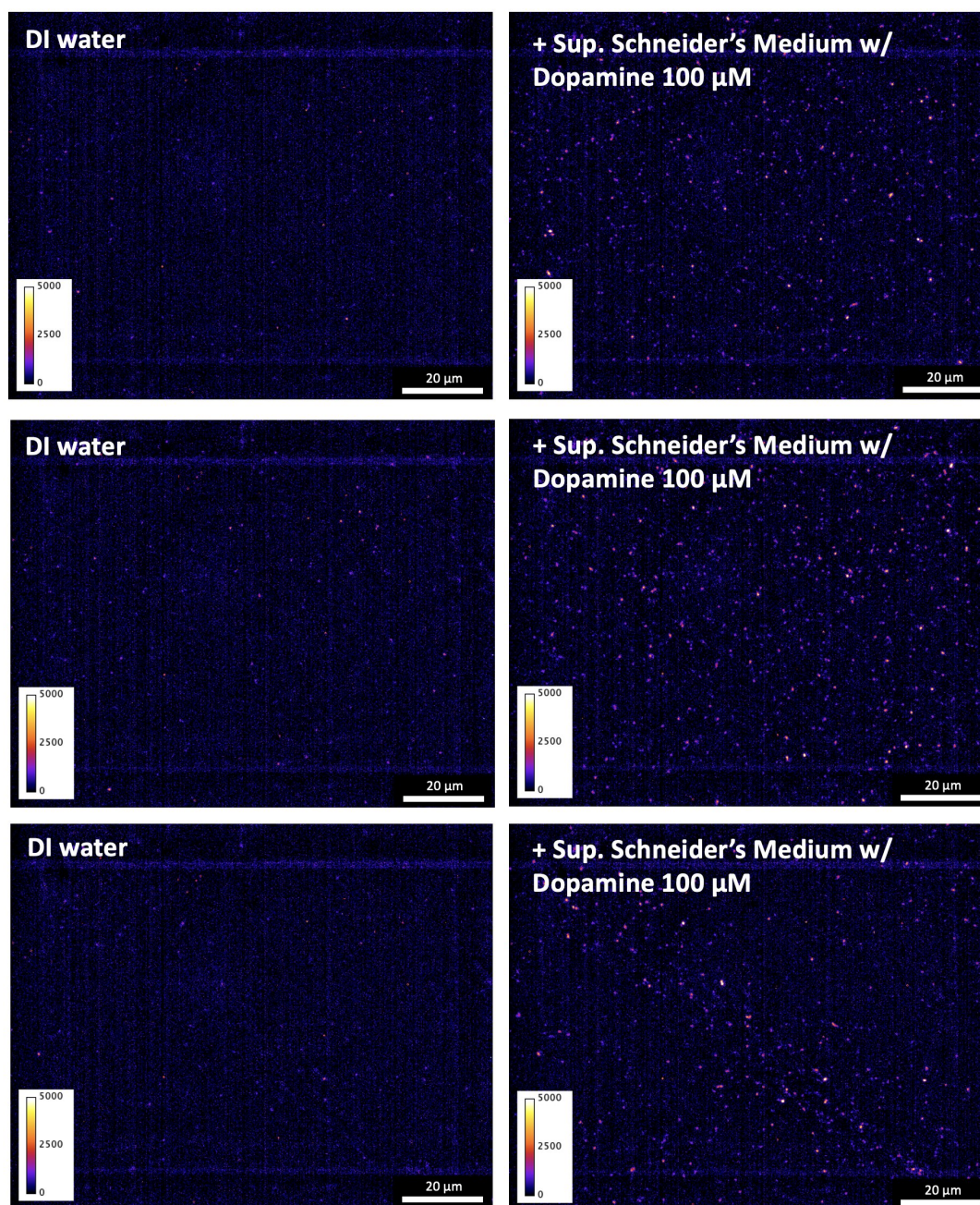


Figure E.15 – Single molecule response of LNA_{every5}-SWCNT sensor films in DI water to the addition of supplemented Schneider's medium spiked with 100 μM dopamine (final concentration: = 9.1 μM). Films were initially wetted with 100 μL of DI water and incubated for 15 min prior to adding 10 μL of supplemented Schneider's medium freshly prepared with 100 μM dopamine. Three representative images of LNA_{every5} sensor films before (**left**) and after (**right**) the addition of medium were acquired. All samples were incubated for 15 min post medium addition prior to acquiring the images (excitation: 780 nm, emission filter: 980 nm LP, exposure time: 1 s). Backgrounds were subtracted using a Gaussian blur filter (sigma = 25).

Appendix E. Outlook on Potential Applications of XNA-SWCNTs for Improved Optical Biosensing

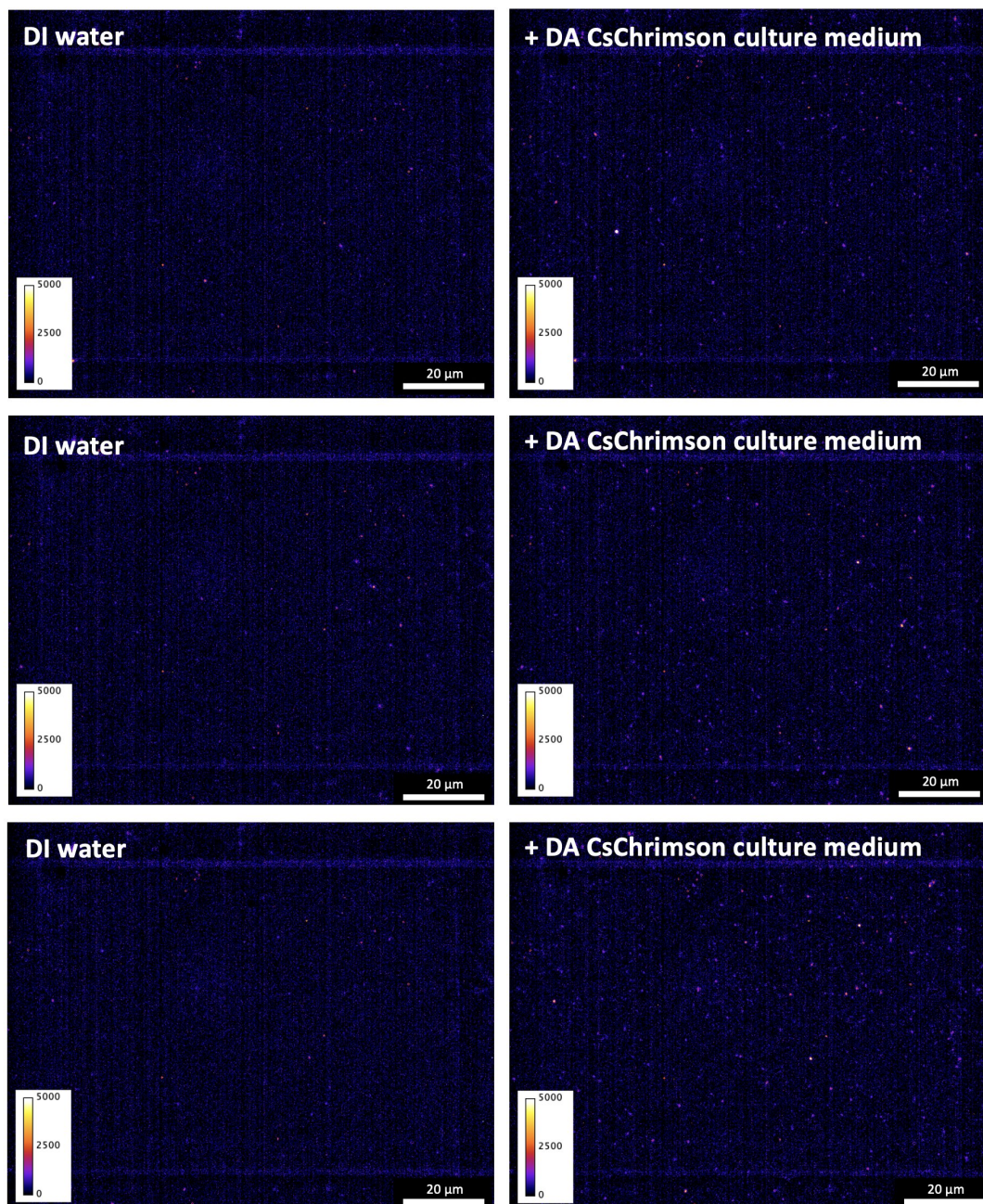


Figure E.16 – Single molecule response of LNA_{every5}-SWCNT sensor films in DI water to the addition of medium extracted from a neuronal cell culture containing transgenic dopamine neurons induced to express CsChrimson (DA-CsChrimson). Cells were grown on poly-L-lysine coated glass bottom petri dishes for 72 h at room temperature in supplemented Schneider's medium, which was replenished as necessary to prevent the culture from drying out. Films were initially wetted with 100 μL of DI water and incubated for 15 min prior to adding 10 μL of the extracted medium. Three representative images of LNA_{every5} sensor films before (**left**) and after (**right**) the addition of medium were acquired. All samples were incubated for 15 min post medium addition prior to acquiring the images (excitation: 780 nm, emission filter: 980 nm LP, exposure time: 1 s). Backgrounds were subtracted using a Gaussian blur filter (sigma = 25).

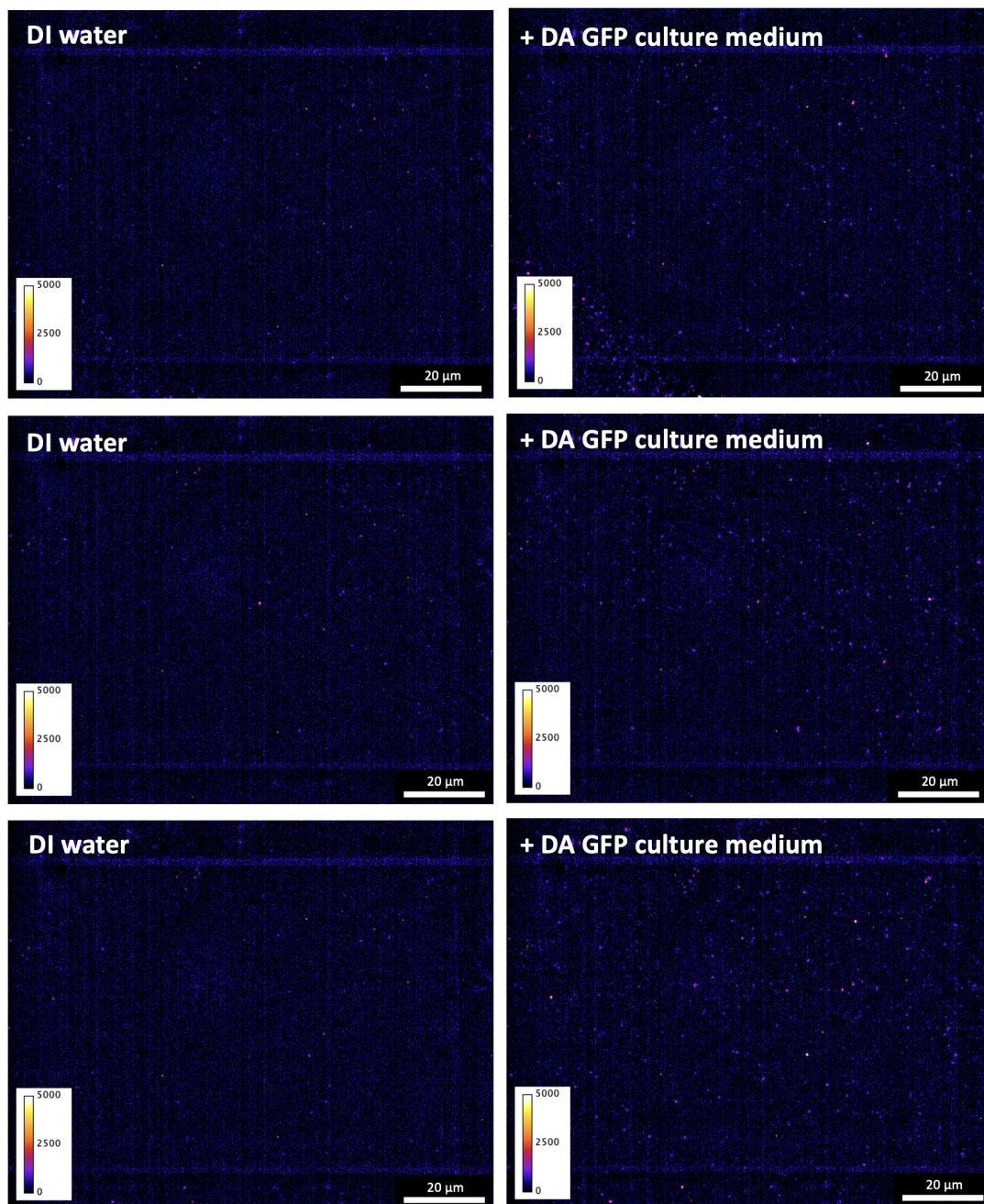


Figure E.17 – Single molecule response of LNA_{every5}-SWCNT sensor films in DI water to the addition of medium extracted from a neuronal cell culture containing transgenic dopamine neurons induced to express GFP (DA-GFP). Cells were grown on poly-L-lysine coated glass bottom petri dishes for 72 h at room temperature in supplemented Schneider's medium, which was replenished as necessary to prevent the culture from drying out. Films were initially wetted with 100 μL of DI water and incubated for 15 min prior to adding 10 μL of the extracted medium. Three representative images of LNA_{every5} sensor films before (**left**) and after (**right**) the addition of medium were acquired. All samples were incubated for 15 min post medium addition prior to acquiring the images (excitation: 780 nm, emission filter: 980 nm LP, exposure time: 1 s). Backgrounds were subtracted using a Gaussian blur filter (sigma = 25).

Appendix E. Outlook on Potential Applications of XNA-SWCNTs for Improved Optical Biosensing

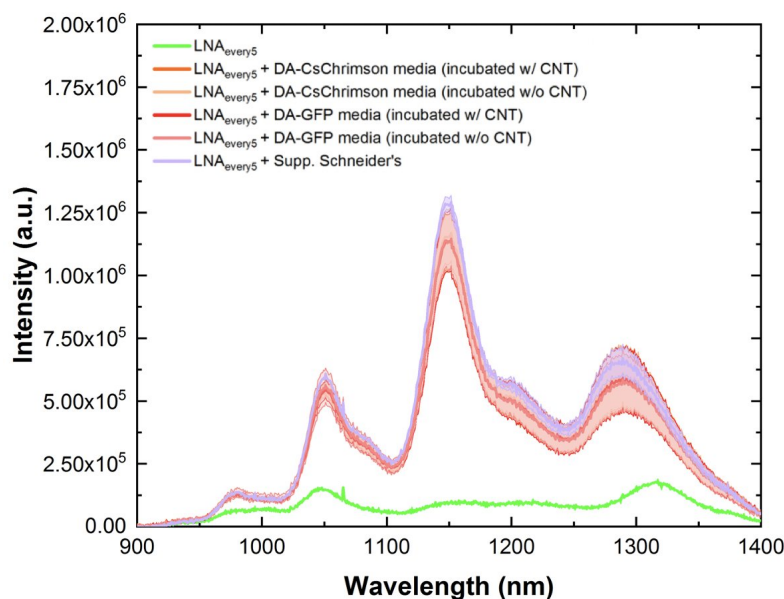


Figure E.18 – Fluorescence response of LNA_{every5}-SWCNTs towards the addition of medium extracted from *Drosophila* neuronal cell cultures (excitation: 660 nm, exposure time: 10 s). Included are the spectra before (green) and following addition supplemented Schneider's medium (purple), or medium extracted from the cell culture. The solid line represents the average wavelength shift and all shaded regions represent 1 σ standard deviation (n = 3 technical replicates). All cell cultures contained transgenic dopamine neurons induced to either express GFP (DA-GFP) or CsChrimson (DA-CsChrimson). Cells were grown for 48 h on poly-L-lysine coated glass bottom well plates either with (w/ CNT) or without (w/o CNT) nanotubes present.

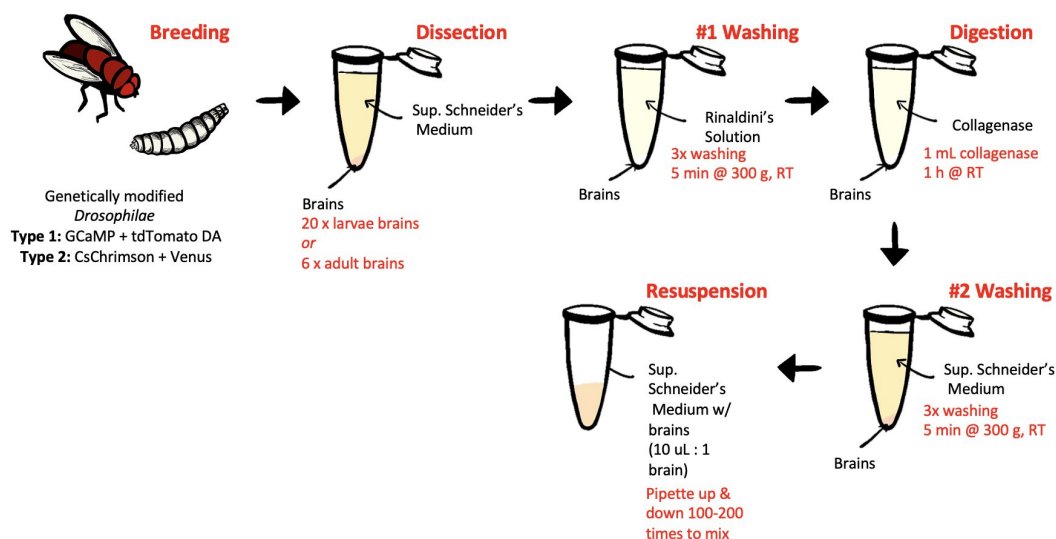


Figure E.19 – Schematic of the protocol used to extract *Drosophila* neurons from adult or larvae brains. Neurons resuspended in supplemented Schneider's medium could then be plated in either 96-well plates or glass-bottom petri dishes.

E.2 XNA-SWCNTs for miRNA Detection

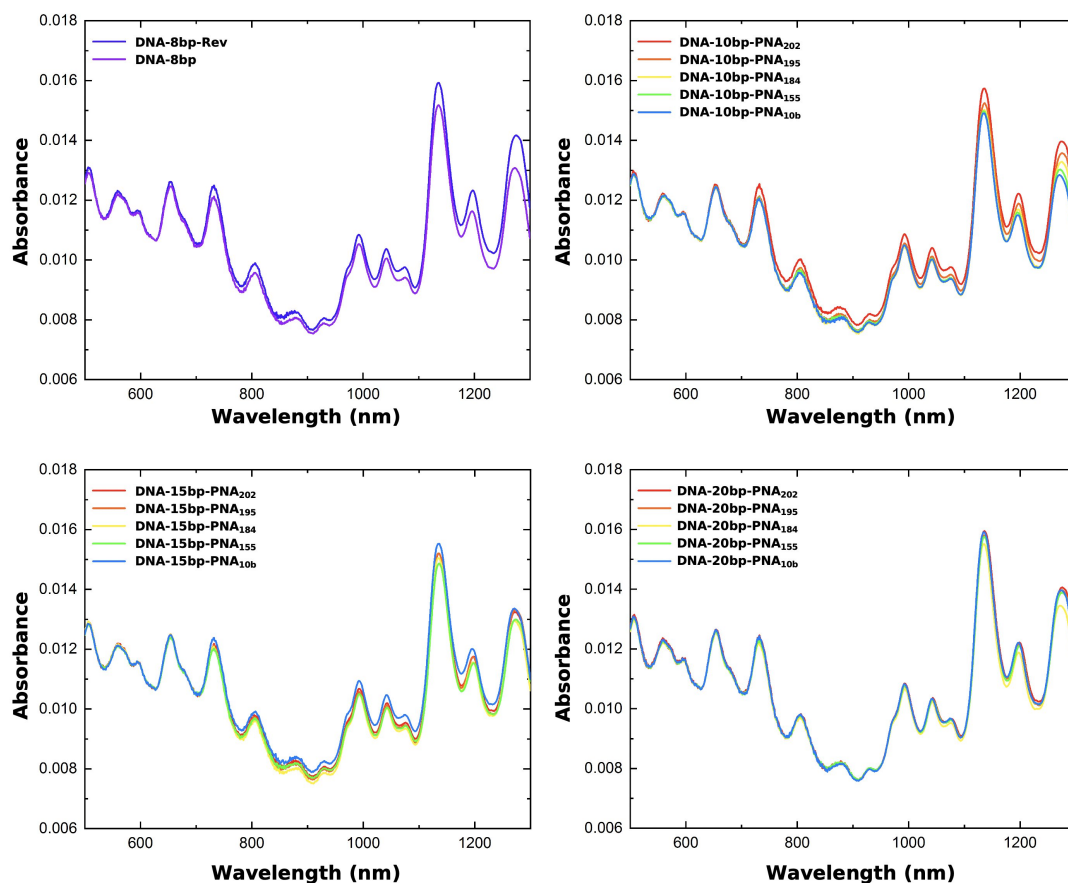


Figure E.20 – Normalized absorbance spectra for all DNA-SWCNT suspensions used in this study. All DNA-SWCNT suspensions were prepared using MeOH assisted surfactant exchange. DNA sequences used are detailed in **Appendix Table E.1**. All spectra were normalized to concentration using an extinction coefficient of 0.036 mg/L at Abs_{632nm}.

Appendix E. Outlook on Potential Applications of XNA-SWCNTs for Improved Optical Biosensing

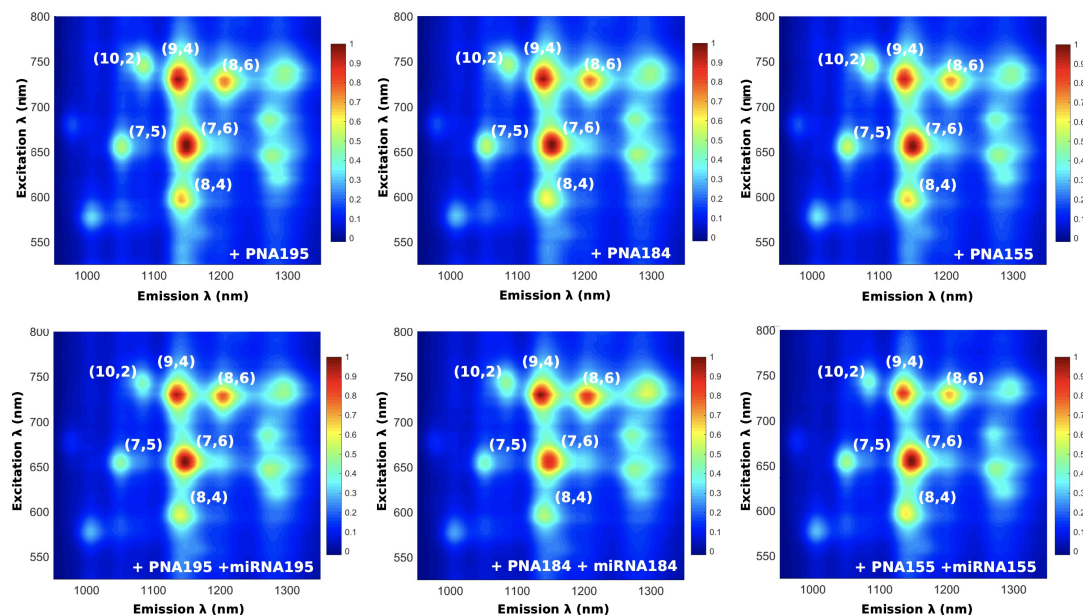


Figure E.21 – PLE maps of the PNA-DNA_{8bp-rev}-SWCNT solutions (PNA₁₉₅, PNA₁₈₄, and PNA₁₅₅) before (**top**) and after (**bottom**) addition of complementary miRNA (final concentration: PNA = 9.5 μ M, miRNA = 4.8 μ M). The predominate chiralities are labelled in white. All fluorescence intensities were normalized to the maximum intensity in each plot.

Name	Sequence (5' to 3')	Length	GC content	Hybrid portion length	GC content in hybrid
DNA _{8bp} -rev	GTG TGT GTG TGT GTG TGT GTG AAG AGA C	28 bases	50%	8 bases	50%
DNA _{8bp}	GTG TGT GTG TGT GTG TGT GTG AGA GAA G	28 bases	50%	8 bases	50%
PNA _{10b} -DNA _{10bp}	GTG TGT GTG TGT GTG TGT GTG AGA GAA GGT	30 bases	50%	10 bases	50%
PNA ₁₅₅ -DNA _{10bp}	GTG TGT GTG TGT GTG TGT GTG AGA GAA GTT	30 bases	47%	10 bases	40%
PNA ₁₈₄ -DNA _{10bp}	GTG TGT GTG TGT GTG TGT GTG AGA GAA GTG	30 bases	50%	10 bases	50%
PNA ₁₉₅ -DNA _{10bp}	GTG TGT GTG TGT GTG TGT GTG AGA GAA GCG	30 bases	53%	10 bases	60%
PNA ₂₀₂ -DNA _{10bp}	GTG TGT GTG TGT GTG TGT GTG AGA GAA GAA	30 bases	47%	10 bases	40%
PNA _{10b} -DNA _{15bp}	GTG TGT GTG TGT GTG TGT GTG AGA GAA GGT GTT TA	35 bases	46%	15 bases	40%
PNA ₁₅₅ -DNA _{15bp}	GTG TGT GTG TGT GTG TGT GTG AGA GAA GTT GGG GA	35 bases	51%	15 bases	53%
PNA ₁₈₄ -DNA _{15bp}	GTG TGT GTG TGT GTG TGT GTG AGA GAA GTG GGA AT	35 bases	49%	15 bases	47%
PNA ₁₉₅ -DNA _{15bp}	GTG TGT GTG TGT GTG TGT GTG AGA GAA GCG GTT AT	35 bases	49%	15 bases	47%
PNA ₂₀₂ -DNA _{15bp}	GTG TGT GTG TGT GTG TGT GTG AGA GAA GAA GGG TA	35 bases	49%	15 bases	47%
PNA _{10b} -DNA _{20bp}	GTG TGT GTG TGT GTG TGT GTG AGA GAA GGT GTT TAA GCC A	40 bases	48%	20 bases	45%
PNA ₁₅₅ -DNA _{20bp}	GTG TGT GTG TGT GTG TGT GTG AGA GAA GTT GGG GAT AGT G	40 bases	50%	20 bases	50%
PNA ₁₈₄ -DNA _{20bp}	GTG TGT GTG TGT GTG TGT GTG AGA GAA GTG GGA ATA GTC A	40 bases	48%	20 bases	45%
PNA ₁₉₅ -DNA _{20bp}	GTG TGT GTG TGT GTG TGT GTG AGA GAA GCG GTT ATA AAG A	40 bases	45%	20 bases	40%
PNA ₂₀₂ -DNA _{20bp}	GTG TGT GTG TGT GTG TGT GTG AGA GAA GAA GGG TAC GGG A	40 bases	53%	20 bases	55%

Table E.1 – List of DNA sequences used to prepare the solutions of SWCNTs used in this study. All sequences consisted of a (GT)₁₀- anchor sequence and 8 - 20 nucleotide for conjugation with the complementary PNA sequence. All suspensions were prepared using MeOH assisted surfactant exchange. Solutions were stored at 4°C to prevent aggregation. PNA was added to the mixtures immediately prior to measurement.

Appendix E. Outlook on Potential Applications of XNA-SWCNTs for Improved Optical Biosensing

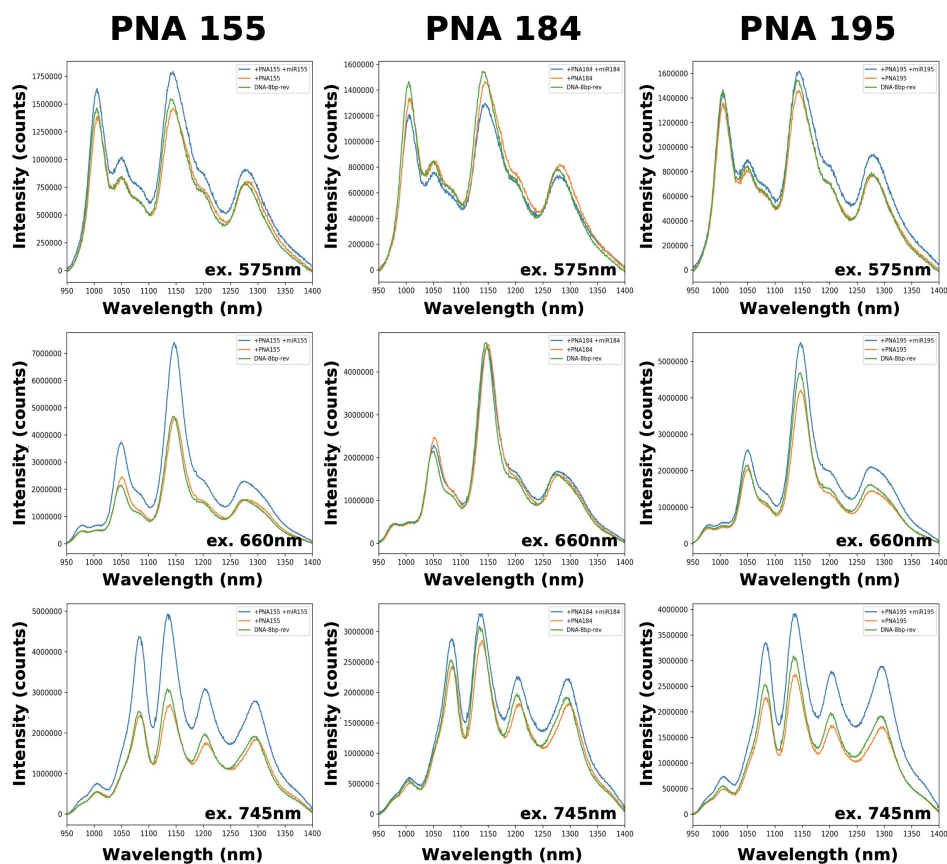


Figure E.22 – Spectra extracted from PLE maps to compare the intensity and wavelength positions of the DNA_{8bp-rev}-SWCNTs (green), the PNA-DNA_{8bp-rev}-SWCNTs (orange), and the PNA-DNA_{8bp-rev}-SWCNTs following the addition of complementary miRNA (blue) for hybrids formed using PNA₁₅₅ (left), PNA₁₈₄ (center), or PNA₁₉₅ (right) (final concentration: PNA = 9.5 μ M, miRNA = 4.8 μ M). The wavelength of the excitation laser used is indicated in the lower right corner.

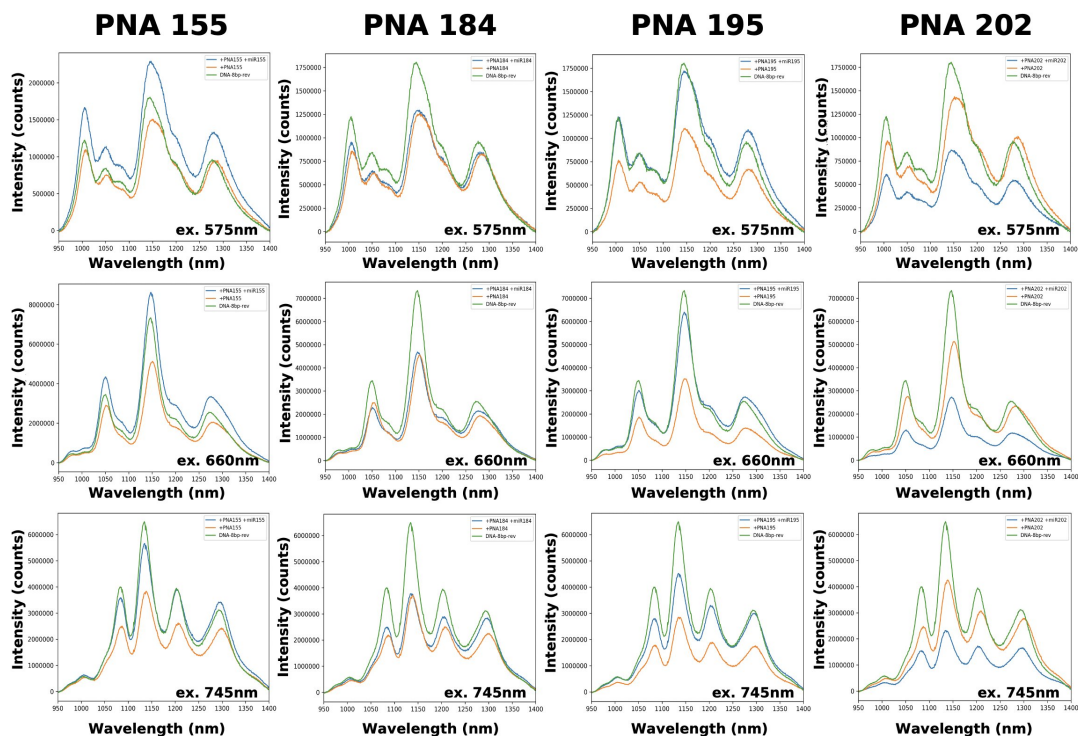


Figure E.23 – Spectra extracted from PLE maps to compare the intensity and wavelength positions of the DNA_{8bp-rev}-SWCNTs (green), the PNA-DNA_{8bp-rev}-SWCNTs (orange), and the PNA-8bp-rev-SWCNTs following the addition of complementary miRNA (blue) for hybrids formed using PNA₁₅₅, PNA₁₈₄, PNA₁₉₅, or PNA₂₀₂ (final concentration: PNA = 9.5 μ M, miRNA = 4.8 μ M). All samples were incubated overnight (16 h) prior to acquiring the PLE maps. The wavelength of the excitation laser used is indicated in the lower right corner.

Appendix E. Outlook on Potential Applications of XNA-SWCNTs for Improved Optical Biosensing

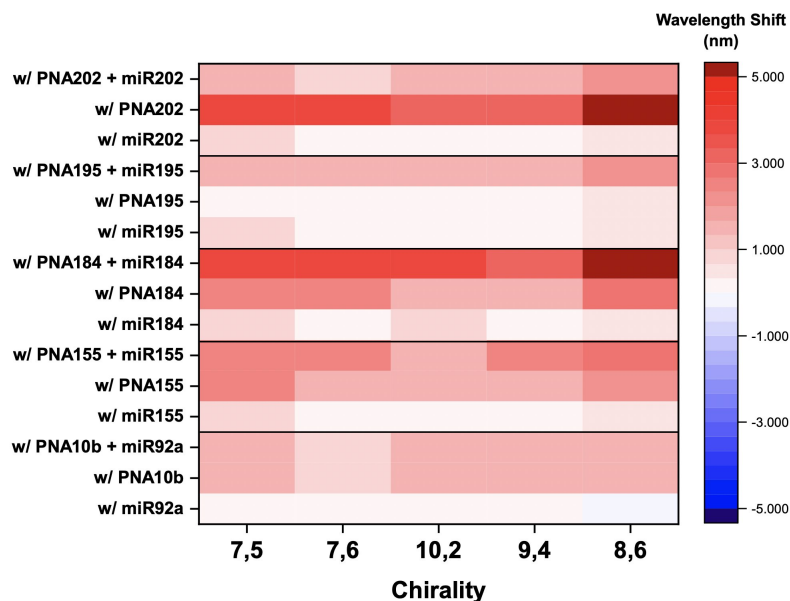


Figure E.24 – Fluorescence wavelength shift of the (7,5), (7,6), (10,2), (9,4), and (8,6) peaks following the addition of PNA, miRNA, or PNA + miRNA to DNA_{8bp-rev}-SWCNTs (final concentration: PNA = 9 μ M, miRNA = 1 μ M). All wavelength shifts were calculated versus the peak positions for DNA_{8bp-rev}-SWCNTs. **Red** indicates a redshift in the wavelength position of the chirality peak and **blue** represents a blueshift in the wavelength position.

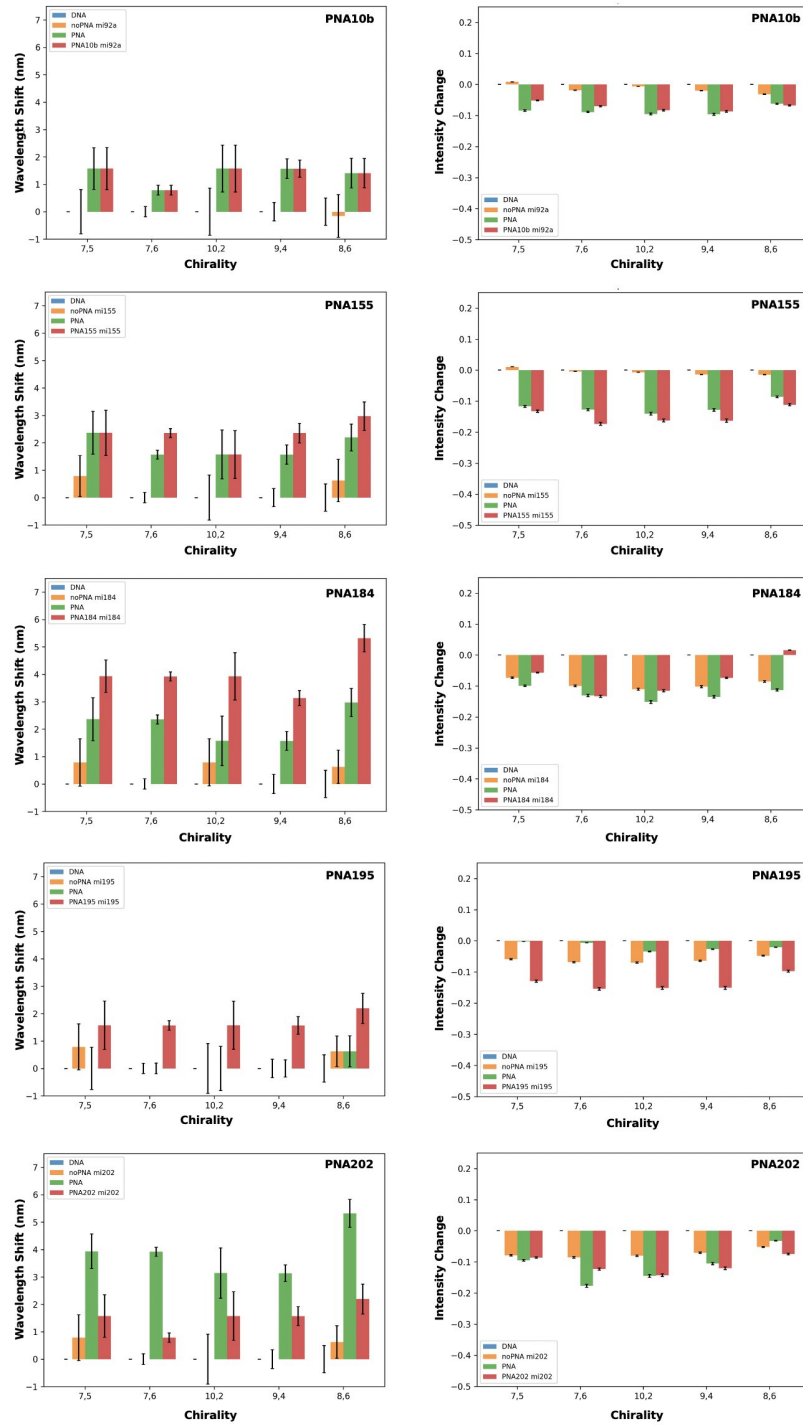


Figure E.25 – Comparison of the chirality dependent wavelength shifts (**left**) and intensity changes (**right**) for DNA_{8bp-rev}-SWCNTs following addition of miRNA (orange), PNA (green), and PNA with miRNA (red) (final concentration: PNA = 9 μ M, miRNA = 1 μ M). All wavelength shifts were calculated versus the wavelength positions for DNA_{8bp-rev}-SWCNTs. For DNA_{8bp-rev}-SWCNTs, error bars represent 1 σ standard deviation (n = 5 technical replicates). For all other samples error bars represent the error on the fit of the peak (3 σ from one technical replicate). For PNA_{10b} (**top**) non-complementary miRNA (miR92a) was added while for all other samples the respective complementary miRNA was added.

Appendix E. Outlook on Potential Applications of XNA-SWCNTs for Improved Optical Biosensing

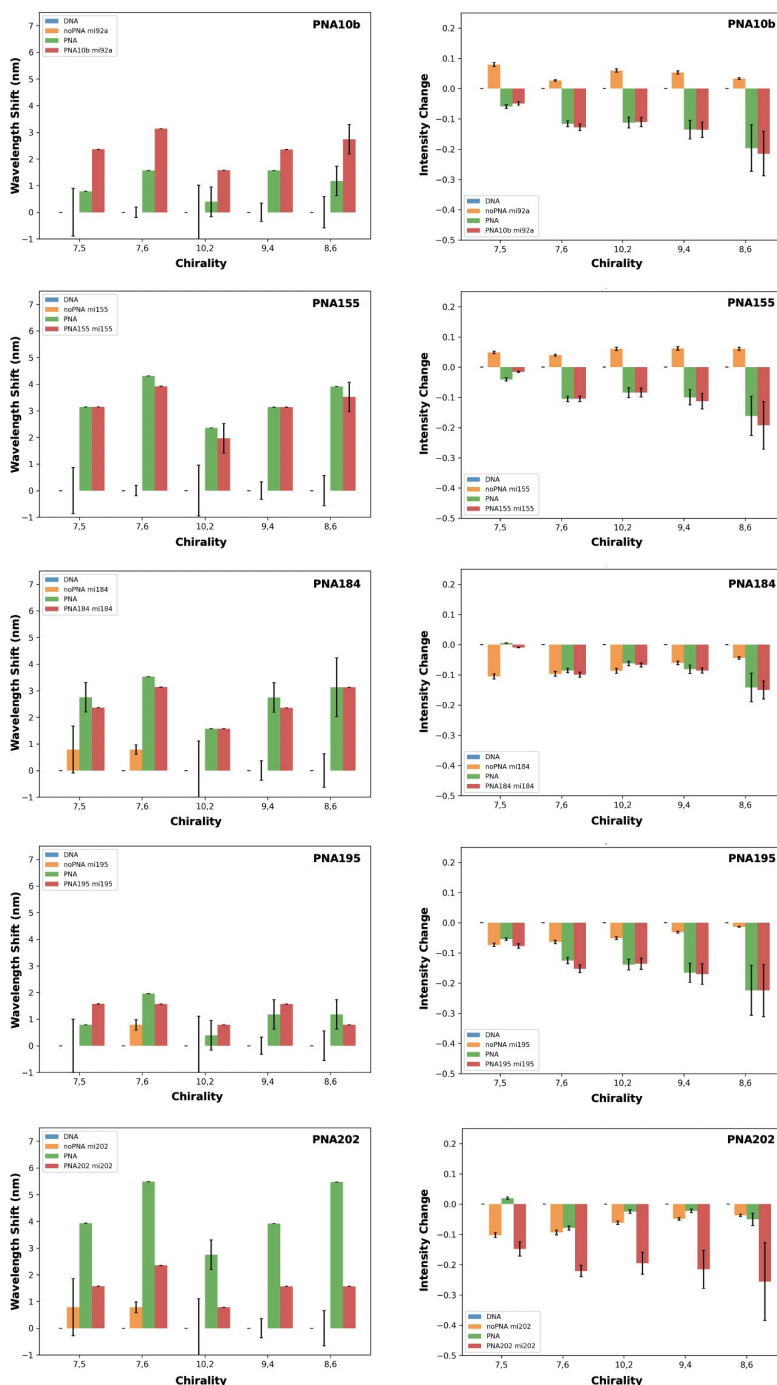


Figure E.26 – Comparison of the chirality dependent wavelength shifts (**left**) and intensity changes (**right**) for DNA_{8bp}-SWCNTs following addition of miRNA (**orange**), PNA (**green**), and PNA with miRNA (**red**) (final concentration: PNA = 9 μ M, miRNA = 1 μ M). All wavelength shifts were calculated versus the wavelength positions for DNA_{8bp}-SWCNTs. For DNA_{8bp}-SWCNTs, error bars represent 1 σ standard deviation (n = 5 technical replicates). For all PNA samples with and without miRNA, error bars represent 1 σ standard deviation (n = 2 technical replicates). For miRNA additions in the absence of PNA error bars represent the error on the fit of the peak (3 σ from one technical replicate). For PNA_{10b} (**top**) non-complementary miRNA (miR92a) was added while for all other samples the respective complementary miRNA was added.

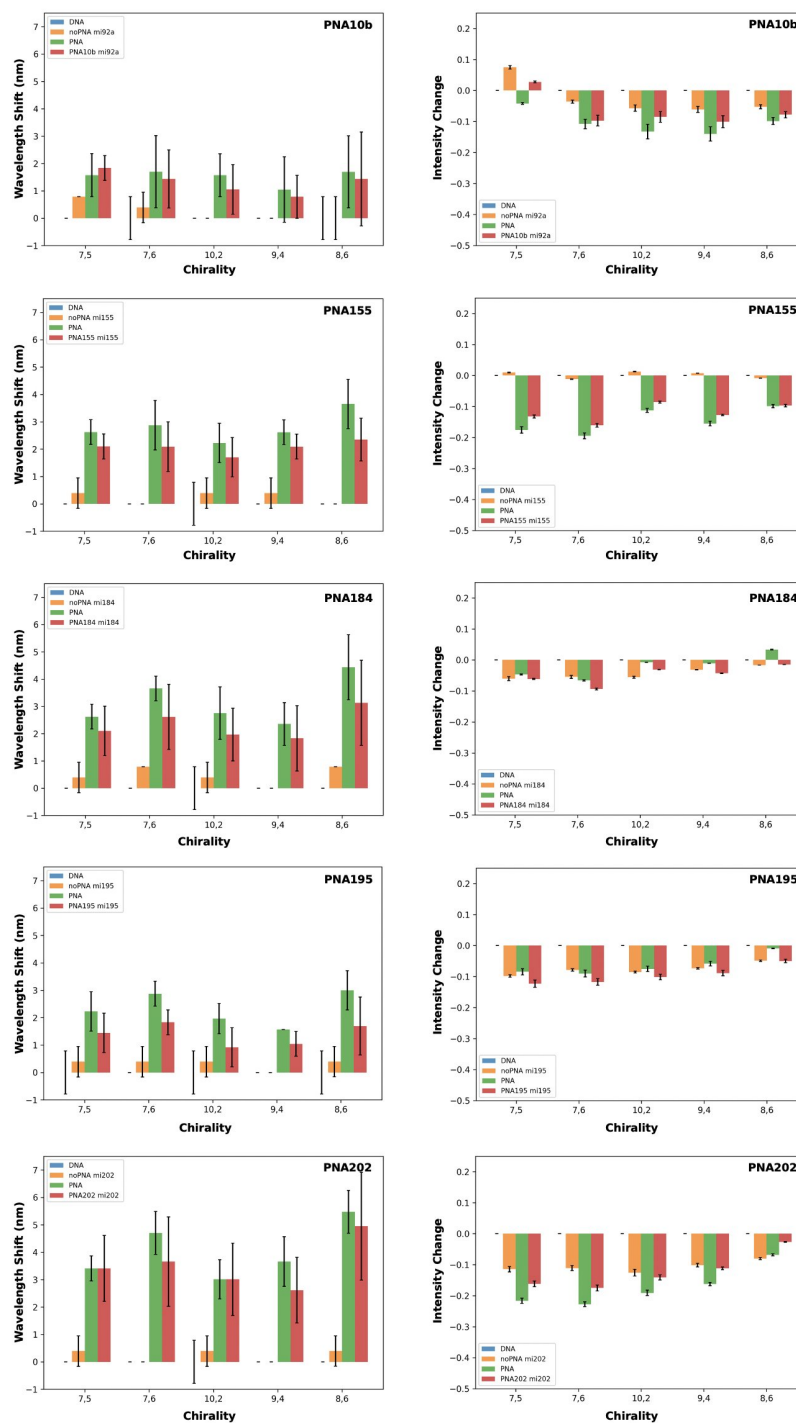


Figure E.27 – Comparison of the chirality dependent wavelength shifts (**left**) and intensity changes (**right**) for DNA_{10bp}-SWCNTs following addition of miRNA (**orange**), PNA (**green**), and PNA with miRNA (**red**) (final concentration: PNA = 9 μ M, miRNA = 1 μ M). All wavelength shifts were calculated versus the wavelength positions for DNA_{10bp}-SWCNTs. For DNA_{10bp}-SWCNTs and miRNA additions in the absence of PNA, error bars represent 1 σ standard deviation ($n = 2$ technical replicates). For all other samples, error bars represent 1 σ standard deviation ($n = 3$ technical replicates). For PNA_{10b} (**top**) non-complementary miRNA (miR92a) was added while for all other samples the respective complementary miRNA was added.

Appendix E. Outlook on Potential Applications of XNA-SWCNTs for Improved Optical Biosensing

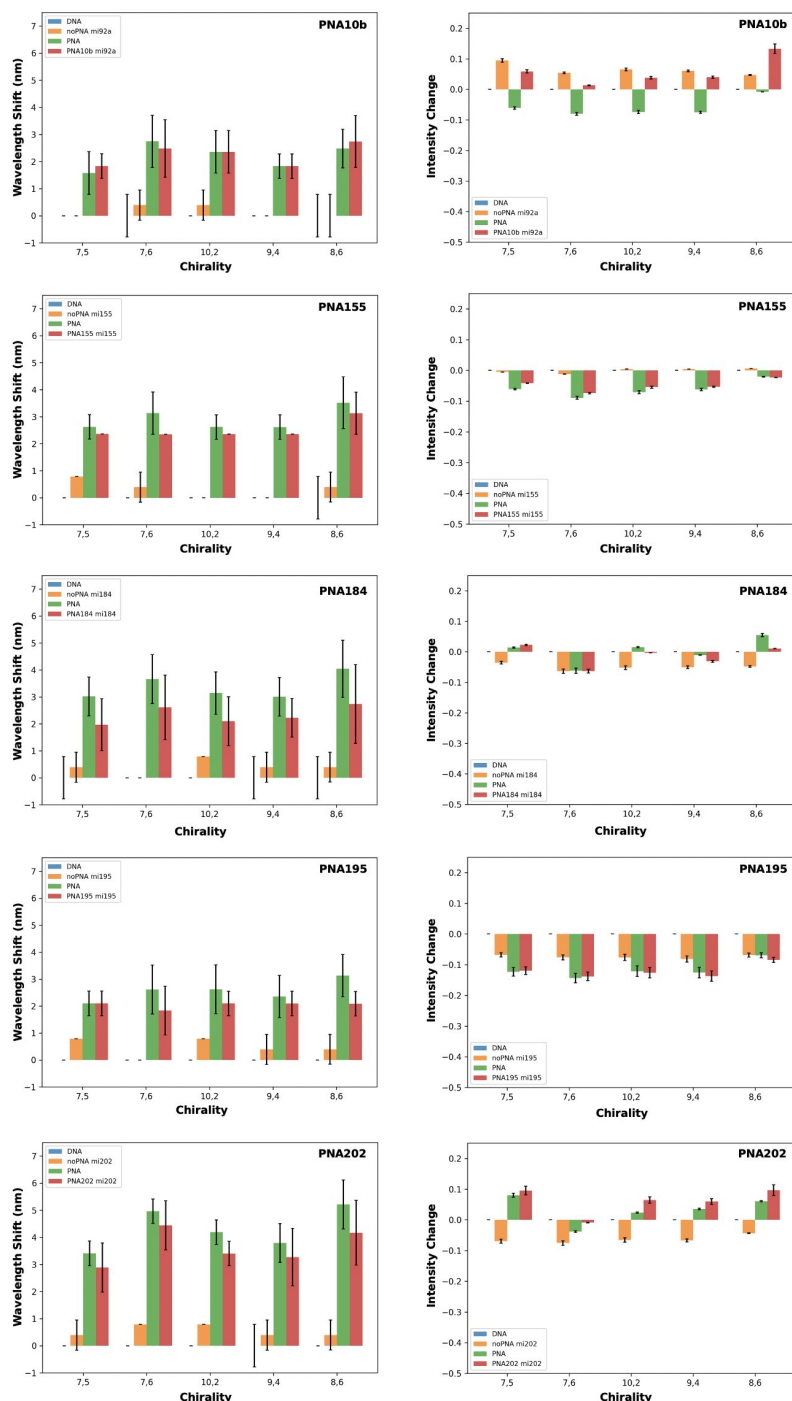


Figure E.28 – Comparison of the chirality dependent wavelength shifts (**left**) and intensity changes (**right**) for DNA_{15bp}-SWCNTs following addition of miRNA (**orange**), PNA (**green**) and PNA with miRNA (**red**) (final concentration: PNA = 9 μ M, miRNA = 1 μ M). All wavelength shifts were calculated versus the wavelength positions for DNA_{15bp}-SWCNTs. For DNA_{15bp}-SWCNTs and miRNA additions in the absence of PNA, error bars represent 1 σ standard deviation ($n = 2$ technical replicates). For all other samples, error bars represent 1 σ standard deviation ($n = 3$ technical replicates). For PNA_{10b} (**top**) non-complementary miRNA (miR92a) was added while for all other samples the respective complementary miRNA was added.

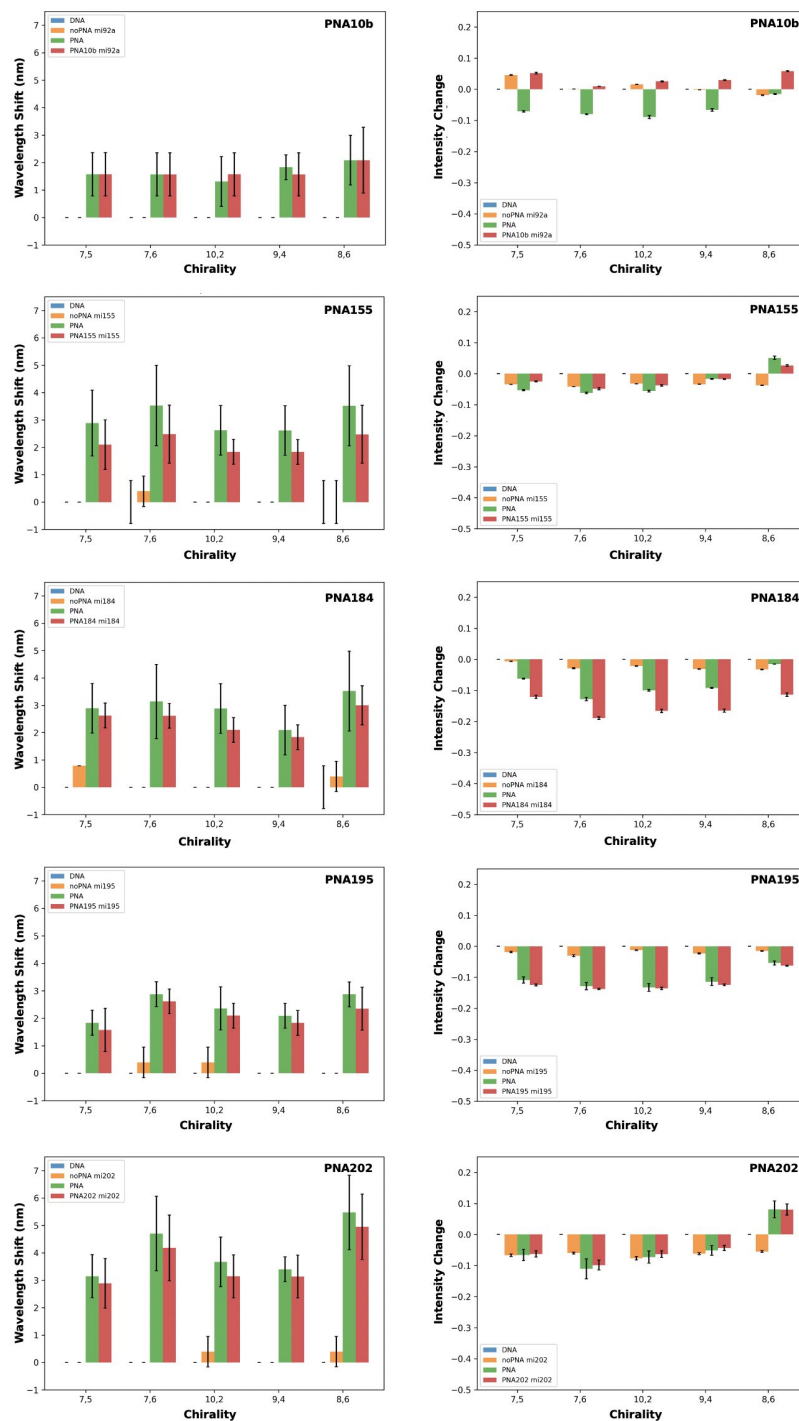


Figure E.29 – Comparison of the chirality dependent wavelength shifts (**left**) and intensity changes (**right**) for DNA_{15bp}-SWCNTs following addition of miRNA (**orange**), PNA (**green**), and PNA with miRNA (**red**) (final concentration: PNA = 9 μ M, miRNA = 1 μ M). All wavelength shifts were calculated versus the wavelength positions for DNA_{20bp}-SWCNTs. For DNA_{20bp}-SWCNTs and miRNA additions in the absence of PNA, error bars represent 1 σ standard deviation ($n = 2$ technical replicates). For all other samples, error bars represent 1 σ standard deviation ($n = 3$ technical replicates). For PNA_{10b} (**top**) non-complementary miRNA (miR92a) was added while for all other samples the respective complementary miRNA was added.

Appendix E. Outlook on Potential Applications of XNA-SWCNTs for Improved Optical Biosensing

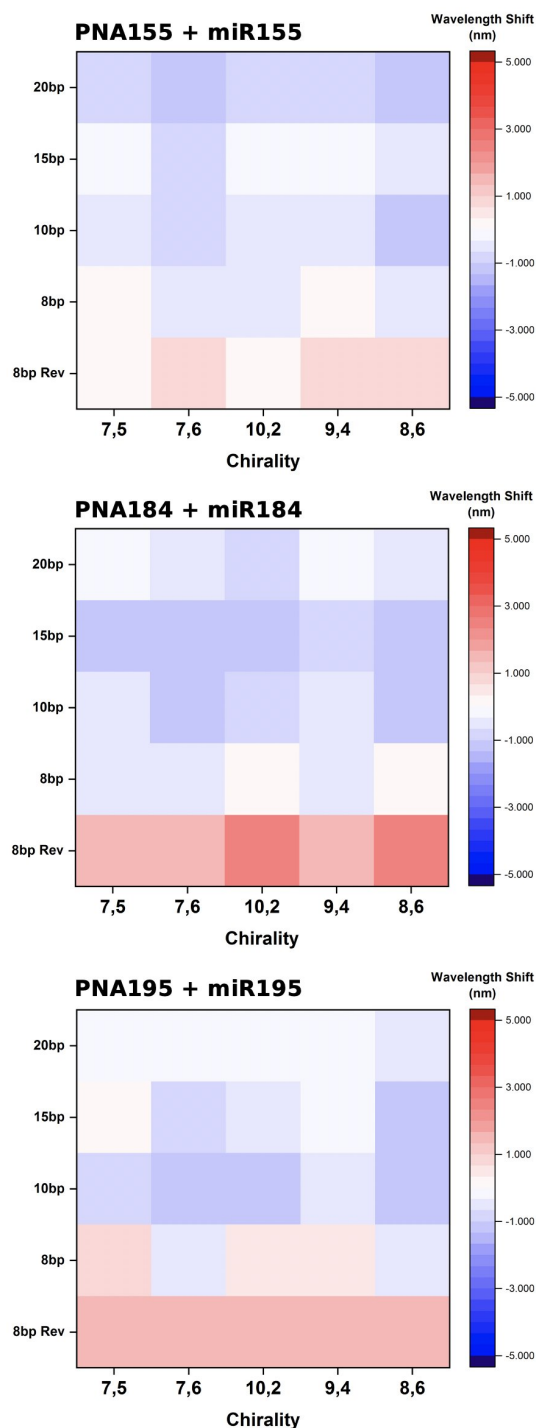


Figure E.30 – Dependency of the wavelength shifting response of PNA₁₅₅, PNA₁₈₄ - and PNA₁₉₅-DNA-SWCNTs on the length of the DNA hybrid portion. Comparison of the wavelength shift following addition of complementary miRNA to PNA-DNA-SWCNTs (final concentration: PNA = 9 μ M, miRNA = 1 μ M). PNA-DNA-SWCNTs were formed using different lengths for the hybrid portion in the DNA sequence (8, 10, 15, or 20 bases) as well as different directionalities for the hybridization (anti-parallel (rev) or parallel). All wavelength shifts were calculated versus the wavelength position of each chirality for the respective PNA-DNA-SWCNTs prior to miRNA addition. **Red** indicates a redshift in the wavelength position of the chirality peak, and **blue** represents a blueshift in the wavelength position.

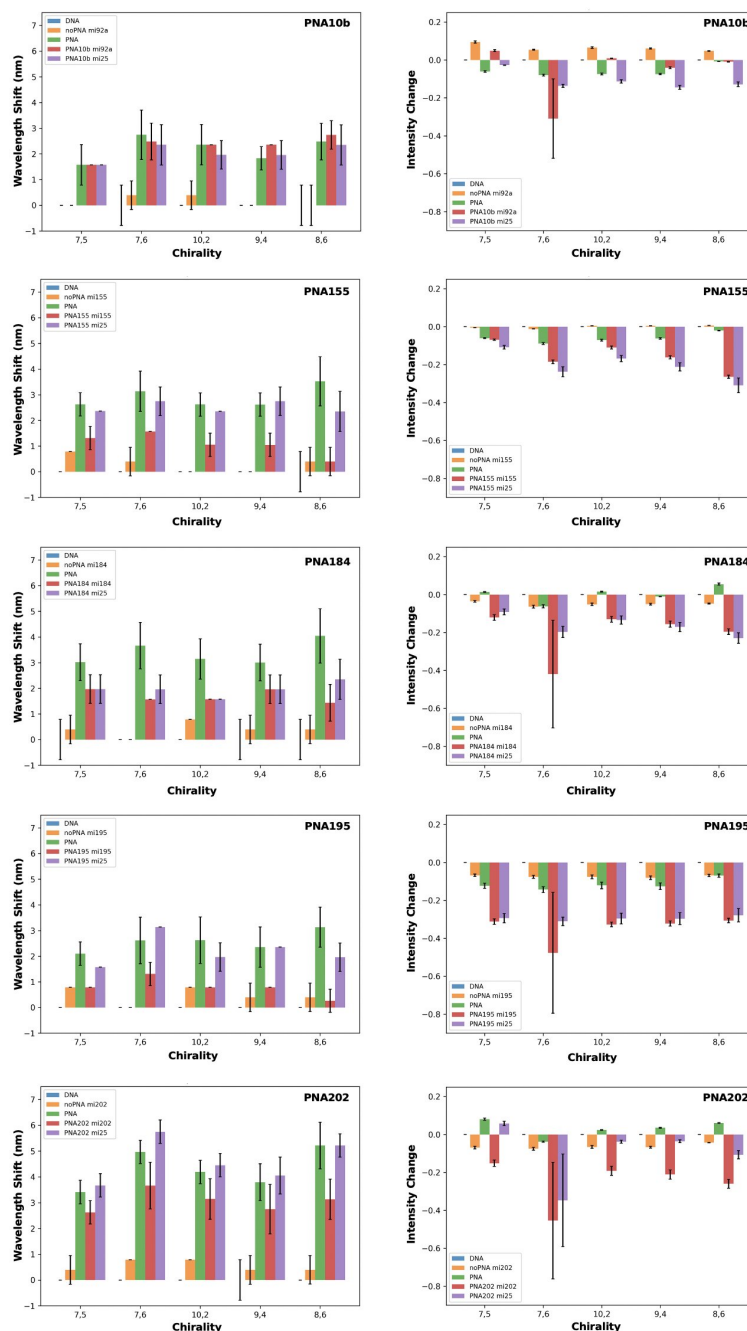


Figure E.31 – Comparison of the chirality dependent wavelength shifts (**left**) and intensity changes (**right**) for DNA_{15bp}-SWCNTs following addition of miRNA (orange), PNA (green), and PNA with either complementary (red) or non-complementary (purple) miRNA. Higher relative concentrations of miRNA were added to increase the ration of miRNA:PNA (final concentration: PNA = 9.4 μ M, miRNA = 5.7 μ M). Complementary miRNA was added to PNA₂₀₂-, PNA₁₉₅-, PNA₁₈₄-, and PNA₁₅₅-DNA_{15bp}-SWCNTs, as well as the non-complementary miR25 for comparison. Two different non-complementary miRNAs (miR25 and miR92a) were added to PNA_{10b}-DNA_{15bp}-SWCNTs. All wavelength shifts were calculated versus the wavelength position of the chiralities for the respective DNA_{15bp}-SWCNT solution prior to any addition. For complementary miRNA additions error bars represent 1 σ standard deviation (n = 3 technical replicates), for all other samples error bars represent 1 σ standard deviation (n = 2 technical replicates).

Appendix E. Outlook on Potential Applications of XNA-SWCNTs for Improved Optical Biosensing

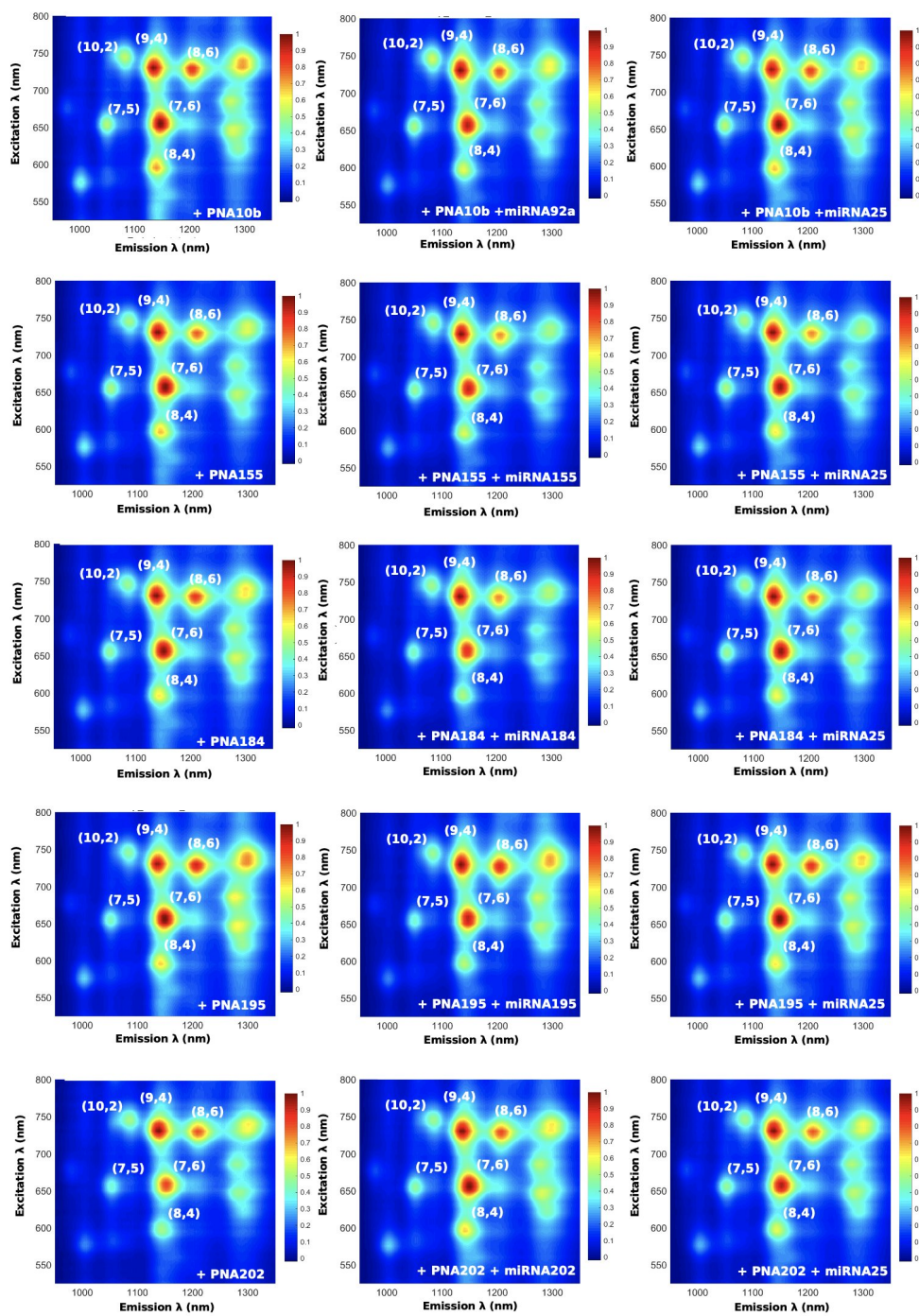


Figure E.32 – PL maps of the PNA-15bp-SWCNT solutions (PNA_{10b}, PNA₁₅₅, PNA₁₈₄, PNA₁₉₅, and PNA₂₀₂) before (**left**) and after addition of complementary (**center**) and non-complementary (miR25, **right**) miRNA (final concentration: PNA = 9.4 μ M, miRNA = 5.7 μ M). For the PNA_{10b}-DNA_{15bp}-SWCNT solution two non-complementary miRNAs were added (miR92a - **center**, miR25 - **right**). The predominate chiralities are labelled in white. All fluorescence intensities were normalized to the maximum intensity in each plot.

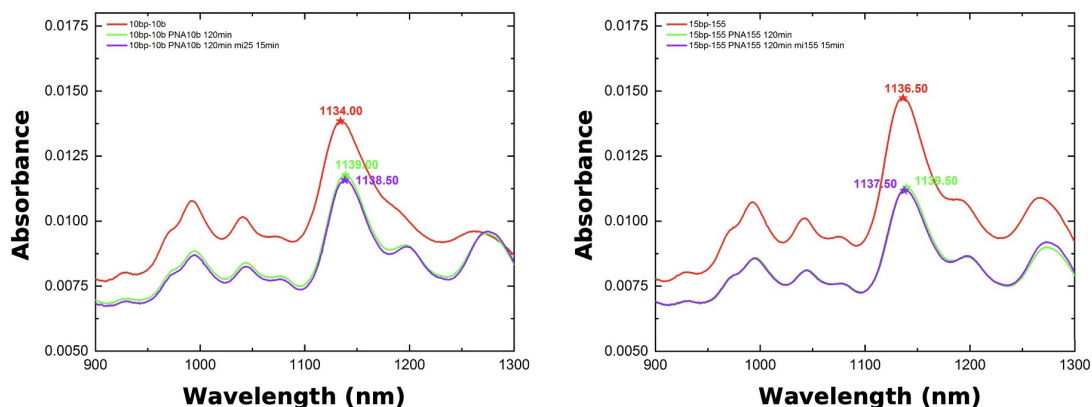


Figure E.33 – Comparison of the normalized absorbance spectra for DNA_{15bp}-SWCNTs (**red**), PNA₁₅₅-DNA_{15bp}-SWCNTs or PNA_{10b}-DNA_{15bp}-SWCNTs before (**green**) and after the addition of either complementary or non-complementary miRNA (**purple**). Samples were incubated for 15 min following the addition of miRNA prior to acquiring the spectrum. PNA-DNA samples were incubated for 120 min prior to addition of the miRNA sequence (final concentrations: PNA = 9.4 μ M, miRNA = 5.7 μ M).

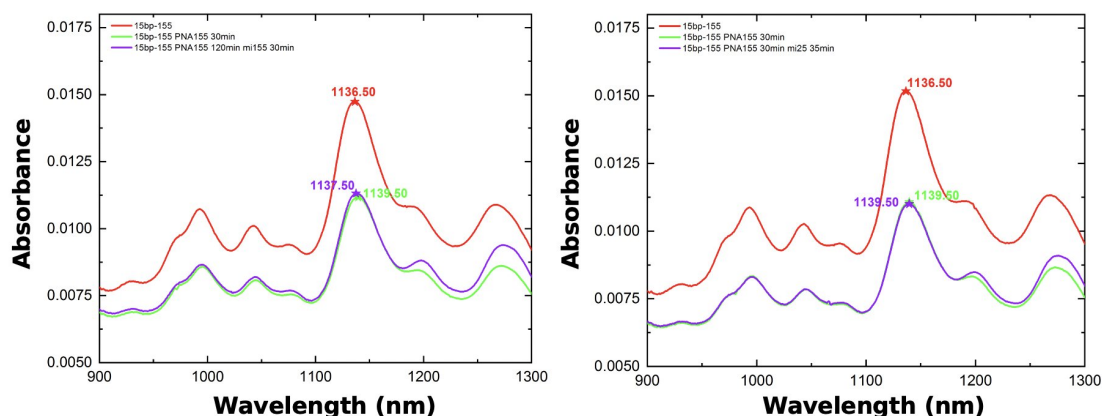


Figure E.34 – Comparison of the normalized absorbance spectra for DNA_{15bp}-SWCNTs (**red**), PNA₁₅₅-DNA_{15bp}-SWCNTs (**green**), and PNA₁₅₅-DNA_{15bp}-SWCNTs following the addition of either complementary (miR155, **left**) or non-complementary (miR25, **right**) miRNA (**purple**). Samples were incubated for 30 min following the addition of PNA prior to acquiring the spectrum. PNA-DNA samples used for miRNA detection were incubated for 2 h prior to addition of the miRNA sequence (final concentrations: PNA = 9.4 μ M, miRNA = 5.7 μ M).

Appendix E. Outlook on Potential Applications of XNA-SWCNTs for Improved Optical Biosensing

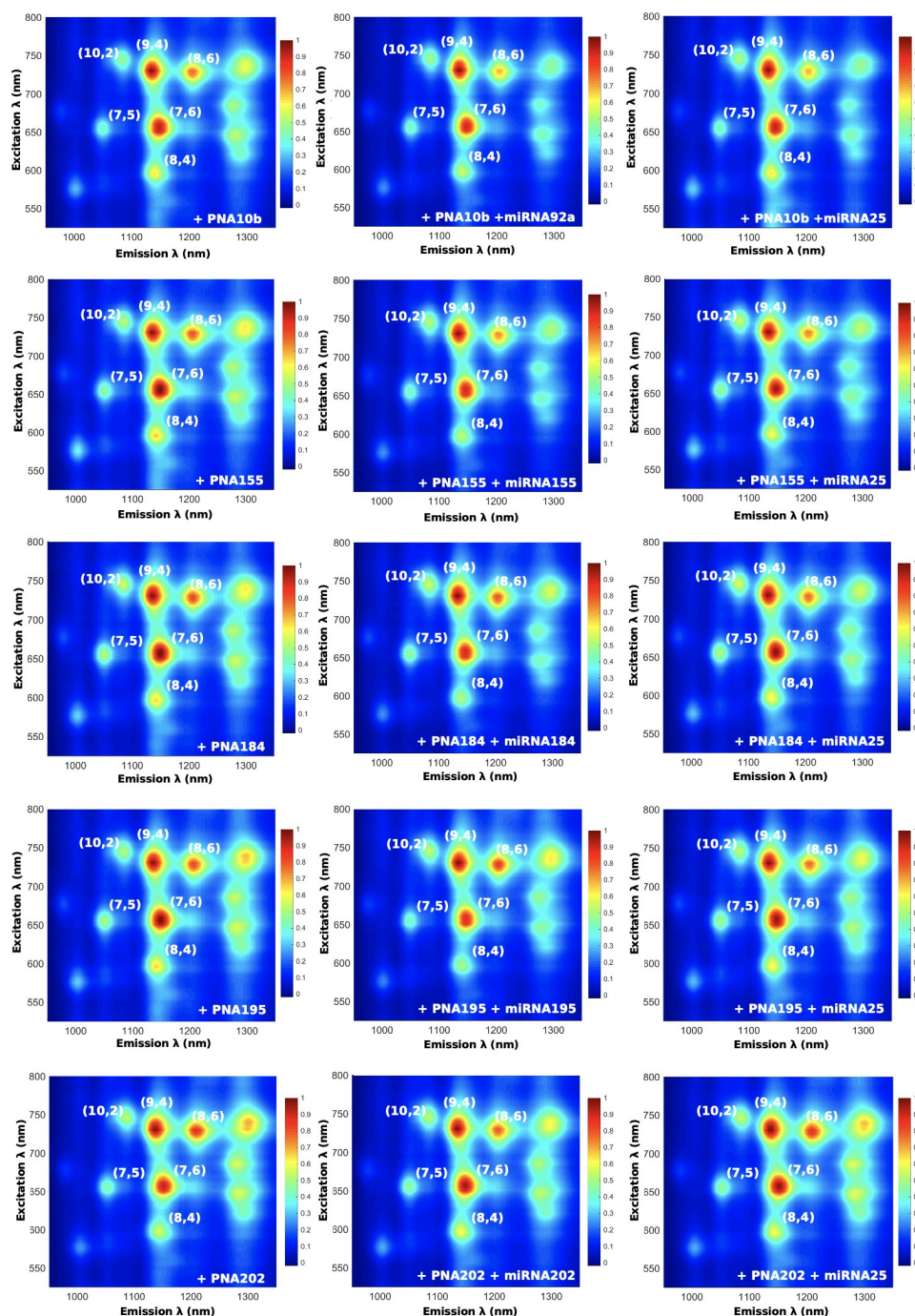


Figure E.35 – PL maps of the PNA-10bp-SWCNT solutions (PNA_{10b}, PNA₁₅₅, PNA₁₈₄, PNA₁₉₅, and PNA₂₀₂) before (**left**) and after addition of complementary (**center**) and non-complementary (miR25, **right**) miRNA (final concentration: PNA = 9.4 μ M, miRNA = 5.7 μ M). For the PNA_{10b}-DNA_{10bp}-SWCNT solution two non-complementary miRNAs were added (miR92a - **center**, miR25 - **right**). The predominate chiralities are labelled in white. All fluorescence intensities were normalized to the maximum intensity in each plot.

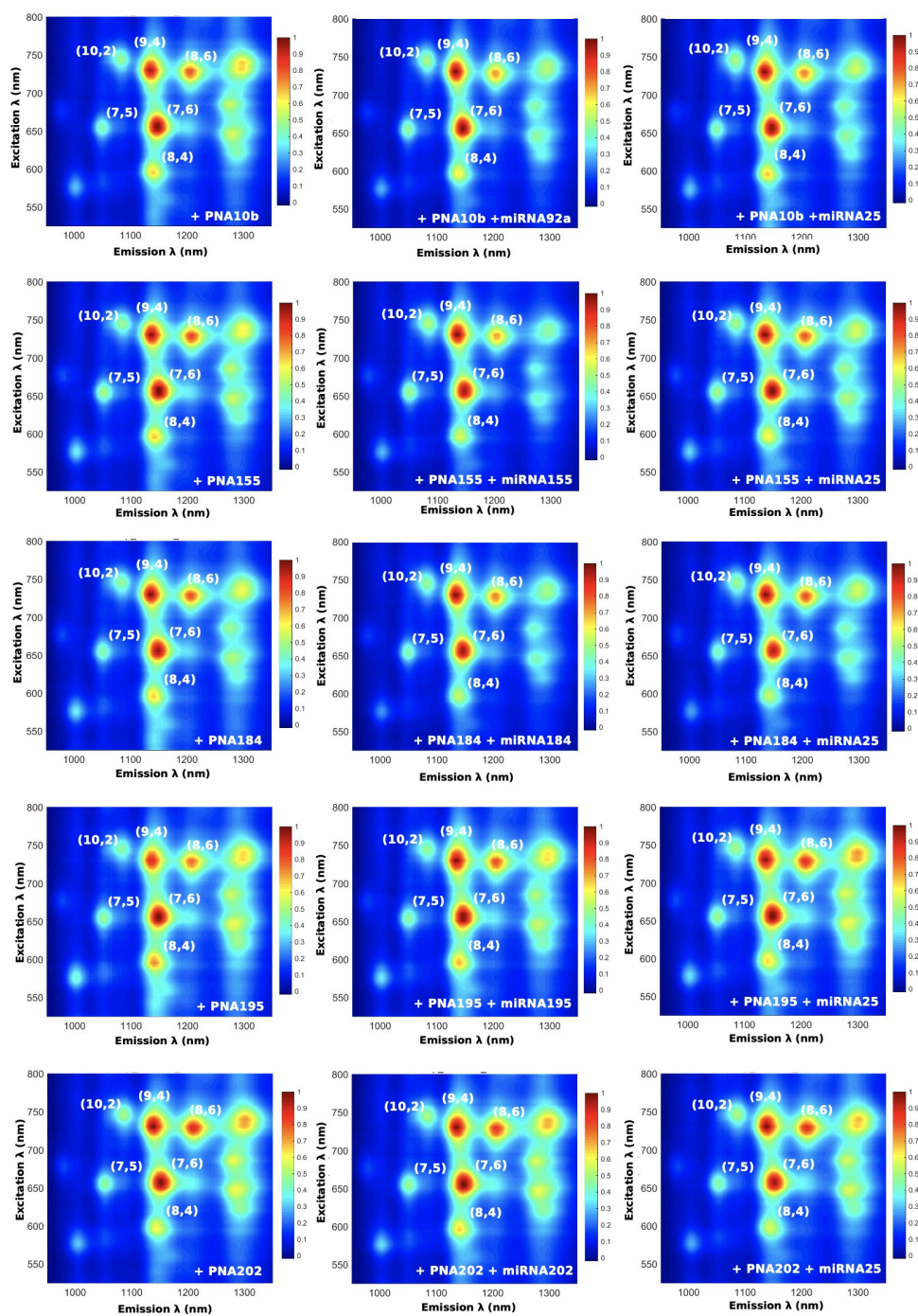


Figure E.36 – PLE maps of the PNA-20bp-SWCNT solutions (PNA_{10b}, PNA₁₅₅, PNA₁₈₄, PNA₁₉₅, and PNA₂₀₂) before (**left**) and after addition of complementary (**center**) and non-complementary (miR25, **right**) miRNA (final concentration: PNA = 9.4 μ M, miRNA = 5.7 μ M). For the PNA_{10b}-DNA_{20bp}-SWCNT solution two non-complementary miRNAs were added (miR92a - **center**, miR25 - **right**). The predominant chiralities are labelled in white. All fluorescence intensities were normalized to the maximum intensity in each plot.

Appendix E. Outlook on Potential Applications of XNA-SWCNTs for Improved Optical Biosensing

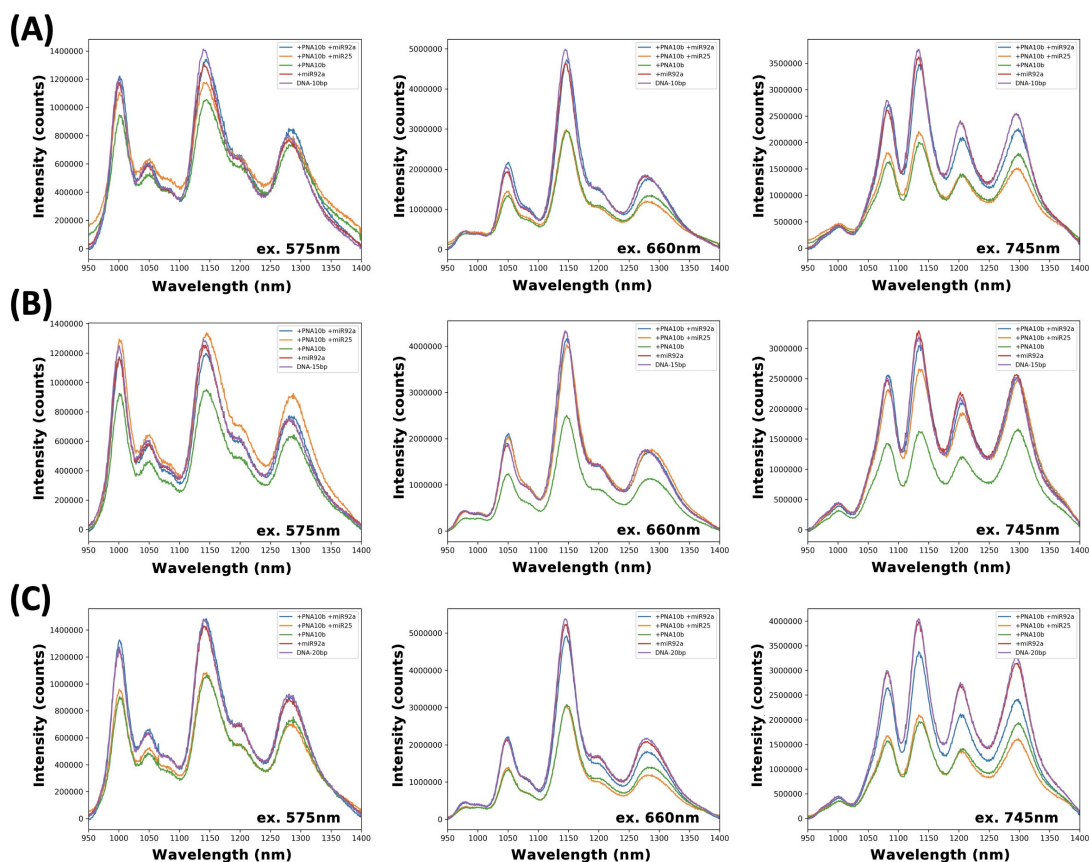


Figure E.37 – Spectra extracted from PLE maps to compare the intensity and wavelength positions of the PNA_{10b}-DNA-SWCNTs with different hybrid section lengths ((A) 10, (B) 15, or (C) 20 bases) following the addition of non-complementary miRNA (miR92a - blue, miR25 - orange) (final concentration: PNA = 9.4 μ M, miRNA = 5.7 μ M). Spectra for the respective DNA-SWCNTs (purple), PNA-DNA-SWCNTs (green), and DNA-SWCNTs following miRNA addition in the absence of PNA (red) are also included for comparison. The wavelength of the excitation laser used is indicated in the lower right corner.

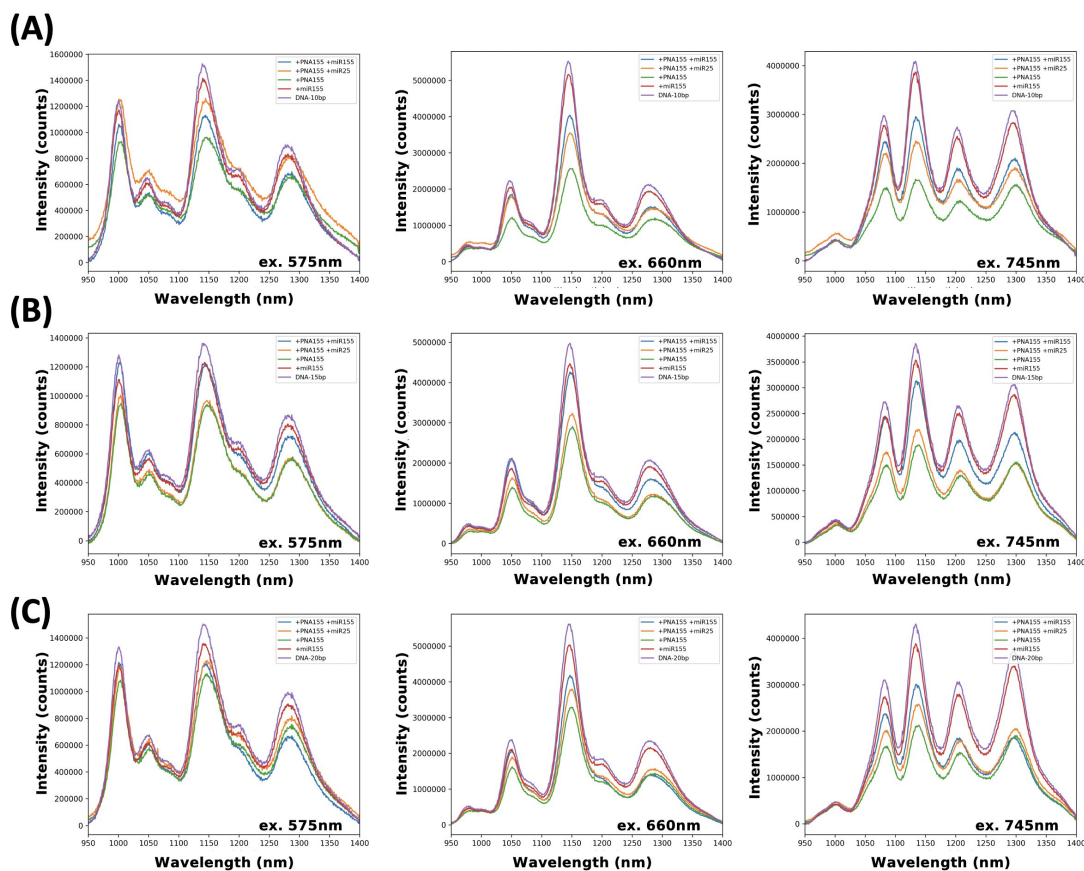


Figure E.38 – Spectra extracted from PLE maps to compare the intensity and wavelength positions of the PNA₁₅₅-DNA-SWCNTs with different hybrid section lengths ((A) 10, (B) 15, or (C) 20 bases) following the addition of complementary (blue) and non-complementary miRNA (miR25 - orange) (final concentration: PNA = 9.4 μ M, miRNA = 5.7 μ M). Spectra for the respective DNA-SWCNTs (purple), PNA-DNA-SWCNTs (green), and DNA-SWCNTs following miRNA addition in the absence of PNA (red) are also included for comparison. The wavelength of the excitation laser used is indicated in the lower right corner.

Appendix E. Outlook on Potential Applications of XNA-SWCNTs for Improved Optical Biosensing

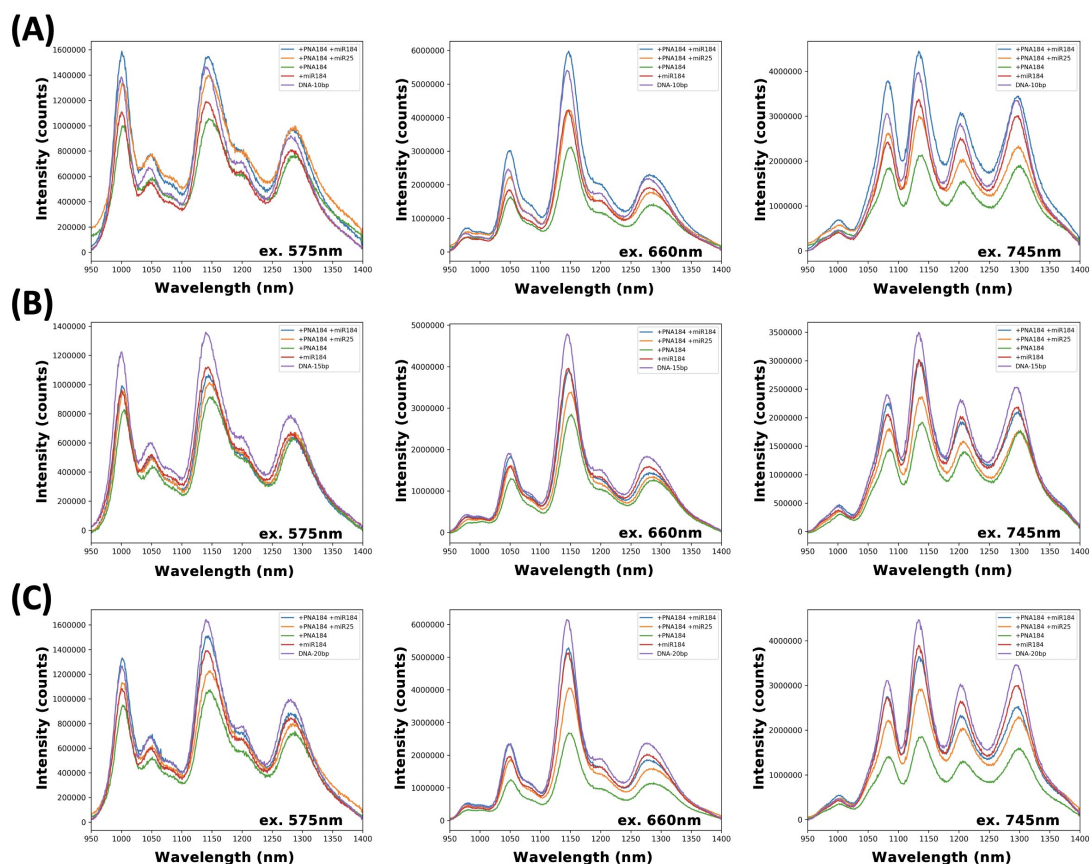


Figure E.39 – Spectra extracted from PLE maps to compare the intensity and wavelength positions of the PNA₁₈₄-DNA-SWCNTs with different hybrid section lengths ((A) 10, (B) 15, or (C) 20 bases) following the addition of complementary (blue) and non-complementary miRNA (miR25 - orange) (final concentration: PNA = 9.4 μ M, miRNA = 5.7 μ M). Spectra for the respective DNA-SWCNTs (purple), PNA-DNA-SWCNTs (green), and DNA-SWCNTs following miRNA addition in the absence of PNA (red) are also included for comparison. The wavelength of the excitation laser used for comparison. The wavelength of the excitation laser used is indicated in the lower right corner.

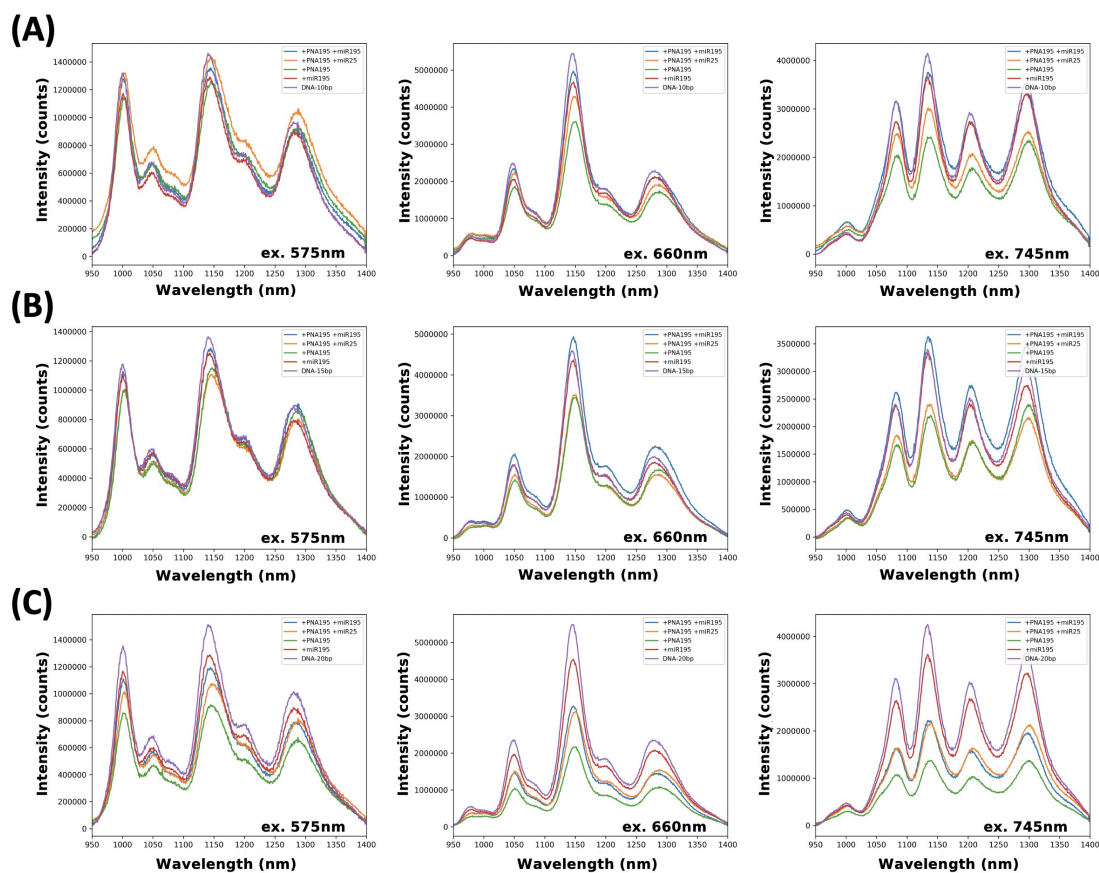


Figure E.40 – Spectra extracted from PLE maps to compare the intensity and wavelength positions of the PNA₁₉₅-DNA-SWCNTs with different hybrid section lengths ((A) 10, (B) 15, or (C) 20 bases) following the addition of complementary (blue) and non-complementary miRNA (miR25 - orange) (final concentration: PNA = 9.4 μ M, miRNA = 5.7 μ M). Spectra for the respective DNA-SWCNTs (purple), PNA-DNA-SWCNTs (green), and DNA-SWCNTs following miRNA addition in the absence of PNA (red) are also included for comparison. The wavelength of the excitation laser used is indicated in the lower right corner.

Appendix E. Outlook on Potential Applications of XNA-SWCNTs for Improved Optical Biosensing

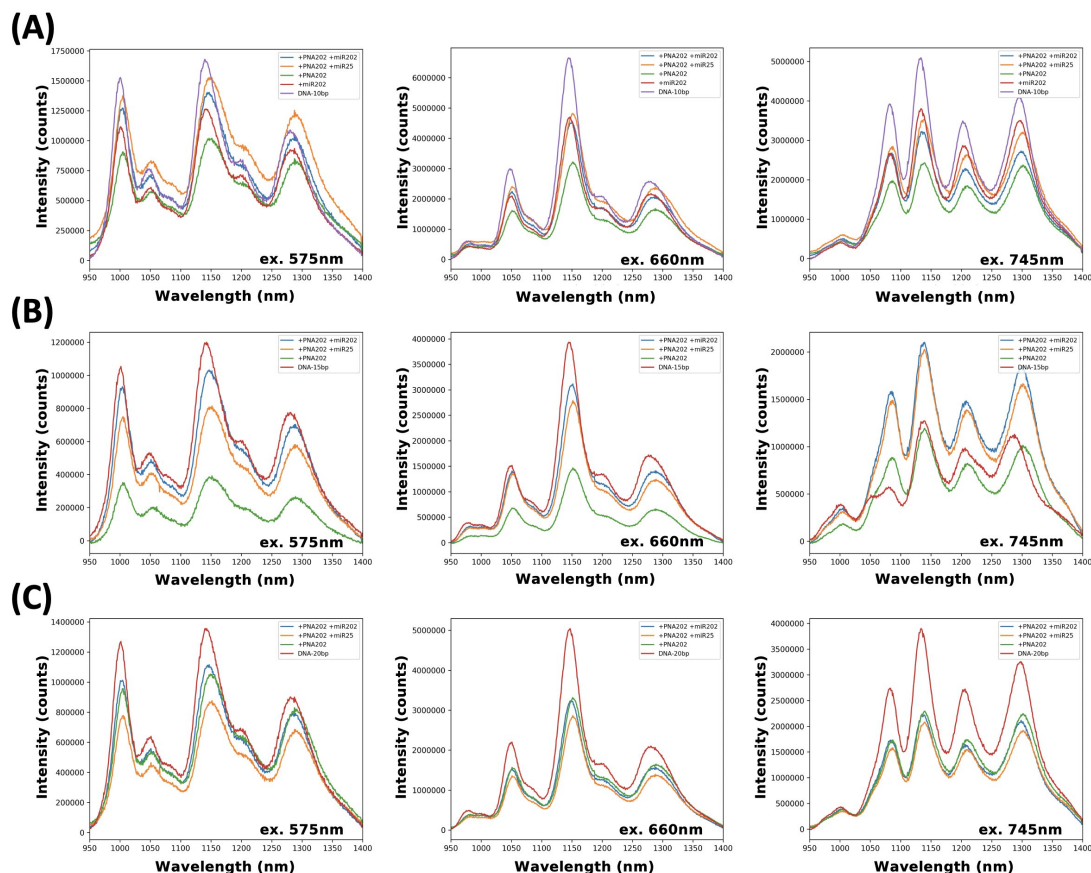


Figure E.41 – Spectra extracted from PLE maps to compare the intensity and wavelength positions of the PNA₁₉₅-DNA-SWCNTs with different hybrid section lengths ((A) 10, (B) 15, or (C) 20 bases) following the addition of complementary (blue) and non-complementary miRNA (miR25 - orange) (final concentration: PNA = 9.4 μ M, miRNA = 5.7 μ M). Spectra for the respective DNA-SWCNTs (purple), PNA-DNA-SWCNTs (green), and DNA-SWCNTs following miRNA addition in the absence of PNA (red) are also included for comparison. The wavelength of the excitation laser used is indicated in the lower right corner.

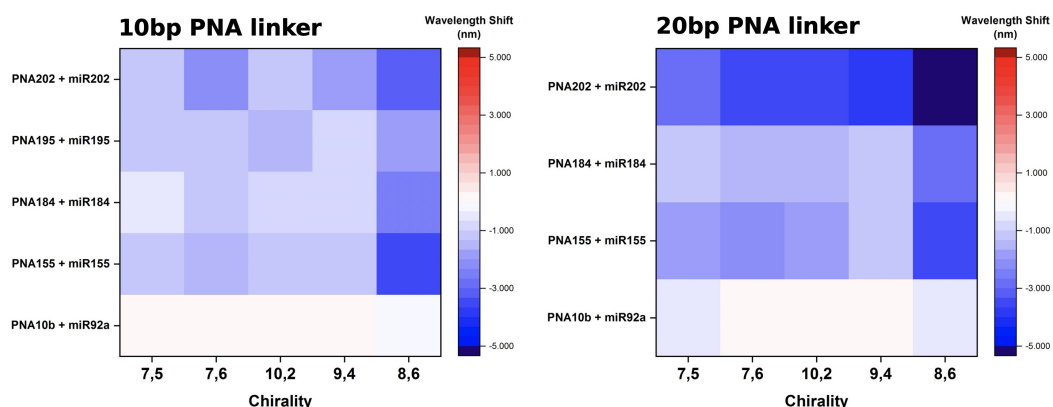


Figure E.42 – Fluorescence wavelength shift response of PNA-DNA_{10bp}-SWCNTs and PNA-DNA_{20bp}-SWCNTs to complementary and non-complementary miRNA (final concentration: PNA = 9.4 μ M, miRNA = 5.7 μ M). complementary miRNA was added to PNA₂₀₂-, PNA₁₉₅-, PNA₁₈₄-, and PNA₁₅₅-DNA_{15bp}-SWCNTs. Non-complementary miRNAs (miR92a) were added to PNA_{10b}-DNA_{15bp}-SWCNTs. All wavelength shifts were calculated versus the wavelength position of the chiralities for the respective PNA-DNA_{10bp}-SWCNT or PNA-DNA_{20bp}-SWCNT solution prior to miRNA addition. **Red** and **blue** indicate a redshift or blueshift in the wavelength position, respectively.

Bibliography

1. Mobed, A., Hasanzadeh, M., Ahmadalipour, A. & Fakhari, A. Recent advances in the biosensing of neurotransmitters: Material and method overviews towards the biomedical analysis of psychiatric disorders. *Analytical Methods* **12**, 557–575 (2020).
2. Leopold, A. V., Shcherbakova, D. M. & Verkhusha, V. V. Fluorescent Biosensors for Neurotransmission and Neuromodulation: Engineering and Applications. *Frontiers in Cellular Neuroscience* **13** (2019).
3. Rodeberg, N. T., Sandberg, S. G., Johnson, J. A., Phillips, P. E. & Wightman, R. M. Hitchhiker's Guide to Voltammetry: Acute and Chronic Electrodes for in Vivo Fast-Scan Cyclic Voltammetry. *ACS Chemical Neuroscience* **8**, 221–234 (2017).
4. Sames, D., Dunn, M., Karpowicz, R. J. & Sulzer, D. Visualizing neurotransmitter secretion at individual synapses. *ACS Chemical Neuroscience* **4**, 648–651 (2013).
5. Patriarchi, T. *et al.* Ultrafast neuronal imaging of dopamine dynamics with designed genetically encoded sensors. *Science* **360**, 1–22 (2018).
6. Sun, F. *et al.* A Genetically Encoded Fluorescent Sensor Enables Rapid and Specific Detection of Dopamine in Flies, Fish, and Mice. *Cell* **174**, 481–496.e19 (2018).
7. Palmer, A. E., Qin, Y., Park, J. G. & McCombs, J. E. Design and application of genetically encoded biosensors. *Trends in Biotechnology* **29**, 144–152. arXiv: NIHMS150003 (2011).
8. Bachilo, S. M. *et al.* Structure-Assigned Optical Spectra of Single-Walled Carbon Nanotubes. *Science* **298**, 2361–2366 (2002).
9. O'Connell, M. J. *et al.* Band Gap Fluorescence from Individual Single-Walled Carbon Nanotubes. *Science* **297**, 593–597 (2002).
10. Harvey, J. D. *et al.* A carbon nanotube reporter of microRNA hybridization events in vivo. *Nature Biomedical Engineering* **1**, 1–11 (2017).
11. Harvey, J. D., Baker, H. A., Ortiz, M. V., Kentsis, A. & Heller, D. A. HIV Detection via a Carbon Nanotube RNA Sensor. *ACS Sensors* **4**, 1236–1244 (2019).
12. Williams, R. M., Lee, C. & Heller, D. A. A Fluorescent Carbon Nanotube Sensor Detects the Metastatic Prostate Cancer Biomarker uPA. *ACS Sensors* **3**, 1838–1845 (2018).

Bibliography

13. Kruss, S. *et al.* Carbon nanotubes as optical biomedical sensors. *Advanced Drug Delivery Reviews* **65**, 1933–1950 (2013).
14. Kruss, S. *et al.* Neurotransmitter detection using corona phase molecular recognition on fluorescent single-walled carbon nanotube sensors. *Journal of the American Chemical Society* **136**, 713–724 (2014).
15. Beyene, A. G. *et al.* Ultralarge Modulation of Fluorescence by Neuromodulators in Carbon Nanotubes Functionalized with Self-Assembled Oligonucleotide Rings. *Nano Letters* **18**, 6995–7003 (2018).
16. Bisker, G. *et al.* Protein-targeted corona phase molecular recognition. *Nature Communications* **7**, 1–14 (2016).
17. Beyene, A. G. *et al.* Imaging striatal dopamine release using a nongenetically encoded near infrared fluorescent catecholamine nanosensor. *Science Advances* **5**, 1–12 (2019).
18. Louie, S. G. in *Carbon Nanotubes* 113–145 (Springer Berlin Heidelberg, Berlin, Heidelberg, 2001).
19. O’Connell, M. (J. *Carbon nanotubes : properties and applications* 319 (CRC/Taylor & Francis, 2006).
20. Ebert, L. B. *Science of fullerenes and carbon nanotubes* 437–438. arXiv: arXiv:1011.1669v3 (Academic Press, 1997).
21. Saito, R., Dresselhaus, G. & Dresselhaus, M. S. *Physical Properties of Carbon Nanotubes* (1998).
22. Weisman, R. B. & Bachilo, S. M. Dependence of optical transition energies on structure for single-walled carbon nanotubes in aqueous suspension: An empirical Kataura plot. *Nano Letters* **3**, 1235–1238 (2003).
23. Dukovic, G. *et al.* Structural dependence of excitonic optical transitions and band-gap energies in carbon nanotubes. *Nano Letters* **5**, 2314–2318 (2005).
24. Gelao, G., Marani, R. & Perri, A. G. A Formula to Determine Energy Band Gap in Semiconducting Carbon Nanotubes. *ECS Journal of Solid State Science and Technology* **8**, M19–M21 (2019).
25. Wang, F, Dukovic, G., Brus, L. E. & Heinz, T. F Time-resolved fluorescence of carbon nanotubes and its implication for radiative lifetimes. *Physical Review Letters* **92**, 17–20 (2004).
26. Heller, D. A. *Biopolymer-Mediated Analyte Detection Via Photoluminescence Modulation of Single-Walled Carbon Nanotubes* PhD thesis (University of Illinois, 2000).
27. Hartschuh, A. *et al.* Single carbon nanotube optical spectroscopy. *ChemPhysChem* **6**, 577–582 (2005).

28. Kataura, H. *et al.* Optical properties of single-wall carbon nanotubes. *Synthetic Metals* **103**, 2555–2558 (1999).
29. Choi, J. H. & Strano, M. S. Solvatochromism in single-walled carbon nanotubes. *Applied Physics Letters* **90**, 88–91 (2007).
30. Gillen, A. J. & Boghossian, A. A. Non-covalent Methods of Engineering Optical Sensors Based on Single-Walled Carbon Nanotubes. *Frontiers in Chemistry* **7**, 1–13 (Sept. 2019).
31. Kim, M. *et al.* Fluorescent Carbon Nanotube Defects Manifest Substantial Vibrational Reorganization. *Journal of Physical Chemistry C* **120**, 11268–11276 (2016).
32. Kwon, H. *et al.* Molecularly Tunable Fluorescent Quantum Defects. *Journal of the American Chemical Society* **138**, 6878–6885 (2016).
33. Sykes, M. E. *et al.* Ultrafast Exciton Trapping at sp³ Quantum Defects in Carbon Nanotubes. *ACS Nano* **13**, 13264–13270 (2019).
34. Chio, L. *et al.* Electrostatic Assemblies of Single-Walled Carbon Nanotubes and Sequence-Tunable Peptoid Polymers Detect a Lectin Protein and Its Target Sugars. *Nano Letters*, [acs.nanolett.8b04955](https://doi.org/10.1021/acs.nanolett.8b04955) (Apr. 2019).
35. Gillen, A. J., Kupis-Rozmyslowicz, J., Gigli, C., Schürgers, N. & Boghossian, A. A. Xeno Nucleic Acid Nanosensors for Enhanced Stability Against Ion-induced Perturbations. *The Journal of Physical Chemistry Letters*, [acs.jpclett.8b01879](https://doi.org/10.1021/acs.jpclett.8b01879) (2018).
36. Polo, E. & Kruss, S. Impact of Redox-Active Molecules on the Fluorescence of Polymer-Wrapped Carbon Nanotubes. *Journal of Physical Chemistry C* **120**, 3061–3070 (2016).
37. Zubkovs, V., Schuergers, N., Lambert, B., Ahunbay, E. & Boghossian, A. A. Mediatorless, Reversible Optical Nanosensor Enabled through Enzymatic Pocket Doping. *Small* **13**, 1701654 (2017).
38. Phan, T. G. & Bullen, A. Practical intravital two-photon microscopy for immunological research: faster, brighter, deeper. *Immunology and Cell Biology* **88**, 438–444 (2010).
39. Hong, G., Antaris, A. L. & Dai, H. Near-infrared fluorophores for biomedical imaging. *Nature Biomedical Engineering* **1** (2017).
40. Boghossian, A. A. *et al.* Near-infrared fluorescent sensors based on single-walled carbon nanotubes for life sciences applications. *ChemSusChem* **4**, 848–863 (2011).
41. Heller, D. A. *et al.* Concomitant length and diameter separation of single-walled carbon nanotubes. *Journal of the American Chemical Society* **126**, 14567–14573 (2004).
42. Feltz, A. *Physiology of Neurons* 5 (CRC Press/Taylor & Francis, 2020).
43. Südhof, T. C. Calcium control of neurotransmitter release. *Cold Spring Harbor Perspectives in Biology* **4** (2012).
44. Südhof, T. C. The presynaptic active zone. *Neuron* **75**, 11–25 (2012).

Bibliography

45. Südhof, T. C. The Synaptic Vesicle Cycle. *Annual Review of Neuroscience* **27**, 509–547 (2004).
46. Luo, F., Sclip, A., Jiang, M. & Südhof, T. C. Neurexins cluster Ca²⁺ channels within the presynaptic active zone. *The EMBO Journal* **39**, 1–14 (2020).
47. Beyene, A. G., Delevich, K., Yang, S. J. & Landry, M. P. New Optical Probes Bring Dopamine to Light. *Biochemistry* **57**, 6379–6381 (2018).
48. Scimemi, A. & Beato, M. Determining the neurotransmitter concentration profile at active synapses. *Molecular Neurobiology* **40**, 289–306 (2009).
49. Ledonne, A. & Mercuri, N. B. Current concepts on the physiopathological relevance of dopaminergic receptors. *Frontiers in Cellular Neuroscience* **11**, 1–9 (2017).
50. Civelli, O. Orphan GPCRs and neuromodulation. *Neuron* **76**, 12–21. arXiv: NIHMS150003 (2012).
51. Grace, A. A. Phasic Versus Tonic Dopamine Release and the Modulation of Dopamine System Responsivity: A Hypothesis for the Etiology of Schizophrenia. *Neuroscience* **41**, 1–24 (1991).
52. Cabib, S. & Puglisi-Allegra, S. Stress, depression and the mesolimbic dopamine system. *Psychopharmacology* **128**, 331–342 (1996).
53. Davie, C. A. A review of Parkinson's disease. *British Medical Bulletin* **86**, 109–127 (2008).
54. Bass, C. E. *et al.* Optogenetic control of striatal dopamine release in rats. *Journal of Neurochemistry* **114**, 1344–1352 (2010).
55. Hyman, S. E. Neurotransmitters. *Current Biology* **15**, 749–754 (2015).
56. Wu, H.-c., Chang, X., Liu, L., Zhao, F. & Zhao, Y. Chemistry of carbon nanotubes in biomedical applications, 1036–1052 (2010).
57. Südhof, T. C. The synaptic vesicle cycle: a cascade of protein-protein interactions. *Nature* **375**, 645–653 (1995).
58. Dunn, M. *et al.* Designing a norepinephrine optical tracer for imaging individual noradrenergic synapses and their activity in vivo. *Nature Communications* **9**, 1–13 (2018).
59. Del Bonis-O'Donnell, J. T. *et al.* Dual Near-Infrared Two-Photon Microscopy for Deep-Tissue Dopamine Nanosensor Imaging. *Advanced Functional Materials* **27**, 1–10 (2017).
60. Jain, A., Homayoun, A., Bannister, C. W. & Yum, K. Single-walled carbon nanotubes as near-infrared optical biosensors for life sciences and biomedicine. *Biotechnology Journal* **10**, 447–459 (2015).
61. Gillen, A. J. *et al.* Templating colloidal sieves for tuning nanotube surface interactions and optical sensor responses. *Journal of Colloid and Interface Science* **565**, 55–62 (Apr. 2020).

62. Kruss, S. *et al.* High-resolution imaging of cellular dopamine efflux using a fluorescent nanosensor array. *Proceedings of the National Academy of Sciences* **114**, 1789–1794 (2017).
63. O'Brien, J., Hayder, H., Zayed, Y. & Peng, C. Overview of microRNA biogenesis, mechanisms of actions, and circulation. *Frontiers in Endocrinology* **9**, 1–12 (2018).
64. Szafranska, A. E. *et al.* Analysis of MicroRNAs in Pancreatic Fine-Needle Aspirates Can Classify Benign and Malignant Tissues. *Clinical chemistry* **54**, 1716–1724 (2008).
65. Barshack, I. *et al.* MicroRNA expression differentiates between primary lung tumors and metastases to the lung. *Pathology Research and Practice* **206**, 578–584 (2010).
66. Hoshida, Y. *et al.* Gene expression in fixed tissues and outcome in hepatocellular carcinoma. *New England Journal of Medicine* **359**, 1995–2004 (2008).
67. Wang, J., Chen, J. & Sen, S. MicroRNA as Biomarkers and Diagnostics. *Journal of Cellular Physiology* **231**, 25–30 (2016).
68. Iorio, M. V. *et al.* MicroRNA signatures in human ovarian cancer. *Cancer Research* **67**, 8699–8707 (2007).
69. Hayes, J., Peruzzi, P. P. & Lawler, S. MicroRNAs in cancer: Biomarkers, functions and therapy. *Trends in Molecular Medicine* **20**, 460–469 (2014).
70. Kim, J. H. *et al.* A luciferase/single-walled carbon nanotube conjugate for nearInfrared fluorescent detection of cellular ATP. *Angewandte Chemie - International Edition* **49**, 1456–1459 (2010).
71. Ruscito, A. & DeRosa, M. C. Small-molecule binding aptamers: Selection strategies, characterization, and applications. *Frontiers in Chemistry* **4**, 1–14 (2016).
72. Sela-Culang, I., Kunik, V. & Ofran, Y. The structural basis of antibody-antigen recognition. *Frontiers in Immunology* **4**, 1–13 (2013).
73. Zhang, J. *et al.* Molecular recognition using corona phase complexes made of synthetic polymers adsorbed on carbon nanotubes. *Nature Nanotechnology* **8**, 959–968 (2013).
74. Zhang, J. *et al.* Single molecule detection of nitric oxide enabled by d(AT)₁₅ DNA adsorbed to near infrared fluorescent single-walled carbon nanotubes. *Journal of the American Chemical Society* **133**, 567–581 (2011).
75. Harvey, J. D., Baker, H. A., Mercer, E., Budhathoki-Uprety, J. & Heller, D. A. Control of Carbon Nanotube Solvatochromic Response to Chemotherapeutic Agents. *ACS Applied Materials and Interfaces* **9**, 37947–37953 (2017).
76. Bisker, G. *et al.* Insulin Detection Using a Corona Phase Molecular Recognition Site on Single-Walled Carbon Nanotubes. *ACS Sensors* **3**, 367–377 (2018).

Bibliography

77. Mann, F. A., Herrmann, N., Meyer, D. & Kruss, S. Tuning selectivity of fluorescent carbon nanotube-based neurotransmitter sensors. *Sensors* **17** (2017).
78. Lambert, B., Gillen, A. J., Schuergers, N., Wu, S. J. & Boghossian, A. A. Directed evolution of the optoelectronic properties of synthetic nanomaterials. *Chemical Communications* **55**, 3239–3242 (2019).
79. Beyene, A. G., McFarlane, I. R., Pinals, R. L. & Landry, M. P. Stochastic Simulation of Dopamine Neuromodulation for Implementation of Fluorescent Neurochemical Probes in the Striatal Extracellular Space. *ACS Chemical Neuroscience* **8**, 2275–2289 (2017).
80. Salem, D. P. *et al.* Ionic strength mediated phase transitions of surface adsorbed DNA on single-walled carbon nanotubes. *Journal of the American Chemical Society* **139**, 16791–16802 (2017).
81. Pearse, B. M. Clathrin: A unique protein associated with intracellular transfer of membrane by coated vesicles. *Proceedings of the National Academy of Sciences of the United States of America* **73**, 1255–1259 (1976).
82. Robinson, M. S. Forty Years of Clathrin-coated Vesicles. *Traffic* **16**, 1210–1238 (2015).
83. Pan, J., Li, F. & Choi, J. H. Single-walled carbon nanotubes as optical probes for bio-sensing and imaging, 6511–6522 (2017).
84. Liu, Z., Yang, K. & Lee, S.-t. Single-walled carbon nanotubes in biomedical imaging (2011).
85. Maeda, Y. *et al.* Dispersion of single-walled carbon nanotube bundles in nonaqueous solution. *Journal of Physical Chemistry B* **108**, 18395–18397 (2004).
86. Coleman, J. N. Liquid-phase exfoliation of nanotubes and graphene. *Advanced Functional Materials* **19**, 3680–3695 (2009).
87. Jeng, E. S., Moll, A. E., Roy, A. C., Gastala, J. B. & Strano, M. S. Detection of DNA hybridization using the near-infrared band-gap fluorescence of single-walled carbon nanotubes. *Nano Letters* **6**, 371–375 (2006).
88. Hertel, T., Himmelein, S., Ackermann, T., Stich, D. & Crochet, J. Diffusion Limited Photoluminescence Quantum Yields in 1-D Semiconductors : Single-Wall Carbon Nanotubes. *ACS Nano* **4**, 7161–7168 (2010).
89. Wu, S.-J. *et al.* Restriction Enzyme Analysis of Double-Stranded DNA on Pristine Single-Walled Carbon Nanotubes. *ACS Applied Materials & Interfaces*, acsami.8b12287 (2018).
90. Antonucci, A., Kupis-Rozmysłowicz, J. & Boghossian, A. A. Noncovalent Protein and Peptide Functionalization of Single-Walled Carbon Nanotubes for Biodelivery and Optical Sensing Applications. *ACS Applied Materials and Interfaces* **9**, 11321–11331 (2017).

91. Saifuddin, N., Raziah, A. Z. & Junizah, A. R. Carbon nanotubes: A review on structure and their interaction with proteins. *Journal of Chemistry* **2013** (2013).
92. O'Connell, M. J. *et al.* Reversible water-solubilization of single-walled carbon nanotubes by polymer wrapping. *Chemical Physics Letters* **342**, 265–271 (2001).
93. Dresselhaus, M. S., Dresselhaus, G. & Saito, R. Carbon fibers based on C₆₀ and their symmetry. *Physical Review B* **45** (1992).
94. Hamada, N., Sawada, S. I. & Oshiyama, A. New one-dimensional conductors: Graphitic microtubules. *Physical Review Letters* **68**, 1579–1581 (1992).
95. Saito, R., Dresselhaus, G. & Dresselhaus, M. S. Electronic structure of double-layer graphene tubules. *Journal of Applied Physics* **60**, 2204–2206. arXiv: 0402594v3 [arXiv:cond-mat] (1992).
96. Wildoer, J. W. G., Venema, L. C., Rinzler, A. G., Smalley, R. E. & Dekker, C. Electronic structure of atomically resolved carbonnanotubes. *Nature* **391** (1998).
97. Angelikopoulos, P. & Bock, H. The science of dispersing carbon nanotubes with surfactants. *Physical Chemistry Chemical Physics* **14**, 9546–9557 (2012).
98. Kato, Y., Inoue, A., Niidome, Y. & Nakashima, N. Thermodynamics on soluble carbon nanotubes: How do DNA molecules replace surfactants on carbon nanotubes? *Scientific Reports* **2**, 1–7 (2012).
99. Oh, H., Sim, J. & Ju, S. Y. Binding affinities and thermodynamics of noncovalent functionalization of carbon nanotubes with surfactants. *Langmuir* **29**, 11154–11162 (2013).
100. Tummala, N. R. & Striolo, A. SDS Surfactants on Carbon Nanotubes. **3**, 595–602 (2009).
101. Tummala, N. R. & Striolo, A. Role of counterion condensation in the self-assembly of SDS surfactants at the water-graphite interface. *Journal of Physical Chemistry B* **112**, 1987–2000 (2008).
102. Angelikopoulos, P. & Bock, H. Directed self-assembly of surfactants in carbon nanotube materials. *Journal of Physical Chemistry B* **112**, 13793–13801 (2008).
103. Nonoguchi, Y., Tani, A., Murayama, T., Uchida, H. & Kawai, T. Surfactant-driven amphoteric doping of carbon nanotubes. *Chemistry - An Asian Journal* (2018).
104. Haggemueller, R. *et al.* Comparison of the quality of aqueous dispersions of single wall carbon nanotubes using surfactants and biomolecules. *Langmuir* **24**, 5070–5078 (2008).
105. Bergler, F. F., Stahl, S., Goy, A., Schöppler, F. & Hertel, T. Substrate-Mediated Cooperative Adsorption of Sodium Cholate on (6,5) Single-Wall Carbon Nanotubes. *Langmuir* **32**, 9598–9603 (2016).

Bibliography

106. Hirsch, A. Functionalization of single-walled carbon nanotubes. *Angewandte Chemie - International Edition* **41**, 1853–1859 (2002).
107. Wenseleers, W. *et al.* Efficient isolation and solubilization of pristine single-walled nanotubes in bile salt micelles. *Advanced Functional Materials* **14**, 1105–1112 (2004).
108. Crochet, J., Clemens, M. & Hertel, T. Quantum yield heterogeneities of aqueous single-wall carbon nanotube suspensions. *Journal of the American Chemical Society* **129**, 8058–8059 (2007).
109. Blanch, A. J., Lenahan, C. E. & Quinton, J. S. Optimizing surfactant concentrations for dispersion of single-walled carbon nanotubes in aqueous solution. *Journal of Physical Chemistry B* **114**, 9805–9811 (2010).
110. Matarredona, O. *et al.* Dispersion of Single-Walled Carbon Nanotubes in Aqueous Solutions of the Anionic Surfactant NaDDBS. *The Journal of Physical Chemistry B* **107**, 13357–13367 (2003).
111. Xin, X., Xu, G. & Li, H. *Dispersion and Property Manipulation of Carbon Nanotubes by Self-Assemblies of Amphiphilic Molecules* (2013).
112. Vo, M. D. & Papavassiliou, D. V. Effects of Temperature and Shear on the Adsorption of Surfactants on Carbon Nanotubes. *Journal of Physical Chemistry C* **121**, 14339–14348 (2017).
113. Vo, M. D., Shiau, B., Harwell, J. H. & Papavassiliou, D. V. Adsorption of anionic and non-ionic surfactants on carbon nanotubes in water with dissipative particle dynamics simulation. *Journal of Chemical Physics* **144** (2016).
114. Islam, M. F., Rojas, E., Bergey, D. M., Johnson, A. T. & Yodh, A. G. High weight fraction surfactant solubilization of single-wall carbon nanotubes in water. *Nano Letters* **3**, 269–273. arXiv: 9906424v1 [arXiv:cond-mat] (2003).
115. Angelikopoulos, P. & Bock, H. The differences in surfactant adsorption on carbon nanotubes and their bundles. *Langmuir* **26**, 899–907 (2010).
116. Xu, J. *et al.* Strongly Bound Sodium Dodecyl Sulfate Surrounding Single-Wall Carbon Nanotubes. *Langmuir* **33**, 5006–5014 (2017).
117. Tummala, N. R., Morrow, B. H., Resasco, D. E. & Striolo, A. Stabilization of aqueous carbon nanotube dispersions using surfactants: Insights from molecular dynamics simulations. *ACS Nano* **4**, 7193–7204 (2010).
118. Wang, H. *et al.* Dispersing single-walled carbon nanotubes with surfactants: A small angle neutron scattering study. *Nano Letters* **4**, 1789–1793 (2004).
119. Moore, V. C. *et al.* Individually Suspended Single-Walled Carbon Nanotubes in Various Surfactants. *Nano Letters* **3**, 1379–1382 (2003).

120. Sun, Z. *et al.* Quantitative evaluation of surfactant-stabilized single-walled carbon nanotubes: Dispersion quality and its correlation with zeta potential. *Journal of Physical Chemistry C* **112**, 10692–10699 (2008).
121. White, B., Banerjee, S., O'Brien, S., Turro, N. J. & Herman, I. P. Zeta-potential measurements of surfactant-wrapped individual single-walled carbon nanotubes. *Journal of Physical Chemistry C* **111**, 13684–13690 (2007).
122. Yurekli, K., Mitchell, C. A. & Krishnamoorti, R. Small-angle neutron scattering from surfactant-assisted aqueous dispersions of carbon nanotubes. *Journal of the American Chemical Society* **126**, 9902–9903 (2004).
123. Johnson, R. R., Kohlmeyer, A., Johnson, A. T. C. & Klein, M. L. Free Energy Landscape of a {DNA}–carbon Nanotube Hybrid Using Replica Exchange Molecular Dynamics. *Nano Letters* **9**, 537–541 (2009).
124. Zheng, Y., Bachilo, S. M. & Weisman, R. B. Quenching of Single-Walled Carbon Nanotube Fluorescence by Dissolved Oxygen Reveals Selective Single-Stranded DNA Affinities. *Journal of Physical Chemistry Letters* **8**, 1952–1955 (2017).
125. Yum, K., McNicholas, T. P., Mu, B. & Strano, M. S. Single-walled carbon nanotube-based near-infrared optical glucose sensors toward in vivo continuous glucose monitoring. *Journal of Diabetes Science and Technology* **7**, 72–87 (2013).
126. Bonis-O'Donnell, J. T. D. *et al.* Chemometric Approaches for Developing Infrared Nanosensors To Image Anthracyclines. *Biochemistry* **58**, 54–64 (2019).
127. Dong, L., Joseph, K. L., Witkowski, C. M. & Craig, M. M. Cytotoxicity of single-walled carbon nanotubes suspended in various surfactants. *Nanotechnology* **19** (2008).
128. Dong, L., Witkowski, C. M., Craig, M. M., Greenwade, M. M. & Joseph, K. L. Cytotoxicity effects of different surfactant molecules conjugated to carbon nanotubes on human astrocytoma cells. *Nanoscale Research Letters* **4**, 1517–1523 (2009).
129. Bansal, J., Singh, I., Bhatnagar, P. K. & Mathur, P. C. DNA sequence detection based on raman spectroscopy using single walled carbon nanotube. *Journal of Bioscience and Bioengineering* **115**, 438–441 (2013).
130. Zheng, M. *et al.* DNA-assisted dispersion and separation of carbon nanotubes. *Nature materials* **2**, 338–342 (2003).
131. Heller, D. A. *et al.* Optical Detection of DNA Conformational Polymorphism on Single-Walled Carbon Nanotubes. *Science* **311**, 508–511 (2006).
132. Enyashin, A. N., Gemming, S. & Seifert, G. DNA-wrapped carbon nanotubes. *Nanotechnology* **18** (2007).

Bibliography

133. Kupis-Rozmysłowicz, J., Antonucci, A. & Boghossian, A. A. Engineering the Selectivity of the DNA-SWCNT Sensor. *ECS Journal of Solid State Science and Technology* **5**, M3067–M3074 (2016).
134. Zheng, M. *et al.* Structure-Based Carbon Nanotube Sorting by Sequence-Dependent DNA Assembly. *Science* **302**, 1545–1548 (2003).
135. Johnson, R. R., Johnson, A. T. C. & Klein, M. L. Probing the structure of DNA-carbon nanotube hybrids with molecular dynamics. *Nano Letters* **8**, 69–75 (2008).
136. Li, C. & Shi, G. Carbon nanotube-based fluorescence sensors. *Journal of Photochemistry and Photobiology C: Photochemistry Reviews* **19**, 20–34 (2014).
137. Safaee, M. M., Gravely, M., Rocchio, C., Simmeth, M. & Roxbury, D. DNA Sequence Mediates Apparent Length Distribution in Single- Walled Carbon Nanotubes. *ACS Applied Materials & Interfaces* (2018).
138. Jena, P. V., Safaee, M. M., Heller, D. A. & Roxbury, D. DNA-Carbon Nanotube Complexation Affinity and Photoluminescence Modulation Are Independent. *ACS Applied Materials and Interfaces* **9**, 21397–21405 (2017).
139. Safaee, M. M., Gravely, M., Rocchio, C., Simmeth, M. & Roxbury, D. DNA Sequence Mediates Apparent Length Distribution in Single-Walled Carbon Nanotubes. *ACS Applied Materials and Interfaces* **11**, 2225–2233 (2019).
140. Chattopadhyay, D., Galeska, I. & Papadimitrakopoulos, F. A route for bulk separation of semiconducting from metallic single-wall carbon nanotubes. *Journal of the American Chemical Society* **125**, 3370–3375 (2003).
141. Peng, H., Alvarez, N. T., Kittrell, C., Hauge, R. H. & Schmidt, H. K. Dielectrophoresis field flow fractionation of single-walled carbon nanotubes. *Journal of the American Chemical Society* **128**, 8396–8397 (2006).
142. Krupke, R., Hennrich, F., Löhneysen, H. v. & Kappes, M. M. Separation of metallic from semiconducting single-walled carbon nanotubes. *Science (New York, N.Y.)* **301**, 344–347. arXiv: arXiv:1011.1669v3 (2003).
143. Krupke, R., Hennrich, F., Kappes, M. M. & Löhneysen, H. V. Surface conductance induced dielectrophoresis of semiconducting single-walled carbon nanotubes. *Nano Letters* **4**, 1395–1399 (2004).
144. Huang, X., Mclean, R. S. & Zheng, M. High-resolution length sorting and purification of DNA-wrapped carbon nanotubes by size-exclusion chromatography. *Analytical Chemistry* **77**, 6225–6228 (2005).
145. Strano, M. S. *et al.* Understanding the nature of the DNA-assisted separation of single-walled carbon nanotubes using fluorescence and raman spectroscopy. *Nano Letters* **4**, 543–550 (2004).

146. Lustig, S. R., Jagota, A., Khripin, C. & Zheng, M. Theory of structure-based carbon nanotube separations by Ion-exchange chromatography of DNA/CNT hybrids. *Journal of Physical Chemistry B* **109**, 2559–2566 (2005).
147. Tu, X. & Zheng, M. A DNA-based approach to the carbon nanotube sorting problem. *Nano Research* **1**, 185–194 (2008).
148. Zheng, M. & Semke, E. D. Enrichment of single chirality carbon nanotubes. *Journal of the American Chemical Society* **129**, 6084–6085 (2007).
149. Tu, X., Manohar, S., Jagota, A. & Zheng, M. DNA sequence motifs for structure-specific recognition and separation of carbon nanotubes. *Nature* **460**, 250–253 (2009).
150. Zhang, M. *et al.* Single-step total fractionation of single-wall carbon nanotubes by counter-current chromatography. *Analytical Chemistry* **86**, 3980–3984. arXiv: NIHMS150003 (2015).
151. Arnold, M. S., Green, A. A., Hulvat, J. F., Stupp, S. I. & Hersam, M. C. Sorting carbon nanotubes by electronic structure using density differentiation. *Nature Nanotechnology* **1**, 60–65 (2006).
152. Khripin, C. Y., Fagan, J. A. & Zheng, M. Spontaneous partition of carbon nanotubes in polymer-modified aqueous phases. *Journal of the American Chemical Society* **135**, 6822–6825 (2013).
153. Ao, G., Khripin, C. Y. & Zheng, M. DNA-controlled partition of carbon nanotubes in polymer aqueous two-phase systems. *Journal of the American Chemical Society* **136**, 10383–10392 (2014).
154. Ao, G. & Zheng, M. in *Current Protocols in Chemical Biology* 1, 43–51 (John Wiley & Sons, Inc., Hoboken, NJ, USA, Mar. 2015).
155. Ao, G., Streit, J. K., Fagan, J. A. & Zheng, M. Differentiating Left- and Right-Handed Carbon Nanotubes by DNA. *Journal of the American Chemical Society* **138**, 16677–16685 (2016).
156. Subbaiyan, N. K. *et al.* Bench-top aqueous two-phase extraction of isolated individual single-walled carbon nanotubes. *Nano Research* **8**, 1755–1769 (2015).
157. Jeng, E. S., Nelson, J. D., Prather, K. L. & Strano, M. S. Detection of a single nucleotide polymorphism using single-walled carbon-nanotube near-infrared fluorescence. *Small* **6**, 40–43 (2010).
158. Etheridge, A., Lee, I., Hood, L., Galas, D. & Wang, K. Extracellular microRNA: a new source of biomarkers. *Mutat Res.* **717**, 85–90 (2011).
159. Mishra, P. J. MicroRNAs as promising biomarkers in cancer diagnostics. *Biomarker Research* **2**, 19 (2014).

Bibliography

160. Bertoli, G., Cava, C. & Castiglioni, I. Micrnas: New biomarkers for diagnosis, prognosis, therapy prediction and therapeutic tools for breast cancer. *Theranostics* **5**, 1122–1143 (2015).
161. Wang, J., Chen, J. & Sen, S. MicroRNA as Biomarkers and Diagnostics. *Journal of Cellular Physiology* **231**, 25–30 (2016).
162. Hamam, R. *et al.* Circulating microRNAs in breast cancer : novel diagnostic and prognostic biomarkers. *Cell Death and Disease* **8** (2017).
163. Kim, J. H. *et al.* The rational design of nitric oxide selectivity in single-walled carbon nanotube near-infrared fluorescence sensors for biological detection. *Nature Chemistry* **1**, 473–481 (2009).
164. Xu, Y., Pehrsson, P. E., Chen, L., Zhang, R. & Zhao, W. Double-stranded DNA single-walled carbon nanotube hybrids for optical hydrogen peroxide and glucose sensing. *Journal of Physical Chemistry C* **111**, 8638–8643 (2007).
165. Landry, M. P. *et al.* Single-molecule detection of protein efflux from microorganisms using fluorescent single-walled carbon nanotube sensor arrays. *Nature Nanotechnology* **12**, 368–377 (2017).
166. Bisker, G. *et al.* A Mathematical Formulation and Solution of the CoPhMoRe Inverse Problem for Helically Wrapping Polymer Corona Phases on Cylindrical Substrates (2015).
167. Ulissi, Z. W., Zhang, J., Sresht, V., Blankschtein, D. & Strano, M. S. 2D Equation-of-State Model for Corona Phase Molecular Recognition on Single-Walled Carbon Nanotube and Graphene Surfaces (2015).
168. Landry, M. P. *et al.* Experimental tools to study molecular recognition within the nanoparticle corona. *Sensors* **14**, 16196–16211 (2014).
169. Lee, K., Nojoomi, A., Jeon, J., Lee, C. Y. & Yum, K. Near-Infrared Fluorescence Modulation of Refolded DNA Aptamer-Functionalized Single-Walled Carbon Nanotubes for Optical Sensing. *ACS Applied Nano Materials* **1**, acsanm.8b01377 (2018).
170. Barone, P. W. & Strano, M. S. Reversible control of carbon nanotube aggregation for a glucose affinity sensor. *Angewandte Chemie - International Edition* **45**, 8138–8141 (2006).
171. Yoon, H. *et al.* Periplasmic binding proteins as optical modulators of single-walled carbon nanotube fluorescence: Amplifying a nanoscale actuator. *Angewandte Chemie - International Edition* **50**, 1828–1831 (2011).

172. Mohamad, N. R., Marzuki, N. H. C., Buang, N. A., Huyop, F. & Wahab, R. A. An overview of technologies for immobilization of enzymes and surface analysis techniques for immobilized enzymes. *Biotechnology and Biotechnological Equipment* **29**, 205–220. arXiv: arXiv:1011.1669v3 (2015).
173. Huang, W. *et al.* Attaching Proteins to Carbon Nanotubes via Diimide-Activated Amidation. *Nano Letters* **2**, 311–314 (2002).
174. Jiang, K. *et al.* Protein immobilization on carbon nanotubes via a two-step process of diimide-activated amidation. *Journal of Materials Chemistry* **14**, 37–39 (2004).
175. Gao, Y. & Kyratzis, I. Covalent Immobilization of Proteins on Carbon Nanotubes Using the. *October* **19** (2008).
176. Neves, L. F. F. *et al.* Targeting single-walled carbon nanotubes for the treatment of breast cancer using photothermal therapy. *Nanotechnology* **24** (2013).
177. Nepal, D. & Geckeler, K. E. pH-sensitive dispersion and debundling of single-walled carbon nanotubes: Lysozyme as a tool. *Small* **2**, 406–412 (2006).
178. Holt, B. D., McCorry, M. C., Boyer, P. D., Dahl, K. N. & Islam, M. F. Not all protein-mediated single-wall carbon nanotube dispersions are equally bioactive. *Nanoscale* **4**, 7425–7434 (2012).
179. Ma, Q., Lee, D., Tan, Y. Q., Wong, G. & Gao, Z. Synthetic genetic polymers: Advances and applications. *Polymer Chemistry* **7**, 5199–5216 (2016).
180. Pinheiro, V. B. & Holliger, P. The XNA world: Progress towards replication and evolution of synthetic genetic polymers. *Current Opinion in Chemical Biology* **16**, 245–252. arXiv: 1509.01236 (2012).
181. Pinheiro, V. B., Loakes, D. & Holliger, P. Synthetic polymers and their potential as genetic materials. *BioEssays* **35**, 113–122 (2013).
182. Ghosh, S. & Chakrabarti, R. Spontaneous Unzipping of Xylonucleic Acid Assisted by a Single- Walled Carbon Nanotube : A Computational Study. *The Journal of Physical Chemistry B*, 3642–3652 (2016).
183. Anosova, I. *et al.* The structural diversity of artificial genetic polymers. *Nucleic Acids Research* **44**, 1007–1021 (2016).
184. Pinheiro, V. B. & Holliger, P. Towards XNA nanotechnology: New materials from synthetic genetic polymers. *Trends in Biotechnology* **32**, 321–328 (2014).
185. Wang, L., Yang, C. J., Medley, C. D., Benner, S. A. & Tan, W. Locked Nucleic Acid Molecular Beacons. *Journal of American Chemical Society* **127**, 15664–15665 (2005).
186. Taylor, A. I., Arangundy-Franklin, S. & Holliger, P. Towards applications of synthetic genetic polymers in diagnosis and therapy. *Current opinion in chemical biology* **22**, 79–84 (2014).

Bibliography

187. Sun, J. & Zuckermann, R. N. Peptoid polymers: A highly designable bioinspired material. *ACS Nano* **7**, 4715–4732 (2013).
188. Iverson, N. M. *et al.* In Vivo Biosensing Via Tissue Localizable Near Infrared Fluorescent Single Walled Carbon Nanotubes. *Nature Nanotechnology* **8**, 873–880 (2013).
189. Giraldo, J. P. *et al.* A Ratiometric Sensor Using Single Chirality Near-Infrared Fluorescent Carbon Nanotubes: Application to in Vivo Monitoring. *Small* **11**, 3973–3984 (2015).
190. Welsher, K. *et al.* A route to brightly fluorescent carbon nanotubes for near-infrared imaging in mice. *Nature Nanotechnology* **4**, 773–780 (2009).
191. Heller, D. A., Baik, S., Eurell, T. E. & Strano, M. S. Single-walled carbon nanotube spectroscopy in live cells: Towards long-term labels and optical sensors. *Advanced Materials* **17**, 2793–2799 (2005).
192. Iijima, S. Helical microtubules of graphitic carbon. *Nature* **354**, 56–58. arXiv: arXiv: 1011.1669v3 (1991).
193. Iijima, S. & Ichihashi, T. Single-shell carbon nanotubes of 1-nm diameter. *Nature* **363**, 603–605. arXiv: 9809069v1 [arXiv:gr-qc] (1993).
194. Nakashima, N., Okuzono, S., Murakami, H., Nakai, T. & Yoshikawa, K. DNA Dissolves Single-walled Carbon Nanotubes in Water. *Chemistry Letters* **32**, 456–457 (2003).
195. Cathcart, H. *et al.* Spontaneous debundling of single-walled carbon nanotubes in DNA-based dispersions. *Journal of Physical Chemistry C* **111**, 66–74 (2007).
196. Cathcart, H. *et al.* Ordered DNA wrapping switches on luminescence in single-walled nanotube dispersions. *Journal of the American Chemical Society* **130**, 12734–12744 (2008).
197. Hersam, M. C. Progress towards monodisperse single-walled carbon nanotubes. *Nature Nanotechnology* **3**, 387–394 (2008).
198. Lin, S. & Blankschtein, D. Role of the Bile Salt Surfactant Sodium Cholate in Enhancing the Aqueous Dispersion Stability of Single-Walled Carbon Nanotubes : A Molecular Dynamics Simulation Study. *Journal of Physical Chemistry B* **114**, 15616–15625 (2010).
199. Grossiord, N., Van Der Schoot, P., Meuldijk, J. & Koning, C. E. Determination of the surface coverage of exfoliated carbon nanotubes by surfactant molecules in aqueous solution. *Langmuir* **23**, 3646–3653 (2007).
200. Nair, N., Kim, W. J., Braatz, R. D. & Strano, M. S. Dynamics of surfactant-suspended single-walled carbon nanotubes in a centrifugal field. *Langmuir* **24**, 1790–1795 (2008).
201. Boghossian, A. A., Choi, J. H., Ham, M. H. & Strano, M. S. Dynamic and reversible self-assembly of photoelectrochemical complexes based on lipid bilayer disks, photosynthetic reaction centers, and single-walled carbon nanotubes. *Langmuir* **27**, 1599–1609 (2011).

-
202. Ham, M. H. *et al.* Photoelectrochemical complexes for solar energy conversion that chemically and autonomously regenerate. *Nature Chemistry* **2**, 929–936 (2010).
203. Dougherty, D. A. Cation- π Interactions in Chemistry and Biology : A New View of Benzene , Phe , Tyr , and Trp. *Science* **271** (1996).
204. Ma, J. C. & Dougherty, D. A. The cation- π interaction. *Chemical Reviews* **97**, 1303–1324 (1997).
205. Tardani, F. & La Mesa, C. Attempts to control depletion in the surfactant-assisted stabilization of single-walled carbon nanotubes. *Colloids and Surfaces A: Physicochemical and Engineering Aspects* **443**, 123–128 (2014).
206. Hilmer, A. J. *et al.* Role of adsorbed surfactant in the reaction of aryl diazonium salts with single-walled carbon nanotubes. *Langmuir* **28**, 1309–1321 (2012).
207. Suttipong, M., Tummala, N. R., Kitiyanan, B. & Striolo, A. Role of surfactant molecular structure on self-assembly: Aqueous SDBS on carbon nanotubes. *Journal of Physical Chemistry C* **115**, 17286–17296 (2011).
208. Hao, L., Lu, R., Leaist, D. G. & Poulin, P. R. Aggregation number of aqueous sodium cholate micelles from mutual diffusion measurements. *Journal of Solution Chemistry* **26**, 113–125 (1997).
209. Wijmans, C. M. & Linse, P. Surfactant Self-Assembly at a Hydrophilic Surface. A Monte Carlo Simulation Study. *The Journal of Physical Chemistry* **100**, 12583–12591 (1996).
210. Wijmans, C. M. & Linse, P. Monte Carlo simulations of the adsorption of amphiphilic oligomers at hydrophobic interfaces. *The Journal of Chemical Physics* **106**, 328–338 (1997).
211. Sugioka, H., Matsuoka, K. & Moroi, Y. Temperature effect on formation of sodium cholate micelles. *Journal of Colloid and Interface Science* **259**, 156–162 (2003).
212. Karachevtsev, V. A., Glamazda, A. Y., Leontiev, V. S., Lytvyn, O. S. & Dettlaff-Weglikowska, U. Glucose sensing based on NIR fluorescence of DNA-wrapped single-walled carbon nanotubes. *Chemical Physics Letters* **435**, 104–108 (2007).
213. Kurnosov, N. V., Leontiev, V. S. & Karachevtsev, V. A. Probing the Influence of Amino Acids on Photoluminescence from Carbon Nanotubes Suspended with DNA. *Journal of Fluorescence*, 1951–1958 (2016).
214. Xu, Y., Pehrsson, P. E., Chen, L., Zhang, R. & Zhao, W. Double-stranded DNA single-walled carbon nanotube hybrids for optical hydrogen peroxide and glucose sensing. *Journal of Physical Chemistry C* **111**, 8638–8643 (2007).
215. Barone, P. W. & Strano, M. S. Single walled carbon nanotubes as reporters for the optical detection of glucose. *Journal of diabetes science and technology (Online)* **3**, 242–252 (2009).

Bibliography

216. National Center for Biotechnology Information. *Tryptophan*, CID=6305
217. National Center for Biotechnology Information. *Serotonin*, CID=5202
218. Wu, F. H., Zhao, G. C., Wei, X. W. & Yang, Z. S. Electrocatalysis of tryptophan at multi-walled carbon nanotube modified electrode. *Microchimica Acta* **144**, 243–247 (2004).
219. Ghoreishi, S. M., Behpour, M., Ghoreishi, F. S. & Mousavi, S. Voltammetric determination of tryptophan in the presence of uric acid and dopamine using carbon paste electrode modified with multi-walled carbon nanotubes. *Arabian Journal of Chemistry* **10**, S1546–S1552 (2013).
220. John, C. E. & Jones, S. R. *Fast Scan Cyclic Voltammetry of Dopamine and Serotonin in Mouse Brain Slices* (CRC Press/Taylor & Francis, 2007).
221. Nasirizadeh, N., Shekari, Z., Zare, H. R., Ardakani, S. A. & Ahmari, H. Developing a sensor for the simultaneous determination of dopamine, acetaminophen and tryptophan in pharmaceutical samples using a multi-walled carbon nanotube and oxadiazole modified glassy carbon electrode. *Journal of the Brazilian Chemical Society* **24**, 1846–1856 (2013).
222. Zhou, J., Sheng, M., Jiang, X., Wu, G. & Gao, F. Simultaneous determination of dopamine, serotonin and ascorbic acid at a glassy carbon electrode modified with carbon-spheres. *Sensors (Switzerland)* **13**, 14029–14040 (2013).
223. National Center for Biotechnology Information. *Dopamine*, CID=681
224. Zhang, J. *et al.* A Rapid, Direct, Quantitative, and Label-Free Detector of Cardiac Biomarker Troponin T Using Near-Infrared Fluorescent Single-Walled Carbon Nanotube Sensors. *Advanced Healthcare Materials* **3**, 412–423 (2014).
225. Salem, D. P. *et al.* Chirality dependent corona phase molecular recognition of DNA-wrapped carbon nanotubes. *Carbon* **97**, 147–153 (2016).
226. Yang, J., Zhang, Z., Zhang, D. & Li, Y. Quantitative analysis of the (n,m) abundance of single-walled carbon nanotubes dispersed in ionic liquids by optical absorption spectra. *Materials Chemistry and Physics* **139**, 233–240 (2013).
227. Streit, J. K., Fagan, J. A. & Zheng, M. A Low Energy Route to DNA-Wrapped Carbon Nanotubes via Replacement of Bile Salt Surfactants. *Analytical Chemistry* **89**, 10496–10503 (2017).
228. Levenberg, K. A Method for the Solution of Certain Non-Linear Problems in Least Squares. *Quarterly of Applied Mathematics* **2**, 164–168 (1944).
229. Marquardt, D. W. An Algorithm for Least-Squares Estimation of Nonlinear Parameters. **11** (1963).

-
230. Newville, M., Stensitzki, T., Allen, D. B. & Ingargiola, A. LMFIT: Non-Linear Least-Square Minimization and Curve-Fitting for Python (Sept. 2014).
231. Metropolis, N., Rosenbluth, A. W., Rosenbluth, M. N., Teller, A. H. & Teller, E. Equation of state calculations by fast computing machines. *The Journal of Chemical Physics* **21**, 1087–1092 (1953).
232. Jones, M. *et al.* Analysis of photoluminescence from solubilized single-walled carbon nanotubes. *Physical Review B - Condensed Matter and Materials Physics* **71**, 1–9 (2005).
233. Silvera-Batista, C. A., Wang, R. K., Weinberg, P. & Ziegler, K. J. Solvatochromic shifts of single-walled carbon nanotubes in nonpolar microenvironments. *Physical Chemistry Chemical Physics* **12**, 6990–6998 (2010).
234. Liu, H., Tanaka, T. & Kataura, H. One-step separation of high-purity (6,5) carbon nanotubes by multicolumn gel chromatography. *Physica Status Solidi (B) Basic Research* **248**, 2524–2527. arXiv: arXiv:1507.02142v2 (2011).
235. Rocha, J. D. R., Bachilo, S. M., Ghosh, S., Arepalli, S. & Weisman, R. B. Efficient spectrofluorimetric analysis of single-walled carbon nanotube samples. *Analytical chemistry* **83**, 7431–7437 (2011).
236. Carlson, L. J., Maccagnano, S. E., Zheng, M., Silcox, J. & Krauss, T. D. Fluorescence efficiency of individual carbon nanotubes. *Nano Letters* **7**, 3698–3703 (2007).
237. Vialla, F. *et al.* Unifying the low-temperature photoluminescence spectra of carbon nanotubes: The role of acoustic phonon confinement. *Physical Review Letters* **113**, 1–5. arXiv: arXiv:1406.0773v1 (2014).
238. Stancik, A. L. & Brauns, E. B. A simple asymmetric lineshape for fitting infrared absorption spectra. *Vibrational Spectroscopy* **47**, 66–69 (2008).
239. Lu, R. *et al.* Rapid mesoscale volumetric imaging of neural activity with synaptic resolution. *Nature Methods* **17**, 291–294 (2020).
240. Rong, G., Corrie, S. R. & Clark, H. A. In vivo biosensing: progress and perspectives. *ACS Sensors*, acssensors.6b00834 (2017).
241. Beyene, A. G., Yang, S. J. & Landry, M. P. Tools and trends for probing brain neurochemistry. *Journal of Vacuum Science & Technology A* **37**, 040802 (2019).
242. Horton, N. G. *et al.* In vivo three-photon microscopy of subcortical structures within an intact mouse brain. *Nature Photonics* **7**, 205–209 (2013).
243. Beyene, A. G. *et al.* Ultralarge Modulation of Fluorescence by Neuromodulators in Carbon Nanotubes Functionalized with Self-Assembled Oligonucleotide Rings. *Nano Letters* **18**, 6995–7003 (2018).

Bibliography

244. Meyer, D. *et al.* Transport and programmed release of nanoscale cargo from cells by using NETosis. *Nanoscale* **12**, 9104–9115 (2020).
245. Nißler, R. *et al.* Quantification of the Number of Adsorbed DNA Molecules on Single-Walled Carbon Nanotubes. *Journal of Physical Chemistry C* **123**, 4837–4847 (2019).
246. Ju, S.-Y., Kopcha, W. P. & Papadimitrakopoulos, F. Brightly Fluorescent Single-Walled Carbon Nanotubes via an Oxygen-Excluding Surfactant Organization. *Science* **323**, 1319 (2009).
247. Piao, Y. *et al.* Brightening of carbon nanotube photoluminescence through the incorporation of sp³ defects. *Nature Chemistry* **5**, 840–845. arXiv: NIHMS150003 (2013).
248. Zubkovs, V. *Protein Bioconjugation to Carbon Nanotubes for Near-Infrared Sensing* PhD thesis (Ecole Polytechnique Federale de Lausanne, 2019).
249. Lee, M. A. *et al.* Implanted Nanosensors in Marine Organisms for Physiological Biologging: Design, Feasibility, and Species Variability. *ACS Sensors* **4**, 32–43 (2019).
250. Yang, Y., Sharma, A., Noetinger, G., Zheng, M. & Jagota, A. Pathway-Dependent Structures of DNA-Wrapped Carbon Nanotubes: Direct Sonication vs Surfactant/DNA Exchange. *The Journal of Physical Chemistry C* **124**, 9045–9055 (2020).
251. Green, M. R. & Sambrook, J. *Molecular Cloning: A Laboratory Manual* 4th (Cold Spring Harbor Laboratory Press, 2012).
252. Godin, A. G. *et al.* Single-nanotube tracking reveals the nanoscale organization of the extracellular space in the live brain. *Nature Nanotechnology* **12**, 238–243 (2017).
253. Gao, Z., Danné, N., Godin, A. G., Lounis, B. & Cognet, L. Evaluation of Different Single-Walled Carbon Nanotube Surface Coatings for Single-Particle Tracking Applications in Biological Environments. *Nanomaterials* **7**, 393–404 (2017).
254. Brege, J. J., Gallaway, C. & Barron, A. R. Fluorescence quenching of single-walled carbon nanotubes in SDBS surfactant suspension by metal ions: Quenching efficiency as a function of metal and nanotube identity. *Journal of Physical Chemistry C* **111**, 17812–17820 (2007).
255. Brege, J. J., Gallaway, C. & Barron, A. R. Fluorescence Quenching of Single-Walled Carbon Nanotubes with Transition-Metal Ions. *The Journal of Physical Chemistry C* **2**, 4270–4276 (2009).
256. Brege, J. & Barron, A. Using fluorescence quenching of single walled carbon nanotubes with metal ions as a probe of surfactant. *Main Group Chemistry* **10**, 89–104 (2011).
257. Jin, H. *et al.* Divalent ion and thermally induced DNA conformational polymorphism on single-walled carbon nanotubes. *Macromolecules* **40**, 6731–6739 (2007).

-
258. Ions, R. E. & Correlations, T. S. Significant FRET between SWNT / DNA and Rare Earth Ions : A Signature of Their Spatial Correlations. *ACS nano*, 6052–6059 (2011).
259. Kim, S.-J. *et al.* Metal-particle-induced enhancement of the photoluminescence from biomolecule-functionalized carbon nanotubes. *Nanoscale research letters* **9**, 85–91 (2014).
260. Niyogi, S. *et al.* Selective aggregation of single-walled carbon nanotubes via salt addition. *Journal of the American Chemical Society* **129**, 1898–1899 (2007).
261. Koh, B. & Cheng, W. Mechanisms of carbon nanotube aggregation and the reversion of carbon nanotube aggregates in aqueous medium. *Langmuir* **30**, 10899–10909 (2014).
262. Lyons, J. W. & Kotin, L. the Effect of Magnesium Ion on the Secondary Structure of Deoxyribonucleic Acid. *Journal of the American Chemical Society* **87**, 1781–1785 (1965).
263. Landry, M. P. *et al.* Comparative Dynamics and Sequence Dependence of DNA and RNA Binding to Single Walled Carbon Nanotubes. *Journal of Physical Chemistry C* **18**, 10048–10058. arXiv: 15334406 (2015).
264. Harvey, J. D., Zerze, G. H., Tully, K. M., Mittal, J. & Heller, D. A. Electrostatic Screening Modulates Analyte Binding and Emission of Carbon Nanotubes. *The Journal of Physical Chemistry C* **122**, 10592–10599 (2018).
265. Wang, J. *et al.* The variation in urinary calcium levels in adult patients with fracture and surgical intervention. *Journal of Orthopaedic Surgery and Research* **12**, 1–7 (2017).
266. Guyton, A. C. & Hall, J. E. *Textbook of Medical Physiology* 11th, 1011–1018. arXiv: 9809069v1 [arXiv:gr-qc] (Elsevier, 2006).
267. Metheny, N. M. *Fluid and Electrolyte Balance* 5th (Jones & Bartlett Learning, 2012).
268. Berkow, R., Fletcher, A. J. & Beers, M. H. *The Merck Manual of Diagnosis and Therapy* 1003–1019 (Merck Research Laboratories, 1992).
269. Kastenholz, M. A., Schwartz, T. U. & Hünenberger, P. H. The Transition between the B and Z Conformations of DNA Investigated by Targeted Molecular Dynamics Simulations with Explicit Solvation. *Biophysical Journal* **91**, 2976–2990 (2006).
270. Zheng, M. & Diner, B. A. Solution redox chemistry of carbon nanotubes. *Journal of the American Chemical Society* **126**, 15490–15494 (2004).
271. Nugraha, A. R. T. *et al.* Dielectric constant model for environmental effects on the exciton energies of single wall carbon nanotubes. *Applied Physics Letters* **97**, 091905 (2010).
272. Larsen, B. A. *et al.* Effect of solvent polarity and electrophilicity on quantum yields and solvatochromic shifts of single-walled carbon nanotube photoluminescence. *Journal of the American Chemical Society* **134**, 12485–12491 (2012).

Bibliography

273. Pohl, F. M. & Jovin, T. M. Salt-induced co-operative conformational change of a synthetic DNA: Equilibrium and kinetic studies with poly(dG-dC). *Journal of Molecular Biology* **67**, 375–396 (1972).
274. Pohl, F. M., Jovin, T. M., Baehr, W. & Holbrook, J. J. Ethidium bromide as a cooperative effector of a DNA structure. *Proceedings of the National Academy of Sciences of the United States of America* **69**, 3805–3809 (1972).
275. Wang, A. H., Gessner, R. V., van der Marel, G. A., van Boom, J. H. & Rich, A. Crystal structure of Z-DNA without an alternating purine-pyrimidine sequence. *Proceedings of the National Academy of Sciences of the United States of America* **82**, 3611–3615 (1985).
276. Miyahara, T., Nakatsuji, H. & Sugiyama, H. Helical structure and circular dichroism spectra of DNA: A theoretical study. *Journal of Physical Chemistry A* **117**, 42–55 (2013).
277. Guéron, M., Demaret, J. & Filoche, M. A unified theory of the B-Z transition of DNA in high and low concentrations of multivalent ions. *Biophysical Journal* **78**, 1070–1083 (2000).
278. Obika, S. *et al.* Synthesis of 2'-O,4-C-methyleneuridine and -cytidine. Novel bicyclic nucleosides having a fixed C3, -endo sugar puckering. *Tetrahedron Letters* **38**, 8735–8738 (1997).
279. Koshkin, A. A. *et al.* LNA (Locked Nucleic Acids): Synthesis of the adenine, cytosine, guanine, 5-methylcytosine, thymine and uracil bicyclonucleoside monomers, oligomerisation, and unprecedented nucleic acid recognition. *Tetrahedron* **54**, 3607–3630 (1998).
280. Kaur, H., Arora, A., Wengel, J. & Maiti, S. Thermodynamic, counterion, and hydration effects for the incorporation of locked nucleic acid nucleotides into DNA duplexes. *Biochemistry* **45**, 7347–7355 (2006).
281. You, Y., Moreira, B. G., Behlke, M. A. & Owczarzy, R. Design of LNA probes that improve mismatch discrimination. *Nucleic Acids Research* **34** (2006).
282. Owczarzy, R., You, Y., Groth, C. L. & Tataurov, A. V. Stability and mismatch discrimination of locked nucleic acid-DNA duplexes. *Biochemistry* **50**, 9352–9367 (2011).
283. Kim, D. S. *et al.* Electrochemical detection of dopamine using periodic cylindrical gold nanoelectrode arrays. *Scientific Reports* **8**, 1–10 (2018).
284. Marceglia, S. *et al.* Dopamine-dependent non-linear correlation between subthalamic rhythms in Parkinson's disease. *Journal of Physiology* **571**, 579–591 (2006).
285. Kandimalla, R. & Reddy, P. H. Therapeutics of Neurotransmitters in Alzheimer's Disease. *Journal of Alzheimer's Disease* **57**, 1049–1069 (2017).
286. Jamwal, S. & Kumar, P. Insight Into the Emerging Role of Striatal Neurotransmitters in the Pathophysiology of Parkinson's Disease and Huntington's Disease: A Review. *Current Neuropharmacology* **17**, 165–175 (2018).

-
287. World Health Organisation. *Neurological Disorders: Public Health Challenges* (World Health Organization, 2006).
288. Jeong, S., Yang, D., Beyene, A., Gest, A. M. & Landry, M. High Throughput Evolution of Near Infrared Serotonin Nanosensors, 673152 (2019).
289. Paviolo, C. *et al.* Nanoscale exploration of the extracellular space in the live brain by combining single carbon nanotube tracking and super-resolution imaging analysis. *Methods* **174**, 91–99 (2020).
290. Eaton, M. E. *et al.* L-type Ca^{2+} channel blockers promote Ca^{2+} accumulation when dopamine receptors are activated in striatal neurons. *Brain Res Mol Brain Res* **131**, 65–72. arXiv: NIHMS150003 (2004).
291. Patel, J. C., Witkovsky, P., Avshalumov, M. V. & Rice, M. E. Mobilization of calcium from intracellular stores facilitates somatodendritic dopamine release. *Journal of Neuroscience* **29**, 6568–6579 (2009).
292. Brini, M., Calì, T., Ottolini, D. & Carafoli, E. Neuronal calcium signaling: Function and dysfunction. *Cellular and Molecular Life Sciences* **71**, 2787–2814 (2014).
293. Catoni, C., Calì, T. & Brini, M. Calcium, dopamine and neuronal calcium sensor 1: Their contribution to Parkinson's disease. *Frontiers in Molecular Neuroscience* **12**, 1–8 (2019).
294. Campbell, J. F., Tessmer, I., Thorp, H. H. & Erie, D. A. Atomic Force Microscopy Studies of DNA-Wrapped Carbon Nanotube Structure and Binding to Quantum Dots. *Journal of the American Chemical Society* **130**, 10648–10655 (2008).
295. Vogel, R. *et al.* High-Resolution Single Particle Zeta Potential Characterisation of Biological Nanoparticles using Tunable Resistive Pulse Sensing. *Scientific Reports* **7**, 1–13 (2017).
296. Cedervall, T. *et al.* Understanding the nanoparticle-protein corona using methods to quantify exchange rates and affinities of proteins for nanoparticles. *Proceedings of the National Academy of Sciences of the United States of America* **104**, 2050–2055 (2007).
297. Heller, D. A. *et al.* Multimodal optical sensing and analyte specificity using single-walled carbon nanotubes. *Nature Nanotechnology* **4**, 114–120 (2009).
298. Pinals, R. L., Yang, D., Lui, A., Cao, W. & Landry, M. P. Corona Exchange Dynamics on Carbon Nanotubes by Multiplexed Fluorescence Monitoring. *Journal of the American Chemical Society* **142**, 1254–1264 (2020).
299. Pinals, R. L. *et al.* Protein Corona Composition and Dynamics on Carbon Nanotubes in Blood Plasma and Cerebrospinal Fluid. *bioRxiv*, 2020.01.13.905356 (2020).
300. Gravely, M., Safaei, M. M. & Roxbury, D. Biomolecular Functionalization of a Nanomaterial to Control Stability and Retention within Live Cells. *Nano Letters* **19**, 6203–6212 (2019).

Bibliography

301. Egger, B., Van Giesen, L., Moraru, M. & Sprecher, S. G. In vitro imaging of primary neural cell culture from *Drosophila*. *Nature Protocols* **8**, 958–965 (2013).
302. Zubkovs, V. *et al.* Spinning-disc confocal microscopy in the second near-infrared window (NIR-II). *Scientific Reports* **8**, 1–10 (2018).
303. Gong, X., Sharma, A. K., Strano, M. S. & Mukhopadhyay, D. Selective assembly of DNA-conjugated single-walled carbon nanotubes from the vascular secretome. *ACS Nano* **8**, 9126–9136 (2014).
304. Klapoetke, N. C. *et al.* Independent optical excitation of distinct neural populations. *Nature Methods* **11**, 338–346 (2014).
305. Brand, A. H. & Perrimon, N. Targeted gene expression as a means of altering cell fates and generating dominant phenotypes. *Development* **118**, 401–415 (1993).
306. Lu, M. *et al.* An analysis of human microRNA and disease associations. *PLoS ONE* **3**, 1–5 (2008).
307. Krepelkova, I. *et al.* Evaluation of miRNA detection methods for the analytical characteristics necessary for clinical utilization. *BioTechniques* **66**, 277–284 (2019).
308. Zöllner, H., Hahn, S. A. & Maghnouj, A. in *miRNA Maturation. Methods in Molecular Biology (Methods and Protocols)* 121–134 (Humana Press, Totowa, NJ, USA, 2013).
309. Schmittgen, T. D. *et al.* Real-time PCR quantification of precursor and mature microRNA. *Methods* **44**, 31–38 (2008).
310. Kappel, A. *et al.* MicroRNA in vitro diagnostics using immunoassay analyzers. *Clinical Chemistry* **61**, 600–607 (2015).
311. Nielsen, P. E., Egholm, M., Berg, R. H. & Buchardt, O. Sequence-selective recognition of DNA by strand displacement with a thymine-substituted polyamide. *Science* **254**, 1497–1500 (1991).
312. Válczi, A. *et al.* Sensitive and specific detection of microRNAs by northern blot analysis using LNA-modified oligonucleotide probes. *Nucleic acids research* **32** (2004).
313. Castoldi, M., Schmidt, S., Benes, V., Hentze, M. W. & Muckenthaler, M. U. miChip: An array-based method for microRNA expression profiling using locked nucleic acid capture probes. *Nature Protocols* **3**, 321–329 (2008).
314. Vester, B. & Wengel, J. LNA (Locked Nucleic Acid): High-affinity targeting of complementary RNA and DNA. *Biochemistry* **43**, 13233–13241 (2004).
315. Castoldi, M., Benes, V., Hentze, M. W. & Muckenthaler, M. U. miChip: A microarray platform for expression profiling of microRNAs based on locked nucleic acid (LNA) oligonucleotide capture probes. *Methods* **43**, 146–152 (2007).

-
316. Petersen, M. & Wengel, J. LNA: A versatile tool for therapeutics and genomics. *Trends in Biotechnology* **21**, 74–81 (2003).
317. Song, R., Ro, S. & Yan, W. In situ hybridization detection of microRNAs. *Methods Mol Biol.* **629**, 287–294. arXiv: [14601](#) (2010).
318. Egholm, M. *et al.* PNA hybridizes to complementary oligonucleotides obeying the Watson-Crick hydrogen-bonding rules. *Nature* **365**, 566–568 (1993).
319. Hyrup, B. & Nielsen, P. E. Peptide nucleic acids (PNA): Synthesis, properties and potential applications. *Bioorganic and Medicinal Chemistry* **4**, 5–23 (1996).
320. Nielsen, P. E. Applications of peptide nucleic acids. *Current Opinion in Biotechnology* **10**, 71–75 (1999).
321. Ray, A. & Nordén, B. Peptide nucleic acid (PNA): its medical and biotechnical applications and promise for the future. *The FASEB Journal* **14**, 1041–1060 (2000).
322. Paulasova, P. & Pellestor, F. The peptide nucleic acids (PNAs): A new generation of probes for genetic and cytogenetic analyses. *Annales de Genetique* **47**, 349–358 (2004).
323. Chaput, J. C., Yu, H. & Zhang, S. The emerging world of synthetic genetics. *Chemistry and Biology* **19**, 1360–1371 (2012).
324. Nielsen, P. E. DNA Analogues with Nonphosphodiester Backbones. *Annual Review of Biophysics and Biomolecular Structure* **24**, 167–183 (1995).
325. Igloi, G. L. Variability in the stability of DNA-peptide nucleic acid (PNA) single-base mismatched duplexes: Real-time hybridization during affinity electrophoresis in PNA-containing gels. *Proceedings of the National Academy of Sciences of the United States of America* **95**, 8562–8567 (1998).
326. Simpson, J. R., Fagan, J. A., Becker, M. L., Hobbie, E. K. & Hight Walker, A. R. The effect of dispersant on defects in length-separated single-wall carbon nanotubes measured by Raman spectroscopy. *Carbon* **47**, 3238–3241 (2009).
327. Dresselhaus, M. S., Dresselhaus, G., Saito, R. & Jorio, A. Raman spectroscopy of carbon nanotubes. *Physics Reports* **409**, 47 (2005).



Curriculum Vitae

Alice J. Gillen

PHD · CHEMISTRY AND CHEMICAL ENGINEERING

☎ (+353) 85-776-7987 | ✉ alice.gillen@epfl.ch | 🔗 [linkedin.com/in/alice-gillen-4b86a463/](https://www.linkedin.com/in/alice-gillen-4b86a463/) | ORCID iD: 0000-0002-8328-1017

Education

Ecole Polytechnique Federale de Lausanne (EPFL)

Lausanne, Switzerland

PHD IN CHEMISTRY AND CHEMICAL ENGINEERING

Oct. 2016 - Sept. 2020

- Elected PhD Representative for the School of Chemistry and Chemical Engineering
- President of ECS Swiss Student Chapter
- Safety representative (COSEC) for the Laboratory of Nanobiotechnology
- **Thesis:** Optical Biosensors for Improved Neurochemical Sensing Using Single-Walled Carbon Nanotubes

Trinity College, University of Dublin

Dublin, Ireland

BA MOD. HONS. IN NANOSCIENCE, PHYSICS AND CHEMISTRY OF ADVANCED MATERIALS

Sept. 2011 - May. 2015

- Graduated First Class Honours
- Recipient of *Gold Medal* and *Henderson-Lloyd Prize*
- **Thesis:** Investigation of the early stages of the surface layer formation on cycled HE-NCM vs. LTO electrodes using XPS and SEM

Employment History

Laboratory of Nanobiotechnology, EPFL (Prof. Ardemis Boghossian)

Lausanne, Switzerland

RESEARCH ASSISTANT

Oct. 2016 - PRESENT

- PhD student in the Laboratory of Nanobiotechnology (LNB) in the group of Prof. Ardemis Boghossian at EPFL. Current research aims at designing improved optical biosensors for neurochemical sensing applications using single-walled carbon nanotubes.

IB Credit, J.P. Morgan

London, United Kingdom

CREDIT RISK ANALYST

Aug. 2015 - Sep. 2016

- Worked as an analyst within the JP Morgan Graduate Programme in the Structured Finance and Real Estate Credit team. Performed transaction analysis and credit review of clients, due diligence and deal execution process for EMEA Real Estate and Structured Finance transactions. Analysed credit quality of clients, and recommended product risk mitigation strategies for transactions.

Magnetism and Spin Electronics group, Trinity College Dublin (Prof. J.M.D Coey)

Dublin, Ireland

RESEARCH ASSISTANT

Dec. 2014 - Jun. 2015

- Research assistant in the Magnetism and Spin Electronics group at Trinity College Dublin working under the supervision of Prof. J.M.D Coey and Dr. Lorena Monzon. Projects focused on the effect of tetraalkylammonium cations on bubble coalescence and the stability behaviour of electrochemically generated nano and micro-bubbles.

Electrochemical Energy Storage Group, Paul Scherrer Institute (Prof. Dr. Ing. Petr Novak)

Villigen, Switzerland

RESEARCH ASSISTANT

Sept. 2014 - Dec. 2014

- Undertook a three month research project in the Electrochemical Energy Storage group working under the supervision of Dr. Mario El Kazzi and Dr. Claire Villevielle. The project focused on studying the early stages of surface layer formation on electrodes in cycled Lithium-ion based cells using Scanning Electron Microscopy and X-ray Photoemission Spectroscopy.

Magnetism and Spin Electronics group, Trinity College Dublin (Prof. J.M.D Coey)

Dublin, Ireland

RESEARCH ASSISTANT

May. 2014 - Aug. 2014

- Research assistant in the Magnetism and Spin Electronics group at Trinity College Dublin working under the supervision of Prof. J.M.D Coey and Dr. Lorena Monzon. Project focused on examining the stability behaviour of electrochemically generated nano and micro-bubbles.

Skills

Soft Skills	Leadership, Project Management & Planning, Teamwork, Critical Thinking, Problem Solving, Spoken & Written Communication
Instrumental	Fluorescence spectroscopy, UV-vis-NIR, NIR fluorescence confocal microscopy, Atomic force microscopy (AFM), Zeta Potential, DLS, Circular Dichroism, Scanning Electron Microscopy (SEM), Functionalisation of nanomaterials, Raman spectroscopy, <i>Drosophila</i> neuron culturing
Software	Mac OSX, Windows, \LaTeX , Microsoft Office, OriginLab, ImageJ, Adobe (Illustrator, Photoshop), MATLAB, ChemDraw, Gwyddion, Python
Languages	English (native), French (intermediate), Irish (basic)

Honors & Awards

2020	MT180 My Thesis in 180 seconds - Public Vote (1st round)	EPFL, Switzerland
2020	MIT ChemE Rising Star	MIT, USA
2019	1st Place , Bionanotechnology NSEF Graduate Student Award for best presentation	2019 AIChE Annual Meeting
2019	2nd Place , Nanoscale Science and Engineering Poster Award	2019 AIChE Annual Meeting
2019	2nd Place , B Symposia Best Poster Award	235th ECS Meeting
2019	Travel award for the 235th ECS Meeting	Electrochemistry Society
2019	Travel grant from Materials Chemistry Division	Royal Society of Chemistry
2019	EPFL representative with poster presentation	Global Young Scientists Summit
2018	Travel award for the 233rd ECS Meeting	Electrochemistry Society
2018	Chemistry Travel award	SCNAT & SCS
2017	Academia-Industry Training (AIT) programme - selected to represent the Swiss team at the India camp	Swissnex
2015	Henderson-Lloyd Prize - awarded for achieving the highest overall score in the Moderatorship Examinations	Trinity College Dublin
2015	Gold Medal	Trinity College Dublin
2015	Highly Commended Mathematics & Physics	Global Undergraduate Awards
2013	D.C. Pepper Prize in Chemistry - awarded for achieving the highest score in Senior Freshman Chemistry	Trinity College Dublin
2013	1st Place & Best Female Speaker , Broad Curriculum Chemistry	Trinity College Dublin
2013	First Class Book Prize	Trinity College Dublin
2012	First Class Book Prize	Trinity College Dublin
2011	Women in Physics Scholarship	Trinity College Dublin
2011	Entrance Scholarship	Trinity College Dublin

Professional Memberships

International Society of Electrochemistry (ISE)

MEMBER

Royal Society of Chemistry (RSC)

AFFILIATE MEMBER

Swiss Chemical Society (SCS)

STUDENT MEMBER

Electrochemical Society (ECS)

STUDENT MEMBER

American Chemical Society (ACS)

STUDENT MEMBER

American Association for the Advancement of Science (AAAS)

STUDENT MEMBER

European Association of Science Editors (EASE)

STUDENT MEMBER

American Institute of Chemical Engineers (AIChE)

GRADUATE STUDENT MEMBER

Publications

Near-Infrared Optical Detection of Dopamine Based on Xeno Nucleic Acid (XNA) Sensors

[ALICE J. GILLEN](#), ALESSANDRA ANTONUCCI, MELANIA REGGENTE, DANIEL MORALES, ARDEMIS A. BOGHOSSIAN

In preparation

Modifying DNA-SWCNT Sensors for Improved Dopamine Detection

[ALICE J. GILLEN](#), BENJAMIN LAMBERT, ALESSANDRA ANTONUCCI, ARDEMIS A. BOGHOSSIAN

In preparation

Directed Evolution of Nanosensors for the Simultaneous Detection of Mycotoxins

BENJAMIN LAMBERT, AFSANEH TAHERI, SHANG-JUNG WU, [ALICE J. GILLEN](#), ARDEMIS BOGHOSSIAN

In preparation

Near-Infrared Imaging of Heterocysts using Single-Walled Carbon Nanotubes

ALESSANDRA ANTONUCCI, [ALICE J. GILLEN](#), MELANIA REGGENTE, BENJAMIN LAMBERT, ARDEMIS A. BOGHOSSIAN

In preparation

Biotechnology Applications of Nanocarbons in Plant and Algal Systems

ALESSANDRA ANTONUCCI, [ALICE J. GILLEN](#), ARDEMIS A. BOGHOSSIAN

Submitted

Near-Infrared Confocal Imaging of Single-Walled Carbon Nanotube Uptake in Bacteria

ALESSANDRA ANTONUCCI, NILS SCHUERGERS, VITALIJS ZUBKOV, MELANIA REGGENTE, [ALICE J. GILLEN](#), BENJAMIN LAMBERT, ELISABETTA CARATA, LUCIANA DINI, ARDEMIS A. BOGHOSSIAN

Submitted

Synthetic biology: a solution to tackle nanomaterial challenges

BENJAMIN LAMBERT, [ALICE J. GILLEN](#), ARDEMIS A. BOGHOSSIAN

The Journal of Physical Chemistry Letters

2020

Transport and programmed release of nanoscale cargo from cells by using NETosis

DANIEL MEYER, SABA TELELE, ANNA ZELEN, [ALICE J. GILLEN](#), ALESSANDRA ANTONUCCI, ELSA NEUBERT, ROBERT NISSLER, FLORIAN MANN, LUISE ERPENBECK, ARDEMIS A. BOGHOSSIAN, SARA KOSTER, SEBASTIAN KRUSS

Nanoscale

2020

Templating colloidal sieves for tuning nanotube surface interactions and optical sensor responses

[ALICE J. GILLEN](#), DANIEL SIEFMAN, SHANG-JUNG WU, CLAIRE BOURMAUD, BENJAMIN LAMBERT, ARDEMIS BOGHOSSIAN

Journal of Colloid and Interface Science

2019

Non-covalent Methods of Engineering Optical Sensors Based on Single-Walled Carbon Nanotubes

[ALICE J. GILLEN](#), ARDEMIS BOGHOSSIAN

Frontiers in Chemistry

2019

Enhancing bioelectricity generation in microbial fuel cells and biophotovoltaics with nanomaterials

MOHAMMED MOUHIB, ALESSANDRA ANTONUCCI, MELANIA REGGENTE, AMIRMOSTAFA AMIRJANI, [ALICE J. GILLEN](#), ARDEMIS A. BOGHOSSIAN

Nano Research

2019

Directed evolution of the optoelectronic properties of synthetic nanomaterials

BENJAMIN LAMBERT, [ALICE J. GILLEN](#), NILS SCHUERGERS, SHANG-JUNG WU, ARDEMIS A. BOGHOSSIAN

Chemical Communications

2019

Restriction Enzyme Analysis of Double-Stranded DNA on Pristine Single-Walled Carbon Nanotubes

SHANG-JUNG WU, NILS SCHUERGERS, KUN-HAN LIN, [ALICE J. GILLEN](#), CLEMENCE CORMINBOEUF, ARDEMIS A. BOGHOSSIAN

ACS Applied Materials & Interfaces

2018

Xeno Nucleic Acid Nanosensors for Enhanced Stability Against Ion-Induced Perturbations

[ALICE J. GILLEN](#), JUSTYNA KUPIS-ROZMYSLWICZ, CARLO GIGLI, NILS SCHUERGERS, ARDEMIS A. BOGHOSSIAN

The Journal of Physical Chemistry Letters

2018

Generation and stability of freestanding aqueous microbubbles

J.M.D COEY, MATTHIUS MOBIUS, [ALICE J. GILLEN](#), SIDDARTHA SEN

Electrochemistry Communications

2017

Effect of Tetraalkylammonium Cations on Gas Coalescence at a Hydrogen-Evolving Microelectrode

LORENA M. A. MONZON, [ALICE J. GILLEN](#), MATTHIUS MOBIUS, J.M.D COEY

Langmuir

2015

Investigation of the early stages of surface layer formation on cycled HE-NCM vs. LTO electrodes using XPS

[A. J. GILLEN](#), C. VILLEVIEILLE, E. BERG JAMSTORP, P. NOVAK AND M. EL KAZZI

Paul Scherrer Institute, Annual Reports

2014

Conference Proceedings & Posters

Engineering Xeno Nucleic Acid Nanosensors for Enhanced Stability

[ALICE J. GILLEN](#), JUSTYNA KUPIS-ROZMYSLWICZ, CARLO GIGLI, NILS SCHUERGERS, ARDEMIS A. BOGHOSSIAN

2019 AIChE Annual Meeting

Orlando FL, USA (2019)

Directed Evolution of the Optoelectronic Properties of Synthetic Nanomaterials

BENJAMIN P. LAMBERT, [ALICE J. GILLEN](#), NILS SCHUERGERS, SHANG-JUNG WU, ARDEMIS A. BOGHOSSIAN

2019 AIChE Annual Meeting

Orlando FL, USA (2019)

Engineering Xeno Nucleic Acid Nanosensors for Enhanced Stability	<i>Poster Session - 2019 AIChE Annual Meeting</i>
<u>ALICE J. GILLEN</u> , JUSTYNA KUPIS-ROZMYSLWICZ, CARLO GIGLI, NILS SCHUERGERS, ARDEMIS A. BOGHOSSIAN	<i>Orlando FL, USA (2019)</i>
The Impact of Exposed Surface Area on the Response of SWCNT Optical Sensors	<i>2019 AIChE Annual Meeting</i>
<u>ALICE J. GILLEN</u> , DANIEL J. SIEFMAN, SHANG-JUNG WU, CLAIRE BOURMAUD, BENJAMIN P. LAMBERT, ARDEMIS A. BOGHOSSIAN	<i>Orlando FL, USA (2019)</i>
Characterization of Double-Stranded DNA (dsDNA) on Single-Walled Carbon Nanotubes (SWCNTs)	<i>2019 AIChE Annual Meeting</i>
SHANG-JUNG WU, NILS SCHUERGERS, <u>ALICE J. GILLEN</u> , ARDEMIS A. BOGHOSSIAN	<i>Orlando FL, USA (2019)</i>
The Impact of Exposed Surface Area on the Response of SWCNT Optical Sensors	<i>235th Electrochemistry Annual Meeting</i>
<u>ALICE J. GILLEN</u> , DANIEL J. SIEFMAN, SHANG-JUNG WU, CLAIRE BOURMAUD, BENJAMIN P. LAMBERT, ARDEMIS A. BOGHOSSIAN	<i>Dallas TX, USA (2019)</i>
Directed Evolution of the Optoelectronic Properties of Synthetic Nanomaterials	<i>235th Electrochemistry Annual Meeting</i>
BENJAMIN P. LAMBERT, <u>ALICE J. GILLEN</u> , NILS SCHUERGERS, SHANG-JUNG WU, ARDEMIS A. BOGHOSSIAN	<i>Dallas TX, USA (2019)</i>
Xeno Nucleic Acids for Enhancing the Optical Stability of Nanosensors	<i>Poster Session - 235th Electrochemistry Annual Meeting</i>
<u>ALICE J. GILLEN</u> , CARLO GIGLI, ARDEMIS A. BOGHOSSIAN	<i>Dallas TX, USA (2019)</i>
Characterization of Double-Stranded DNA (dsDNA) on Single-Walled Carbon Nanotubes (SWCNTs)	<i>Poster Session - 235th Electrochemistry Annual Meeting</i>
SHANG-JUNG WU, NILS SCHUERGERS, <u>ALICE J. GILLEN</u> , ARDEMIS A. BOGHOSSIAN	<i>Dallas TX, USA (2019)</i>
Xeno Nucleic Acid Nanosensors for Enhanced Stability	<i>GYSS@one-north, Global Young Scientists Summit</i>
<u>ALICE J. GILLEN</u> , JUSTYNA KUPIS-ROZMYSLWICZ, CARLO GIGLI, NILS SCHUERGERS, ARDEMIS A. BOGHOSSIAN	<i>Singapore (2019)</i>
Xeno Nucleic Acid Nanosensors for Enhanced Stability	<i>AIChE Annual Meeting 2018</i>
<u>ALICE J. GILLEN</u> , JUSTYNA KUPIS-ROZMYSLWICZ, CARLO GIGLI, NILS SCHUERGERS, ARDEMIS A. BOGHOSSIAN	<i>Pittsburgh PA, USA (2018)</i>
Characterization of Double-Stranded DNA (dsDNA) on Single-Walled Carbon Nanotubes (SWCNTs)	<i>AIChE Annual Meeting 2018</i>
SHANG-JUNG WU, NILS SCHUERGERS, KUN-HAN LIN, <u>ALICE J. GILLEN</u> , CLEMENCE CORMINBOEUF, ARDEMIS A. BOGHOSSIAN	<i>Pittsburgh PA, USA (2018)</i>
Xeno Nucleic Acid Nanosensors for Enhanced Stability	<i>Poster Session - AIChE Annual Meeting 2018</i>
<u>ALICE J. GILLEN</u> , JUSTYNA KUPIS-ROZMYSLWICZ, CARLO GIGLI, NILS SCHUERGERS, ARDEMIS A. BOGHOSSIAN	<i>Pittsburgh PA, USA (2018)</i>
Characterization of Double-Stranded DNA (dsDNA) on Single-Walled Carbon Nanotubes (SWCNTs)	<i>Poster Session - AIChE Annual Meeting 2018</i>
SHANG-JUNG WU, NILS SCHUERGERS, KUN-HAN LIN, <u>ALICE J. GILLEN</u> , CLEMENCE CORMINBOEUF, ARDEMIS A. BOGHOSSIAN	<i>Pittsburgh PA, USA (2018)</i>
Xeno Nucleic Acid Nanosensors for Enhanced Stability	<i>SCS Fall Meeting 2018</i>
<u>ALICE J. GILLEN</u> , JUSTYNA KUPIS-ROZMYSLWICZ, CARLO GIGLI, NILS SCHUERGERS, ARDEMIS A. BOGHOSSIAN	<i>Lausanne, Switzerland (2018)</i>
Restriction Enzyme Analysis of Double-Stranded DNA on Pristine Single-Walled Carbon Nanotubes	<i>SCS Fall Meeting 2018</i>
SHANG-JUNG WU, NILS SCHUERGERS, KUN-HAN LIN, <u>ALICE J. GILLEN</u> , CLEMENCE CORMINBOEUF, ARDEMIS A. BOGHOSSIAN	<i>Lausanne, Switzerland (2018)</i>
Xeno Nucleic Acids for Enhancing the Optical Stability of Nanosensors	<i>233rd Electrochemistry Society Meeting</i>
<u>ALICE J. GILLEN</u> , JUSTYNA KUPIS-ROZMYSLWICZ, CARLO GIGLI, NILS SCHUERGERS, ARDEMIS A. BOGHOSSIAN	<i>Seattle WA, USA (2018)</i>
Quantum Yield Effects of Modified DNA Sequences on Single-Walled Carbon Nanotube (SWCNT) Fluorescence	<i>233rd Electrochemistry Society Meeting</i>
<u>ALICE J. GILLEN</u> , BENJAMIN P. LAMBERT, DANIEL MOLINA-ROMERO, ARDEMIS A. BOGHOSSIAN	<i>Seattle WA, USA (2018)</i>
Characterization of Double-Stranded DNA (dsDNA) on Single-Walled Carbon Nanotubes (SWCNTs)	<i>233rd Electrochemistry Society Meeting</i>
SHANG-JUNG WU, NILS SCHUERGERS, <u>ALICE J. GILLEN</u> , ARDEMIS A. BOGHOSSIAN	<i>Seattle WA, USA (2018)</i>
Locked Nucleic Acid-Wrapped Single-Walled Carbon Nanotubes Based Optical Sensor for microRNAs Detection	<i>AIChE Annual Meeting 2016</i>
JUSTYNA KUPIS-ROZMYSLWICZ, <u>ALICE J. GILLEN</u> , NILS SCHUERGERS, KATARZYNA PIERZCHALA, ARDEMIS A. BOGHOSSIAN	<i>San Fransico CA, USA (2016)</i>
Nanoscale PEEM Spectroscopy Combined With XPS to Elucidate The Surface Reaction Mechanism of Cycled Li-Ion Battery Electrodes	<i>International Battery Association 2016</i>
DANIELA LEANZA, CARLOS A. F. VAZ, <u>ALICE J. GILLEN</u> , PETR NOVAK, MARIO EL KAZZI	<i>Nantes, France (2016)</i>